Formation and desorption of organic molecules: Resolving their emission in a prominent protostellar hot core and its outflow

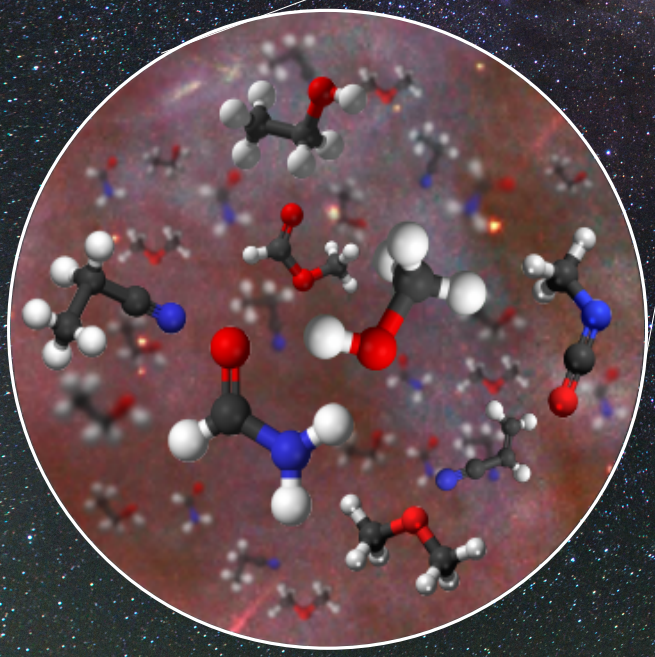

Laura Ann Busch

2023

Cover page background image: The central region of the Milky Way
seen from the ALMA site. *Image credit ESO/B. Tafreshi*

Max-Planck-Institut für Radioastronomie Bonn

Formation and desorption of organic molecules: Resolving their emission in a prominent protostellar hot core and its outflow

Dissertation
zur
Erlangung des Doktorgrades (Dr. rer. nat.)
der
Mathematisch-Naturwissenschaftlichen Fakultät
der
Rheinischen Friedrich-Wilhelms-Universität Bonn

vorgelegt von

Laura Ann Busch

aus
Wolgast, Mecklenburg-Vorpommern, Deutschland

Bonn 2023

Angefertigt mit Genehmigung der Mathematisch-Naturwissenschaftlichen Fakultät der Rheinischen Friedrich-Wilhelms-Universität Bonn

1. Gutachter:	Prof. Dr. Karl M. Menten
2. Gutachter:	Prof. Dr. Frank Bigiel
Tag der Promotion:	14 Dec 2023
Erscheinungsjahr:	2024

RHEINISCHE FRIEDRICH–WILHELMS–UNIVERSITÄT BONN

Abstract

by Laura Ann Busch

for the degree of

Doctor rerum naturalium

Star-forming regions are known to be sites of a rich chemistry involving a variety of molecules. Interstellar complex organic molecules (COMs) are thereby of particular interest. They might act as precursors to larger and potentially prebiotic species that eventually get incorporated into planets or smaller bodies (such as comets) and could participate in the emergence of life.

Many COMs have first been detected and, since then, extensively studied in protostellar environments such as Sgr B2 (N)orth, which is one of the most prominent high-mass star-forming regions in the Milky Way located in the Galactic centre region. It contains several hot (molecular) cores. A hot core represents the heated region of gas and dust that surrounds a high-mass protostar. COMs are highly abundant in the gas of hot cores and their emission is thus bright. The occurrence of the high gas-phase abundances of COMs in these sources results from their formation at high temperature in the gas phase itself or from their sublimation from icy dust-grain surfaces into the gas phase. Many molecules are in fact believed to form in the ice mantles of dust grains, which can either occur during the cold phase prior to the birth of a stellar embryo or during the so-called warm-up phase, when the young protostar gradually heats the surrounding material. Subsequently, the sublimation of COMs can either proceed thermally (i.e. be induced by a gradual increase in dust grain temperature) or non-thermally (e.g. through shocks or interaction with cosmic rays). In hot cores the bulk of the COMs that are formed in the solid phase desorbs thermally. There are essentially two ways in which COMs could desorb thermally: alongside water, which is the most abundant species of the grains' ice mantles, or at their individual desorption temperature, which depends on how strongly they are bound to the grain surface. Which process occurs is yet to be confirmed by observations, which was one of the goals of this thesis.

To tackle this question, we used data taken with the Atacama Large Millimetre/submillimetre array (ALMA) towards Sgr B2 (N). The high angular resolution provided by ALMA allowed us to spatially resolve the COM emission in our target source, Sgr B2 (N1), which is the most massive hot core in the region. This enabled us to study variations in molecular composition by deriving abundances of a dozen of COMs at various positions within the source. Besides abundances, we derived gas temperatures and could thus investigate the relation between the two quantities. We found a steep increase of the COM abundances around 100 K, leading us to conclude that COMs co-desorb with water. Furthermore, we observed non-zero abundances of COMs below 100 K, which suggests a different desorption process at low temperature. With these two results, it is the first time that COM desorption is

spatially resolved in the interstellar medium. Comparing our observational results to predictions of astrochemical models, we could infer the formation of certain COMs on dust-grain surfaces.

The second goal of this thesis was to investigate the impact of shocks, provoked by the outflow of Sgr B2 (N1), on the molecular composition. Comparing the observed abundances to the chemical composition at positions that are not exposed to the outflow revealed segregation between O- and N-bearing molecules, with the former being depleted at the outflow positions. Based on the comparison with astrochemical models and with observed chemical compositions of other sources that are exposed to shocks, we proposed a scenario that may be able to explain the chemical segregation, which was also previously observed in various sources. Our scenario presents a new perspective on this process that, however, still needs to be confirmed by chemical models.

Similar studies of other protostellar sources at high angular resolution in the future could probe whether the results obtained for Sgr B2 (N1) (e.g. regarding desorption processes or the impact of the outflow on the chemical composition) are common at this stage of star formation or are specific to this hot core. It would be of particular interest to compare Sgr B2 (N1), which is a high-mass young stellar object located in the Galactic centre region, with low-mass analogues, on the one hand, and with sources located in the Galactic disk, where physical conditions greatly differ, on the other hand.

List of publications

Publications related to this thesis

1. *Resolving desorption of complex organic molecules in a hot core: Transition from non-thermal to thermal desorption or two-step thermal desorption?*
   L. A. Busch, A. Belloche, R. T. Garrod, H. S. P. Müller, and K. M. Menten, A&A, 665, A96 (2022), DOI: 10.1051/0004-6361/202243383

2. *Shocking Sgr B2 (N1) with its own outflow: A new perspective on segregation between O- and N-bearing molecules*
   L. A. Busch, A. Belloche, R. T. Garrod, H. S. P. Müller, K. M. Menten, 2023, arXiv:2310.11339, accepted for publication in A&A.

Other Publications

3. *Living on the edge of the Milky Way's central molecular zone: G1.3 is the more likely candidate for gas accretion into the CMZ*
   L. A. Busch, D. Riquelme, R. Güsten, K. M. Menten, T. G. S. Pillai, and J. Kauffmann, A&A, 668, A183 (2022), DOI: 10.1051/0004-6361/202244870

4. *The dynamically young outflow of the Class 0 protostar Cha-MMS1*
   L. A. Busch, A. Belloche, S. Cabrit, P. Hennebelle, B. Commerçon, A&A, 633, A126 (2020), DOI: 10.1051/0004-6361/201936432

As of Jan 5th, 2024

Contents

Nomenclature

Frequently used acronyms

ALMA	Atacama Large Millimetre/submillimetre Array
CDMS	Cologne database for molecular spectroscopy
CMB	Cosmic microwave background
CMZ	Central molecular zone
CNM	Cold Neutral Medium
COM	Complex organic molecule
FWHM	Full-width at half maximum
GC	Galactic centre
HIM	Hot ionised medium
HPBW	Half power beam width
IR	Infrared
ISM	Interstellar medium
JPL	Jet propulsion laboratory
LTE	Local thermodynamic equilibrium
LVINE	Linewidth- and velocity-corrected integrated emission
PA	Position angle
PAH	Polycyclic aromatic hydrocarbon
MDC	Massive dense core
ReMoCA	Re-exploring molecular complexity with ALMA
RMS	Root-mean-square
Sgr B2 (N)	Sagittarius B2 North
S/N	Signal-to-noise ratio
UV	Ultra violet
WIM	Warm ionised medium
WNM	Warm neutral medium

Physical Constants

Speed of light (in vacuum)	$c = 2.9979 \times 10^{10}\,\mathrm{cm\,s^{-1}}$
Planck's constant	$h = 6.626 \times 10^{-27}\,\mathrm{erg\,s}$
Boltzmann's constant	$k_\mathrm{B} = 1.381 \times 10^{-16}\,\mathrm{erg\,K^{-1}}$
Mass H atom	$m_\mathrm{H} = 1.673 \times 10^{-24}\,\mathrm{g}$
Molecular weight per hydrogen molecule	$\mu = 2.8$

Astronomical Constants

Astronomical unit	$1\,\mathrm{au} = 1.496 \times 10^{13}\,\mathrm{cm}$
Parsec	$1\,\mathrm{pc} = 3.086 \times 10^{18}\,\mathrm{cm}$
Solar mass	$1\,M_\odot = 1.989 \times 10^{27}\,\mathrm{g}$
Solar luminosity	$1\,L_\odot = 3.9 \times 10^{33}\,\mathrm{erg\,s^{-1}}$
Electronvolt	$1\,\mathrm{eV} = 1.6021 \times 10^{-19}\,\mathrm{J}$
Jansky	$1\,\mathrm{Jy} = 10^{-23}\,\mathrm{erg\,s^{-1}\,cm^{-2}\,Hz^{-1}}$

Frequently used molecules

H_2	Hydrogen molecule
CO	Carbon monoxide
H_2O	Water
SO	Sulphur monoxide
SO_2	Sulphur dioxide
SiO	Silicon monoxide
OCS	Carbonylsulfid
CH_3SH	Methyl mercaptan
CH_3OH	Methanol
C_2H_5OH	Ethanol
CH_3OCH_3	Dimethyl ether
CH_3OCHO	Methyl formate
CH_3CHO	Acetaldehyde
HNCO	Isocyanic acid
CH_3NCO	Methyl isocyanate
NH_2CHO	Formamide
HC_3N	Cyanoacetylene
HC_5N	Cyanodiacetylene
CH_3CN	Methyl cyanide
C_2H_3CN	Vinyl cyanide
C_2H_5CN	Ethyl cyanide

1

Introduction

This chapter contains:

The question of the emergence of life on Earth has excited peoples' curiosity, be they scientists or not, since forever. How Earth actually came by its water and organic material is still debated though (for a recent review on astrochemistry in the context of planet formation see Öberg & Bergin 2021). One theory describes the (partial) delivery of organic (i.e. carbon-bearing) molecules and water by comets and asteroids to the planet at some point in time, from which life as we know it might have developed. In 2009, Elsila et al. reported for the first time on the detection of the simplest amino acid, glycine, in samples of the comet 81P/Wild 2 that had been brought back to Earth. This was not a singular instance: Altwegg et al. (2016) found glycine to be an in-situ constituent of comet 67P and, for example, only recently, several amino acids have been found in samples returned from an asteroid (Naraoka et al. 2023). Comets contain the most primitive material in the solar system as they are thought to have assembled from the material that also formed the planets and the sun itself. Having formed in a large distance from the sun and residing in these far-away cold orbits, their chemical composition remains largely unprocessed. This raises the question of the initial chemical composition

of the material from which comets formed and how much of their present-day molecular content was synthesised at a later stage on these bodies themselves.

Despite the harsh environments in interstellar space outside the solar system, molecules have been observed in numerous sources of vastly different physical conditions and, actually, the rate at which new molecules are detected has drastically increased, especially, over the last decade (McGuire 2022). Figure 1.1 presents cumulatively the number of detected molecules per year subdivided by the number of atoms that they contain. This graph shows not only that the number of newly detected molecules increases with time, but, more remarkably, these molecules get increasingly more complex (although new di- and triatomic molecules are still found). Molecules with more than 13 atoms, big carbon chains and rings (e.g. polycyclic aromatic hydrocarbons, PAHs), even fullerenes such as C_{60} (i.e. a ball of C atoms) have been found. Amongst the detected species there are not only stable neutral molecules, but also ions and radicals. The latter are highly reactive species as they have at least one unpaired electron. In contrast to Earth, where radicals would nearly instantaneously react with another atom or molecule, the low-density conditions in space enable these species to exist in detectable amounts. As will be seen, these molecules play a crucial role in interstellar chemistry, especially in building molecular complexity. Complex organic molecules (COMs) possess, as per definition, more than five atoms with at least one carbon atom[1] (Herbst & van Dishoeck 2009).

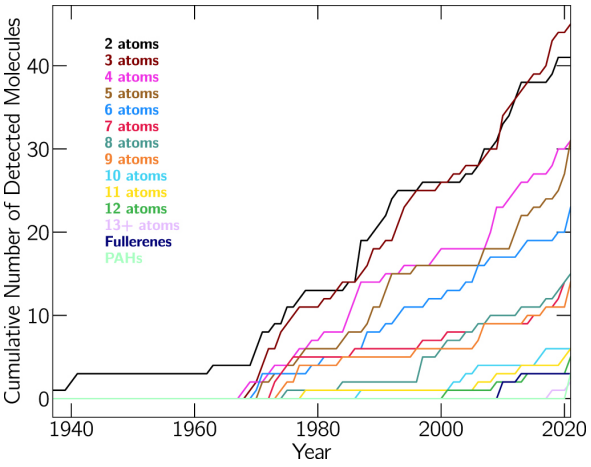

Figure 1.1: Number of newly detected molecules per year categorised based on the number of contained atoms, taken from McGuire (2022).

The big change in the detection rate of new molecules came with the advances of radio astronomy in the 1970s, where molecules were mostly identified through their rotational emission spectra in the wavelength regime from centimetres to submillimetres. Afterwards, the perpetual improvements of receiver technology in terms of instantaneous bandwidth and sensitivity (to detect more and fainter spectral lines, respectively, in one observational setup) at existing radio observatories and new observational facilities, led to a steepening of the detection rate from four to six molecules per year since early 2000, and is rising even more steeply since ~2015. To date, we have detected about 300 interstellar molecules[2].

With this high rate of new detections and the evermore increasing complexity of the new species, this really is the golden age of astrochemistry. The overarching goal of this field of research is to understand where, when, and how the precursors of life are formed and, thereby, to establish a chemical link from the earliest stages of star formation up to the formation of planets. Therefore, it is of key importance to investigate the starting and possible end point of molecular complexity in the interstellar matter that participates in the process of star and planet formation, and to find out which physical processes are involved in the build-up and break-down of complexity at different times and in different physical environments. This thesis aims to provide

[1] Because this is far from the complexity of terrestrial complex molecules, some astronomers also refer to these species as interstellar complex organic molecules (iCOMs), however, in this thesis these molecules are simply referred to as COMs.

[2] List of detected interstellar molecules: https://cdms.astro.uni-koeln.de/classic/molecules

some of the puzzle pieces needed to achieve this goal. By observing the emission of primarily COMs in the vicinity of a high-mass star precursor (or protostar), the impact of the various physical processes that occur at this stage of star formation on the COMs' abundances is investigated in order to put better constraints on the their formation and destruction mechanisms.

Before going into detail on the scientific goals of this thesis, Sect. 1.1 first presents an introduction to the interstellar medium (ISM), its constituents and how it can be divided into different phases. Section 1.2 gives an overview of important chemical reactions that are needed to build up molecular complexity and briefly explains why astrochemical models are indispensable. The formation process of high-mass stars, which are characterised by masses higher than 8 $M_\odot$, and their influence on the chemistry in the ambient medium are described in Sect. 1.3. The source of interest in this work, the high-mass star-forming region Sagittarius B2 North (or Sgr B2 (N)), and its host environment the Milky Way's central molecular zone (CMZ) are introduced in Sect. 1.4. At last, the objectives of this thesis are presented in Sect. 1.5. The following sections are mainly based on Yamamoto (2017), Draine (2010), Tielens (2005), and Ceccarelli et al. (2022), otherwise references are explicitly given.

1.1 The interstellar medium

The Milky Way is a typical barred spiral galaxy with a mass of about 10^{12} $M_\odot$. About 90% of this mass is dark, meaning whatever its constituents are, they do not interact with light and remain invisible to the eye and telescope. The other 10% are visible. Of this small fraction of mass, all the stars in the Milky Way represent about 90% of it. The rest resides in the ISM and, despite its tiny contribution to the total mass of the Galaxy, it plays a crucial role on all spatial scales: from planet to star to galaxy formation and beyond. The main constituent of the ISM is **gas**, of which 98% are hydrogen and helium and the remaining 2% are heavier elements, principally carbon, nitrogen, and oxygen. Depending on the interstellar region that is observed, these elements and less abundant ones can be found in dominantly ionised form, atomic form, or locked up in a variety of molecular species. In the case of hydrogen, about 60% remain in atomic form, H (also referred to as HI), while the other 40% are found in ionised form, H^+ (or HII), and molecular form, H_2, to roughly equal measures. Because interstellar gas exists in various physical states, each of these states will have different observational probes that help characterise the gas. This is taken up on in Sects. 1.1.1 and 1.1.2.

Another component of the ISM is presented by **dust grains**, which are small solid particles of sizes that are typically a fraction of 1 μm. They mainly consist of silicates and carbonaceous material and can be coated by ice mantles in cold interstellar environments. The dust is mixed with the gas and its mass represents about 1% of the mass of the gas. Dust grains have the ability to scatter and absorb background starlight, leading to its reddening or extinction. When aligned by a magnetic field, large dust grains can polarise starlight through selective absorption. In addition to these indirect observations, dust can directly be identified through its infrared (IR) continuum emission, also as it re-emits the absorbed higher-energy starlight. Moreover, dust is an essential driver of chemistry in the ISM (see Sect. 1.2.2).

There are **cosmic rays** in the ISM, which are high-velocity (often relativistic) particles consisting of mostly protons, ~10% helium and other heavier nuclei, and 1% electrons. As they propagate through space they interact with the ISM, thereby heating or even ionising it. In particular, ionisation induced by cosmic rays is an important mechanism that is required to start interstellar chemistry (see Sect. 1.2.1). The interstellar radiation field comprises **photons** from across the electromagnetic

spectrum. Photons from stars dominate the radiation field from the far-UV (young massive stars) to the near-IR (old stars). Emission from dust dominates in the mid-IR to submillimetre wavelength regimes. At millimetre wavelengths, there is also a contribution from the cosmic microwave background (CMB) radiation. Photons in the X-ray energy regime originate from hot plasma (or coronal gas, see Sect. 1.1.1). **Magnetic fields** are suppliers of energy and pressure in the ISM and are able to control the dynamics of the gas and lead to dust-grain alignment. Violent phenomena such as stellar winds and supernova explosions inject energy and cause **turbulence** as shock waves expand into the ambient medium. In the dissipation process of turbulence the involved energy is converted to heat.

In summary, the ISM is far from being static and its constituents far from being uniformly distributed in space. The perpetual interaction between gas and dust with cosmic rays and photons, and their constant exposure to some kind of radiation field, magnetic fields, or shocks ensures that the ISM is always changing with regard to its physical state and chemical composition. However, despite all the variations that the ISM can be found in, it can roughly be divided into phases that come with characteristic densities and temperatures as well as chemical compositions.

1.1.1 Phases of the ISM

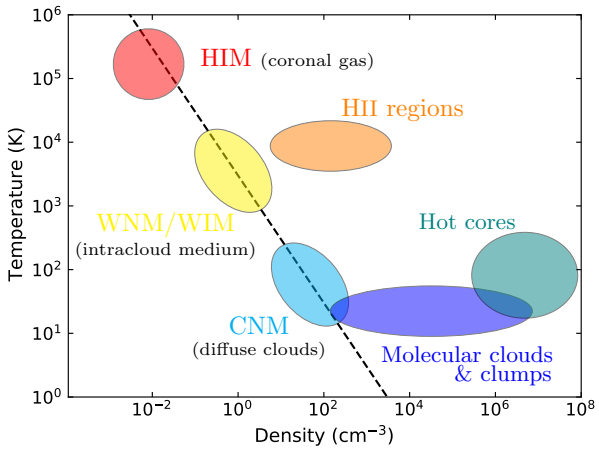

Figure 1.2: Phases of the ISM roughly categorised by their characteristic densities and temperatures. The dashed line corresponds to a constant pressure showing that the hot ionised medium (HIM), the warm neutral/ionised medium (WNM/WIM), and the cold neutral medium (CNM) are in approximate pressure equilibrium. The WIM of HII regions, dense molecular clouds, and even denser molecular clumps and cores are overpressured regions. The figure is adapted from Yamamoto (2017).

Figure 1.2 shows the rough classification of the ISM into different phases with characteristic densities and temperatures. The hot ionised medium (HIM or coronal gas) contains the most dilute and hottest gas. The temperatures were elevated by shocks induced by, for example, the expansion of a supernova. As the name suggests, all hydrogen is ionised, but not only H, also all other elements that were contained in the pre-shocked gas. This phase occupies the largest volume in the Galaxy, likely up to 50%. It can be observed through absorption lines of highly ionised elements at UV and optical wavelengths against a bright background source or in continuum emission (e.g. synchrotron, bremsstrahlung, recombination). As the HIM expands, it cools (on timescales of Myr) until a phase transition occurs. The warm ionised and warm neutral media (WIM and WNM, respectively) are characterised by roughly similar densities of a few particles per cm^3 on average and temperatures of $\sim 10^3$–10^4 K. They are distinguished by the state that essentially hydrogen, but also other species are in. The ionisation source of the WIM can likely be associated with radiation from massive stars. Similarly to the HIM, the WIM can be observed with absorption lines of ionised elements and in free-free continuum emission. The WNM can be traced with HI emission and absorption. The WNM and WIM are often referred to as

the intracloud medium between the HIM and the cold neutral medium (CNM). The CNM assembles in diffuse clouds that are typically observed at temperatures of about 100 K and densities of a few tens of particles per cm^3 in emission and absorption of HI and molecular tracers such as CO or, for example, small hydrides (e.g. CH, CH^+, and others, Jacob et al. 2022).

Based on the ideal gas law, according to which $p \propto nT$, where p is the pressure, n the number density and T the temperature, one finds that the above-described phases can be arranged along a constant pressure line when inserting typical values for n and T. This implies that these phases are in approximate pressure equilibrium. HII regions, which are a specific high-density type of the WIM, do not lie on the constant-pressure line. These are over-pressured ionised regions that are created by the UV radiation of high-mass (proto)stars (see Sect. 1.3) and that expand due to these stars' winds. Also not in pressure equilibrium with the other phases of the ISM are molecular clouds, because they are self-gravitating entities. Due to the high densities, these clouds are greatly opaque to UV radiation, such that hydrogen can exist in molecular form without being dissociated, along with many other molecules, such as CO, which is widely used to observe these clouds. It is in these clouds that stars are born in substructures that can be referred to as clumps and, further up the density chain, cores, from which protostars emerge, ultimately.

The above description shows that stellar evolution plays a crucial role in the evolution of the ISM. Stars form from the material in molecular clouds, process it through nuclear fusion during their lives, and, eventually, give back the gas, which they have enriched with heavier elements, as their lives end. In particular, throughout their lifetimes, high-mass stars have a large impact on the ISM, its physical state and dynamics. Already from earliest evolutionary stages on, it is their stellar winds and ionising radiation that, in the form of HII regions, expand into the ambient medium, thereby injecting energy on cloud scales. Supernova explosions that mark the death of high-mass stars impact the ISM on much larger scales and, all together, they account for the pressure regulation of the ISM in the galaxy. The formation of this type of stars and the impact of high-mass protostars on their surrounding ISM is subject of Sect. 1.3.

1.1.2 From diffuse to dense clouds

The definitions for diffuse, translucent, and dense clouds are not standardised. A now commonly used classification for the different types of clouds was introduced by Snow & McCall (2006) and is illustrated in Fig. 1.3. The figure shows how the fractional abundance of hydrogen and carbon, where $n_H = n(H) + 2n(H_2)$ and $n(C) \sim n(C^+) + n(C) + n(CO)$, change as gas column density, in terms of the total H column density, increases. Accordingly, hydrogen in **diffuse atomic** clouds is (nearly) entirely atomic, while carbon is still ionised, because the ionisation potential of C is lower than that of H (11.2 eV versus 13.6 eV). As density increases from a few tens to a few hundred particles per cm^3, the shielding of H_2 molecules becomes efficient, such that the molecular fraction exceeds 0.1, while carbon is still ionised. These clouds are referred to as **diffuse molecular**. Gas temperatures in both types of diffuse clouds are similar with values of ~30–100 K. **Translucent** clouds are associated with densities about a factor 10 higher than in diffuse molecular clouds and temperatures below 50 K. Hydrogen is mostly molecular here and the abundance of C^+ decreases rapidly, while abundances of neutral C and CO increase. Therefore, translucent clouds are characterised by a fraction of ionised carbon that is below 0.5, while the fraction of CO is still below 0.9. In **dense molecular** clouds densities exceed 10^4 cm^{-3} and carbon is mostly locked up in CO with a fraction above 0.9. Protected from the dissociative UV photons, molecular diversity can develop in the interior of dense clouds (see

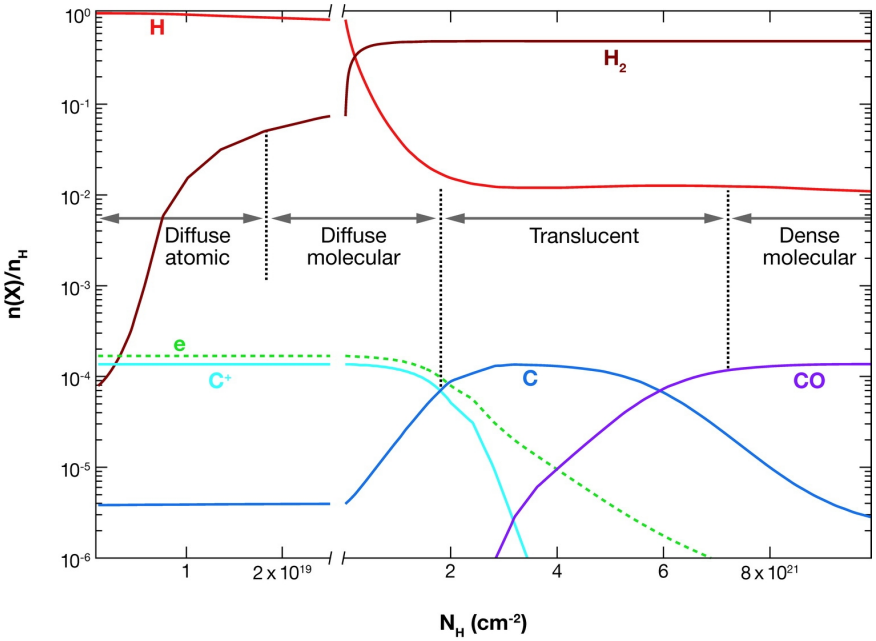

Figure 1.3: Classification of cloud types from diffuse atomic to dense molecular, based on the column density of total hydrogen (in either form) and depending on the state that hydrogen and carbon are found in. The figure is taken from Snow & McCall (2006).

Sect. 1.2). Observations of CO and other tracers revealed that such dense clouds can harbour a number of substructures that are often referred to as clumps, in which cores may be embedded (see Fig. 1.2), where stars can be born, eventually. Similar to the cloud types, there is no clear definition for these expressions. Although, there is some overlap in their characteristics, clumps are typically associated with parsec-sized clouds that have densities of $\sim 10^4$–10^5 cm^{-3}, while cores have sizes of a few 10^{-2} pc and densities that are higher by about a factor 10. So-called hot cores, which are indicated in Fig. 1.2, correspond to the dense material surrounding and heated by a newly-born high-mass protostar (see Sect. 1.3.2).

1.2 Chemistry in dense molecular clouds

The chemistry that takes place in dense molecular clouds is greatly different from that in diffuse clouds, as the high densities prevent UV photons from penetrating deep into the interior of the dense clouds, thereby protecting molecules from being dissociated. The following sections provide an introduction to the formation and destruction processes of simple molecules and how molecular complexity is built up in these clouds, including reactions and their efficiencies in the gas phase (Sect. 1.2.1) as well as on dust-grain surfaces (Sect. 1.2.2). These two sections are mostly based on Yamamoto (2017). Because the molecular composition of a source changes with time and, thus, observations only provide a snapshot of the current molecular content, chemical models are of key importance to understanding the underlying processes involved in the formation and destruction of molecules over time. Therefore, and because the comparison of observational results obtained in this thesis with predictions of chemical models plays a major role, Sect. 1.2.3 gives a brief overview of input and output parameters of astrochemical kinetics models.

1.2.1 Gas-phase chemistry

Gas-phase chemistry in the ISM is facilitated via collisions between particles. Obviously, the conditions in the ISM are vastly different from the conditions on Earth, with pressures usually less than 10^{-12} bar. Accordingly, the chemistry proceeds slowly, on the order of thousands of years, so that a chemical thermodynamic equilibrium is rarely, maybe never, reached. The formation and destruction of a given species might involve one or more of the following processes:

a) Neutral-neutral reaction $\left(k(300\,\mathrm{K}) \sim 10^{-10}\,\mathrm{cm^3\,s^{-1}}\right)$

b) Ion-neutral reaction $\left(k(300\,\mathrm{K}) \sim 10^{-9}\,\mathrm{cm^3\,s^{-1}}\right)$

c) Ion-electron recombination $\left(k(300\,\mathrm{K}) \sim 10^{-7}\,\mathrm{cm^3\,s^{-1}}\right)$

d) Cosmic-ray induced ionisation or dissociation $\left(\zeta_0 \sim 10^{-17}\,\mathrm{s^{-1}}\right)$

e) Photoionisation or photodissociation $\left(\text{secondary UV photons} : \sim 100 - 1000\zeta_0\right)$

f) Radiative association $\left(k(300\,\mathrm{K}) \lesssim 10^{-16}\,\mathrm{cm^3\,s^{-1}}\ \text{for small},\ 10^{-11}\,\mathrm{cm^3\,s^{-1}}\ \text{for large molecules}\right)$.

The parameters in parentheses are the collisional rate coefficient, $k(T)$, and the cosmic-ray ionisation rate, ζ_0 (e.g. van der Tak & van Dishoeck 2000). The values only present rough orders of magnitude for these coefficients for a temperature of $T = 300$ K. Some reactions and their corresponding rate coefficients are listed in Table 5.3 in Yamamoto (2017) and examples for photodissociation rates by secondary UV photons are given in Gredel et al. (1989). These processes take place either between two atoms or molecules or, in cases (d)–(e), it only needs one of those species. Three-body reactions are highly unlikely due to the prevailing low volume densities[3]. For a pair of species, several reactions in the above list may be in competition. For example, an ionic species may react with a neutral atom or molecule to form two or more new species (process b) or one new species (process f). In the former reaction, excess energy is converted to kinetic energy of the products, while in the latter a photon is emitted to get rid of the excess energy. The ionic reactant may also recombine with an electron instead (process c). The time needed to proceed with a reaction decides which reaction dominates. The timescale of a chemical reaction essentially depends on the collisional rate coefficient, k, which can be measured in laboratory experiments or computed theoretically. A reaction does not necessarily lead to unique products, but different species may be produced with different probabilities. The probabilities of all possible reaction channels are referred to as branching ratios. These are specific to a reaction and can be derived experimentally or computationally. The total reaction rate then corresponds to the sum of individual reaction rates weighted by the branching ratios.

How likely a reaction is to occur depends on a number of parameters. One important factor to consider is whether the production of a set of species releases or consumes energy, in other words, whether a reaction proceeds exo- or endothermically, respectively. In cold dense clouds only exothermic reactions can occur efficiently. The rate coefficients stated in the above list show that ion-neutral reactions proceed faster than reactions between neutrals. The coefficient of neutral-neutral reactions depends on the gas temperature, T, and such a reaction often has an additional activation barrier

[3] They may become important in certain environments, such as circumstellar envelopes.

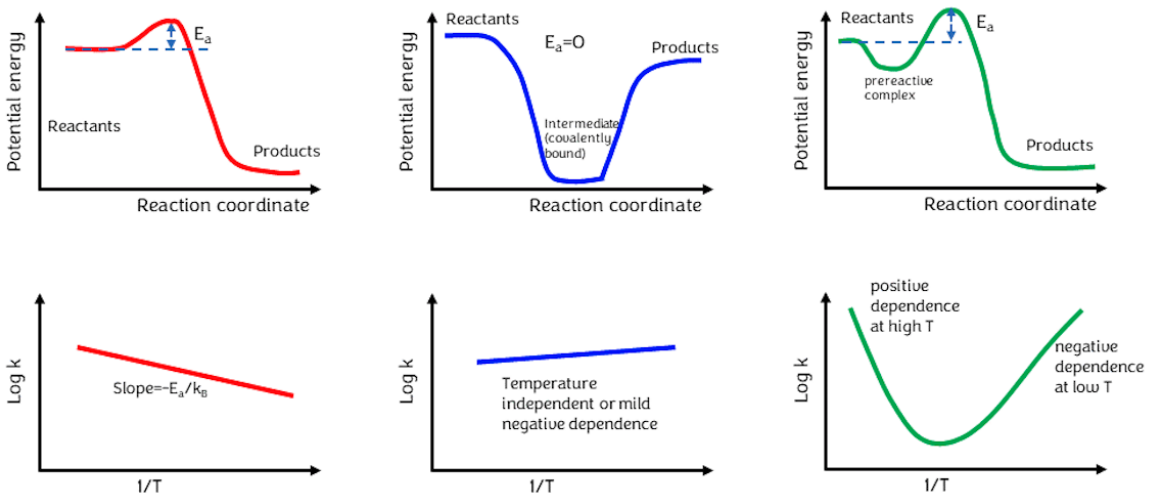

Figure 1.4: Schematic distribution of potential energy *(top row)* and temperature dependence of the reaction rate k *(bottom row)* for reactions that possess an energy barrier E_a (red), that do not have such a barrier (blue), and that have a barrier, but the reactants form a pre-reactive complex (green) that is characterised by a minimum in potential energy preceding the barrier. The figure is taken from Ceccarelli et al. (2022).

to overcome. Figure 1.4 shows schematically the energy distribution and temperature dependency of different types of reactions. The left column illustrates the presence of an energy barrier, E_a, for a reaction, which appears in an additional factor to the reaction rate, $\exp\left(\frac{-E_a}{k_B T}\right)$ and describes the probability per collision for this reaction. The successful collision of two species leads to the formation of a transition or intermediate state. The factor E_a then corresponds to the energy required for the bond-breaking and the rearrangement of atoms to go through this high-energy state and create the products. In some cases, E_a is small such that the kinetic energy of the reactants may be enough to overcome the barrier. In other cases, especially at low temperatures, activation barriers are substantially high such that these reactions do not take place. Only at higher temperatures, the rate coefficient increases and the reaction may be possible to proceed (see Fig. 1.4). The exceptions are neutral-neutral reactions where one or both reactants are radicals. No activation barriers are involved, because these species have one or more unpaired electrons that can directly bond to the other species[4]. The energy profile of barrierless reactions are shown in the top-middle panel of Fig 1.4. These reactions proceed either independently of temperature or with a slightly negative dependency (bottom-middle panel). Some reactions that have an activation barrier and, therefore, proceed more efficiently at high temperatures, can occur at low temperatures if the reactants form a pre-reactive complex, which settles in a minimum of potential energy that precedes the barrier. This leads to tunneling through the activation barrier at temperatures below a certain threshold (right column in Fig. 1.4).

Ion-neutral reactions proceed mostly barrierlessly and exhibit only a weak to moderate overall temperature dependence. Therefore, in low-temperature environments, such as dark clouds or prestellar cores, reactions between an ion and a neutral are generally faster. One specific type of ion-neutral

[4] However, rate coefficients for reactions involving radicals are difficult to measure in the laboratory on Earth due to their extremely reactive nature. The reaction rates come from theoretical calculations.

reactions that is of key importance for interstellar chemistry is the formation of protonated hydrogen, H_3^+, which proceeds efficiently even at low temperatures due to its high exothermicity (e.g. Oka 2006):

$$H_2 \xrightarrow{\text{c.r.}} H_2^+ \xrightarrow{H_2} H_3^+, \tag{1.1}$$

where H_2 is ionised by cosmic rays (c.r.) and reacts with another H_2 to form H_3^+. Protonated H_2 is a key species in astrochemistry as it is involved in a variety of reactions that produce larger molecules (e.g. Herbst & Klemperer 1973). These subsequent reactions involve a proton transfer. Such reactions depend on the proton affinity of a species, that is, how willingly it will take on a proton. Many species have a higher proton affinity than H_2. In these cases, the proton transfer from H_3^+ to the other species takes place. For example, this plays an important role in the build-up of the organic (i.e. C-bearing) molecular content. The carbon chemistry in dense clouds starts off with the following reactions

$$C \xrightarrow{\text{c.r.}} C^+ \xrightarrow{H_2} CH_2^+ \xrightarrow{H_2} CH_3^+, \tag{1.2}$$

$$C \xrightarrow{H_3^+} CH^+ \xrightarrow{H_2} CH_2^+ \xrightarrow{H_2} CH_3^+, \tag{1.3}$$

where the H or H_2 that are produced in these reactions besides the hydrocarbon is not written. The next reaction of the CH_3^+ molecule with an H_2 is endothermic, however, it can form CH_5^+ in a radiative-association reaction. This process is generally extremely slow (it can be more efficient for larger molecules, see list above), but it is able to produce significant amounts of CH_5^+ because of the large H_2 reservoir. Still, this process competes with electron recombination to produce CH_2 or CH and with the reaction with an O atom to form either HCO^+ or H_2CO^+. Similarly, CH_5^+ acts as a reactant in a number of reactions either with electrons (leading to recombination), with atomic oxygen, or with CO. The neutral hydrides CH, CH_2, CH_3, and CH_4 that have been produced through recombination along the way may further react with ions. Reactions with O and C atoms only work for the first three hydrides as they are radicals, while methane (CH_4) is a stable molecule. As the chemistry evolves, larger hydrocarbons can form that, in turn, act as building blocks for even more complex species.

The other two elements that are fairly abundant in a variety of interstellar molecules are oxygen and nitrogen. Oxygen atoms have already been involved in some of the reactions above. Another important molecule for interstellar chemistry is water, which is a product of electron recombination of H_3O^+, which in turn forms via

$$O \xrightarrow{H_3^+} OH^+ \xrightarrow{H_2} H_3O^+. \tag{1.4}$$

The subsequent recombination with an electron creates water in one fourth of the reactions, else OH (Jensen et al. 2000). The reaction between OH and O then produces O_2. Many of the subsequent reactions that involve one of the above products (O_2, OH, H_2O) and C or C^+ will eventually form CO and other chemically important species such as formaldehyde (H_2CO).

Because the N atom has a lower proton affinity than H_3^+, the reaction between the two does not take place. Instead N^+, which is formed through the dissociation of N_2 by He^+ or cosmic rays, can undergo hydrogenation (i.e. addition of H) to form ammonia

$$N^+ \xrightarrow{H_2} NH^+ \xrightarrow{H_2} NH_2^+ \xrightarrow{H_2} NH_3^+ \xrightarrow{H_2} NH_4^+ \xrightarrow{e} NH_3. \tag{1.5}$$

The formation process of the initial N_2 includes several slowly proceeding reactions that make the molecule's formation slow itself. Interestingly, although the reaction $N^+ + H_2$ is endothermic it occurs anyway, because freshly-produced N^+ possesses a fairly high kinetic energy and it meets H_2 before this energy is lost, as H_2 is highly abundant. Nitrogen-bearing molecules that are important for the build-up of molecular complexity are the isomers HCN and HNC, which are final products of a set of reactions that were initiated by the reaction between CN and H_3^+.

The above review clearly shows that ionisation of small molecules or atoms by cosmic rays is key in starting the chemistry in dense clouds. The standard rate at which cosmic rays ionise H_2, as the most abundant molecule, in a dense cloud is of the order 10^{-17} s^{-1} (cf. above list of reactions). Ultraviolet photons from an external radiation field cannot penetrate into the dense cloud deep enough to cause significant ionisation. However, cosmic rays are able to locally produce a secondary UV radiation field. A cosmic ray itself or electrons, which are released as cosmic rays ionise H_2, can excite another H_2 molecule, which relaxes again by emitting a UV photon. The rate at which these secondary UV photons cause ionisation and dissociation is higher than for direct cosmic-ray ionisation by ∼2–3 orders of magnitude (see list above).

Naturally, as new molecules are formed, those acting as reactants are destroyed. Considering destruction mechanisms for a certain molecule is important to understand its chemistry. One pathway includes the protonation of a species and its subsequent recombination with an electron that, due to the large amount of energy released in this reaction, often ends in the dissociation of the molecule, rather than its neutralisation (e.g. Geppert et al. 2006; Hamberg et al. 2010). Such a dissociative recombination often presents the final step in a succession of protonations. For example, this is the case for reactions 1.4 and 1.5. Dissociation also occurs, for example, upon a molecule's interaction with cosmic rays or their induced UV radiation field.

1.2.2 Grain-surface chemistry

Besides protecting the molecules from being photodissociated and, thereby allowing molecular complexity to build up, dust (1% of the gas mass) itself plays a crucial role in the formation of molecules. Particularly, in dense and cold clouds, the collision of an atom or a molecule with a dust grain can lead to its adsorption or accretion onto the dust grain surface. The adsorbed species usually sticks to the surface through physisorption not chemisorption, meaning that there is no chemical bond (i.e. electron transfer) and the species is technically able to move (diffuse) on the surface. The rate at which particles are adsorbed depends on the species' number density in the gas phase, a sticking coefficient (which is between 0 and 1 and corresponds to the probability of a species actually being adsorbed after a collision), and the rate coefficient for collisions with a grain. On the other hand, the species can also desorb from the grain surface back to the gas phase. Whether a species stays on the grain depends on its characteristic binding energy, with which it sticks to the surface. This value depends on the composition and structure of the grain surface itself. Similar to the rate coefficients of gas-phase reactions, the binding energy of a species can be measured in laboratory experiments or estimated in theoretical calculations. Because the intrinsic properties of interstellar dust grains are uncertain and can vary from one source to another, binding energies are anything but certain (e.g. Ligterink & Minissale 2023). In whatever case, a species' binding or desorption energy is typically associated with a desorption temperature[5]. For example, if the dust grain has a temperature

[5] This temperature is time-dependent (e.g. Ceccarelli et al. 2022). Any pure ice will sublimate on some timescale. Because the time in laboratory experiments is much shorter, the measured desorption temperature will be higher than in the ISM.

of about 20 K, CO molecules desorb; in contrast, H_2O requires a temperature of ~100 K (as has been shown, e.g. in desorption experiments, Collings et al. 2004). As the density of a cloud increases and the temperature decreases, assuming the absence of any nearby heating source, more species are successively accreted and stay on the surface (i.e. they are depleted from the gas phase), which leads to the build-up of ice mantles on the dust grains.

The most important mechanism that takes place on dust-grain surfaces is the formation of H_2 molecules, as there is no efficient way of forming it in the gas phase. As an H atom is accreted from the gas phase to the grain surface, it will settle on an 'adsorption site', which is a local minimum in the interaction potential between the atom and the surface. The atom can 'hop' from one site to another even at low temperatures. As soon as it meets another H atom, the two will react to form H_2. The reaction produces enough energy to detach the molecule from the surface. This hopping or diffusive reaction is referred to as Langmuir-Hinshelwood mechanism and is schematically depicted in Fig. 1.5. It may also be that a gas-phase H atom is directly adsorbed to a site that already contains another H atom. This reaction will also lead to the formation of H_2 and its instant release to the gas phase. This is referred to as the Eley-Rideal mechanism (Fig. 1.5) and does not require any diffusion. Tunneling of an H atom plays only a minor role for the H_2 formation on dust grains.

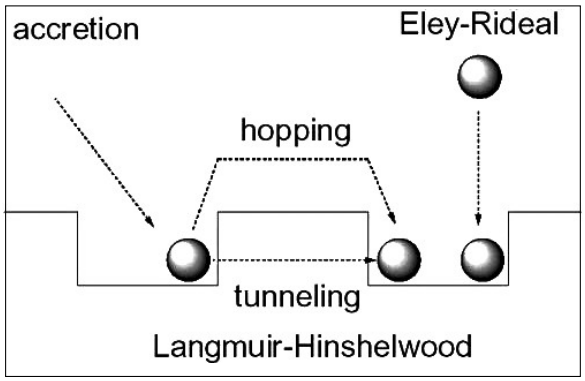

Figure 1.5: Possible reaction processes on dust grain surfaces, that either involve hopping from one site to another (diffusive, *Langmuir-Hinshelwood*) or not (prompt, *Eley-Rideal*). Tunneling may be possible for hydrogen only. The figure was taken from ifa.hawaii.edu.

Diffusive reaction processes typically are the dominant mechanisms for grain-surface chemistry, as abundances of most reactants are usually not high enough on the adsorption site for the prompt formation to be efficient. The advantage of grain-surface chemistry is that the grain can act as a third body that absorbs the energy for a reaction that involves two species and results in only one product. In the gas phase the preservation of the newly-formed molecule would require a radiative association, which is a slow process in comparison to others, as stated above. One difference from the formation of H_2 is that the newly formed molecules will, in almost all cases, remain on the grain surfaces at low temperatures, build the ice mantle of the grain, and may engage in other reactions to produce more complex species. In addition, diffusion on the grain surface proceeds only slowly, if at all, for all species heavier than H and H_2. The species have to overcome a diffusion barrier, which is a fraction of the binding energy and, hence, also depends on the structure and composition of the grain surface. Because H is the most mobile species, the reaction that produces larger molecules most efficiently at low temperatures is hydrogenation. Methanol, the simplest of the COMs, is formed in this way:

$$\mathrm{CO} \xrightarrow{\mathrm{H}} \mathrm{HCO} \xrightarrow{\mathrm{H}} \mathrm{H_2CO} \xrightarrow{\mathrm{H}} \mathrm{CH_3O} \xrightarrow{\mathrm{H}} \mathrm{CH_3OH}. \tag{1.6}$$

In fact, because CO and H_2CO are stable molecules (i.e. not radicals), the reaction with H has a substantial activation barrier. In these cases, tunneling of H through the chemical barrier becomes important. This has been studied in laboratory experiments (e.g. Watanabe et al. 2003). In the same

way, but typically without activation barriers, grain-surface species such as H_2O (addition of H to atomic O; or H_2 + OH), CH_4 (addition of H to atomic C), and NH_3 (addition of H to atomic N) are produced . All these species, amongst others, have been confirmed as abundant ice species in observations, with water generally being the most abundant (e.g. Boogert et al. 2015; McClure et al. 2023).

The chemistry does not stop here. Although not directly confirmed in observations yet, the formation and, thus, presence of COMs in the ice mantles is widely accepted, for example, based on models that include grain-surface chemistry, which can well reproduce observed abundances of COMs (e.g. Garrod et al. 2008). For example, the hydrogenation of HC_3N produces vinyl and ethyl cyanide (C_2H_3CN and C_2H_5CN, respectively), or the reaction of HCO and CH_3O may form methyl formate (CH_3OCHO). Because for the latter reaction the two reactants are heavy, they are not very mobile unless the temperature is high enough. Alternatively, both can react in a prompt reaction, when one of the reactants is adsorbed from the gas phase to the site in which the other resides (which is rather unlikely in practice), or as one of the reactants is formed in the process of methanol formation (see reaction 1.6) and the other happens to be in the same or a nearby site. The latter process is referred to as a three-body reaction, because the last step proceeds almost instantaneously (e.g. Jin & Garrod 2020). Similar to the Eley-Rideal mechanism, this last process does not require any diffusion of the radicals. This is especially important for the build-up of molecular complexity in those regions, where low temperatures prohibit diffusion of all species but H and H_2. That this process can actually form COMs has also been shown in laboratory experiments (e.g. Fedoseev et al. 2015, 2017; Chuang et al. 2016).

COMs are typically observed in emission in the gas phase, but are difficult to identify as solid species in the ice mantle. The fact that COMs are detected in the gas phase while many of them are thought to form in the ice mantles of dust grains means that they can at some point desorb from the grain surfaces. There are many possible ways for molecules to desorb (see e.g. Ceccarelli et al. 2022). For example, molecules can thermally desorb as a consequence of protostellar heating. The dust grain as a whole or molecules that reside on it can be processed by shock waves, cosmic rays, or UV photons. This can enable additional surface reactions to take place or lead to the release of molecules to the gas phase. Some grain-surface reactions may actually release enough energy to overcome the binding energy of the newly-formed molecule leading to its chemical desorption.

1.2.3 Astrochemical models – in a nutshell

Because observations only provide a snapshot of the chemistry of a source, astrochemical models are necessary to understand the involved processes that lead to the detection of some molecules in a certain amount while others may remain undetected. Typically, the comparison between the model and the observation (or between observations of different sources) is based on abundances, which are not expressed as number densities (in units of particles/cm^3) but rather as fractional abundance with respect to hydrogen (or other molecules). Because interstellar chemistry does not reach equilibrium, the abundance of a molecule is time-dependent. Models provide this time evolution of a molecule's abundance as their main output. The comparison with the observed abundance then helps to put constraints on the age of the source and its physical history.

There exists a variety of astrochemical models that focus on different aspects of the chemistry. However, from Sects. 1.2.1 and 1.2.2 it is evident that both gas-phase and grain-surface chemistry as well as their interaction need to be considered for a more complete picture. In fact, the observational

results obtained in this thesis were compared to a three-phase model (Garrod et al. 2022, G22 hereafter). Instead of considering the grain surface as a single chemical entity, this model distinguishes between the ice-surface layers of a grain and its bulk-ice mantle that lies underneath. Accordingly, interactions between all three phases (the bulk ice with the ice surface and the ice surface with the gas phase) are included.

Various input parameters go into such models, amongst these is the chemical network of a molecule. This includes any type of reaction that is known or suspected to form and destroy the species in the solid and gas phase together with the rate coefficients and branching ratios to tell the efficiencies of all these reactions. These parameters are inserted into differential rate equations, one for each molecule, that are then solved for the abundance at each time step. Rate equations are introduced in Sect. 2.1.3. Some reaction rates and branching ratios have been derived in laboratory experiments. For those species and reactions that have not been the subject of any experiment, estimated values from theoretical calculations are used, if available. Sometimes extrapolations have to be made if values have been determined for only a limited temperature range. Some reactions have not been studied with neither approach, which is when assumptions are used based on chemical intuition or analogies to related molecules, which can be incorrect. Another input parameter is the chemical content at the starting point of the model. In the G22 models, for example, the chemistry starts from elemental abundances. Moreover, the physical conditions play a crucial role such as density, temperature, cosmic-ray flux, internal or external radiation fields, and whether these change over time. Currently, there is no perfect model for interstellar chemistry, because all input parameters, those mentioned above and others (e.g. grain sizes and compositions), have uncertainties and because of the increasing number of newly detected molecules. Therefore, it is crucial to keep updating these models with new constraints from observations and laboratory work in order to make better predictions, which will in turn help to better understand how interstellar chemistry proceeds.

1.3 From dense cores to high-mass protostars

If a dense molecular cloud or a part of it exceeds a critical mass, it becomes gravitationally unstable and starts collapsing. In a first approximation, this threshold depends on density and temperature, that is the higher the density and the lower the temperature the more likely a collapse is initiated. However, this threshold can vary in the presence of, for example, turbulence and magnetic fields. As material accretes towards a gravitational centre, higher-density clumps form, then cores, in which stars are born, eventually. The formation process of low-mass (solar-type) star precursors has been studied in great detail, while that of high-mass star ($M > 8\,M_{\odot}$, luminosity $> 10^3\,L_{\odot}$, spectral types O and B) precursors is still debated. Section 1.3.1 briefly introduces the evolutionary stages during low-mass star formation, summarises the problems that occur when trying to apply this sequence to the formation of high-mass stars, and provides a possible scenario for the high-mass case as proposed by Motte et al. (2018). Section 1.3.2 describes observational characteristics of the chemistry in the vicinity of high-mass protostars.

1.3.1 Low- versus high-mass star formation

The first stage in the low-mass star formation process is associated with a **starless or prestellar core**. This phase is characterised by isothermal contraction, meaning that radiation emitted by dust and molecules can leave the core freely, which keeps the temperature at a value of ∼10 K. Only when the density reaches $\sim 10^{11}$ cm^{-3}, the dust becomes opaque to radiation, hence, trapping the radiation inside. The radiation pressure stalls the collapse for a short period of time and a **first stable core** emerges. As accretion onto this core continues, the temperature rises until H_2 molecules get dissociated at 1500 K. This process consumes a large amount of energy leading to a second collapse, after which a second core emerges marking the beginning of the **protostellar phase**. During this stage the protostar is still growing in mass as accretion of cloud material onto to the young stellar object continues. This material has a non-zero angular momentum and, due to conservation of angular momentum, will eventually assemble in a disk. Simultaneously, an outflow is launched perpendicular to the disk that acts as an agent to take away some of the angular momentum. The launching mechanisms of outflows are not fully understood yet, however, the most likely origin is the interplay of gas dynamics in the disk with magnetic fields. When accretion has slowed down significantly, because nearly all material has already been accreted or dissipated by growing stellar feedback, the protostar enters the stage of a **T-Tauri star**. At early times of this stage, some accretion from a small disk may still be ongoing ('classical' T-Tauri), at late stages, accretion does not occur anymore ('weak-line' T-Tauri). For a more detailed view on low-mass star formation, readers are directed to reviews, for example, by Andre et al. (2000), Rosen et al. (2020), and references therein.

When trying to apply this evolutionary sequence to high-mass star formation, the biggest problem that arises is that the radiation pressure increases rapidly as the protostar gains mass, which at some point prevents further accretion of material (e.g. Beuther et al. 2007). Consequently, stars with masses of several tens of solar masses should not exist, but they do. Observing high-mass stars and their precursors is challenging. Only 1% of the stellar population is massive and star-forming regions that produce high-mass stars are located at distances from us on kiloparsec scales. Nonetheless, observations show that stars with more than 100 $M_\odot$ exist. Therefore, different theories have been put forward that try to explain the formation of high-mass stars. One scenario of how the high-mass progenitors evolve is schematically shown in Fig. 1.6 and was introduced by Motte et al. (2018), according to which one distinguishes between six phases:
(1) The starting points of high-mass star formation are molecular cloud complexes (∼100 pc in size, 10^5-10^6 $M_\odot$ in mass) that perhaps already contain a cluster of young massive stars, but are also hosts to massive parsec-sized clouds. In the gravitational centres of these clouds, so-called ridges (if more elongated) or hubs (if more spherical) emerge and seem to present the focus points of filaments that contain large amounts of gas.
(2) In these hubs/ridges IR-quiet massive dense cores (MDCs) form, which are massive cloud fragments of sub-pc size, that harbour low-mass prestellar cores. Observationally, these starless MDCs manifest themselves as high-density regions ($\gtrsim 10^6$ cm^{-3}), with weak or no mid-IR, and without any signpost of star formation such as HII regions, outflows, or hot cores (see Sect. 1.3.2).
(3) Based on observations, ridges/hubs were found to undergo global collapse, which results in accretion of material onto MDCs through gas streams. This does not only increase the mass of the MDCs but also the mass of the low-mass prestellar cores that reside inside. Ultimately, this turns the low-mass prestellar cores into low-mass protostars.
(4) As accretion from larger scales down to the MDC centre continues efficiently, the MDC grows

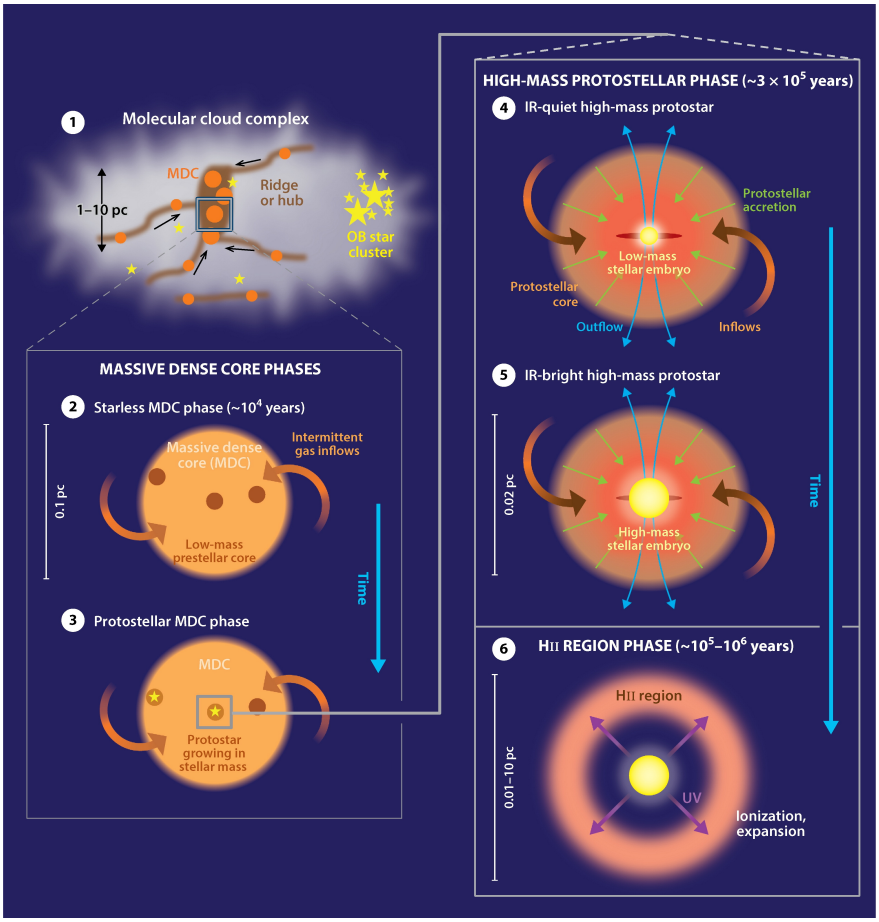

Figure 1.6: One possible scenario for the formation of a high-mass protostar proposed by Motte et al. (2018).

into an IR-quiet high-mass protostar on a scale of ~0.02 pc, which still containing only low-mass protostars. In contrast to IR-quiet MDCs, protostellar activity can be observed at this stage such as outflows and hot cores.

(5) The high-mass protostar turns from IR-quiet to IR-bright, when its mass exceeds 8 $M_\odot$ and a sharp increase in luminosity occurs. At this stage a hyper-compact (HC) HII region develops. These are strong emitters of free-free emission at centimetre wavelength and are either indeed associated with an extremely young HII region (<0.05 pc in size with 10^6 cm^{-3} still quenched by infalling material) or with other sources of ionised material, for example ionised accretion flows or a photo-evaporating disk structure (e.g. Keto 2003).

(6) The increasing UV radiation field originating from the growing protostar results in the growth of the HII region from HC to ultra-compact (~0.1 pc in size) to compact (<0.5 pc) and, finally, to classical (~10 pc, e.g. Garcia-Segura & Franco 1996; Churchwell 2002). Each phase that an HII region goes through is characterised by a number of parameters such as its size, density, or line profile of detected recombination lines. As a consequence of the growing HII region, together with the powerful outflow and stellar winds, accretion onto the protostar ceases eventually.

The advantage of this scenario is that it does not require the presence of high-mass prestellar cores. There are very few sources observed that have been proposed as candidates for such high-mass prestellar cores, but their existence is not confirmed. In contrast to the above sequence, which is a type of the competitive accretion model (e.g. Bonnell et al. 2001), a scenario that starts from a high-mass prestellar core is known as monolithic collapse or turbulent accretion model (e.g. McKee & Tan 2003). In this model, an isolated dense core collapses, however, it must possess a high degree of turbulence or strong magnetic fields that slow down the collapse and enable mass to be accumulated on longer timescales. As the protostar is born the radiation-pressure problem remains. However, numerical simulations show that it is possible to continue accretion when material assembles in some kind of disk-like structure. This is closest to the low-mass star scenario. Understanding high-mass star formation remains an active field of research and is regularly subject to reviews that address theoretical and observational advances that have been made (e.g. Beuther et al. 2007; Tan et al. 2014; Motte et al. 2018).

1.3.2 Hot-core chemistry

As a high-mass protostar is born, it starts heating the ambient material, which has a great impact on the chemistry. The heating results in thermal desorption of the dust grains' ice mantles, which releases molecules, including many COMs, into the gas phase. This region around the high-mass protostar that is bright in emission of COMs is called a hot (molecular) core (or hot corino in case of a low-mass protostar). Hot cores are commonly characterised with a gas temperature above 100 K (e.g. van Dishoeck & Blake 1998). This is associated with the desorption temperature of water, which is the main constituent of the ice mantles (cf. Sect. 1.2.2). Whether COMs desorb at the same temperature or not is an open question, which is addressed in this thesis (see Sect. 1.5). The COMs that are released through thermal desorption are not only those that have been produced in the dense cloud prior to the birth of the protostar. During the gradual warm-up of the protostellar environment from the primary 10 K in the dense cloud to the 100 K that mark the beginning of the hot-core phase, grain-surface chemistry gains in efficiency. Species on the surface (other than H and H_2) become more mobile, due to the extra energy, and find each other to form larger molecules (e.g. Garrod et al. 2008). In particular, reactions between two radicals play an important role at this stage. Moreover, due to the increasing gas temperature, gas-phase reactions become more efficient. The evolution of chemistry during star formation, especially also during the protostellar phase, was recently reviewed by Jørgensen et al. (2020) and Ceccarelli et al. (2022).

At this stage in the star-formation process, the chemistry is not only impacted by the protostellar heating, but also shocks, for example, caused by interaction of the material with the protostellar outflow (e.g. Arce et al. 2008) or by accretion shocks that may occur at the disk-envelope interface (e.g. Csengeri et al. 2019). The potentially sharp increase in temperature that results from the passage of a shock wave through the material can lead to drastic changes in the gas and dust molecular content (e.g. Burkhardt et al. 2019). On the one hand, reactions in the gas phase that have high activation barriers or those that are endothermic may now proceed. However, some species may also be dissociated. Thermal desorption is accelerated and likely even more refractory material (that has a condensation temperature of >1300 K, conversely to volatile material, Lodders 2003) from the grain core can be sublimated, depending on the shock strength. The grain may also be sputtered, which would result in further release of solid-phase species to the gas phase. The exact impact of shocks, due to accretion and outflows in the high-mass protostellar phase, on the chemistry of, especially, COMs has not been studied extensively neither observationally nor in chemical shock models. The impact of an outflow on the chemical composition of a hot core is investigated in this thesis (see Sect. 1.5).

1.4 Zoom-in on the high-mass star forming region Sagittarius B2 (N)

The source of interest in this thesis, Sgr B2 (N1), is the most massive dense core of the high-mass star forming region Sgr B2 (N), which is embedded in the Sgr B2 cloud complex. Due to its location in the Milky Way's central molecular zone (CMZ), which is the largest reservoir of molecular gas in the Galaxy ($2-6\times10^7\,M_\odot$) found in a ~300 pc radius around the central black hole Sgr A*, it presents a perfect laboratory to study (high-mass) star formation under extreme conditions. The physical and chemical properties of CMZ clouds, the physical processes that these clouds are exposed to, and what this means for star formation are described in Sect. 1.4.1. Section 1.4.2 zooms in on the cloud complex Sgr B2 and, in particular, explains why Sgr B2 (N) and its most massive hot core are excellent targets to study COMs. Section 1.4.1 is based on a recent review by Henshaw et al. (2023) that discusses in detail the advances made in the field of star formation in the CMZ.

1.4.1 Molecular clouds in the CMZ

The CMZ extends from roughly -1° to 1.7° Galactic longitude and $\pm0.5^\circ$ Galactic latitude. The gas in this region spans a total velocity range of $|v| \sim 150$ km s^{-1}. Figure 1.7 shows a false three-colour image of the CMZ, where orange traces emission from cold dust at 1.1 mm, emission from warm polycyclic aromatic hydrocarbons at 8 μm is associated with teal, and pink corresponds to emission from hot ionised gas at 20 cm. Some of the well-known CMZ clouds and cloud complexes are labelled, including Sgr C, the 20 km s^{-1} and 50 km s^{-1} clouds, Sgr B2, the so-called Brick, and a couple of clouds encompassed by the latter two complexes in projection, which are commonly referred to as the dust ridge. The location of the central black hole Sgr A* is indicated as well. The CMZ is a region of extremes in many aspects that do not only have a great influence on the motion of molecular clouds so close to the gravitational centre of the Galaxy, but also on their physical and chemical conditions, and ultimately, on the star-formation process.

All of the clouds and cloud complexes shown in Fig. 1.4 orbit the central black hole within a radius of 100 pc and contain most of the dense molecular gas in the CMZ. It is in this '100 pc stream' that most of the present star formation in the Galactic centre takes place. How exactly these clouds are distributed in three-dimensional space and how exactly their orbits look like is not certain yet. At the present day, there are two scenarios that seem likely, which are shown schematically in Fig. 1.7. Accordingly, the clouds might move on two spiral arms (e.g. Sawada et al. 2004) or on open eccentric orbits (Kruijssen et al. 2015). Both scenarios locate Sgr B2 and the dust-ridge clouds in front of Sgr A* (when viewing the CMZ from Earth), which was shown to be likely the case in multiple studies (e.g. Reid et al. 2009; Chuard et al. 2018). The positions of Sgr C, the 20 km s^{-1} and 50 km s^{-1} clouds relative to Sgr A* are debated, they may be located in front of or behind the black hole. Currently, the open-orbit scenario seems to be the preferred one. However, in this scenario it remains unclear, how the 100 pc stream connects to the dust lanes, through which the CMZ is supplied with new material from the inner Galaxy, and to clouds located in the larger-scale Galactic centre region (e.g. the 1.3° complex). In the spiral-arm scheme, these features are included.

The star-formation rate in the CMZ was derived in numerous studies. Amongst other techniques, counting sources that are signposts of stars and star formation, such as young stellar objects, HII regions, or supernova remnants, seems to provide the most accurate values with a mean of $0.07^{+0.08}_{-0.02}\,M_\odot$ yr^{-1} (see Table 1 in Henshaw et al. 2023). This rate is a factor 10 lower than what can be expected from the amount of dense gas that resides in the CMZ (Longmore et al. 2013). The two quantities were shown

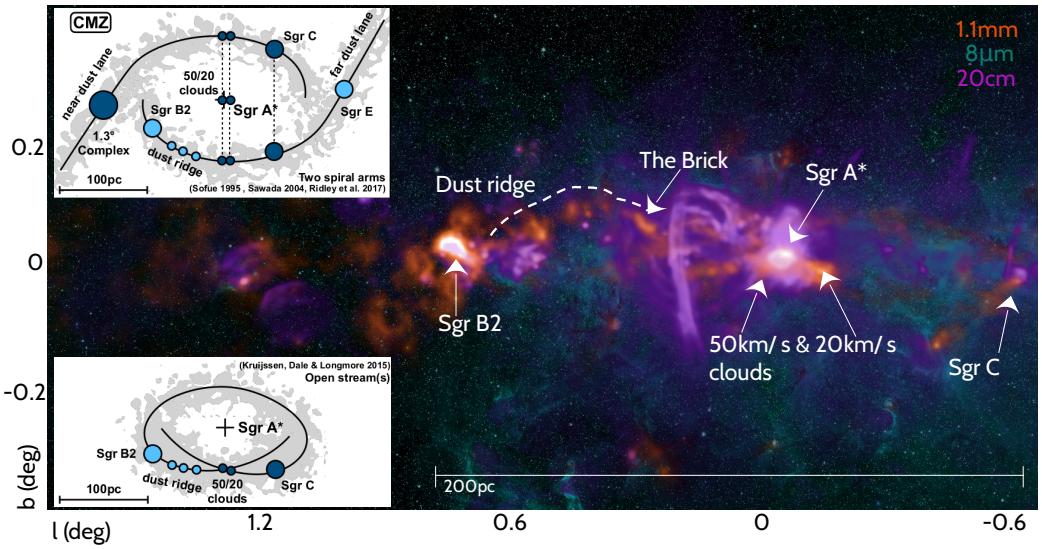

Figure 1.7: The central molecular zone (CMZ) in the galactic coordinate system observed at 1.1 mm showing cold dust emission, at 8 μm tracing emission from warm PAHs, and at 20 cm associated with emission from hot ionised gas coming from HII regions and supernovae. The left-hand panels show two possible top views of the CMZ illustrating how the labelled clouds and cloud complexes might orbit the central black hole Sgr A*. *Image Credit: A. Ginsburg/NRAO/AUI/NSF and Henshaw et al. (2023).*

to follow a linear trend considering a variety of sources, including Galactic plane clouds, extragalactic CMZs, and other galaxies as a whole. A plausible explanation is that the CMZ goes through episodic star formation and that it finds itself in a more quiescent phase at the present day. The main candidates for causing a temporal halt of star formation are stellar feedback and varying mass of the CMZ due to episodic inflow of new material. In a phase of starburst, the turbulent energy injected by stellar winds and supernovae would eventually prevent star formation to continue until the turbulence dissipates and material would accumulate again such that on timescales of a few tens of Myr star formation could be reactivated.

The reason why some clouds are devoid in star formation, despite meeting the requirements in terms of available dense gas, may be attributed to the prevailing physical conditions that have long been known to differ from clouds in the Galactic plane (see also, e.g. Güsten & Philipp 2004). On scales of a few parsec, clouds in the CMZ possess masses of $\sim 10^4$–$10^5\ M_\odot$ yielding densities of $\gtrsim 10^4$ cm^{-3}, which makes them denser on average than their Galactic-plane counterparts. The gas temperature in these CMZ clouds reaches tens of K, even exceeds 100 K in some clouds, which is higher than the typical values of 10–20 K found in disk clouds. However, the dust is observed at temperatures of about 20 K in the CMZ (also higher than in disk clouds) (e.g Tang et al. 2021), implying that dust and gas are thermally decoupled and they were proposed to remain decoupled for densities $< 10^7$ cm^{-3} (Clark et al. 2013). At the present day, the most promising candidates for the globally elevated gas temperatures are mechanical heating, due to turbulence, and cosmic rays. In fact, the cosmic-ray flux is a factor 10–100 higher than the standard value derived in the Galactic disk, even in the densest regions such as Sgr B2 (N) (Bonfand et al. 2019). The sources of cosmic rays in the CMZ are likely supernova explosions, HII regions, or/and past activity of the black hole Sgr A*. Therefore, there can

also be local variations. On the other hand, the larger velocity dispersion in CMZ clouds derived from observed spectral lines of molecules implies indeed the presence of a higher level of turbulence on parsec scales (e.g. Shetty et al. 2012). The dominant source of turbulence is still debated, but is likely a combination of several mechanisms, such as stellar feedback (supernova explosions in particular), inflow of material to the CMZ, and cloud-cloud interactions (also as a consequence of inflow and the movement of clouds in the Galactic gravitational potential). Observations have shown that less than 10% of the cloud mass is found in gravitationally bound clumps (e.g. Lu et al. 2019) leading to the questions whether there is a mechanism preventing the formation of such denser substructures in CMZ clouds, and ultimately, star formation. A prime candidate for causing this is the enhanced degree of turbulence. This implies that in addition to the scenario of episodic star formation, due to stellar feedback or episodic mass inflow or both, the extreme physical conditions to which the dense clouds in the CMZ are exposed prevent star formation to proceed at conditions typical for disk clouds.

The CMZ is not only an excellent laboratory to study star formation in an extreme environment, but also chemistry. The high number of supernovae that explode within smaller radii than in the Galactic plane enrich the material with heavier elements, which manifests observationally in higher metallicities and an increased cosmic-ray flux. Dust temperatures may never go as low as in disk clouds possibly influencing the composition of ice mantles. In Galactic-plane clouds, the emission of some molecules or some transitions of a given molecule probe specific properties of the gas. For example, some molecules can only be excited in high-density gas, while the formation of others relies on the presence of shocks. Because of the on average higher densities and higher level of turbulence in the CMZ, the emission of such molecular tracers is widespread across CMZ clouds (shown in molecular surveys, e.g. Riquelme et al. 2010; Jones et al. 2012). COMs have been detected in many CMZ clouds, also those that are devoid in star formation (Requena-Torres et al. 2006, 2008). The rich gas-phase chemistry in these clouds is thought to be mainly driven by shocks and the enhanced cosmic-ray flux. One of these sources in the CMZ, namely G+0.693−0.027 (G0.693 hereafter), has been targeted to study its molecular composition in particular. Over the past years, several new detections have been made there, including complex amines (Zeng et al. 2021; Rivilla et al. 2021b) or the phosphorus monoxide ion (PO^+, Rivilla et al. 2022a), for example. A comparison of the chemical composition in G0.693 with the one that we derive for the hot core Sgr B2 (N1) in the course of this thesis is of particular interest. Both are located in the Sgr B2 cloud complex and, hence, possibly started from similar initial chemical and physical conditions, however, G0.693 does not show signs of star formation (cf. goals of this thesis in Sect. 1.5).

1.4.2 Sagittarius B2 North

The brightest region after Sgr A* in Fig. 1.7 is Sgr B2, one of the most prominent high-mass star-forming regions in our entire Galaxy. There exist several ideas on how the starburst-like formation of stars might have been triggered in Sgr B2, for example, through tidal compression during pericentre passage 0.75 Myr ago (Longmore et al. 2013), or through collisions of clouds (Zeng et al. 2020). The latter may be a consequence of gas piling up at the current location of Sgr B2 close to the apocentre (see Fig. 1.7 and Hatchfield et al. 2021). Most of the star formation happens in the dense molecular regions Sgr B2 (M)ain, (N)orth, and (S)outh, where their names are associated with their relative locations in the equatorial plane within the Sgr B2 cloud complex as can be seen in Fig. 1.8. Numerous high-mass protostars (e.g. Bonfand et al. 2017), (ultra)compact HII regions (e.g. Gaume et al. 1995), and other signposts of (high-mass) star formation have been observed towards these regions. The

densest parts are embedded in a region of moderate density, which in turn is embedded in a low-density envelope (Schmiedeke et al. 2016). Figure 1.8 shows a sketch of Sgr B2, including the aforementioned components, and lists key characteristics such as the projected size, R, gas and stellar mass, M, luminosity, L, and H_2 volume density, $n(H_2)$. Besides being a site of star formation, Sgr B2 (N) and (M) already contain protoclusters of young (high-mass) stars. Comparing the stellar and gas mass for these two reveals that Sgr B2 (N) has still a lot of gas left while in Sgr B2 (M) a large fraction of gas has already been converted to stars (Ginsburg et al. 2018). Additional dust continuum sources that have been identified in the Sgr B2 cloud complex are Sgr B2 (NE) and Sgr B2 (deepS) (Schmiedeke et al. 2016). They are located further to the northeast from Sgr B2 (N) and further to the south of Sgr B2 (S), respectively (see Fig. 1.8). Moreover, the approximate distances of G.0693 to Sgr B2 (N) (Zeng et al. 2020), which was introduced in Sect.1.4.1, and of Sgr B2 to Sgr A* are indicated.

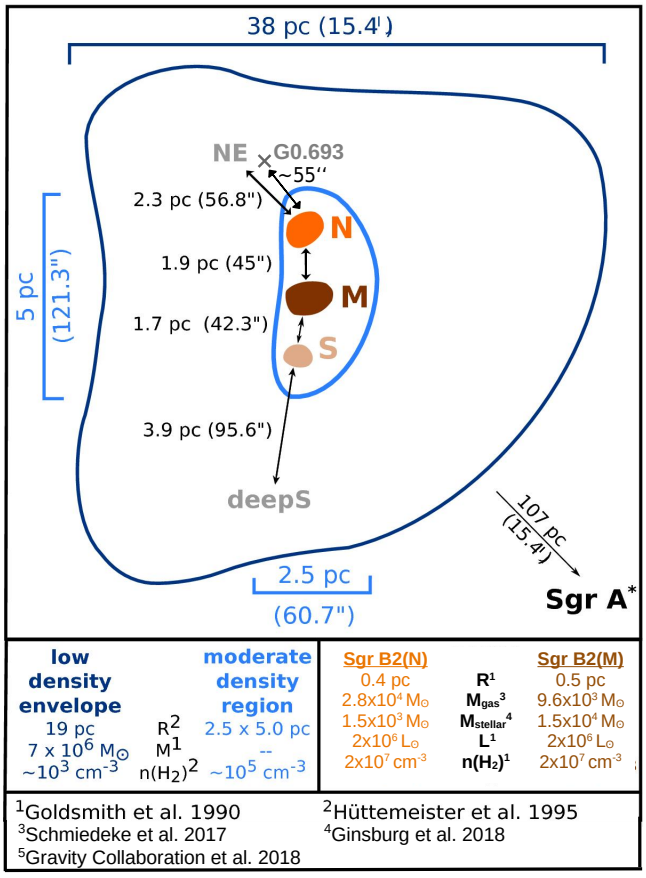

Figure 1.8: Schematic structure of the Sgr B2 cloud complex based on Hüttemeister et al. (1995a). This version is taken from Schmiedeke et al. (2016), updates have been adopted from (Schwörer 2020). The location of G0.693 was added.

From the beginning of molecular astronomy in the late 1960s and over the following decades, Sgr B2 has been established as a perfect hunting ground to detect new species, especially also COMs (McGuire 2022). The complexity of the molecular content in Sgr B2 (N) and (M) could already be investigated in single-dish observations. For example, a detailed inventory can be found in Belloche et al. (2013). Subsequent interferometric observations at high angular resolution were able to spatially resolve individual continuum sources, which made it possible to put better constraints on the origin of COMs, their abundances, and how these are affected by the prevailing physical conditions and ongoing processes in these individual sources.

Figure 1.9 zooms in on the most central region of Sgr B2 (N). The map shows continuum emission at 1 mm (Sánchez-Monge et al. 2017), mostly originating from dust, and reveals the locations of the main and most massive hot core Sgr B2 (N1), the secondary hot core N2, and N3, which is one of three recently detected hot cores (N4 and N5 lie outside the shown field, Bonfand et al. 2017). Based on the 1 mm continuum data that was observed with the Atacama large millimetre/submillimetre array (ALMA), additional continuum peaks have been reported (blue crosses in Fig. 1.9, Sánchez-Monge et al. 2017). The nature of these sources still needs to be investigated in detail, however, many of them likely contain high-mass young stellar objects. In addition, filaments have been identified that seem to converge towards Sgr B2 (N1) and

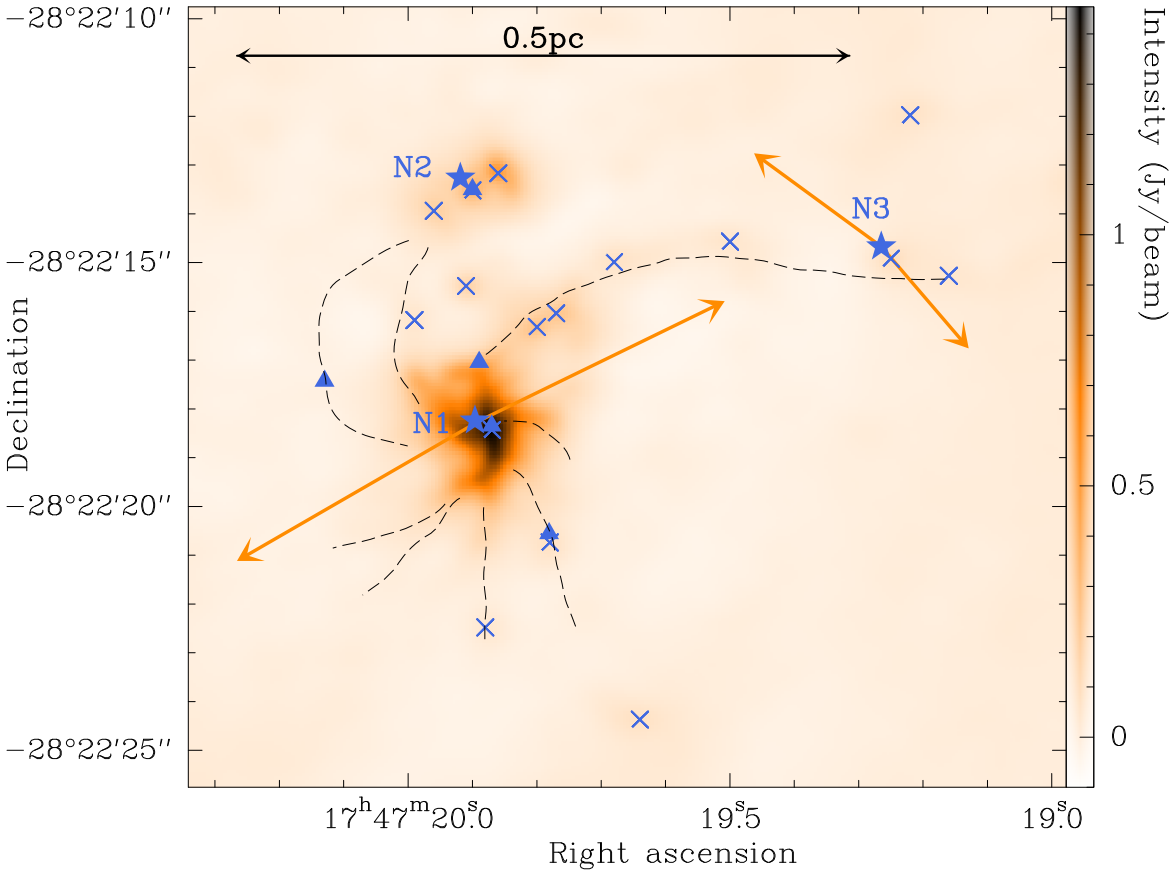

Figure 1.9: Continuum map at 1 mm (in colour scale) observed with the ALMA interferometre towards the high-mass star forming region Sgr B2 (N) (Sánchez-Monge et al. 2017). The hot cores N1–N3 are marked with star symbols (hot cores N4–N5, which were recently identified along with N3 (Bonfand et al. 2017), are out of the field of view. The orange arrows indicate the approximate directions along which the protostellar outflows driven by N1 and N3 expand. Black dashed lines roughly indicate filaments through which material may be transported to the main hot core N1 (Schwörer et al. 2019). Blue crosses mark additional continuum sources identified based on the 1 mm continuum data, and triangles mark the locations of HII regions identified based on observations at 1.3 cm and 7 mm (Gaume et al. 1995; De Pree et al. 2015).

possibly funnel material to the hot core (black dashed lines in Fig. 1.9, Schwörer et al. 2019). These filaments were not only seen in continuum emission, but also in line emission of various molecules, including COMs. The three new hot cores N3–N5 were identified based on data taken as part of the EMoCA (Exploring Molecular Complexity with ALMA, Belloche et al. 2016) survey, which was observed in the 3 mm spectral window again with ALMA. Thanks to the high angular resolution along with a high sensitivity, the new hot cores (and their outflows, if present) were identified based on the high spectral-line density, implying the presence of COMs, and the dust continuum emission in these sources (Bonfand et al. 2017). In addition, new COMs were detected (*i*-C_3H_7CN and CH_3NHCHO, Belloche et al. 2014, 2017). This data set also enabled to map the outflows of N1 (Higuchi et al. 2015) as well as N3 and N5 (Bonfand et al. 2017) and to study in detail the gas molecular composition of the

hot cores N2–N5 (Bonfand et al. 2019). The most massive hot core Sgr B2 (N1) was excluded from the last study due to remaining observational limitations. Overcoming these limitations and studying the emission of COMs in the main hot core is now possible using the EMoCA survey's successor, the ReMoCA (Re-exploring Molecular Complexity with ALMA) survey (Belloche et al. 2019), which has a higher angular resolution by a factor 3–4 and a higher sensitivity by a factor ~3. The analysis of the data taken as part of this survey towards Sgr B2 (N1) is the main focus of this thesis. The main science questions that are addressed are explained in the following section.

1.5 Scientific goals and outline of this thesis

At the beginning of this chapter, it was shown how the number of newly detected molecules has been rising dramatically for the past few years and that these new molecules become increasingly complex. This is exciting and fuels the debate on life and its origins. This whole chapter showed how diverse the chemistry in the ISM can be and that there remains a lot to discover when it comes to a molecule's journey from the earliest stages of star formation to its incorporation into planets on which life may emerge one day. To establish such a chemical link between the phases of star formation, one needs to understand the ways to form and destroy a molecule and to find the physical processes that are involved along the way.

The hot core Sgr B2 (N1) is an excellent target to address this task. As stated in Sect. 1.4.2, the high-mass star-forming protocluster Sgr B2 (N), in which the hot core is embedded, has been the hunting ground for new species since the beginnings of molecular astrophysics, especially regarding COMs. The high-angular resolution of the ReMoCA survey makes it possible to resolve the spatially widely extended emission of COMs that is associated with Sgr B2 (N1). This enables to study the variation in COM abundances as a function of temperature, which is set by the heating source at the centre of the hot core. In addition, the impact of the powerful outflow that is driven by Sgr B2 (N1) on the molecular content can be investigated as well as the potential presence of accretion shocks and their influence on the chemistry at the foot points of the filaments, that is where they hit the denser material of the hot core. The two projects that this thesis is comprised of tackle essentially the first two aspects by addressing the following science question, respectively:

1. Based on model predictions (e.g. Garrod et al. 2008, 2022) and results of laboratory experiments (e.g. Collings et al. 2004; Martín-Doménech et al. 2014), there are two possible ways of thermal desorption in a hot core, which essentially depend on the COMs ability to diffuse through the different layers of the dust grain's ice mantle. If they do so, they may eventually end up at the outermost surface and desorb at their individual desorption temperature, that depends on their binding energy to the grain surface. If they do not have the ability to diffuse, they remain trapped in the ice mantle that dominantly consists of water. In this case, COMs would need to wait for water to leave the grain surface at its desorption temperature, thereby uncovering the ice layers below. To this date there has not yet been direct observational proof for either of the two mechanisms due to observational limitations, especially, in terms of angular resolution. Therefore, finding the dominating process of thermal desorption in Sgr B2 (N1) is the main objective of the first project (Chapter 3). To achieve this goal, spatially resolved gas-phase abundance profiles are derived as a function of distance to the centre of the hot core, hence, temperature. A steep increase in the abundances within a narrow temperature range provides observational evidence for desorption, that is the sudden enrichment of a molecule in the gas due

to its sublimation from the dust-grain surface. Therefore, these abundance profiles additionally give hints on whether a COM is actually formed on dust grains or rather in the gas phase.

2. As described in Sect. 1.3.2, a shock has a great impact on both the physical conditions and the chemistry of the material with which it interacts. The goal of the second project (Chapter 4) is to study the impact of the protostellar outflow driven by Sgr B2 (N1) on the chemical composition in the hot core. To do so, molecular abundances for positions in the outflow lobes are derived and compared with the molecular content of positions that are not impacted by the outflow. This will help shed light on physical and chemical processes that may have been facilitated by the interaction of the outflow with the ambient gas and dust leading to the observed chemical segregation. The obtained results are further compared to the molecular content of other sources that are exposed to shocks, for example G+0.693−0.027, which was introduced in Sect. 1.4.1. Because this source is less dense, this comparison provides information on whether the impact of a shock on a source's molecular composition is the same, independent of initial conditions. In addition, in order to understand the structure of Sgr B2 (N1)'s outflow and whether it matches the general notion of protostellar outflows, the molecular emission is mapped and its morphology investigated.

The results obtained in the course of this thesis provide insights into the chemistry that takes place in hot cores, that is during the protostellar stage of high-mass star formation. However, they also present important puzzle pieces that help to take a step forward in the pursuit of one of the overarching goals of astrochemistry, which concerns the evolution of molecules from dense clouds to planets, because both desorption of molecules and their exposure to shocks are not limited to the protostellar phase. Based on the comparison of our observational results with predictions of astrochemical models, we can argue on the completeness of a molecule's chemical network used in the models and, where necessary, discuss additional formation and destruction routes that are not (yet) included in those models. Besides possibly missing chemical reactions, the impact of different physical conditions (e.g. density and cosmic-ray flux) in Sgr B2 (N1) than assumed in the models on the molecular abundances is investigated.

This thesis is structured as follows: Chapter 2 provides some physical background on how to identify molecules in space, that is, based on their observed rotational spectra and how to derive abundances from these observations. It also includes an introduction to radioastronomical observations performed with a single antenna and with a combination of multiple dishes that form an interferometre. At last, the ReMoCA survey is introduced, including details on the observations with the ALMA interferometre, the structure of the obtained data set, and the methods of analysing the data. Results obtained in the course of the first project are published in Busch et al. (2022) and summarised in Ch. 3. The corresponding article can be found in Appendix A. Chapter 4 contains the article on the second project (Busch et al. 2023, submitted to A&A) in its current status (second reviewing phase). Concluding remarks are provided in Chapter 5.

2

Observations & methods of analysis

This chapter contains:

This chapter provides the physical background that is needed for the analysis of the observed data. At the centre of astrochemistry is the determination of column densities of species. As it is hard to know the three-dimensional structure of a cloud, the column density is often the only measurable quantity of a molecule. It represents the number density of a species enclosed in the telescope beam integrated along the line of sight between the observer and the source. The column density is not only a measure for how abundant a molecule is in a cloud, but it also provides information on the physical conditions that prevail in this cloud, as will be explored further in this thesis. How column densities can be derived from observational data is described in Sect. 2.1. Some important parameters that need to be considered when performing observations in the radio-wavelength regime either with a single antenna or with an array of antennas are briefly explained in Sect. 2.2. Section 2.3 combines the knowledge obtained in the preceding sections and introduces the observational data used in this thesis along with the methods of data analysis. The following sections are based on Yamamoto (2017), Draine (2010), Lequeux et al. (2005), Wilson et al. (2008), and Klein (2006).

2.1 From observed spectral features to column densities

In order to derive molecular column densities from observational data, a few principles need to be introduced first. The radiation that is received from molecules is not continuous, but discrete. Observed spectral features can be associated to the energy radiated or absorbed by a given species, as it gets excited to a higher energy level or decays to a lower one. This energy (or frequency, $E = h\nu$) is unique to a given chemical species. In this thesis, transitions between rotational energy levels of molecules are observed and analysed. A description of energy levels in general and a more detailed look into the occurrence of rotational spectra are provided in Sect. 2.1.1. In Sect. 2.1.2, the radiative transfer equation is derived, which describes the propagation of an electromagnetic wave from its origin to the observer and how the intensity of the radiation changes as it encounters interstellar matter. Section 2.1.3 introduces the energy-level structure of molecules and describes the varied mechanisms by which they are populated and how these populations change over time due to interactions with photons and other molecules. Based on this, a formalism for determining or estimating column densities is eventually derived.

2.1.1 Rotational spectra of molecules

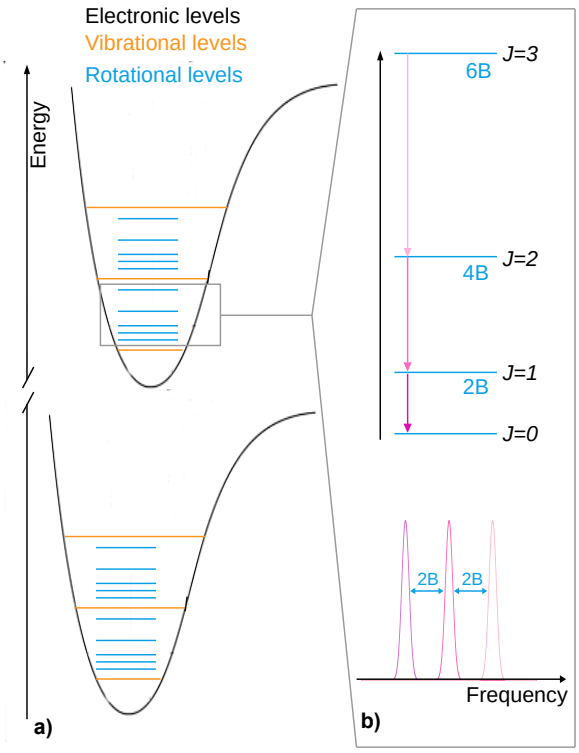

Figure 2.1: *Panel a:* Simplistic energy-level distribution of a molecule. *Panel b:* Sketch of rotational levels, J, and transitions in a diatomic molecule, where B is the rotational constant.

When molecules possess an electric dipole moment, which arises due to an intrinsic charge distribution, they can interact with radiation. Molecular spectral lines can be observed across the electromagnetic spectrum from UV to radio wavelengths. Electronic transitions occur, just as in atoms, when an electron in the molecule changes its energy level from one electronic state to another. The energy associated with this kind of transition is usually of several eV, which translates to a wavelength in the UV regime or frequencies of $\sim 10^{15}$–10^{16} Hz. Different to atoms, a molecule can also vibrate and rotate. This means that within a given electronic state, a molecule finds itself in the vibrational ground state or in a vibrationally excited state and in each of these vibrational states, it can occupy one of several rotational levels, as well. This is schematically shown in Fig. 2.1a. Changing vibrational states results in a rovibrational transition with an energy that is typically a fraction of an eV, which translates to a wavelength in the mid-IR regime, and a frequency of a few 10^{14} Hz. Rotational transitions between two rotational levels in a given vibrational state occur at energies of meV, that is in the centimetre- to submillimetre-wavelength regimes or at frequencies from $\sim 10^{9}$ to a few

10^{11} Hz. This thesis focusses on the analysis and interpretation of rotational transitions (in various vibrational states) from several molecules in order to infer the chemical composition and physical conditions of the observed source.

Starting from the assumption of a molecule as a rigid rotor, meaning that its rotation does not lead to any deformation of the body, the energy of a rotational level, $E_{\rm rot}$, is expressed in terms of the angular velocity, ω, of the rotation movement and the moment of inertia, I:

$$E_{\rm rot} = \frac{1}{2}(\omega_x\ \omega_y\ \omega_z)\begin{pmatrix} I_{xx} & I_{xy} & I_{xz} \\ I_{yx} & I_{yy} & I_{yz} \\ I_{zx} & I_{zy} & I_{zz} \end{pmatrix}\begin{pmatrix} \omega_x \\ \omega_y \\ \omega_z \end{pmatrix}, \tag{2.1}$$

where x, y, z denote the possible rotation axes. The diagonal elements of the matrix are the moments of inertia around the respective subscripted axis. The off-diagonal elements hence present the combination of rotation around different pairs of axes. From diagonalising the inertia matrix, one can find the principle axes such that the off-diagonal elements become zero. The moment of inertia itself depends on the mass of the molecule and on the distance of the individual atoms to the centre of mass. For principle axes *a, b, c* this yields:

$$I_{rr} = \sum_{j=1}^{N} m_j r_j^2 \qquad \text{with } r = \{a, b, c\}, \tag{2.2}$$

where m_j is the mass of atom j and N is the total number of atoms. By introducing the angular momentum, $P_r = \omega_r\, I_{rr}$, the rotational energy can be written as

$$E_{\rm rot} = \frac{P_a^2}{2I_{aa}} + \frac{P_b^2}{2I_{bb}} + \frac{P_c^2}{2I_{cc}}. \tag{2.3}$$

Diatomic and linear molecules

In the simplest case of a diatomic (or linear) molecule, there is no rotation axis along the chemical bond ($P_a = 0$), hence, rotation only occurs around the axes perpendicular to it. In the centre-of-mass system one has $m_1 r_1 = m_2 r_2$ and $R = r_1 + r_2$. Rearranging and inserting these expressions in Eq. (2.2) yields

$$r_1 = \frac{m_2 R}{(m_1 + m_2)} \tag{2.4}$$

$$I_{rr} = m_1 r_1^2 + m_2 r_2^2 = \frac{m_1 m_2}{(m_1 + m_2)} R^2 = \mu R^2, \tag{2.5}$$

where μ is the reduced mass of the diatomic molecule. From the above considerations, it follows that $I_{bb} = I_{cc} \equiv I$ and the rotational energy becomes

$$E_{\rm rot} = \frac{1}{2I}(P_b^2 + P_c^2) \equiv \frac{P^2}{2I}, \tag{2.6}$$

where P is the total angular momentum. Because the energy levels are quantised, meaning that they possess specific energy values, one needs to invoke quantum theory to derive the separation between

the levels. Without going into detail, one exchanges P with its eigenvalues, which are expressed in terms of the rotational quantum number, J, as $\hbar^2 J(J+1)$ with $J = 0, 1, 2, \ldots$. This yields the rotational energy (in units of frequency)

$$\frac{E_{\rm rot}}{h} = \frac{h}{8\pi^2 I} J(J+1) \equiv BJ(J+1) \qquad \text{with } \hbar = \frac{h}{2\pi}, \tag{2.7}$$

where B is the rotational constant. Accordingly, the rotational energy level associated with $J = 0$ corresponds to the ground rotational state, the first rotationally excited state corresponds to $J = 1$ with an energy of $2B$ (in frequency units), and so on. This is schematically shown in Fig. 2.1b. A rotational transition (in a non-degenerate vibrational state) can only occur if the selection rule $\Delta J = \pm 1$ is fulfilled. The frequency, $\nu_{\rm rot}$, that is associated with a rotational transition from state $J+1$ to J then is

$$\frac{\Delta E_{\rm rot}}{h} = \nu_{\rm rot} = \nu_{J+1} - \nu_J = 2B(J+1). \tag{2.8}$$

Therefore, spectral lines resulting from $J+1 \rightarrow J$ rotational transitions are spaced in frequency by a factor $2B$ (see Fig. 2.1b). Since B depends on the moment of inertia, hence, on the mass of a molecule, this constant is characteristic of a species. This means that the frequencies of rotational transitions are specific to a molecule, which makes the observation of rotational spectra an excellent tool to identify molecules in space[1].

In reality, a molecule is not a rigid rotor and its rotation will lead to some distortion due to centrifugal forces. This centrifugal distortion effect can be treated by adding a second-order perturbation to Eq. (2.7), which will result in a shift of the energy levels with respect to the unperturbed ones. However, the contribution of this perturbation to the rotational energy is usually orders of magnitude smaller than that of the first term.

Symmetric and asymmetric top rotors

The above considerations get more complicated when a molecule contains more atoms and its structure is non-linear. For these molecules, rotation around all three principle axes has to be taken into account (see Eq. 2.3). However, the internal structure of some molecules exhibits some kind of symmetry such that two moments of inertia out of the three can take the same value. These molecules are referred to as symmetric top rotors. Assuming that the rotation axis, a, is the symmetry axis of the molecule and the total angular momentum is $P^2 = P_a^2 + P_b^2 + P_c^2 = P_a^2 + 2P_b^2$, its rotational energy levels can be written as

$$E_{\rm rot} = \frac{P_a^2}{2I_{aa}} + \frac{P_b^2}{I_{bb}} = \frac{P_a^2}{2I_{aa}} + \frac{P^2 - P_a^2}{2I_{bb}} = \frac{P^2}{2I_{bb}} + P_a^2 \left(\frac{1}{2I_{aa}} - \frac{1}{2I_{bb}} \right). \tag{2.9}$$

[1] Before molecules can be identified in space, they need to be synthesised and their rotational spectra studied in laboratories here on Earth. These laboratory experiments provide the exact frequencies of the transitions and other spectroscopic properties such as level energies or decay probabilities. The latter is described by the Einstein A coefficient (see Sect. 2.1.3) and depends on the dipole moment (see Eq. 2.29), which is derived either experimentally or theoretically. Spectroscopic properties of molecules are catalogued, for example, in the Cologne database for molecular spectroscopy (CDMS, Endres et al. 2016) or the Jet Propulsion Laboratory (JPL, Pearson et al. 2010) catalogue.

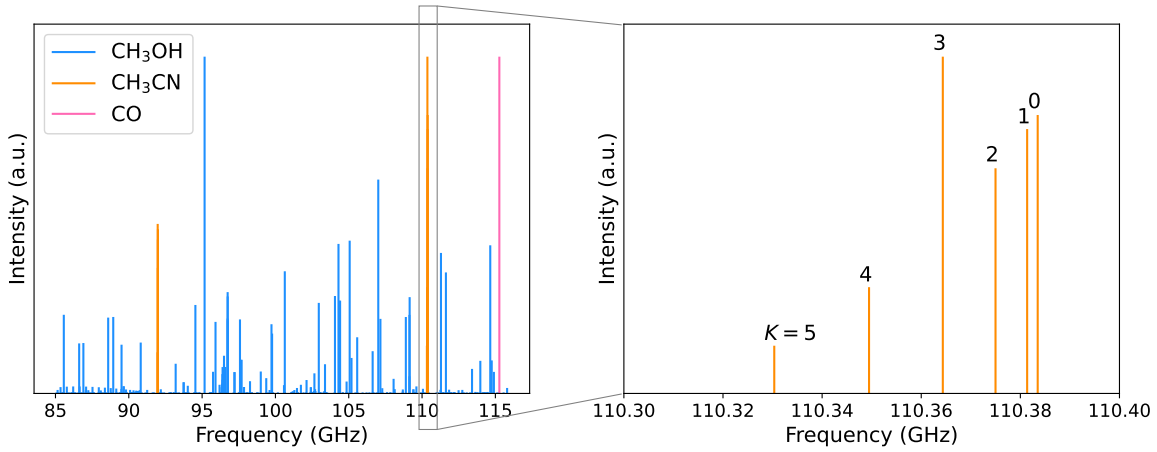

Figure 2.2: Rotational transitions in the 3 mm spectral window (*left*) of the diatomic molecule CO, symmetric top rotor CH_3CN (methyl cyanide), and asymmetric top rotor CH_3OH (methanol), and a zoom-in on the K structure of the $J = 6 - 5$ transition of CH_3CN (*right*). The intensities are given in arbitrary units (a.u.).

Substituting Eq. (2.9) with the eigenvalues from quantum theory, $P^2 \rightarrow \hbar^2 J(J+1)$ and $P_a^2 \rightarrow \hbar^2 J_A(J_A+1) \equiv \hbar^2 K^2$, yields the rotational energy levels (in units of frequency)

$$\frac{E_{\rm rot}}{h} = BJ(J+1) + K^2(A-B), \tag{2.10}$$

where A and B are the rotational constants associated with moments of inertia I_{aa} and I_{bb}, respectively. Centrifugal distortion effects have been neglected here. If $A > B$ the molecule is referred to as a prolate symmetric rotor, while if $A < B$, it is called an oblate symmetric rotor. According to Eq. (2.10), the energy levels of symmetric molecules are characterised by two quantum numbers, J and K, where $K = (0, 1, ..., J-1, J)$ for a given J. The selection rules for a rotational transition are $\Delta J = \pm 1$ and $\Delta K = 0$, hence, transitions for a given J can be expressed as $(J+1)_K \rightarrow J_K$.

Most non-linear molecules in interstellar space do not show any kind of symmetry such that $I_{aa} \neq I_{bb} \neq I_{cc}$. Then, all three moments of inertia contribute to the energy of a rotational level, which is characterised by three quantum numbers, J, K_{-1} and K_{+1}. A rotational level is written as $J_{K_{-1},K_{+1}}$, and rotational transitions have to obey $\Delta J = 0, \pm 1$. There are two rotational levels to each J and K_{-1} or K_{+1} (except for K_{-1} or $K_{+1} = 0$). The extent to which these levels differ in energy depends on the moments of inertia and on the values of J and K_{-1} or K_{+1}. The selection rules for K_{-1} and K_{+1} depend on the direction of the electric dipole moment.

Figure 2.2 gives an idea of how the rotational spectra of the diatomic molecule CO, the symmetric top rotor methyl cyanide (CH_3CN), and the asymmetric top rotor methanol (CH_3OH) can look like in the frequency range from 85 to 116 GHz, which is the range analysed in this thesis. The intensity scale is arbitrary. While only the $J = 1 - 0$ transition of CO is covered in this frequency range, for CH_3CN, transitions $J = 5_K - 4_K$ (with $K = 0 - 5$) and $6_K - 5_K$ (with $K = 0 - 6$) are available. The K structure for the latter transition is shown in a zoom-in in the right panel of Fig. 2.2. For methanol, numerous rotational transitions can be seen in this frequency range that do not show a specific pattern. There can be additional processes that complicate the rotational spectra of molecules, for example, fine- and hyperfine-splitting structure, which arise due to quantum-mechanical effects caused by a non-zero electronic and nuclear spin, respectively.

2.1.2 Radiative transfer equation

The specific (i.e. per unit frequency dν) intensity, I_ν, of an electromagnetic wave describes the energy per unit area, dA, unit time, dt, and unit solid angle, dΩ, hence, is given by

$$I_\nu = \frac{\mathrm{d}E}{\mathrm{d}\nu \mathrm{d}t \mathrm{d}A \mathrm{d}\Omega}. \tag{2.11}$$

As the radiation travels through space, it interacts with interstellar matter and its intensity gets altered due to emission, absorption, and scattering processes. The change in intensity along the pathway, s, due to absorption and emission (i.e. neglecting scattering) is described by

$$\mathrm{d}I_\nu = -\alpha_\nu I_\nu \mathrm{d}s + j_\nu \mathrm{d}s, \tag{2.12}$$

where the first term presents the net change due to absorption with attenuation coefficient, α_ν, and the second term is the net change due to emission with emissivity parameter, j_ν. Formalisms for these two coefficients are given in Sect. 2.1.3. The absorption capability of a medium is commonly expressed by the opacity or optical depth, τ_ν, such that

$$\tau_\nu = \int \alpha_\nu \mathrm{d}s. \tag{2.13}$$

A medium is said to be optically thin if $\tau_\nu << 1$, which means that all photons can escape. In an optically thick medium, where $\tau_\nu > 1$, photons can get re-absorbed and, hence, are trapped inside the medium. When inserting Eq. (2.13) in (2.12), one finds

$$\mathrm{d}I_\nu = -I_\nu \mathrm{d}\tau_\nu + S_\nu \mathrm{d}\tau_\nu, \tag{2.14}$$

where $S_\nu = \frac{j_\nu}{\alpha_\nu}$ is referred to as the source function. A general solution to this differential equation can be obtained by multiplying each side with a factor e^{τ_ν} and integrating from a starting point, where $\tau_\nu = 0$, to a certain depth into the cloud, where opacity has a value of τ_ν. This results in

$$\begin{aligned} \mathrm{e}^{\tau_\nu}\left(\mathrm{d}I_\nu + I_\nu \mathrm{d}\tau_\nu\right) &= \mathrm{d}\left(\mathrm{e}^{\tau_\nu} I_\nu\right) = \mathrm{e}^{\tau_\nu} S_\nu \mathrm{d}\tau_\nu \\ \Rightarrow I_\nu(\tau_\nu)\mathrm{e}^{\tau_\nu} - I_\nu(\tau_\nu = 0) &= \int_0^{\tau_\nu} S_\nu(\tau)\mathrm{e}^{\tau}\mathrm{d}\tau \\ \Rightarrow I_\nu(\tau_\nu) &= I_\nu(0)\mathrm{e}^{-\tau_\nu} + \int_0^{\tau_\nu} S_\nu(\tau)\mathrm{e}^{(\tau-\tau_\nu)}\mathrm{d}\tau. \end{aligned} \tag{2.15}$$

Assuming that the radiation field in a uniform medium has reached thermodynamic equilibrium, then $\mathrm{d}I_\nu = 0$ and hence, $I_\nu = S_\nu$. In these conditions the rate of absorption and emission processes must be balanced, following Kirchhoff's law of radiation. This behaviour describes a blackbody, whose intensity is given by the Planck function

$$B_\nu(T) = \frac{2h\nu^3}{c^2}\left[\exp\left(\frac{h\nu}{k_B T}\right) - 1\right]^{-1}, \tag{2.16}$$

where c is the speed of light, k_B the Boltzmann constant, and h the Planck constant. The intensity, $B_\nu(T)$, solely depends on the temperature of the medium, T (i.e. the excitation temperature, T_{ex}, as

will be defined in Sect. 2.1.3), not on its structure or composition. In this uniform medium, which is described with a single temperature, S_ν is independent of τ. The intensity of the background radiation, $I_\nu(0)$ at $\tau_\nu = 0$, is often assumed to originate from the cosmic microwave background (CMB), whose emission itself is described with a Planck function at $T_{\rm CMB} = 2.73$ K. Based on these considerations, Eq. (2.15) can be solved, resulting in

$$I_\nu = B_\nu(T_{\rm CMB})\mathrm{e}^{-\tau_\nu} + B_\nu(T)(1-\mathrm{e}^{-\tau_\nu}). \tag{2.17}$$

For observations at (sub)millimetre wavelengths, astronomers often express the intensity in units of a temperature. This is done by introducing the radiation or brightness temperature $J(T_B)$:

$$J(T_B)[\mathrm{K}] = \frac{c^2}{2k_B\nu^2}I_\nu = \frac{h\nu}{k_B}\left[\exp\left(\frac{h\nu}{k_B T_B}\right)-1\right]^{-1}, \tag{2.18}$$

which yields for Eq. (2.17)

$$J(T_B) = J(T_{\rm CMB})\mathrm{e}^{-\tau_\nu} + J(T)(1-\mathrm{e}^{-\tau_\nu}) \tag{2.19}$$

Typically the background emission is removed in radio-astronomical observations by performing 'on-off' observations, where the telescope is alternately pointed to the source (or 'on' position) and to a position that is free of emission from the source of interest (or 'off' position). The radiative transfer equation is then written as

$$\Delta J(T_B) = J(T_B) - J(T_{\rm CMB}) = [J(T) - J(T_{\rm CMB})](1-\mathrm{e}^{-\tau_\nu}). \tag{2.20}$$

2.1.3 Deriving column densities

Molecules can be excited and de-excited to certain energy levels via collisions and radiative processes. The latter include absorption as well as stimulated and spontaneous emission of a photon. Considering the simple case of a two-level system with an upper level u and a lower level l (see Fig. 2.3), which is exposed to a mean radiation field, $\bar{I}_\nu = \frac{1}{4\pi}\int I_\nu \mathrm{d}\Omega$, then, if the system is in statistical equilibrium (steady state), the number density of each population, n_i, is time-independent and it follows

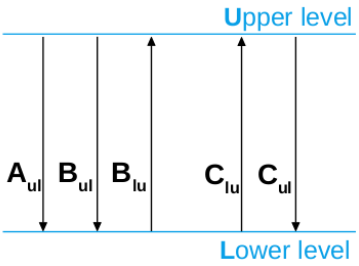

Figure 2.3: Sketch of radiative and collisional (de)population of a two-level system.

$$\frac{\mathrm{d}n_u}{\mathrm{d}t} = 0 = n_l\left(B_{lu}\bar{I}_\nu + C_{lu}n_{\rm c}\right) - n_u\left(A_{ul} + B_{ul}\bar{I}_\nu + C_{ul}n_{\rm c}\right), \tag{2.21}$$

which can be rewritten as

$$\underbrace{n_l B_{lu}\bar{I}_\nu}_{\text{(I)}} + \underbrace{n_l C_{lu}n_{\rm c}}_{\text{(II)}} = \underbrace{n_u A_{ul}}_{\text{(III)}} + \underbrace{n_u B_{ul}\bar{I}_\nu}_{\text{(IV)}} + \underbrace{n_u C_{ul}n_{\rm c}}_{\text{(V)}}, \tag{2.22}$$

where the individual terms present the following processes:

(I) Radiative excitation from l to u through absorption of a photon with a probability per unit time

of $B_{lu}\bar{I}_\nu$, where B_{lu} is the Einstein B coefficient for absorption,

(II) Collisional excitation from l to u with collisional rate coefficient, C_{lu}. This process depends on the abundance of the collision partner, n_c (essentially $n(\mathrm{H_2})$ in dense clouds),

(III) Radiative de-excitation from u to l through spontaneous emission of a photon, which occurs with a probability per unit time of A_{ul}, which is the Einstein A coefficient,

(IV) Radiative de-excitation from u to l through stimulated emission of a photon, which occurs with a probability per unit time of $B_{ul}\bar{I}_\nu$, where B_{ul} is the Einstein B coefficient for this process, and

(V) Collisional de-excitation from u to l with collisional rate coefficient, C_{ul}, which again depends on n_c.

The densities of the level populations $n_{u,l}$ can be related via the Boltzmann equation

$$\frac{n_u}{n_l} = \frac{g_u}{g_l}\exp\left(-\frac{h\nu}{k_B T_\mathrm{ex}}\right), \tag{2.23}$$

where $g_{u,l}$ are the statistical weights of levels u and l, respectively, $E_{ul} = h\nu$ with $\nu = \nu_{ul}$ is the energy separation between the two levels, and T_ex is the excitation temperature of the transition between levels l and u. The upwards collisional rate coefficient is linked to the downwards one via

$$\frac{C_{lu}}{C_{ul}} = \frac{g_u}{g_l}\exp\left(-\frac{h\nu}{k_B T_\mathrm{kin}}\right), \tag{2.24}$$

where T_gas is the gas or kinetic temperature that is associated with the collision partner.

Critical density

First, assuming that there is no external radiation field, that is neglecting terms (I) and (IV), and using the relation in Eq. (2.24), the rate equation (2.22) can be written as

$$n_l \frac{g_u}{g_l} C_{ul} n_\mathrm{c} \exp\left(-\frac{h\nu}{k_B T_\mathrm{kin}}\right) = n_u A_{ul} + n_u C_{ul} n_\mathrm{c}, \tag{2.25}$$

Solving this for the ratio of the level populations yields

$$\frac{n_u}{n_l} = \frac{g_u}{g_l}\exp\left(-\frac{h\nu}{k_B T_\mathrm{kin}}\right)\frac{1}{\frac{n_\mathrm{cr}}{n_\mathrm{c}} + 1} \qquad \text{with } n_\mathrm{cr} \equiv \frac{A_{ul}}{C_{ul}}, \tag{2.26}$$

where n_cr is the critical density, which is a characteristic density at which collisional de-excitation from level u to l can compete with the spontaneous radiative decay. Accordingly, if the density exceeds the critical value ($n_\mathrm{c} > n_\mathrm{cr}$), collisions dominate the de-excitation process and the term $(n_\mathrm{cr}/n_\mathrm{c} + 1)^{-1}$ tends towards 1. In this case, equalising Eq. (2.26) and (2.23) shows that T_kin tends towards T_ex, meaning that the level-population distribution is set by the local conditions of the gas that the molecule resides in. This defines the state of local thermodynamic equilibrium (LTE) and the level populations are said to be thermalised. On the other hand, if $n_\mathrm{c} < n_\mathrm{cr}$, radiative decay becomes important and levels are usually sub-thermally excited, where the population of levels is described by $T_\mathrm{ex} < T_\mathrm{kin}$. Usually, conditions of LTE are not achieved in the ISM, however, in this thesis, the closest vicinity of a protostar

is targeted, where densities are $\sim 10^7$ cm^{-3} (Bonfand et al. 2017) and thus, are high enough such that the assumption of LTE is valid. Also, the critical density as defined above represents only a rough estimate of the real value as it does not take into account the multilevel nature of molecules (or atoms) and the possible presence of an external radiation field. Moreover, it only applies to optically thin emission. Optically thick emission causes radiative trapping and there will be an effective critical density $n_{\mathrm{cr,eff}} \sim \frac{n_{\mathrm{cr}}}{\tau_\nu}$ (e.g. Sect. 2.6.1 in Elitzur 1992), where τ_ν is the peak line optical depth.

Einstein coefficients and optical depth

If one now assumes that only radiative processes take part in the (de-)population of levels, that is neglecting terms (II) and (V), one can work out the relations between the Einstein coefficients B_{lu}, B_{ul}, and A_{ul}. The mean specific intensity of the radiation field, $\bar{I}_\nu$, in LTE follows the Planck distribution in Eq. (2.16), which is isotropic. Using this, where $T_{\mathrm{ex}} \equiv T$, and Eq. (2.23), Eq. (2.22) can be written as

$$n_u \frac{g_l}{g_u} B_{lu} \left[1 - \exp\left(-\frac{h\nu}{k_B T}\right)\right]^{-1} = n_u A_{ul} \frac{c^2}{2h\nu^3} + n_u B_{ul} \left[\exp\left(\frac{h\nu}{k_B T}\right) - 1\right]^{-1}. \tag{2.27}$$

This needs to be true even in the extreme cases of $T \longrightarrow 0$ and $T \longrightarrow \infty$ and one finds

$$g_l B_{lu} = g_u B_{ul} = \frac{c^2}{2h\nu^3} g_u A_{ul}. \tag{2.28}$$

Therefore, B_{ul} and B_{lu} can be determined by knowing A_{ul} and the statistical weights, $g_{u,l}$. The Einstein A coefficient is computed using

$$A_{ul} = \frac{64\pi^4 \nu^3 \mu^2 S_{ul}}{3hc^3 g_u}, \tag{2.29}$$

where μ is the electric dipole moment to the transition and S_{ul} is the line strength. For example, for the transition $J+1 \longrightarrow J$ in a diatomic or linear molecule, $S_{ul} = J+1$ and $g_u = 2J+3$. The Einstein A coefficient can be looked up in tables of molecular databases (e.g. CDMS and JPL). Furthermore, the Einstein coefficients are used in the description of the absorption coefficient and emissivity, which were introduced in Sect. 2.1.2. For some randomised isotropic radiation, they are

$$j_\nu = \frac{h\nu}{4\pi} \Phi_\nu n_u A_{ul} \tag{2.30}$$

$$\alpha_\nu = \frac{h\nu}{4\pi} \Phi_\nu (n_l B_{lu} - n_u B_{ul}), \tag{2.31}$$

where Φ_ν describes the line profile, in other words, it is the probability to find photons within the frequency interval $[\nu, \nu + \mathrm{d}\nu]$ such that $\int \Phi_\nu \mathrm{d}\nu = 1$. Using the relations (2.23) and (2.28), the attenuation coefficient can be written as

$$\alpha_\nu = \frac{c^2 n_u A_{ul}}{8\pi\nu^2 \mathrm{d}\nu} \left[\exp\left(\frac{h\nu}{k_B T_{\mathrm{ex}}}\right) - 1\right], \tag{2.32}$$

where the line profile is approximated with $\Phi_\nu = {}^1/_{\mathrm{d}\nu}$ with a width of $\mathrm{d}\nu$. In Sect. 2.1.2, the optical depth, $\tau_\nu = \int \alpha_\nu \mathrm{d}s$, was introduced and can now be rearranged using Eq. (2.32). Introducing the

column density, $N_u = \int n_u \mathrm{d}s$, the optical depth becomes

$$\tau_\nu = \frac{c^2 A_{ul}}{8\pi\nu^2 \mathrm{d}\nu} \left[\exp\left(\frac{h\nu}{k_B T_{\mathrm{ex}}}\right) - 1\right] N_u. \tag{2.33}$$

Column density

Assuming that monochromatic radiation travels through an optically thin medium (i.e. $\tau_\nu << 1$), which has a temperature of T_{ex}, the radiative transfer equation in Eq. (2.19) simplifies to

$$J(T_B) = J(T_{\mathrm{ex}})\tau_\nu, \tag{2.34}$$

where the background radiation was neglected for simplicity. By inserting Eqs. (2.18) and (2.33), an expression for the column density of level u can be derived, which is

$$\begin{aligned} J(T_B) &= \frac{h\nu}{k_B}\left[\exp\left(\frac{h\nu}{k_B T_{\mathrm{ex}}}\right) - 1\right]^{-1} \frac{c^2 A_{ul}}{8\pi\nu^2 \mathrm{d}\nu}\left[\exp\left(\frac{h\nu}{k_B T_{\mathrm{ex}}}\right) - 1\right] N_u \\ \Rightarrow N_u &= \frac{8\pi k_B \nu \int J(T_B)\mathrm{d}\nu}{hc^2 A_{ul}}, \end{aligned} \tag{2.35}$$

where $\int J(T_B)\mathrm{d}\nu$ is the integrated intensity (in brightness temperature scale) in the interval $[\nu, \nu+\Delta\nu]$. Instead of a frequency interval, intensities are often rather integrated in the velocity regime, using the relation $\frac{\mathrm{d}\nu}{\nu} = -\frac{\mathrm{d}v}{c}$. In LTE, the upper-level column density of level u with energy, E_u, is related to the total column density, N_{tot}, as

$$\frac{N_u}{N_{\mathrm{tot}}} = \frac{g_u}{Q(T_{\mathrm{ex}})} \exp\left(-\frac{E_u}{k_B T_{\mathrm{ex}}}\right) \quad \text{with} \quad Q(T_{\mathrm{ex}}) = \sum_i g_i \exp\left(-\frac{E_i}{k_B T_{\mathrm{ex}}}\right), \tag{2.36}$$

where $Q(T_{\mathrm{ex}})$ is the partition function. Values of the partition function of a given species are tabulated as a function of temperature in molecular databases. Often the values need to be interpolated, sometimes extrapolated, for observed temperatures. Using Eqs. (2.35) and (2.36) one finds a relation between the observed intensity of a transition and the total column density of the molecule, which is

$$N_u = \frac{8\pi k_B \nu^2 J(T_B)\mathrm{d}v}{hc^3 A_{ul}} = \frac{g_u N_{\mathrm{tot}}}{Q(T_{\mathrm{ex}})} \exp\left(-\frac{E_u}{k_B T_{\mathrm{ex}}}\right). \tag{2.37}$$

This equation is the basis for a population-diagram analysis, which is used in this thesis and is introduced in detail in Sect. 2.3.3. Because this method uses rotational transitions, the partition function sums over all possible rotational levels, and, in LTE, all these levels are described with the same rotational temperature (i.e. $T_{\mathrm{rot}} \equiv T_{\mathrm{ex}}$).

In contrast, if the medium is optically thick ($\tau_\nu >> 1$), photons that are emitted inside the cloud are re-absorbed and are not able to leave the cloud. Therefore, the observed intensity from such a source originates only from the surface. This is also reflected in the radiative transfer equation (2.19), which can be approximated with $J(T_B) = J(T_{\mathrm{ex}})$ in this case. Column densities cannot be computed for optically thick emission. One needs to find optically thin proxies in order to do so. For example, this

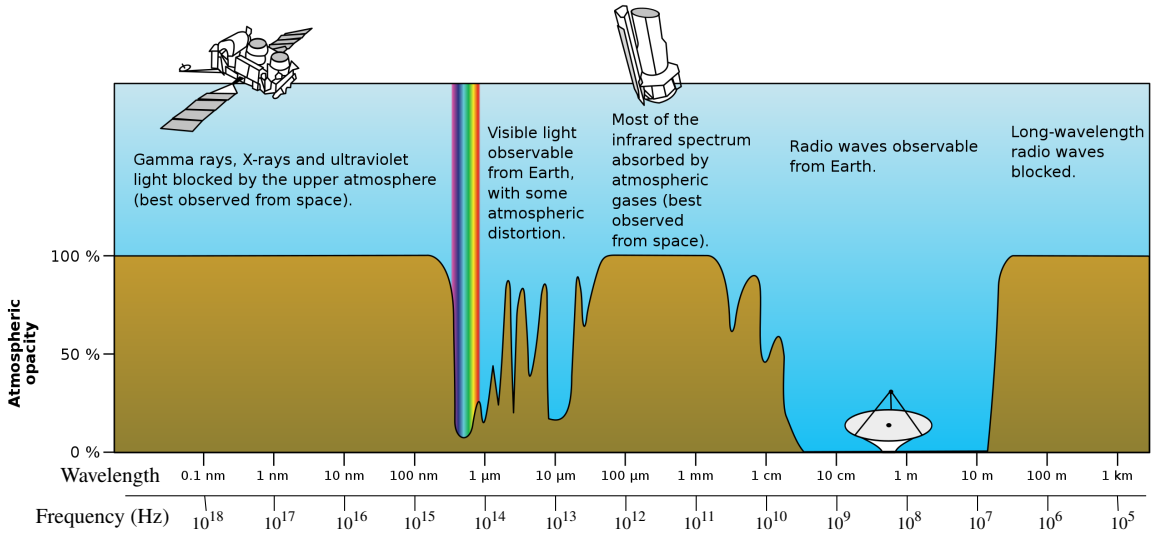

Figure 2.4: The atmospheric window showing how opaque the Earth's atmosphere is to radiation of a given wavelength. *Image credit: NASA/Public domain*.

is often the approach that is used to determine CO column densities. As the second most abundant molecule, emission from its main isotopologue, $^{12}C^{16}O$, is often optically thick. Instead, column densities are derived from $^{13}C^{16}O$ or $^{12}C^{18}O$, which are less abundant and thus, their emission is optically thin. If the isotopic ratios are known, the column densities of the rarer isotopologue can be converted to that of the main isotopologue.

2.2 Introduction to radio-astronomical observations

The opacity of the Earth's atmosphere to radiation depends on the wavelength. Figure 2.4 illustrates this behaviour. Accordingly, the atmosphere is completely opaque to all radiation with wavelengths shorter than a few hundred nanometres, that is, γ-rays, X-rays, and most of the UV (i.e. frequencies of $\nu \gtrsim 10^{15}$ Hz). Therefore, observations in this wavelength regime should be done with space stations. The same is true for large portions of the infrared regime from a few tens to hundreds of μm. Observations at optical wavelength can be performed with ground-based telescopes, so do observations in the radio window, which extends over a wavelength regime from a few millimetres to a few metres ($\sim 10^{10} - 10^{7}$ Hz).

Ground-based telescopes are also used for observations in the (sub-)millimetre wavelength regime ($\sim 10^{10} - 10^{11}$ Hz). Preferably, the telescopes that operate in this wavelength regime should be located at high altitudes and in low-humidity sites, such as the Atacama desert in Chile. This is because molecules in the atmosphere such as H_2O (water vapour) as well as O_2 and O_3 efficiently absorb the incoming radiation. The atmosphere does not only absorb radiation, it also contributes thermal noise to the observed data. The following sections do not go into detail on radio-astronomical observations, but rather provide a brief overview on fundamental parameters that play a role in the context of this thesis.

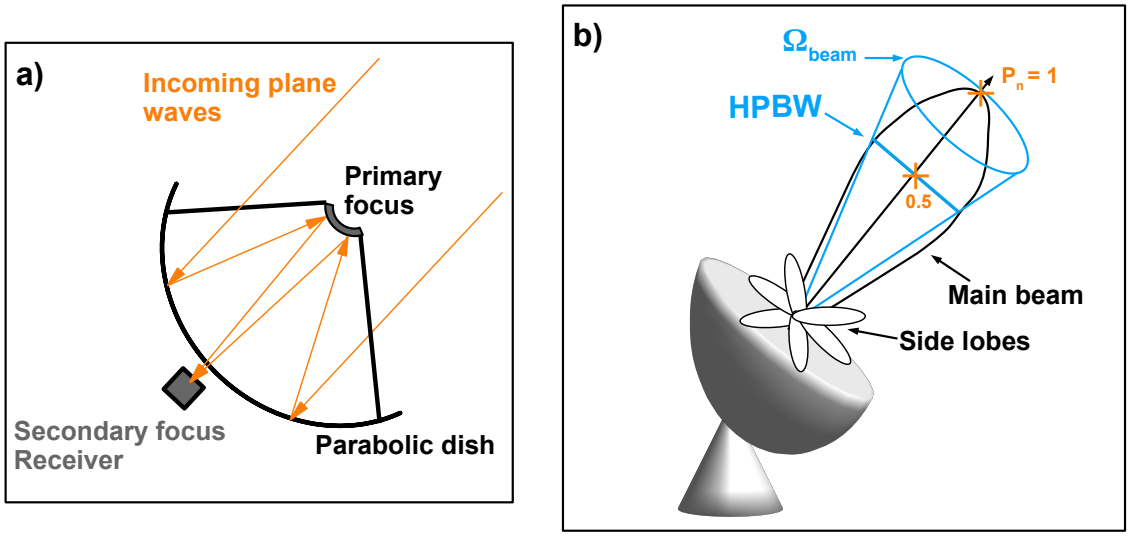

Figure 2.5: *Panel a:* Sketch of the pathway of incoming radiation (orange) to the receiver. *Panel b:* Sketch of the beam or power pattern of an antenna consisting of the main beam and side lobes. The main-beam solid angle, $\Omega_{\rm beam}$, and half-power beam width, HPBW (or $\theta_{\rm HPBW}$), are marked in blue.

2.2.1 Measuring radiation with a single antenna

Radio astronomy utilises parabolic shaped dishes to observe the faint radio signals coming from space. Because of the large distances to astronomical sources, the incoming electromagnetic waves can always be treated as planar. Figure 2.5a demonstrates the pathway of rays that are incident on the dish. They are reflected and re-directed to a primary focal point and further to a secondary focus, where a receiver detects the signal and processes it to a digital quantity. The power that is received by an antenna per frequency bandwidth, P_ν, corresponds to the sky brightness, I_ν, collected with an effective area, $A_{\rm eff}$, and over a solid angle, $\mathrm{d}\Omega_A$,

$$P_\nu = \frac{1}{2} A_{\rm eff} \iint I_\nu(\theta, \phi) \mathrm{d}\Omega_A. \tag{2.38}$$

The factor $\frac{1}{2}$ takes into account that only one polarisation of the typically unpolarised incoming radiation can be detected by the antenna. Although most of the power is directed to one focus point, which yields the main lobe or main beam, the antenna collects signals from all other angles, which creates additional side lobes. Radiation is directed to the side lobes, for example, due to surface inaccuracies of the dish or diffraction at the support legs that hold the instrumentation at the primary focus. This response behaviour of an antenna is described by the power pattern, $P_n(\theta, \phi)$ (the subscript n indicates that it is normalised to the peak of the response), which can be incorporated in the solid angle of the antenna as

$$\Omega_A = \iint_{4\pi} P_n(\theta, \phi) \mathrm{d}\Omega. \tag{2.39}$$

The normalised power pattern $P_n(\theta)$ of the main beam (also primary beam) can typically be approximated with a Gaussian distribution as

$$P_n(\theta) = \exp\left(-a\theta^2\right). \tag{2.40}$$

Introducing the half-power beam width, θ_{HPBW}, which marks the point at which the normalised signal drops to 0.5 (see also Fig. 2.5b), the factor a can be determined by

$$\frac{1}{2} = \exp\left(-a\frac{\theta_{\mathrm{HPBW}}^2}{4}\right) \quad \Longleftrightarrow \quad a = \frac{4\ln(2)}{\theta_{\mathrm{HPBW}}^2}. \tag{2.41}$$

Inserting this into Eq. (2.40), the solid angle of the main beam, Ω_{beam}, becomes (Condon & Ransom 2015)

$$\begin{aligned}\Omega_{\mathrm{beam}} &= \iint_{\mathrm{beam}} P_n(\theta)\mathrm{d}\Omega = 2\pi \int \exp\left(-\frac{4\ln(2)}{\theta_{\mathrm{HPBW}}^2}\theta^2\right)\theta\mathrm{d}\theta \quad \text{with } \sin\theta \approx \theta \\ &= \frac{\pi\theta_{\mathrm{HPBW}}^2}{4\ln(2)} \int_{y(0)}^{y(\theta_{\mathrm{max}})} \exp(-y)\,\mathrm{d}y \qquad \text{with } y = \frac{4\ln(2)}{\theta_{\mathrm{HPBW}}^2}\theta^2 \\ &\approx \frac{\pi\theta_{\mathrm{HPBW}}^2}{4\ln(2)},\end{aligned} \tag{2.42}$$

where it is approximated that if $\theta_{\mathrm{HPBW}} << \theta$, then $\exp(-y) \to 0$.

Typically the observed angular size, Ω_{obs}, of an extended astronomical source is also assumed to be represented by a Gaussian distribution (or a superposition of multiple ones). Taking advantage of the fact that the convolution of two Gaussian distributions is still a Gaussian, the actual size of the source, Ω_S, can be obtained by deconvolving, that is subtracting the beam from the observed distribution, such that $\Omega_S = \Omega_{\mathrm{obs}} - \Omega_{\mathrm{beam}}$. In order to convert the observed brightness to the true brightness of a source, one introduces the beam filling factor, B, which is

$$B = \frac{\Omega_S}{\Omega_{\mathrm{obs}}} = \frac{\theta_S^2}{\theta_S^2 + \theta_{\mathrm{HPBW}}^2}. \tag{2.43}$$

Accordingly, if the source size is of the order of the beam size or smaller, then, $B < 1$ and the true brightness temperature will actually be higher than the observed one. This effect is referred to as beam dilution. For sources that are much more extended than the beam, which are said to fill the beam, the beam filling factor approaches 1 and the observed brightness temperature corresponds to the brightness temperature of the source. The beam size, θ_{HPBW}, for a Gaussian beam corresponds to the angular resolution of the antenna, which characterises the smallest structures that the antenna is able to separate and depends on the diameter of the dish, D, and the observed wavelength, λ, as follows

$$\theta_{\mathrm{HPBW}} = \frac{k\lambda}{D}, \tag{2.44}$$

where k is a constant of order unity that depends on the illumination of the dish. This shows that for a fixed λ, the diameter has to be larger to achieve a higher resolution. However, a single-dish antenna

cannot be built arbitrarily large. Deformation through gravity and differential heating by the sun cause surface inaccuracy and lead to sensitivity loss. Therefore, to obtain higher angular resolutions, one has to use interferometers (see Sect. 2.2.2).

The quantity that is obtained from integrating the sky brightness towards an observed source convolved with the power pattern subtended by a solid angle is the flux density, F_ν (in units of $\mathrm{W\,m^{-2}\,Hz^{-1}}$),

$$F_\nu = \iint_{\mathrm{source}} I_\nu(\theta,\phi) P_n(\theta,\phi)\mathrm{d}\Omega. \tag{2.45}$$

Because radio-signals from astronomical sources are extremely weak, the unit Jansky [Jy] is commonly used (after Karl G. Jansky, the pioneer of radio astronomy), where $1\,\mathrm{Jy} = 10^{-26}\,\mathrm{W\,m^{-2}\,Hz^{-1}}$. Assuming that the main-beam solid angle can be expressed by using Eq. (2.42) and inserting Eq. (2.18) for I_ν, the flux density can be written as

$$F_\nu = I_\nu \Omega_{\mathrm{beam}} = \frac{2k_B\nu^2}{c^2} J(T_B)\frac{\pi\theta^2_{\mathrm{HPBW}}}{4\ln(2)}. \tag{2.46}$$

The sensitivity of radio-astronomical observations is expressed in terms of the root-mean-square, *rms* or σ, which describes the noise level delivered after a given time by the receiver that collects the signal transmitted by the antenna. This is computed using the radiometre formula (e.g. Klein 2006):

$$\sigma \propto \frac{T_{\mathrm{sys}}}{\sqrt{N}} = \frac{T_{\mathrm{sys}}}{\sqrt{t\Delta\nu}}, \tag{2.47}$$

where $N = t\Delta\nu$ is the number of measurements, t is the integration time that the telescope spent on the source, and $\Delta\nu$ is the spectral resolution that is proportional to the channel width of the receiver's frequency band. The system temperature, T_{sys}, combines all noise signals that have been collected by the antenna such that $T_{\mathrm{sys}} = \Delta T_{\mathrm{source}} + T_{\mathrm{rec}} + T_{\mathrm{atmo}} + T_{\mathrm{gr}} + \ldots$, where the first term corresponds to the noise coming from the source itself and the second to fourth terms present the contribution from the receiver system, Earth's atmosphere, and any emission or reflections from the ground, respectively. The signal-to-noise ratio, $S/N = \frac{J(T_B)}{\sigma}$, determines the significance of, for example, the detection or non-detection of a spectral line that originates from a molecular rotational transition. It is common to claim a detection when the observed peak intensity exceeds 3σ.

2.2.2 Interferometers

To achieve higher angular resolution in radio-astronomical observations, individual antennas can be combined to form an interferometer. The antennas are placed in a plane that is projected to the so-called (u, v) plane, which is perpendicular to the line of sight of the observed source, and describes the location of antennas at coordinates (u, v). The projected distances between these antennas are also called baselines. When pointing all antennas simultaneously to the same location in the sky, the power received at two antennas can be correlated, where the relative time delays of the incoming signals at antennas needs to be taken into account, also as the Earth rotates. Using the signals that were sampled in the (u, v) plane, the brightness distribution on the sky can be recovered by applying an inverse Fourier transform during the data-imaging process. As there is a limited number of antennas,

there will be gaps of signal in the (u, v) plane. Therefore, the true brightness distribution remains unknown, however, interpolating the sampled data in the imaging process fills the gaps to obtain a best-fit solution.

This observing technique always produces images or maps of sources, whose field of view is limited by the response pattern of the individual antennas and corresponds to the HPBW of the primary Gaussian-shaped beam, which is computed using Eq. (2.44). The HPBW of the beam that is synthesised during the imaging process from the data observed with all antennas corresponds to the actual angular resolution, which depends on the longest baseline between antenna pairs. In a first approximation, one can simply exchange in Eq. (2.44) the diameter of the single dish with the longest baseline, B_{max}. However, there will often only be a small number of antenna pairs (maybe only one) that cover this distance. Using the resulting beam size inevitably leads to a loss in sensitivity. Therefore, one would rather use an average value for the longest baseline, which is covered by more pairs of antennas. For example, it was found in simulations for the Atacama Large Millimetre/submillimetre Array (ALMA) that using the 80^{th} percentile projected baseline yields more robust values of angular resolution (see, e.g. Sect. 7.4 in the ALMA Partnership et al. 2016). When observing with an interferometre, there is not only a limit to the smallest distinguishable scales, but there is also a maximum largest scale that can be observed. This occurs due to the natural limit for the smallest baselines, physically, because of the diameter of the antenna dishes, and in projection due to shadowing, which occurs when a source is observed at low elevation above the horizon. Similar to the longest baselines, there may only be one pair of antennas covering the smallest baseline, hence, an average value for the smallest baseline should be used. In the case of ALMA, the 5^{th} percentile shortest baseline is best suited (Sect. 7.6 in the ALMA Partnership et al. 2016). Observed structures that extend over this 'maximum recoverable scale' cannot be seen by the interferometre and are filtered out. This effect is referred to as spatial filtering. The flux density that is lost in the process can be recovered, for example, by combining the interferometric data with single-dish observations, that are sensitive to the emission extending over larger scales. The sensitivity (in $\mathrm{Jy\,beam^{-1}}$) of an interferometric image (e.g. Wilson et al. 2008) obtained using N individual antennas is

$$\sigma_S = \frac{2k_B T_{\mathrm{sys}}}{A_{\mathrm{eff}}\sqrt{N(N-1)t\Delta\nu}}, \tag{2.48}$$

and, using Eq. (2.46), in units of temperatures

$$\sigma = \frac{\lambda^2 T_{\mathrm{sys}}}{A_{\mathrm{eff}}\Omega_{\mathrm{beam}}\sqrt{N(N-1)t\Delta\nu}}. \tag{2.49}$$

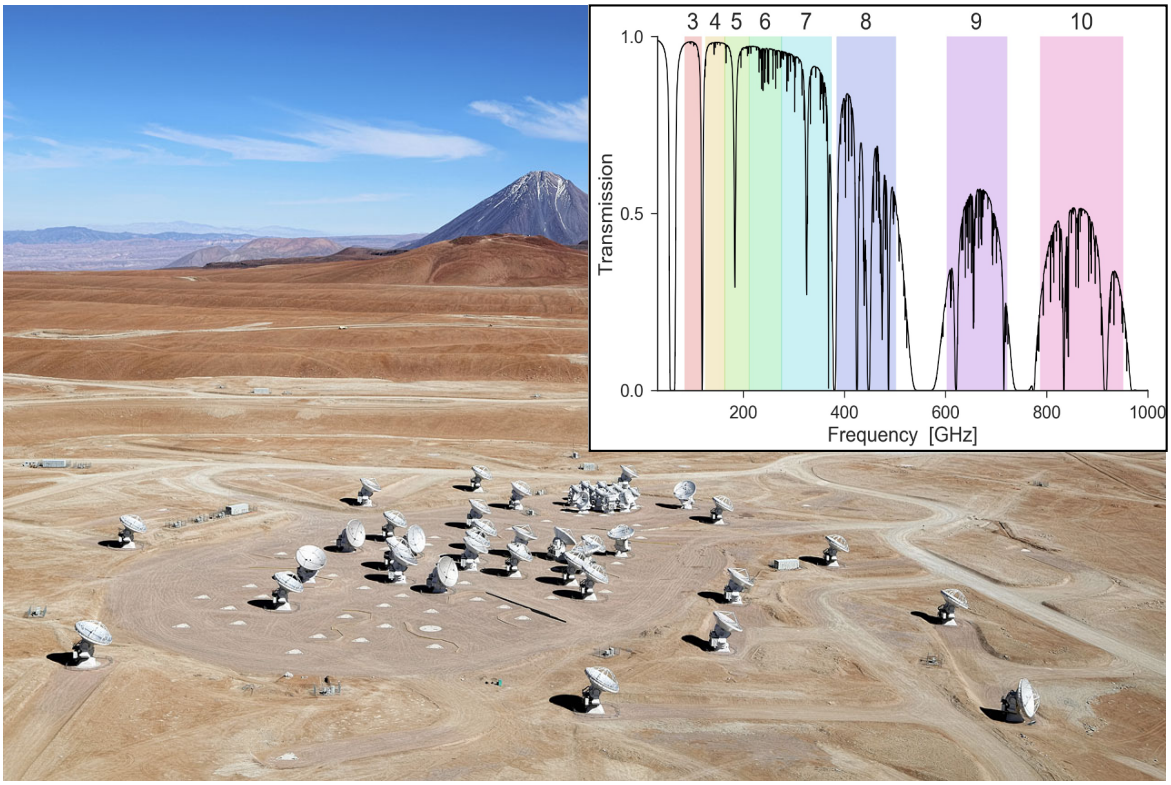

Figure 2.6: Some 12 m antennas of the ALMA interferometre from above. Also visible is the Atacama compact array (ACA), consisting of twelve closely spaced 7 m and four 12 m antennas used in single-dish mode. The top-right panel shows the atmospheric transmission windows and frequency bands used for observations at ALMA. *Image credit:Clem & Adri Bacri-Normier/ESO* and *ALMA/NRAO/Ke Zhang*.

2.3 The ReMoCA survey

Molecules rarely come alone. In particular, identifying and analysing the emission of COMs in hot cores (or corinos) is challenging as the observed spectra approach the confusion limit, meaning that there is line emission in nearly every frequency bin and spectral features of several species may be blended. To securely detect COMs and analyse their emission in these regions, we need unbiased line surveys over large frequency bands observed at high angular resolution and high sensitivity. All this is provided by ALMA, which was used for the observations of the imaging spectral-line survey ReMoCA, whose continuum and spectral-line data that were obtained in the course of these observations are analysed in this thesis. The following sections give an overview on the observing strategy of the survey, the structure of the obtained data, and methods of the data analysis.

2.3.1 Observations with ALMA

The ALMA interferometre is located in one of the driest places on Earth: the Atacama desert in the Chilean Andes at an altitude above 5000 m. The observatory is the result of an international

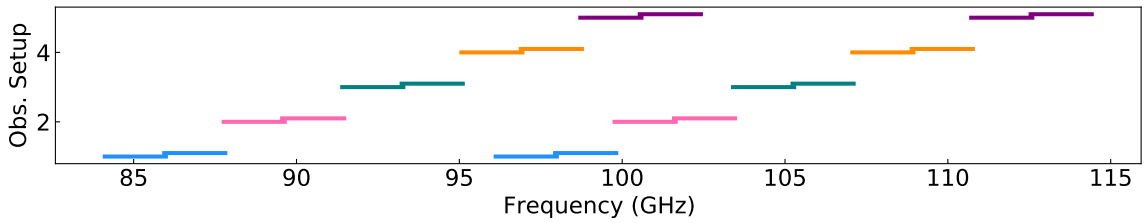

Figure 2.7: Observing strategy for the ReMoCA survey. Each color represents a different tuning. Each tuning provides four spectral windows covering 1.9 GHz each, two in the lower sideband and two in the upper sideband, as illustrated by the colored segments.

collaboration between countries in Europe, North America, East Asia, and the host country Chile. The interferometre consists of in total 66 antennas that can be moved to different positions to form different configurations. Of the 66 antennas, 16 antennas (twelve 7 m and four 12 m dishes) are closely spaced and belong to the Atacama compact array (ACA). The other 50 antennas, each of which having a diameter of 12 m, are spaced such that they cover a variety of baselines. The absolute minimum and maximum baselines that are currently available span 15 m and ~16 km, respectively. Different antenna configurations result in different angular resolutions. The highest resolution handed out by ALMA to date was 9 mas (milliarcseconds). Figure 2.6 shows some of the antennas from above, including the ACA, together with the magnificent landscape of the Chajnator plain in the Atacama desert. ALMA operates in certain frequency bands, which are adjusted to atmospheric windows where the transmission of the Earth's atmosphere allows for astronomical observations. The atmospheric windows are shown in the top-right panel of Fig. 2.6, together with the ALMA bands 3–10 in colour, which cover in total the frequency range from 84 to 950 GHz. For next year (2024), band 1 is expected to become operational, which will cover 35–50 GHz. As can be seen in Fig 2.6, the transmission for the lower frequency bands is quite high for the weather condition displayed here, while it degrades heavily for bands 8–10. Hence, observations at these frequencies require the best (driest) weather.

The ReMoCA survey was observed with the main ALMA array in observational cycle 4 (i.e. between October 2016 and July 2017). The antennas were pointed to the position $(\alpha, \delta)_{\mathrm{J2000}} = (17^{\mathrm{h}}47^{\mathrm{m}}19\overset{\mathrm{s}}{.}87, -28^{\circ}22'16\overset{''}{.}00)$ marking the phase centre of the observations. This position lies halfway between the main hot core Sgr B2 (N1) and the secondary hot core N2, which are separated by $4.9''$ (i.e. ~40 000 au or ~0.2 pc in projection). The survey covers nearly the entire ALMA band 3, precisely, frequencies from 84.1 GHz to 114.4 GHz. Due to the design of the receiver instrumentation, this frequency band cannot be observed at once. Instead, five individual frequency setups (S1–S5) were observed, where one setup covers two times ~4 GHz with a gap of 8.3 GHz in between them. This is shown in Fig. 2.7, where each colour represents one observational setup. Moreover, each setup is divided into four spectral windows (W0–W3) of 1875 MHz bandwidth, indicated with the increments in Fig. 2.7. Adjacent spectral windows overlap by 50 MHz to ensure a good data quality at the band edges. Each spectral window is divided into a number of channels originally separated by 244.141 kHz. During the post-processing of the data, this was smoothed to a lower number of channels separated by 488.3 kHz (or 1.3–1.7 $\mathrm{km\,s^{-1}}$ depending on the observed frequency). Further technical details on each observation run are listed in Table 1 in Belloche et al. (2019) and summarised below. Each observational setup was observed four times for 47–50 min each. During the observation period, there was a change in antenna configuration, such that the number of individual dishes and the

Table 2.1: Observational details of the ReMoCA survey (Belloche et al. 2019).

S[a]	W[b]	Frequency	Synthesised beam		rms[d]	
			($\theta_{\rm max} \times \theta_{\rm min}$)	PA[c]		
		(GHz)	($''\times''$)	(°)	mJy beam^{-1}	(K)
1	0	84.112–85.990	0.86×0.67	–84	0.98	0.29
	1	85.938–87.815	0.90×0.66	–87	0.94	0.26
	2	96.116–97.993	0.74×0.59	–84	0.92	0.27
	3	97.941–99.818	0.72×0.57	–86	0.94	0.29
2	0	87.763–89.640	0.85×0.62	87	1.02	0.30
	1	89.588–91.465	0.93×0.61	83	1.05	0.28
	2	99.766–101.643	0.72×0.60	83	0.82	0.23
	3	101.591–103.468	0.72×0.62	66	0.74	0.19
3	0	91.403–93.280	0.70×0.62	89	0.85	0.28
	1	93.228–95.105	0.69×0.59	–86	0.81	0.27
	2	103.405–105.282	0.63×0.53	–85	0.87	0.29
	3	105.230–107.107	0.61×0.52	–86	0.92	0.31
4	0	95.062–96.939	0.57×0.46	–53	0.39	0.20
	1	96.887–98.764	0.56×0.45	–53	0.39	0.20
	2	107.064–108.942	0.51×0.41	–54	0.43	0.22
	3	108.890–110.767	0.50×0.40	–54	0.45	0.23
5	0	98.714–100.591	0.43×0.30	–78	0.69	0.66
	1	100.539–102.417	0.42×0.29	–78	0.68	0.66
	2	110.717–112.594	0.39×0.26	–77	0.81	0.78
	3	112.542–114.419	0.38×0.25	–77	0.95	0.90

Notes. [a] Setup. [b] Spectral window. [c] Position angle. [d] Median rms noise level measured in the channel maps of the continuum-removed data cubes.

individual baselines were different for setups 1–3 and 4–5. Both antenna configurations counted about 40–46 antennas, there can be variations when some antennas were not available for various reasons. The resulting baselines are between ~15 and 1100 m for setups 1–3 and between ~17 and 3600 m for setups 4–5. Hence, the observations are sensitive to scales up to a few arcseconds (cf. Tables 7.1 and 7.2 in ALMA Partnership et al. 2016) and down to half an arcsecond on average (see below and Table 2.1). The calibration, deconvolution, and imaging of the observed data were not part of the thesis, but were performed previously. Details on these procedures can be found in Belloche et al. (2019).

The final data were stored in 20 individual three-dimensional data cubes, one for each spectral window. Figure 2.8 illustrates the structure of such a data cube with two position axes and one spectral axis. The position axes are subdivided into a number of pixels, whose sizes depend on the angular resolution and are thus larger for observational setups 1–3 ($\sim 0.12'' \times 0.12''$) than for setups 4–5 ($\sim 0.06'' \times 0.06''$). The spectral axis can interchangeably be expressed in units of velocity, v, or

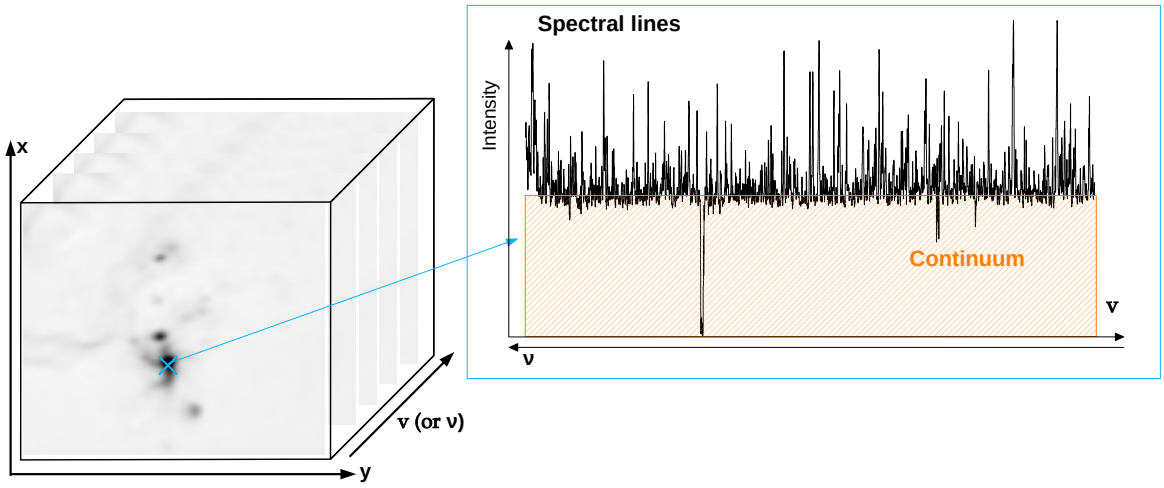

Figure 2.8: Sketch of the data structure obtained for ReMoCA. The data comes in three-dimensional cubes *(left)* that consist of two position axes (i.e coordinates) and one spectral axis (i.e. frequency ν or velocity v). The observed spectra *(right)* show spectral-line features as well as continuum emission.

frequency, ν, according to the relation

$$\frac{\Delta\nu}{\nu_{\rm ref}} = \frac{\nu - \nu_{\rm ref}}{\nu_{\rm ref}} = -\frac{\Delta v}{c}, \tag{2.50}$$

where $\nu_{\rm ref}$ is the frequency at a given reference channel, where $v = 0$ km s^{-1}. On the one hand, this data structure allows to extract a spectrum at a given position (or pixel) to study the flux density across the frequency band. On the other hand, by taking one spectral channel per pixel, a channel map can be constructed, with which the spatial distribution of the flux density in the observed field of view at a given frequency can be studied. One may also add up several channels to derive integrated intensity maps (see Sect. 2.3.3). Table 2.1 summarises some of the technical details of each spectral window, which include the exact range of covered frequencies, the beam sizes synthesised from the interferometric data, and median noise levels of the spectral (i.e. continuum-subtracted) data cubes. The synthesised beams have the shape of a 2D elliptical Gaussian, with a minor and a major axis, $\theta_{\rm min}$ and $\theta_{\rm maj}$ (or HPBW$_{\rm min,maj}$), respectively, with the major axis rotated by a position angle (here defined east from north). The mean synthesised beam ($HPBW$, or mean angular resolution) is given by the geometrical mean, $\sqrt{\theta_{\rm min} \times \theta_{\rm maj}}$. The reduced data cubes contain both the continuum emission and the spectral line features as can be seen in the spectrum in Fig. 2.8. To properly analyse both, they have to be separated. For the ReMoCA survey, a constant value was assumed for the continuum emission in each spectral window in each pixel that was then subtracted from the observed flux densities. This process is also referred to as baseline subtraction. The observed continuum flux density can vary between the spectral windows for a given position as it depends on frequency and angular resolution, which becomes evident in the next section. The flux densities of the data cubes are given in units of Jy beam^{-1} and can be converted to Kelvin using the relation in Eq. (2.46).

2.3.2 Analysing continuum data

Because H_2 is the most abundant species in molecular clouds, cloud properties such as their density or mass are inferred from the H_2 column densities. However, observing H_2 is challenging as it is a symmetric molecule and, thus, possesses no electric dipole moment that would result in rotational transitions in the (sub)mm wavelength regime. The molecule can undergo rotational transitions, however, as these have a quadrupolar origin, they are extremely faint. In order to still derive H_2 column densities, $N(H_2)$, and determine the cloud properties, other proxies are observed. One widely used tracer for H_2 column densities is the continuum emission from dust grains[2]. Dust grains are emitters of thermal radiation, hence, their flux density distribution can be described with a Planck function, $B_\nu(T_d)$, at a dust temperature, T_d. Then, the observed flux (in Jy beam^{-1}) at frequency, ν, is determined using the radiative transfer equation (cf. Eq. 2.19)

$$S_\nu^{\rm beam} = \Omega_{\rm beam} B_\nu(T_d)(1 - {\rm e}^{-\tau}), \tag{2.51}$$

assuming that $T_d >> T_{\rm CMB} = 2.73$ K and hence, that the background CMB radiation can be neglected. The grain temperature is set by the radiative energy balance (e.g. Tielens 2005), which states that the emitted and absorbed energies, in terms of photons, are equal. This entails a number of dependencies for T_d on, for example, the external radiation field and the efficiency at which photons are absorbed and emitted, which in turn depends on the grain size and composition. However, thanks to the high densities in Sgr B2 (N1), two assumptions can be made: that the dust is well coupled with the gas, such that $T_d \approx T_{\rm gas}$, and that LTE can be applied, such that $T_{\rm gas} = T_{\rm rot}$, meaning that the dust temperature can be approximated with the rotational temperature, $T_{\rm rot}$, derived from molecular line emission. The derivation of $T_{\rm rot}$ is explained in Sect. 2.3.3. As will be seen, values of $T_{\rm rot}$ typically exceed 100 K, hence, neglecting $T_{\rm CMB}$ in Eq. (2.51) is applicable.

Rearranging Eq. (2.51) results in an expression for the dust opacity, $\tau = \tau_\nu$, which is

$$\tau = -\ln\left(1 - \frac{S_\nu^{\rm beam}}{\Omega_{\rm beam} B_\nu(T_d)}\right). \tag{2.52}$$

The general description of the opacity is given in Eq. (2.13). For dust emission, the optical depth is regarded as a function of dust mass opacity, κ_ν [cm^2 g^{-1}], instead of the attenuation coefficient, α_ν [cm^{-1}], such that $\tau = \int \alpha_\nu {\rm d}s = \int \kappa_\nu \rho_{\rm D} {\rm d}s$, where $\rho_{\rm D}$ is the mass density of the dust grains. The dust mass opacity can be computed using a power law (e.g. Erickson et al. 1981; Tielens 2005)

$$\kappa_\nu = \kappa_0 \left(\frac{\nu}{\nu_0}\right)^\beta, \tag{2.53}$$

where κ_0 is a reference value at frequency ν_0 and β is the emissivity spectral index of the dust. An appropriate reference value, $\kappa_0(\nu_0)$, can be taken from experimental or numerical studies that investigated the frequency dependence of κ_ν for different grain compositions (e.g. Ossenkopf & Henning 1994; Demyk et al. 2014). The emissivity spectral index can be computed using observations of the dust emission at two frequencies (see below).

[2] Another widely-used tracer is CO. The molecule's integrated intensity is commonly converted to $N(H_2)$ by assuming a constant CO–to–H_2 conversion factor (see Bolatto et al. 2013, and references therein). In the course of this thesis, emission from the optically thin isotopologue $C^{18}O$ is used, besides the dust emission, to derive H_2 column densities.

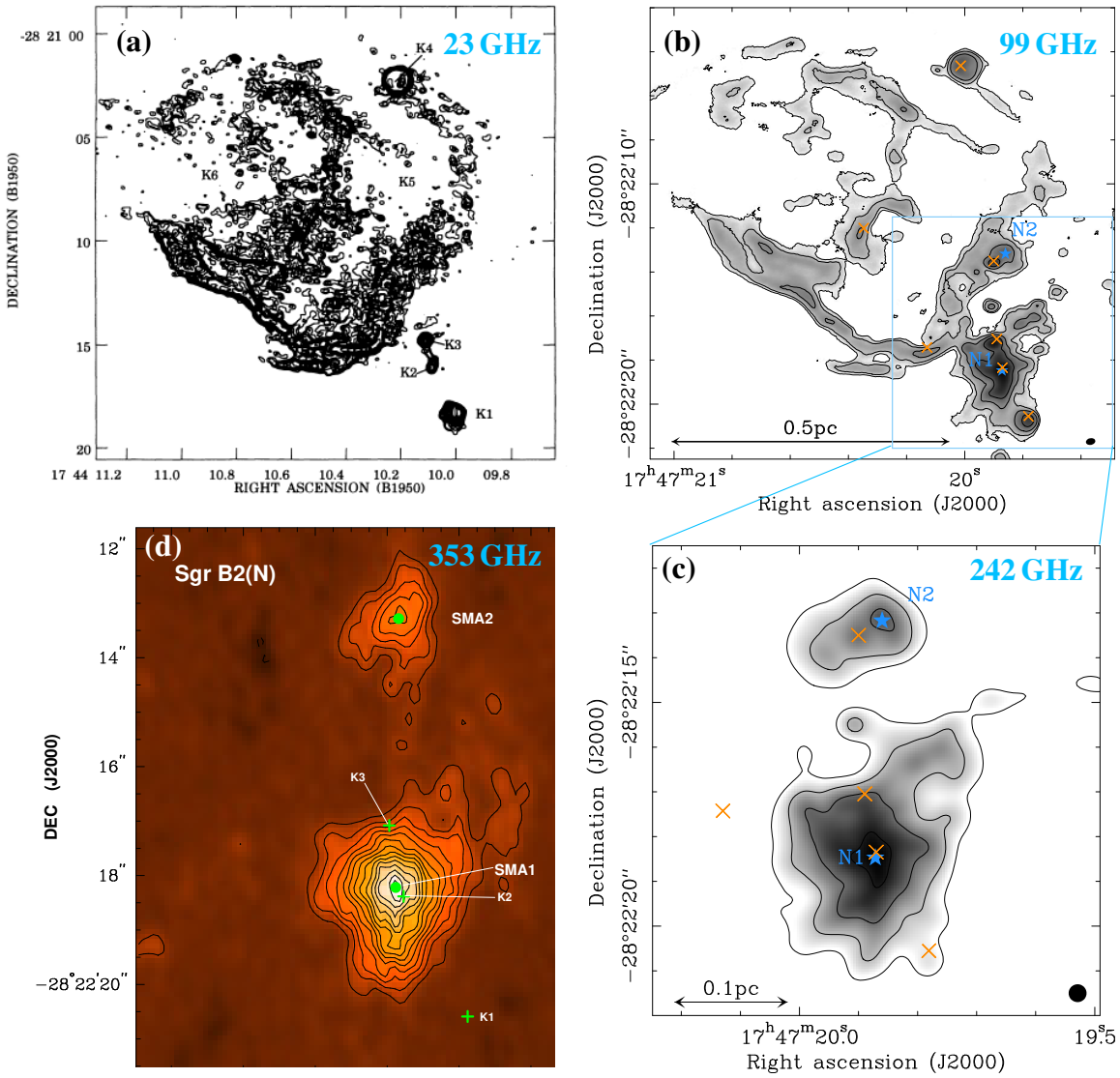

Figure 2.9: Multi-frequency view of Sgr B2 (N): *Panel a:* Continuum map at 23 GHz (1.3 cm, taken from Gaume et al. 1995) shows the free-free emission from the HII regions K1–K6. *Panel b:* Continuum map at 99 GHz (3 mm) extracted from the ReMoCA survey presents a mixture of the free-free emission from HII regions (orange crosses) with dust emission from mainly the hot cores N1 and N2. *Panel c:* Continuum map at 242 GHz (~1.3 mm, Sánchez-Monge et al. 2017) is dominated by the dust emission, but some free-free emission (e.g. for K1) is still observed. *Panel d:* Continuum map at 352 GHz (850 μm, taken from Qin et al. 2011) shows the dust emission towards SMA1 (or N1) and SMA2 (or N2). Panels a–b and c–d show roughly the same field of view, respectively.

Assuming that the H_2 column density, $N(H_2)$, is related to the dust column density, N_D, via a constant proportionality factor, C, one finds

$$\begin{aligned} \int n(\mathrm{H_2})\mathrm{d}s &= C \int n_\mathrm{D}\mathrm{d}s \\ \frac{M_\mathrm{gas}}{\mu_{\mathrm{H_2}} m_\mathrm{H} V} &= C\,\frac{M_\mathrm{D}}{m_\mathrm{D} V} = C\,\frac{\chi M_\mathrm{gas}}{m_\mathrm{D} V} \\ \Rightarrow C &= \frac{m_\mathrm{D}}{\chi \mu_{\mathrm{H_2}} m_\mathrm{H}}, \end{aligned} \tag{2.54}$$

where n is the volume density of either component, m is the mass of the H atom or the mean mass of a single dust grain, $\mu_{\mathrm{H_2}} = 2.8$ is the mean molecular weight (Kauffmann et al. 2008), and M the total mass of H_2 (or the gas) and dust, respectively, in the same volume, V. As standard, the gas-to-dust ratio, χ, is assumed to be 100. The H_2 column density can then be computed with

$$\begin{aligned} N(\mathrm{H_2}) &= \frac{m_\mathrm{D}}{\chi \mu_{\mathrm{H_2}} m_\mathrm{H}} N_\mathrm{D} \\ &= \frac{\tau}{\chi \mu_{\mathrm{H_2}} m_\mathrm{H} \kappa_\nu} \qquad \text{with } m_\mathrm{D} N_\mathrm{D} = m_\mathrm{D} \int n_\mathrm{D}\mathrm{d}s = \int \rho_\mathrm{D}\mathrm{d}s = \frac{\tau}{\kappa_\nu}, \end{aligned} \tag{2.55}$$

where τ is derived from the observed flux with Eq. (2.52) and κ_ν with Eq. (2.53) such that

$$N(\mathrm{H_2}) = \frac{1}{\chi \mu_{\mathrm{H_2}} m_\mathrm{H}} \times -\ln\left(1 - \frac{S_\nu^\mathrm{beam}}{\Omega_\mathrm{beam} B_\nu(T_d)}\right) \times \frac{1}{\kappa_0}\left(\frac{\nu}{\nu_0}\right)^{-\beta}. \tag{2.56}$$

Using Eq. (2.56) at two frequencies, ν_1 and ν_2, taking the ratio of the two equations, and rearranging it, one obtains the dust emissivity spectral index, β,

$$\beta = \ln\left\{\ln\left(1 - \frac{S_{\nu_2}}{\Omega_{\mathrm{beam},2} B_{\nu_2}(T_d)}\right) \times \left[\ln\left(1 - \frac{S_{\nu_1}}{\Omega_{\mathrm{beam},1} B_{\nu_1}(T_d)}\right)\right]^{-1}\right\} \times \frac{1}{\ln\left(\frac{\nu_2}{\nu_1}\right)}. \tag{2.57}$$

Although thermal emission from dust largely contributes to the continuum emission observed towards Sgr B2 (N) at the frequencies covered by the ReMoCA survey, it is not the only contributor, as demonstrated in Fig. 2.9, where continuum maps at four frequencies towards the source are presented. At the lowest frequency (23 GHz, Fig. 2.9a), the continuum map, taken from Gaume et al. (1995), shows the distribution of the free-free emission that originates from thermal plasma in HII regions. Accordingly, Sgr B2 (N) contains multiple compact HII regions (e.g. K1–K4) but also an extremely spatially extended one (K6). Conversely, at the highest frequency (353 GHz, Fig. 2.9d, taken from Qin et al. (2011)), the contribution of free-free emission drops to zero and is dominated by the thermal emission from dust grains associated with the dense cores Sgr B2 (N1) (or SMA1) and N2 (or SMA2). Panels (b) and (c) of Fig. 2.3.2 show continuum maps at intermediate frequencies, where Fig. 2.9b (99 GHz) was extracted from the ReMoCA survey and the data for the map at 242 GHz was taken from Sánchez-Monge et al. (2017). This implies that the continuum emission towards Sgr B2 (N) as observed by ReMoCA in the 3 mm spectral window is a mixture of both thermal dust emission and free-free emission stemming from the HII regions. At 242 GHz, dust emission dominates, however,

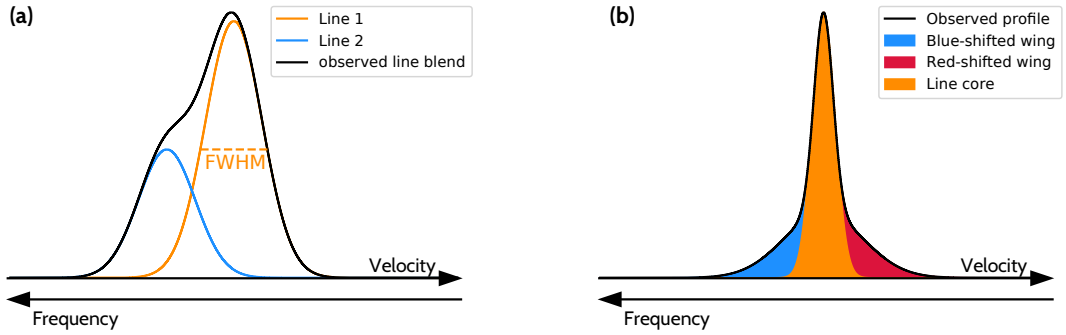

Figure 2.10: Sketch of possible reasons for deviations from Gaussian line profiles showing *a)* blending of two lines potentially coming from two different molecules and *b)* line wings that indicate the presence of additional blue- and red-shifted emission (e.g. from an outflow).

some minor contribution from free-free emission (e.g. at K1) is still evident. Regions, in which emission of either origin dominates, can be identified by computing the spectral index, α (not to be confused with the attenuation coefficient, α_ν), which is defined as $S_\nu \propto \nu^\alpha$, from the observed total fluxes at two different frequencies. In the course of project 1, a spectral-index map for the region of Sgr B2 (N1) was derived using the continuum maps shown in Fig. 2.9b and c. For optically thin emission, Eq. (2.51) can be approximated as $S_\nu \propto B_\nu(T)\tau$, which depends on frequency as follows

$$B_\nu(T)\tau \propto \begin{cases} \nu^2 \nu^\beta = \nu^{2+\beta}, & \text{for dust emission} \\ \nu^2 \nu^{-2.1} = \nu^{-0.1}, & \text{for free-free emission (e.g. Mezger \& Henderson 1967).} \end{cases} \tag{2.58}$$

For optically thick emission, it is $S_\nu \propto B_\nu \propto \nu^2$ in either case, and in some regions a mixture of both can be expected. Values of β in dense cores are expected to range from $\lesssim$1 to 2 (e.g. Kwon et al. 2009; Schnee et al. 2009), which means that $\alpha = 2 + \beta \sim 2.5 - 4$ for optically thin dust emission.

2.3.3 Analysing spectral line data

As described in Sect. 2.1.1, the (rotational) transitions are unique identifiers of the molecule that emits them as they are observed at specific frequencies. Although discrete, the spectral lines have a natural line width, which is the consequence of the energy uncertainty in the level populations due to their finite lifetime, according to Heisenberg's uncertainty principle. The lines are additionally broadened as the molecules are typically in motion. This velocity dispersion depends on the temperature and density of the gas and could additionally be influenced by turbulence, for example. Typically, the observed line profile can be well approximated by a one-dimensional Gaussian distribution as

$$\Phi_v = A_0 \exp\left(-\frac{(v - v_{\rm sys})^2}{2\sigma_v^2}\right) \qquad \text{with } \Delta v_{\rm FWHM} = \sqrt{8\ln 2}\,\sigma_v, \tag{2.59}$$

where A_0 is the amplitude, $v_{\rm sys}$ is the systemic or line-of-sight velocity of the cloud in which the molecules reside, and σ_v the one-dimensional velocity dispersion, which is related to the observed

width (i.e. full width at half maximum, Δv_{FWHM}) of the spectral line. Naturally, a non-zero systemic velocity (Doppler) shifts the spectral lines away from their rest frequencies (according to Eq. 2.50) to lower or higher values depending on whether the observed cloud moves away from or towards us, respectively.

In a chemically rich source such as Sgr B2 (N1), the observed spectral features can deviate from a Gaussian distribution due to several reasons. Figure 2.10 depicts two possible reasons, where in panel (a) the observed feature is a blend of two or more spectral lines originating from the same or from different molecules. Especially in the second project of this thesis that concerns the molecular emission associated with the protostellar outflow of Sgr B2 (N1), profiles such as that shown in panel (b) are commonly seen. Outflow emission is typically observed at higher absolute velocities than the source itself, which manifests in line wings at red- and blue-shifted velocities relative to the systemic velocity of the line core that, in this case, is associated with emission from the hot core itself. The true observed spectral lines towards positions that show outflow emission can be more complicated than what is shown in Fig. 2.10b. For example, instead of the wings there often are additional velocity components that have Gaussian-like line profiles and can be treated as individual emission lines. Another effect that results in deviation from Gaussian profiles is presented in high line optical depth. Because the probability of absorption of a photon is higher closer to the systemic velocity, the line gets saturated or self-absorbed.

The first step in the analysis of this kind of data is the assignment of spectral lines to a molecule. This was done with the help of radiative transfer models, with which synthetic spectra of a molecule can be computed. In addition to identifying molecules, the modelled spectra ultimately provide a number of properties of the molecule and of the region from which the emission originates. The results obtained from the models were verified with a population-diagram analysis. In addition, the spatial extent and the overall morphology of molecular emission was investigated based on integrated intensity maps. All these steps are explained in detail in the following.

Integrated intensity maps

The advantage of having a 3D data cube is that the molecular emission can be mapped. Usually, this is done by simply integrating the emission over the spectral line, that is adding up the intensity in each channel that covers the line and multiplying by the channel width (in $\mathrm{km\,s^{-1}}$), at each position (or pixel) of the map. In a source such as Sgr B2 (N1), this is not as easily done. The average systemic velocity of the hot core is assumed to be $v = 62\ \mathrm{km\,s^{-1}}$ in this thesis. However, observed molecular lines show that there is a velocity gradient, with velocities ranging from ~55 to 75 $\mathrm{km\,s^{-1}}$. Similarly, there are differences in the FHWM of spectral lines over the same region, where lines can be as narrow as 3 $\mathrm{km\,s^{-1}}$ and as broad as ~10 $\mathrm{km\,s^{-1}}$ (cf. Fig. B.2 in Busch et al. 2022). During the second project, the outflow emission at red- and blue-shifted velocities, was mapped as well. Because a larger velocity interval needs to be included in the integration, in this case, it is likely that contaminating emission from other molecules may be unintentionally considered as well, which biases the emission maps. When deriving integrated intensity maps in the course of this thesis, these problems are taken care of as well as possible. The exact integration strategies are explained in detail in the respective publications.

Radiative transfer modelling

In order to assign spectral lines to a certain molecule and derive the molecule's column density, the software Weeds (Maret et al. 2011) was used, which is an extension of the GILDAS/CLASS software[3] developed by IRAM (Institut de radioastronomie millimétrique) for the purpose of spectral-line analysis. Weeds basically solves the radiative transfer equation and determines level populations based on a handful of input parameters. The radiative transfer equation is similar to Eq. (2.19), but has an extra term that takes into account an additional component of continuum emission, $J(T_{\rm cont})$. Usually, this corresponds to the dust emission that is associated with the source of the molecular line emission. Specifically for the analysis done as part of this thesis, the values of the baselines that were subtracted from the spectral-line data were used as $J(T_{\rm cont})$ for a given position and spectral window. This does only work as long as the dust emission is optically thin, since $J(T_{\rm cont})$ is treated separately from the line emission as another background source in Weeds. The radiative transfer equation can then be written as

$$J(T_B) = [J(T_{\rm ex}) - J(T_{\rm CMB})](1 - \mathrm{e}^{-\tau_\nu}) + J(T_{\rm cont})\mathrm{e}^{-\tau_\nu}. \tag{2.60}$$

By rearranging, one finds the formalism that is used by Weeds to compute a spectrum for one component with an arbitrary beam filling factor, B, which is

$$J(T_B) = J(T_{\rm cont}) + B[J(T_{\rm ex}) - J(T_{\rm CMB}) - J(T_{\rm cont})](1 - \mathrm{e}^{-\tau_\nu}) \tag{2.61}$$

Hence, the output spectrum essentially comprises two terms: the background continuum, which is assumed to be optically thin and spatially extended, and the spectral-line emission. The actual output spectrum that is stored in a variable by Weeds is continuum-subtracted. In order to solve Eq. (2.61), the brightness temperature has to be derived, which is done by using the expression of the optical depth from Eq. (2.33) and the relation between upper-level and total column density from Eq. (2.37). This yields

$$\tau_\nu = \frac{c^2 A_{ul}}{8\pi\nu^2}\Phi_\nu \frac{g_u N_{\rm tot}}{Q(T_{\rm rot})}\left[\exp\left(\frac{h\nu}{k_B T_{\rm rot}}\right) - 1\right]\exp\left(-\frac{E_u}{k_B T_{\rm rot}}\right). \tag{2.62}$$

The parameters that are specific to each transition of a given molecule (ν, A_{ul}, and g_u) are taken from a database, widely from the CDMS or the JPL catalogue. If the value for the partition function at $T_{\rm rot}$ does not exist in the database, an extra- or interpolation of the existing data is performed by Weeds. The total column density of the molecule, $N_{\rm tot}$, the rotational temperature $T_{\rm rot}$, and dv in terms of the width (FWHM) of the lines are provided by the user. The two remaining user-chosen input parameters are the angular size of the emitting region, based on which the beam filling factor is computed for the given beam size, and the source velocity, which is where the spectral lines have their peak intensity and which is needed to visualise the modelled spectrum correctly. This last parameter and the FWHM of the spectral lines are typically determined based on the observed lines by fitting 1D Gaussian profiles to them, provided the observed lines are neither blended with other lines nor optically thick. As mentioned in Sect. 2.2.1, the angular size of the observed emitting region is typically assumed to have a 2D Gaussian distribution. However, the molecular emission observed towards Sgr B2 (N1) reveals a lot of structure with extended and more compact emission superimposed. For the greatest

[3] https://iram.fr/IRAMFR/GILDAS/

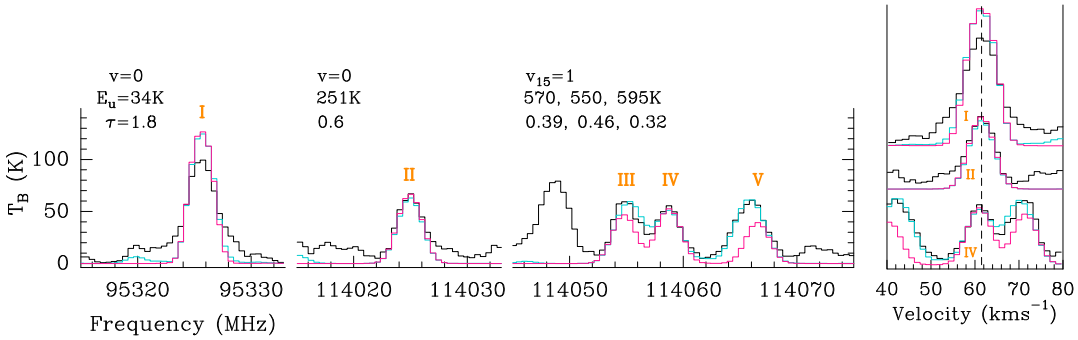

Figure 2.11: Some observed rotational transitions (I)–(V) of C_2H_3CN in vibrational states $v = 0$ (ground state) and $v_{15} = 1$ extracted from the ReMoCA survey at one position (black) and shown as a function of frequency (*left*) and velocity (*right*). The pink spectrum corresponds to the Weeds model for this molecule at this position and blue indicates the model that contains all here identified molecules. The upper-level energies of the transitions and their peak opacities computed by Weeds are given below the vibrational state. The black dashed line marks the systemic velocity used for the model.

parts the emission is extended, meaning that it fills the beam, therefore, the beam filling factor was assumed to be unity, by assuming a source size of $2''$ in all instances. Starting from an educated guess as an input for the column density and rotational temperature, based on values from other molecules or from previous studies, the values were iterated based on the results from the population diagrams (see below). The optimisation of these two parameters were however made by visually inspecting the observed and synthetic spectra, thereby, making sure that the model does not overestimate any of the molecule's observed transitions. A molecule is said to be detected when there are at least a handful of unblended lines (the more the better) above a threshold of 3σ, where σ is the noise level in the whole spectrum (see Table 2.1). For each molecule (of a selection of molecules) and each vibrational state, for which rotational transitions were detected, one Weeds model was derived. The input parameters for each vibrational state are allowed to differ in theory, however, in the analysis here, the same values were found to fit well the rotational spectra of all vibrational states of a molecule. The individual models of all molecules were subsequently linearly added to construct a complete Weeds model, which helps to identify blended lines and determine the individual contributions of different transitions. Simply adding up the spectra is correct only if all transitions are optically thin. In addition to the synthesised spectrum, Weeds also provides the opacity for each transition that is computed from the given set of input parameters.

An example of a Weeds model is shown in Fig. 2.11. In black are parts of an observed spectrum extracted from the ReMoCA survey at one position. Pink shows the derived Weeds model for C_2H_3CN and blue the complete Weeds model of all molecules identified at this position (incl. the pink model). It is evident that the model for line (I) overestimates the observed intensity, indicating that T_{ex} is not uniform along the line of sight (as is assumed in Eq. (2.61)). Instead, there are two or more gas components at different T_{ex} captured in the beam towards this position. For line (II) the model matches well the observed spectrum. For the last three spectral lines (III)–(V), the blue model is a good match of the observed spectrum between 114.052–114.069 GHz and shows that C_2H_3CN is not the only molecule contributing to the observed spectral features, but there are contributions from at least one other identified molecule. Peak line opacities for each transition provided by Weeds are displayed in Fig. 2.11 and reveal that all transitions, except for line (I), are moderately optically thin ($\tau < 1$). The right panel shows essentially the same as the left panel, but instead of frequencies, velocities are

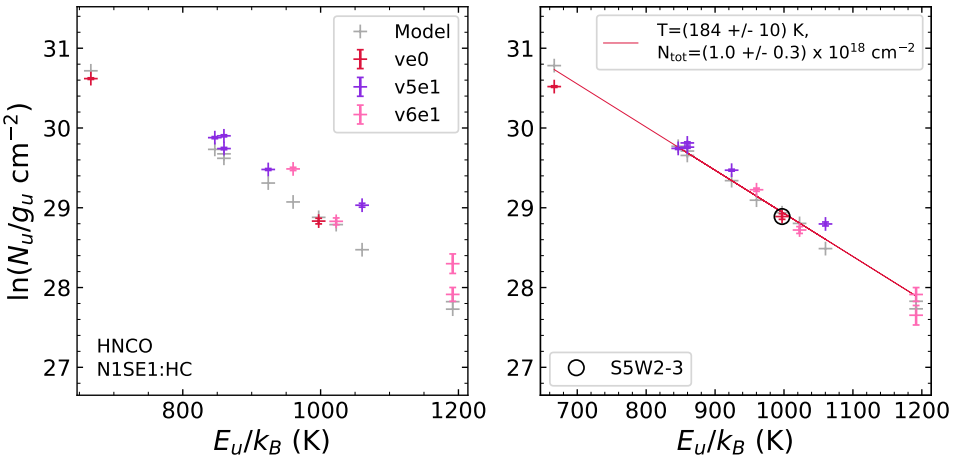

Figure 2.12: One example of a population diagram for HNCO, taken from Paper II. Observed data points are shown in various colours as indicated in the top-right corner of the left panel, while synthetic data points are shown in grey. The *left diagram* contains the original entries, while in the *right diagram* corrections for opacity and contamination by other molecules have been considered for both the observed and synthetic populations. The red line is a linear fit to all observed data points (in linear-logarithmic space). The result of the fit is shown in the top-right corner of the right panel. The black circle indicates an observed data point from spectral windows 2–3 of observational setup 5 (the rest is from setup 4).

shown on the x axis. The black dashed line indicates the source or systemic velocity that was used for the Weeds model of this molecule at this position.

Population diagrams

By rearranging Eq. (2.37), one finds the formalism on which population diagrams are based (Goldsmith & Langer 1999; Mangum & Shirley 2015)

$$\ln\left(\frac{N_u}{g_u}\right) = \ln\left(\frac{N_{\rm tot}}{Q(T_{\rm rot})}\right) - \frac{E_u}{k_B T_{\rm rot}} \tag{2.63}$$

The known parameters in this equation are E_u for each transition of a molecule, g_u, and N_u. The latter is computed from integrating intensities over the whole spectral line according to Eq. (2.37). Plotting the left-hand side of Eq. (2.63) against the upper-level energy $\frac{E_u}{k_B}$ (in units of K), the data points should lie on a straight line if LTE was applicable and hence, $T_{\rm rot}$ was the same for all transitions. Then, the rotational temperature can be determined from the slope of a linear fit to the data points. In addition, using the value of $T_{\rm rot}$, one can compute the partition function, Q, and obtain the total column density, $N_{\rm tot}$, for the molecule from the y intercept of the linear fit.

As an example, Fig. 2.12 shows one of the population diagrams that will be published in Paper II (cf. Ch. 4). In both panels, the entries from the observations are shown in various colours, where each colour represents one vibrational state. The entries from the model are indicated in grey. The left panel shows the original data, while two correction factors were applied to the observed and modelled entries in the right plot. The first correction factor concerns the line optical depth. As briefly mentioned in Sect. 2.1.3, high opacities prevent us from deriving the column density in the whole cloud, because radiation is only received from a certain depth within a cloud. In the worst case, only

the surface radiation is detected. However, if the opacity is moderate, it is possible to correct for it. Neglecting any background emission, the radiative transfer equation can be written as

$$J(T_B) = J(T_{\rm rot})(1 - {\rm e}^{-\tau_\nu}) = J(T_{\rm rot})\frac{1 - {\rm e}^{-\tau_\nu}}{\tau_\nu}\tau_\nu = J_{\rm thin}(T_B)\frac{1 - {\rm e}^{-\tau_\nu}}{\tau_\nu}, \tag{2.64}$$

where $J_{\rm thin}(T_B)$ is the simplification of the radiative transfer equation in the case of an optically thin transition (Eq. 2.34). Accordingly, multiplying the observed intensity $J(T_B)$ that suffers from optical depth with the correction factor $\frac{\tau_\nu}{1-{\rm e}^{-\tau_\nu}}$ yields the intensity expected in the optically thin case (Goldsmith & Langer 1999; Mangum & Shirley 2015). As mentioned above, Weeds computes the optical depth for each transition, which is used to determine the respective correction factor. However, when τ exceeds a certain value, the observed spectral lines can deviate greatly from the expected Gaussian distribution in a way, that Weeds is no longer able to predict the true intensity of the transition. Then, the correction factor will most likely be underestimated, and so will be the observed data point in the population diagrams. This likely applies to the entry at lowest upper-level energy in Fig. 2.12, where the observed entry is below the modelled one, suggesting that the transition is optically thick and that the correction factor cannot totally account for the missing intensity. In practice, those transitions, for which Weeds computes opacities of $\tau_\nu \gtrsim 2 - 3$, are not taken into account in the population diagram of the respective molecule. If they were considered, the slope of the linear fit would be underestimated, hence, the temperature overestimated.

The observed spectra towards Sgr B2 (N1) are full of emission lines (see, e.g. the spectrum in Fig. 2.8). Hence, the probability that two or more transitions from different molecules overlay or blend is high. Blended lines can obviously not be used to derive a population diagram of the molecule, as the value of integrated intensity would be overestimated. Only if the amount of contaminating emission is known, it can be subtracted from the value of integrated intensity. This can be done by using the complete Weeds model that combines all the individual models from identified molecules. In this way, for example, line (V) in Fig. 2.11 can be included to the analysis, because the molecule(s) and its contribution to the emission seen at this frequency is known. This can only work if all transitions that contribute to the line are optically thin. Comparing the two diagrams in Fig. 2.12, it is evident that this correction was significant for the transition at E_u ~1050 K (purple) and one transition at ~1900 K, for example.

This method of data analysis has a few disadvantages compared to the radiative transfer modelling. For example, in the latter the dust continuum emission is taken into account, which is not done and cannot properly be done in the formalism of the population diagram. In addition, the two corrections that are applied to the entries in the population diagrams depend on the output Weeds model. Therefore, larger weight is put onto the results obtained from the Weeds models in the course of this thesis. Another correction factor that is applied to the final column densities obtained from both methods takes into account contributions of vibrational states that are not considered in the partition functions provided by the databases, but that are populated at the high temperatures derived towards Sgr B2 (N1). The general expression for the correction factor, $C_{\rm vib}$, is given by (e.g. Endres et al. 2016)

$$C_{\rm vib} = \prod_i \left[1 - \exp\left(\frac{-E_{{\rm vib},i}}{k_B T_{\rm rot}}\right)\right]^{-1}, \tag{2.65}$$

which is the product over all known vibrational modes i.

3

Resolving desorption of complex organic molecules in a hot core

This chapter provides a summary on the first publication that is associated with this thesis:

'Resolving desorption of complex organic molecules in a hot core: Transition from non-thermal to thermal desorption or two-step thermal desorption?'

Laura A. Busch[1], Arnaud Belloche[1], Robin T. Garrod[2], Holger S. P. Müller[3], Karl M. Menten[1]

[1] Max-Planck-Institut für Radioastronomie, Auf dem Hügel 69, 53121 Bonn, Germany

[2] Departments of Chemistry and Astronomy, University of Virginia, Charlottesville, VA 22904, USA

[3] I. Physikalisches Institut, Universität zu Köln, Zülpicher Str. 77, 50937 Köln, Germany

Astronomy & Astrophysics, 2022, 665, A96, DOI: 10.1051/0004-6361/202243383

The article can be found in its entirety in Appendix A.
Author contribution: LB carried out the analysis of the continuum and spectral-line data, including the radiative transfer modelling of the spectra and the derivation of the population diagrams. The interpretation of the results was done by LB, AB, and RG. A first draft of the article, including all figures (except for Fig. D.3, which was provided by RG) and tables, was written by LB and the manuscript was edited by LB, AB, and RG. HM contributed the text for Appendix A. All co-authors have reviewed the paper as well as an anonymous A&A referee.

Introduction

As described in detail in Sect. 1.5, the main goal of this first project was to find observational evidence for the thermal desorption of COMs and whether it happens alongside water, along with other objectives that concern the formation and destruction processes of COMs. To tackle this task, data that were obtained as part of the imaging spectral-line survey ReMoCA, which was introduced in Sect. 2.3, were analysed. The survey targeted the whole Sgr B2 (N) region (see Sect. 1.4.2), however, this project focussed on the main, most massive hot core Sgr B2 (N1), mainly because the COM emission is spatially very extended and well resolved thanks to ReMoCA's high angular resolution.

Morphology of continuum and COM emission

First, the continuum emission was investigated. As described in detail in Sect. 2.3.2, the continuum emission at 3 mm is a combination of free-free emission that originates from HII regions and dust emission. This was demonstrated in the article by visually comparing a continuum map extracted from the ReMoCA data at 99.2 GHz with a map at 242 GHz, which was published by Sánchez-Monge et al. (2017). The mix of dust and free-free emission was further quantified by computing a spectral-index map. The spectral-line analysis started with an inspection of the morphology of the molecular emission. For this purpose linewidth- and velocity-corrected integrated emission (LVINE) maps were computed. The LVINE method is an extension of the VINE method (Calcutt et al. 2018), which, in addition to velocity gradients, takes into account variations of the line widths across the mapped region when integrating intensities at each pixel of the map. LVINE maps have been computed for six O-bearing COMs, including the ^{13}C isotopologue of methanol (CH_3OH), seven N-bearing species, of which six are COMs, and three molecules that contain both N and O, including two COMs. The analysis of the morphology of these maps showed that the molecules fall into two (maybe three) main groups, which are illustrated in Fig. 3.1a. This figure shows that most O-bearing COMs have extended and structured emission (dark blue contour), while most N-bearing COMs have a more compact morphology. The emission of some of the N- and (N+O)-bearing molecules is more structured (light blue contour), while others have a smoother distribution of emission (pink contour). Based on these maps, the selection of positions was done at which temperatures and molecular abundances were subsequently derived. The centre of the hot core ($r < 0.5''$) could not be analysed because of the high optical depth of the dust continuum that obscures the line emission. Starting from a radius of ~$0.5''$ from the centre of the hot core, twelve positions to the south and ten positions to the west in intervals of $0.3''-0.5''$ were selected.

Profiles of COM abundance and rotational temperature and their implications

At each of these position, the spectrum of each selected COM was modelled with Weeds and population diagrams were derived as explained in Sect. 2.3.3, from which rotational temperatures and column densities were obtained. The set of molecules that we analysed consists of ten COMs: those listed in Fig. 3.1 and $^{13}CH_3OH$. They were selected based on their number of bright spectral lines available in the ReMoCA data.

The resulting spatially resolved profiles of rotational temperature reveal a linear dependence with distance to the centre of Sgr B2 (N1) in a log-log plot. The power-law indices range from −0.4 to −0.8, which is similar to other sources (e.g. Beltrán et al. 2018; Gieser et al. 2021) and can be expected for a collapsing envelope heated internally by a young stellar object (e.g. Kenyon et al. 1993). The column densities were converted to abundances with respect to CH_3OH and H_2, where the H_2 column densities were derived from the dust continuum emission and from emission of the lowest J–rotational transition 1–0 of $C^{18}O$ as described in Sect. 2.3.2. The spatially resolved gas-phase abundance profiles were investigated as a function of distance and rotational temperature for each COM. In particular, the observed trends as a function of temperature were then used to compare with predictions of state-of-the-art astrochemical models (see Sect. 1.2.3 for a brief introduction to such models) that were performed by Robin Garrod and published in Garrod et al. (2022). In general, these abundance profiles can be divided into three temperature regimes, which is schematically shown in Fig. 3.1b:

(I) Most profiles show a steep increase in abundance over multiple orders of magnitude at around

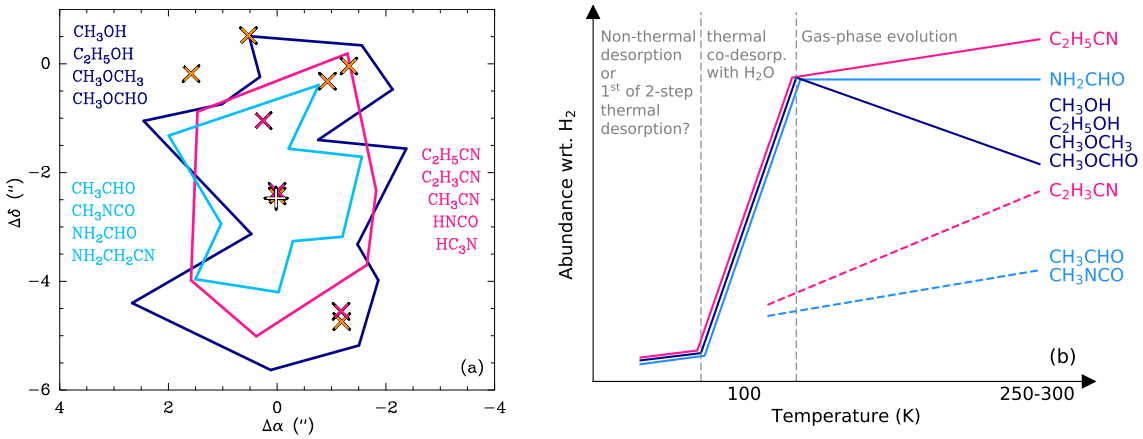

Figure 3.1: This figure corresponds to Fig. 15 in Busch et al. (2022). *Panel a:* Sketch of the three different types of morphology observed in LVINE maps of molecules. The molecules, COMs and simpler ones, that show the respective morphology are listed in the colour of the contour. The markers indicate locations of additional continuum sources. The position offsets are given with respect to the ReMoCA phase centre. *Panel b:* Schematic overview of the observed COM abundance profiles as a function of temperature and their interpretation (see (I)–(III) in the main text). The colours are the same as in (a), connecting the abundance profile of a COM to its observed emission morphology. Solid and dashed lines of a given colour indicate a similar morphology but different types of abundance profile.

100 K, suggesting that the bulk of these COMs desorbs thermally at this temperature from the dust grains to the gas phase. Because this steep rise is observed at roughly the same temperature, the desorption of COMs likely happens alongside water and does not depend on the binding energy of the COMs to the dust-grain surfaces. This is in good agreement with the predictions of the models and indirectly suggests that diffusion of species in the ice mantles of dust grains is not efficient.

(II) At higher temperatures (i.e. shorter distance to the hot-core centre), the abundance profiles either decrease (pointing to the destruction of the molecule in the gas phase), increase (pointing to further production in the gas phase), or show a plateau. The behaviour of each species is compared in detail to its model predictions in Sect. 4.4 in the article.

(III) The non-zero abundance values observed for some COMs at temperatures below ~100 K suggest that a different desorption process is at work. We proposed that COMs may be released from the grains through non-thermal processes, such as chemical desorption, interaction with cosmic rays, or turbulence. Another thermal desorption process at lower temperatures is however not excluded, for example, due to reduced binding energies of COMs in CO-dominated ice layers. Before the onset of the protostellar heating during the gravitational collapse of the cloud, the temperature can drop below 15–20 K. At these temperatures CO freezes out from the gas phase onto the dust-grain surfaces. As the environment starts heating up, due to the birth of the protostar, COMs that reside in these outermost CO-rich ice layers may be able to desorb at temperatures below 100 K. The bulk of the COM would remain trapped in the water-rich ice layers underneath.

Based on both the above qualitative comparison between observed and modelled abundance profiles and another quantitative comparison between modelled and observed peak abundances, a detailed discussion was done on possible formation and destruction processes for each individual COM. If differences between the models and the observations are identified for a given species, this may indicate that its chemical network used by the models is not complete. In these cases, alternative ways are discussed in the article that may reduce the difference if they are included to the network. Additionally, the possible influence of the physical conditions and their (spatial) variations (e.g. density, cosmic-ray flux, warm-up timescale) in Sgr B2 (N1), which may differ from the assumptions made in the models, on the formation and destruction of molecules was discussed. Ultimately, the relative molecular abundances derived at each position in Sgr B2 (N1) and differences between the gas molecular compositions at each position can, to a great extent, be traced back to the (presumably) dominant formation and destruction pathways of the individual COMs. However, as mentioned above, the efficiency for some of these pathways that lead to this conclusion still require confirmation by the astrochemical models, as they are not included yet. At last, we investigated whether the binding energy has any minor influence on the desorption process of the COMs, however, no convincing correlations were found.

In conclusion, this article presents the first spatially resolved study of the COM desorption process in a star-forming region. The abundance profiles and the peak abundances, which were taken from these profiles, in comparison with the models provide useful information on the formation and destruction processes of COMs that can be used to update astrochemical models, in particular, regarding their underlying chemical networks of COMs, and to better understand chemical segregation between species or groups of species (e.g. O- and N-bearing molecules) that has previously been observed and studied in other sources.

4

The impact of Sgr B2 (N1)'s outflow on the chemistry in the hot core

This chapter consists of the current version of the following manuscript (excluding the Overview), which has been submitted to A&A and is currently in the second reviewing phase. The numbering of sections and figures is adjusted to this thesis and thus deviates from the original manuscript. Same applies to the corresponding appendix, which can be found in Appendix B.

'Shocking Sgr B2 (N1) with its own outflow: A new perspective on segregation of O- and N-bearing molecules'

Laura A. Busch[1], Arnaud Belloche[1], Robin T. Garrod[2], Holger S. P. Müller[3], Karl M. Menten[1]

[1] Max-Planck-Institut für Radioastronomie, Auf dem Hügel 69, 53121 Bonn, Germany

[2] Departments of Chemistry and Astronomy, University of Virginia, Charlottesville, VA 22904, USA

[3] I. Physikalisches Institut, Universität zu Köln, Zülpicher Str. 77, 50937 Köln, Germany

Astronomy & Astrophysics, 2023, under review

Author contribution: LB carried out the analysis of the spectral-line data, including the radiative transfer modelling of the spectra and the derivation of the population diagrams. The interpretation of the results was done by LB, AB, and RG. A first draft of the article, including all figures (except for Fig. C.10, which was provided by RG) and tables, was written by LB and the manuscript was edited by LB, AB, and RG. All co-authors have reviewed the paper as well as Elisabeth Mills, who acts as the A&A referee.

Overview

Observationally, protostellar outflows and jets manifest themselves as bipolar structures emanating from the location of their driving sources with velocities ranging from a few $\mathrm{km\,s^{-1}}$ to several hundreds of $\mathrm{km\,s^{-1}}$. They serve as an agent to remove angular momentum from the young protostar-disk system. The launching mechanism of outflows is most likely the consequence of the interaction between magnetic fields and the dense material in the rotating accretion disk around the young stellar object.

Therefore, the process of material ejections is closely linked to the process of accretion. For example, knot-like structures in the observed spatial distribution of outflow emission hint at episodic ejection, which in turn is associated with episodic accretion. A protostellar outflow typically contains several components in terms of velocity and degree of collimation. The fastest and most collimated features are referred to as jets, while more loosely-collimated lower-velocity material is rather termed outflow. For a recent review on observations of protostellar outflows, the reader is referred to Bally (2016). The multi-component nature of protostellar outflows is also seen in terms of chemical composition as they often contain an ionised, atomic, and molecular component. In spectral-line observations, emission from an outflow is observed as high-velocity line wings (cf. Fig. 2.10b). Molecular jet components are commonly observed, for example, in emission of shock-excited H_2, in emission of SiO and SO, whose abundances are enhanced in shocked gas, or in high-velocity CO emission (Lee 2020; Tychoniec et al. 2021, and references therein). Molecular outflow components are thought to consist of envelope material that got entrained, thereby accelerated by the jet, or of disk material that was blown away by wide-angle winds (e.g. Tychoniec et al. 2021). Outflows are observed in emission of various molecules. In particular, emission of COMs has also been detected in outflows of low-mass (e.g. Arce et al. 2008; De Simone et al. 2020) and high-mass protostars (e.g. Palau et al. 2017). As briefly discussed in Sect. 1.3.2, when the outflow hits the ambient lower-velocity medium, a shock is produced that accelerates the medium, heats it (temporarily up to hundreds or thousands of K), and compresses it. Higher temperatures can facilitate endothermic reactions or reactions with high activation barriers in the gas phase, while collisions between particles become more frequent in the compressed material. In addition, the high temperatures lead to sublimation of ice species and more-strongly bound (refractory) species from dust grains. Dust grains can also get completely sputtered when the shock is strong enough. All this can lead to enhanced abundances of some COMs in the gas phase, while other species may be destroyed. Studying the molecular content in sources that are impacted by shocks can provide important information on the molecules' formation and destruction pathways and how these depend on environmental changes in, for example, temperature or density. Using again the data taken as part of the ReMoCA survey, this second project of the thesis aims to understand the impact of the outflow that is driven by Sgr B2 (N1) on the molecular composition in the hot core (see also Sect. 1.5).

4.1 Introduction

At the center of astrochemistry is the study of the formation and destruction pathways of molecules, whose knowledge is mandatory for an understanding how the chemistry of the interstellar medium evolves along with the star-formation process. Out of the variety of species that have been detected in the interstellar medium so far (see, e.g. McGuire 2022), complex organic molecules (COMs, carbon-bearing molecules of six or more atoms, Herbst & van Dishoeck 2009) are of particular interest as they present the building blocks of more complex species from which life, as we know it from Earth, may have emerged. By now, COMs have been detected in the solid and gas phase towards a wide variety of sources that cover all the stages of star formation (see Jørgensen et al. (2020) for a recent review): in cold dark clouds (e.g. Taquet et al. 2017; Agúndez et al. 2021; Zeng et al. 2018), prestellar cores (e.g. Bacmann et al. 2012; Jiménez-Serra et al. 2016), protostellar environments (e.g. Belloche et al. 2013; Jørgensen et al. 2016; Pagani et al. 2017), protoplanetary disks (e.g. Walsh et al. 2016; van der Marel et al. 2021; Brunken et al. 2022), and small bodies in the Solar System (Altwegg

et al. 2019; Naraoka et al. 2023).

COMs can be formed in the solid phase on the surface or in the ice mantle of dust grains, and in the gas phase. Gas-phase reactions are efficient in producing COMs mainly at high temperatures ($\gtrsim$100 K) although some reactions may produce some COMs also at low temperatures (Balucani et al. 2015). A substantial number of COMs is thought to form on dust grains and, subsequently, desorb thermally at a certain temperature or non-thermally. Depending on the species, the production in the solid phase can start as early as during the prestellar phase, that is at extremely low temperatures during the collapse phase before the onset of protostellar heating, or later on when the protostar gradually heats its environment (e.g. Garrod et al. 2022). Detectable amounts of COMs in the gas phase in low-temperature environments such as prestellar cores are likely the consequence of mainly non-thermal desorption processes that release the molecules from the dust grain surfaces. These processes include interactions with cosmic rays or with the secondary ultraviolet photons that these cosmic rays produce upon interaction with the gas, or various chemical processes (e.g. Ruaud et al. 2015; Shingledecker et al. 2018; Jin & Garrod 2020; Paulive et al. 2021).

COMs may also desorb as a consequence of grain processing by the passage of a shock. For example, shock-chemistry likely plays a substantial part in enriching the gas of clouds in the Galactic central molecular zone (CMZ) that are devoid of star formation with COMs and simpler species (e.g. Requena-Torres et al. 2006, 2008). In addition, enhanced cosmic-ray fluxes in the CMZ also impact the chemistry of these clouds (e.g. Indriolo et al. 2015). One of these CMZ clouds that has been the target for many recent follow-up studies on COMs is G+0.693−0.027 (G0.693 hereafter), which is located in the cloud complex Sagittarius B2 (Sgr B2 hereafter) and has no signs of active star formation. Over the past few years, the detection of many molecules, including COMs, several of them being even new interstellar detections, have made G0.693 one of the chemically richest sources in the Galaxy (e.g. Rivilla et al. 2021a,b, 2022a,b, 2023; Jiménez-Serra et al. 2022; Zeng et al. 2023). Shocks may also be provoked by protostellar outflows that travel through the material of the parental cloud of their driving source. For example, this has been associated with the the detection of various COMs at positions that are exposed to the outflow of the low-mass protostar L1157 (e.g. Arce et al. 2008).

Thermal desorption is naturally expected to account for the high COM abundances observed in hot corinos and hot cores that surround low- and high-mass protostars, respectively. It was proposed that a COM can thermally desorb either alongside water at the desorption temperature of water, that is $\gtrsim$100 K, or depending on the COM's individual binding energy, with which it sticks to the dust grain surface. Which of the processes occurs in three-phase astrochemical models (which distinguish the surface and bulk layers of the ice mantles) depends mainly on a molecule's ability to diffuse in the bulk ice and from the bulk ice to the surface of the grain (e.g. Garrod 2013) or its disability to do so (Garrod et al. 2022). Accordingly, if the COM reaches the outermost layer of the grain surface, it will desorb at its characteristic desorption temperature.

In our previous study (Busch et al. 2022, Paper I hereafter), we addressed exactly this question. We used the data of the ReMoCA survey (Re-exploring Molecular Complexity with ALMA, Belloche et al. 2019) that were obtained with the Atacama Large Millimetre/submillimetre Array (ALMA) towards the massive star-forming region Sgr B2 (N)orth, which is located in the Galactic centre region at a distance of 8.2 kpc from the sun (Reid et al. 2019). Figure 4.1 provides an overview of observed sources and features in the region surrounding the two main hot cores N1 and N2. Thanks to the subarcsecond angular resolution of ReMoCA, we resolved the COM emission in the main hot core Sgr B2 (N1) and derived abundance profiles of various COMs towards the south and west directions starting from

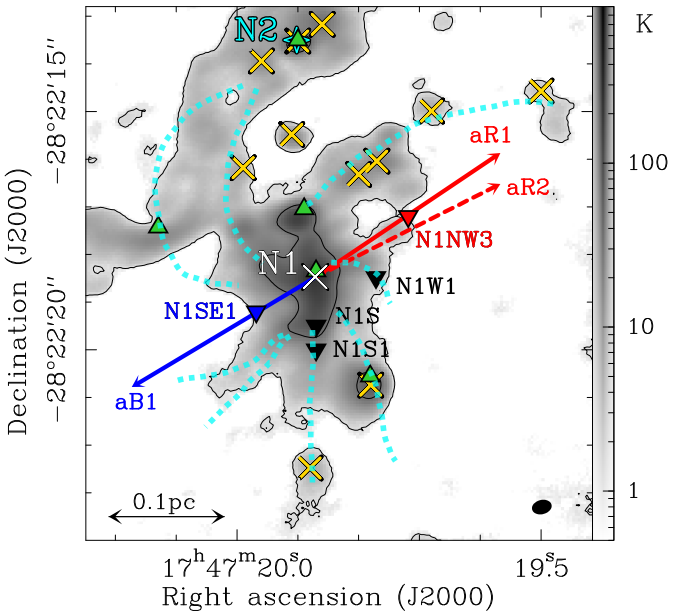

Figure 4.1: Continuum map at 99 GHz extracted from the ReMoCA survey data of the central region of Sgr B2 (N) in grey scale with contour steps 3σ and 81σ, where $\sigma = 0.4$ K. The centre of the main hot core N1 is marked in white and was determined based on the ReMoCA data in Busch et al. (2022). The position of the secondary hot core N2 is shown with a cyan tetragon reported by Bonfand et al. (2017) on the basis of the EMoCA survey. Emission peaks of HII regions (Gaume et al. 1995; De Pree et al. 2015) are marked with green triangles, continuum sources identified by Sánchez-Monge et al. (2017) based on their 1 mm ALMA data with yellow crosses. Filaments identified by Schwörer et al. (2019) based on the same 1 mm (continuum and spectral-line) data are roughly indicated in cyan. The blue and red arrows labelled aB1, aR1, and aR2 indicate the outflow axes identified in this work based on SO emission (see Sect. 4.3.1). Positions N1SE1 and N1NW3, which are located along these axes, were analysed in this work; positions N1S, N1S1, and N1W1, which are not associated with the outflow, were studied in Busch et al. (2022), but have been revisited in this work. The HPBW is shown in the bottom-right corner. The map is not corrected for primary beam attenuation.

$\sim 0.5''$ from the hot-core centre and going up to a distance of $d = 5''$ and $4''$, respectively. This analysis included positions N1S ($d = 1''$), N1S1 ($d = 1.5''$), and N1W1 ($d = 1.3''$), which are marked in Fig. 4.1. A steep increase in the observed abundance profiles of most COMs over one or more orders of magnitude at around $\sim$100 K ($d \sim 3 - 4''$) suggests that the bulk of these molecules desorbs thermally at this temperature. A comparison with most recent chemical models performed by Garrod et al. (2022) revealed that the similarity in the COMs' desorption temperatures provides observational evidence for the thermal co-desorption process of COMs and water. Moreover, we discussed that the derived non-zero abundance values at temperatures <100 K might result from non-thermal desorption processes or another thermal desorption process, for example as a consequence of reduced binding energies of COMs in water-poor outer ice layers that would be rich in CO at low temperatures. The observed abundance profiles of some COMs suggest that gas-phase formation purely or partly accounts for an increase in these COMs' abundances in the gas phase at temperatures above 100 K.

In this earlier work we focussed on the thermal desorption process. Therefore, to reduce the chance of contributions to COM abundances by non-thermal (shock-induced) desorption, we intentionally avoided to analyse positions that are associated with the outflow powered by Sgr B2 (N1) (see Fig. 4.1 and Higuchi et al. 2015; Schwörer 2020). The goal of the present work is to study the chemistry in the outflow (or in regions impacted by the outflow) and to investigate its role in the formation, destruction, and desorption behaviour of mainly complex but also simpler molecules. In particular, we want to find out if the gas molecular composition in the outflow shows significant differences to that derived in Paper I. This includes a comparison of abundances between 'outflow' positions N1SE1 and N1NW3 (see Fig. 4.1 and Sect. 4.3.3) and 'hot-core' positions N1S, N1S1, and N1W1 (Paper I).

An outflow driven by Sgr B2 (N1) was long proposed to account for red- and blue-shifted line emission observed in spectra of simpler molecules such as SO, SO_2, SiO, HC_3N, but also, for example C_2H_5CN or C_2H_3CN (Lis et al. 1993; Liu & Snyder 1999; Belloche et al. 2013). A large number of spots showing intense maser emission in the 22 GHz water line have been observed in the close vicinity of the hot core (McGrath et al. 2004). These are signposts of high-mass star formation, in particular, shock-related events such as protostellar outflows as these masers are the results of shock chemistry and are collisionally pumped (Elitzur et al. 1989). Higuchi et al. (2015) used the data of the EMoCA survey (Exploring Molecular Complexity with ALMA, Belloche et al. 2016), ReMoCA's predecessor, which has an angular resolution of $\sim 2''$, to map SO_2 and SiO emission. These maps revealed a bipolar outflow, with a dynamical age of of ~5 kyr and a total mass of 2000 $M_\odot$. Schwörer (2020) studied the outflow of Sgr B2 (N1) in emission of mainly simple molecules such as SiO, SO, SO_2, HNCO, and others, but also CH_3OH based on ALMA observations at 1.3 mm with an angular resolution of $\sim 0.5''$ and $\sim 0.05''$. The observed morphology of the outflow emission suggests that it may be interacting with material associated with the HII region located in the northeast and that it may be framed by some of the identified filaments (see also Schwörer et al. 2019), provided that all sources lie at the same distance along the line of sight. Schwörer (2020) also derived an outflow mass of 230 $M_\odot$, which is a factor 10 lower than the value from Higuchi et al. (2015), due to a different way of derivation, a total kinetic energy output of $\sim 10^{48}$ erg, a dynamical age of 3–7 kyr, and a mass ejection rate of $\sim 0.05\ M_\odot\ \mathrm{yr}^{-1}$. Assuming a kinetic temperature of 250 K and a core radius of 0.03 pc, the author estimated a total luminosity of $\sim 6 \times 10^6\ L_\odot$ for Sgr B2 (N1), a total gas-and-dust mass of 2000 $M_\odot$, and a stellar mass content of 800–3000 $M_\odot$, based on which he proposed that multiple sources at the centre of Sgr B2 (N1) drive outflows that appear to be one. In this case, the intriguing rather clear separation of blue-shifted emission in the southeastern lobe and red-shifted emission in the northwestern lobe would be largely fortuitous. Independently of the number of driving sources, the outflow of Sgr B2 (N1) is one of the most massive and powerful protostellar outflows known to date.

In this work we want to study the impact of the outflow on the COM inventory in Sgr B2 (N1) and how this compares to other sources in which the molecular content is influenced by shocks, which are L1157-B1, a region located in the blue-shifted lobe of the outflow driven by the low-mass protostar L1157, and G0.693. The comparison to the latter is of particular interest as it is located within the same cloud complex as Sgr B2 (N1), exposed to likely similar physical processes as the positions in Sgr B2 (N1) that are impacted by the outflow, however, G0.693 has a lower density. The article is structured as follows: Section 4.2 provides details on the observations and the data analysis including the LTE modelling of spectra and the derivation of population diagrams. In Sect. 4.3 we present our results, which are discussed and compared with observational results of the other shock-dominated regions and with astrochemical models in Sect. 4.4. The conclusions are provided in Sect. 4.5.

4.2 Observations and method of analysis

4.2.1 The ReMoCA survey

We made use of data that were obtained as part of the imaging spectral-line survey ReMoCA (Belloche et al. 2019) towards Sgr B2 (N) with ALMA. The phase centre at $(\alpha, \delta)_{J2000} = (17^h47^m19\overset{s}{.}87, -28^\circ22'16\overset{''}{.}00)$ is located north of Sgr B2 (N1), halfway to the secondary hot core Sgr B2 (N2). Five observational setups (S1–S5) were observed, each delivering data in four spectral windows, covering the frequency range from 84 to 114 GHz in total. Different antenna configurations yielded angular resolutions that vary from ∼0.75″ in setup 1 to ∼0.3″ in setup 5. Further details on the observations as well as average rms noise levels for each spectral window can be found in Table 2 of Belloche et al. (2019). Details on the data reduction can also be found in the latter article. The size (HPBW) of the primary beam varies from 69″ at 84 GHz to 51″ at 114 GHz (ALMA Partnership et al. 2016) and the spectral resolution of the reduced spectra is 488 kHz, which translates to 1.7–1.3 km s^{-1}.

4.2.2 LTE modelling with Weeds

In order to identify molecules in the observed spectra and to determine the properties of their emission, we performed radiative transfer modelling with Weeds (Maret et al. 2011). Weeds is an extension of the GILDAS/CLASS software[1] and is used to produce synthetic spectra under the assumption of local thermodynamic equilibrium (LTE). Assuming LTE conditions in Sgr B2 (N) is appropriate given the high volume densities of $\sim 10^7$ cm^{-3} that have been derived towards the source (Bonfand et al. 2017).

The modelling procedure is performed in the same way as in Paper I. Weeds requires five input parameters for each molecule: total column density, rotational temperature, size of the emission region, velocity offset with respect to the systemic velocity of the source, and linewidth (FWHM). The last two parameters have been derived by applying one-dimensional Gaussian fits to optically thin and unblended transitions of a molecule. Column density and rotational temperature were first selected by eye and adjusted subsequently, based on results that were obtained from a population diagram analysis (see Sect. 4.2.3). Following Paper I, the size of the emission region was fixed to a value of 2″, based on the assumption of resolved emission. The identification of a molecular species is validated when the synthetic spectrum correctly predicts each observed transition. By adding up the synthetic spectra of all individual species, we derive a combined model of molecules. More details on the modelling procedure can be found in Belloche et al. (2016). All Weeds parameters determined for each molecule at each selected position (see Sect. 4.3.3) are summarised in Tables B.1–B.4. The modelling of synthetic spectra relies on spectroscopic information, which, for most parts, are taken from the CDMS (Cologne Database for Molecular Spectroscopy, Endres et al. 2016) or the JPL (Jet Propulsion Laboratory, Pearson et al. 2010) spectroscopy database. For some COMs, we provided an extended description on the laboratory background and on the vibrational spectroscopy in Paper I.

4.2.3 Population diagrams

To support the results of the LTE modelling, we derived population diagrams that yield rotational temperature, T_{rot}, and column density, N_{col}, of a molecule. This analysis is based on the following

[1] https://www.iram.fr/IRAMFR/GILDAS/

formalism (Mangum & Shirley 2015):

$$\ln\left(\frac{N_u}{g_u}\right) = \ln\left(\frac{8\,\pi\,k_B\,\nu^2\int J(T_B)\mathrm{d}v}{c^3\,h\,A_{\mathrm{ul}}\,g_u\,B}\right) = \ln\left(\frac{N_{\mathrm{tot}}}{Q(T_{\mathrm{rot}})}\right) - \frac{E_u}{k_B T_{\mathrm{rot}}}, \tag{4.1}$$

where N_u is the upper-level column density, g_u the upper-level degeneracy, E_u the upper-level energy, k_B the Boltzmann constant, c the speed of light, h the Planck constant, $B = \frac{\text{source size}^2}{\text{source size}^2 + \text{beam size}^2}$ the beam filling factor, A_{ul} the Einstein A coefficient, N_{tot} the total column density, and Q the partition function. Integrated intensities in brightness temperature scale, $J(T_B)$, are obtained over a visually selected velocity range, dv, in the baseline-subtracted spectra.

Following the strategy of Paper I, we only use setups 4–5 because of their higher angular resolutions compared to setups 1–3. Only in the case of NH_2CHO, setups 1–3 were used because there are not enough lines in the higher angular-resolution setups to construct a population diagram for this COM. Population diagrams for relevant species and positions (see Sect. 4.3.3) can either be found in Paper I or in Appendix B.1. Values for column density and rotational temperature can be found in Tables B.1–B.4. For each molecule and position, there exist two diagrams: the left panel that shows the original integrated intensities and the right panel, in which two correction factors (discussed below) have been applied to the data points. If there is contaminating emission from other species or from other velocity components of the same species, due to line blending, its contribution is subtracted from the value of integrated intensity, where we used the information of the complete Weeds model that was created based on the individual spectra of the molecules analysed here.

Moreover, some spectral lines may be affected by high optical depth. To account for this, the integrated intensities of both the observed and modelled transitions were multiplied with a correction factor, $\frac{\tau}{1-e^{-\tau}}$ (e.g. Mangum & Shirley 2015). The opacity values were taken from our Weeds model for the respective transition. However, the Weeds model has only limited capabilities in treating high optical depths leading to an underestimation of the correction factor at very high values. Therefore, we did not consider a transition in the population diagram when the opacity exceeded a value of ~2–3. After applying these two corrections, some small scatter between the observed and modelled data points and amongst the observed points remains, which can have multiple reasons that we elaborated on in Sect. 3.4 of Paper I.

In each population diagram, the data points follow a linear trend implying that the level distributions can be explained by a single temperature. The error bars shown in the population diagrams only include the standard deviation coming from integrated intensities and a quadratically added additional contribution of 1σ, where σ is the median noise level measured in channel maps of the continuum-removed data cubes taken from Table 2 in Belloche et al. (2019), to account for the uncertainty in the continuum level (Paper I). We applied a linear fit to the observed data points to obtain the rotational temperature and column density. To avoid giving too much weight to the most intense or contaminated lines, the fit does not take into account the uncertainties of the data points.

In some cases, a molecule may be detected but the number of available transitions is insufficient to derive a population diagram. By using a 3σ upper limit for the intensity of non-detected lines, we derive upper limits for the entries in the population diagrams to, in turn, obtain an upper limit on the temperature and an estimate of the column density. In two cases, the linear fit did not provide a reliable result, and so we fixed the temperature in the population diagram to obtain a column density value.

In comparison to the radiative transfer models, a population-diagram analysis is affected by a few

more uncertainties, which we discussed in detail in Paper I. For example, in the Weeds models the background continuum is taken into account in the equation of radiative transfer, while it is not (and cannot be properly) when fitting the population diagrams (cf. Goldsmith & Langer 1999). Moreover, the correction factors that we apply to the observed and modelled values in the population diagrams depend on the Weeds model. On the one hand the opacity correction is an output of the Weeds model. On the other hand, although to some extent we can reduce the contribution of contaminating emission, it cannot be avoided entirely when deriving the population diagrams, while for the Weeds models we ensure that the modelled intensity of a transition for any given molecule does not exceed the contribution of that transition to the observed spectrum. Therefore, our analysis is focused on the results derived from the radiative transfer modelling, while we use the population diagrams to support those results.

4.3 Results

4.3.1 Outflow morphology

In the following, we investigate the morphology of the outflow as seen in emission of various molecules. In Sect. 4.3.1, we focus on typical shock-tracing molecules, namely SO and SiO. Then, to better take into account velocity and linewidth gradients across Sgr B2 (N1), we computed linewidth- and velocity-corrected integrated emission (LVINE) maps, which are introduced in Sect. 4.3.1, for SO (Sect. 4.3.1) and other species (Sect. 4.3.1).

SiO and SO emission

In the case of SiO, we analysed its $J = 2 - 1$ transition at 86.85 GHz, which is covered in observational setup 1, that is at lower angular resolution (~0.7″). For SO, we used its $J = 2_3 - 1_2$ transition at 99.3 GHz, which is covered in setup 5 with a two times higher angular resolution than for the SiO line (~0.3″). We present integrated-intensity maps of the two molecules in Fig. 4.2 on top of a continuum map at 99 GHz which has contributions of both dust emission and free-free emission from ionised gas (see Paper I for a detailed description of the continuum). We integrated over the blue- and red-shifted emission and show the maps in separate panels. The pixel-dependent integration starts from the first channel that no longer shows absorption (starting from the systemic velocity, v_{sys}) and progresses up to the respective outer integration limits. For blue- and red-shifted SO emission, these outer limits are fixed at 15 and 115 km s^{-1}, respectively, while for SiO emission, these are at 5 and 130 km s^{-1}, respectively. To illustrate the choice of integration intervals, Fig. 4.3 shows the spectra of both transitions towards two positions in the outflow (N1NW3 and N1SE1, see Fig. 4.1) and one position that is primarily not associated with the outflow (N1S, see also Paper I). The positions N1NW3 and N1SE1 are further analysed in Sect. 4.3.3. The spectra reveal absorption at velocities close to v_{sys}, but also prominent red-shifted (wing)emission towards N1NW3 and blue-shifted emission towards N1SE1, which is indicative of the outflow. In addition, a second SO transition at 109.25 GHz ($J = 3_2 - 2_1$, orange), which is only in emission, is shown for comparison of the line profiles. The integrated-intensity maps of Fig. 4.2 may contain some contaminating emission from other molecules as can be seen from additional spectral lines in the integration interval in Fig. 4.3, especially for N1S. On the other hand, because the outer integration limits were set such that contaminating emission

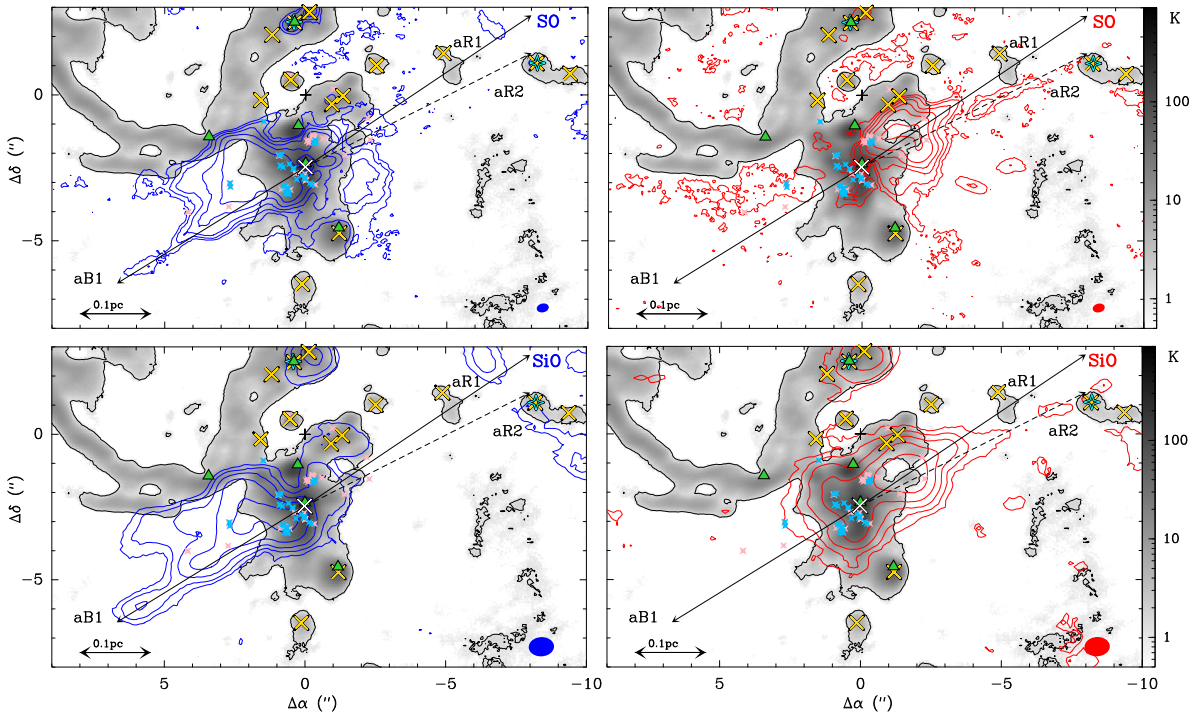

Figure 4.2: Continuum emission at 99 GHz in grey scale overlaid by contours of SO $J = 2_3 - 1_2$ at 99.3 GHz (*top*) and SiO $J = 2 - 1$ at 86.85 GHz (*bottom*) integrated intensities. The inner integration limits vary such that channels that contain deep absorption are excluded. The outer integration limits are fixed at 15 and 115 km s^{-1} for blue- and red-shifted SO emission, respectively, and 5 and 130 km s^{-1} for blue- and red-shifted SiO emission, respectively (see also Fig. 4.3). The blue and red contours start at 5σ and then increase by a factor of 2, where $\sigma = 10.5$ (SO, blue), 10.8 (SO, red), 4.5 (SiO, blue), and 5.8 K km s^{-1} (SiO, red) and corresponds to an average noise level that was measured in the respective map. The black contour indicates the 3σ level of the continuum emission (see Fig. 4.1). Based on the SO maps, we identify collimated features possibly tracing outflow axes that are shown as solid and dashed black arrows and labelled aB1, aR1, and aR2. The markers are the same as in Fig. 4.1. In addition to N2, the hot core N3 identified by Bonfand et al. (2017) is marked with a cyan tetragon. Blue and pink star markers indicate H_2O maser spots (McGrath et al. 2004) with blue- and red-shifted velocities, respectively, with respect to $v_{sys} \equiv 62$ km s^{-1}. The HPBW is shown in the bottom-right corner of each panel. The position offsets are given with respect to the ReMoCA phase centre (black cross). The maps are not corrected for primary beam attenuation.

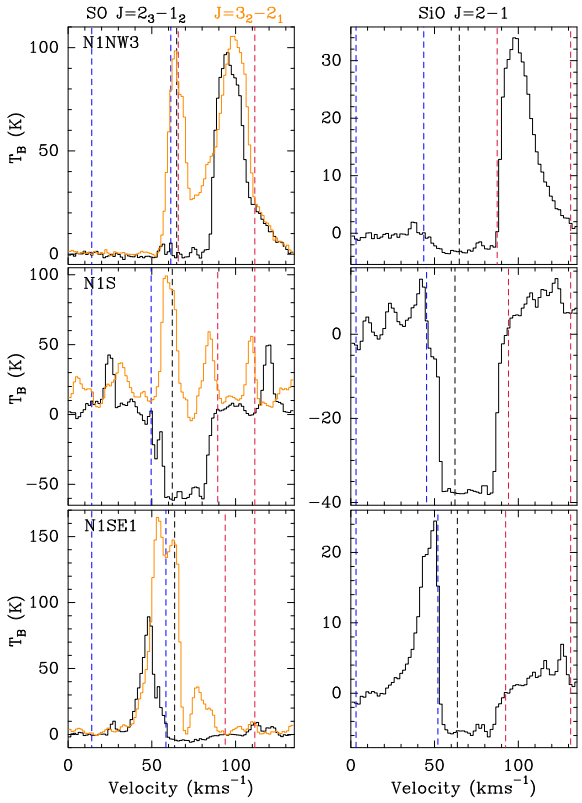

Figure 4.3: Spectra of SO $J = 2_3 - 1_2$ at 99.3 GHz, SO $J = 3_2 - 2_1$ at 109.25 GHz, and SiO $J = 2 - 1$ at 86.85 GHz towards a position in the red-shifted lobe (N1NW3, *top row*), N1S (*middle row*), and a position in the blue-shifted lobe (N1SE1, *bottom row*). The black dashed lines mark the systemic velocities of 64.8 km s^{-1} (N1NW3), 62.2 km s^{-1} (N1S), and 63.6 km s^{-1} (N1SE1), while the dashed blue and red lines indicate the inner and outer limits used to integrate the blue- and red-shifted emission shown in Fig. 4.2. While the outer limits are fixed values, the inner limits are pixel-dependent and set such that channels that contain absorption features close to the systemic velocity are excluded.

could be excluded at some positions, outflow emission at higher velocities may be missed at other positions (see, e.g. red-shifted SO emission at N1S and N1SE1).

Although the morphology has some complexity to it, blue-shifted emission is dominantly observed to the southeast, while red-shifted emission extends to the northwest. There is some overlap of both in the closest vicinity of the hot core's centre. The longest features labelled in the blue- (aB) and red-shifted (aR2) emission maps, which are at position angles of 120° and −64° east from north, respectively, starting from the continuum peak of Sgr B2 (N1), stand out due of their strong collimation in the SO maps. They do not appear as narrow in the SiO maps due to the lower angular resolution. These features extend up to 0.3 pc (blue) and 0.38 pc (red). There was only one detached contour in the CO map shown by Schwörer (2020) hinting at this spatially extended feature. The position angles correspond more or less to those stated by Higuchi et al. (2015), who mapped the outflow in SiO emission using the EMoCA survey. Neither the high degree of collimation nor the maximum spatial extent seen here could be identified in the EMoCA data, due to the lower angular resolution and lower sensitivity of that survey. Moreover, in contrast to the SiO maps shown by Higuchi et al. (2015), we are

able to identify an additional feature (aR1) in the SO maps, which also has some degree of collimation but a smaller spatial extent than aR2. The position angles of features aR1 and aR2 differ only by a few degree, which possibly indicates precession of the outflow. There is also another blue-shifted feature extending to the east at a position angle of ~95°, whose possible origins are discussed in Sect. B.3.2, where the outflow morphology is described in more detailed also in comparison to other species.

As noted by Schwörer (2020), the blue- and red-shifted emissions seem to have multiple meeting points with continuum emission. The blue-shifted emission extending to the east follows the continuum (free-free) emission of the large HII region located in the northeast (cf. Gaume et al. 1995), while the emission along aB1 seems to be framed by one of the filaments identified by Schwörer et al. (2019, see also Fig. 4.1). Similarly, the red-shifted emission seems to be embedded in the filamentary structure of the continuum emission. Additionally, in the northwest portion of mainly the SiO maps, the outflow of N3, another hot core (Bonfand et al. 2017), can be identified. The red-shifted collimated feature aR2 seems to extend up to the location of N3, with which it might be interacting if they were located at the same distance along the line of sight. To the north, there is also emission that is associated with the hot core Sgr B2 (N2).

Despite the difference in angular resolution of their maps, both molecules trace generally the same morphology. Only, there is red-shifted emission in the SiO maps towards the south(east), which is not as prominently observed in the SO maps. Given that it still coincides with continuum emission, there might be some contamination coming from another species. We cannot be conclusive as this is the only SiO transition covered by ReMoCA. In contrast, the SO emission reveals faint red-shifted emission to the east that follows the structure of the HII region, which may further be associated with the two H_2O masers that are observed at red-shifted velocities in this region (pink markers). In the map of blue-shifted SO emission, there is an extension towards the (south)west that is not observed in SiO.

LVINE maps for SO

The molecular emission towards Sgr B2 (N1) reveals gradients in both peak velocity (from $\lesssim 60\,\mathrm{km\,s^{-1}}$ up to $\sim 70\,\mathrm{km\,s^{-1}}$, see Schwörer et al. (2019) and Paper I) and linewidth (from ~3 to $12\,\mathrm{km\,s^{-1}}$). In order to account for this when integrating intensities in Paper I, we first derived peak-velocity and linewidth maps for the region around Sgr B2 (N1) (see Fig. B.2 in Paper I). For this purpose, we used a transition of ethanol, which remains sufficiently optically thin even at closest distances to the centre of the hot core, and a bright methanol line beyond the distances where ethanol is no longer securely detected. Subsequently, the peak velocities and linewidths were used to adjust the integration limits in each pixel of the LVINE maps. This LVINE method is an extension of the VINE method (Calcutt et al. 2018) in that we also consider the variations in linewidth. Here we used this method and the peak velocity and linewidth maps from Paper I to determine the inner integration limits for the integrated-intensity maps of the blue- and red-shifted emission. We first find the channels for which the velocity is $v_t \pm FWHM_t$ for the blue- and red-shifted emission, respectively, where v_t and $FWHM_t$ are the peak velocity and linewidth of the template spectral lines (ethanol in the inner part, methanol in the outer part). To obtain the inner integration limits, we apply a shift of another two channels outwards to avoid as much emission from the hot-core component as possible. The outer integration limits are pixel-independent, fixed values that were defined based on a comparison of spectra as, for example, shown in Fig. 4.3, but over a larger area. Because emission of the SO and SiO transitions used for Fig. 4.2 suffer from strong self-absorption over large portions of the maps and

over a large velocity interval, they cannot be used. In the case of SO, we instead use its transition at 109.25 GHz and show the LVINE maps for red-and blue-shifted emission in Fig. 4.4a. It reveals essentially the same morphology as in Fig. 4.2 with collimated features (labelled aB1, aR1, aR2 in Fig. 4.2) but the bulk of emission showing a wide opening angle. Additional structures are discussed while comparing to other molecules in Sect. 4.3.1 or in Appendix B.3. In the case of SiO, there is no transition unaffected by self-absorption in the ReMoCA survey.

Emission from other molecules

In addition to these typical outflow tracers, primarily blue-shifted components had been detected in lines of HC_3N and COMs such as C_2H_5CN and C_2H_3CN in the past (e.g. Belloche et al. 2013). While inspecting spectra extracted from positions along the blue-shifted lobe, we identified for multiple COMs one or more emission component(s) in addition to that associated with the hot core, that is at v_{sys}. In general, these additional components are more prominent for N- and S-bearing species than for (N+O)- or O-bearing species, when detected at all for the latter. As an example, Fig. 4.5 shows spectra of C_2H_5CN and HNCO towards the same positions as in Fig. 4.3. In each panel, two transitions of the respective molecule are shown, which were selected based on their similar upper-level energies and Einstein A coefficients and thus have similar intensities. The difference of the two spectra ($black - orange$) inside the integration limits (dashed red and blue lines) is shown below the respective panel. The profiles for C_2H_5CN at N1S agree well for velocities close to the average systemic velocity of 62 km s^{-1}. There is no clear hint of additional components or prominent wing emission within the velocity interval limited by the blue and red dashed lines, which would be indicative of the presence of an outflow. Most of the emission seen in these velocity intervals can likely be associated with other molecules, given that the black and orange spectra behave differently. This is also true for HNCO at this position, however, the contamination by emission from other molecules is more severe. In contrast, at N1SE1 the two transitions agree well between 45 and 70 km s^{-1} for both C_2H_5CN and HNCO proving that the orange and black emissions that are observed in this velocity range come from the same molecule and are not contaminated by other species. Therefore, in addition to the component that is associated with the hot core at 63.6 km s^{-1} at this position, there is a second one at blue-shifted velocities, which peaks at ~54 km s^{-1}. There is some contaminating emission in the orange spectra at ~30 km s^{-1} for C_2H_5CN and at ~32 and ~72 km s^{-1} for HNCO. At N1NW3, the two transitions of ethyl cyanide show similar line profiles between 60 and 100 km s^{-1}, again with one 'hot-core' component at 64.8 km s^{-1} and one component at red-shifted velocities. The latter peaks at ~74 km s^{-1} and shows extended wing emission towards higher velocities. At blue-shifted velocities, there is some emission in the orange spectrum around ~52 km s^{-1} and in the black spectrum at 30–35 km s^{-1} that is not seen in the other spectrum, respectively, again suggesting that this emission comes from another molecule. Emission of HNCO is much weaker at this position and the line profiles of the two transitions only agree within 60–67 km s^{-1}. Emission at other velocities is most likely contamination from other molecules.

To determine the extent of the blue- and red-shifted emission for different molecules, we compute LVINE maps (see Sect. 4.3.1). However, this is not an easy task because line emission is pervasive over large spatial scales, hence the risk of contamination by emission from another species is high, as was seen by the comparison of C_2H_5CN and HNCO spectra in Fig 4.5. In these spectra we mark the peak velocities derived from the template line, v_t, with dashed black lines and the integration limits for the blue- and red-shifted emission with dashed blue and red lines, respectively. This shows

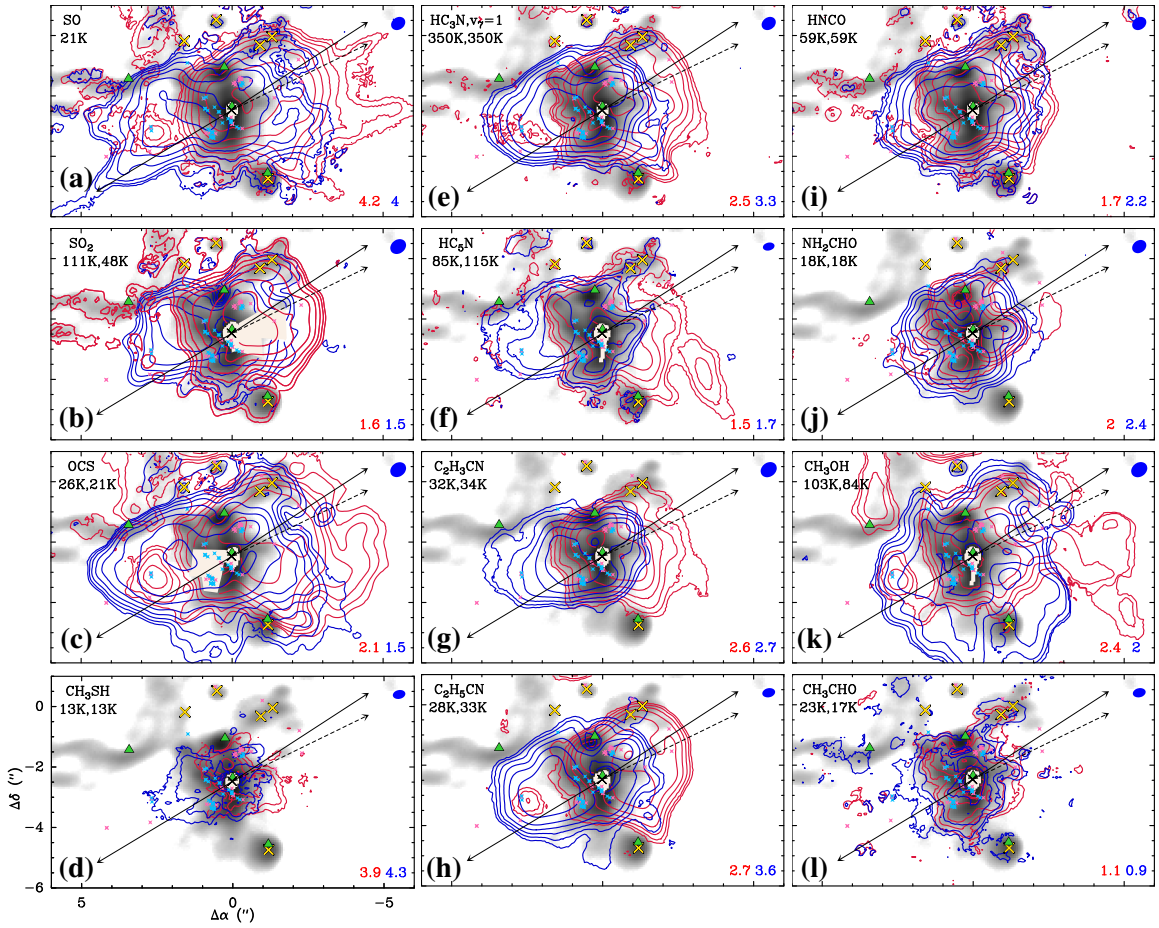

Figure 4.4: LVINE maps of blue- and red-shifted emission (blue and red contours, respectively) of S-bearing molecules *(a–d)*, N-bearing molecules *(e–h)*, and (N+O)- and O-bearing species *(i–l)*. The contour steps start at 5σ and then increase by a factor of 2, where σ is an average noise level measured in an emission-free region in each map and is given in K km s^{-1} in the bottom-right corner in each panel. The grey scale in all panel shows the continuum emission at 99 GHz (see Fig. 4.2). The closest region around Sgr B2 (N1) is masked out (beige areas) due to high frequency- and beam-size-dependent continuum optical depth (see Appendix C in Paper I). For OCS and SO_2, the masked region was extended due to contamination by emission from another species that was identified in their spectra. Markers and arrows are the same as in Fig. 4.2. The upper-level energies of the transitions used to produce the maps are shown in the top-left corner in each panel. Other properties of the transitions and the outer integration limits are summarised in Table B.5. The HPBW is shown in the top-right corner in each panel. The position offsets are given with respect to the ReMoCA phase centre.

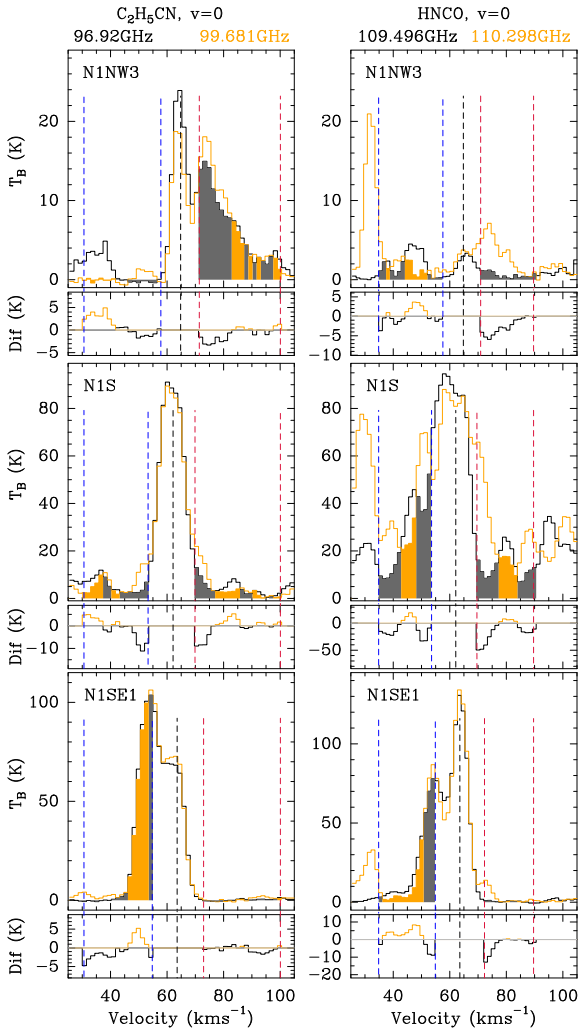

Figure 4.5: Spectra of two transitions of C_2H_5CN and HNCO towards a position in the red-shifted lobe (N1NW3, *top row*), N1S (*middle row*), and a position in the blue-shifted lobe (N1SE1, *bottom row*). The black and orange spectra show the transitions whose frequencies are given in the respective colour at the top. Additional line properties can be found in Table B.5. The black dashed lines are the same as in Fig. 4.3, while the dashed blue and red lines indicate the fixed outer and pixel-dependent inner limits used to integrate the blue- and red-shifted emission shown in Fig. 4.4. The difference (Dif) of the two spectra ($black - orange$) within the integration intervals is shown below the respective panel. The filled histograms and the colour of the difference spectra indicate which transition was used in each channel for the integration of the blue-shifted and red-shifted emission in order to minimise the contamination by other species.

that with the defined inner integration limits, we avoid (almost) all emission from the component at $\sim v_t$, however, in that way parts of the lower-velocity blue- and red-shifted emission are also partly excluded. Moreover, as described above, the velocity ranges defined for integration most likely contain contaminating emission from other species. In order to reduce the contamination in the LVINE maps for the blue- and red-shifted emission, we had to develop a different strategy, in which we made use of two transitions for each molecule to derive the LVINE maps. This procedure is explained in Appendix B.3.1 and illustrated with the filled histograms (and coloured difference spectrum) in Fig. 4.5.

In Fig. 4.4 we show the final LVINE maps for a variety of COMs and simpler molecules, where the grey scale shows the continuum map at 99 GHz as in Fig. 4.2. Overall, the bipolar structure with blue-shifted emission extending to the (south)east and red-shifted emission to the (north)west can be identified for S- and N-bearing molecules. For O- and (N+O)-bearing species this bipolarity is less striking, if evident at all. None of the other molecules shows a secure detection of the narrow feature observed for SiO and both transitions of SO (labelled aB1, aR1, aR2 in Fig. 4.2), which might be the result of the absence of the molecule at these far distances, but could also be an issue of insufficient sensitivity or excitation. At some positions that show bright continuum emission from the dense core, there is also a substantial overlay of blue- and red-shifted emission. Especially in this region, we cannot reliably determine whether the outflow is the only origin of the emission, also given that some blue and red contours follow almost exactly the contour of the continuum emission, which makes the interpretation of the emission morphology more challenging in this region. Moreover, the filaments identified in the continuum emission (see Fig. 4.1) are also observable in blue- and red-shifted molecular emission (Schwörer et al. 2019), which presents another difficulty in this decision. In addition to these general trends, a lot of structure is observed in the morphology of blue- and red-shifted emission that is described in further detail in Appendix B.3.2. To identify at which velocities the collimated features aB1, aR1, and aR2 appear and to denote additional low- or high-velocity features, each LVINE map is split into two, showing lower-velocity and higher-velocity emission (see Figs. B.4–B.6), respectively. Moreover, velocity-channel maps are presented in Fig. B.7.

4.3.2 Position-velocity diagrams

Figure 4.6 shows position-velocity (PV) diagrams of the two transitions of SiO and SO used in Fig. 4.2, which have both an upper-level energy in temperature unit lower than <10 K, and the second transition of SO with a higher upper-level energy of 21.1 K. Positions close to the hot core's centre and those containing emission from other species are masked. The two transitions at lower upper-level energies present deep absorption close to the hot-core centre between velocities of ~50 and 85 km s^{-1} for SiO and in a slightly narrower velocity range for SO. The SO transition at 109 GHz with slightly higher upper-level energy is not as heavily absorbed and presents emission over the whole velocity range from ~25 km s^{-1} to 120 km s^{-1}. Towards the southeast along aB1, we highlight two features: B1 is spatially compact, but elongated along the velocity axis reaching highest blue-shifted velocities ($\lesssim$30 km s^{-1}), while B2 is spatially the most extended feature that still reaches down to 30 km s^{-1}. The latter represents the blue-shifted emission that extends farthest in the position-position maps (see, e.g. the velocity-channel map at 40 km s^{-1} for SO in Fig. B.7). Given that B1 is more compact and faster than B2, the latter may present an older ejection event that decelerated while gaining a greater distance from the hot-core centre, which hints at episodic ejection. Due to its closeness to the centre, a feature in the position-position maps cannot unambiguously be assigned to B1. For the red-shifted emission along aR1, there are at least two intensity peaks recognisable for the SO transition at 109 GHz. There

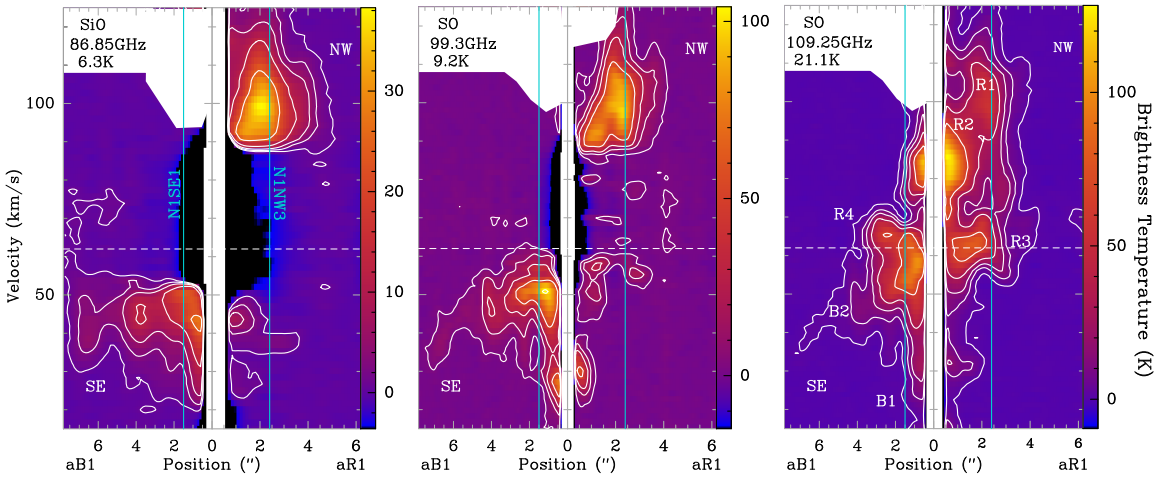

Figure 4.6: Position-velocity (PV) diagrams of SiO at 86.8 GHz and SO at 99.3 GHz and 109.252 GHz taken along the solid black arrows labelled aB1 and aR1 in Fig. 4.2. Here, the position labelled 0 corresponds to the centre of the hot core. Contours are at 5σ, 25σ, and then increase by a factor 2, where σ = 0.12 K for SiO and 0.5 K and 0.32 K for the two SO transitions, respectively, and was measured in an emission-free region in the respective data cubes. Pixels with intensities less than -30σ are shown in black. The positions N1SE1 and N1NW3 are indicated with light-blue solid lines. Regions close to the centre and those containing contaminating emission from other species are masked in white. The white dashed line marks an average systemic velocity of 62 km s^{-1}. The frequency and upper-level energy of the respective transition are written in the upper-left corner. Highlighted features in blue-shifted emission towards the southeast (SE, in the position-position maps) include B1 (elongated along velocity axis), B2 (elongated along both axes). Intensity peaks in red-shifted emission towards the northwest (NW) are labelled R1 and R2, and red-shifted emission close to the systemic velocity are labelled R3 (NW) and R4 (SE).

is a bright feature at ~82 km s^{-1} close to the hot-core centre (labelled R2), which is not prominent in the other two PV diagrams due to absorption at these velocities. The second peak, labelled R1, at ~100 km s^{-1} is observed for all transitions. These features likely correspond to intensity peaks P5 (for R2) and P6 (for R1) that were identified in the LVINE maps of SO and other species in Sect. B.3.2. Spatially extended emission at ~55 to 65 km s^{-1} labelled R3 (towards NW) and R4 (SE) can likely be associated with the hot core itself. The emission from the SO transition at 109 GHz also reveals that within distances of ~2″ there is blue- and red-shifted in either direction even at velocities far from the systemic velocity. It is not entirely excluded that at least some of this emission comes from other species, especially at closest distances to the hot-core centre, where line emission is pervasive.

Figure B.8 shows PV diagrams of all the molecules for which we show LVINE maps in Fig. 4.4 and, in addition, for CH_3NCO, C_2H_5OH, CH_3OCHO, and CH_3OCH_3. The closest regions to the centre of the hot core and regions that are certainly contaminated with emission from other species are masked in white. We compare the distribution of emission of the various molecules to that of the SO transition at 109 GHz, which is again shown in this figure in the upper left panel and its contours (black) in all other panels. Emission along B2 is clearly identified for all S- and N-bearing molecules, HNCO, and CH_3OH. Emission from all other O-bearing molecules, NH_2CHO, and CH_3NCO remains compact in both the spatial and velocity domains. The highest-velocity feature B1 is, besides in SO emission, evident in emission of OCS, HC_3N, C_2H_3CN, and C_2H_5CN. It may also be seen for some other molecules such as SO_2 and HC_5N, however, we identified contaminating emission at these positions

and velocities for these two molecules. Although the emission for the four molecules mentioned above can likely be associated with B1, we cannot definitely exclude that there may be contamination. At red-shifted velocities, R2 can be identified in emission of N- and simple S-bearing molecules, HNCO, and CH_3OH, for some more prominently than for others. However, the emission of all these molecules does generally not peak at velocities as high as for SO. Emission at R1 is evident for SO, SO_2, OCS, and HC_3N, faintly for C_2H_5CN. Additionally, in the PV diagrams of SO, OCS, C_2H_5CN, and some of the O-bearing COMs there may be some kind of cavity evident at around 70 km s^{-1} and ∼1.5″ in the northwestern direction.

4.3.3 Radiative transfer analysis

In order to understand the impact of the outflow on the gas molecular inventory, we derived molecular abundances for two positions, one in each lobe of the outflow, and we compare them to results obtained previously in Paper I for the hot core (Sect. 4.3.3) and later to results of other sources (Sect. 4.4.2). In this section, we first describe the process of selecting the positions and molecules for the analysis, before presenting the results derived from the radiative transfer modelling and population diagram methods.

Line and position selection

We adopted the selection of COMs from Paper I, which includes CH_3OH, C_2H_5OH, CH_3OCH_3, CH_3OCHO, CH_3CHO, C_2H_3CN, C_2H_5CN, NH_2CHO, and CH_3NCO. We added a few more species, which are CH_3CN, HC_3N, HC_5N, NH_2CN, and HNCO. Some of these may not have been analysed in Paper I because there were not enough transitions when considering setups 1–3 and 4–5 separately or due to high line optical depth out to large distances, or because the molecules' lines were too weak to be considered in the previous study. Moreover, we included the S-bearing species OCS and CH_3SH, both of which are expected to be indicators of shock chemistry. We do not analyse SO_2 here because there are not enough transitions available for a reliable radiative transfer modelling. We have not shown LVINE maps for CH_3CN, because the molecule's various K-ladder transitions for a given J are blended.

We looked for a position to the SE along the collimated high-velocity feature seen in SO emission labelled aB1 in Fig. 4.2 and chose N1SE1, which is at a distance of 1.5″ from the continuum peak of Sgr B2 (N1). The position naming is based on that started in Paper I and depends on the distance to the continuum peak. This position is sufficiently distant from the centre of the hot core to not be too contaminated by the pervasive line emission arising in the hot core itself, while showing intense blue-shifted emission, where detected (see Fig. 4.4). The position selection in the red-shifted lobe was more difficult to do, because the red-shifted emission is not as intense as the blue-shifted emission in general. We looked for a position along one of the outflow axes identified in the red-shifted SO emission maps, that is either along aR1 or aR2. Moreover, we searched for a position that clearly showed a red-shifted component in CH_3OH as we want to compute abundances with respect to this COM (among others) in the following in order to compare between the positions and with other sources. At a distance of ∼2″ along aR1, there is a peak in the continuum map (see Fig. 1 in Paper I) and in emission of some COMs that may be associated with another source. Closer to the centre of Sgr B2 (N1), the component close to the systemic velocity and the red-shifted one become hardly distinguishable, which makes it difficult to model them. Therefore, we selected position N1NW3 at a distance of ∼2.5″ along aR1. In the following, we distinguish the pair of velocity components at a

given position by adding HC for the hot-core component close to the systemic velocity and OF for the supposedly outflow component at red- or blue-shifted velocities. In Figs. B.9–B.11 we show a selection of transitions for each selected molecule towards the two positions in order to validate the presence of at least one component in addition to the hot-core component.

The observed spectra of the selected species were modelled with Weeds (see Sect. 4.2.2) and population diagrams were derived (see Sect. 4.2.3) for both components at N1SE1 and N1NW3 in order to obtain rotational temperatures and column densities. To compare with results that were previously obtained in Paper I, we additionally use column density values derived at positions N1S (at a distance of 1″ from the hot core's centre to the south), N1S1 (1.5″ to the south), and N1W1 (1.5″ to the west). All positions are marked in Fig. 4.1.

Temperatures and velocities

First, we investigate whether the outflow positions N1SE1 and N1NW3 show significant differences in the derived rotational temperatures compared to the positions that are not exposed to the outflow and potential shocks that are associated with it. In Fig. B.12 we compare the rotational temperatures used to obtain the Weeds models with the results from the population diagrams at each position. The temperature values derived from the latter method deviate only marginally if at all from those used in the models, thereby validating the models. In Fig. 4.7 we compare the rotational temperatures of the various velocity components and positions in the hot core and in the outflow. Assuming that positions N1SE1 and N1NW3 experience shocks due to their location in the outflow lobes, one might expect elevated temperatures as a consequence of these shocks. However, in this regard the outflow positions do not stand out compared to the previously analysed positions (N1S, N1S1, and N1W1). Interestingly, at N1SE1, temperatures derived for the blue-shifted component (N1SE1:OF) are lower than or similar to the values in the hot-core component (N1SE1:HC). In addition, N-bearing molecules tend to have slightly higher rotational temperatures with a mean of ∼210 K (excluding NH_2CN) than the O-bearing molecules with ∼170 K at N1SE1:HC. With only two O-bearing COMs detected at N1SE1:OF such a trend cannot be clearly identified.

In addition, we explore possible correlations between velocity, linewidth, and temperature in Fig. 4.8. Figure 4.8a shows temperatures in comparison with the velocity offset from the source velocity v_{sys} = 62 km s^{-1}, where markers at $v_{off} < -7$ and >11 km s^{-1} correspond to the blue- and red-shifted emission, respectively. Each set of marker and colour represents one molecule. Filled markers represent N1SE1, unfilled markers N1NW3. When the molecule is detected in both the hot-core and outflow components at a given position, these two identical markers are connected by a line. This shows again that, in general, temperatures are lower in the outflow (OF) than in the hot-core component (HC) at N1SE1, except for CH_3SH and HC_3N, whose temperature values, however, have a higher uncertainty. A clear trend is not visible for N1NW3, only the much lower temperature for HC_3N in the outflow component stands out. Figure 4.8b shows the distribution of linewidths as a function of velocity offset, using the same marker and color scheme as in Fig. 4.8a. The outflow components generally show larger linewidths, which may arise from a higher degree of turbulence or blending of multiple narrower, unresolved velocity components. At N1NW3, the linewidth derived for methanol in the hot core seems to be larger than in the outflow, however, the outflow component is fairly weak in emission and may come with greater uncertainty, also in linewidth. Figures 4.8c and d show the distribution of line widths as a function of rotational temperature for N1SE1 and N1NW3, respectively, however, no trend is visible.

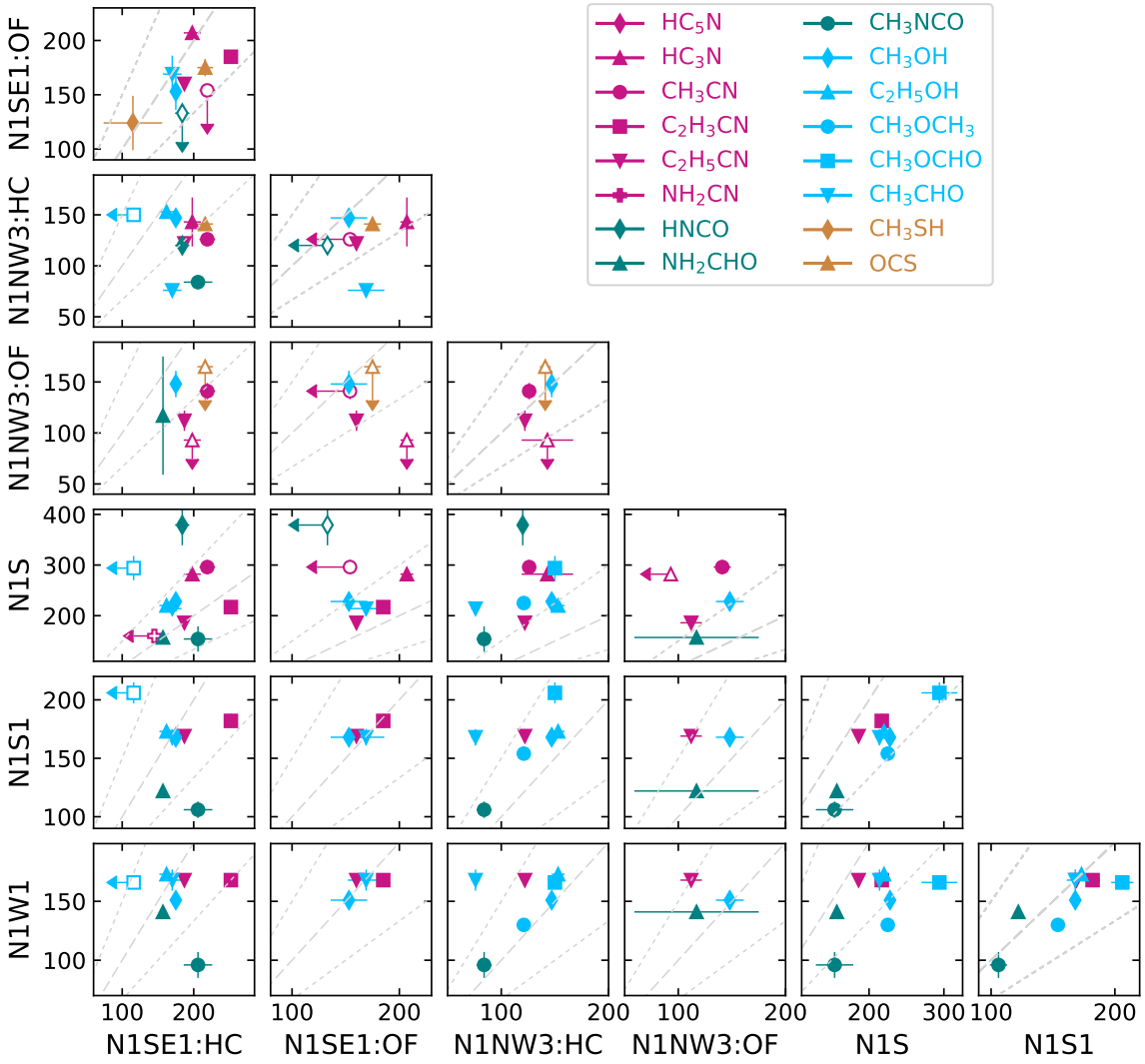

Figure 4.7: Rotational temperatures (in K) for various positions towards Sgr B2 (N1) derived with the population-diagram analysis. Pink markers indicate N-bearing species, teal markers (N+O)-bearers, blue O-bearers, and orange S-bearers. Arrows indicate upper limits. The grey dashed line shows where temperatures are equal. The two grey dotted lines indicate a factor 1.5 difference from unity.

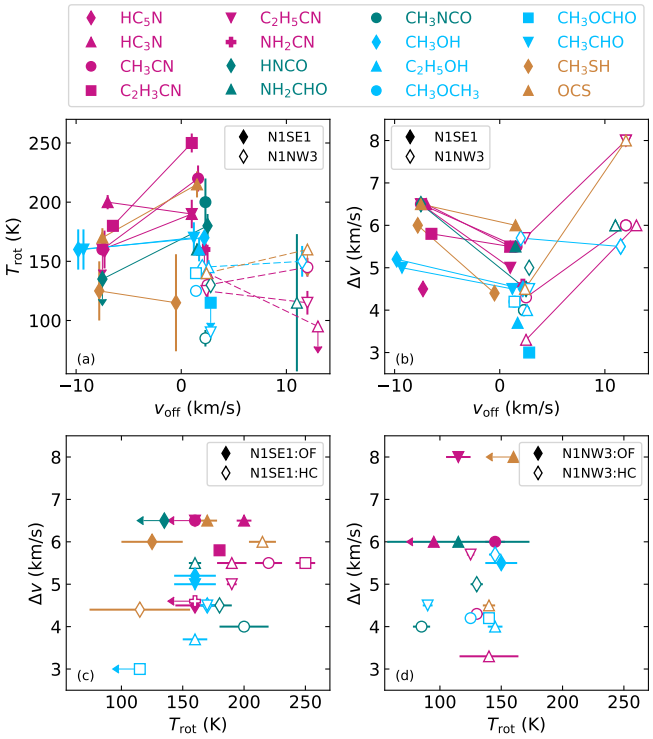

Figure 4.8: Correlation plots for Weeds model parameters: *Panel a:* Velocity offset $v_{\rm off}$ from the systemic velocity ($v_{\rm sys}$ = 62 km s^{-1}) versus rotational temperature $T_{\rm rot}$. *Panel b:* Offset $v_{\rm off}$ versus linewidth Δv ($FWHM$). *Panels c–d:* Temperature $T_{\rm rot}$ versus linewidth. Pink markers indicate N-bearing species, teal markers (N+O)-bearers, blue O-bearers, and orange S-bearers. Markers showing $|v_{\rm off}|$ values larger than 7 km s^{-1} in (a) and (b) correspond to the blue- and red-shifted components of positions N1SE1 (filled markers) and N1NW3 (empty markers), respectively. In panels (c) and (d) empty markers present the hot-core component at N1SE1 and N1NW3, respectively. Uncertainties on the temperature values are taken from the results of the population diagrams. Arrows indicate upper limits.

Column densities and abundances

We show the column densities that were used for the Weeds models in Fig. B.13. The values are similar to those derived from the fit in the population diagrams underlining their reliability (cf. Tables B.1–B.4). Following Paper I, we multiplied the column densities by a temperature-dependent vibrational correction factor, when necessary. Unfilled bars indicate upper limits on the column density, which were obtained by fixing all other parameters in the models to median values that were derived from other molecules. Figure B.13 shows in addition the column densities derived in Paper I for the positions N1S, N1S1, and N1W1 (see also Fig. 4.1 to locate these positions). For molecules that were not analysed in Paper I, we computed a Weeds model and derived a population diagram (HC_3N, CH_3SH, and HNCO, see Fig. B.1) or took values from other studies (2.8×10^{18} cm^{-2} for CH_3CN and 2.6×10^{16} cm^{-2} for NH_2CN from Müller et al. (2021) and Kisiel et al. (2022) towards N1S, respectively). For positions N1S1 and N1W1, these molecules were not considered.

To better compare the chemical compositions between the outflow and hot-core components and,

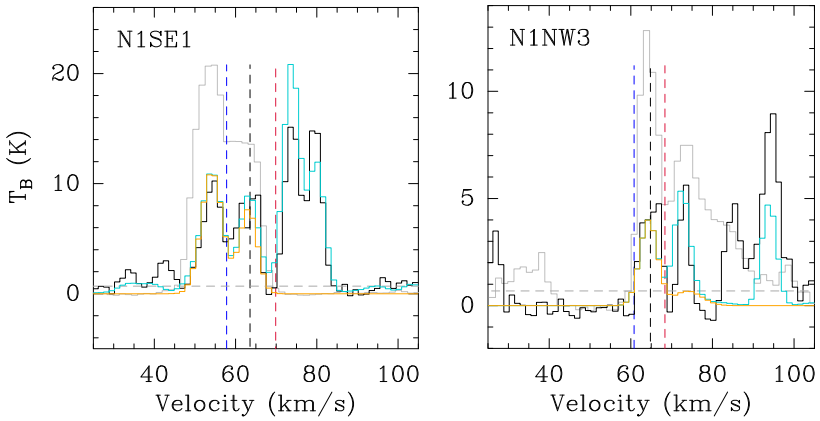

Figure 4.9: Observed spectrum of $C^{18}O$ $J = 1 - 0$ (black) overlaid by the respective Weeds models for both the outflow and hot-core components (orange) and the total Weeds model of all yet identified species at these positions (blue). For comparison, the grey spectrum shows the ethyl cyanide transition at 96.92 GHz scaled down by a factor 5 for N1SE1 and a factor 2 for N1NW3 (see also Fig. 4.5). The vertical black dashed lines mark the systemic velocities, while vertical red and blue dashed lines show the pixel-dependent inner limits used to integrate the blue- and red-shifted emissions (see also Fig. 4.5). The grey horizontal line indicates the 3σ level, where $\sigma = 0.23$ K.

later, between the results obtained for Sgr B2 (N1) and those of other sources, we compute abundances with respect to H_2, CH_3OH, and C_2H_5CN. Deriving abundances with respect to H_2 is difficult because there may be dust emission for the hot-core components, however, this cannot simply be applied to the outflow components. Therefore, we estimated the H_2 column densities from $C^{18}O$ $J = 1 - 0$ emission by fixing all parameters in the Weeds model, except for the column density, to average values derived for other molecules for a given component. The observed spectrum and the corresponding Weeds model are shown in Fig. 4.9 for N1SE1 and N1NW3. There is a minor contribution from the blue-shifted component of HNCO, $v = 0$ to the hot-core component of $C^{18}O$ at N1SE1, otherwise, the $C^{18}O$ spectral lines seem clean, although we cannot exclude further minor contamination by other species. If the assumed rotational temperature in the Weeds models were higher or lower by 80 K, the $C^{18}O$ column densities would differ by at most a factor 2. Assuming that CO remains a good tracer of H_2 column densities at these positions impacted by the outflow, we multiply the $C^{18}O$ column densities with a $C^{16}O$-to-$C^{18}O$ ratio of 250 ± 30 (Henkel et al. 1994) and a H_2-to-CO conversion factor of 10^4 to obtain H_2 column densities. This yields N_{H_2}(N1SE1:HC) = $(1.0 \pm 0.3) \times 10^{24}$ cm^{-2}, N_{H_2}(N1SE1:OF) = $(1.6 \pm 0.5) \times 10^{24}$ cm^{-2}, and N_{H_2}(N1NW3:HC) = $(3.8 \pm 1.2) \times 10^{23}$ cm^{-2}. The errors include an uncertainty on the $C^{18}O$ column density, where we assume $\Delta N_{C^{18}O} = 0.3 N_{C^{18}O}$, and the uncertainty on the CO isotopologue ratio. The values at N1SE1 are a factor 2–3 lower than the one at N1S1 shown in Fig. 8 in Paper I, which is at the same distance from the centre of Sgr B2 (N1) to the south, and a factor 10 lower than at N1S, which is 0.5″ closer to the centre. The difference in H_2 column density between N1NW3:HC and N1W3, which are at the same distance, is less than a factor 2. The $C^{18}O$ transition is not detected for N1NW3:OF because of a blend with stronger emission from HNCO, $v = 0$. The H_2 column densities at N1S and N1S1 are taken from Table E.24 in Paper I, where for the latter we use the value derived from $C^{18}O$, while for N1S, the value derived from dust emission had to be used, because the $C^{18}O$ transition was also seen in absorption whose contribution could not be determined.

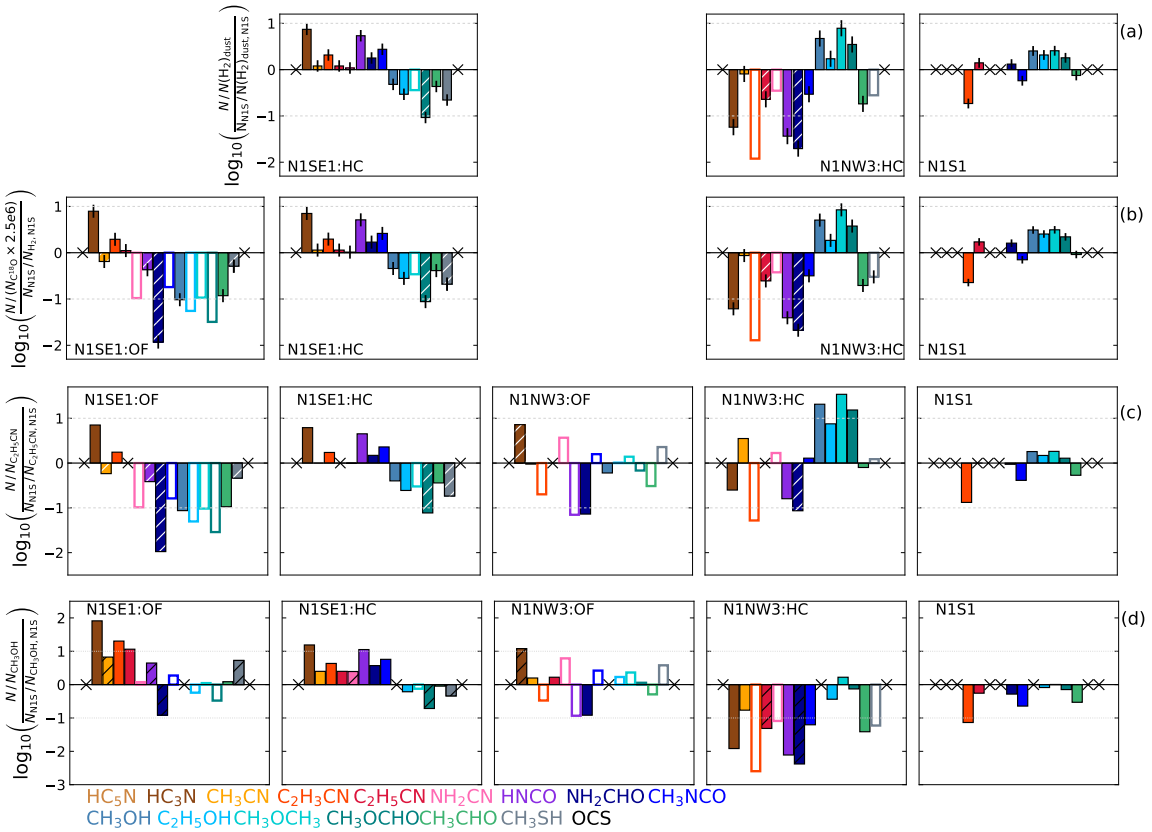

Figure 4.10: Comparison of the gas molecular content in the hot-core and outflow components at N1SE1 and N1NW3 amongst each other and with positions N1S and N1S1, which were analysed in Paper I. *Rows a–b:* Abundances with respect to H_2 normalised to the value derived for N1S, where H_2 column densities were derived from a) dust emission at 242 GHz and b) $C^{18}O$ for all components but N1S, for which the value from dust emission was used in both rows. Component N1NW3:OF is not shown, because $C^{18}O$ is difficult to identify due to contamination by another molecule. *Rows c–d:* Same as (b), but abundances with respect to C_2H_5CN and CH_3OH are shown, respectively. In all panels, hatched bars indicate when the rotational temperature in a population diagram (PD) was fixed (NH_2CN at N1SE1:HC and CH_3SH at N1S), the molecule was detected but a PD could not be derived (NH_2CHO at N1SE1:OF), or only an upper limit for the rotational temperature in the PD was derived. Empty bars show upper limits. HC_5N and OCS are not shown as we do not have the column densities of the two molecules at N1S.

In Figs. 4.10a and b, we show abundances with respect to H_2 normalised to the values at N1S. The H2 column densities were derived either from a) dust continuum emission at 242 GHz (Sánchez-Monge et al. 2017, Paper I) or b) $C^{18}O$ emission. For the former we assume that the dust temperature is equal to the rotational temperature of ethanol as done in Paper I, which yields N_{H_2}(N1SE1:HC) = (9.5 ± 2.7) × 10^{23} cm^{-2} and N_{H_2}(N1NW3:HC) = (4.0 ± 1.6) × 10^{23} cm^{-2}. The error bars include an uncertainty on the dust temperature of 20% and on the continuum level, that is the baseline, of 1σ = 1.67 K. The abundances with respect to H_2 revealed that C_2H_5CN abundances are comparable at N1SE1, N1S, and N1S1. Therefore, we additionally show abundances with respect to this COM in Fig. 4.10c. Figure 4.10d shows abundances with respect to methanol as this COM is commonly used to compare the chemical inventories between different sources.

Outflow (OF) components: Abundances with respect to H_2 and C_2H_5CN (Fig. 4.10a–c) reveal that the O- and (N+O)-bearing molecules are less abundant in N1SE1:OF than at N1S, also N1S1, by factors of a few up to an order of magnitude, or even almost two orders of magnitude in the case of NH_2CHO. The O-bearing molecules C_2H_5OH, CH_3OCH_3, and CH_3OCHO are not even detected in the outflow components, only CH_3OH and CH_3CHO are. On the other hand, HC_5N is only securely detected in the outflow component at N1SE1. The molecule is not shown in Fig. 4.10 because it is not detected at N1S. Abundances of CH_3CN and C_2H_3CN at N1SE1:OF differ only slightly from the values at N1S, while HC_3N is more abundant. At N1NW3:OF, only HC_3N, CH_3CN, NH_2CHO, and CH_3OH are detected and follow similar trends as at N1SE1:OF, except that the CH_3OH abundance is more similar to N1S. The comparison with abundances with respect to CH_3OH presents a quite opposite trend, at least for N1SE1:OF, where abundances for N-bearing molecules, except for NH_2CN, are higher by roughly 1–2 orders of magnitude in this component than for N1S and N1S1. Also, CH_3SH abundances are enhanced at N1SE1:OF. However, NH_2CHO abundances are lower in both outflow components compared to N1S, as was seen in abundances with respect to C_2H_5CN. Abundances of HNCO are higher in N1SE1:OF and lower in N1NW3:OF than in N1S.

Hot-core (HC) components: At N1SE1:HC, O-bearing molecules and CH_3SH are less abundant than at N1S and N1S1, similarly to the outflow component at this position but not as severely. Also similar to N1SE1:OF, abundances of N-bearing molecules, except for HC_3N, are comparable at N1SE1:HC and N1S. In contrast, (N+O)-bearing species are either similarly or more abundant in N1SE1:HC than in N1S, N1S1, and N1SE1:OF. The hot-core component at N1NW3 behaves differently compared to N1SE1:HC: in general, N- and (N+O)-bearing molecules are less abundant in N1NW3:HC, while O-bearing species are enhanced, except for CH_3CHO. Abundances with respect to CH_3OH reveal an enhancement of N- molecules in N1SE1:HC compared to N1S and N1S1, similar to the outflow component, but not as prominent. Moreover, all (N+O)-bearing species have enhanced abundances in N1SE1:HC. Abundances of O-bearing species are comparable to the values found for N1S and N1S1. At N1NW3:HC, abundances with respect to methanol for N- and (N+O)-bearing molecules as well as CH_3CHO are lower than at N1S and N1SE1:HC by 1–3 orders of magnitude. Most O-bearing species, except for CH_3CHO, show similar abundances to N1S and N1S1.

In summary, we do not only identify differences in the gas molecular inventory between the blue- and red-shifted components and all hot-core components analysed here, but also between the hot-core components at positions N1SE1 and N1NW3 and at N1S and N1S1. The most remarkable result are the much lower abundances of O-bearing molecules in the outflow component N1SE1:OF

with respect to H_2 and C_2H_5CN compared to N1S, while abundances of N-bearing molecules are comparable to N1S (except for HC_3N). A similar trend is seen for the comparison between the hot-core component at this position N1SE1:HC and N1S. In contrast, (N+O)-bearing molecules are more abundant in N1SE1:HC and less abundant in N1SE1:OF than at N1S. The comparison between abundances with respect to H_2 (or C_2H_5CN) and to CH_3OH shows that, in this case, the latter may not be the best molecule to normalise to, as its abundance with respect to H_2 changes a lot between the different components.

4.4 Discussion

4.4.1 Morphology of blue- and red-shifted emission

The blue- and red-shifted SiO and SO emission shown in Fig. 4.2 revealed a bipolar nature, however, especially at close distances to the centre of Sgr B2 (N1), more structure is seen that is not simply bipolar. Because of the complex morphology, not only seen in the maps of SO and SiO, but also other molecules (see Figs. 4.4, B.4–B.6, and B.7), it is challenging to disentangle the contribution of the outflow and other sources, such as the dense core itself or filaments, and to connect this to the gas molecular inventory that we have derived for blue- and red-shifted velocity components. Because of this complex structure, one might speculate whether Sgr B2 (N1) is a site of an explosive outflow event. For example, this was observed in Orion (e.g. Zapata et al. 2017), where such an event is not only characterised by a large number of observed finger-like structures originating from a common location, but also emission from COMs has been detected in the surrounding regions embedded in Orion KL that are supposedly impacted by the explosion (e.g. Zapata et al. 2011; Favre et al. 2017; Pagani et al. 2019). Zapata et al. (2017) reported on the observational differences of regular protostellar and explosive outflows. Although there are multiple finger-like structures identified in the emission morphology of SO and SiO in Sgr B2 (N1) (labelled aB1 and aR1–2 in Fig. 4.2 and, potentially, aB2 and aR3 in Fig. B.4), the rather clear separation of blue- and red-shifted emission with their spatial extension to the (south)east and (north)west, respectively, with at least some degree of collimation, suggests that we see a protostellar outflow. However, as also noted by Schwörer (2020), there might exist several protostars hidden from us by dust at the centre of Sgr B2 (N1) that could each drive an outflow. Still, the clear bipolar structure may speak against such a scenario of multiple driving sources unless there is a mechanism that roughly aligns these outflows in the same direction.

We highlighted three collimated features in emission of SO and SiO that we labelled aB1, aR1, and aR2 in Fig. 4.2. Their high degree of collimation, their detection at extremely high blue- and red-shifted velocities (see also velocity-channel maps in Fig. B.7), and their extension to large distances from the hot-core centre let us conclude that at least these three structures can be associated with the outflow. Determining any physical properties for these outflow features is difficult because of the highly uncertain inclination to the observer. The opening angle of the lobes is another factor of uncertainty due to the complex morphology of the outflow emission. Considering that blue- and red-shifted emission are fairly well separated, the inclination for the most collimated feature observed in SO have a value between 10° and 80°. However, if we consider all blue-shifted emission to the southeast, which is observed with a much wider opening angle (up to 60°), not only for SO, but also for all other molecules, the inclination may rather have a value between 30° and 60°. We estimate a maximum projected length along aB1 (feature B2 in the PV diagrams in Fig. 4.6) of $\sim 7''$, which corresponds to 0.3 pc, and a projected velocity of $v_{of} = v_{sys} - v_{max} \sim 62 - 35 = 27\,\mathrm{km\,s^{-1}}$ (cf. channel

maps of SO in Fig. B.7). If this collimated feature was however inclined by 80° to the line of sight (i.e. almost edge on), the true velocity would be as high as 150 km s^{-1}. On the other hand, if it were seen with an inclination of 10°, its spatial extent could reach up to 1 pc. These most extreme values of inclination result in a lower limit on the dynamical age of 2 kyr and an upper limit of 57 kyr. Similar values can be obtained for the red-shifted structure along aR1. Assuming an intermediate inclination of 45° yields an age of ∼10 kyr. The second blue-shifted feature B1 identified in the PV diagrams, is spatially more compact (maybe 1″) but reaches higher velocities ($v_{\rm of}$ = 37 km s^{-1}) and, hence, is younger with an age of at most 6 kyr for an inclination of 10°, but it could also be younger than 1 kyr for higher inclinations.

The blue-shifted component at ∼55 km s^{-1} that we have analysed at N1SE1 can likely be associated with feature B2 in the PV diagrams shown in Fig. B.8, that is the older one. On the other hand, the red-shifted component at N1NW3, which is only detected for a handful of molecules, cannot easily be assigned to one of the features identified in the PV diagram of SO, but rather coincides with more extended, less intense SO emission. Understanding the impact of the outflow on the emission morphology of the various molecules studied here and on their abundances derived for the outflow and hot-core components at N1SE1 and N1NW3 is the subject of the next sections.

4.4.2 Comparison to chemical composition of other sources impacted by shocks

In this section we compare molecular abundances that we derived with those of other sources that are known for their organic chemistry substantially driven by shocks. We look at G0.693, which is a position located not far from Sgr B2 (N) in the Sgr B2 molecular cloud complex. As many other CMZ clouds, G0.693 was found to be rich in COMs that are similarly or even more abundant than in known hot cores and corinos despite the absence of any sign of star formation (Requena-Torres et al. 2006, 2008; Armijos-Abendaño et al. 2015). Instead, the extraordinary conditions in the Galactic centre (GC) region were made responsible, such as large-scale shocks and an enhanced cosmic-ray flux (e.g. Henshaw et al. 2023). The richness in COMs across CMZ clouds and the only small variations in their abundances raise the question whether these represent the initial chemical conditions of the gas that eventually forms stars in the GC, such as in Sgr B2 (N). The 40 positions in the CMZ that had been observed in the original study by Requena-Torres et al. (2006) corresponded to peaks in SiO emission (Martín-Pintado et al. 1997). Therefore, although shocks traced by SiO emission in the CMZ are ubiquitous, these 40 positions seem to experience either frequent or exceptionally strong shocks that may cause enrichments of COMs in the gas. For example, a cloud-cloud collision has been proposed as the driver of shocks in G0.693 (Zeng et al. 2020). In particular, this source was the focus of many follow-up studies that reported on several new molecular detections (e.g. Jiménez-Serra et al. 2022, and references therein). This does not mean, however, that these molecules are not present in other CMZ clouds with similar physical conditions.

In addition to the fact that the positions studied by Requena-Torres et al. (2006) may only represent the material that is most strongly impacted by shocks in the CMZ, it is also likely that the chemical composition of the gas phase presently measured at these positions has been modified by the shocks, which in turn means that the current gas-phase composition of these positions may not directly probe (after desorption induced by the shocks) the chemical composition of the dust grains during the prestellar phase in the CMZ. In this sense, we do not consider the chemical composition of G0.693 as representing the chemical composition of the dust-grain mantles in Sgr B2 during the prestellar phase. We rather see G0.693 as revealing the gas-phase composition after the impact of shocks on

prestellar gas and dust, which motivates our comparison of the outflow components in Sgr B2 (N1) to this source.

Based on observations with the IRAM 30 m telescope and their follow-up study with the Green Bank 100 m Telescope (GBT) towards positions in the Galactic centre region, including G0.693, Requena-Torres et al. (2006, 2008) derived column densities for O-bearing molecules. After that, other studies aimed to investigate further the chemical inventory of G0.693, for example, Armijos-Abendaño et al. (2015) who performed observations with the Mopra 22 m telescope and derived column densities for many molecules, Zeng et al. (2018) who studied N-bearing molecules based on observations with the IRAM 30 m telescope and the GBT, and Rodríguez-Almeida et al. (2021) who used the IRAM 30 m and Yebes 40 m telescopes to study primarily S-bearing molecules. Molecular column densities that were derived towards G0.693 in the various studies are summarised in Table B.6.

The low-mass protostar L1157-mm drives an outflow that produces shocks upon encounter with the ambient interstellar medium (Bachiller & Pérez Gutiérrez 1997). Towards this outflow, multiple spots of shock-excited emission have been observed that reveal a rich and complex chemistry (e.g. Benedettini et al. 2007; Arce et al. 2008; Lefloch et al. 2017, cf. Table B.6). Amongst these, the most studied one is L1157-B1, which is located in the blue-shifted outflow lobe. It has been the target of numerous observations at lower angular resolution (see column LR in Table B.6), from which abundances of many molecules were derived. Interferometric studies towards L1157-B1 revealed evidence for spatial and chemical segregation of different molecules. For the clump L1157-B1b, some abundances have been derived (see column HR (B1b) in Table B.6).

In Fig. 4.11 we compare molecular abundances with respect to H_2 between G0.693, L1157-B1, and the outflow positions N1SE1 and N1NW3 in Sgr B2 (N1). The outflow component at N1NW3 is not shown as we could not derive a value for the H_2 column density. We use H_2 column densities of 1.35×10^{23} cm^{-2} for G0.693 (Martín et al. 2008) and 2.0×10^{21} cm^{-2} for L1157-B1 (Lefloch et al. 2017). In Appendix B.5 we provide more details on the observations and the method of analysis used in the studies on these two sources. In the right column of Fig. 4.11, we show abundances with respect to H_2 towards G0.693, where we used the results of Zeng et al. (2018) for N- and (N+O)-bearing species, except for NH_2CHO, for which we used an updated value from Zeng et al. (2023), those of Rodríguez-Almeida et al. (2021) for CH_3SH and C_2H_5OH, those of Requena-Torres et al. (2008) for CH_3OH and CH_3OCHO, and those of Requena-Torres et al. (2006) for CH_3CHO. The study by Armijos-Abendaño et al. (2015) was performed at slightly lower angular resolution, hence, we only use their OCS column density. In the cases where multiple studies reported on the column density of a molecule, we show this range of values as error bars in Fig. 4.11. The larger difference in column density for HC_5N may result from different excitation temperatures that were used to model the molecule: Armijos-Abendaño et al. (2015) derived ~32 K from a rotation diagram analysis that is twice that of Zeng et al. (2018), who used the software `madcuba`. This may similarly apply to the results of NH_2CHO, however, it cannot explain the difference for CH_3OH as both studies assumed the same excitation temperature, however, Armijos-Abendaño et al. (2015) used only one transition to compute the column density. For L1157-B1, we used the values obtained from single-dish observations because more such data are available and because the spatial scales of a few 1000 au probed by observations with the IRAM 30 m telescope towards L1157-B1 (at a distance of 352 pc, Zucker et al. 2019) are more similar to those probed with the ReMoCA survey towards Sgr B2 (N1). The values are shown in the left column of Fig. 4.11.

In the top panel of Fig. 4.11, we compare abundances with respect to H_2 between G0.693 and L1157-B1. Abundances of O- and (N+O)-bearing molecules are similar in both sources, except for

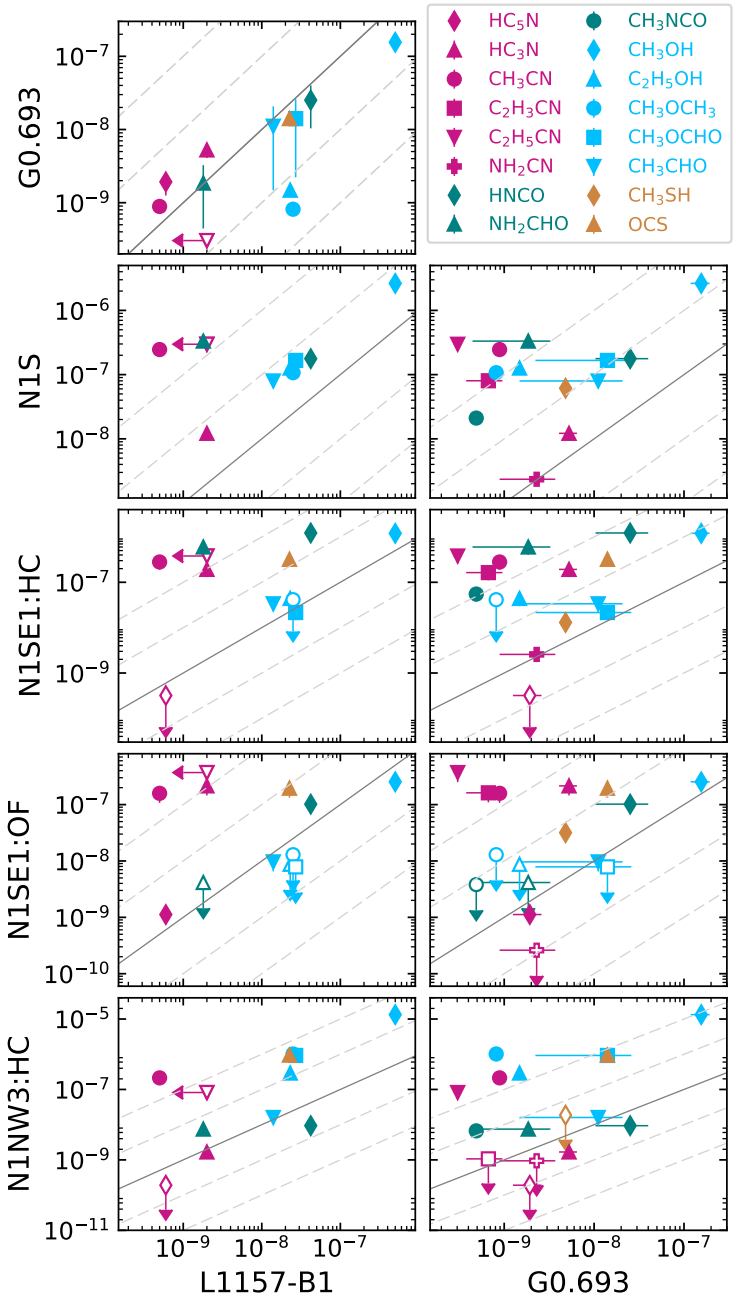

Figure 4.11: Molecular abundances with respect to H_2 for the outflow (OF) and hot-core (HC) components at N1SE1, for N1NW3:HC, and for N1S, G0.693, and L1157-B1. Pink markers indicate N-bearing species, teal markers (N+O)-bearers, blue O-bearers, and orange S-bearers. Unfilled markers with arrows indicate upper limits. The grey solid line shows where abundances are equal. The grey dotted lines indicate factors 10 and 100 from unity.

C_2H_5OH and CH_3OCH_3, which are an order of magnitude less abundant in G0.693. Abundances of N-bearing molecules are generally higher in G0.693 by factors of a few. However, there is a tendency towards higher abundances for O-bearing molecules in comparison to N-bearing species in both sources, except for C_2H_5OH and CH_3OCH_3 in G0.693. In Fig. B.14, we additionally compare abundances with respect to CH_3OH, which reveals a similar trend as seen in Fig. 4.11. The similarities in the molecular inventory, also noted by Zeng et al. (2018), suggest that similar processes may drive the chemistry in the two sources.

The detailed comparison of G0.693 and L1157-B1 with the positions in Sgr B2 (N1) based on Fig. 4.11 can be found in Appendix B.5. The key points are summarised in the following. No general trend between the two other sources and any position in Sgr B2 (N1) can be observed. Abundances with respect to H_2 that were derived for N1S are all higher than in G0.693 and L1157-B1 by ~1–2 orders of magnitude. At positions N1SE1 and N1S in Sgr B2 (N1), the cyanides (and HC_3N at N1SE1:OF) are more abundant by two orders of magnitude or more than in G0.693 and L1157-B1. The abundances of most O-bearing molecules at N1SE1:OF are likely lower than in the other two sources. The lack of any correlation between the molecular abundances between the outflow position in Sgr B2 (N1) and the other two sources suggests that a shock may impact the material differently or that the boundary physical conditions are different. A discussion on possible explanations for the chemical differences is provided in Sect. 4.4.5.

4.4.3 Comparison to hot-core models

As in Paper I, we compare our results to recent astrochemical models performed by Garrod et al. (2022, G22 hereafter). As a 3-phase model it considers the chemistry within the bulk ice, the grain/ice surface, and the gas phase as well as physical processes connecting one phase to the other. The physical setup compares to earlier models (Garrod et al. 2008; Garrod 2013; Garrod et al. 2017), in which two stages are distinguished: a cold collapse phase (stage 1), that takes place before the onset of the protostellar heating, and a subsequent warm-up phase (stage 2). Stage 1 happens on a timescale of $\sim 10^6$ yr. During this time, the density increases from 3×10^3 to 2×10^8 cm^{-3}, the dust temperature decreases from ~15 K to ~8 K, and the gas temperature is kept constant at a value of 10 K. Subsequently, in stage 2 gas and dust temperatures increase in the same manner, as they are assumed to be well coupled during this stage. The density is fixed to the final value of stage 1. Three different timescales are regarded for stage 2, meaning that the warm-up to 200 K either lasts 10^6 yr (slow), 2×10^5 yr (medium), or 4×10^4 yr (fast). The maximum temperature reached in the models is 400 K. The main differences of the new models (G22) compared to the previous ones (amongst other changes) are the inclusion of non-diffusive chemical reactions and the absence of bulk diffusion for all species but H and H_2. The latter leads to the trapping of species (including COMs) in the water-dominated ice mantles of grains until water itself desorbs at a temperature $\gtrsim$100 K. This co-desorption process of molecules with water is associated with a steep increase in gas-phase abundances at this characteristic temperature. The resolved abundance profiles that we derived in Paper I revealed such a steep increase at ~100 K for multiple COMs (see Fig. 15 in Paper I), based on which we could confirm that this process releases the bulk of these COMs to the gas phase in Sgr B2 (N1). For COMs that did not show this steep increase we proposed a dominant formation route in the gas phase or a lack of sensitivity.

In Appendix B.6, we provide a detailed comparison between the modelled peak abundances in the slow and fast warm-up phases with the observed abundances towards both components at positions N1SE1, N1NW3:HC, N1S and N1S1 (derived in Paper I), and towards G0.693 and L1157-B1 that were

discussed in Sect. 4.4.2. The comparison shows that none of the components is perfectly reproduced by any model (see Figs. B.15 and B.16). In the following, we summarise some trends that can be deduced from this comparison regarding formation and destruction pathways for mainly O- and N-bearing molecules that play a role for the discussion on the impact of the outflow on the chemistry in Sgr B2 (N1) in Sect. 4.4.5, also including some knowledge gained in Paper I.

From Paper I, we learned that O-bearing molecules (CH_3OH, C_2H_5OH, CH_3OCH_3, CH_3OCHO) are mainly produced in the solid phase and desorb thermally, in agreement with the models. CH_3CHO and C_2H_3CN are efficiently produced in the hot gas phase and C_2H_5CN showed evidence for both solid- and gas-phase formation, although the gas-phase formation of C_2H_5CN is not (yet) included in the G22 models. Results for NH_2CHO and CH_3NCO were less conclusive, but also likely suggest formation in both phases. The detection of HC_5N in only the outflow component N1SE1:OF suggests that its formation may proceed more efficiently in the post-shock gas. According to the G22 model, there are two periods (at ~200 K and $\gtrsim$350 K) during which the molecule is efficiently produced in the gas phase. This can be seen in Fig. B.17, which shows qualitatively at what times and temperatures of the pre- and protostellar evolution the molecule is dominantly formed (green) or destroyed (blue) in the G22 models (of which this kind of figure is an output). A dramatic temporal temperature increase caused by a shock (possibly no longer traced by the derived rotational temperatures in Sgr B2 (N1)) may have accelerated the formation that is associated with the second period. At these high temperatures, atomic N is sourced from ammonia (NH_3) via H abstraction in the models and reacts with hydrocarbons (e.g. C_2H_5) to form HC_5N. In a similar way, HC_3N can be produced at high temperatures. We speculate that this may also be the case for the larger cyanides, but such a formation route is not included in the current models. Wing emission in NH_3 observed towards Sgr B2 (N1) indicates that the molecule is present in the outflow (Mills et al. 2018).

Ammonia is a widely used tracer of temperature in interstellar gas, especially also for CMZ clouds, where detections of metastable transitions with high upper-level energies ($E_u \gtrsim 500$ K) imply temperatures of $\gtrsim$ 300 K (e.g. Hüttemeister et al. 1995b; Wilson et al. 2006; Riquelme et al. 2013; Mills & Morris 2013; Candelaria et al. 2023). These hot components are usually observed in addition to a colder component (< 100 K), which is traced by the lower-energy transitions, and maybe warm gas at temperatures in between. Although the hot NH_3 component is often associated with more tenuous gas than the core of the CMZ clouds, where most of the other molecules are located, Mills & Morris (2013) found that the hot component rather follows the morphology and kinematics of HC_3N, which is associated with the denser gas. A systematic study on changes in the abundance of hot NH_3 and HC_3N or HC_5N as a function temperature may confirm the proposed chemical link between the species.

In Paper I, we found that the destruction of some O-bearing COMs seems to proceed more efficiently than predicted by the models. As a possible reason we stated that higher volume densities than assumed in the model may lead to an accelerated destruction, which remains to be confirmed by the models, however. If this were a consequence of higher densities, it may (partially) explain the reduced abundances of O-bearing molecules at N1SE1, assuming that a shock wave compresses the material through which it passes. The possible impact of higher densities and (temporally) higher temperatures on the chemistry in the post-shock gas in Sgr B2 (N1) are further discussed in Sect. 4.4.5.

4.4.4 Comparison to shock models

Burkhardt et al. (2019) modelled the evolution of chemistry in a C-shock at a speed of 20 km s^{-1} and distinguished between multiple regimes of chemistry. Within the first 50 yr after the shock has passed,

rapid formation of molecules on dust grains takes place due to enhanced mobility of species, shortly after which sputtering of grains releases the molecules to the gas phase. As a consequence, one would find the entire ice inventory in the gas phase at these times, which would mainly include methanol and other O-bearing species. The dust is heated faster than the gas ($T_{\rm dust,max} \sim 35$ K) and the latter reaches its peak temperature around 1000 yr ($T_{\rm gas,max} \sim 1000$ K) after the shock has passed. This is when also enhanced gas-phase formation starts to proceed efficiently. Species that benefit from this include, for example, CH_3CHO and NH_2CHO in the Burkhardt et al. models. Molecules that do not show a significant change in their gas-phase abundances at this stage are HNCO, CH_3OCH_3, and CH_3OH. After 10^4 yr in the model, the environment has cooled back to its low initial temperature, which is when species start to return to the solid state. For some species such as NH_2CHO, CH_3CHO, or CH_3OCHO, gas-phase formation continues as the precursor molecules are still available.

The physical conditions of the material that is impacted by the shock in this model are quite different from what we expect for Sgr B2 (N1). Due to the close vicinity of, especially, N1SE1 but also N1NW3, densities and temperatures in the pre- and post-shock gas are likely higher than in the model, where the maximum post-shock density is $\sim 3 \times 10^5$ cm^{-3}. Therefore, we may also expect that thermal desorption, as a consequence of the protostellar heating, released ice species already in the pre-shock phase and we do not expect any redeposition phase to occur. Therefore, we would expect that a shock in Sgr B2 (N1) may result in an increase of the gas temperature, compression of the material, and release of additional solid material from the dust grains that did not (yet) desorb thermally. When trying to sort the various higher-velocity features that we identified in the PV diagrams in Fig. B.8 in some sort of timeline, feature B2 could be an older ejection event, because it is spatially the most extended and its peak velocity with respect to the hot core is lower than that of the faster and more compact feature B1. This additionally suggests that it may have decelerated. Therefore, post-shock gas-phase chemistry may be proceeding efficiently in B2 and enriching (or depleting) the gas phase with (of) species, including COMs. Accordingly, if B2 was an older ejection event, the peak sputtering phase may have gone by (if it happened at all), meaning that there was enough time to reduce abundances of molecules that are mainly the product of grain-surface chemistry, provided they do not have additional formation routes in the gas phase. From our observations in comparison with the G22 model, this would include the O-bearing COMs CH_3OH, CH_3OCHO, CH_3OCH_3, but also NH_2CN and CH_3SH. Unfortunately, the behaviour of N-bearing species from the pre- to the post-shock phase was not studied in Burkhardt et al. (2019), which would be important to see whether enhanced gas-phase formation is expected, as it was indicated by the abundances with respect to CH_3OH in the outflow of Sgr B2 (N1). For the faster feature B1 we estimated a younger age (it could be younger than 1000 yr if seen at high inclination). At this age, we might expect to find the source in the phase of rapid ice mantle evaporation. However, at these short distances to the centre of the hot core, all ice has likely been sublimated and further processed in the hot gas phase prior to any shock. Therefore, it may not be surprising to observe this feature only securely in emission of SO, SiO, OCS, HC_3N, C_2H_3CN, and C_2H_5CN and not in emission of CH_3OH, C_2H_5OH, or CH_3OCH_3, which are products of grain-surface chemistry. This could be supported by taking into account the results from Paper I, where abundance profiles of the latter three COMs decrease with shorter distances to the hot-core centre, while that of C_2H_3CN increases, which we explained with destruction and formation of these COMs in the gas phase, respectively.

4.4.5 Implications for the chemistry in Sgr B2 (N1)

The following discussion is focussed on position N1SE1, since not many molecules are detected in N1NW3:OF and the hot-core component seems to still be influenced by the nearby continuum source. The behaviour of abundances with respect to H_2 (also C_2H_5CN) suggests that O-bearing molecules might be less abundant (i.e. more efficiently destroyed) in N1SE1:HC, and even less in N1SE1:OF, than at N1S, while abundances of N-bearing species are similar in all components. In both G0.693 and L1157-B1, the rotational temperatures derived for various molecules (10–30 K) are generally much lower than the kinetic temperature (50–140 K, Zeng et al. 2018; Mendoza et al. 2018; Codella et al. 2020) determined for these sources. This is a consequence of low volume densities (10^{4-5} cm^{-3}, Armijos-Abendaño et al. 2015) and results in sub-thermal excitation. Rotational temperatures that we derived in both components at N1SE1 and N1NW3 are generally above 100 K and reach up to 200 K depending on the molecule. Hence, the volume density at these positions must be high. It may be that densities are even higher than towards N1S. This may be supported by the presence of numerous bright H_2O masers (McGrath et al. 2004) that need high densities to be excited ($\sim10^9$ cm^{-3}, Hollenbach et al. 2013). At this point we are not certain about the exact relation between the two components at N1SE1 (and N1NW3) and the outflow. This discussion is taken up on in Sect. 4.4.6. In general, the passage of a shock (e.g. provoked by an outflow) is capable of compressing material and although temperatures are high in the outflow component at N1SE1, the values are lower than in the hot-core component at this position. This may suggest that the former could be more shielded, due to the higher densities, from external heating sources, provided that this temperature difference is not an effect of projection.

Effects of a high volume density and high temperature

An enhanced volume density may accelerate the gas-phase production of molecules, provided the reactants are sufficiently abundant. For example, we mentioned in Appendix B.6.2 that, according to the G22 models, HC_3N and HC_5N can be produced from atomic N at temperatures of >350 K. Atomic nitrogen at these temperatures is the product of the breakdown of ammonia through successive H abstraction, which may not only be involved in the formation of the cyanopolyynes but potentially also in the gas-phase formation of the complex cyanides. As the equivalent for O-bearing molecules, one might think of sourcing atomic O from H_2O or CO that may then be involved in the formation of larger molecules. However, the destruction reactions for these two molecules have much higher barriers than for NH_3, which makes them unlikely to proceed even in shocked gas. Even if atomic O was available, there are currently (almost) no reactions known that include atomic O to produce O-bearing COMs. Hence, if an enhanced gas-phase formation is restricted to N-bearing molecules, due to the availability of reactants such as atomic N, then this explains why abundances of other products of gas-phase chemistry, such as CH_3CHO, are not enhanced. This may also apply to CH_3OCH_3 and CH_3OCHO as the G22 models include formation routes in the gas phase for these two COMs, which involve CH_3OH and CH_3OCH_3 as reactants, respectively.

On the other hand, in order to explain a decrease in the observed abundances of some (O-bearing) COMs towards higher temperatures steeper than in the model, we discussed in Paper I that densities higher than assumed in the model may cause a more efficient destruction of these COMs in the gas phase. Such a scenario may explain the lower abundances of O-bearing molecules relative to H_2 that we derived towards N1SE1. However, whether there are destruction mechanisms proceeding in higher-density gas that only apply to a specific group of molecules, that is O- and not N-bearing

species, is uncertain. This may rather imply that a lack of gas-phase formation routes, able to compete against the destruction of O-bearing molecules, results in the segregation. Still, O-bearing molecules are less abundant than expected from N1S. Instead of the continuous destruction in the higher-density post-shock gas, reactions with energy barriers favouring certain products may have been able to proceed as a result of the brief temperature peak during the passage of the shock. For example, we may speculate that reactions that involve O-bearing COMs and produce H_2O tend to have lower barriers than reactions that involve N-bearing COMs and produce HCN, because the former have a higher exothermicity as water is a more stable molecule than HCN. However, this mechanism itself needs to be confirmed in models. Furthermore, these reactions likely need thousands of K to proceed efficiently, hence, this would require a shock stronger than in the model of Burkhardt et al. (2019), where $T_{\rm gas,max} = 1000\,{\rm K}$.

An important factor impacting the molecular content in the post-shock gas is dust. As described in Sect. 4.4.4, the passage of a shock in a cold environment leads to the desorption of grain-surface species either due to the temporal temperature increase or because the dust grains get sputtered. Because we do not see an enhancement of species that are mainly the product of grain-surface chemistry (e.g. C_2H_5OH, CH_3OCH_3, and CH_3OCHO), the relation between the dust and the shock may be different for the outflow of Sgr B2 (N1). Because of the short distance of N1SE1 (and N1NW3) to the centre of the hot core, temperatures were likely high enough for thermal desorption to proceed in the pre-shock gas. Therefore, the gas phase has probably already been enriched with grain-surface species, but also with products of high-temperature gas-phase chemistry, before the shock hit the material. In that case, a shock may not have a great impact on the sublimation of ice-mantle species any more, but still on the release of less volatile species, such as Si to form SiO in the gas phase. Moreover, we do not expect the initial dust composition (set before warm-up) to be much different for the various positions because of the short distances of N1SE1 and N1NW3 to the centre of the hot core. Therefore, this cannot be the reason for chemical differences.

A shock-preceding hot-core phase

Based on the above discussion, the present-day gas chemical content of the outflow component at N1SE1 (in some way also the hot-core component) has probably been dominantly influenced by two processes: a phase of hot-core chemistry, including thermal desorption of ice species and gas-phase chemistry, that preceded a shock impact, as well as compression and heating of the material by the shock. Accordingly, most of the ice species have already desorbed to the gas phase before the shock passed, meaning that the shock caused the release of primarily less volatile species. In the post-shock gas, some N-bearing molecules are efficiently formed, thereby, likely counteracting any destruction reactions, while there are no gas-phase formation routes for most O-bearing COMs. In contrast, these seem to be even more efficiently destroyed (when compared to N1S) either due to the increase in density or temperature, although the exact process is uncertain. Assuming that N1S is representative of pre-shock molecular composition in Sgr B2 (N1) and N1SE1:OF of the post-shock composition, the impact of a shock on O- and N-bearing molecules in Sgr B2 (N1) is schematically shown in Fig. 4.12.

This scenario may be able to explain several observed differences between Sgr B2 (N1), G0.693, and L1157-B1 (see Fig. 4.11). For a direct comparison, G0.693 is also shown in Fig. 4.12. Abundances of the cyanides are higher in both N1S and N1SE1 than in G0.693 and L1157-B1 suggesting that these species were initially produced in the hot pre-shock gas and, in the post-shock gas, formation and destruction may be competing, which holds up the high abundances. Given that G0.693 and L1157-B1

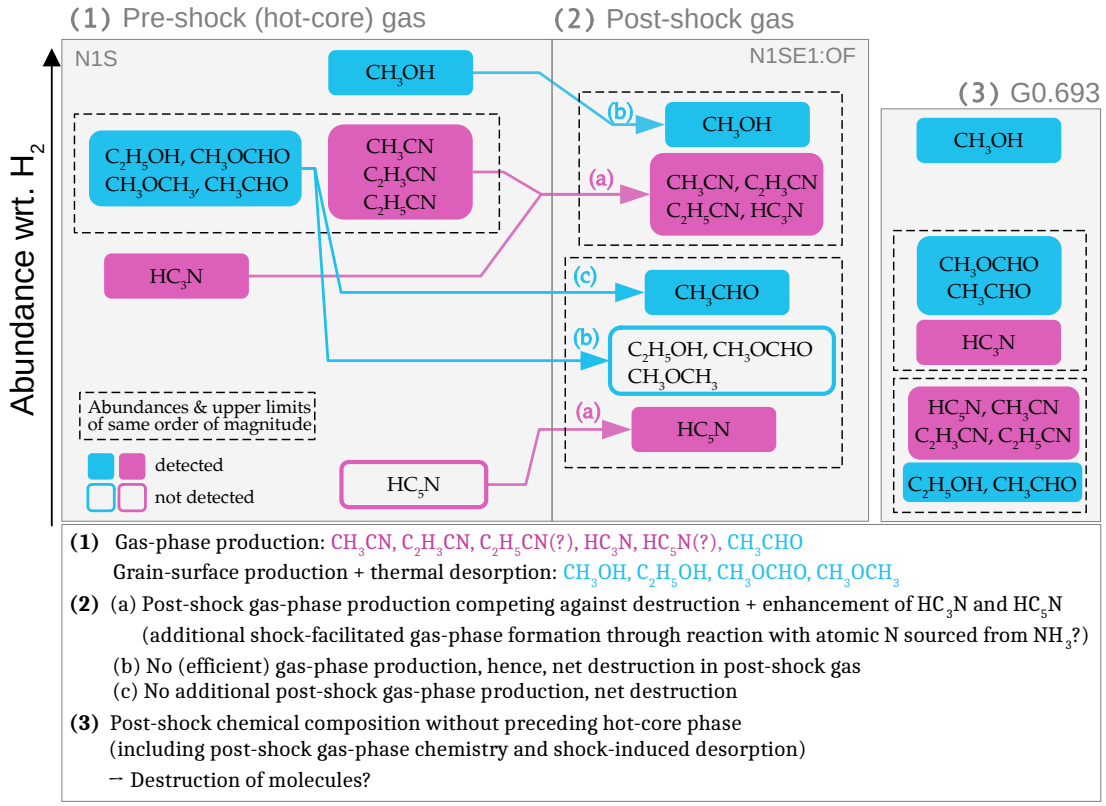

Figure 4.12: Illustrative behaviour of abundances of O-bearing COMs (blue) and N-bearing molecules (pink, including cyanopolyynes and cyanides) in Sgr B2 (N1) in (1) the pre-shock gas (here represented by N1S) and (2) the post-shock gas (N1SE1:OF) in comparison to (3) G+0.693−0.027. Involved physical processes or chemical reactions are discussed in detail in Sects. 4.4.3–4.4.5; key points are provided below the figure. Boxes filled with colors indicate detections while empty ones represent upper limits. Dashed boxes enclose molecules with similar abundances (within an order of magnitude).

did not go through a phase of hot-core chemistry, this may explain the much lower abundances of cyanides compared to Sgr B2 (N1). This may also apply to HC_3N and HC_5N in these sources. In Sgr B2 (N1), HC_3N has a high abundance at N1S, meaning that it is also a product of hot-core chemistry (be it on grain surfaces or in the gas phase). However, it is about a factor 10 more abundant at N1SE1, and with that similarly enhanced as the cyanides compared to G0.693 and L1157-B1, maybe suggesting that there is an additional gas-phase formation route (possibly from atomic N). This also applies to N1NW3:OF where the HC_3N abundance is as high as for N1SE1. The non-detection of HC_5N in all hot-core components in Sgr B2 (N1) and the similar abundance in N1SE1:OF, G0.693, and L1157-B1 may indicate that this species is not primarily a product of hot-core chemistry (at temperatures below 350 K), but was rather efficiently formed later in the post-shock gas. Because O-bearing molecules generally tend to be similarly or more abundant than N-bearing molecules in G0.693 and L1157-B1, they may not be as efficiently destroyed as in N1SE1, which may be a consequence of the lower volume densities than at N1SE1 or of a less violent shock that did not facilitate certain gas-phase (destruction) reactions. Especially for the comparison of G0.693 and

Sgr B2 (N1), taking into account the higher cosmic-ray flux and its influence on the chemistry in the different density environments may also be of importance.

Ultimately, in order to confirm the proposed scenario in which gas and dust in Sgr B2 (N1) are exposed to efficient protostellar heating before the passage of a shock, we would need to run shock models. The assumed physical conditions in the chemical models, with which we compared the observational results, do not exactly apply to those expected in the outflow of Sgr B2 (N1). The G22 models do not include shocks and the models of Burkhardt et al. (2019) were designed to predict the impact of the L1157 outflow on the ambient material, which is overall colder and less dense than in Sgr B2 (N1). Therefore, we need shock models that take into account overall higher pre- and post-shock densities as well as higher initial temperatures. Moreover, the effect of hot-core chemistry in the pre-shock phase, including thermal desorption due to protostellar heating as well as gas-phase chemistry, should be investigated. Finally, both the G22 models and the models of Burkhardt et al. (2019) assume a standard cosmic-ray ionisation rate. Exploring the impact of higher cosmic-ray ionisation rates, which are known to prevail in the CMZ (e.g. Indriolo et al. 2015), on shock models would be interesting.

4.4.6 Implications for the outflow morphology

Based on the integrated intensity maps shown in Figs. 4.2 and B.4–B.6, it is difficult to disentangle structures that solely originate from the outflow. Although most of the hot-core emission can be avoided thanks to the LVINE method, some emission may still be included in the integration. Filamentary structures have also been identified (see Fig. 4.1 and Schwörer et al. 2019) in dust continuum emission and in emission of some molecules at red- and blue-shifted velocities. The gas molecular content that we derived in N1SE1:OF along with rotational temperatures that are lower than in N1SE1:HC and the presence of H_2O masers suggest that this component may be characterised by a high volume density, possibly even higher than at N1S. Moreover, the similar behaviour of molecular abundances in N1SE1:HC and OF imply that the hot-core component at this position may also be influenced to some extent by what drives the chemistry in the outflow component. The molecular component of a protostellar outflow can often be subdivided into a fast molecular jet characterised by a high degree of collimation, a more loosely-collimated low-velocity outflow, and the walls of an outflow cavity (e.g. Tychoniec et al. 2021). Molecules that can be observed in a fast collimated jet are usually species such as H_2, SO, SiO, or CO, although the latter may also trace the outflow cavity; (for an illustration, see the well-studied case of the low-mass protostellar outflow HH 211 Gueth & Guilloteau 1999; Hirano et al. 2006). The collimated emission features that we observe for SO and SiO (labelled aB1, aR1, and aR2 in Fig. 4.2) and that remain visible up to very high blue- and red-shifted velocities may represent such a jet. The bulk of the emission from all analysed molecules in the outflow is observed at lower velocities and with a much wider opening angle suggesting that it may represent a kind of lower-velocity outflow, if all of the emission is indeed associated with an outflow. This wider-angle outflow may contain dominantly material that was entrained and accelerated by the jet as it propagates through the envelope or material that originates from some kind of disk and ended up in the outflow through disk winds. Because the behaviour of abundances in the hot-core component at N1SE1 is somehow similar to that of the outflow component, the former may be associated with some kind of cavity wall, whose density or temperature was increased by the shock, however, to a lesser extent than in the outflow component itself. This would not be a typical cavity wall, which is exposed to the UV radiation from the protostar and thus traced by photochemistry. This component in Sgr B2 (N1) is still

embedded in the hot core and shielded from UV radiation. However, it remains questionable how the shock impacted the density or temperature while the systemic velocity of this component does not show any signs of interaction with an outflow. On the other hand, one might speculate whether N1SE1:HC represents the chemical composition prior to the shock impact, which would mean that this hot-core component was different from N1S to begin with. However, we cannot tell what kind of process would lead to such differences.

4.4.7 Implications for segregation of O- and N-bearing species in other sources

Multiple observational studies revealed differences between species, in particular, O- and N-bearing molecules in their emission morphology or in values of rotational temperature and abundances. For example, early observations (e.g. Caselli et al. 1993) revealed chemical differences between the hot core and the compact ridge in Orion. These two environments come with different physical properties (e.g. Tercero et al. 2010), where the hot core is hotter (>200 K) and denser ($\gtrsim 10^7$ cm^{-3}) than the ridge (~100 K and ~10^6 cm^{-3}) and shows high abundances of N-bearing molecules, while the compact ridge is dominated by emission of O-bearing molecules (Blake et al. 1987; Crockett et al. 2014; Pagani et al. 2019). Chemical models, that took into account the different observed physical conditions, predicted that hot gas-phase chemistry played a more important role in the hot core (Caselli et al. 1993; Crockett et al. 2015). In addition, the outflow driven by the nearby young stellar object IRc2 was proposed to maybe have an impact on the observed molecular content (Caselli et al. 1993). More recently, the chemical segregation in the Orion KL region was explored with ALMA in the context of the explosive outflow event (already mentioned in Sect. 4.4.1) that happened in this region about 500–550 yr ago (Gómez et al. 2008) and is probably impacting the chemistry in the various sources contained in this region (Zapata et al. 2011; Pagani et al. 2017, 2019). With this in mind, if the Orion hot core was indeed a typical hot core, that is, if it contained an internal heating source (Wilkins et al. 2022), which is debated (e.g. Zapata et al. 2011; Orozco-Aguilera et al. 2017), it might have gone through a phase of thermal desorption and high-temperature gas-phase chemistry before it started to interact with the shock originating from this explosion. Similar to our observations, the hot-core region in Orion KL is bright in emission from, for example, the cyanides, HC_3N, and OCS, but also from CH_3OH and HNCO. As shown in earlier studies, most of these molecules reveal only weak emission, if any at all, in the compact ridge while emission of some O-bearing COMs such as CH_3OCH_3 and CH_3OCHO peak here. This could be more similar to what is observed in G0.693 and L1157-B1, also based on the lower temperatures associated with this source. However, other O-bearing molecules, for example C_2H_5OH, do not show emission as bright. The segregation between O-bearing COMs was studied by Tercero et al. (2018), who proposed that the availability of different radicals (CH_3O and CH_2OH) as reactants might play a role. Besides the compact ridge and the hot core, there are more sources in this region that are bright in emission of some molecules and lack emission of others. Ultimately, Orion KL reveals a high degree of chemical diversity and further investigation is needed to understand the impact of the explosive event on the chemistry in the various embedded sources and whether some of the involved processes resemble what we propose for the outflow position in Sgr B2 (N1), where also the different timescales since the passage of a shock need to be considered.

Allen et al. (2017) derived the molecular composition towards four continuum sources (A, B1, B2, B3) in the high-mass star-forming region G35.20-0.74N and found that abundances with respect to H_2 of N-bearing species, especially C_2H_3CN and C_2H_5CN, are higher in sources A and B3 and lower, if they were detected at all, in sources B1 and B2. Amongst other ideas, the authors proposed

a scenario in which an enhanced gas-phase formation accounts for the enhancement in N-bearing molecules in A and B3, based on derived temperatures that are higher in these sources than in B1 and B2 (similar to the early Orion KL studies). Based on the interpretation of our observed results, where cyanides are produced in the hot gas phase, it may not be too surprising that their abundances are higher in the hotter sources B3 and A ($T > 250$ K) than in B1 and B2 ($T < 180$ K). However, in B3 also O-bearing molecules are generally more abundant than in the other sources, or at least similarly abundant. Again, based on our results, where O-bearing molecules are destroyed in the high-temperature gas phase, this may be the more puzzling result. However, the authors used average kinetic temperatures for their classification of the sources that they derived using CH_3CN emission. The actual range of temperatures shows that the sources could be more similar to each other. Recently, Zhang et al. (2022) reported on a spiral-like structure around B1 in SO_2 emission, which is associated with a disk and which also coincides with the continuum peaks B3 and B2. In addition, sources A and B1 drive outflows (e.g. Zhang et al. 2022) and there is also SiO emission associated with the filament in which all sources are embedded. Therefore, one or more sources could be impacted by shocks. For example, this may have heated up B3, which enabled the production of N-bearing species.

Observations towards the hot-core precursor G328.2551–0.5321 (Csengeri et al. 2019) revealed an enhancement in abundances with respect to methanol of O-bearing molecules towards two position that the authors associated with a disk. The enhancement was proposed to result from accretion shocks, that sputtered the dust grains and, thereby, released the molecules into the gas phase. On the other hand, N-bearing molecules showed a more spherical distribution that the authors associated with the thermal desorption of these species from dust grains. They proposed that this source may be in an early evolutionary stage. If we assume that this source is indeed of a younger age and is possibly on the verge of becoming a hot core similar to Sgr B2 (N1), the explanation for the chemical segregation given by the authors together with the observed velocity structure and derived temperatures can hardly be connected to any scenario that we proposed in Paper I or here in this work.

Another mechanism, that has been introduced as a potential driver of chemical segregation is carbon-grain sublimation. van 't Hoff et al. (2020) proposed that a rise in temperature to >300 K provoked by an accretion burst may lead to the thermal sublimation of less-volatile carbon-rich species from dust grains that will preferably react with N-bearing species in the gas phase. The possible additional release of ammonium salts could enhance the amount of nitrogen (and N-bearing species) that would be available for reactions. Observationally, this would manifest in intense and compact emission of cyanides, where these high temperatures are reached, and in enhanced abundances of these species (see also Nazari et al. 2023). Furthermore, rotational temperatures of N-bearing species should be elevated compared to O-bearing molecules. At N1SE1 in Sgr B2 (N1) temperatures likely exceeded 300 K temporarily as a consequence of a shock and the values that we derived tend to be slightly higher for N-bearing species (cf. Fig. 4.7). Abundances of the cyanides with respect to H_2 are similarly high in N1S and N1SE1 suggesting that either abundances remain more or less unchanged or that enhanced gas-phase formation competes against their destruction in the post-shock gas. We proposed that atomic N sourced from NH_3 may be involved in the gas-phase formation. Nonetheless, it is not excluded that carbon-grain sublimation contributes reactants for the formation of cyanides. However, because the high temperatures required for this process result from a violent event that is an accretion burst or the impact of a protostellar outflow, refractory carbonaceous material (and ammonium salts?) could also be released non-thermally, for example through grain sputtering, leading to the same observational features.

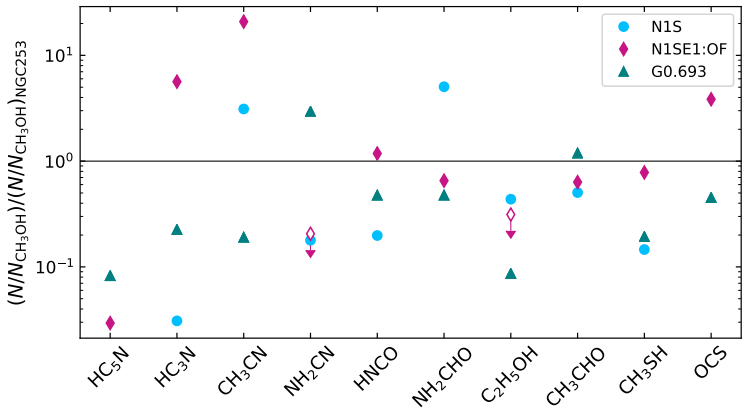

Figure 4.13: Abundances with respect to CH_3OH derived towards N1SE1:OF and N1S in Sgr B2 (N1) and G0.693 normalised by the values observed towards the central molecular zone of the nearby starburst galaxy NGC 253 (Martín et al. 2021). Empty markers with arrows indicate upper limits.

4.4.8 Comparison to extragalactic sources

The results obtained towards CMZ sources, such as Sgr B2 (N1) and its outflow or G0.693 can also be used to shed light onto the chemistry of clouds in the central regions of other galaxies, given that these may similarly be exposed to enhanced cosmic-ray fluxes and shocks with or without star formation. For example, unveiling the chemical composition towards the central molecular zone of the starburst galaxy NGC 253 is the goal of the ALCHEMI (ALMA Comprehensive High-resolution Extragalactic Molecular Inventory, Martín et al. 2021) survey. Figure 4.13 compares abundances with respect to CH_3OH towards N1SE1:OF and N1S in Sgr B2 (N1) and G0.693 normalised by the values observed towards NGC 253. The values for NGC 253 were taken from (Martín et al. 2021), who derived these from the data observed with the Atacama compact array (ACA) of ALMA at a resolution of 15″ (260 pc at a distance of 3.5 Mpc). The scatter between NGC 253 and Sgr B2 (N1) as well as G0.693 is large and no clear trend can be identified. Nonetheless, the results of the higher angular-resolution data observed with the 12 m ALMA array may resolve chemical segregations and reveal similarities to Sgr B2 (N1) or G0.693.

4.5 Summary

We aimed to study the impact of a high-mass protostellar outflow on the chemistry of COMs and a few simpler molecules in the ambient medium. Our target source, Sgr B2 (N1), which is the most massive hot core embedded in the high-mass star-forming protocluster Sgr B2 (N), has long been suspected to drive a powerful outflow, based on the detection of multiple velocity components and wing emission in molecular spectra (Lis et al. 1993; Liu & Snyder 1999) and the presence of bright water masers (McGrath et al. 2004). Later, the outflow was mapped and studied in emission of some, mainly simpler molecules (Higuchi et al. 2015; Schwörer 2020). Using the high-angular resolution and high sensitivity data obtained as part of the ReMoCA spectral line survey, we derived integrated intensity maps for SO and SiO as well as as well as four other simple species and twelve COMs. For one position in the blue-shifted lobe (N1SE1) and one in the red-shifted lobe (N1NW3), rotational

temperatures and abundances with respect to H_2, C_2H_5CN, and CH_3OH were derived for, in total, 16 species using LTE radiative transfer models and population diagrams. The resulting abundances for the outflow (OF) and hot-core components (HC) at both positions (with a greater focus on N1SE1) were compared to results obtained previously in Paper I (i.e. hot core positions not impacted by the outflow, mainly N1S), the gas molecular content of G0.693 and L1157-B1, and predictions of hot-core models and shock models. The main results of this work are summarised in the following:

- The morphology of the SO and SiO maps shows that blue-shifted emission extends towards the southeast and red-shifted emission towards the northwest. Although this bipolarity can be identified, the morphology reveals complex structure, with various emission peaks that appear at different velocities. Most striking are highly collimated features in both blue- and red-shifted emission that are observed at high velocities, which may be associated with molecular jets. However, the bulk of emission is found at lower velocities with a larger opening angle.

- The blue- and red-shifted emission of other S- and N-bearing molecules reveal a similar bipolar structure as SiO and SO following the lower-velocity, wider-angle emission in large parts. This component may be associated with a low-velocity molecular outflow that consists of material entrained by the jet or pushed by some kind of disk wind. The (N+O)-bearing molecules HNCO and NH_2CHO show more compact blue- and red-shifted emission similar to CH_3CHO. Methanol reveals extended emission, which does not simply follow the bipolar structure seen for other molecules.

- Rotational temperatures derived from the 16 selected molecules are not too different from those obtained for N1S and go rarely below 100 K in both the outflow and hot-core components at N1SE1 and N1NW3.

- Abundances with respect to H_2 and C_2H_5CN show that purely O-bearing molecules are less abundant in N1SE1:HC and even less in N1SE1:OF than in N1S, while most values for N-bearing molecules are similar in these components. However, HC_3N is more abundant in both components at N1SE1 and in N1NW3:OF than in N1S and HC_5N is only detected in N1SE1:OF.

- The high rotational temperatures in N1SE1:HC and OF together with the presence of H_2O masers in this region suggest that volume densities are high. The compression of material can likely be explained by a shock passage.

- While the gas molecular inventories of G0.693 and L1157-B1 reveal similar trends, where O-bearing molecules tend to be more abundant than N-bearing species, there is no correlation with any component in Sgr B2 (N1). This suggests that a shock impacted the chemistry in Sgr B2 (N1) in a different way, likely because the initial conditions in the pre-shock gas were different and present-day volume densities are likely higher at N1SE1 in Sgr B2 (N1).

We propose a scenario for N1SE1 in which the pre-shock material went through a phase of hot-core chemistry, during which thermal desorption and high-temperature gas-phase formation enriched the gas, before a shock, provoked by any interaction with the outflow from Sgr B2 (N1), hit the material. This means that the shock is not the main driver of ice sublimation, but still of the release of less volatile species. In addition, the shock led to compression of material and possibly a temporary rise

in temperatures to hundreds of K if not 1000 K or more, which has a great impact on the chemistry in the post-shock gas. Accordingly, the segregation of particularly O- and N-bearing molecules in Sgr B2 (N1) and its outflow and the chemical differences to G0.693 and L1157-B1 may be explained as follows:

- Cyanides were formed in the hot gas phase at N1SE1 prior to the shock. Gas-phase formation in the post-shock gas competes with the molecules' destruction keeping the abundances at pre-shock values.
- Abundances of HC_3N and HC_5N are higher at N1SE1 than N1S, suggesting that these species benefit from post-shock gas-phase formation, which may involve atomic N that was sourced from the destruction of NH_3.
- Oxygen-bearing molecules do not possess gas-phase formation routes neither in the pre- nor post-shock gas that could compete against their destruction. Moreover, they seem to be destroyed more efficiently, however, the exact process is uncertain. Methanol is still observed because it is generally abundant. Acetaldehyde is produced in the gas phase, which does not seem to entirely uphold its pre-shock abundances.

In order to confirm these trends, we would need to run shock chemical models that take into account higher initial densities and temperatures than typically assumed and a pre-shock gas that has already been enriched with molecules during a phase of hot-core chemistry before any shock impact. In any case, this study provides new perspectives on shock chemistry as our results differ from the more 'classical' picture, in which the post-shock gas is enriched by grain-surface species and some products of enhanced gas-phase chemistry. Accounting for the higher cosmic-ray ionisation rate that is prevalent in Sgr B2 would also be important.

5

Concluding remarks

In this thesis, we studied the emission of complex organic molecules (COMs) in Sgr B2 (N1), which is the most massive hot core in the high-mass star-forming region Sgr B2 (N) that is located in the central region of the Milky Way. Thanks to the high angular resolution of the data taken with ALMA as part of the imaging spectral-line survey ReMoCA, we were able to spatially resolve the COM emission towards Sgr B2 (N1). This enabled us to study the spatial distribution of the emission of various COMs, by means of integrated intensity maps, and to probe variations in rotational temperature and molecular abundance across the hot core. Values of COM rotational temperature and column density were obtained by employing radiative transfer models using the Weeds package in the GILDAS software and from population diagrams. The two projects that this thesis is composed of were built around the following main science questions:
(I) Which process dominates the thermal desorption of COMs from dust-grain surfaces to the gas phase? Does it occur via co-desorption with water or does the desorption temperature of a given COM depend on its binding energy with which it sticks to the grain surface?
(II) What impact does the protostellar outflow that originates from the centre of Sgr B2 (N1) have on the chemical composition in the hot core?
In the pursuit to answer these two questions, we also studied the formation and destruction mechanisms of COMs and unveiled chemical segregation. The results that were obtained in the course of the first project are published in Busch et al. (2022) and summarised in Chapter 3. The current manuscript that contains the results of the second project (Busch et al., 2023, subm. to A&A) can be found in Chapter 4. In the following, we list again briefly the main conclusions associated to Paper I:

- The derived abundance (with respect to H_2) profiles of various COMs as a function of rotational temperature revealed a steep increase at ~100 K. In comparison to state-of-the-art astrochemical models (Garrod et al. 2022, G22 hereafter), this suggests that these COMs desorb thermally, likely alongside water.

- At temperatures below 100 K, non-zero abundance values for some COMs point to a different desorption process that either proceeds thermally or non-thermally. Together with the observational evidence for the thermal co-desorption with water, this is the first time that the transition between two desorption processes of COMs has been spatially resolved in the interstellar medium (ISM).

- The behaviour of the abundance profiles at temperatures >100 K provides observational evidence

for whether a COM is further produced or rather destroyed in the higher-temperature gas phase. Possibly involved processes have been discussed for each studied COM, based on a comparison with the G22 models. Accordingly, many O-bearing COMs are primarily produced on dust grains and desorb, while most N-bearing COMs seem to have efficient formation pathways in the gas phase (as well).

and Paper II:

- The comparison of abundances with respect to H_2 between positions in Sgr B2 (N1) that are exposed to the outflow (i.e. the material likely experiencing a shock upon interaction with the outflow) and positions that are not revealed similar values for N-bearing molecules and lower values for O-bearing species at one of the outflow positions, namely N1SE1.

- Given the short distance of N1SE1 to the centre of Sgr B2 (N1), it is likely that the material at this position went through a phase of 'hot-core' chemistry, which includes thermal desorption of ice species and efficient gas-phase chemistry due to the protostellar heating, before being impacted by the outflow. This proposed scenario is the result of a detailed comparison of our observational results with the G22 models, with shock models (Burkhardt et al. 2019), and with the chemical compositions that have been derived in other sources that are exposed to shocks.

- A summary of observational indications for such a shock-preceding phase of hot-core chemistry based on the observed molecular abundances in Sgr B2 (N1) can be found in Chapter 4. It makes use of the fact that most N-bearing species can efficiently be produced in the gas phase, especially, as temperatures further increase, while most O-bearing COMs do not possess efficient gas-phase formation routes. The occurrence of such a scenario still requires confirmation by shock-chemical models that need to be adjusted to the pre- and post-shock conditions of Sgr B2 (N1). Nonetheless, with this work, we provide a new perspective on the chemical segregation between O- and N-bearing molecules, which has previously been observed in numerous sources.

How can these findings help astrochemists answer the big questions that remain in this field of research, for example, when and how does molecular complexity start and end in the ISM and how does the chemistry evolve from the cold dense cloud up to planets?

From prestellar cores to protostars to protoplanetary disks

Until only a few years back, hot cores and hot corinos were the primary locations to hunt for new COMs and to study already known ones. Although they are still widely investigated, the search for COMs has recently been extended towards other environments. Astrochemical models assumed that these molecules needed the warmth of the young stellar object in order to be formed in the first place. For example, radicals were proposed to become mobile within the ice mantles of dust grains during the warm-up phase, which allows them to react with one another to form larger species that would then desorb at a later time. For example, Garrod et al. (2008) found that this kind of chemistry is able to reproduce the molecular composition of Sgr B2 (N) to a great extent. However, starting from the early 2010s, more and more observations of COMs in cold regions were reported, such as in prestellar cores (e.g. Bacmann et al. 2012; Jiménez-Serra et al. 2016) and dark clouds (e.g. Vasyunina et al. 2014; Taquet et al. 2017). This primarily concerns saturated COMs; long carbon-chain species, which

are unsaturated molecules, had previously been detected in starless cores (e.g. Kalenskii et al. 2004). These new observations challenged the then-existing models and new mechanisms to form COMs at these cold temperatures were needed. They were delivered in terms of non-diffusive reactions on dust-grain surfaces (e.g. Jin & Garrod 2020) or gas-phase reactions (e.g. Balucani et al. 2015). We found indirect observational evidence that non-diffusive reactions likely play an important role in the formation of COMs. The thermal desorption of COMs alongside water, which we proposed to happen in Sgr B2 (N1) based on our analysis of the ReMoCA data, is the result of the absence of diffusion for all species heavier than H_2 on dust grains in the G22 models. If diffusion were efficient, each COM would rather desorb at its own desorption temperature that depends on its binding energy to the grain surface (e.g. Garrod et al. 2008). In addition to this, with the molecular inventories that are now gradually determined for sources in the prestellar phase, a comparison with the results obtained in this thesis for Sgr B2 (N1) (and hot cores/corinos in general) can be done. This will help shed light on the question whether chemistry (or parts of it) is inherited from the earlier stages of the star-formation process.

On the other hand, the results that we obtained for Sgr B2 (N1) may also be used to understand how much of the chemical inventory from the protostellar phase may be incorporated in protoplanetary disks. So far, not many COMs have been detected in the gas phase in planet-forming disks around more-evolved young stellar objects. Detected molecules include CH_3OH (Walsh et al. 2016) and CH_3CN (Loomis et al. 2018). Nonetheless, these two, together with other simpler organics such as formaldehyde (H_2CO) and formic acid (HCOOH), which have also been identified in such disks (e.g. Favre et al. 2018; Öberg et al. 2017), represent building blocks for more complex species. Their presence in the gas phase hint at their active non-thermal desorption from grain surfaces or/and low-temperature gas-phase chemistry. Therefore, there is no reason to believe that other COMs are not present at this stage of star formation, which is supported by the very recent detection of CH_3OCH_3 and the tentative detection of CH_3OCHO (Brunken et al. 2022). Protoplanetary disks can generally be divided into three layers (e.g. Ceccarelli et al. 2022): i) a hot surface layer, where the UV photons of the protostar dissociate molecules and ionise atoms; ii) a warm molecular layer, where molecules can survive in the gas phase (including COMs) because the UV radiation does not penetrate deeper; and iii) a cold (outer) midplane (with densities up to $\sim 10^{11}$ cm^{-3}), where most species are frozen out onto dust grains. Accordingly, a lack of COM detections in disks may partially be explained by obscuration of the line emission by large amounts of dust along the line of sight or by the small spatial extent of the warm molecular layer itself that leads to (beam-averaged) column densities that are too low to be detected. One interesting result from observations of CH_3OH, HCOOH, and CH_3CN in the protoplanetary disk TW Hydra is that the N-bearing COM is brighter than the other two species. This is intriguing, because CH_3CN is thought to be a product of high-temperature gas-phase chemistry, which was also inferred from our observational results towards Sgr B2 (N1) in agreement with the G22 models. Ideas for alternative production mechanisms of CH_3CN in the disk are introduced and discussed in Ceccarelli et al. (2022). Although the exact mechanism is not clear yet, this observation suggests that both inheritance and in-situ chemistry could play a role.

Sgr B2 (N1) – One of many?

An obvious question that arises from this study on Sgr B2 (N1) concerns the hot core's uniqueness in comparison to other protostellar sources. More specifically, how do the observational results for Sgr B2 (N1) compare to other high-mass young stellar objects inside and outside the Galactic centre

region and how do the results compare to hot corinos (i.e. low-mass protostars)? In fact, an overall good correlation between the molecular composition of the secondary hot core Sgr B2 (N2) and that of the low-mass protostar IRAS 16293–2422 B (IRAS 16293 B hereafter) was found by Jørgensen et al. (2020, see their Fig. 9). This presents observational evidence that not only the chemistry (including the degree of molecular complexity) in low- and high-mass protostellar sources may be widely comparable, but also between sources in the Galactic disk (IRAS 16293 B) and the Galactic centre region (Sgr B2 (N2)). Molecules that deviate from this correlation are, for example, the N-bearing molecules HC_3N, C_2H_3CN, and C_2H_5CN, which are more abundant (with respect to HNCO) in Sgr B2 (N2). The authors proposed that this group of molecules may possess similar formation routes. Based on our results in Sgr B2 (N1) we may go one step further and speculate whether higher overall temperatures in Sgr B2 (N2) drive a more efficient gas-phase chemistry, which benefits the formation of these three species. Indeed, rotational temperatures derived for the three species in IRAS 16293 B are around 100 K (Calcutt et al. 2018), while temperatures in Sgr B2 (N2) are between ~140 and 200 K (Belloche et al. 2016). Conversely, for some O-bearing molecules (e.g. CH_3OH, C_2H_5OH, CH_3OCHO) rotational temperature were found to be $\gtrsim$250 K in IRAS 16293 B (Jørgensen et al. 2018), while temperatures derived in Sgr B2 (N2) are around 150 K for these species (Bonfand et al. 2017). Because abundances relative to CH_3OH are in good agreement between the two sources, this suggests that either abundances with respect to H_2 are independent of temperature or that the abundances of CH_3OH and the other O-bearing species behave similarly with temperature. Our results towards Sgr B2 (N1) may rather speak for the latter because the abundances of these species decrease as temperatures increase.

This kind of comparison is likely to be expanded in the near future. Until now, large molecular inventories have only been determined for a few exceptional sources. Especially studies on high-mass young stellar objects have often focussed on Sgr B2 or Orion. In order to improve our knowledge on the chemistry in the protostellar phase (and during star formation in general), we need to observe larger samples of young stellar objects to increase the statistics. Luckily, there are several (large) ALMA projects[1] that are currently being observed and that will investigate just this, such as, for example, COMPASS (Complex Organic Molecules in Protostars with ALMA Spectral Survey, PI: J. Jørgensen), which covers a sample of multiple low-mass protostars, CoCCoA (Complex Chemistry in hot Cores with ALMA, PI: B. McGuire), which looks at 25 hot cores, and ACES (The ALMA CMZ Exploration Survey, PI: S. Longmore), which studies star formation across the central molecular zone (CMZ) of the Galaxy. When the time comes to interpret observed molecular compositions, the results that we obtained for Sgr B2 (N1) could serve as a template in many aspects. This includes the nature of the desorption process of COMs or the impact of protostellar outflows on the molecular content. In addition, the impact of cosmic rays should be further investigated, as Sgr B2 (N) was found to be exposed to a higher cosmic-ray flux (Bonfand et al. 2019) due to its location in the CMZ. Segregation between O- and N-bearing molecules will likely be observed in some (or all) sources, where Sgr B2 (N1) could also be a starting point for studies on this phenomenon and help put better constraints on the underlying processes. Besides all these, further investigation of the chemistry in regions that are exposed to shocks can provide valuable information on the evolution of chemistry and on dependencies of the molecular composition to environmental changes that are caused by shocks (e.g. temporal increase in temperature).

[1] ALMA large programs: https://almascience.eso.org/alma-data/lp.

Towards understanding interstellar molecular complexity

To date, about 300 molecules have been identified in the ISM, where about half of them has been detected within the last 15 years (McGuire 2022). The rate at which new molecules are detected has rapidly increased over the last five years. This also applies to the detection of increasingly more complex species in the ISM. Not only do the molecules contain an increasing number of atoms, some even possess exotic structural properties in the context of interstellar chemistry. For example, a branched COM has been detected (i.e. *iso*-propyl cyanide, *i*-C_3H_7CN, Belloche et al. 2014). In contrast to its straight-chain structural isomer[2] (i.e. *normal*-propyl cyanide, *n*-C_3H_7CN), the -CN group of the branched molecule is attached to the C atom that is in the middle of the three-carbon backbone (cf. Fig 5.1a). Belloche et al. (2014) found that *n*-C_3H_7CN is only a factor 2.5 more abundant than *i*-C_3H_7CN in Sgr B2 (N2). Moreover, models predict that for the next species in this alkyl cyanide series (butyl cyanide, C_4H_9CN), the branched isomers may be more abundant than the straight-chain isomer (Garrod et al. 2017). In fact, one of the initial objectives of the ReMoCA survey was to search for C_4H_9CN and its isomers. Unfortunately, they remained undetected.

Other examples include the recent detections of aromatic molecules that contain one or two hexagonal rings of C atoms, which are benzonitrile (C_6H_5CN, McGuire et al. 2018) and cyanonaphtalene (1- and 2-$C_{10}H_7CN$, McGuire et al. 2021), which are illustrated in Fig 5.1c. The latter molecule does not only represent the largest molecule (19 atoms) that we currently know in the ISM (besides fullerenes), it is also the first identified member of the group of polycyclic aromatic hydrocarbons (PAHs), which have long been identified to be collectively responsible for emission features observed in the infrared spectra of various sources, for example, photon-dominated regions (e.g. Tielens 2005; Draine & Li 2007). These features appear because of specific vibration motions (e.g. of C–C or C–H bonds) that can occur in various species. Therefore, while observations of these vibrational spectra did not allow to identify individual PAHs, radio astronomy made it possible. However, it remains challenging to identify PAHs based on their rotational spectra because the emission lines are extremely faint.

Besides, as mentioned in the introduction, the holy grail regarding complex species in astrochemistry would be the detection of the simplest amino acid glycine (or any amino acid) outside the solar system. Technically, we are not that far away. Belloche et al. (2008) reported on the first detection of amino acetonitrile (NH_2CH_2CN) in Sgr B2 (N). This molecule could potentially be a direct precursor of glycine (NH_2CH_2COOH) as discussed in Jiménez-Serra et al. (2020, see also their Fig. 1) or Choe (2023). Glycine may however also form from smaller radicals (Ioppolo et al. 2021). Other prebiotic species have already been discovered in space (cf. Fig 5.1b), for example urea ($NH_2C(O)NH_2$, detected for the first time based on the ReMoCA data by Belloche et al. 2019), ethanolamine ($NH_2CH_2CH_2OH$, representing the hydrophilic head of the simplest phospholipid in cell membranes, detected towards G+0.693−0.027 by Rivilla et al. 2021b), or glycolaldehyde ($CH_2(OH)CHO$, the simplest sugar, first detected towards Sgr B2 (N) by Hollis et al. 2000). At last, only very recently, a new article by Rivilla et al. (2023) reported on the detection of glycolamide ($NH_2C(O)CH_2OH$), which is an isomer of glycine, towards G+0.693−0.027 (cf. Fig 5.1d). Understanding the formation of these molecules requires detailed knowledge of the formation and destruction pathways of their precursors. Therefore, it remains necessary to study (by now) 'moderately' complex molecules, as was done in the course of this thesis, in different environments, to improve our knowledge on their chemical networks. Moreover, the comparison of our observational results with the predictions of state-of-the-art astrochemical

[2] Isomers are molecules that contain the same atoms, but the atoms or groups of atoms are arranged differently.

models showed that there is still room for improvement, even for the precursor species that have long been identified. Along with new observational data and revised models, laboratory experiments are needed to update our knowledge on, for example, reaction rates or binding energies of molecules. Moreover, we will continue to need measurements of rotational spectra of rarer isotopologues of known molecules or in their higher vibrational states, and of new species, which can then be searched for in the interstellar medium.

– All in all, it is a very exciting time to work in the field of astrochemistry right now! –

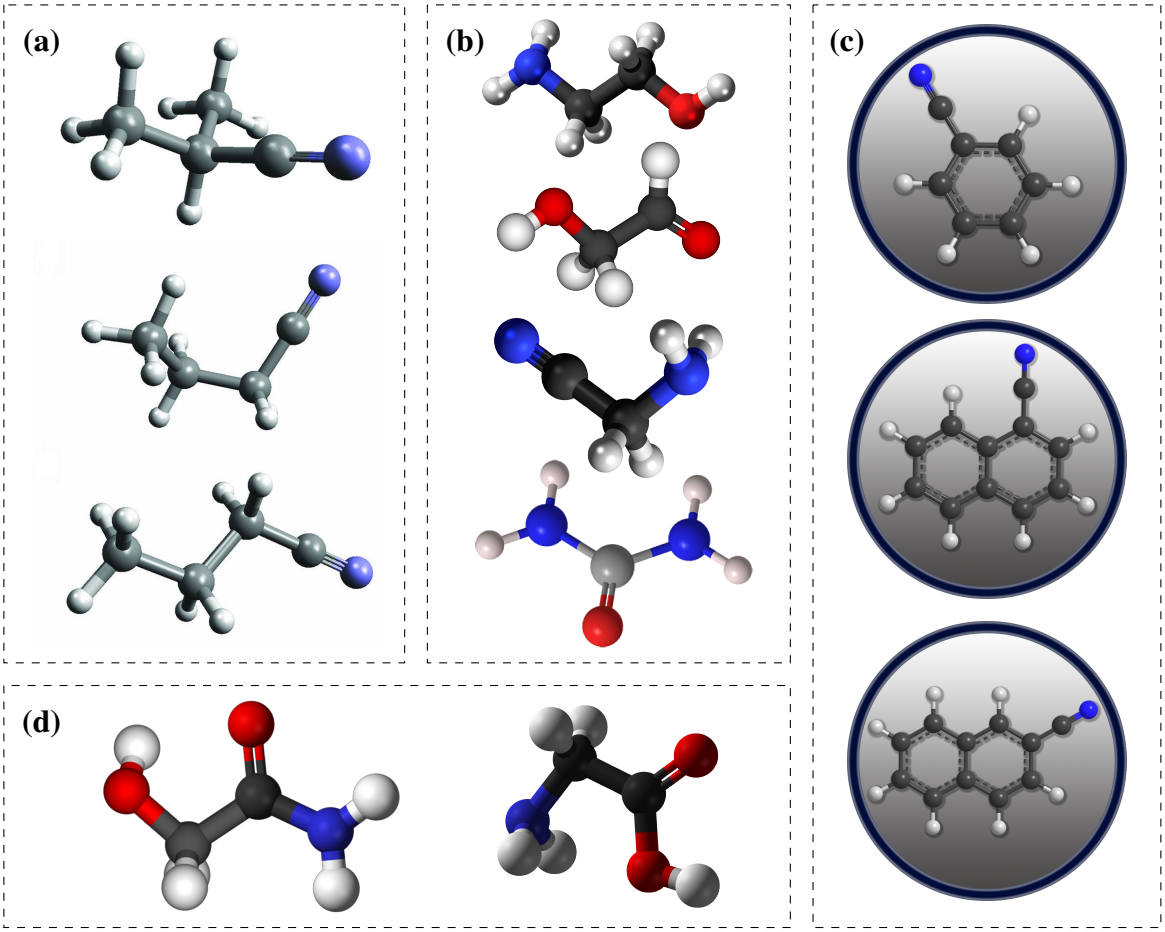

Figure 5.1: Illustration of the molecules mentioned in the last paragraph of this chapter. Grey or black spheres represent carbon atoms, red are oxygen atoms, and blue are nitrogen atoms. *Panel a:* Branched and straight-chain propyl cyanide with *iso*-C_3H_7CN, *gauche-normal*-C_3H_7CN, *anti-normal*-C_3H_7CN from top to bottom (taken from Belloche et al. 2014). *Panel b, top to bottom:* Ethanolamine ($NH_2CH_2CH_2OH$), glycolaldehyde ($CH_2(OH)CHO$), amino acetonitrile (NH_2CH_2CN), and urea ($NH_2C(O)NH_2$). *Panel c, top to bottom:* Benzonitrile (c-C_6H_5CN) and cyanonaphtalene (1– and 2–$C_{10}H_7CN$). *Image credit: B. McGuire/homepage*. *Panel d, left to right:* Glycolamide ($NH_2C(O)CH_2OH$) and glycine (NH_2CH_2COOH).

A

Paper I: Resolving desorption of complex organic molecules in a hot core

This appendix contains the original article associated with the publication Busch et al. (2022) that has been published in the journal *Astronomy & Astrophysics*. A summary of the results and conclusions can be found in Chapter 3.

A&A 665, A96 (2022)
https://doi.org/10.1051/0004-6361/202243383

Astronomy & Astrophysics

Resolving desorption of complex organic molecules in a hot core

Transition from non-thermal to thermal desorption or two-step thermal desorption?

Laura A. Busch[1,⋆], Arnaud Belloche[1], Robin T. Garrod[2], Holger S. P. Müller[3], and Karl M. Menten[1]

[1] Max-Planck-Institut für Radioastronomie, Auf dem Hügel 69, 53121 Bonn, Germany
e-mail: labusch@mpifr-bonn.mpg.de
[2] Departments of Chemistry and Astronomy, University of Virginia, Charlottesville, VA 22904, USA
[3] I. Physikalisches Institut, Universität zu Köln, Zülpicher Str. 77, 50937 Köln, Germany

Received 21 February 2022 / Accepted 21 June 2022

ABSTRACT

Context. The presence of many interstellar complex organic molecules (COMs) in the gas phase in the vicinity of protostars has long been associated with their formation on icy dust grain surfaces before the onset of protostellar activity, and their subsequent thermal co-desorption with water, the main constituent of the grains' ice mantles, as the protostar heats its environment to ∼100 K.
Aims. Using the high angular resolution provided by the Atacama Large Millimetre/submillimetre Array (ALMA), we want to resolve the COM emission in the hot molecular core Sagittarius B2 (N1) and thereby shed light on the desorption process of COMs in hot cores.
Methods. We used data taken as part of the 3 mm spectral line survey Re-exploring Molecular Complexity with ALMA (ReMoCA) to investigate the morphology of COM emission in Sagittarius B2 (N1). We also used ALMA continuum data at 1 mm taken from the literature. Spectra of ten COMs (including one isotopologue) were modelled under the assumption of local thermodynamic equilibrium (LTE) and population diagrams were derived for these COMs for positions at various distances to the south and west from the continuum peak. Based on this analysis, we produced resolved COM rotation temperature and column density profiles. H_2 column density profiles were derived from dust continuum emission and $C^{18}O$ 1–0 emission and used to derive COM abundance profiles as a function of distance and temperature. These profiles are compared to astrochemical models.
Results. Based on the morphology, a rough separation into O- and N-bearing COMs can be done. The temperature profiles span a range of 80–300 K with power-law indices from −0.4 to −0.8, which is in agreement with expectations of protostellar heating of an envelope with optically thick dust. Column density and abundance profiles reflect a similar trend as seen in the morphology. While abundances of N-bearing COMs peak only at the highest temperatures, those of most O-bearing COMs peak at lower temperatures and remain constant or decrease towards higher temperatures. Many abundance profiles show a steep increase at ∼100 K. To a great extent, the observed results agree with results of astrochemical models that, besides the co-desorption with water, predict that O-bearing COMs are mainly formed on dust-grain surfaces at low temperatures, while at least some N-bearing COMs and CH_3CHO are substantially formed in the gas phase at higher temperatures.
Conclusions. Our observational results, in comparison with model predictions, suggest that COMs that are exclusively or, to a great extent, formed on dust grains desorb thermally at ∼100 K from the grain surface, likely alongside water. A dependence on the COM binding energy is not evident from our observations. Non-zero abundance values below ∼100 K suggest that another desorption process of COMs is at work at these low temperatures: either non-thermal desorption or partial thermal desorption related to the lower binding energies experienced by COMs in the outer, water-poor ice layers. In either case, this is the first time that the transition between two regimes of COM desorption has been resolved in a hot core.

Key words. astrochemistry – methods: observational – stars: formation – ISM: molecules – submillimeter: ISM – ISM: clouds

1. Introduction

To date, more than 270 molecules have been detected in space[1] and the detection rate is speeding up thanks, in particular, to the perpetual advancement of broad-band receivers on single-dish telescopes such as the Yebes 40 m, IRAM 30 m telescopes, or the Green Bank Telescope allowing for observations of sensitive spectral-line surveys that cover a wide range of frequencies (McGuire 2022). Observations of molecules help us understand the structure and evolution of the interstellar medium (ISM) and shed light on the various phases of the star-formation process from diffuse clouds ($n_H \sim 10^2$–10^3 cm^{-3}), to dense clouds and cores with densities beyond 10^8 cm^{-3}, and to protostellar and protoplanetary disks (for a recent review see Jørgensen et al. 2020). Amongst these, observations of complex organic molecules (COMs), which are carbon-bearing molecules that

⋆ Member of the International Max Planck Research School (IMPRS) for Astronomy and Astrophysics at the Universities of Bonn and Cologne.
[1] See https://cdms.astro.uni-koeln.de/classic/molecules

consist, per definition, of at least six atoms (Herbst & van Dishoeck 2009), are of special interest as they are potential precursors of even more complex and possibly prebiotic species. Therefore, they may play a role in the build-up of the complex organic and prebiotic inventory seen in meteorites and comets in the Solar System and, going one step further, in the emergence of life on Earth.

Many COMs have first been detected in the close vicinity of high- and low-mass protostars. These regions are referred to as hot cores and hot corinos, respectively. The spatial extent of these regions is usually associated with a gas temperature of ∼100 K (Jørgensen et al. 2020). The characteristic temperature of ∼100 K denotes the point when water desorbs from the dust grain surfaces, along with many other species, perhaps including the COMs themselves. At the end of the cold collapse phase of a dense cloud core, an ice mantle consisting of mostly water (with traces of, e.g. CO, CO_2, and NH_3, Boogert et al. 2015) covers the grain. A widely accepted paradigm for the production of COMs was the photodissociation of molecules in this ice mantle, notably methanol, producing radicals that would become mobile, and thus reactive, during the gradual warm-up of dust grains that occurs once a protostar is born and starts heating up its collapsing envelope (Garrod & Herbst 2006). At high enough temperatures, both the simple and complex molecules would thermally desorb from the grains into the gas phase. The release of the simple species in particular could also induce gas-phase chemistry. Recent models by Garrod et al. (2022), which include non-diffusive surface and bulk-ice chemistry, indicate that significant COM production on dust grains may actually occur at low temperatures when the simple ices themselves are beginning to form, which is in agreement with recent experimental findings involving the co-deposition of atomic H and simple molecules such as CO (e.g. Fedoseev et al. 2015).

Assuming that COMs are indeed formed on the dust grains (which does not rule out complementary gas-phase formation in some cases), their temperature-dependent desorption behaviour will be important to the observed spatial morphologies of their emission regions. The desorption of COMs from the grains has been studied in the laboratory using interstellar ice analogues (e.g. Collings et al. 2004; Martín-Doménech et al. 2014), but the precise temperature dependence is complex. In particular, for a COM more volatile than water, the desorption of that molecule from a water ice mixture may partially occur at a relatively low temperature, corresponding to direct thermal desorption, perhaps mediated by some diffusive transport of molecules through surface-pore structures. Another component would be trapped within the water-ice structure, eventually co-desorbing with the water, and therefore, exhibiting a similar desorption temperature as water itself.

Astrochemical models have typically used simple treatments for the desorption of COMs; so-called two-phase models (e.g. Garrod 2008), which consider the grain-surface ices to be a single physical phase, and three-phase models (e.g. Garrod 2013), which distinguish the bulk ice from the ice-mantle surface, usually allow molecules to desorb according to their own binding energies, meaning that there is no trapping of any kind. The more recent three-phase model of Garrod et al. (2022) adopts the other extreme; material in the bulk ice is trapped beneath the upper layer, meaning that only a small fraction of COMs in the bulk is able to desorb until water rapidly begins to desorb at its own characteristic desorption temperature (Viti et al. 2004, used an empirical treatment to model temperature-dependent molecular desorption, but did not include actual grain-surface chemistry, only desorption). There has so far been no direct observational confirmation of the co-desorption of COMs with water, mainly because the angular resolution of observations has been insufficient to resolve the temperature gradient as traced by the COM emission, which is needed to pinpoint their desorption temperatures. The alternative picture, in which COMs do not desorb alongside water but according to their own independent binding energies, would lead to the appearance of COMs at different temperatures even below 100 K. This dependence on binding energy has neither been confirmed nor refuted observationally, either, again due to observational limitations.

Moreover, observations of COMs in the absence of protostars in cold ($T \lesssim 20$ K) regions, for example the dark cloud TMC–1 (e.g. Agúndez et al. 2021, and references therein) or prestellar cores (Bacmann et al. 2012; Jiménez-Serra et al. 2016, 2021; Scibelli & Shirley 2020), but also in protostellar outflows such as L1157 (Codella et al. 2015, 2017) and, for example the shocked region (while quiescent in star formation) G+0.693−0.027 located in the Galactic centre region (e.g. Requena-Torres et al. 2006; Zeng et al. 2018), point to additional or purely non-thermal desorption processes. These processes may include grain-sputtering and subsequent release of COMs into the gas phase due to shock passing induced by outflows, accretion shocks (e.g. Csengeri et al. 2019), or cloud interactions, desorption after interaction of molecules on dust grain surfaces with cosmic rays (Shingledecker et al. 2018; Paulive et al. 2021), or other diffusive and non-diffusive reactions taking place on the dust surface that lead to the chemical desorption of COMs (e.g, Ruaud et al. 2015; Jin & Garrod 2020).

The investigation of COMs and the many possible ways for them to arrive in the gas phase is one of the objectives of the ReMoCA (Re-exploring Molecular Complexity with ALMA) survey (Belloche et al. 2019), an imaging spectral line survey performed at 3 mm with the Atacama Large Millimetre/submillimetre Array (ALMA) towards the giant molecular cloud Sagittarius B2 (hereafter Sgr B2), which is located at a distance of 8.2 kpc from the sun (Reid et al. 2019) in the Galactic centre region. Sgr B2 hosts two sites of active high-mass star formation. Amongst them, Sagittarius B2 North (hereafter Sgr B2 (N)) has a high record of first detections of interstellar molecules turning it into an excellent target to look out for COMs. Observations towards this region revealed several high-mass protostars with hot cores (Bonfand et al. 2017), HII regions (Gaume et al. 1995; De Pree et al. 2015), filaments through which accretion probably happens (Schwörer et al. 2019), and outflows (Higuchi et al. 2015; Bonfand et al. 2017). Therefore, it fulfils the requirements to study all thermal and non-thermal desorption processes mentioned above.

Before ReMoCA, its predecessor, the EMoCA survey (Exploring Molecular Complexity with ALMA, Belloche et al. 2016), which itself succeeded a spectral line survey of Sgr B2 (N) and (M) with the IRAM 30 m single-dish telescope (Belloche et al. 2013), already allowed to study Sgr B2 (N) in the 3 mm spectral window at a high angular resolution of 1.6″. Insights that were obtained from the data of this survey included first detections of new COMs such as *i*-C_3H_7CN (Belloche et al. 2014) and CH_3NHCHO (Belloche et al. 2017, 2019), a detailed study on the complex chemistry in translucent clouds along the line of sight (Thiel et al. 2017), the discovery of three new hot cores and their outflows, if present (Bonfand et al. 2017), and an inventory of COMs in the hot cores Sgr B2 (N2–N5) (Bonfand et al. 2019). The latter analysis does not include the main and most massive hot core Sgr B2 (N1) because the observed line forest at the confusion limit, spectral lines that have full width at half maximum (FWHM) of ∼7 km s^{-1} and

additional line wings, and the high column density and optical depth of the dust continuum made it challenging to probe the inner part of this hot core at this wavelength. Now, with the ReMoCA survey and its sub-arcsecond angular resolution and four-times better sensitivity, it becomes possible to resolve the COM emission in Sgr B2 (N1).

In this work, we aim to shed light on the thermal desorption process, in particular on the question whether COMs co-desorb with water or rather depending on their binding energies. To do so, we studied the morphology of the emission of 16 organic molecules and chose ten of them, all COMs, for further analysis. The spectra of these ten COMs (including one isotopologue) were modelled under the assumption of local thermodynamic equilibrium (LTE) and population diagrams were derived. Based on this analysis, we derived resolved profiles of rotation temperature and COM abundance starting from ∼0.5″ distance from the continuum peak and proceeding to the point of non-detection for each COM. By comparing these profiles with results from state-of-the-art astrochemical models, we want to trace (back) each species' evolution in the solid and gas phases, and the transition from one phase to the other in order to answer the question above. The article is structured as follows: Sect. 2 provides details on the used data and the LTE modelling of the spectra. In Sect. 3 we present our results including an analysis of the continuum data, a description of the morphology of the COM emission, and the path towards derivation of the COM abundance profiles. The discussion on the results is done in Sect. 4 including the comparison to chemical models and a conclusion is provided in Sect. 5.

2. Observations and method of analysis

2.1. The ReMoCA survey

The observations of the ReMoCA line survey were conducted with the ALMA interferometre and cover the complete frequency range from 84.1 to 114.4 GHz. The phase centre is located at $(\alpha, \delta)_{J2000} = (17^h47^m19\overset{s}{.}87, -28°22'16\overset{''}{.}00)$ halfway between Sgr B2 (N1) and (N2). The survey is split into five observational setups, called S1 to S5, each of which delivers four spectral windows. The observations were performed with different antenna configurations, which yield mean synthesised beam sizes that vary from ∼0.75″ in setup 1 to 0.3″ in setup 5. The detailed list of covered frequency ranges, beam sizes, and average rms noise levels for all spectral windows can be found in Table 2 of Belloche et al. (2019). We refer to the latter article for more details on the observations and the data reduction. The FWHM of the primary beam varies between 69″ at 84 GHz and 51″ at 114 GHz (ALMA Partnership 2016). The reduced spectra have a spectral resolution of 488 kHz, which translates to 1.7–1.3 km s^{-1}.

2.2. 1.3 mm ALMA data

Sánchez-Monge et al. (2017) observed Sgr B2 (N) and (M) with ALMA using an extended configuration. The continuum map used here was obtained at 242 GHz with a synthesised beam of 0.4″. The average rms noise level in the map is 12.7 mK. The phase centre is located at $(\alpha, \delta)_{J2000} = (17^h47^m19\overset{s}{.}887, -28°22'15\overset{''}{.}76)$ but was shifted to the phase centre of the ReMoCA data in this work. More details on these observations are presented in Sánchez-Monge et al. (2017).

2.3. LTE modelling

To analyse the spectral line data, we performed radiative transfer modelling under conditions of LTE, which is appropriate given the high densities found towards Sgr B2 (N) (∼10^7 cm^{-3}, Bonfand et al. 2017). The spectral line emission has already been split from the continuum emission as reported by Belloche et al. (2019) (see their paper for details), who performed a preliminary baseline subtraction, which has been improved subsequently (Melosso et al. 2020). Another subtraction was performed in this work, when residual baseline issues were identified, however, only for spectra at distances larger than 2″ from Sgr B2 (N1) because of the difficulty of distinguishing between the continuum and the pervasive line emission.

The line identification and modelling of the spectra were done with Weeds (Maret et al. 2011), which is an extension of the GILDAS/CLASS software[2]. To produce a synthetic spectrum, Weeds requires five input parameters, which are: total column density, rotational temperature, source size, velocity offset with respect to the systemic velocity of the source, and line width (FWHM). We performed 1D Gaussian fits to optically thin and unblended transitions, from which we obtained the velocity offset and the line width. Column density and rotational temperature were determined in an iterative way. From a first model, in which these parameters were selected by eye, we derived population diagrams (see Sect. 3.4), which also yield column density and rotational temperature. The Weeds parameters were adjusted until the model and the results of the population diagram were in good agreement. The molecular emission is assumed to follow a 2D Gaussian distribution in Weeds. Because the COM emissions show extended but also small-scale structures, the determination of the source size is challenging and is discussed in more detail in Sect. 3.2.

A species is identified when the synthetic spectrum correctly predicts each observed transition. Models of all analysed species were subsequently combined to a complete synthetic spectrum, in which blending of lines is treated by adding up the model predictions of individual species. More details on the modelling procedure can be found in Belloche et al. (2016).

The spectroscopic calculations used to create the models are based on the CDMS (Cologne Database for Molecular Spectroscopy, Endres et al. 2016) or JPL (Jet Propulsion Laboratory, Pearson et al. 2010) catalogues in most instances. We provide details on the laboratory background and on the vibrational spectroscopy in Appendix A. The former is necessary to give credit to at least the most important contributors who often carried out the respective measurements to support the radio astronomical community. The latter is important to account for the molecules in excited vibrational states which are populated at excited temperatures such as in our work but may be characterised too little or not at all or may be too weak to be detected securely.

3. Astronomical results

3.1. Continuum emission at 1.3 and 3 mm

Figure 1 shows the continuum map at 1.3 mm (242 GHz, Sánchez-Monge et al. 2017) in colour scale and a ReMoCA continuum map at 3 mm (99.2 GHz) with contours. The continuum at 1.3 mm is dominated by dust emission and peaks towards the two main hot cores N1 and N2. We show continuum peak positions of Sgr B2 (N1) derived by various authors along with the position determined by us in the following way: using continuum maps obtained from setup 5, which is the ReMoCA setup of highest angular resolution, and computing the peak position by intensity-weighting the four brightest pixels, we located the

[2] https://www.iram.fr/IRAMFR/GILDAS/

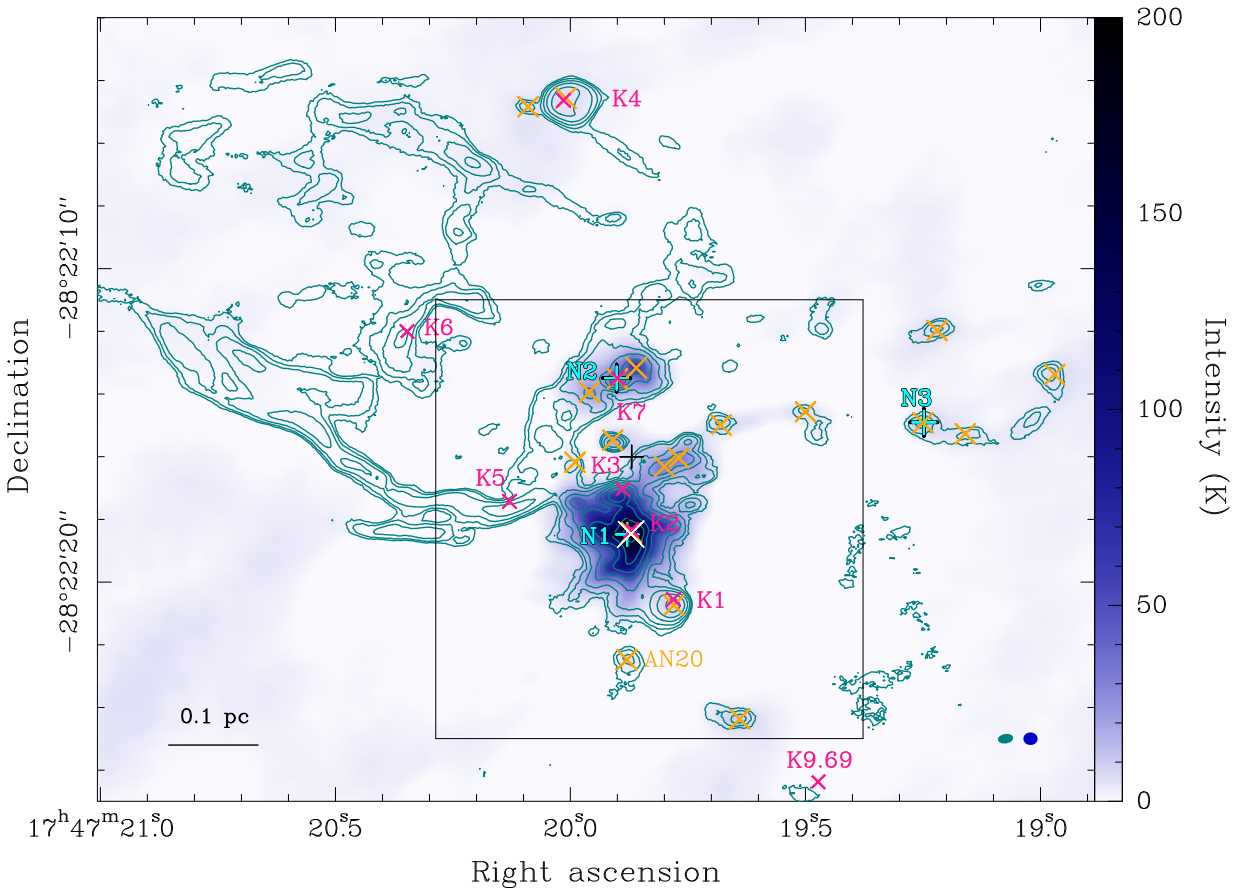

Fig. 1. Continuum maps at 242 GHz (Sánchez-Monge et al. 2017) shown in colour scale and at 99.2 GHz (ReMoCA) shown with teal contours. The contour steps start at 3σ and then increase by a factor of 2 with σ = 0.4 K the rms noise level of the continuum map at 99.2 GHz. The black cross shows the phase centre of the ReMoCA observations. The white cross shows the intensity-weighted 3 mm continuum peak determined in this work. Orange crosses indicate 1.3 mm continuum sources from Sánchez-Monge et al. (2017), cyan crosses the continuum peaks of the hot cores N1 and N2 as well as the line density peak of N3 reported by Bonfand et al. (2017) on the basis of the EMoCA survey at 1.6″ resolution, and pink crosses HII regions reported by Gaume et al. (1995) (K1–K6, K9.69) and De Pree et al. (2015) (K7) with the VLA. The black box indicates the region for which spectral indices are determined as shown in Fig. 2. The respective synthesised beams for both maps are shown in the lower right corner.

3 mm continuum peak at $(0.02 \pm 0.03, -2.47 \pm 0.04)''$ from the phase centre (see the white cross in Fig. 1).

In addition to N1 and N2, hot core N3 is indicated, which has only been discovered recently (together with N4 and N5, which are located outside the field shown in Fig. 1, Bonfand et al. 2017). Further continuum sources at 1.3 mm have been identified by Sánchez-Monge et al. (2017), those of which located within the shown field are indicated with orange crosses in Fig. 1. Each of these sources has a counterpart in the 3 mm continuum map as can be seen from the contours suggesting that a substantial part of the continuum emission traces dust. One exception is HII region K1 which is seen at both wavelengths but whose emission seems to be dominated by free-free emission even at 1.3 mm (see Fig. 2 and Sánchez-Monge et al. 2017). Moreover, there are features that are not seen at 1.3 mm, for example the large-scale structure to the north-east. It resembles the one reported by Gaume et al. (1995), who performed observations of the continuum towards Sgr B2 (N) at 1.3 cm with the VLA. At this wavelength, free-free emission originating from HII regions dominates over dust. Therefore, the continuum at 3 mm is not exclusively tracing dust but also free-free emission to a substantial extent. The positions of the HII regions reported by Gaume et al. (1995) and De Pree et al. (2015) are indicated with pink crosses in Fig. 1, and all (except K9.69) are associated with intensity peaks in the 3 mm continuum map.

We created a spectral index map using the 1.3 and 3 mm continuum maps and show the result in Fig. 2. The spectral index α is computed by

$$\alpha = \ln\left(\frac{S_{242}}{S_{99.2}}\right) \times \frac{1}{\ln\left(\frac{242\,\mathrm{GHz}}{99.2\mathrm{GHz}}\right)}, \quad (1)$$

where S_{242} and $S_{99.2}$ are the flux densities measured at each position in the continuum map of the respective frequency. We smoothed the 3 mm data to the resolution of the 1.3 mm data for a more precise analysis. The spectral index was only computed above a flux density threshold of 1σ, where σ is the average noise level in the respective continuum map. For most parts in Fig. 2, the spectral index has values ranging from 2.5 to $\gtrsim$4 suggesting prevalence of optically thin dust emission. In

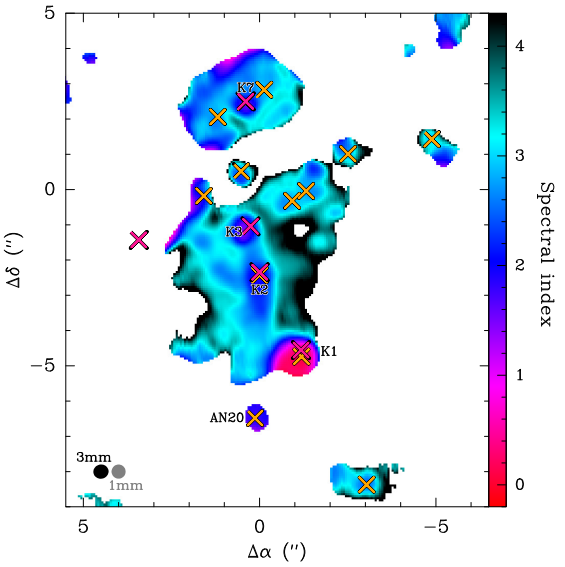

Fig. 2. Spectral index map derived from the 1.3 and 3 mm continuum emission for the region around N1 and N2 indicated with the black box in Fig. 1. The crosses indicate the same sources of respective colour as in Fig. 1. The synthesised beams (after smoothing for the 3 mm map) are shown in the lower left corner. The position offsets are given with respect to the ReMoCA phase centre.

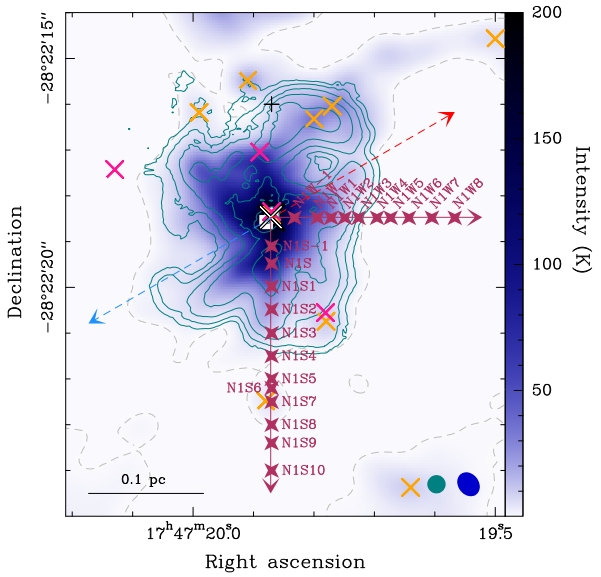

Fig. 3. Continuum at 242 GHz (Sánchez-Monge et al. 2017) in colour scale overlaid by a Line-width- and Velocity-corrected INtegrated Emission (LVINE) map of C_2H_5OH (97.139 GHz, E_u = 264 K) shown with teal contours. The contour steps start at 3σ and then increase by a factor of 2 with σ = 8.3 K km s^{-1}. The grey dashed contour indicates the 3σ level of the continuum with σ = 12.7 mK. The closest region around Sgr B2 (N1) is masked out due to high continuum optical depth (see Appendix C). Coloured crosses indicate continuum sources introduced in Fig. 1. The black cross shows the phase centre of the ReMoCA observations. Red and blue dashed arrows indicate the outflow axis reported by Higuchi et al. (2015). The beams of the maps are shown in the respective colour in the lower right corner. Maroon arrows indicate the directions along which positions (maroon star symbols) are chosen for the subsequent analysis (see Sect. 3.3).

some regions the spectral index is smaller than 2–2.5 including the HII regions K1, K3, and K7 (Gaume et al. 1995), but also AN 20 (Sánchez-Monge et al. 2017), whose nature is not certainly known. Besides at 99.2 GHz and 242 GHz, the latter source was detected at 40 GHz (Rolffs et al. 2011; Sánchez-Monge et al. 2017) suggesting a possible contribution of free-free emission to the observed flux. K1 even shows values <1, which is most likely the result of a mixture of dust and free-free emission (see also Sánchez-Monge et al. 2017).

We also expect a contribution of free-free emission originating from K2 to the continuum at the position of Sgr B2 (N1) as they are nearly co-located. Because we want to derive H_2 column densities from the 3 mm dust emission at positions close to Sgr B2 (N1) it is important to disentangle the contributions of free-free and dust emission, particularly at this position. De Pree et al. (2015) reported a flux density of 80 mJy for K2 at 44.2 GHz for a size of the emitting region of 0.22″ × 0.1″. Given a total peak continuum flux of 190 mJy beam^{-1} at the position of Sgr B2 (N1) at 99.2 GHz for a beam size of 0.4″, free-free emission contributes ∼40% to this flux assuming that the free-free emission is optically thin ($\alpha_{\rm ff,thin}$ = −0.1) above 44.2 GHz.

An advantage of the 3 mm continuum is that dust opacities are smaller at this wavelength than at 1.3 mm. To confirm this, we estimated the optical depth τ at the position of Sgr B2 (N1) and the position N1S (0.00,−3.48)″ (see Fig. 3), which was used for analysis in Belloche et al. (2019). The flux density at the position of Sgr B2 (N1) was corrected for the contribution of free-free emission as derived above, while for N1S the contribution is negligible. We used the equation presented in Bonfand et al. (2017), which is

$$\tau = -\ln\left(1 - \frac{S_\nu^{\rm beam}}{\Omega_{\rm beam} B_\nu(T_d)}\right), \quad (2)$$

Table 1. Optical depth at 1.3 and 3 mm assuming two different dust temperatures.

Position	$\Delta\alpha$ (″)	$\Delta\delta$ (″)	T_d (K)	$\tau_{1.3\rm mm}$	$\tau_{3\rm mm}$
N1	0.02	−2.47	200	2.58	0.83
			250	1.32	0.60
N1S	0.00	−3.48	200	0.67	0.40
			250	0.49	0.30

where $\Omega_{\rm beam} = \frac{\pi}{4\ln 2} \times HPBW_{\rm min} \times HPBW_{\rm maj}$ is the beam solid angle, $S_\nu^{\rm beam}$ the peak flux density, and $B_\nu(T_d)$ the Planck function of the dust emission evaluated for the dust temperature T_d. Because the optical depth is sensitive to the dust temperature we assumed two values: T_d = 200 K and 250 K. We used the smoothed map for a direct comparison of the 1.3 and 3 mm continuum and therefore, a beam size of $HPBW_{\rm min} = HPBW_{\rm maj}$ = 0.4″. The results are summarised in Table 1 and show that opacities are lower for the observations at 3 mm at both positions. We have a closer look at the optical depth in Sect. 3.5 when we derive H_2 column densities.

An effect biasing the comparison between the continuum levels may be spatial filtering by the ALMA interferometre, which occurs as a consequence of limited (u, v) coverage at

shortest baselines. This leads to a lower sensitivity to larger-scale emission, in other words, emission that is extended beyond a certain spatial scale might be filtered out, which eventually leads to a decrease of the observed flux density. This maximum recoverable scale depends on the length of the shortest baseline (ALMA Partnership 2016). For the observations at 1.3 mm, 34–36 antennae were used covering baselines from 30 m to 650 m and hence, ensuring sensitivity to structures on scales of 0.4–5″ at an angular resolution of 0.4″ (Sánchez-Monge et al. 2017). The ReMoCA survey has been observed with different configurations using 36–46 antennae that cover baselines from 15 m to 3600 m (cf. Table 2 in Belloche et al. 2019). Therefore, maximum scales that can be recovered at 100 GHz are between ∼3″ and ∼8″ for the highest and lowest angular resolutions, respectively (see Table 7.1 in ALMA Partnership 2016). Because the two datasets have a similar maximum recoverable scale the spectral index map in Fig. 2 should be reliable for the scales traced by both.

3.2. Spatial distribution of COMs

To explore the morphology of the COM emission we created Line-width- and Velocity-corrected INtegrated Emission maps (LVINE). The LVINE method is an extension of the VINE method, which was introduced by Calcutt et al. (2018), and takes into account gradients of velocity and spectral line width in the observed region. The LVINE method is explained in more detail in Appendix B.

Figure 3 shows the 1.3 mm continuum map in colour scale, which is overlaid by contours of an LVINE map of a C_2H_5OH transition at 97.139 GHz (E_u = 264 K). The continuum exhibits a lot of structure that was associated with filaments by Schwörer et al. (2019), who described the continuum emission at 1.3 mm in detail. The authors reported on the differences in the morphology of O- and S-bearing COM emission that follows the structured continuum emission, which can also be seen for C_2H_5OH in Fig. 3, and N-bearing species, which reveal a more spherical morphology. In order to investigate these reported differences, we show LVINE maps of emission from various COMs in Fig. 4.

Similarly to C_2H_5OH, the emissions of CH_3OH, its ^{13}C isotopologue, CH_3OCH_3, and CH_3OCHO, all of which are O-bearing COMs, closely follow the morphology of the continuum. The distribution of CH_3CHO emission is slightly different, however, it shows the tendency of the morphology seen for the other O-bearing COMs. The emissions of the N-bearing COMs such as $^{13}CH_3CN$, C_2H_5CN, C_2H_3CN, and $HC^{13}CCN$ share a similar morphology that is less structured and more compact around the central region of Sgr B2 (N1), with the latter two showing the smallest spatial extent. The morphology of HNCO emission is similar to the N-bearing COMs. The spatial distributions of CH_3NCO, NH_2CHO, and NH_2CH_2CN emissions are similar, with the latter being more compact, and follow a slightly different morphology as it shows the compactness of the N-bearing COMs with a pattern similar to what is seen for the O-bearing COMs. i-C_3H_7CN and n-C_3H_7CN emissions are extremely compact and weak and cannot be compared to the other COMs. In summary, we observe a spatial segregation of species, approximately between O- and N-bearing COMs. Moreover, there may even be indications of a third group.

The determination of the physical size of the emission region is challenging because the morphology for all COMs does not simply follow a 2D Gaussian profile as assumed by Weeds, instead it shows extended emission as well as structures on smaller scales. In the following we assume that we always resolve the emission region. In the Weeds model we set the size (FWHM) of the emission region to 2″, which yields a beam filling factor of approximately 1 and thus, satisfies the requirement.

In the region closest to Sgr B2 (N1) we found that the continuum becomes optically thick and obscures the COM emission. Therefore, the true intensity of the COM emission is unknown and this inner region is masked in the maps shown in Figs. 3 and 4. The determination of the mask size is explained in Appendix C. It varies between the observational setups and spectral windows because the opacity effect on the continuum is higher for higher frequency and higher angular resolution.

3.3. Line and position selection

We focussed our analysis on commonly abundant O- and N-bearing COMs, that show numerous strong lines and have enough lines that are not optically thick. This selection comprises CH_3OH (methanol), C_2H_5OH (ethanol), CH_3OCH_3 (dimethyl ether), CH_3OCHO (methyl formate), CH_3CHO (acetaldehyde), CH_3NCO (methyl isocyanate), C_2H_5CN (ethyl cyanide), C_2H_3CN (vinyl cyanide), and NH_2CHO (formamide).

As discussed above, optical depth of the continuum at its peak, and therefore obscuration of the COM emission, prevents us from starting our analysis at this position. Therefore, Belloche et al. (2019) selected a position that is 1″ to the south of Sgr B2 (N1) for their analysis and called it N1S. Spectral lines at this position suffer less from masking by the continuum. Moreover, they have moderate average line widths of ∼5 km s^{-1} and do not show wings, which would be indicative of emission originating from the outflow of Sgr B2 (N1) (Higuchi et al. 2015). Based on this reasoning, we decided to start from this position and go further south in order to determine the COM rotational temperature and column density profiles along this direction. The positions were chosen so that they are approximately one beam size apart (0.5″). The transition to source AN 20 was analysed with an additional position (N1S6). The analysis was continued up to the distance where none of the selected COMs is detected any longer. This maximum distance varies for different COMs and can either result from the limited sensitivity of the observations or is due to the prevailing chemical or physical conditions. The used positions to the south are indicated with maroon star symbols in Fig. 3 and listed in Table E.1, where we adopt the naming from Belloche et al. (2019) and term positions N1Si (i = 1,2,...) with increasing distance starting from N1S. Additionally, we studied the position N1S-1, which is at a distance of 0.6″ from Sgr B2 (N1). During the analysis we found that this position is already affected by the high continuum optical depth, severely in spectral windows 2 and 3 of observational setup 5, which cover the highest frequencies and have the highest angular resolution. Therefore, transitions covered by these spectral windows at N1S-1 were not used in the following (see also Appendix C).

The results obtained southwards are compared to another direction. Because in this study we focussed on the COMs' behaviour under the influence of heating by the protostar, that is the process of thermal desorption, we did not use directions towards the south-east and north-west as they correspond to the axis of the Sgr B2 (N1) outflow (Higuchi et al. 2015). The outflow induces shocks in the ambient gas, which may trigger non-thermal desorption of COMs. The impact of the outflow on the COM emission will be topic of a forthcoming paper. To the north, there are multiple continuum sources that may bias the

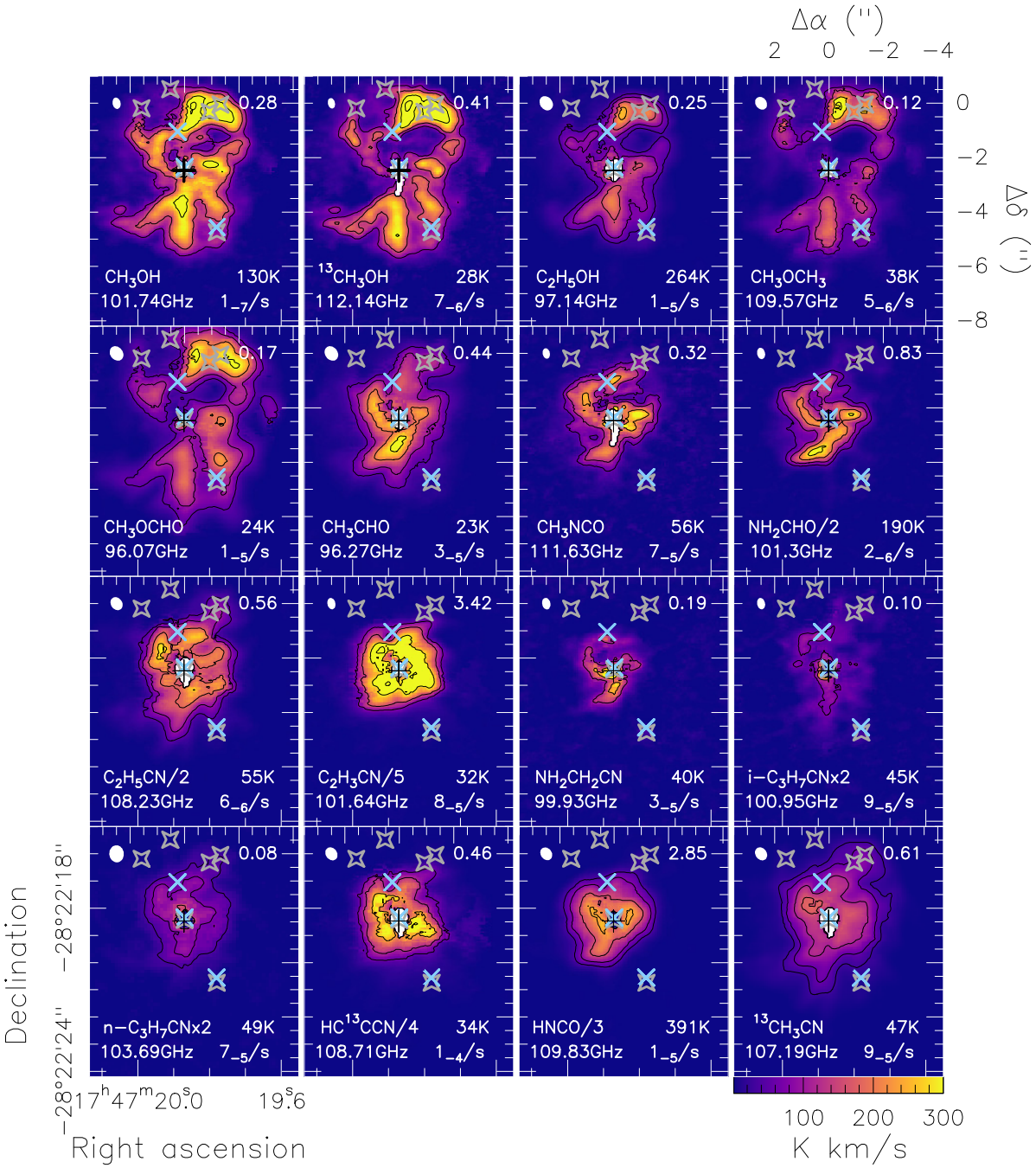

Fig. 4. LVINE maps of various COMs. Integrated intensities of C_2H_5CN are scaled down by a factor of 2, those of C_2H_3CN by a factor 5, $HC^{13}CCN$ by a factor 4, HNCO by a factor 3, and NH_2CHO by a factor 2. Integrated intensities of *i*-C_3H_7CN and *n*-C_3H_7CN are scaled up by a factor 2, respectively. Because the noise level within each map is not uniform due to the pixel-dependent integration limits, contours are at 15, 30, 60, and 90% of the respective peak intensity and additional signal-to-noise maps are shown in Fig. D.1. The name of the COM and the frequency of the used transition are shown in the lower left corner. Upper level energies and Einstein A coefficients (where $x_{-y}/\mathrm{s} = x \times 10^{-y}\,\mathrm{s}^{-1}$) are shown in the lower right, optical depth at position N1S in the upper right, and the synthesised beam in the upper left corner. The closest region around Sgr B2 (N1) is masked out due to high frequency- and beam-size-dependent continuum optical depth (see Appendix C). The black cross indicates the position of Sgr B2 (N1) determined in this work. HII regions reported by Gaume et al. (1995) are shown with blue crosses, continuum sources reported by Sánchez-Monge et al. (2017) with grey polygons.

results of COM abundances and to the north-east, we face uncertain contributions of free-free emission (see Fig. 1) to the continuum. Therefore, these directions were not used, instead, we decided to go west as indicated with maroon symbols in Fig. 3. The positions are listed in Table E.1. Because the molecular emission seemed slightly less spatially extended than to the south (cf. Fig. 4), the positions where the emission is more intense are chosen in a somewhat smaller distance from each other. Similar to N1S, we refer the distance at 1″ from Sgr B2 (N1) to as N1W and then increase numbers with increasing distance. Additionally, we looked at position N1W-1 which is at a distance of 0.5″ from Sgr B2 (N1). Positions closer to Sgr B2 (N1) in either direction were not used because the continuum becomes optically thick.

In Appendix E we provide the parameters used for the LTE modelling of the selected COMs at each position. Additionally, we show observed spectra for each COM at position N1S (or N1S1 for CH_3OCH_3) together with the synthetic spectra in Appendix F. These figures only show transitions that have been used to create the respective population diagram (see Sect. 3.4).

3.4. COM rotational temperature and column density profiles

At each position selected in the previous section we derived population diagrams in order to determine the rotational temperature $T_{\rm rot}$ and column density $N_{\rm col}$ profiles for each COM. In the population diagrams we plot the natural logarithm of the upper level column density N_u divided by the level degeneracy g_u against the upper level energy E_u (Mangum & Shirley 2015) as they are related by

$$\ln\left(\frac{N_u}{g_u}\right) = \ln\left(\frac{8\,\pi\,k_B\,\nu^2\int J(T_B)\mathrm{d}v}{c^3\,h\,A_{\rm ul}\,g_u\,B}\right) = \ln\left(\frac{N_{\rm tot}}{Q(T_{\rm rot})}\right) - \frac{E_u}{k_B T_{\rm rot}}, \quad (3)$$

where k_B is the Boltzmann constant, c the speed of light, h the Planck constant, $B = \frac{\text{source size}^2}{\text{source size}^2 + \text{beam size}^2}$ the beam filling factor, $A_{\rm ul}$ the Einstein A coefficient, $N_{\rm tot}$ the total column density, and Q the partition function. Intensities in brightness temperature scale $J(T_B)$ are integrated over a manually selected velocity range dv.

In Fig. 5 the population diagram for CH_3OH towards N1S is shown as an example including data points for the observed as well as the modelled transitions. We used the vibrational ground state $v = 0$ and the first and second torsionally excited states $v = (1, 2)$ of CH_3OH, all of which were modelled with the same Weeds input parameters. We considered setups 1–3 and 4–5 separately and used different input parameters for both, if necessary, because of their different angular resolutions that can vary by more than a factor of 2 (see Fig. C.1 of Motiyenko et al. 2020 for another version of this population diagram of methanol that includes all setups). Without this separation, we might introduce larger scatter in the population diagram because different beams may see different portions of the gas. Because rotational temperatures derived from the population diagrams for either setups 1–3 or 4–5 differ by at most 3σ, where σ is the error on the linear fit, and in roughly two thirds of the cases the difference is even $\lesssim 1\sigma$ we only used the higher-resolution setups 4–5 to determine the temperature and column density profiles in the following. Except for $^{13}CH_3OH$ and NH_2CHO, for which we had to use setups 1–3, there are enough transitions of each COM detected in setups 4–5 to make reliable linear fits to the data in the population diagrams. Population diagrams for all analysed COMs and for all possible positions can be found in Appendix G. All vibrational states of a

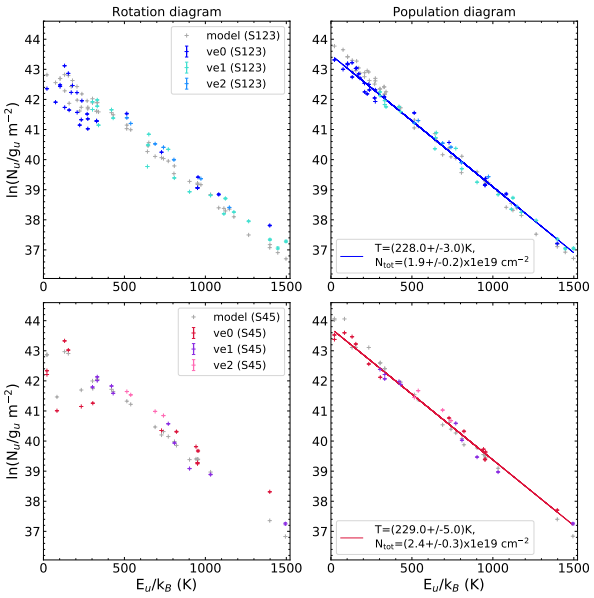

Fig. 5. Population diagram for CH_3OH towards Sgr B2 (N1S), where setups 1–3 and 4–5 are considered separately in the *upper* and *lower row*, respectively. Observed data points are shown in colours as indicated in the upper right corner in the *left panel* while the synthetic data points are shown in grey. No corrections are applied in the *left panel* while in the *right panel* corrections for opacity and contamination by other molecules have been considered for both the observed and synthetic populations. The blue and red lines are linear fits to the observed data points (in linear-logarithmic space) obtained with setups 1–3 and 4–5, respectively. The results of the fit are shown in the *right panels*.

COM that were used during the analyses are indicated in these population diagrams and are summarised in Table G.1.

We applied two corrections to the data points, which are only considered in the right panels of Fig. 5 and Figs. G.1–G.21. First, although we selected only transitions that are not too contaminated some contamination is inevitable due to high spectral line intensity. Therefore, we created a complete Weeds model that includes all transitions of all species used for the analysis. Based on this model, the contamination of neighbouring transitions of at least other identified species was estimated and subtracted from the integrated intensities.

Second, to consider possible effects of line optical depth we multiplied the integrated intensities of both the observed and modelled transitions with a correction factor $\frac{\tau}{1-e^{-\tau}}$ (see Goldsmith & Langer 1999; Mangum & Shirley 2015), where we used the opacities obtained from our Weeds model for the respective transition. Depending on the species, the upper level energy of a transition, and the distance to Sgr B2 (N1), opacities can be extremely high, which cannot be properly accounted for in our simple Weeds model. Hence, the correction factor might not be able to counteract the effect on the intensity. This may be seen for the lowest upper-level energy transitions of CH_3OH from setups 4–5 in Fig. 5, for which we obtained an optical depth of ∼3 from the model. When corrected for it, the data points (red) remain slightly below the fitted line, while the model (grey) overestimates the observation for these two transitions. Therefore, we only considered transitions in the population diagram that have opacities of $\lesssim$2–3 for all molecules.

After applying these two corrections, deviations between the observed and synthesised data points are generally small indicating that our chosen input parameters for the Weeds modelling are reliable. However, scatter amongst the observed data points can still occur due to a remaining contamination by unidentified lines, line opacity effects, or inaccurate baseline subtraction due to line confusion. Furthermore, the Weeds model was produced by taking into account the background continuum temperature, which is given by the baseline level initially subtracted from the spectra. Due to the different angular resolutions of the observational setups, the continuum level varies, which can introduce scatter amongst both the observed and synthesised data points. Moreover, at positions close to Sgr B2 (N1), we face the problem that the continuum starts becoming optically thick and therefore, hiding the line emission from our view. Because in Weeds the continuum is only considered as another background source, the model does not perform properly in this situation. Accordingly, intensities of some transitions may be overestimated by the model resulting in larger scatter in the population diagrams of observed data points. This is indeed evident in population diagrams at position N1S-1, where the continuum can be expected to become optically thick. Because transitions covered by spectral windows 2 and 3 of observational setup 5 suffer most from this effect they were not included for the analysis at this position as mentioned in Sect. 3.3.

At larger distances, where the COM emission becomes weak, scatter amongst the observed data points may be introduced when the larger beams of setup 4 capture material closer to the protostar that is no longer seen with the smaller beams of setup 5. For COMs and positions for which this effect is severe, we used spectra from setup 5 that are smoothed with a 2D Gaussian kernel to the angular resolution of spectral window 3 of setup 4.

For CH_3OCHO, and to a lesser extent for CH_3NCO, we noticed a systematic deviation of observed points from setups 4 and 5. We do not know the reason for this for sure. This is not caused by the different angular resolutions of the setups as smoothing the spectra of setup 5 to the resolution of setup 4 does not yield improvement. A possible explanation may however be filtering of extended emission by ALMA (see Sect. 3.1) which would affect setup 5 more than setup 4 due to the average shortest baselines that are longer for setup 5 (see Table 1 in Belloche et al. 2019). Data points observed with setup 5 would be expected to lie below those of setup 4 if emission was filtered, which is what we see in the population diagrams of these two molecules. However, this effect cannot be confirmed quantitatively and its impact remains questionable as it is not clear why the two mentioned COMs should be more affected than others.

Many of the above-mentioned uncertainties cannot be meaningfully quantified. Therefore, the error bars shown in the population diagrams only reflect the standard deviation from fitting and an additional factor of 1σ, where σ is the median noise level measured in channel maps of the continuum-removed data cubes taken from Table 2 in Belloche et al. (2019), to account for the uncertainty in the continuum level. However, the fit was performed by not weighting the data points by the errors in order to avoid giving too much weight to extremely strong lines and contaminated lines.

The data points in all population diagrams follow a linear trend meaning a single temperature can explain the level distribution for each molecule at each position. Therefore, we fitted a straight line to the observed data points in all cases and obtained the desired temperature profiles for each COM. We performed the fit only as far as positions N1S4 and N1W4, respectively, for reasons explained below. The profiles are shown as solid lines in Fig. 6 and the slopes of the linear fits to these profiles are summarised in Table 2. The errors on the data points correspond to values obtained from the population diagrams and determine the uncertainty on the temperature profiles. Few profiles seem to deviate from a straight line at shorter distances to Sgr B2 (N1). Therefore, we applied an additional fit to the data that includes only those positions at larger distances from Sgr B2 (N1) that seemingly lie on a straight line (dashed lines in Fig. 6). The second fit is kept only when the slopes of both fits differ by more than 15%.

Table 2. Slopes of the rotational temperature profiles shown in Fig. 6.

COM	South		West	
	All[(a)]	Far[(b)]	All[(c)]	Far[(d)]
CH_3OH	−0.67(4)	–	−0.56(7)	−0.80(6)
$^{13}CH_3OH$	−0.67(4)	–	−0.68(5)	–
C_2H_5OH	−0.74(7)	–	−0.73(5)	–
CH_3OCH_3	−0.69(5)	–	−0.94(9)	–
CH_3OCHO	−0.84(8)	–	−0.52(6)	–
CH_3CHO	−0.70(6)	–	−0.82(13)	−1.16(21)
CH_3NCO	−0.29(6)	−0.46(17)	−0.43(8)	−0.66(17)
C_2H_5CN	−0.52(8)	−0.74(3)	−0.48(6)	−0.59(9)
C_2H_3CN	−0.59(9)	–	−0.48(2)	–
NH_2CHO	−0.30(14)	−0.51(19)	−0.30(5)	−0.39(8)

Notes. The values in parentheses show the uncertainties in units of the last digit. [(a)]Linear fit was done using temperatures at all positions up to N1S4 (except for C_2H_3CN (N1S3), CH_3NCO (N1S3) and NH_2CHO (N1S2)). [(b)]Linear fit was done for positions beyond 1″ for CH_3NCO and NH_2CHO or 1.5″ for C_2H_5CN and up to maximum distances from (a). [(c)]Linear fit was performed for all positions up to N1W4 for CH_3OH and $^{13}CH_3OH$ or N1W3 for the rest, except for CH_3OCH_3 (N1S–N1S2). [(d)]Linear fit was done for positions beyond 1″ and up to maximum distances from (c).

To the south, CH_3OH, CH_3OCH_3, and CH_3OCHO are the COMs detected farthest from Sgr B2 (N1) with a reliable temperature determination beyond a distance of 3.5″. Especially for CH_3OH and CH_3OCH_3, it is evident in Fig. 6 that the rotational temperatures beyond this distance (corresponding to positions N1S5–N1S7) lie above the fit. These slightly higher temperatures can possibly be associated with the continuum source AN 20 (see Figs. 1 and 3) that heats the gas in addition to Sgr B2 (N1). Therefore, we excluded these positions from the fit of the temperature profiles. To the west, there seems to be a drop in temperature at positions N1W4 and N1W5 for CH_3OCHO and less pronounced for C_2H_5CN and a subsequent rise to $\gtrsim$100 K at larger distances. Therefore, position N1W4 was not included in the fit for these two molecules. A same trend may be expected for CH_3OCH_3 and C_2H_3CN, however, these molecules are not detected at these two positions. They reappear at larger distances. Remarkably, there is a change in velocity and line width starting from N1W5. Up to this position, spectral lines are detected at $v_{lsr} \sim 65$ km s^{-1} with $FWHM \sim 5$ km s^{-1}. This component is undetected at larger distances, instead the line appears at $v_{lsr} \sim 69$ km s^{-1} and is extremely narrow with $FWHM \sim 2$–3 km s^{-1} (indicated with crosses in all figures where necessary). This is also evident in the peak-velocity map in Fig. B.2. We did not include these positions to the fit of the temperature profile.

The slopes of the southbound profiles for the O-bearing COMs vary in a range from −0.6 to −0.8 when including all positions up to N1S4, except CH_3OCHO, whose profile is slightly steeper. However, given the apparent separation of data points

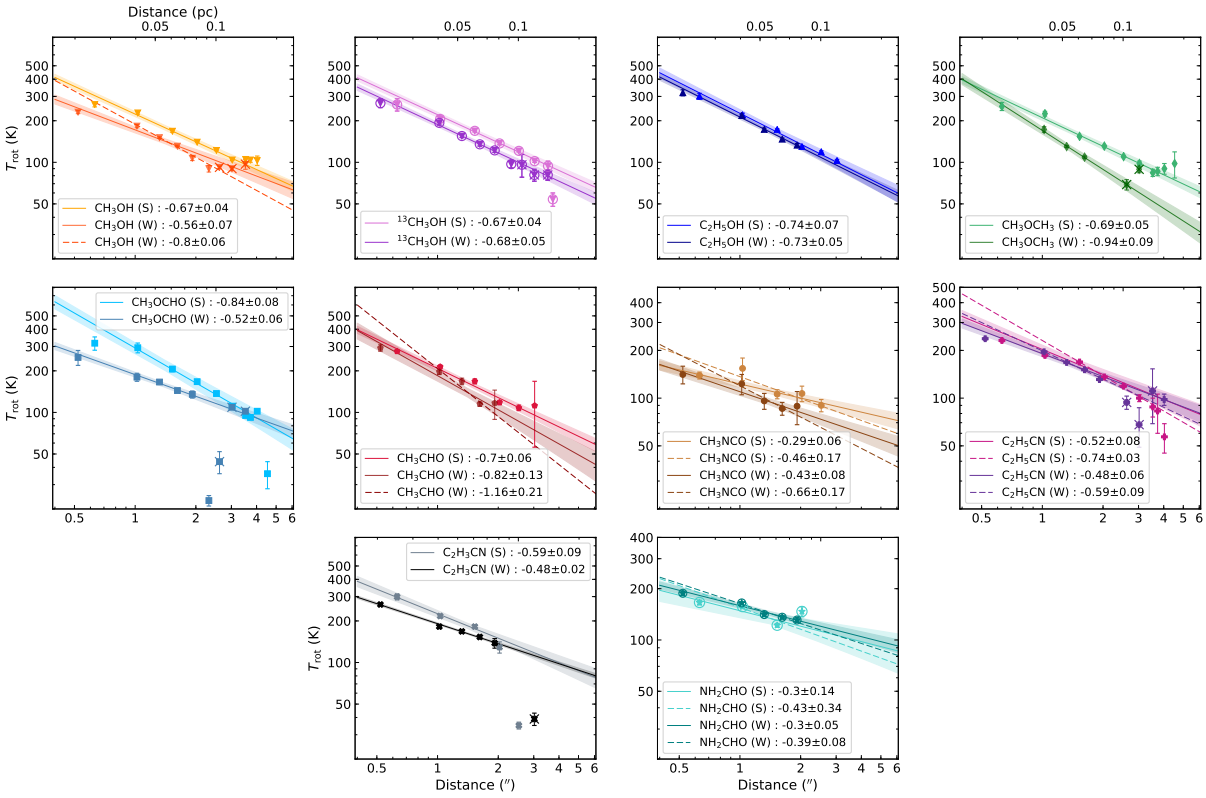

Fig. 6. Rotational temperature profiles to the south (S) and west (W), where temperatures for all COMs are taken from the linear fit in the population diagrams using setups 4–5, except for $^{13}CH_3OH$ and NH_2CHO, for which setups 1–3 have to be used (encircled symbols). Solid lines show the fit including all positions up to N1W4 (except for CH_3OCHO and C_2H_5CN) to the west and up to N1S4 to the south while dashed lines indicate the fit using only positions beyond 1″ (CH_3OH (W), CH_3CHO (W), CH_3NCO (W), C_2H_5CN (W), NH_2CHO) or 1.5″ (C_2H_5CN (S)) and up to N1S4 and N1W4, respectively. Additional crosses on the markers indicate positions for which the velocity offset changed from $\lesssim$2 to ∼7 km s^{-1}. The shaded areas indicate the uncertainty on the fit using all positions. The fit results are shown in the respective legend and are summarised in Table 2.

from setups 4 and 5 at some positions for this molecule, we may expect a greater overall uncertainty for its profile. The westbound profiles of CH_3OH, its ^{13}C isotopologue, C_2H_5OH, and CH_3CHO show similar slopes as their southbound counterparts. The westbound profile of CH_3OCH_3 has a much steeper slope of −1, while that of CH_3OCHO has a much shallower slope (approximtely −0.5) than to the south. When including only points farther away from Sgr B2 (N1), CH_3OH shows a slightly steeper slope of −0.81, which is still in the above-mentioned range. Also, CH_3CHO has a steeper slope of −1.15.

The slopes of the N-bearing COMs, except NH_2CHO, are slightly shallower (−0.4 to −0.6, NH_2CHO: −0.3) than those of the O-bearing COMs when including all points. Only when the closest positions to Sgr B2 (N1) are excluded, C_2H_5CN and NH_2CHO show steeper slopes that are comparable to those of the O-bearing COMs. The slopes of the westbound profiles of the N-bearing COMs are similar to the southbound ones. When considering only larger distances, the slopes of C_2H_5CN and CH_3NCO again become similar to those of the O-bearing COMs. The slope of NH_2CHO remains shallow. Up to now, it is unclear what may cause a deviation from a linear fit with all points included and the difference between the COMs. Aside from an underestimation of uncertainties, possible reasons may be presented in an underestimation of line optical depth or the absence of a species in the closest vicinity of Sgr B2 (N1). In the latter case, we may then observe a cloud layer where this species is still abundant and which has a lower temperature. In the case of NH_2CHO (also $^{13}CH_3OH$) the larger beams of setups 1–3 may influence the result, especially to the west, since the distances between positions are smaller than the average beam size and hence, adjacent positions are not independent of each other.

The temperature profile ($T \propto D^{\gamma}$) is derived from the diffusion equation (e.g. Kenyon et al. 1993). The slope γ varies depending on whether the dust emission is optically thin $\gamma = -\frac{2}{4+\beta}$ or thick $\gamma = -\frac{1-n}{4-\beta}$, where β is the dust emissivity spectral index, which likely varies in a range from 0.5 to 2 at 3 mm in dense cores (e.g. Kwon et al. 2009; Li et al. 2017), and n is the density power law index, which typically is $n = -1.5$ for a free-falling envelope (Shu 1977). Assuming these values the slope γ varies from $\sim[-0.3, -0.4]$ for optically thin and $\sim[-0.7, -1.3]$ for optically thick dust emission. Therefore, the slopes derived above that include all positions generally lie in between these ranges with the tendency towards the range for optically thick continuum.

Total column density profiles for each COM were obtained from the linear fit performed in the population diagrams and are shown in Fig. 7, where the errors on the data points again correspond to those obtained from the population diagrams. In addition, column densities used for the modelling with Weeds are shown as dotted lines. Usually, the difference is less than

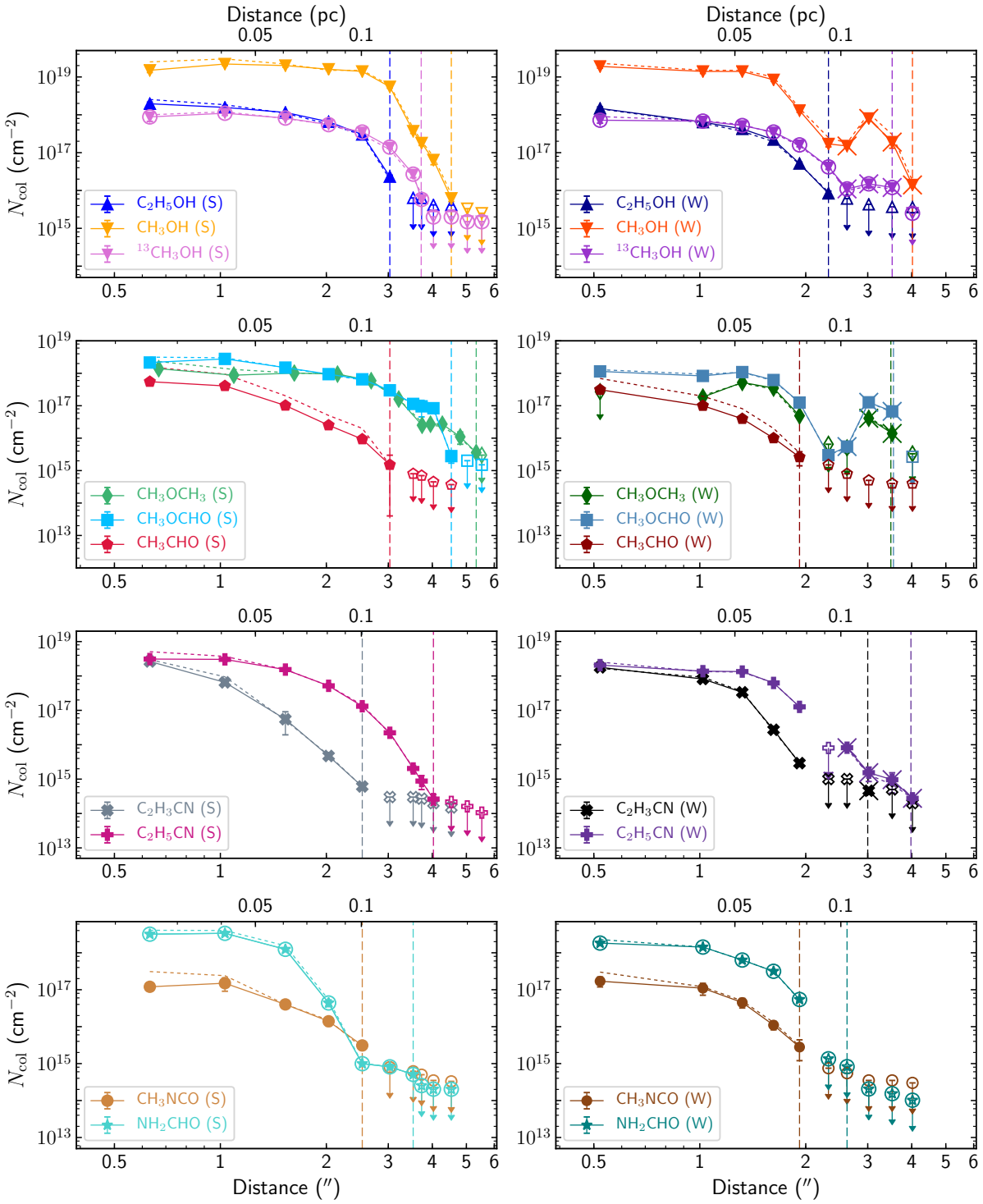

Fig. 7. COM column density profiles to the south (S) and west (W), where solid curves show the total column densities derived from the linear fit in the population diagrams using setups 1–3 for $^{13}CH_3OH$ and NH_2CHO (encircled symbols) and setups 4–5 for the rest of the COMs. Dotted curves indicate column densities used during the radiative transfer modelling with Weeds. Additional crosses on the markers indicate positions for which the velocity offset changed from $\lesssim$2 to ~7 km s^{-1}. Isolated unfilled markers with arrows indicate upper limits. Vertical lines mark the distance from Sgr B2 (N1) beyond which a COM is no longer detected.

a factor 2, except for CH_3CHO and CH_3NCO, for which the difference can be up to a factor 3–4 for some positions. This is mainly caused by the fact that the Weeds model considers the background continuum, while it is ignored (and cannot be properly accounted for) when fitting the population diagram. For this reason, we only use column densities from Weeds in the following. To all values we applied a vibrational correction factor that accounts for contributions to the column density by vibrational states, in the cases where the partition function provided by the various databases does not include this contribution that cannot be neglected at the high temperatures measured here. Southbound profiles of almost all O-bearing species resemble a plateau between 0.5″ and 2.5″ and then start to decrease at larger distances from Sgr B2 (N1), with those of CH_3OH and C_2H_5OH dropping more abruptly than CH_3OCH_3 and CH_3OCHO. The column density of CH_3CHO rather continuously decreases with increasing distance. To the south, column densities of N-bearing COMs decrease similarly to CH_3CHO, with C_2H_3CN and NH_2CHO showing a steeper decrease of column density with increasing distance from Sgr B2 (N1).

At close distances, the westbound profiles of all COMs, except CH_3OCH_3, behave similarly to their southbound counterparts with values that are equal or slightly smaller. The column density of CH_3OCH_3 decreases towards Sgr B2 (N1) such that at N1S-1, we were not able to derive a population diagram and hence, only an upper limit from the Weeds model was determined by extrapolating its temperature profile. At large distances the west- and southbound profiles start deviating from each other. On the one hand, C_2H_5OH, CH_3CHO, and CH_3NCO are only detected to shorter westward distances than to the south, while on the other hand, CH_3OH and CH_3OCHO show a cavity to the west, where column densities drop by up to two orders of magnitude reaching a minimum at N1W4–N1W5 only to increase again beyond these distances. This coincides with the drop in temperature seen in Fig. 6. This cavity is also observed for CH_3OCH_3, C_2H_3CN, and C_2H_5CN, because although they are not even detected at positions N1W4 and, for the former two, N1W5, their column densities can be determined at the larger distances. For $^{13}CH_3OH$, this drop in column density is less pronounced if evident at all. This may be because it has been smeared out due to the larger beam sizes of setups 1–3 that are used for this COM. NH_2CHO is detected up to position N1W5, however only upper limits (see below) could be determined. According to these, NH_2CHO may show a trend similar $^{13}CH_3OH$ concerning the cavity.

At some position at farther distance from Sgr B2 (N1) some COMs may still be detected, however, the linear fit in the population diagram did not yield a reliable result. In theses cases we fixed the rotational temperature by extrapolating the derived temperature profile of the respective species shown in Fig. 6 in order to determine column densities. Vertical lines in Fig. 7 indicate the largest projected distance from Sgr B2 (N1) up to which the COM is still detected and its column density can be derived. Accordingly, the COMs disappearing southwards first are C_2H_3CN and CH_3NCO, followed by CH_3CHO and C_2H_5OH, NH_2CHO, C_2H_5CN, and at last CH_3OH, CH_3OCHO, and CH_3OCH_3. Due to the cavity in column density, such a statement is difficult to make to the west. However, all COMs that are detected farthest from Sgr B2 (N1) to the south are also the ones detected at largest distances to the west, which is also seen in Fig. D.2, where these maximum distances are summarised. At distances beyond the shown vertical lines and at positions of the cavity, if necessary, upper limits for the column densities were determined, where the rotational temperature was again obtained from extrapolating the respective temperature profile. These upper limits were computed assuming an average velocity offset and line width determined from detected molecules at a specific position and making sure that the Weeds model for the undetected species did not overestimate the intensity over a 3σ threshold, where σ was taken from Table 2 in Belloche et al. (2019).

3.5. H_2 column densities from dust

Assuming that LTE conditions apply to the COMs, the rotational temperatures derived in Sect. 3.4 correspond to the kinetic temperature of the gas. Moreover, assuming that the gas is well coupled to the dust, the kinetic temperature of the gas also corresponds to that of the dust. Based on this, we computed again optical depth using Eq. (2), however, this time, we made use of the rotational temperatures derived in Sect. 3.4 and determined optical depth as a function of distance from Sgr B2 (N1) for both the continua at 1.3 and 3 mm. The profiles are shown in Fig. 8a. We used the temperature profile of C_2H_5OH because its population diagrams together with the temperature profile seem to be the most reliable amongst the COMs analysed here. The error bars correspond to an uncertainty that allows the dust temperature to differ by 20% from the gas temperature, which dominates over other uncertainties.

Based on the contribution of free-free emission to the 3 mm continuum at the position of Sgr B2 (N1) derived in Sect. 3.1, we estimated the remaining contribution at closest distance to Sgr B2 (N1) considered here (~0.2″, which is roughly half the average beam size of spectral window 0 of setup 5) to be ~16% and negligible at larger distances. The continuum at 1.3 mm has no significant contribution of free-free emission.

The results shown in Fig. 8a demonstrate again that the 3 mm continuum is less optically thick than the 1.3 mm continuum. Opacities are generally lower and the difference between the two continua is more pronounced to the west. The maximum distance from Sgr B2 (N1) denotes where the continuum is detected above 2σ. At positions N1S4 and N1S5, the continuum at 242 GHz drops below 1σ, hence, we used an upper limit of 2σ at these positions in the following. At distances beyond 3.5″ (corresponding to positions N1S5–N1S7), the optical depth increases again, which can be associated with continuum source AN 20 (see Figs. 1 and 3), whose location coincides with these positions.

To the south, the profile for both frequencies slightly decreases at shorter distance to Sgr B2 (N1) between 0.6″ and 0.2″, which may be the result of an underestimation of the continuum level. The continuum at both frequencies corresponds to the baseline, which is subtracted from the spectra. At these short distances, line emission is detected in almost every channel making the identification of the true baseline level more difficult. We checked the already baseline-subtracted spectra (done by Belloche et al. 2019) at the closest distance to Sgr B2 (N1) and estimated a possibly remaining continuum level of at most 20 K that would lead to an increase of the current level by about 10%. Therefore, missing continuum emission cannot fully account for the lower optical depth at short distances at least at 99.2 GHz. Though we accounted for a possible difference between gas and dust temperature in the error bars, we may still underestimate the optical depth, hence the dust temperature, that is assumed to be the gas temperature, may be overestimated. The underestimation of optical depth would in turn lead to an underestimation of H_2 column densities to an unknown extent. Therefore, southbound

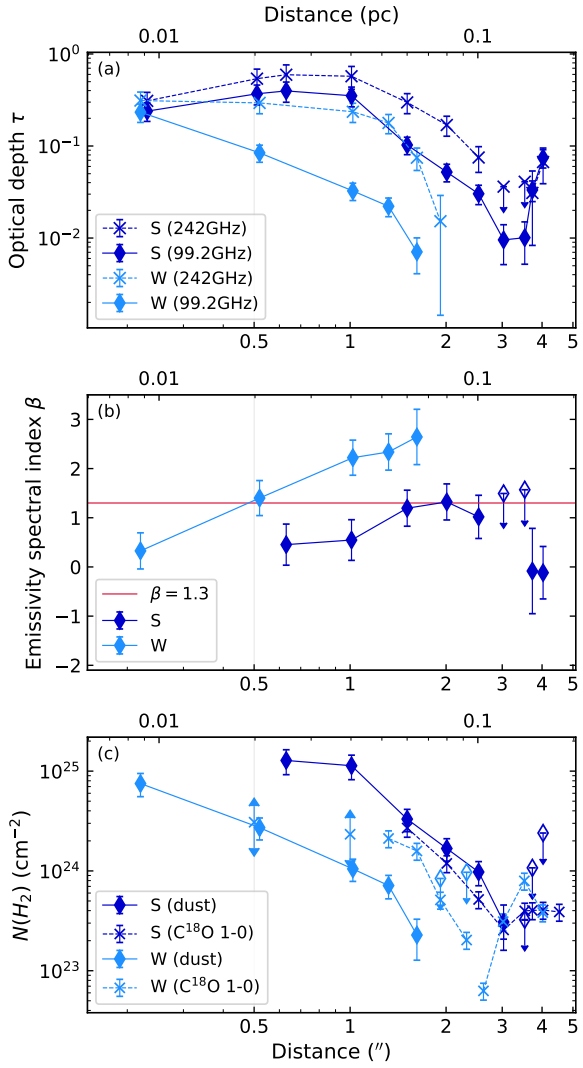

Fig. 8. Physical properties of Sgr B2 (N1) derived from dust continuum emission and $C^{18}O$ 1–0 emission. *Panel a*: optical depth τ as a function of distance from Sgr B2 (N1) in south (S) and west (W) directions and for the 1.3 mm and 3 mm continua, respectively. The 3 mm data have been corrected for free-free emission. *Panel b*: emissivity spectral index β as a function of distance from Sgr B2 (N1) derived from the optical depth ratio of the 1.3 mm and 3 mm data shown in (a). *Panel c*: H_2 column densities derived from the 3 mm continuum emission, using $\beta = 1.3$ (adopted from Bonfand et al. 2019, see text), and from $C^{18}O$ 1–0 emission using conversion factors of $C^{16}O/C^{18}O = 250 \pm 30$ (Henkel et al. 1994) and $H_2/C^{16}O = 10^4$ (Rodríguez-Fernández et al. 2001). The break in the (dashed) westbound profile indicates the observed velocity shift of the line from ~64 to 69 km s^{-1}. In all panels upper and lower limits are indicated with arrows.

distances to Sgr B2 (N1) smaller than 0.6″ are not considered in the following.

From the optical depth H_2 column densities $N(H_2)$ can be derived using

$$N(H_2) = \frac{\tau}{\mu_{H_2}\, m_H\, \kappa_\nu}, \tag{4}$$

where $\mu_{H_2} = 2.8$ is the mean molecular weight per hydrogen molecule, m_H the mass of an hydrogen atom, and κ_ν the dust mass opacity. The latter follows a power law given by:

$$\kappa_\nu = \frac{\kappa_0}{\chi}\left(\frac{\nu}{\nu_0}\right)^\beta, \tag{5}$$

where $\chi = 100$ is the standard gas-to-dust ratio and κ_0 is the dust mass absorption coefficient at frequency ν_0.

Assuming that H_2 column densities derived from the 1.3 mm and the 3 mm continuum yield the same result, the dust emissivity spectral index can be derived using the formalism introduced by Bonfand et al. (2017), which in our case leads up to

$$\beta = \ln\left(\frac{\tau_{99.2}}{\tau_{242}}\right) \times \frac{1}{\ln\left(\frac{99.2\,\mathrm{GHz}}{242\,\mathrm{GHz}}\right)}, \tag{6}$$

where $\tau_{99.2}$ and τ_{242} are continuum optical depths at the respective frequency. We show β as a function of distance from Sgr B2 (N1) to the south and west in Fig. 8b. The points at largest distance to the south corresponding to N1S5–N1S7 are not reliable as these positions are attributed to AN 20 and the contribution of free-free emission there is unknown. To the south, β has a value 0.4 at closest distances to Sgr B2 (N1) and increases to 1.3 at larger distances while to the west, β increases from roughly 0 up to a value of ~2.5. Based on these profiles, it is, therefore, difficult to assign a single β value that is able to describe the dust in both directions. Furthermore, β as well as κ rely on the dust properties, which are generally highly uncertain. Therefore, we decided to follow the approach described in Bonfand et al. (2019), who derived κ as a function of wavelength for $\beta = 1.2$ (see their Fig. F.1) and compared their results to models by Ossenkopf & Henning (1994). Ultimately, they used $\beta = 1.3$, which fits best the model that includes no ice mantles and assumes a gas density of 10^6 cm^{-3}. Accordingly, they used $\kappa_0 = 1.99$ cm^2 g^{-1} at $\nu_0 = 230$ GHz (i.e. $\lambda_0 = 1.3$ mm). In the following we adopt these values for κ_0 and β and assume an uncertainty of $\Delta\beta = 0.5$.

With optical depth and the dust mass opacity at hand, H_2 column densities can be derived using Eq. (4). The results are shown in Fig. 8c. H_2 column densities are listed in Table E.24, together with the continuum intensity and optical depth. In both directions we determined a maximum H_2 column density of $\sim 10^{25}$ cm^{-2}, which agrees well with the value of $(1.3 \pm 0.2) \times 10^{25}$ cm^{-2} derived by Bonfand et al. (2017) for Sgr B2 (N1), based on the data of the EMoCA survey, and a minimum value of $\sim 2 \times 10^{23}$ cm^{-2}. However, the westbound profile decreases faster and at already shorter distances than the southbound one. At positions where H_2 column densities were determined along both directions, the westbound values are lower than the southbound ones by a factor of a few or even by roughly one order of magnitude. If free-free emission was indeed contributing to the continuum emission of AN 20, H_2 column densities would be lower. Therefore, we consider the values at positions N1S5–N1S7 as upper limits. To the west, we added upper limits of 2σ.

3.6. H_2 column densities from $C^{18}O$

Additionally, H_2 column densities were derived from CO, where we used the $J = 1{-}0$ rotational transition of its isotopologue $^{12}C^{18}O$. Upper level column densities of this isotopologue were converted to those of the main one $^{12}C^{16}O$ by multiplying with the $C^{16}O/C^{18}O$ isotopic ratio of 250 ± 30 (Henkel et al. 1994)

A&A 665, A96 (2022)

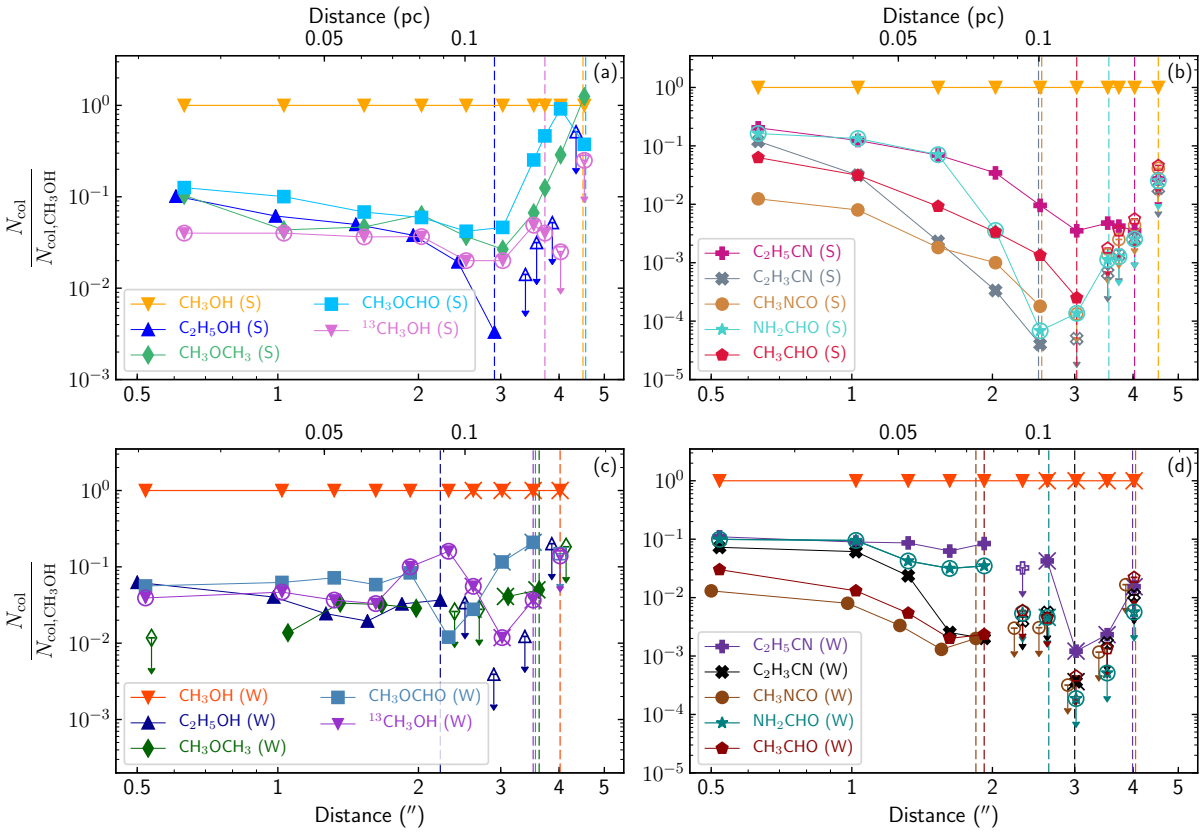

Fig. 9. COM abundance profiles with respect to CH_3OH to the south (S, *a–b*) and to the west (W, *c–d*) based on data from observational setups 1–3 (encircled symbols) and 4–5. Additional crosses on the markers indicate positions for which the velocity offset changed from $\lesssim 2$ to ~ 7 km s^{-1}. Unfilled symbols with arrows indicate upper limits. Vertical dashed lines mark the distance from Sgr B2 (N1) beyond which the respective COM is no longer detected.

and subsequently, to H_2 column densities by multiplying with 10^4 (Rodríguez-Fernández et al. 2001). We used the opacity-corrected column densities of the Weeds model, for which we fixed the temperature and the velocity offset to that of ethanol. The resulting H_2 column density profiles are shown in Fig. 8c. Column densities of H_2 and $C^{18}O$, and Weeds parameters are summarised in Table E.24. At distances of $\lesssim 1''$, only upper limits were determined to the west as the line is too contaminated by emission from other species at the two closest positions[3]. However, at these positions, the baseline subtraction may be overestimated due to spectral confusion, such that the upper limit could well be higher. Therefore we also show lower limits. At positions N1S-1 and N1S column densities could not be computed because there is an absorption component absorbing the emission at the respective velocity. Between distances of 1.5″ and 3″ the southbound profiles of H_2 column densities derived from dust and $C^{18}O$ follow the same trend, with values from $C^{18}O$ being only slightly smaller. The westbound profiles show greater difference. The value estimated at N1W-1 is in agreement with the one derived from dust while at N1W, the H_2 column density estimated from $C^{18}O$ may be larger. At even larger distances from Sgr B2 (N1) the column densities derived from the dust are surprisingly smaller than the column densities derived from $C^{18}O$ by a factor 4–5 or even more, which cannot be explained by contamination alone. In both directions, we are able to go to farther distances with the profile from $C^{18}O$ emission.

3.7. COM abundances as a function of distance and temperature

Figure 9 shows COM abundances relative to CH_3OH as a function of distance from Sgr B2 (N1) to the south (panels a–b) and to the west (panels c–d). Figures 10 a–d and 11 a–d show COM abundances relative to H_2 derived from dust and $C^{18}O$ 1–0 emissions, respectively, as a function of distance from Sgr B2 (N1) in both directions. For a better comparison, the abundance profiles are normalised to the respective value at 1.5″ distance to Sgr B2 (N1) as is shown in panels e–h, respectively. Given the resemblance of the H_2 column density profiles to the south, also the abundance profiles are similar, where possible to compare. Abundance profiles that were derived from dust continuum emission cover a distance range from 0.6″ to 3″ to the south (we refer to these profiles as S_D hereafter) and 0.5″ to ∼2″ to the west (W_D hereafter). The range is shorter for W_D because of the

[3] One of the contaminating species at lower frequencies is HNCO, $v = 0$. Emission coming from higher frequencies could not be assigned to a molecule. However, in comparison with other molecules, there may be a blue-shifted component of $C^{18}O$ originating from the outflow, which may then also apply to HNCO. At distances of >1″, the remaining contamination to the line core of $C^{18}O$ seems vanishingly low.

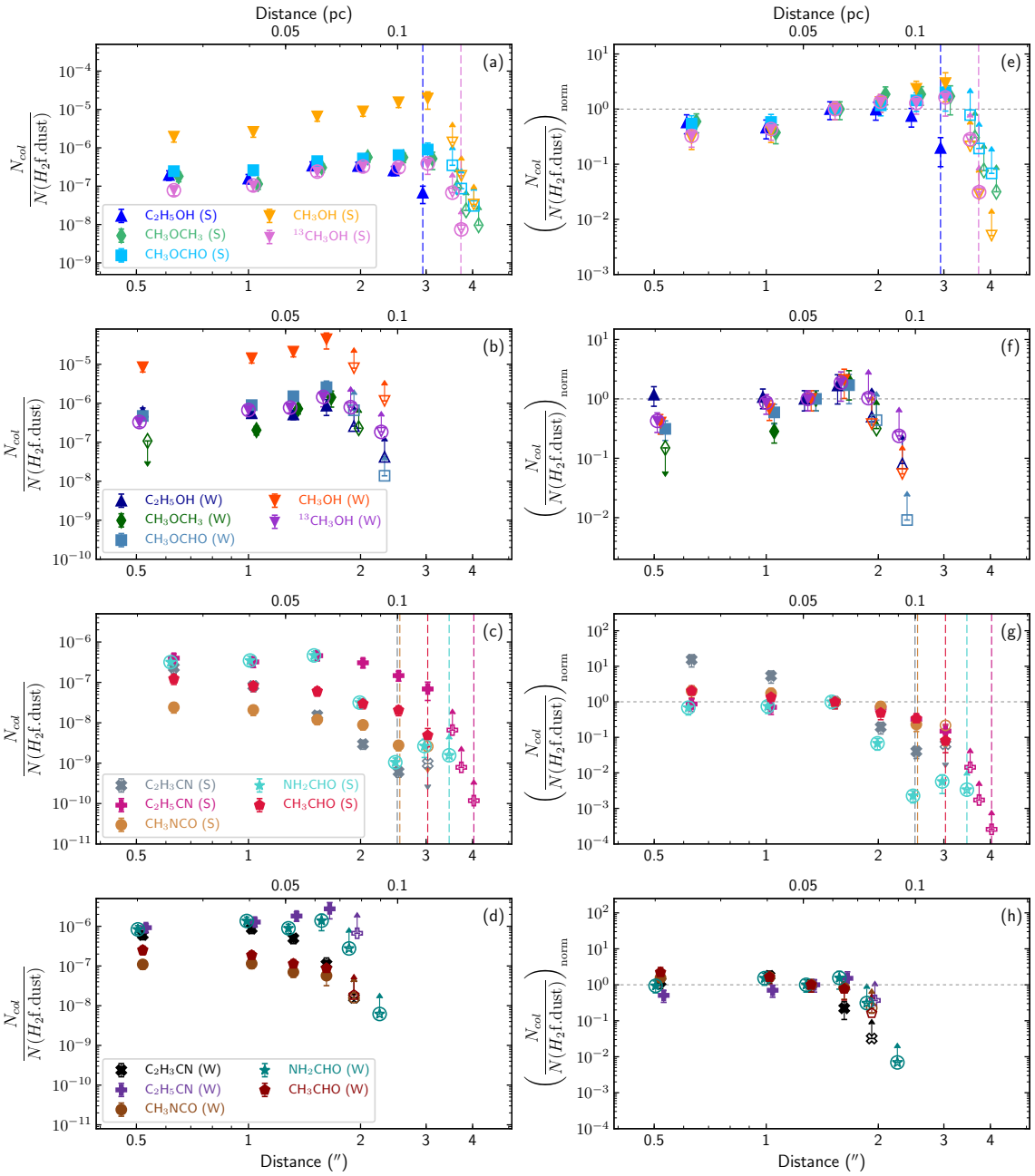

Fig. 10. COM abundance profiles with respect to H_2 (f. dust = derived from dust emission) to the south (S) and to the west (W) based on data from observational setups 1–3 (encircled symbols) and 4–5. *Panels a–d*: original COM abundances. Panels *e–h*: abundances normalised to the value at 1.5″ distance to Sgr B2 (N1). Unfilled symbols with arrows pointing downwards or upwards indicate upper or lower limits, respectively. Vertical dashed lines mark the distance from Sgr B2 (N1) beyond which the respective COM is no longer detected.

lack of H_2 column density at farther distances. In contrast, abundance profiles that were derived by using $C^{18}O$ reach farther out to maximum distances of 4.5″ to the south (S_{CO} hereafter) and 3.5″ to the west (W_{CO} hereafter). However, at distances ≤1″, there are only lower and upper limits for W_{CO} or no values at all for S_{CO}. Moreover, with the cavity observed for W_{CO}, peak abundances for the COMs are more difficult to locate.

Figure 12 also shows COM abundances relative to H_2 derived from dust (panels a–e) and $C^{18}O$ 1–0 emissions (panels f–j), but as a function of rotation temperature using the temperatures derived in Sect. 3.4. The temperatures covered by the abundance profiles are in a range of ∼100–300 K for S_D, well-above 100 K for W_D, and between ∼80 and 170–200 K for S_{CO} and W_{CO}. Therefore, with the additional positions at larger distances for

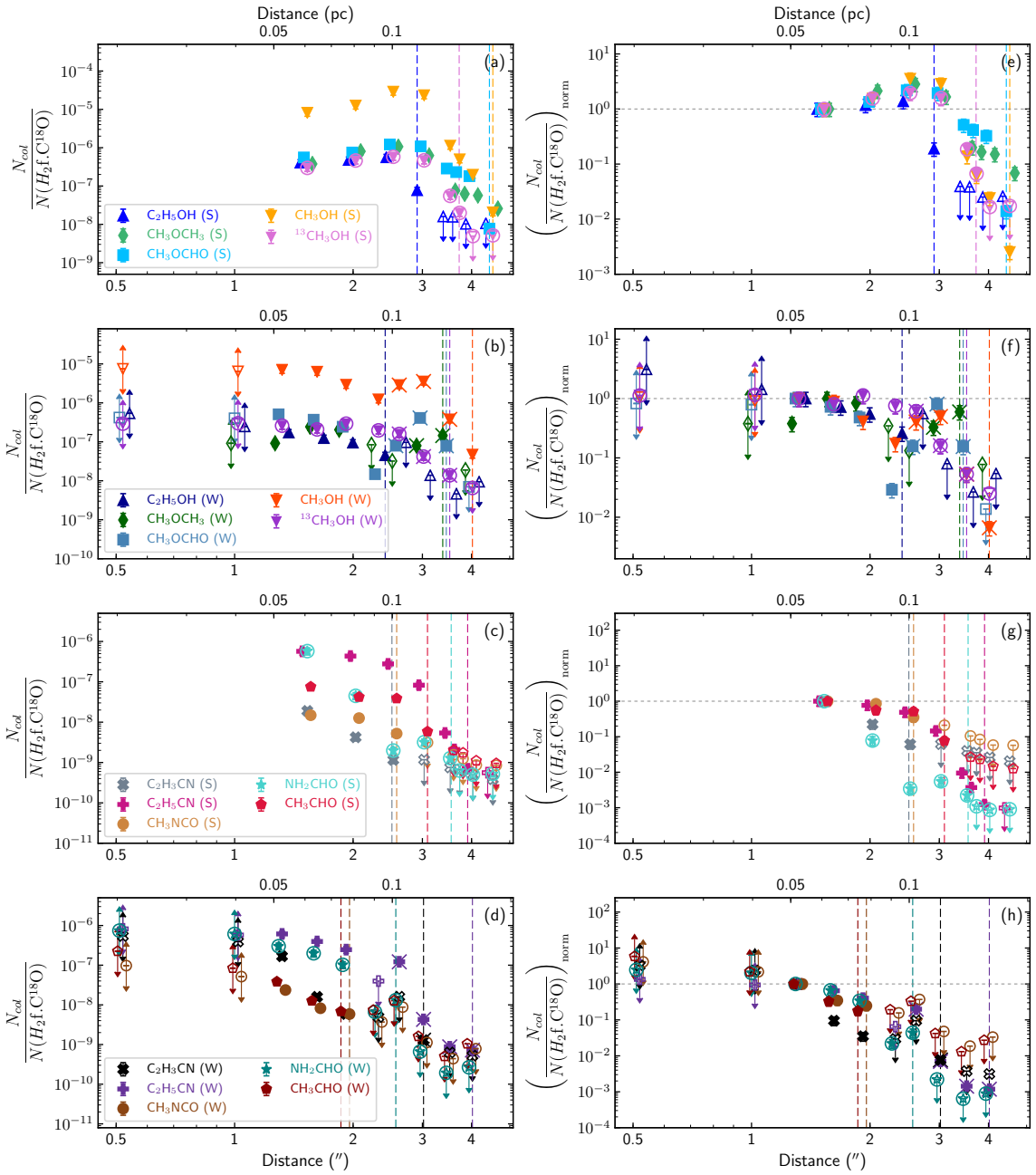

Fig. 11. COM abundance profiles with respect to H_2 (f. $C^{18}O$ = derived from $C^{18}O$ 1–0 emission) to the south (S) and to the west (W) based on data from observational setups 1–3 (encircled symbols) and 4–5. *Panels a–d*: original COM abundances. Panels *e–h*: abundances normalised to the value at 1.5″ distance to Sgr B2 (N1). Unfilled symbols with arrows pointing downwards or upwards indicate upper or lower limits, respectively. Vertical dashed lines mark the distance from Sgr B2 (N1) beyond which the respective COM is no longer detected.

S_{CO} and W_{CO}, also abundances at lower temperatures can be analysed.

3.7.1. Methanol CH_3OH

Methanol abundances increase steeply at around 100 K, that is between 3″ and 4″ distance from Sgr B2 (N1), to peak at 100–130 K corresponding to ∼1.5″ and 3″. Then, the profiles decrease steadily towards higher temperatures and shorter distances for directions S_D, W_D, and S_{CO}. For W_{CO}, the profile remains constant or possibly shows a slight increase towards higher temperatures with a peak that could be above 150 K given the limits on abundance. With little variation, most probably due to the different observational setups used for the analysis, that is

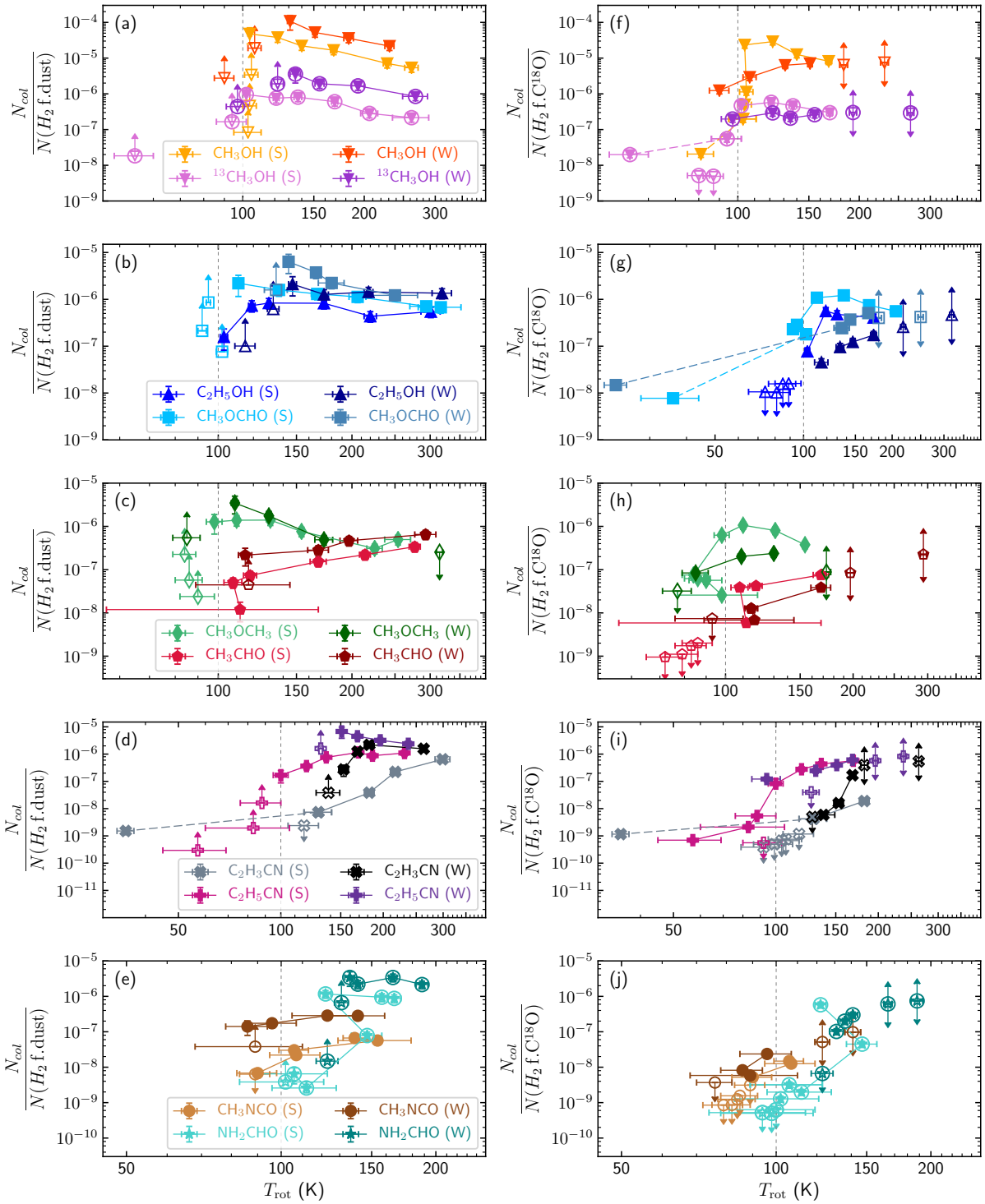

Fig. 12. COM abundance profiles with respect to H_2 to the south (S) and west (W) as a function of rotational temperature taken from Fig. 6. H_2 column densities were derived from either dust emission (f. dust, *a–e*) or $C^{18}O$ 1–0 emission (f. $C^{18}O$, *f–j*). Coloured dashed lines indicate the connection to points for which the temperature was either fixed in the population diagram, where a value was obtained from extrapolating the respective temperature profile, or derived from the population diagram but not considered in the fit to the temperature profiles shown in Fig. 6. Unfilled symbols with arrows pointing downwards or upwards indicate upper or lower limits, respectively. Encircled symbols indicate the species for which data from observational setups 1–3 were used, instead of 4–5.

different angular resolution, $^{13}CH_3OH$ follows the same trend as the main isotopologue.

3.7.2. Ethanol C_2H_5OH

Ethanol and methanol show similar behaviours as can be seen from Fig. 9, where the ethanol abundance profile relative to methanol is relatively flat. However, there is a slight decrease with increasing distance to the south, which is also indicated to the west. This reflects the fact that the abundance of ethanol relative to H_2 stays approximately constant with increasing temperature, while that of methanol decreases, as can be seen in Fig. 12. Abundances with respect to H_2 peak at 120–150 K for all directions (except for W_{CO}), which corresponds to distances of 1.5–2″ for S_D and W_D and 2.3″ for S_{CO}, which is closer to Sgr B2 (N1) and at slightly higher temperatures on average than for methanol. Abundances start decreasing at shorter distances from Sgr B2 (N1) and at higher temperatures than for CH_3OH.

3.7.3. Dimethyl ether CH_3OCH_3

The observed abundance profile as function of both distance and temperature shows similar behaviour compared to ethanol and methanol including a steep increase of abundance at 3–4″ distance to Sgr B2 (N1), corresponding to temperatures of ∼100 K, followed by an abundance peak at 110–130 K, and a subsequent decrease with increasing temperature or shorter distance. However, while the increase of abundance at ∼100 K is slightly less steep than for methanol, as can be seen in the profiles for S_{CO} and W_{CO}, the decrease towards higher temperatures along the west direction is steeper (cf. Fig. 9). The COM is not detected in the cavity of W_{CO}, however, it reappears at larger distances from Sgr B2 (N1).

3.7.4. Methyl formate CH_3OCHO

The abundance profile of CH_3OCHO closely resembles that of CH_3OCH_3, maybe slightly shifted by about +10 K. Abundances increase to peak at temperatures between 110 and 160 K corresponding to distances of 2.5–3″ for all, but W_{CO}, for which it is ∼1.5″. Similar to all other O-bearing COMs, abundance profiles then decrease towards higher temperatures.

3.7.5. Acetaldehyde CH_3CHO

In contrast to the other O-bearing COMs discussed above, the observed abundance profile of CH_3CHO shows a different behaviour as it continuously increases to a peak just below 300 K, which is the maximum temperature measured at closest distance to Sgr B2 (N1) for S_D, W_D, and W_{CO} (cf. Figs. 10–12). For S_{CO}, the maximum temperature is only 170 K due to missing data at positions closest to Sgr B2 (N1). We do not trace temperatures lower than 100 K, therefore, a conclusion on a possibly steeper increase similar to other O-bearing COMs cannot be drawn from the current data.

3.7.6. Vinyl cyanide C_2H_3CN

The observed abundance profile of C_2H_3CN shows an increasing behaviour towards shorter distance and higher temperature, similar to CH_3CHO, but steeper. Moreover, a difference is evident between the southbound and westbound profiles because to the south, the profile increases continuously while to the west, the increase is steeper between ∼120–170 K or 1–2″ and flattens for higher temperatures and shorter distances. The location of the abundance peak shows some variance but may well be at highest temperatures and closest to Sgr B2 (N1) for all cases when considering all uncertainties. The different behaviours of the profiles could possibly be explained by an under- and overestimation of the line opacity to the west and south, respectively, since more transitions throughout all vibrational states, used to derive the population diagram of C_2H_3CN, are optically thick at closest distances to Sgr B2 (N1) compared to the other COMs, which can have an influence on the results of the population diagram. Similar to CH_3CHO, the abundance profiles only reliably go down to temperatures of >100 K and, therefore, we are not able to observe a possible steep increase at these temperatures. And, similar to CH_3OCH_3, vinyl cyanide is not detected in the cavity of W_{CO}, however, it is observed at one more position at a larger distance.

3.7.7. Ethyl cyanide C_2H_5CN

The abundance profiles of C_2H_5CN show a similarly steep increase as the aforementioned O-bearing COMs at distances of 3–4″ from Sgr B2 (N1), which, for S_D and S_{CO}, corresponds to a temperature of around 100 K. For W_D and W_{CO}, the lack of H_2 column density and the cavity, respectively, prevent us from making a statement on the temperature to the west. Abundances then keep gently increasing to a peak at 150–170 K (1.5–2″ distance). Towards higher temperatures and shorter distances, the profile for W_D slightly decreases, while, for the others, the profiles seem to remain flat or to slightly increase. With this behaviour, C_2H_5CN is placed somewhere in between the results seen for C_2H_3CN and CH_3CHO and the other O-bearing COMs.

3.7.8. Methyl isocyanate CH_3NCO

Similar to CH_3CHO, we do not observe a steep increase of abundance for CH_3NCO because the COM is not detected at distances where the increase for other molecules is identified. The profiles do show a continuous increase to a peak at closest distances to Sgr B2 (N1). The same trend is indicated in the profile as function of temperature, however, the error bars on the measured temperatures are large. The temperature of the abundance peak is located at ∼110–150 K.

3.7.9. Formamide NH_2CHO

Abundance profiles of NH_2CHO show a similarly steep increase as methanol, however, starting only at a distance of 2.5″ to Sgr B2 (N1), that is at much shorter distances than for other COMs. The temperature of this increase is uncertain, however, it seems to be above 100 K. The southbound abundance profiles of formamide show a plateau at the largest distances that is at roughly 100 K. The profiles peak at 120–140 K or ∼1.5″ for S_D, S_{CO}, and W_D, and show a subsequent plateau or slight decrease.

4. Discussion

4.1. H_2 column densities

H_2 column densities were derived in two ways: from dust emission as well as from $C^{18}O$ 1–0 emission. While the H_2 column density profiles derived from both show only small differences to the south, the westbound profiles show larger differences at least at distances >1″, where H_2 column densities derived from dust are smaller by factors of a few than those from $C^{18}O$. In Sect. 3.6 we concluded that contamination of the $C^{18}O$ intensity

by other species cannot fully explain this difference. The conversion factors from CO to H_2 may have some greater uncertainties than considered here. Chemical models by Garrod et al. (2022) (hereafter G22) show that the typical CO abundance with respect to H_2 of 10^{-4} is only reached at temperatures of 100–150 K as the molecule co-desorbs with water from dust grain surfaces. Therefore, we may be underestimating this conversion factor at lower temperatures. However, this does not explain the discrepancy of the profiles to the west because temperatures lower than 100 K are reached in only a few cases and the discrepancy is only seen at temperatures >100 K. CO abundances may be further enhanced at higher temperatures when more complex species are destroyed and leave behind CO as one of the final products.

Probably even higher uncertainties exist for the conversion from dust to H_2 due to the unknown dust properties. In Fig. 8b we show the dust emissivity spectral index β, which is directly linked to the dust properties and varies significantly between the south and west directions, but also along one direction. It is rather unlikely that the dust properties vary by this much in one source. Whether β is a constant, however, as is assumed in Fig. 8c, is not certain, either. Whether these uncertainties can explain the differences seen in the H_2 column density profiles to the west or whether environmental differences (e.g. outflow, accretion through filaments) may play a role remains unclear to now.

4.2. Segregation of O- and N-bearing COMs

The morphology of COM emission shown in Fig. 4 suggests a separation of COMs into two, maybe even three groups. Emissions of the O-bearing COMs CH_3OH, C_2H_5OH, CH_3OCHO, CH_3OCH_3, and, to some extent, CH_3CHO are extended and structured following the (dust) continuum emission, while those of the N-bearing COMs C_2H_5CN and C_2H_3CN are more compact and less structured. Morphologies of NH_2CHO and CH_3NCO are in between as these are compact, however, with some structure.

Many observations revealed segregation of O- and N-bearing COMs in other star-forming regions with a variety of explanations. Bisschop et al. (2007) found a segregation of COMs in terms of rotational temperature on the basis of unresolved single-dish observations of seven high-mass young stellar objects. They classified the COMs as either 'hot' or 'cold' species. In their classification, CH_3CHO (amongst others) is a cold species that traces maximum temperatures of <100 K, while CH_3OH, C_2H_5OH, CH_3OCHO, NH_2CHO, C_2H_5CN, and HNCO are hot species because they trace temperatures of >100 K. Although primarily, this is not a segregation of O- and N-bearing COMs, all species of the latter type are classified as hot species by Bisschop et al. (2007). This separation was similarly observed in Orion KL (Crockett et al. 2015) and, with a slightly deviating classification, in the hot corino around the low-mass protostar IRAS 16293–2422B (Jørgensen et al. 2018), where the latter study did only investigate O-bearing COMs. In these last two studies, differences between COMs were also observed in the morphology of the COM emission. This classification into hot and cold species was proposed to primarily arise from differences in the binding energy of the molecules. Cold species have low binding energies. Therefore, they can already thermally desorb at lower temperatures and their emissions are more widespread. Hot species desorb at higher temperatures due to higher binding energies and their emitting area is more compact around the protostar. Although this theory is supported by results of chemical models (Garrod 2013) it is not really confirmed observationally because the true desorption temperatures of COMs in interstellar environments are not known.

Deviations from this classification have been observed, for example in IRAS 16293–2422A (Manigand et al. 2020), where CH_3OH and CH_3OCHO, although being hot species, trace a more extended region. Moreover, most recent observations towards CygX-N30 do not reveal a significant difference in temperature between various COMs in general (van der Walt et al. 2021). Such a classification that depends on binding energies is not straightforward as their values are uncertain and vary depending on the dust composition. We discuss the role of binding energies in more detail in Sect. 4.7.

A temperature-dependent segregation of O- and N-bearing COMs can result from carbon-grain sublimation, which was proposed to occur inside the so-called soot line at $T \gtrsim 300$ K (van 't Hoff et al. 2020). This mechanism would lead to an increase in the abundance of nitriles and hydrocarbons that add to the abundances that are already present due to thermal desorption at lower temperatures. Accordingly, this leads to the observation of N-bearing species at higher excitation temperatures with enhanced column densities and with a more compact morphology than O-bearing species. Therefore, when only regarding the morphology, where the emission of N-bearing COMs is more compactly distributed around the protostar, this mechanism may be able to explain the differences between the COMs observed in Sgr B2 (N1).

A segregation of O- and N-bearing COMs was also observed in the hot core of the massive protostar G328.2551-0.5321 (Csengeri et al. 2019). The observed morphologies of the two families of COMs are completely different. O-bearing COMs show two intensity peaks on either side of the protostar, while the emission of N-bearing COMs is more compact and spherically distributed around it. The authors concluded that abundances of O-bearing COMs are enhanced due to a non-thermal desorption process. They interpreted the two observed intensity peaks in the morphology as tracing the location of material falling onto a disk, thereby, inducing accretion shocks, which enhances the abundance of O-bearing COMs. In contrast, the morphology of N-bearing COMs follows the expectations for thermal desorption from dust grains. The morphology of O-bearing COMs in Sgr B2 (N1) does not present such a behaviour as there is no indication of two distinct intensity peaks on opposite sides of the protostar and at opposite velocity offsets from the source velocity that would imply the presence of a disk (cf. Fig. 4 and the peak velocity map in Fig. B.2a).

Results from most recent chemical models by G22 suggest a separation between O- and N-bearing COMs that is caused by their different main formation pathways on dust grains at low temperatures and in the gas phase, respectively. More details are discussed in Sect. 4.4 when these modelled abundance profiles are compared to our observed ones. Based on this comparison and the discussion on the temperature profiles below, we try to identify which of the aforementioned mechanisms may cause the segregation of O- and N-bearing COMs seen around Sgr B2 (N1).

4.3. Temperature profiles

The variation of the slopes of the rotation temperature profiles derived from various COMs is generally small. They span ranges from −0.6 to −0.8 for O-bearing COMs and from −0.4 to −0.6 for N-bearing COMs (except for NH_2CHO). In Sect. 3.4 we have already shown that our derived values lie in between the theoretical slopes expected for central heating through an envelope

containing optically thin or thick dust, for which a range of dust emissivity indices β of 0.5–2 was assumed. Assuming $\beta = 1.3$, which we used to compute H_2 column densities in Sect. 3.5, the expected power-law indices would be −0.38 or −0.93 for optically thin and thick dust, respectively. Although the values slightly deviate from the observed power-law indices, our results suggest that the COMs in Sgr B2 (N1) along the two analysed directions trace the temperature structure of the collapsing envelope that is heated by the central (proto)star(s).

Temperature profiles have been derived for 22 massive cores as part of the CORE project by Gieser et al. (2021) based on observations of H_2CO and CH_3CN. The slopes span a range from −0.1 to −0.6 with an average value of −(0.4 ± 0.1) excluding three outliers with slopes of −1 to −1.5. With the CORE-extension sample (Gieser et al. 2022), temperature profiles of another ten cores were shown and slopes of −0.1 to −1 reported, where a fit was only applied for those cores whose profiles were resolved and that did not show flat profiles.

An observed temperature profile with a slope of −0.77 was reported for the hot core G31.41+0.31 (Beltrán et al. 2018) and supported by models (Osorio et al. 2009). Models by Nomura & Millar (2004) suggest steeper profiles at similar distances considered here for higher H_2 column densities, which correspond to higher dust optical depths. The modelled temperature profile for Sgr B2 (N2) shows a steepening from far distances to closer distances to the protostar, spanning a range of slopes for the optically thin regime to −0.8 for an optically thicker regime (Bonfand et al. 2019).

Based on this discussion, it seems that, for the scales traced with the ReMoCA survey, the desorption process of COMs in Sgr B2 (N1) is thermally driven, in other words, there is no clear sign in the temperature profiles that would indicate shock chemistry induced by the outflow or accretion shocks, at least not along the two analysed directions. A more detailed discussion on the differentiation between thermal and non-thermal desorption is done in Sect. 4.5, also considering the abundance profiles. In addition to this result, we concluded in Sect. 3.4 that the power-law indices of the temperature profiles are more consistent with expected values for an optically thick dust continuum.

4.4. Abundance profiles

We focussed the discussion on the abundance profiles on a comparison with most recent astrochemical models performed by G22. The chemistry of the G22 models includes new methods for simulating non-diffusive reaction mechanisms, but the general physical and chemical setup is based on earlier works (Garrod 2008, 2013; Garrod et al. 2017). This setup includes two stages: a cold collapse phase (stage 1) and a subsequent warm-up phase (stage 2). In stage 1 the density increases from 3×10^3 to 2×10^8 cm^{-3} and the dust temperature decreases from ∼15 K to 8 K while the gas temperature is kept constant at a value of 10 K on a timescale of $\lesssim 10^6$ yr. In stage 2 the final density of stage 1 is adopted and kept constant. Gas and dust temperatures increase simultaneously as it is assumed that they are well coupled during this stage. Three different timescales of this temperature rise are considered separately: 10^6 yr (slow warm-up), 2×10^5 yr (medium warm-up), and 4×10^4 yr (fast warm-up), which corresponds to the time it takes to reach 200 K, respectively. The models then continue to a maximum temperature of 400 K. In both stages the chemistry takes into account gas-phase, grain/ice-surface, and bulk-ice chemistry, which are all coupled by various thermal and non-thermal processes. Amongst these is the interaction with cosmic rays (CRs) under all conditions,

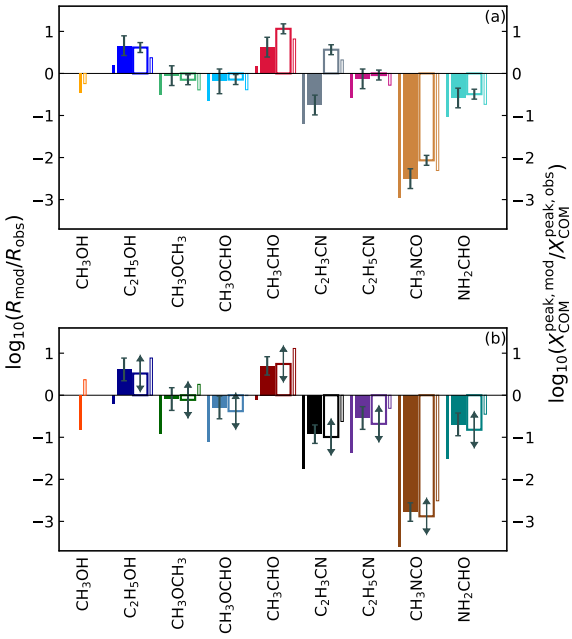

Fig. 13. Comparison between observed peak abundances with respect to H_2 and the modelled ones to the a) south and b) west, where H_2 column densities were derived from dust (thick filled bars) or $C^{18}O$ emission (thick unfilled bars). The peaks are taken from the profiles shown in Fig. 12 and are normalised by the value for CH_3OH to obtain R_{obs}. The position of the peak can differ between the COM and methanol in all four cases. The peaks with respect to CH_3OH in the models, R_{mod}, are taken from Table 17 in Garrod et al. (2022), where we use the values of the slow warm-up model. Thin bars show the ratio of modelled abundance peaks X^{peak}_{mod} and observed ones X^{peak}_{obs}. Observed abundances are with respect to H_2 derived from dust (filled bars) or $C^{18}O$ 1–0 emission (blank bars). Modelled peak abundances are taken from Table 16 in Garrod et al. (2022) and multiplied by a factor 2 to roughly convert to abundances with respect to H_2 (from total H). All values are summarised in Table 3. Arrows pointing downwards or upwards indicate upper or lower limits, respectively.

where the ionisation rate is kept constant at the standard value of $\zeta = 1.3 \times 10^{-17}$ s^{-1}. The most recent model used in G22, however, does include a number of changes compared to the earlier models. We refer the reader to the article for a detailed description of new adjustments and their influence on the COM abundances. Some of the new implementations will, however, be mentioned in the following as they play a crucial role in explaining our observations.

In general, our results are overall best described by the model of the slow warm-up phase, which was previously also found to best explain the observed abundances in Sgr B2 (N2) (G22). To compare the modelled results to our observations and, based on that, make implications on the main formation and destruction pathways of COMs, we created a diagram similar to Fig. 15 of G22, where they show the ratio of peak COM abundances relative to the peak abundance of CH_3OH. The result is shown with thick bars in Fig. 13, where on the left y axis we plot

$$\frac{R_{mod}}{R_{obs}} = \frac{X^{peak,mod}_{COM}}{X^{peak,mod}_{CH_3OH}} \frac{X^{peak,obs}_{CH_3OH}}{X^{peak,obs}_{COM}}, \quad (7)$$

Table 3. Observed (to the south and west) and modelled peak COM abundances and corresponding temperatures.

	South				West					
	$N(H_2)$ from dust		$N(H_2)$ from $C^{18}O$		$N(H_2)$ from dust		$N(H_2)$ from $C^{18}O$			
Molecule	X_{peak}	T_{rot} (K)	X_{peak}	T_{rot} (K)	X_{peak}	T_{rot} (K)	X_{peak}	T_{rot} (K)	X^{mod}_{peak}	T^{mod}_{rot} (K)
CH_3OH	$4.8 \pm 2.3(-5)$	104 ± 1	$2.9 \pm 0.6(-5)$	122 ± 1	$1.1 \pm 0.5(-4)$	131 ± 2	$\geq 5.7(-6)$	≥ 149	1.7(−5)	166
C_2H_5OH	$8.3 \pm 2.1(-7)$	130 ± 1	$5.6 \pm 1.1(-7)$	119 ± 2	$2.1 \pm 0.9(-6)$	147 ± 3	$\geq 1.4(-7)$	≥ 169	1.3(−6)	166
CH_3OCH_3	$1.4 \pm 0.4(-6)$	131 ± 1	$1.1 \pm 0.2(-6)$	110 ± 1	$3.5 \pm 1.5(-6)$	109 ± 2	$\geq 1.9(-7)$	≥ 128	4.4(−7)	200
CH_3OCHO	$2.2 \pm 1.1(-6)$	111 ± 2	$1.2 \pm 0.2(-6)$	137 ± 2	$6.3 \pm 2.8(-6)$	144 ± 3	$\geq 4.1(-7)$	≥ 162	5.0(−7)	225
CH_3CHO	$3.4 \pm 0.9(-7)$	277 ± 8	$7.5 \pm 1.4(-8)$	168 ± 7	$6.5 \pm 1.6(-7)$	293 ± 16	$\geq 3.1(-8)$	≥ 159	5.0(−7)	257
C_2H_3CN	$6.5 \pm 1.6(-7)$	299 ± 15	$1.9 \pm 0.4(-8)$	182 ± 6	$2.2 \pm 0.5(-6)$	182 ± 6	$\geq 1.4(-7)$	≥ 165	4.0(−8)	166
C_2H_5CN	$1.2 \pm 0.3(-6)$	169 ± 1	$5.7 \pm 1.1(-7)$	169 ± 1	$6.8 \pm 3.0(-6)$	151 ± 1	$\geq 4.9(-7)$	≥ 167	3.0(−7)	166
CH_3NCO	$6.7 \pm 1.7(-8)$	139 ± 7	$1.5 \pm 0.3(-8)$	106 ± 7	$2.9 \pm 0.7(-7)$	123 ± 18	$\geq 1.9(-8)$	≥ 85	7.2(−11)	343
NH_2CHO	$1.2 \pm 0.3(-6)$	122 ± 3	$5.8 \pm 1.1(-7)$	122 ± 3	$3.4 \pm 1.5(-6)$	136 ± 3	$\geq 2.4(-7)$	≥ 138	1.1(−7)	166

Notes. Values of observed peak abundance X_{peak} are taken from Fig. 12 and represent COM column densities with respect to H_2, where we consider H_2 column densities derived from either dust (2nd and 6th columns) or $C^{18}O$ 1–0 emission (4th and 8th columns). The modelled peak abundances X^{mod}_{peak} present COM column densities with respect to total H taken from Table 16 from Garrod et al. (2022) multiplied by a factor 2 to roughly convert to abundances with respect to H_2. The values in parentheses show the decimal power, where $x \pm y(z) = (x \pm y) \times 10^z$.

where X^{peak}_{COM} is the peak COM abundance and $X^{peak}_{CH_3OH}$ is the peak abundance of CH_3OH. The observed peak abundances with respect to H_2 are extracted from Fig. 12. The modelled peak abundance ratios are taken from Table 17 in G22. All values are listed together with the corresponding peak-abundance temperature in Table 3. In addition, we show a comparison of modelled and observed peak abundances $X^{peak,mod}_{COM}/X^{peak,obs}_{COM}$ without normalising to CH_3OH (thin bars, right y axis). The modelled peak abundances are taken from Table 16 in G22 and multiplied by a factor 2 to convert to abundances with respect to H_2 (from total H).

Besides peak abundances, the behaviours of the profiles were compared to the model predictions. In particular, we used Figs. 12, 20, and 21 from G22 that present results of the cold and subsequent slow warm-up phase. All three show the time evolution of the COM abundances that is also linked to the temperature increase due to the evolution of the protostar. Figure 12 of G22 presents the abundance profile in the solid and gas phase while Figs. 20–21 of G22 (see also their Figs. 13–14 to find responsible chemical reactions) show the rate at which a COM is dominantly formed or destroyed at each point of the evolution.

4.4.1. Methanol CH_3OH

Methanol is the most abundant COM in the observation as well as the model with peak abundances that differ by factors of a few only (cf. Table 3 and thin bars in Fig. 13). According to the model, CH_3OH is predominately formed in the bulk ice before the onset of the warm-up as seen in Fig. 20 of G22. After co-desorption with water, starting at ∼120 K and finishing at 166 K, the molecule is destroyed in the gas phase, mainly through proton transfer from H_3O^+. This leads to the drop of gas-phase abundance seen towards higher temperatures right after the peak at 166 K in the model. Except for the value of peak abundance that is underestimated by the model (except for W_{CO}), however only by factors of a few, and temperature of this peak that is higher in the model by some tens of Kelvin (see Table 3 and Fig. 13), the model is in good agreement with the observations (cf. Sect. 3.7.1). Therefore, the CH_3OH abundance in Sgr B2 (N1) is most likely enhanced in the gas phase due to thermal desorption at ∼100 K supported by the increase that seems fairly sudden (see also Sect. 4.5).

The similar behaviour of abundances of the main and ^{13}C isotopologues implies that similar formation and destruction mechanisms take place for both species. This also indicates that our model of the CH_3OH emission accounted well for potential optical depth effects. Considering only the abundance plateau, that is distances of $\lesssim 2''$ to Sgr B2 (N1), we find an observed median $^{12}C/^{13}C$ isotopic ratio of 22 and 24 to the south and west, respectively, which is consistent with the value of 25 obtained for methanol and ethanol in Sgr B2 (N2) with the EMoCA survey (Müller et al. 2016) and agrees with expected values for the Galactic centre region.

4.4.2. Ethanol C_2H_5OH

The bulk of C_2H_5OH in the model is produced in the cold phase on dust grains and is effectively destroyed after desorption into the gas phase mainly via proton addition by protonated molecules such as H_3O^+, H_3^+, or HCO^+, which is followed by electron recombination (cf. Fig. 20 of G22). Similar to methanol, some fraction of the protonated molecule does not recombine with an electron, instead, it transfers the proton to NH_3 and goes back to unprotonated ethanol. The observed slight increase of ethanol abundances relative to methanol beyond the abundance peak (cf. Sect. 3.7.2) suggests that ethanol is less effectively destroyed than methanol after desorption to the gas phase, which is not accounted for by the current model.

Observed and modelled values of peak abundance differ by a factor 2.5 at most, except for W_{CO} (factor 10). The observed abundance ratios with respect to methanol shown in Fig. 13 are overproduced by the model by factors 3–5 in all cases. The chemical network of G22 may indeed lack several grain-surface reactions that affect the rate of ethanol production; in particular, reactions between atomic H and the set of C_2H_X species generally result in H addition while H abstraction by atomic H to produce H_2 and a less hydrogen-rich hydrocarbon is not included. Jin et al. (in prep.) have made such adjustments to the network, which could result in a moderate reduction in ethanol

production efficiency on grain surfaces at low temperatures, for example via $C_2H_5 + OH \rightarrow C_2H_5OH$.

4.4.3. Dimethyl ether CH_3OCH_3

In the model the bulk of CH_3OCH_3 is produced on dust grains in the cold collapse phase as well as on the surface during the warm-up phase and co-desorbs with water at $T > 120$ K. In the gas phase, at temperatures $\gtrsim$120 K, CH_3OCH_3 is additionally produced via proton transfer from $CH_3OCH_4^+$ to NH_3. This is an efficient formation pathway because the protonated dimethyl ether is the product of the reaction between two abundant reactants: methanol and protonated methanol. Eventually, this leads to the abundance peak of CH_3OCH_3 at slightly higher temperatures of 200 K and a flat profile as temperature increases (cf. Fig. 12 of G22). With this the modelled profile differs considerably from the observations (cf. Sect. 3.7.3).

Observed and modelled peak abundances differ by factors smaller than 2 for W_{CO} and up to ~8 for W_D, with S_D and S_{CO} in between (cf. Table 3). A similar behaviour of peak abundances between observations and model is seen for methanol, therefore, the observed ratio of both COMs is remarkably comparable to the modelled one in all cases, with differences less than a factor 2 (cf. Fig. 13). In summary, while the model succeeds in reproducing the observed peak abundance of dimethyl ether with respect to methanol, it seems that the destruction of this molecule in the gas phase is more efficient in Sgr B2 (N1) than in the model beyond the position of peak abundance at higher temperatures. Whether that indicates a destruction channel missing in the chemical network of the model or whether this is a result of any geometrical or physical conditions not caught by the model remains uncertain. It is likely that the regions closer to the centre of Sgr B2 (N1) have, in addition to higher temperatures, also higher densities, in which case the destruction may be accelerated. Such an effect is not considered by the model as the density is fixed during the warm-up. However, this would reduce the discrepancy between the observations and the model only if the destruction of dimethyl ether would be more accelerated than that of methanol.

4.4.4. Methyl formate CH_3OCHO

Similar to the aforementioned O-bearing COMs, methyl formate is predominantly produced on dust grains in the cold phase as well as during the warm-up in the model and desorbs into the gas phase as soon as uncovered from water at $\lesssim$166 K (cf. Fig. 20 of G22). Moreover, CH_3OCHO is efficiently produced in the gas phase at temperatures of water desorption via oxygenation of CH_3OCH_2, which was primarily sourced from CH_3OCH_3. This leads to an abundance peak at a higher temperature than for the other COMs. At $T > 200$ K, Fig. 20 of G22 suggests some destruction of the molecule, which is only minor and does not lead to a drop in the gas-phase abundance profile. Similar to CH_3OCH_3, the observed values of peak abundance agree well with the model for W_{CO} and are higher for S_{CO}, S_D, and W_D by factors 2–4 up to an order of magnitude (cf. Table 3). However, when normalised to methanol the observations and the model agree again more or less within the error bars (cf. Fig. 13). The observed decrease in abundance towards higher temperatures (cf. Sect. 3.7.4), which is similar to the other O-bearing COMs, is not reproduced by the model and may demand a more efficient destruction rate of the molecule. Similar to CH_3OCH_3, higher densities closer to Sgr B2 (N1), not taken into account by the model, may accelerate the destruction process.

4.4.5. Acetaldehyde CH_3CHO

According to the model (cf. Fig. 20 of G22), only a minor fraction of CH_3CHO is produced on dust grains in the cold phase and during the warm-up phase, and co-desorbs into the gas phase with water. A significant amount is formed in the gas phase at temperatures of $\gtrsim$150 K via the oxygenation of C_2H_5. This leads to a continuously increasing gas-phase abundance profile in the model, which agrees with the observed results for CH_3CHO (cf. Sect. 3.7.5). Peak abundances to the south agree well with the model predictions, while those to the west are overestimated by the model by factors 5 and 10 (cf. Table 3). When normalised to CH_3OH, the model overestimates the abundance ratio by factors 5–10 for all directions (cf. Fig. 13). In the model the acetaldehyde peak abundance and, in turn, the ratio to methanol are sensitive to the warm-up timescale, where the ratio is higher by a factor 6.4 for the slow than for the fast warm-up (cf. Tables 16 and 18 in G22). Therefore, the overestimation of the observed ratio by the model may be an indication that the warm-up in Sgr B2 (N1) proceeds faster than predicted for the slow warm-up model to which we are comparing here. However, for all other COMs, except for C_2H_5OH, the difference between model and observations is slightly larger when assuming the fast warm-up.

4.4.6. Vinyl cyanide C_2H_3CN

As can be seen in Fig. 21 of G22, there are two main formation phases of C_2H_3CN in the model. Some formation happens on the dust grains before the warm-up phase, however, the bulk of the molecule is produced in the gas phase at temperatures higher than 160 K, predominantly through the reaction of C_2H_4 and CN. This leads to a continuous increase of abundances in the model and could explain the increase seen in the observations (cf. Sect. 3.7.6). However, the values of observed peak abundance are underestimated by the model by a factor 2 for S_{CO} up to more than an order of magnitude for W_D with S_{CO} and W_{CO} in between (cf. Table 3). This discrepancy is also seen in the abundance ratios with respect to methanol, that is, it is underestimated by factors 6–10 in the model for all but S_{CO}, for which the ratio is overestimated by a factor 4 (cf. Fig. 13). G22 mention that the model tends to underestimate abundances of N-bearing COMs including C_2H_3CN, which they attribute to a possible overproduction of HC_3N in the model. They propose that this could be counteracted if HC_3N was hydrogenated on grain surfaces at early stages to form C_2H_3CN and C_2H_5CN, eventually.

4.4.7. Ethyl cyanide C_2H_5CN

Ethyl cyanide is exclusively produced on dust grains in the model, partially during the warm-up phase, but mainly in the cold phase (cf. Fig. 21 of G22). As soon as the molecule arrives in the gas phase after co-desorption with water, it is efficiently destroyed via proton transfer from H_3O^+ leading to a drop in abundance at high temperatures. However, some of the protonated ethyl cyanide goes back to the unprotonated form by transferring the extra proton to NH_3. This behaviour at high temperatures differs significantly from the observations (cf. Sect. 3.7.7).

The observed steeper increase of abundance around 100 K may point to thermal desorption, however, peak abundances are only reached at much higher temperatures suggesting an increase of abundance in the gas phase. Although there currently is no efficient gas-phase formation route for C_2H_5CN included in the model, G22 discussed that the reaction of CH_3^+ and CH_3CN again

leading to $C_2H_5CNH^+$ (see also McEwan et al. 1989) could be efficient in increasing the ethyl cyanide abundance at $T > 100$ K, when the protonated species transfers the extra proton to NH_3.

The observed values of peak abundance are larger than in the model by factors of a few for all cases, except for W_D, for which abundances differ by more than an order of magnitude (cf. Table 3). To the south, the ratio with respect to methanol does, however, agree well with what is expected from the model, while an underestimation by a factor of a few is still evident to the west (cf. Fig. 13). Including the above-mentioned additional gas-phase reaction in the model would probably be able to at least partially counteract the heavy decrease in gas-phase abundance seen in the model and may even somewhat increase the peak abundance to better match the observations. Additionally, there may be another formation channel on dust-grains via multiple hydrogenation of HC_3N as described for C_2H_3CN.

Vinyl and ethyl cyanide are often mentioned together as they share a chemical link. However, there is no such strong link in the new model of G22 compared to former studies (Garrod et al. 2017). Previously, a large fraction of the C_2H_3CN gas-phase abundance was produced from $C_2H_5CNH^+$, which, in turn, was sourced from ethyl cyanide, leading to decreasing abundances of C_2H_5CN with increasing temperature in the gas phase. In the new model, the gas-phase reaction mentioned in Sect. 4.4.6 dominates the formation of C_2H_3CN and weakens the gas-phase relationship of the two COMs (G22).

4.4.8. Methyl isocyanate CH_3NCO

According to the model, CH_3NCO is exclusively produced on dust grains mainly during the warm-up phase through the reaction $CH_3 + OCN \rightarrow CH_3NCO$ (Belloche et al. 2017). Subsequently, a fraction is already destroyed in the grain mantle, where it is hydrogenated to eventually form CH_3NHCHO, a molecule that was recently identified in the interstellar medium (Belloche et al. 2017, 2019). The other fraction desorbs to the gas phase, where it reacts with H_3O^+ resulting in further decrease in abundance (cf. Fig. D.3). Therefore, we would expect similar behaviour of the abundance profile as, for example for C_2H_5OH, for which abundances peak right after the molecule desorbs and decrease significantly towards higher temperatures. If that were the case, it would disagree with the observed abundance profile of CH_3NCO (cf. Sect. 3.7.8).

Moreover, the model underestimates the observed peak abundances by 2–3 orders of magnitude (cf. Fig. 13), which is also the case for the abundance ratios with respect to methanol. G22 argue that this may partly be explained by uncertainties in the activation barriers of reactions occurring on the grain surface. However, the observed trend of the abundance profile may additionally suggest that CH_3NCO is also produced in the gas phase. Halfen et al. (2015) proposed that the reaction of HNCO with CH_3 would be able to efficiently produce CH_3NCO in the gas phase, which is supported by later studies targeting low-mass protostars (Martín-Doménech et al. 2017; Quénard et al. 2018). However, as Halfen et al. (2015) noted, the $CH_3 + HNCO$ reaction that they proposed could be endothermic, and this seems to be confirmed by the calculations of Majumdar et al. (2018). The latter authors proposed alternative formation mechanisms for the grain-surface production of CH_3NCO. These included a barrierless reaction between atomic N and the CH_3CO radical, and the reaction of H with HCN that is trapped in a van der Waals complex with surface CO. In the latter case, in spite of a barrier to hydrogenation of HCN, the resultant product, H_2CN, would have sufficient energy to overcome the barrier to its own reaction with CO to produce CH_2NCO. This radical would then be hydrogenated to methyl isocyanate. The protostellar chemistry model presented by Majumdar et al. (2018) indicates that their proposed mechanisms can achieve gas-phase abundances of the order of 10^{-7} with respect to H_2, following desorption of the ice mantles; these abundances are in line with some of our observed values. It is unclear how the non-diffusive chemistry included in the G22 model might influence the efficiency of mechanisms proposed by Majumdar et al. (2018). Another alternative mechanism for grain-surface production of CH_3NCO, proposed by Vávra et al. (2022), would be a reaction between HNCO and the diradical methylene (CH_2), which is formed during the course of CH_4 production on dust-grain surfaces, and may also be a photoproduct of methane in the bulk ice. Whatever the mechanism, the lack of an efficient gas-phase process to form CH_3NCO would indicate that surface/ice chemistry is at work.

4.4.9. Formamide NH_2CHO

According to the model, NH_2CHO is dominantly produced on dust grains in the cold phase and during the warm-up phase (cf. Fig. 21 of G22). These production mechanisms continue as NH_2CHO starts to co-desorb with water at $T \gtrsim 120$ K and moreover, its abundance is enhanced by hydrogenation of NH_2CO when this radical is uncovered as water desorbs. Also, gas-phase reactions start to produce some NH_2CHO at these temperatures. However, gas-phase production through the reaction of NH_2 and H_2CO (Barone et al. 2015) is responsible only for around 9% of total production in the G22 model. Despite the many formation channels of this COM, the model predicts that it is efficiently destroyed via protonation followed by recombination, which is in disagreement with the observed abundance profile (cf. Sect. 3.7.9).

Also for this N(+O)-bearing COM, the observed peak abundance is higher than the modelled one by factors of a few to the west and by more than an order of magnitude to the south (cf. Table 3). Ratios of abundances with respect to methanol are underestimated by the model by factors 3–7. So far, it is uncertain what causes the difference between model and observations. Based on the observed abundance profiles and in comparison with other COMs, we may expect both thermal desorption at ~100 K, which, however, seems to happen at significantly shorter projected distances than for other COMs, and formation in the gas phase at higher temperatures as also predicted by the model. Because there is no indication for a significant drop in the observed abundances with increasing temperature there may exist an additional supply of NH_2CHO or the molecule may be less efficiently destroyed than in the model or both.

4.5. Resolved desorption of COMs in Sgr B2 (N1)

From Sect. 4.3 we concluded that the temperature profiles derived from the COMs reveal the gradient that is expected from heating of an envelope with optically thick dust by a protostar. This is true for all COMs be they predicted to mainly form in the gas phase such as CH_3CHO or in the solid phase (and then desorb) such as CH_3OH. However, the high angular resolution of the ReMoCA survey allowed us to resolve the abundance profiles of the COMs and to reveal their differences. This allows us to draw conclusions on the prevalent desorption process.

4.5.1. Thermal co-desorption with water

In the case of thermal desorption, we expect a sudden rise in column density and abundance of a COM at the location of desorption, which can either happen at the co-desorption temperature of water and COMs or at a specific desorption temperature that depends on the COM's binding energy to the grain surface or to itself. Perhaps the greatest change implemented to the current model used in G22 compared to the earlier studies (Garrod 2013) is that diffusion in the bulk ice as well as from the bulk ice to the surface layers regardless of the temperature is prohibited for all species except H and H_2. This entails that COMs formed in the bulk ice cannot diffuse to the surface from where they could thermally desorb depending on their binding energy. In the new non-diffusive model of G22 the COMs are trapped in the water ice and the bulk of the COMs can only desorb when water does, which happens at 120–170 K in the model. Based on Fig. 12, COMs that present such an abundance profile with a steep increase at a given temperature in Sgr B2 (N1) and, thereby, are in agreement with the model are CH_3OH, C_2H_5OH, NH_2CHO, and C_2H_5CN, and tentatively, CH_3OCH_3 and CH_3OCHO. However, instead of a temperature $\gtrsim$120 K as predicted by the model, abundances of these species already increase at temperatures ∼100 K. Provided that this behaviour can be associated with their thermal co-desorption with water, then this process seems to start at these low temperatures of about 100 K and to already terminate at ∼100–150 K, corresponding to the peak-abundance temperature of the above-mentioned species (see Fig. 12). Because the binding energy of water is uncertain as it depends on the precise ice structure, the value in the model could well be lower, leading to a lower desorption temperature of water that would be in better agreement with the observations. Jin et al. (in prep.), who use the model of G22, have in fact recently revised the value downwards and achieved a better agreement between their model and observations of Orion KL.

Though all O-bearing COMs except CH_3CHO present an abundance increase at ∼100 K, the column densities of dimethyl ether and methyl formate do not increase as steeply as those of methanol and ethanol (cf. Fig. 7). In the model, gas-phase formation of the two starts as soon as water starts desorbing, which may explain the observed behaviour. Besides, CH_3OCH_3 and CH_3OCHO have lower binding energies than CH_3OH and C_2H_5OH amongst other COMs and water (cf. Table 4), which led to thermal desorption at lower temperatures in earlier models (e.g. Garrod 2013). However, if thermal desorption took place depending on binding energies, we would still expect a steep increase of column density and abundance only at lower temperatures for CH_3OCH_3 and CH_3OCHO, which is not evident in the column density and abundance profiles. However, the observed profiles could also be the result of a two-step thermal desorption process which we elaborate on further in Sects. 4.5.3 and 4.5.4.

The abundance profile of ethyl cyanide increases more steeply around 100 K than at higher temperatures, however, not as steeply as for methanol. This may indicate that only some fraction is released from dust grains at around 100 K, which would be in agreement with desorption either along with water or depending on the binding energy, given its similar values of binding energy as methanol and ethanol (cf. Table 4). Formamide abundances increase steeply, however, only at shorter distances to Sgr B2 (N1) than methanol, that is potentially, at higher temperatures.

A steep increase is not observed for CH_3CHO and C_2H_3CN, which is consistent with the expectation of the model, according to which they are mainly formed in the gas phase. Although a fraction is produced on dust grains and released during water desorption in the model of G22, the amount may not be significant enough to be detected in the observed abundance profiles. The same would apply if desorption depended on the binding energy. Temperatures derived from CH_3NCO have higher uncertainties, nonetheless, the abundance profiles of this COM are similar to those of CH_3CHO suggesting a predominant gas-phase formation. Moreover, although the binding energy of CH_3NCO could be as high as 6500 K, thermal desorption at higher temperatures seems unlikely given the only mild increase of abundance with increasing temperatures.

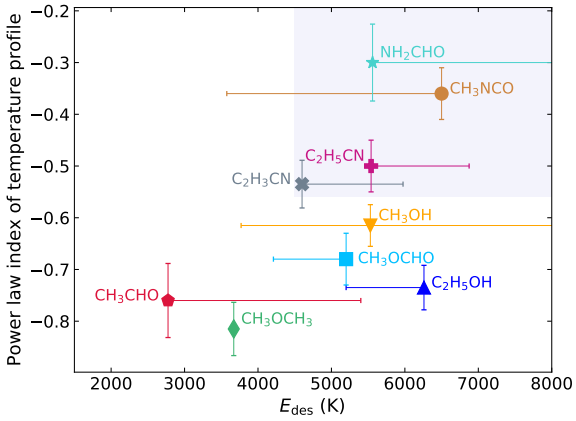

Fig. 14. Binding (or desorption) energies versus the power-law indices of the COM temperature profiles shown in Fig. 6 averaged over the south and west directions. The binding energies are taken from the third column of Table 4, with uncertainties indicating the range of values listed in that table. The lilac rectangle highlights the location of the N-bearing COMs.

In summary, the behaviour of the observed column density and abundance profiles for COMs that are expected to (partially) form on dust grain surfaces and to desorb subsequently suggests that co-desorption with water is likely to take place. Together with the overall good agreement of the model by G22 with our observations, precisely, because the co-desorption with water was implemented amongst other revisions, this process of thermal co-desorption seems to be the prevalent one in Sgr B2 (N1). Mottram et al. (2020) arrived at a similar conclusion for the hot core W3 IRS 4 based on observations with the Northern Extended Millimeter Array (NOEMA). The authors derived CH_3OH and CH_3CN abundances relative to H_2 as a function of temperature that reveal an increase at 80–100 K. However, the low-temperature regime of their profiles consists of measurements done towards two continuum peaks and an outflow position in the vicinity of the hot core rather than a continuous sampling along a certain direction starting from the hot core. Therefore, the evidence for the desorption process of these COMs is less obvious in this source.

Our interpretation of co-desorption of COMs with water also leads us to exclude that the observed segregation of COMs is based on their binding energies as it was proposed for the classification into hot and cold species as introduced in Sect. 4.2. We observe a small difference between O- and N-bearing COMs in the power law indices of the temperature profiles, where the latter have shallower slopes than the former and, therefore, do not trace as high temperatures on average. Naively, for this situation, we would infer that, when observed along the same line of sight,

N-bearing (or N+O-bearing) COMs show lower temperatures because they are destroyed in the hotter regions that are traced by the O-bearing COMs. This is rather the opposite of what is predicted by the chemical models of G22. However, we cannot exclude this kind of behaviour given that the model does not take into account density changes and neither the model nor the observations consider the three-dimensional (3D) structure of the hot core. There also exists a rough dependence of the power-law indices on the binding energy of the COMs as shown in Fig. 14, where N-bearing (or N+O-bearing) COMs have higher binding energies on average and, thus, can stick to the grain surface until higher temperatures are reached. Why this would lead to N-bearing (or N+O-bearing) COMs tracing lower temperatures is unclear to us.

4.5.2. Transition from non-thermal to thermal desorption

Assuming that the increase in abundance at ∼100 K represents the thermal co-desorption of COMs and water into the gas phase, non-zero abundance values at lower temperature, such as the value of 10^{-8} at 80 K for CH_3OH or at ∼55 K for $^{13}CH_3OH$ in Fig. 12f, the value $\sim10^{-9}$ at 55 K for C_2H_5CN in panel (i) of the same figure, and low-temperature values around 10^{-9} for NH_2CHO in panel j, would be the consequence of another desorption process. One possibility would be non-thermal desorption, which would be able to enhance COM abundances at temperatures lower than ∼100 K. The cold-phase chemistry as described in detail by Jin & Garrod (2020) is included in the model of G22, and this includes both chemical desorption and UV-driven desorption of surface molecules. The latter mechanism tends to show only limited ability to desorb molecules at visual extinction values greater than around unity, under the assumption of the standard interstellar radiation field and CR ionisation rate. Chemical desorption (such as desorption induced by the release of chemical energy upon formation of a molecule; see Garrod et al. 2007), on the other hand, is able to drive substantial COM desorption at low temperatures. However, strong desorption occurs during the periods of strongest ice production; at later times in the models, prior to thermal desorption, abundances of COMs relative to H in the gas phase remain below a value of 10^{-11}, which is at least two orders of magnitude lower than the observed values that we suspect may indicate non-thermal desorption of COMs.

However, with its location in the Galactic centre, Sgr B2 (N) resides in a violent environment with enhanced turbulence and enhanced CR fluxes that influence the star-formation process. The enhanced CR flux in Sgr B2 (N) (Bonfand et al. 2019) can work in both directions. CRs and the secondary UV field that they provoke can support formation and non-thermal desorption of some COMs, while they destroy others when upon collision with the dust grains. Non-thermal desorption due to a shock passing and turbulence is most probably the reason for the complex chemistry observed in G+0.693−0.027, a source not far from Sgr B2 (N) without any signposts of active star formation (e.g. Zeng et al. 2018, 2020) although a recent study of this object proposes that it may be on the verge of star formation (Colzi et al. 2022). Shocks are proposed to be induced through a cloud-cloud collision. Multiple studies suggest that these interactions between clouds not only happen in this source but in Sgr B2 in general (Hasegawa et al. 1994; Sato et al. 2000; Armijos-Abendaño et al. 2020; Zeng et al. 2020) and that these may even have triggered the star formation process. Therefore, besides enhanced CR flux, enhanced turbulence could increase the abundance of COMs via non-thermal desorption in the colder gas phase of Sgr B2 (N1). Specifically for this hot core, shocks may also arise from accretion because along the directions analysed here, filaments have been located through which accretion towards Sgr B2 (N1) may happen (Schwörer et al. 2019). However, because we do not see any evidence for accretion shocks in the morphology (as e.g. Csengeri et al. 2019, did in G328.2551–0.5321), we excluded this possibility. Moreover, although we avoided the outflow axes for the analysis in this work, an influence of the outflow of Sgr B2 (N1) can probably not be excluded a priori, especially at shortest distances to the hot core's centre. In this case, however, we would expect a simultaneous increase of temperature in the shocked gas. Because the temperature profiles do not show any evidence for this, we expect the influence of the outflow to also be minor if existent at all along the directions analysed in this work.

4.5.3. Thermal desorption in two steps

Thermal desorption may also take place in two steps. Figure 8 in G22 shows that, although water is still abundant, CO is the main constituent of the outermost ice layers at the end of the cold collapse phase. Therefore, these outermost ice layers can possibly desorb at much lower temperatures (20–30 K) given the low binding energy of CO. If some COMs are also abundant in these layers, their binding energies will be reduced compared to the value that they have for binding to pure water ice. As a result, these COMs may be able to desorb according to their reduced binding energy at temperatures of <100 K. If, after desorption of these CO-rich ice layers, the remaining ice were still mostly CO-related COMs, then the ice would be less polar and binding would presumably be weaker, still allowing for desorption at lower temperatures. Based on Fig. 9 of G22, COMs that seem to be present in these outer ice layers are CH_3OH, C_2H_5OH, CH_3OCH_3, CH_3OCHO, CH_3CHO, but also C_2H_5CN, which is not CO-related. Hence, thermal desorption due to reduced binding energies may not only apply to O-bearing COMs. This process may be able to explain the non-zero abundances at low temperatures for CH_3OH and C_2H_5CN as well as the shallower increase for CH_3OCHO and CH_3OCH_3. The slightly different behaviour shown by methyl formate and dimethyl ether may be due to their somewhat lower binding energies (compared with the other molecules mentioned above), even on water ice. Strong trapping of COMs by H_2O in this picture would then manifest once the upper layers, which are rich in CO, had desorbed along with some COMs. Some COMs would still be present in the more water-rich ice below, to be released at higher temperatures when water desorbs.

4.5.4. Gas-phase production

Gas-phase formation may also present an option to enhance COM abundances at low temperatures. Gas-phase reactions for CH_3OCH_3 and CH_3OCHO may be able to explain their overall shallower increase in abundance at around 100 K. However, it is questionable whether gas-phase formation, for example for NH_2CHO, can explain the non-zero abundance values at low temperatures because, although included in the model, the abundances prior to thermal desorption remain lower than the observed values at low temperatures. This may indicate that gas-phase formation is simply not efficient enough to reproduce the observed abundances or that the reactants are not sufficiently abundant, which is also plausible given the low temperatures, or both. Moreover, for methanol, there is currently no efficient gas-phase formation route that would explain the COM's

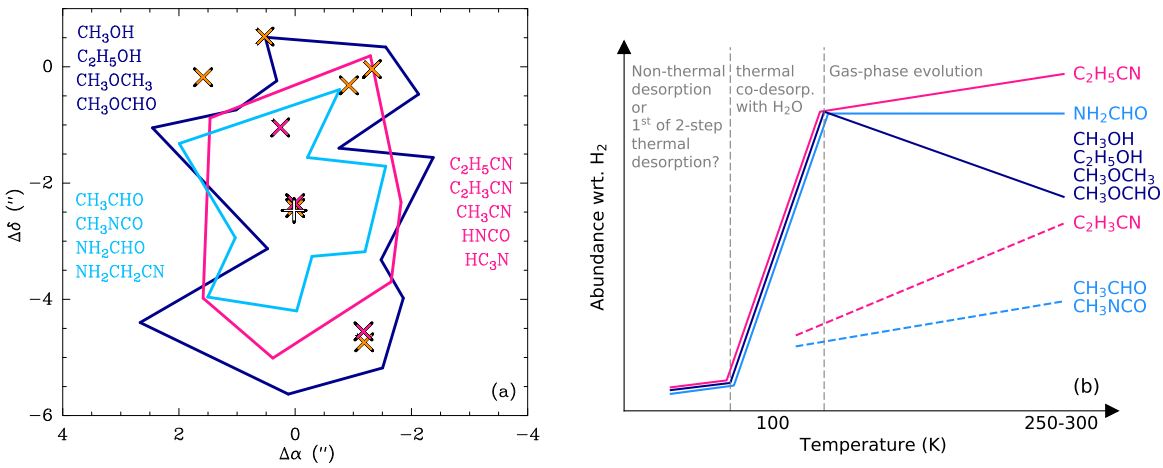

Fig. 15. Panel *a*: Overview sketch of the three different types of morphology observed in the integrated intensity maps of molecular emission built with the LVINE method as shown in Fig. 4. The molecules, COMs and simpler ones, that show the respective morphology are listed in the colour of the contour. The markers are the same as in Fig. 1. Panel *b*: Overview sketch of the different types of abundance profile as a function of temperature (taken from Fig. 12) and their interpretation in terms of desorption process and gas-phase evolution (see Sect. 4.4). The colours are the same as in *a* and indicate the observed emission morphology for the respective COM. Solid and dashed lines of one colour indicate a similar morphology but different types of abundance profile.

non-zero abundances at low temperatures. Eventually, we would exclude gas-phase reactions as the main reason for the non-zero abundances at low temperatures.

4.6. Implications for COM segregation

Taking into account all observational uncertainties and considering the simplicity of the model of G22 in terms of dynamics and geometry, it is striking how well the model can explain the majority of observed results. Moreover, for some of the differences, there may already exist potential explanations that remain to be proven, however. There are plausible reactions that, when added to the chemical network, may already be able to explain differences seen for COMs such as CH_3NCO and C_2H_5CN. Furthermore, although our results are best reproduced under the assumption of a slow warm-up, this may not be the case for Sgr B2 (N1) in reality as perhaps indicated by results from CH_3CHO. According to G22, similar results are possibly obtained for a faster warm-up with enhanced CR flux because the main difference between all three warm-up phases is the exposure time to CRs and their induced secondary UV field, and because CRs present one way of destruction of some COMs on the grain surface as well as in the gas phase. Bonfand et al. (2019) found that a cosmic ray ionisation rate of 50 times that of the standard value best described the COM abundances in the hot cores Sgr B2 (N2–N5) derived on the basis of the lower-angular-resolution survey EMoCA. However, although similar results may be expected for a slow warm-up and a faster warm-up with enhanced CR flux, we can only know for sure if the model is run with these conditions. As already mentioned above, geometry and changes of the density in the warm-up phase are not treated by the current model. On the other hand, our observational results do only consider projected distances and not the underlying 3D structure (e.g. filaments and the outflow).

In Fig. 15a we summarise the three different morphologies of COM emission regions that we identified based on the LVINE maps shown in Fig. 4: (a) extended and structured (dark blue, O-bearing COMs), (b) more compact and uniform (pink, N-bearing COMs, HC_3N, and HNCO), and (c) compact and structured (light blue, CH_3CHO, CH_3NCO, NH_2CHO, NH_2CH_2CN). We also observed differences in the behaviours of the abundance profiles of the various COMs (see Sect. 3.7). Figure 15b shows an overview of the trends seen in the abundance profiles as a function of temperature (taken from Fig. 12). The comparison with model predictions of G22, done for each COM separately in Sect. 4.4, indicates that the observed differences between COM abundance profiles trace back to the COMs' desorption processes at temperatures around 100 K (thermal co-desorption with H_2O) and at lower temperatures (non-thermal or thermal desorption) and their individual formation and destruction pathways at higher temperatures.

Although the differences seen in the COM abundance profiles do not simply match those seen in the morphology of COM emission, the above reasoning may also be able to explain the morphology to some extent. The extended and structured morphology of the emission regions for the four O-bearing COMs that are mainly formed on dust-grains closely follows the dust continuum emission, suggesting a close relation of the dust and these COMs. Emission from the N-bearing (or N+O-bearing) COMs and CH_3CHO is more compactly distributed around the protostar, where higher temperatures, which are required for the gas-phase reactions to become efficient or to take place at all, are expected and observed. Further differences amongst the latter group may be attributed to a mix of solid- and gas-phase formation with different efficiencies. However, whether the N-bearing (or N+O-bearing) molecules that are not analysed in detail follow this classification cannot be concluded from their morphology alone. For example, CH_3CN and HNCO show a similar morphology as ethyl or vinyl cyanide (cf. Fig. 4) and, according to the chemical model, CH_3CN is indeed efficiently produced in the gas phase, while HNCO seems to rather be formed on dust grains and destroyed when arriving in the gas phase (see Fig. 21 of G22).

Based on our observational results, we do not identify an influence on the COM temperature and abundance profiles

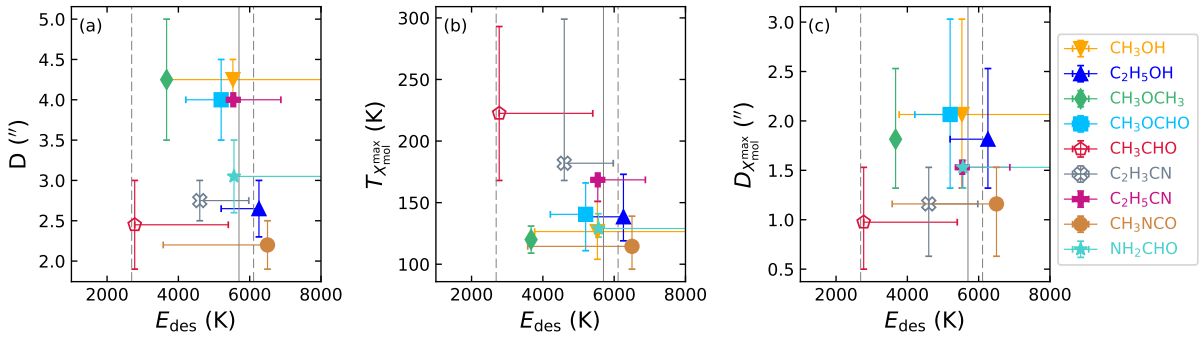

Fig. 16. Various observed properties of the COMs as a function of binding (or desorption) energy E_{des}. The binding energies are taken from the third column of Table 4, with uncertainties indicating the range of values listed in that table. *Panel a*: E_{des} versus the maximum distance to which the respective COM is still detected, where distances are taken from Fig. 7. They represent the mean value from both directions for each COM, respectively. The error bars show the spread in the values. *Panel b*: E_{des} versus the rotation temperature at which the COM abundance relative to H_2 peaks. The values are taken from Fig. 12. They represent the median value from both directions and both methods of H_2 column density derivation for each COM, respectively. The error bars show the spread in the values. *Panel c*: E_{des} versus distance at which the abundance of a COM peaks, where distances are taken from Figs. 10 and 11. In all panels the solid grey line indicates a binding energy of water of 5700 K while the dashed lines show the possible range of values based on other studies (see Table 4). Unfilled symbols indicate species that are mainly formed in the gas phase according to the model by Garrod et al. (2022).

Table 4. Binding energies of water and complex organic molecules investigated in this work from various studies.

Molecule	E_{bin} (K)				
	G13	B19/G22	W17	D18	F20
H_2O	5700	*	5600	2690	3600–6110
CH_3OH	5530	*	5000	4370	3770–8620
C_2H_5OH	6260	*	5200	–	–
CH_3OCH_3	3675	*	–	–	–
CH_3OCHO	4210	5200	–	–	–
CH_3CHO	2775	*	5400	3850	–
CH_3NCO	3575	6500	4700	–	–
C_2H_5CN	6875	5540	–	–	–
C_2H_3CN	5975	4600	–	–	–
NH_2CHO	5560	*	6300	–	5790–11 000

Notes. (*) Same value as in G13.
References. G13: Garrod (2013). B19: Belloche et al. (2019); only for CH_3NCO. G22: Garrod et al. (2022). W17: Wakelam et al. (2017). D18: Das et al. (2018). F20: Ferrero et al. (2020).

due to carbon-grain sublimation (see Sect. 4.2). Although the more compact emission region of N-bearing COMs could have suggested it, the only slightly larger abundance values at highest measured temperatures do not point to a significant enhancement of N-bearing COMs as expected from this process. However, the location of the soot line at ~300 K is only a rough estimate (van 't Hoff et al. 2020) and could well be at higher temperatures that is closer to the protostar such that we cannot observe it due to insufficient angular resolution and the high continuum optical depth.

4.7. The role of binding energies

Although, based on our observational results, thermal desorption of the bulk of a COM seems to happen alongside water and does not depend on binding energies as concluded from Sect. 4.5, the latter may still have an influence on the observed profiles. First, the desorption temperature of water and all other molecules depends on their binding energies. Table 4 lists values of binding energies that were either measured in laboratory experiments (Wakelam et al. 2017; Das et al. 2018; Ferrero et al. 2020) or assumed by chemical models (Garrod 2013; Garrod et al. 2022). For those species, for which multiple values are available, it is evident that these can vary greatly. The binding energy depends on a number of parameters, amongst these are the dust surface composition, that is the material the molecule is bound to, and the surface structure, that is depending on the binding site, a COM may stick more strongly to it. The latter can lead to a range of binding energies for a given COM and dust composition as shown by Ferrero et al. (2020). In Sect. 4.5.1 we already mentioned that a lower binding energy in the model is able to better explain not only our results, but also observations in Orion KL (Jin et al, in prep).

We investigated possible correlations of binding energy with various parameters in Fig. 16, where binding energies were taken from the third column in Table 4. In Fig. 16a we look at the correlation of binding energy with the maximum spatial extent of the COM emission, where we used the maximum projected distance to which COM column densities could be determined from Figs. 7 and D.2. We show the average of the values obtained to the west and south and error bars represent the range of possible values. Although we show all analysed COMs, a relation may not be expected for those that are mainly produced in the gas phase, which are CH_3CHO and C_2H_3CN (unfilled symbols), and possibly also C_2H_5CN, CH_3NCO, and NH_2CHO. The former two are, therefore, not considered in the following discussion. There is no obvious trend visible; however, C_2H_5OH and CH_3NCO, which show the smallest spatial extents, have a higher binding energy than water, which could mean that they remain on the grain surface though uncovered from water because even higher temperatures are required for their desorption. All COMs with a smaller binding energy than water co-desorb with it in the model as soon as they are uncovered, which may explain the small variance amongst them in Fig. 16a. However, we cannot exclude a contribution to the abundance by

non-thermal desorption processes (Sect. 4.5.2) or thermal desorption due to reduced binding energies (Sect. 4.5.3) at these large distances from Sgr B2 (N1), that is low temperatures, which could introduce a bias to this correlation.

Based on the assumption that C_2H_5OH and CH_3NCO have a higher binding energy than water and that they, therefore, stick longer to the grain surface, we may expect a correlation of the binding energy with the temperature of peak abundance, which is shown in Fig. 16b. Here, we used the median value obtained from S_D, W_D, S_{CO}, and W_{CO} extracted from Fig. 12. The error bars indicate the range that is spanned by the four values. No trend is visible, also because the spread in observed temperature values for each COM is large and all COMs could as well peak at the same temperature. Moreover, for most of these species, except for methanol and ethanol, we may expect further enhancement of abundances through gas-phase reactions, either based on the predictions of the model by G22 or based on the observed column density and abundance profiles or both. Additionally, we show the projected distance at which the COM abundances peak in Fig. 16c, where values were taken from Figs. 10 and 11. In this case no correlation is evident at all also because the spread in this parameter for most COMs is large.

Based on the discussion above and in Sect. 4.5, binding energies may not have a great impact on the thermal desorption that is associated with these COMs' peak abundances in the gas phase and they are not the driving source of segregation between COMs in Sgr B2 (N1). Nonetheless, they may have a minor influence on the power-law indices of the temperature profiles, the temperature of peak abundance, and on the maximum spatial extent of COMs at least for those that are mainly formed on dust grains and despite further enhancement of their abundance in the gas phase and (non-)thermal desorption processes. However, as seen in Fig. 16, not only temperatures and distances show a large spread for each COM, also the values of binding energy do, which makes the discussion let alone final conclusion on the role of binding energies difficult.

5. Conclusion

Thanks to the high-angular resolution of the ReMoCA spectral line survey we were able to resolve the hot core region of the main hub Sgr B2 (N1) located in the star-forming protocluster Sgr B2 (N). Our goal was to shed light on the desorption process that releases COMs from dust-grain surfaces, where most of them are believed to form, into the gas phase. For each of a selected number of COMs, we derived rotation temperature, column density, and abundance profiles going south and west from the continuum peak position of Sgr B2 (N1). The two directions were chosen after an inspection of the morphology of the continuum and COM emission and to avoid the outflow driven by Sgr B2 (N1). Abundances were derived with respect to methanol as well as H_2, where column densities of the latter were derived from the dust continuum emission as well as from $C^{18}O$ 1–0 emission. Finally, the observational results were compared to state-of-art astrochemical models performed by Garrod et al. (2022). The main results of this article are the following:

1. Based on the morphology of their emissions, the COMs can be classified into two groups. The O-bearing COMs CH_3OH, C_2H_5OH, CH_3OCH_3, and CH_3OCHO show structured emission that closely follows that of the dust continuum emission. In contrast, N-bearing organic molecules such as C_2H_5CN, C_2H_3CN, CH_3CN, and HC_3N have less structured and more compact morphologies. COMs such as CH_3CHO, NH_2CHO, and CH_3NCO reveal morphologies that are somewhere in between.
2. The temperature profiles derived from all COMs have power-law indices that vary from −0.4 to −0.8, which is in agreement with other observations as well as models and which is consistent with a temperature gradient due to protostellar heating of an envelope with optically thick dust.
3. The southbound H_2 column density profiles derived from dust and $C^{18}O$ emission show similar behaviours with values that agree within the error bars, while the westbound profile from $C^{18}O$ yields higher values by factors of a few than the one from dust, which is surprising and still demands an explanation.
4. The COM column density and abundance profiles support the segregation of COMs seen in the emission morphology. The comparison with astrochemical models indicates that the gas-phase abundance for the majority of O-bearing COMs is dominantly set by their solid-phase abundance as they are mainly formed on dust-grain surfaces during the cold collapse phase. CH_3CHO and C_2H_3CN rather trace the warmer gas-phase chemistry as this is where they are mainly formed. NH_2CHO seems to be produced in both phases and while, up to now, CH_3NCO and C_2H_5CN are exclusively formed on dust grains in the model, observational results suggest (partial) gas-phase formation for these COMs. There exist reactions, that are not yet included in the model but could be promising candidates for the efficient production of these COMs.
5. Most abundance profiles show a steep increase at ∼100 K, and then either a plateau, smooth increase, or drop at higher temperatures. The steep increase can probably be associated with the COMs' thermal desorption from dust grains and given that it occurs at roughly the same temperature for the respective COMs, we suggest that it represents thermal co-desorption of these COMs with water, rather than thermal desorption depending on binding energies. Co-desorption of COMs and water is in agreement with predictions by the models of Garrod et al. (2022), in which this outcome is a consequence of the deactivation of the ability of COMs to diffuse within the bulk ice mantles. No convincing correlation with binding energies has been found.
6. Non-zero abundance values for some COMs at temperatures below ∼100 K, that is before the steep increase associated with co-desorption with water, suggest another desorption process at work at these low temperatures. One explanation would be a partial thermal desorption of molecules from the outer, water-poor (and initially CO-rich) layers of the ice mantles, due to weaker binding caused by the lower water content in those layers. CO would desorb at low temperatures (20–30 K), leaving behind COMs that would be bound less strongly to each other than they would be in a water-rich ice, allowing them to desorb at temperatures <100 K. Most of the COMs in the ice would remain trapped in the water-rich layers beneath. Another explanation would be non-thermal desorption, which could include chemical desorption or photo-desorption. In either case, our observations have resolved and revealed for the first time the transition between two regimes of desorption of COMs in a hot core.

Given that our observational results only consider the projected distance from Sgr B2 (N1) and that the model does not take into account any geometrical changes, it is striking how well the two agree. The comparison to the model were focussed on the results for the slow warm-up phase as they best described the observations. However, we may expect similar results from a faster warm-up with enhanced cosmic-ray flux. The latter is confirmed to exist in Sgr B2 (N1) and may be able to still alter the modelled results if taken into account.

Acknowledgements. This paper makes use of the following ALMA data: ADS/JAO. ALMA#2016.1.00074.S. ALMA is a partnership of ESO (representing its member states), NSF (USA), and NINS (Japan), together with NRC (Canada), NSC and ASIAA (Taiwan), and KASI (Republic of Korea), in cooperation with the Republic of Chile. The Joint ALMA Observatory is operated by ESO, AUI/NRAO, and NAOJ. The interferometric data are available in the ALMA archive at `https://almascience.eso.org/aq/`. Part of this work has been carried out within the Collaborative Research Centre 956, sub-project B3, funded by the Deutsche Forschungsgemeinschaft (DFG) – project ID 184018867. RTG acknowledges funding through the Astronomy & Astrophysics program of the National Science Foundation (grant No. AST 19-06489). The authors would like to thank the developers of the many Python libraries, made available as open-source software, in particular this research has made use of NumPy (Harris et al. 2020), matplotlib (Hunter 2007), and SciPy (Virtanen et al. 2020).

References

Agúndez, M., Marcelino, N., Tercero, B., et al. 2021, A&A, 649, L4
ALMA Partnership (Asayama, S., et al.) 2016, ALMA Cycle 4 Technical Handbook
Anderson, T., Herbst, E., & De Lucia, F. C. 1987, ApJS, 64, 703
Anderson, T., De Lucia, F., & Herbst, E. 1990a, ApJS, 72, 797
Anderson, T., Herbst, E., & De Lucia, F. C. 1990b, ApJS, 74, 647
Armijos-Abendaño, J., Banda-Barragán, W. E., Martín-Pintado, J., et al. 2020, MNRAS, 499, 4918
Bacmann, A., Taquet, V., Faure, A., Kahane, C., & Ceccarelli, C. 2012, A&A, 541, L12
Barone, V., Latouche, C., Skouteris, D., et al. 2015, MNRAS, 453, L31
Baskakov, O. I., Dyubko, S. F., Ilyushin, V. V., et al. 1996, J. Mol. Spectr., 179, 94
Belloche, A., Müller, H. S. P., Menten, K. M., Schilke, P., & Comito, C. 2013, A&A, 559, A47
Belloche, A., Garrod, R. T., Müller, H. S. P., & Menten, K. M. 2014, Science, 345, 1584
Belloche, A., Müller, H. S. P., Garrod, R. T., & Menten, K. M. 2016, A&A, 587, A91
Belloche, A., Meshcheryakov, A. A., Garrod, R. T., et al. 2017, A&A, 601, A49
Belloche, A., Garrod, R. T., Müller, H. S. P., et al. 2019, A&A, 628, A10
Beltrán, M. T., Cesaroni, R., Rivilla, V. M., et al. 2018, A&A, 615, A141
Bisschop, S. E., Jørgensen, J. K., van Dishoeck, E. F., & de Wachter, E. B. M. 2007, A&A, 465, 913
Blake, G. A., Sutton, E. C., Masson, C. R., et al. 1984, ApJ, 286, 586
Bonfand, M., Belloche, A., Menten, K. M., Garrod, R. T., & Müller, H. S. P. 2017, A&A, 604, A60
Bonfand, M., Belloche, A., Garrod, R. T., et al. 2019, A&A, 628, A27
Boogert, A. C. A., Gerakines, P. A., & Whittet, D. C. B. 2015, ARA&A, 53, 541
Brauer, C. S., Pearson, J. C., Drouin, B. J., & Yu, S. 2009, ApJS, 184, 133
Calcutt, H., Jørgensen, J. K., Müller, H. S. P., et al. 2018, A&A, 616, A90
Cazzoli, G., & Kisiel, Z. 1988, J. Mol. Spectr., 130, 303
Cernicharo, J., Kisiel, Z., Tercero, B., et al. 2016, A&A, 587, L4
Codella, C., Fontani, F., Ceccarelli, C., et al. 2015, MNRAS, 449, L11
Codella, C., Ceccarelli, C., Caselli, P., et al. 2017, A&A, 605, L3
Collings, M. P., Anderson, M. A., Chen, R., et al. 2004, MNRAS, 354, 1133
Colzi, L., Martín-Pintado, J., Rivilla, V. M., et al. 2022, ApJ, 926, L22
Coudert, L. H., Çarçabal, P., Chevalier, M., et al. 2002, J. Mol. Spectr., 212, 203
Crockett, N. R., Bergin, E. A., Neill, J. L., et al. 2015, ApJ, 806, 239
Csengeri, T., Belloche, A., Bontemps, S., et al. 2019, A&A, 632, A57
Daly, A. M., Bermúdez, C., López, A., et al. 2013, ApJ, 768, 81
Das, A., Sil, M., Gorai, P., Chakrabarti, S. K., & Loison, J. C. 2018, ApJS, 237, 9
De Pree, C. G., Peters, T., Mac Low, M. M., et al. 2015, ApJ, 815, 123
Durig, J. R., Deeb, H., Darkhalil, I. D., et al. 2011, J. Mol. Struct., 985, 202
Endres, C. P., Drouin, B. J., Pearson, J. C., et al. 2009, A&A, 504, 635
Endres, C. P., Schlemmer, S., Schilke, P., Stutzki, J., & Müller, H. S. P. 2016, J. Mol. Spectr., 327, 95
Fedoseev, G., Cuppen, H. M., Ioppolo, S., Lamberts, T., & Linnartz, H. 2015, MNRAS, 448, 1288
Fernández, J. M., Tejeda, G., Carvajal, M., & Senent, M. L. 2019, ApJS, 241, 13
Ferrero, S., Zamirri, L., Ceccarelli, C., et al. 2020, ApJ, 904, 11
Fukuyama, Y., Odashima, H., Takagi, K., & Tsunekawa, S. 1996, ApJS, 104, 329
Fukuyama, Y., Omori, K., Odashima, H., Takagi, K., & Tsunekawa, S. 1999, J. Mol. Spectr., 193, 72
Garrod, R. T. 2008, A&A, 491, 239
Garrod, R. T. 2013, ApJ, 765, 60
Garrod, R. T., & Herbst, E. 2006, A&A, 457, 927
Garrod, R. T., Wakelam, V., & Herbst, E. 2007, A&A, 467, 1103
Garrod, R. T., Belloche, A., Müller, H. S. P., & Menten, K. M. 2017, A&A, 601, A48
Garrod, R. T., Jin, M., Matis, K. A., et al. 2022, ApJS, 259, 1
Gaume, R. A., Claussen, M. J., de Pree, C. G., Goss, W. M., & Mehringer, D. M. 1995, ApJ, 449, 663
Gerry, M. C. L., & Winnewisser, G. 1973, J. Mol. Spectr., 48, 1
Gieser, C., Beuther, H., Semenov, D., et al. 2021, A&A, 648, A66
Gieser, C., Beuther, H., Semenov, D., et al. 2022, A&A, 657, A3
Goldsmith, P. F., & Langer, W. D. 1999, ApJ, 517, 209
Halfen, D. T., Ilyushin, V. V., & Ziurys, L. M. 2015, ApJ, 812, L5
Haque, S. S., Lees, R. M., Saint Clair, J. M., Beers, Y., & Johnson, D. R. 1974, ApJ, 187, L15
Harris, C. R., Millman, K. J., van der Walt, S. J., et al. 2020, Nature, 585, 357
Hasegawa, T., Sato, F., Whiteoak, J. B., & Miyawaki, R. 1994, ApJ, 429, L77
Heise, H. M., Winther, F., & Lutz, H. 1981, J. Mol. Spectr., 90, 531
Henkel, C., Wilson, T. L., Langer, N., Chin, Y. N., & Mauersberger, R. 1994, Interstellar CNO Isotope Ratios, eds. T. L. Wilson, & K. J. Johnston (Berlin: Springer), 439, 72
Herbst, E., & van Dishoeck, E. F. 2009, ARA&A, 47, 427
Herbst, E., Messer, J. K., De Lucia, F. C., & Helminger, P. 1984, J. Mol. Spectr., 108, 42
Higuchi, A. E., Hasegawa, T., Saigo, K., Sanhueza, P., & Chibueze, J. O. 2015, ApJ, 815, 106
Hunter, J. D. 2007, Comput. Sci. Eng., 9, 90
Ilyushin, V., Kryvda, A., & Alekseev, E. 2009, J. Mol. Spectr., 255, 32
Jiménez-Serra, I., Vasyunin, A. I., Caselli, P., et al. 2016, ApJ, 830, L6
Jiménez-Serra, I., Vasyunin, A. I., Spezzano, S., et al. 2021, ApJ, 917, 44
Jin, M., & Garrod, R. T. 2020, ApJS, 249, 26
Jørgensen, J. K., Müller, H. S. P., Calcutt, H., et al. 2018, A&A, 620, A170
Jørgensen, J. K., Belloche, A., & Garrod, R. T. 2020, ARA&A, 58, 727
Karakawa, Y., Oka, K., Odashima, H., Takagi, K., & Tsunekawa, S. 2001, J. Mol. Spectr., 210, 196
Kenyon, S. J., Calvet, N., & Hartmann, L. 1993, ApJ, 414, 676
Khlifi, M., Nollet, M., Paillous, P., et al. 1999, J. Mol. Spectr., 194, 206
Kisiel, Z., Martin-Drumel, M.-A., & Pirali, O. 2015, J. Mol. Spectr., 315, 83
Kobayashi, K., Sakai, Y., Fujitake, M., et al. 2020, Can. J. Phys., 98, 551
Kryvda, A. V., Gerasimov, V. G., Dyubko, S. F., Alekseev, E. A., & Motiyenko, R. A. 2009, J. Mol. Spectr., 254, 28
Kuriyama, H., Takagi, K., Takeo, H., & Matsumura, C. 1986, ApJ, 311, 1073
Kutzer, P., Weismann, D., Waßmuth, B., et al. 2016, J. Mol. Spectr., 329, 28
Kwon, W., Looney, L. W., Mundy, L. G., Chiang, H.-F., & Kemball, A. J. 2009, ApJ, 696, 841
Lees, R. M., & Baker, J. G. 1968, J. Chem. Phys., 48, 5299
Li, J. I.-H., Liu, H. B., Hasegawa, Y., & Hirano, N. 2017, ApJ, 840, 72
Lovas, F. J., Lutz, H., & Dreizler, H. 1979, J. Phys. Chem. Ref. Data, 8, 1051
Majumdar, L., Loison, J. C., Ruaud, M., et al. 2018, MNRAS, 473, L59
Mangum, J. G., & Shirley, Y. L. 2015, PASP, 127, 266
Manigand, S., Jørgensen, J. K., Calcutt, H., et al. 2020, A&A, 635, A48
Maret, S., Hily-Blant, P., Pety, J., Bardeau, S., & Reynier, E. 2011, A&A, 526, A47
Martín-Doménech, R., Muñoz Caro, G. M., Bueno, J., & Goesmann, F. 2014, A&A, 564, A8
Martín-Doménech, R., Rivilla, V. M., Jiménez-Serra, I., et al. 2017, MNRAS, 469, 2230
McEwan, M. J., Denison, A. B., Huntress, W. T., et al. 1989, J. Phys. Chem. A, 93, 4064
McGuire, B. A. 2022, ApJS, 259, 2
McNaughton, D., Evans, C. J., Lane, S., & Nielsen, C. J. 1999, J. Mol. Spectr., 193, 104
Melosso, M., Belloche, A., Martin-Drumel, M. A., et al. 2020, A&A, 641, A160
Motiyenko, R. A., Tercero, B., Cernicharo, J., & Margulès, L. 2012, A&A, 548, A71
Motiyenko, R. A., Belloche, A., Garrod, R. T., et al. 2020, A&A, 642, A29
Mottram, J. C., Beuther, H., Ahmadi, A. et al. 2020, A&A, 636, A118
Müller, H. S. P., Menten, K. M., & Mäder, H. 2004, A&A, 428, 1019
Müller, H. S. P., Belloche, A., Menten, K. M., Comito, C., & Schilke, P. 2008, J. Mol. Spectr., 251, 319

Müller, H. S. P., Belloche, A., Xu, L.-H., et al. 2016, A&A, 587, A92
Neustock, W., Guarnieri, A., Demaison, J., & Wlodarczak, G. 1990, Z. Nat. A, 45, 702
Nomura, H., & Millar, T. J. 2004, A&A, 414, 409
Osorio, M., Anglada, G., Lizano, S., & D'Alessio, P. 2009, ApJ, 694, 29
Ossenkopf, V., & Henning, T. 1994, A&A, 291, 943
Paulive, A., Shingledecker, C. N., & Herbst, E. 2021, MNRAS, 500, 3414
Pearson, J. C., Sastry, K. V. L. N., Winnewisser, M., Herbst, E., & De Lucia, F. C. 1995, J. Phys. Chem. Ref. Data, 24, 1
Pearson, J. C., Sastry, K. V. L. N., Herbst, E., & De Lucia, F. C. 1996, J. Mol. Spectr., 175, 246
Pearson, J. C., Sastry, K. V. L. N., Herbst, E., & De Lucia, F. C. 1997, ApJ, 480, 420
Pearson, J. C., Brauer, C. S., & Drouin, B. J. 2008, J. Mol. Spectr., 251, 394
Pearson, J. C., Müller, H. S. P., Pickett, H. M., Cohen, E. A., & Drouin, B. J. 2010, J. Quant. Spectr. Rad. Transf., 111, 1614
Pickett, H. M., Cohen, E. A., Brinza, D. E., & Schaefer, M. M. 1981, J. Mol. Spectr., 89, 542
Quénard, D., Jiménez-Serra, I., Viti, S., Holdship, J., & Coutens, A. 2018, MNRAS, 474, 2796
Reid, M. J., Menten, K. M., Brunthaler, A., et al. 2019, ApJ, 885, 131
Requena-Torres, M. A., Martín-Pintado, J., Rodríguez-Franco, A., et al. 2006, A&A, 455, 971
Rodríguez-Fernández, N. J., Martín-Pintado, J., Fuente, A., et al. 2001, A&A, 365, 174
Rolffs, R., Schilke, P., Wyrowski, F., et al. 2011, A&A, 529, A76
Ruaud, M., Loison, J. C., Hickson, K. M., et al. 2015, MNRAS, 447, 4004
Sánchez-Monge, Á., Schilke, P., Schmiedeke, A., et al. 2017, A&A, 604, A6
Sastry, K. V. L. N., Lees, R. M., & De Lucia, F. C. 1984, J. Mol. Spectr., 103, 486
Sato, F., Hasegawa, T., Whiteoak, J. B., & Miyawaki, R. 2000, ApJ, 535, 857
Schwörer, A., Sánchez-Monge, Á., Schilke, P., et al. 2019, A&A, 628, A6
Scibelli, S., & Shirley, Y. 2020, ApJ, 891, 73
Shimanouchi, T. 1972, Nat. Stand. Ref. Data Ser., Nat. Bur. Stand. (U.S.), 39, 1
Shingledecker, C. N., Tennis, J., Le Gal, R., & Herbst, E. 2018, ApJ, 861, 20
Shu, F. H. 1977, ApJ, 214, 488
Smirnov, I. A., Alekseev, E. A., Ilyushin, V. V., et al. 2014, J. Mol. Spectr., 295, 44
Thiel, V., Belloche, A., Menten, K. M., Garrod, R. T., & Müller, H. S. P. 2017, A&A, 605, L6
Tudorie, M., Ilyushin, V., Vander Auwera, J., et al. 2012, J. Chem. Phys., 137, 064304
van der Walt, S. J., Kristensen, L. E., Jørgensen, J. K., et al. 2021, A&A, 655, A86
van 't Hoff, M. L. R., Bergin, E. A., Jørgensen, J. K., & Blake, G. A. 2020, ApJ, 897, L38
Vávra, K., Kolesniková, L., & Belloche, A. 2022, A&A, in press [arXiv:2207.03417]
Virtanen, P., Gommers, R., Oliphant, T. E., et al. 2020, Nat. Methods, 17, 261
Viti, S., Collings, M. P., Dever, J. W., McCoustra, M. R. S., & Williams, D. A. 2004, MNRAS, 354, 1141
Wakelam, V., Loison, J. C., Mereau, R., & Ruaud, M. 2017, Mol. Astrophys., 6, 22
Xu, L.-H., & Lovas, F. J. 1997, J. Phys. Chem. Ref. Data, 26, 17
Xu, L.-H., Fisher, J., Lees, R. M., et al. 2008, J. Mol. Spectr., 251, 305
Zeng, S., Jiménez-Serra, I., Rivilla, V. M., et al. 2018, MNRAS, 478, 2962
Zeng, S., Zhang, Q., Jiménez-Serra, I., et al. 2020, MNRAS, 497, 4896

Appendix A: Spectroscopic calculations

The CH_3OH data were taken from the CDMS (tag 032504). Version 3 is a recalculation of the original work by Xu et al. (2008). The entry includes transitions up to $v_t = 2$, and we used data from these three states. Transitions in the range of our survey were contributed by Lees & Baker (1968), Pickett et al. (1981), Sastry et al. (1984), Herbst et al. (1984), Anderson et al. (1990a), Müller et al. (2004), and Xu et al. (2008). This entry resolves intensity issues that prevailed in earlier entries of the CDMS and JPL catalogues. The partition function takes into account energies up to $v_t = 3$; it should be converged up to ~200 K and should be quite good at 300 K.

We used the $^{13}CH_3OH$ data from the CDMS (tag 033502). Version 2 is a recalculation of Xu & Lovas (1997) with contributions from Haque et al. (1974), Blake et al. (1984), Kuriyama et al. (1986), Anderson et al. (1987), and Anderson et al. (1990b). The intensities were calculated employing scaled partition function values from the main isotopic species. The errors introduced by the scaling are small compared to available alternatives.

The ethanol calculation is from the CDMS catalogue (tag 046524, version 1). It is based on the extensive work by Pearson et al. (2008) with additional data from Pearson et al. (1995, 1996, 1997). The main difference with respect to the JPL catalogue entry are in part very different intensities as shown by Müller et al. (2016). The calculated frequencies are at least nearly identical to those in the JPL catalogue, but no experimental frequencies were merged in the CDMS entry. Vibrational corrections are based on the fundamental frequencies in Durig et al. (2011). We accounted for contributions by overtone and combination states by applying the harmonic oscillator approximation. The errors by this approximation are usually small, especially because the exact energies of low-lying vibrations are frequently not known or, if so, mostly only for the fundamental vibrations.

We employed the CDMS entry for dimethyl ether (tag 046514, version 1). It is based on the analysis of Endres et al. (2009) with additional rest frequencies in the range of our survey from the compilation of Lovas et al. (1979) and from Neustock et al. (1990). We also considered data in the two lowest excited states, $v_{11} = 1$ and $v_{15} = 1$. These data were provided by C. P. Endres and involve unpublished data. The partition function in the CDMS takes into account vibrational contributions up to 500 cm^{-1}. This is sufficient at 100 K and reasonable around 150 K. In order to account for contributions of higher vibrations, we evaluated the ground state contributions first and corrected them subsequently in the harmonic approximation. Most of the fundamental vibrations were taken from Coudert et al. (2002). We took information on the torsional fundamentals from Fernández et al. (2019) and on the COC bending mode from Kutzer et al. (2016).

We use the JPL entry (tag 060003, version 2) for methyl formate, based on Ilyushin et al. (2009), with additional data from Karakawa et al. (2001). The partition function of methyl formate considers $v_t = 1$. Its contribution was first subtracted and, subsequently, vibrational corrections added in the harmonic approximation. The torsional band origin was determined in Tudorie et al. (2012), additional low-lying vibrations were mentioned in Kobayashi et al. (2020), higher lying vibrations were summarised by Shimanouchi (1972).

The acetaldehyde data were communicated by R. A. Motiyenko. They are based on Smirnov et al. (2014) with additional data extending beyond $v_t = 2$. Vibrational contributions were evaluated in the harmonic approximation employing the compilation of Shimanouchi (1972).

We used the CDMS entries (tags 057505 and 057506, version 1 in each case) to identify methyl isocyanate. The entries were generated from the compilation of assignments in Cernicharo et al. (2016). The rotational part of the partition function was determined employing the rigid rotor approximation; this was the best to do given the highly perturbed rotational spectrum. Vibrational corrections were applied in Cernicharo et al. (2016) for states up to 580 K. The errors are small up to ~150 K, but reach the 10% level at 200 K. The vibrational spectrum is unfortunately not known well enough to employ further corrections.

We identified ethyl cyanide employing the CDMS entry (tag 055502, version 2). It is based on Brauer et al. (2009) with frequencies in the range of our survey from Fukuyama et al. (1996). We also used excited state data $v_{20} = 1(A)$ (tag 055513, version 1) and $v_{12} = 1(A)$ (tag 055514, version 1), based on Daly et al. (2013), with previously published $v_{20} = 1$ data from Fukuyama et al. (1999). The vibrational correction factors are available through the CDMS documentation; they were evaluated using Heise et al. (1981).

The vinyl cyanide data are from the CDMS (tag 053515, version 1). They are based on Müller et al. (2008) with data in the range of our survey mainly from Gerry & Winnewisser (1973), Cazzoli & Kisiel (1988), and Baskakov et al. (1996). Data on the two lowest excited vibrational states, $v_{11} = 1$ and $v_{15} = 1$, are from unpublished data by one of us (HSPM) and takes also into account published data from Cazzoli & Kisiel (1988). We applied vibrational corrections using low-lying fundamentals of Kisiel et al. (2015) and higher lying fundamentals of Khlifi et al. (1999). The entry needs to be updated, see Kisiel et al. (2015) and references therein with data also on several excited vibrational states, but the current data are sufficient for the purpose of our study.

We used the CDMS entries for formamide in its ground vibrational state (tag 045512, version 2) and in $v_{12} = 1$ (tag 045516, version 1). They are based on Motiyenko et al. (2012) and contain data in the range of our survey mostly from Kryvda et al. (2009). We consulted McNaughton et al. (1999) for vibrational correction. We summed up first the contributions of the anharmonic NH_2 out of plane vibration and its overtones and applied further vibrational corrections in the harmonic approximation.

Appendix B: LVINE maps

Figures 3 and 4 show Line-width and Velocity-corrected INtegrated Emission (LVINE) maps. The LVINE method is an extension of the VINE method introduced by Calcutt et al. (2018). The authors determined the peak velocity of a bright methanol line at every position in their map in order to integrate intensities of other molecules or transitions of the same molecule over a fixed interval that then was varied around the derived peak velocity. We extended this method by also varying the interval in which intensities are integrated based on the line width at each position.

In order to create maps of peak velocity and line width we looked for a strong line that is neither contaminated nor optically thick. Because it is difficult to find a spectral line that combines all three criteria, we used two lines: an optically thin yet not too strong ethanol transition at 108.44 GHz (E_u = 88 K) for the region closer to Sgr B2 (N1) and a strong methanol transition at 95.91 GHz (E_u = 21 K), at far distances from Sgr B2 (N1). The

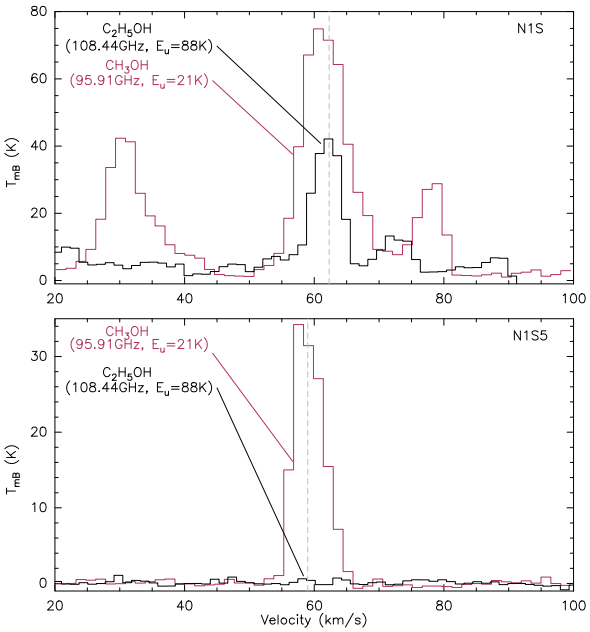

Fig. B.1. Spectra at positions N1S and N1S5 of the transitions of C_2H_5OH (black) and CH_3OH (maroon) that were used to create maps of peak velocity and line width, which are shown in Fig. B.2. The rest frequency and upper level energy of the transition are indicated with the respective molecule and in the respective colour in the upper left corner. The grey dashed line indicates the peak velocities (62.3 km s^{-1} at N1S and 59 km s^{-1} at N1S5).

methanol line is optically thick at positions close to Sgr B2 (N1) ($\tau \sim 3$ at N1S), however, at positions used here, its opacity is moderate ($\tau \sim 0.4$ at N1S5). The two transitions are shown in Fig. B.1 at a position close to Sgr B2 (N1) (N1S), where C_2H_5OH was used, and a position farther away (N1S5), where CH_3OH was used. At each position in the map, that is for each pixel, a 1D Gaussian profile was fitted, from which the peak velocity and line width for the respective map were extracted. If the fitted peak intensity of the ethanol transition at one position dropped below a threshold of 5σ, where σ is the median rms noise level listed in Table 2 in Belloche et al. (2019), then the methanol transition was used instead. The final maps of peak velocity and line width as well as a map that indicates where ethanol, methanol, or neither of the two (None) were used are shown in Fig. B.2 a–c, respectively. When neither the ethanol nor the methanol line had an intensity above the threshold, a fixed value of 64 km s^{-1} was allocated to the peak velocity and a value of 4 km s^{-1} to the line width for this pixel.

The Gaussian fitting happened unsupervised for most parts. However, in some regions an adjustment of input parameters or the refinement of the window, in which the fitting was done, or both was necessary, for example due to additional velocity components that lead to contamination and possibly bias the resulting velocity and line width when taken into account during the fitting process. The decision on the true velocity components was made by inspecting neighbouring positions. The decision on when to intervene was also made in the same way. Although we were able to avoid fatal failures of the fitting procedure in that way, some uncertainties remain hidden. However, with our velocity map we trace the major velocity gradients seen in Sgr B2 (N1), that is the lower velocities (< 62 km s^{-1}) seen to the south and the sudden rise in velocity to ∼70 km s^{-1} to the west. Other less pronounced velocity changes, which were associated with filaments (Schwörer et al. 2019), are evident as well. The line widths for the considered velocity components can be as narrow as 2–3 km s^{-1} and remain generally below a value of 10 km s^{-1}.

Appendix C: Continuum masking

Although for most parts the continuum emission is optically thin (cf. Fig. 2), we identified an increase in optical depth of the continuum at distances $\lesssim$0.5″to Sgr B2 (N1). When the continuum becomes optically thick it obscures the line emission from COMs. Because the Weeds model cannot treat this effect properly an analysis of COM emission in this region is impossible to do. Therefore, we excluded this closest region around Sgr B2 (N1) by creating masks. The definition of the mask size is challenging as the continuum emission depends on angular resolution, hence, on the observational setup and frequency.

To create the masks, we computed the channel-intensity distribution for the continuum-included spectra of each spectral window and determined the intensity at the peak of this distribution $T_{\rm peak}$ and the maximum intensity $T_{\rm max}$. We plot the difference $T_{\rm max} - T_{\rm peak}$ normalised by $T_{\rm max}$ in Fig. C.1. A position in the map was blanked when $T_{\rm peak} < 3\sigma$, where σ is the average noise level in the continuum emission map. In that way, we identified at which distance from Sgr B2 (N1) the emission lines get attenuated due to the increasing continuum optical thickness. As expected, the observational setups of higher angular resolution and higher frequencies are more affected. We decided to use the contour at a value of 0.43 (see red dashed contour in Fig. C.1) to define the mask for each setup. This decision was made based on these maps and also on the comparison to the spectra. It allowed us to keep position N1S in our analysis for all observational setups and N1S-1 for all setups except spectral windows 2 and 3 of setup 5. For these two spectral windows, the Weeds model systematically overestimates intensities at N1S-1 although the model seems to fit otherwise. At this close distance to Sgr B2 (N1) the increasing continuum optical thickness can be expected to attenuate the observed intensity of spectral lines untreated by Weeds. Other reasons may be presented by an overestimation of the source size or filtering of emission by the interferometre.

The approach applied here is not the most accurate because, for example, it does not take into account absorption lines or extremely strong lines from very abundant molecules such as ^{13}CO. However, it is sufficient for our purposes. Accordingly, spectral windows 2 and 3 of setup 5 were excluded from the analysis of position N1S-1 and integrated intensities within the mask are blanked in all respective maps. Figure C.1 further suggests to mask emission originating from the HII regions K3 and K1 for some spectral windows. However, inspecting spectra at the continuum peak positions of the two shows that the continuum is still sufficiently optically thin and the spectral lines are simply weak. Therefore, we do not apply any mask to the HII regions.

Appendix D: Additional figures

Because the noise level within each LVINE map shown in Fig. 4 is not uniform due to the pixel-dependent integration limits, that is, the number of channels over which the integration was performed is different in each pixel, we show signal-to-noise maps

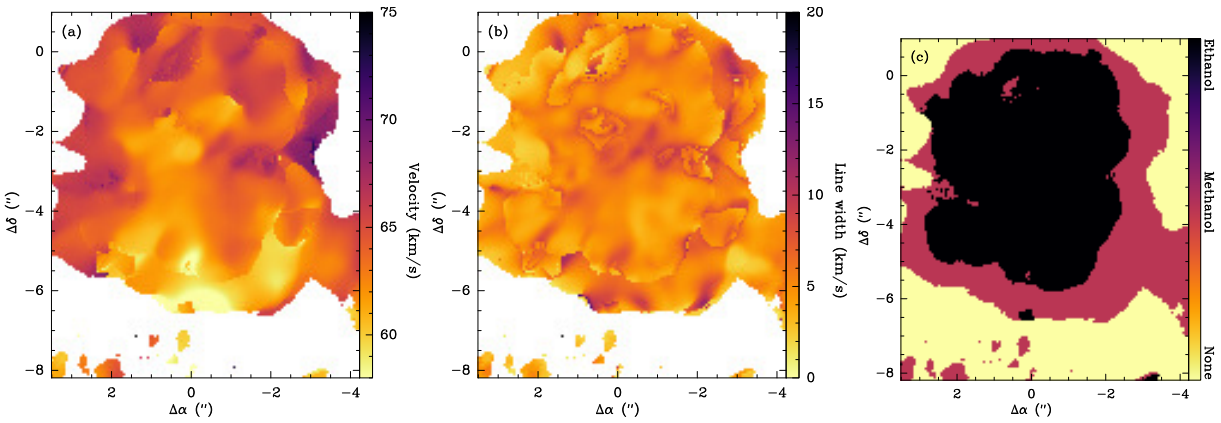

Fig. B.2. Peak velocity **(a)** and line-width map **(b)** of Sgr B2 (N1) created using the 108.44 GHz (E_u = 88 K) transition of C_2H_5OH (black region in c) and the 95.91 GHz (E_u = 21 K) transition of CH_3OH (maroon region in c). The map in panel **(c)** shows at which positions in (a) and (b) either C_2H_5OH (black) or CH_3OH (maroon) was used. The transition from ethanol to methanol happens when the fitted peak intensity of the ethanol line is less than 5σ, where σ is the median rms noise level listed in Table 2 in Belloche et al. (2019). At positions where neither C_2H_5OH nor CH_3OH are detected above this threshold (yellow region) the peak velocity and line width were fixed to values of 64 km s^{-1} and 4 km s^{-1}, respectively, to produce the LVINE maps shown in Fig. 4 and were blanked in a) and b).

in Fig. D.1 complementary to the LVINE maps. Figure D.2 highlights the maximum distances to the south and west to which emission of a certain COM is still detectable. Figure D.3 shows the same as in Fig. 13 in Garrod et al. (2022), but for CH_3NCO. It illustrates the net rate of change in abundance of the COM starting from the cold phase and assuming a subsequent slow warm-up.

Appendix E: Additional tables

Table E.1 lists the positions selected for analysis, which are also indicated in Fig. 3. Tables E.2–E.23 provide the parameters used for the LTE modelling with Weeds of each COM at each position, respectively. Moreover, the results obtained from the population diagrams are shown. Table E.24 lists the H_2 column densities derived from either dust continuum emission or $C^{18}O$ at each position, respectively, along with the dust continuum flux, continuum optical depth, and the model parameters of $C^{18}O$.

Appendix F: Additional figures: Spectra at N1S

Figures F.1–F.10 show observed and synthetic spectra of the analysed COMs at position N1S or, in case of CH_3OCH_3, N1S1. Only transitions that are used to create the respective population diagram are shown.

Appendix G: Population diagrams

Figures G.1–G.11 show population diagrams of CH_3OH, its ^{13}C isotopologue, C_2H_5OH, CH_3OCH_3, CH_3OCHO, CH_3CHO, CH_3NCO, C_2H_5CN, C_2H_3CN, and NH_2CHO for all positions to the south where they are detected. The vibrational states used for each COM are listed in Table G.1. Figures G.12–G.21 show the same for positions to the west.

Table E.1. Selected positions for analysis, also shown in Fig. 3 in terms of equatorial offsets from the continuum peak position of Sgr B2 (N1).

Position	$\Delta\alpha$ (″)	$\Delta\beta$ (″)
N1S-1	0.0	−3.1
N1S	0.0	−3.5
N1S1	0.0	−4.0
N1S2	0.0	−4.5
N1S3	0.0	−5.0
N1S4	0.0	−5.5
N1S5	0.0	−6.0
N1S6	0.0	−6.2
N1S7	0.0	−6.5
N1S8	0.0	−7.0
N1S9	0.0	−7.5
N1S10	0.0	−8.0
N1W-1	−0.5	−2.5
N1W	−1.0	−2.5
N1W1	−1.3	−2.5
N1W2	−1.6	−2.5
N1W3	−1.9	−2.5
N1W4	−2.3	−2.5
N1W5	−2.6	−2.5
N1W6	−3.0	−2.5
N1W7	−3.5	−2.5
N1W8	−4.0	−2.5

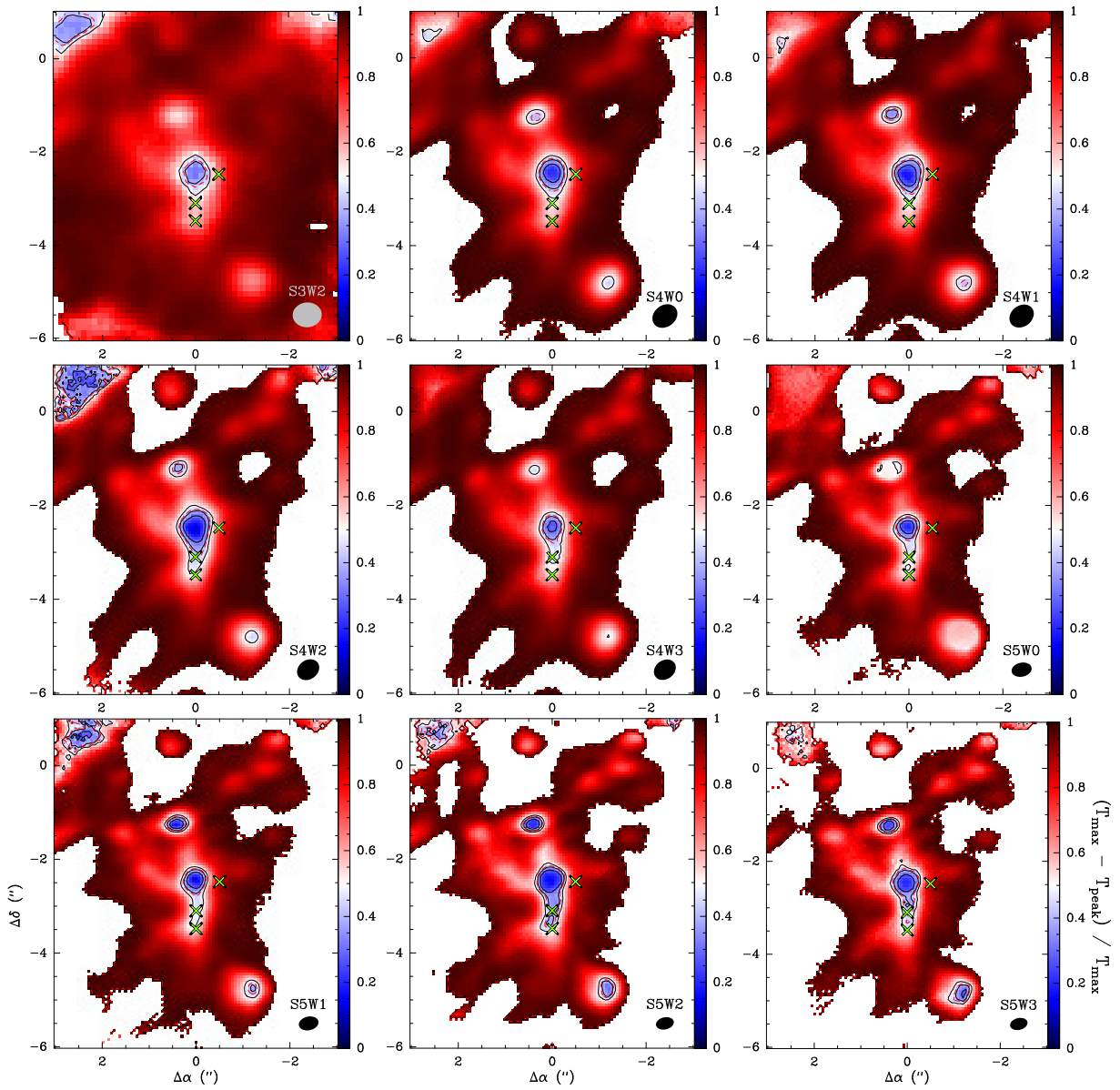

Fig. C.1. Visualisation of the determination of the continuum emission mask needed because of high continuum optical depth towards Sgr B2 (N1). From the channel-intensity distribution of the continuum-included spectra, the intensity at the peak $T_{\rm peak}$ and the maximum intensity $T_{\rm max}$ were determined. The maps in colour-scale and the contours show the difference $T_{\rm max} - T_{\rm peak}$ normalised by $T_{\rm max}$. This ratio was only computed when $T_{\rm peak} > 3\sigma$, where σ is the average noise level in the continuum emission map. The contour steps (black) are 0.3, 0.4, and 0.5. The red dashed contour at a value of 0.43 indicates the boundary of the adopted mask. Green crosses show positions N1S-1 and N1S to the south and N1W-1 to the west. The observational setup and spectral window are shown in the lower right corner together with the respective beam sizes. Only those spectral windows are shown from which molecular transitions are used to create integrated intensity maps (cf. Figs. 3 and 4).

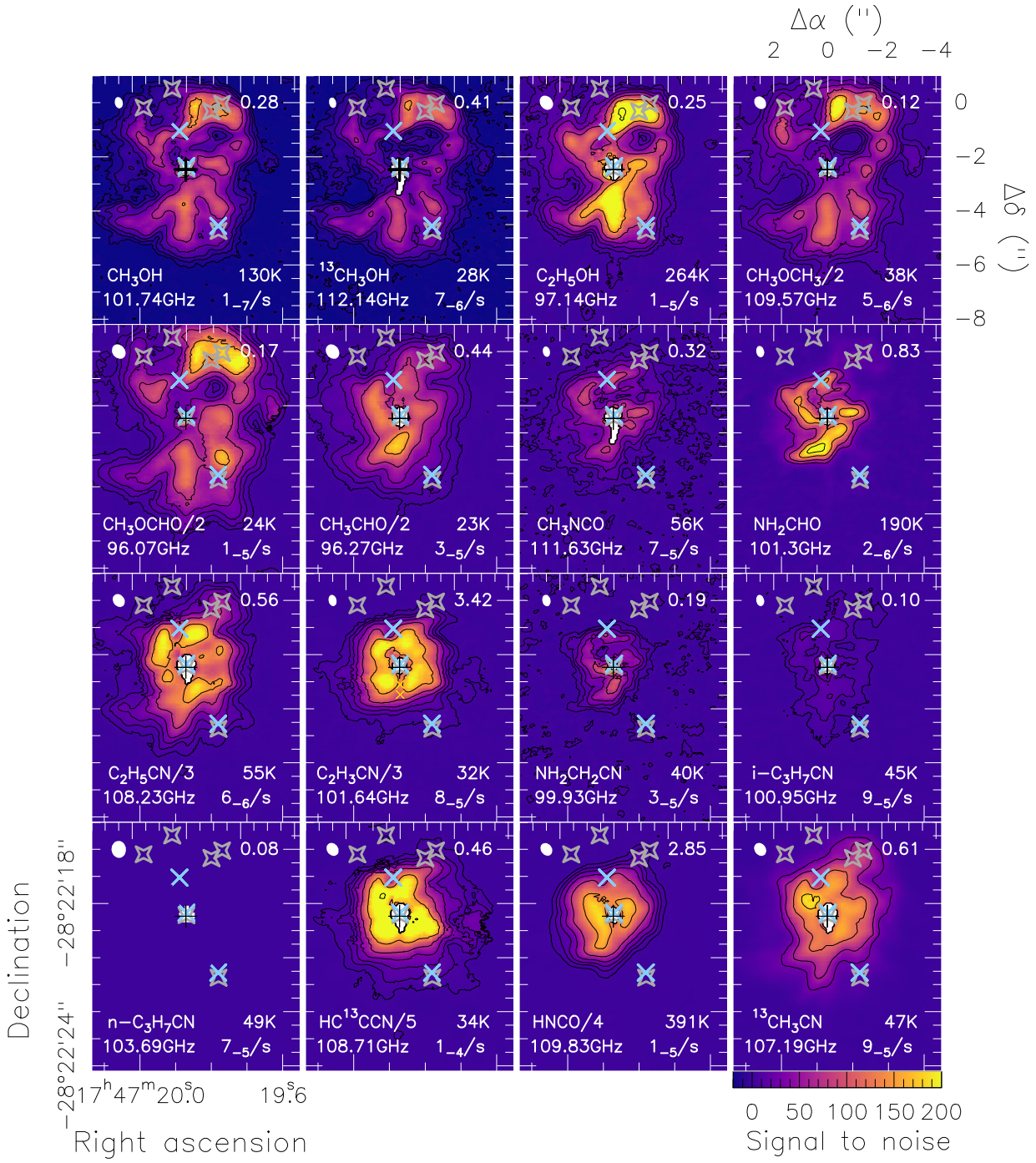

Fig. D.1. Same as Fig. 4, except that instead of integrated intensities the signal-to-noise ratio is shown. The noise is computed by $\sqrt{N} \times \Delta v \times \sigma$, where N is the number of channels over which integration was performed, Δv is the channel separation in km s^{-1}, and σ is the median rms noise level as shown in Table 2 in Belloche et al. (2019). Values of CH_3OCH_3, CH_3OCHO, and CH_3CHO are scaled down by a factor of 2, those of C_2H_5CN and C_2H_3CN by a factor 3, $HC^{13}CCN$ by a factor 5, HNCO by a factor 4. The contour steps are 3, 9, 18, 36, 72, 144, 288, and 576.

Table E.2. Weeds parameters used for COMs at N1S-1.

Molecule[a]	Size[b] ($''$)	$T_{\rm rot,W}$ [c] (K)	$T_{\rm rot,obs}$ [d] (K)	$N_{\rm W}$ [e] ($\rm cm^{-2}$)	$N_{\rm obs}$ [f] ($\rm cm^{-2}$)	$C_{\rm vib}$ [g]	Δv [h] ($\rm km\,s^{-1}$)	$v_{\rm off}$ [i] ($\rm km\,s^{-1}$)
CH_3OH, $v = 0$	2.0	250	262 ± 10	2.5(19)	(1.5 ± 0.2)(19)	1.00	6.0	0.0
$v = 1$	2.0	250	262 ± 10	2.5(19)	(1.5 ± 0.2)(19)	1.00	6.0	0.0
$v = 2$	2.0	250	262 ± 10	2.5(19)	(1.5 ± 0.2)(19)	1.00	6.0	0.0
$^{13}CH_3OH$, $v = 0$	2.0	250	262 ± 27	1.0(18)	(8.8 ± 2.1)(17)	1.00	6.0	0.5
C_2H_5OH, $v = 0$	2.0	300	301 ± 15	2.5(18)	(2.0 ± 0.2)(18)	2.88	6.3	0.3
CH_3OCH_3, $v = 0$	2.0	254	254 ± 17	2.3(18)	(1.4 ± 0.3)(18)	1.16	4.5	1.5
CH_3OCHO, $v = 0$	2.0	320	317 ± 35	3.1(18)	(2.2 ± 0.4)(18)	2.62	5.0	0.5
$v = 1$	2.0	320	317 ± 35	3.1(18)	(2.2 ± 0.4)(18)	2.62	5.0	0.5
CH_3CHO, $v = 0$	2.0	280	277 ± 8	1.6(18)	(5.5 ± 0.4)(17)	1.13	6.0	0.0
$v = 1$	2.0	280	277 ± 8	1.6(18)	(5.5 ± 0.4)(17)	1.13	6.0	0.0
CH_3NCO, $v = 0$	2.0	150	139 ± 7	3.1(17)	(1.2 ± 0.2)(17)	1.00	5.5	−0.2
C_2H_5CN, $v = 0$	2.0	230	231 ± 5	5.1(18)	(3.1 ± 0.2)(18)	2.21	6.8	−0.7
$v_{12} = 1$	2.0	230	231 ± 5	5.1(18)	(3.1 ± 0.2)(18)	2.21	6.8	−0.7
$v_{13} = 2$	2.0	230	231 ± 5	5.1(18)	(3.1 ± 0.2)(18)	2.21	6.8	−0.7
$v_{20} = 1$	2.0	230	231 ± 5	5.1(18)	(3.1 ± 0.2)(18)	2.21	6.8	−0.7
$v_{21} = 2$	2.0	230	231 ± 5	5.1(18)	(3.1 ± 0.2)(18)	2.21	6.8	−0.7
C_2H_3CN, $v = 0$	2.0	300	299 ± 15	3.0(18)	(2.6 ± 0.3)(18)	1.20	6.0	−0.5
$v_{11} = 1$	2.0	300	299 ± 15	3.0(18)	(2.6 ± 0.3)(18)	1.20	6.0	−0.5
$v_{15} = 1$	2.0	300	299 ± 15	3.0(18)	(2.6 ± 0.3)(18)	1.20	6.0	−0.5
NH_2CHO, $v = 0$	2.0	170	166 ± 5	4.1(18)	(3.2 ± 0.3)(18)	1.10	5.3	0.1
$v_{12} = 1$	2.0	170	166 ± 5	4.1(18)	(3.2 ± 0.3)(18)	1.10	5.3	0.1

Notes. [a]COMs and vibrational states used to derive population diagrams. [b]Size of the emitting region. [c]Rotation temperature used for the Weeds model. [d]Rotation temperature derived from the population diagram. [e]Column density used for the Weeds model. [f]Column density derived from the population diagram. [g]Vibrational state correction applied when the partition function does not account for higher-excited vibrational states, where $C_{\rm vib} = C_{\rm vib}(T_{\rm rot,obs})$. [h]$FWHM$ of the transitions. [i]Offset from the source systemic velocity, which was set to $62\,\rm km\,s^{-1}$. Values in parentheses show the decimal power, where $x(z) = x \times 10^z$ or $(x \pm y)(z) = (x \pm y) \times 10^z$.
Upper limits on N_W indicate that a population diagram could not be derived, either because too many transitions are contaminated or the molecule is not detected. The temperatures used for the Weeds model at these positions are determined by extrapolating the temperature profile of the respective molecule that was derived in Sect. 3.4.

Table E.3. Same as Table E.2, but for position N1S.

Molecule	Size ($''$)	$T_{\rm rot,W}$ (K)	$T_{\rm rot,obs}$ (K)	$N_{\rm W}$ ($\rm cm^{-2}$)	$N_{\rm obs}$ ($\rm cm^{-2}$)	$C_{\rm vib}$	Δv ($\rm km\,s^{-1}$)	$v_{\rm off}$ ($\rm km\,s^{-1}$)
CH_3OH, $v = 0$	2.0	220	228 ± 5	3.0(19)	(2.2 ± 0.2)(19)	1.00	5.0	0.5
$v = 1$	2.0	220	228 ± 5	3.0(19)	(2.2 ± 0.2)(19)	1.00	5.0	0.5
$v = 2$	2.0	220	228 ± 5	3.0(19)	(2.2 ± 0.2)(19)	1.00	5.0	0.5
$^{13}CH_3OH$, $v = 0$	2.0	215	206 ± 10	1.2(18)	(1.1 ± 0.1)(18)	1.00	4.5	0.5
C_2H_5OH, $v = 0$	2.0	215	220 ± 7	1.8(18)	(1.6 ± 0.1)(18)	1.85	5.4	0.3
CH_3OCH_3, $v = 0$	2.0	250	225 ± 9	1.3(18)	(8.8 ± 1.0)(17)	1.09	4.5	0.5
$v_{11} = 1$	2.0	250	225 ± 9	1.3(18)	(8.8 ± 1.0)(17)	1.09	4.5	0.5
CH_3OCHO, $v = 0$	2.0	280	294 ± 24	3.0(18)	(2.8 ± 0.4)(18)	2.32	4.0	0.5
$v = 1$	2.0	280	294 ± 24	3.0(18)	(2.8 ± 0.4)(18)	2.32	4.0	0.5
CH_3CHO, $v = 0$	2.0	200	214 ± 6	9.4(17)	(4.1 ± 0.3)(17)	1.05	5.0	0.0
$v = 1$	2.0	200	214 ± 6	9.4(17)	(4.1 ± 0.3)(17)	1.05	5.0	0.0
CH_3NCO, $v = 0$	2.0	150	154 ± 25	2.4(17)	(1.5 ± 0.6)(17)	1.00	5.0	−0.2
C_2H_5CN, $v = 0$	2.0	190	186 ± 4	3.7(18)	(3.0 ± 0.2)(18)	1.69	6.0	−0.1
$v_{13} = 2$	2.0	190	186 ± 4	3.7(18)	(3.0 ± 0.2)(18)	1.69	6.0	−0.1
$v_{20} = 1$	2.0	190	186 ± 4	3.7(18)	(3.0 ± 0.2)(18)	1.69	6.0	−0.1
$v_{21} = 2$	2.0	190	186 ± 4	3.7(18)	(3.0 ± 0.2)(18)	1.69	6.0	−0.1
C_2H_3CN, $v = 0$	2.0	220	217 ± 7	9.4(17)	(6.5 ± 0.6)(17)	1.05	6.0	−0.5
$v_{11} = 1$	2.0	220	217 ± 7	9.4(17)	(6.5 ± 0.6)(17)	1.05	6.0	−0.5
$v_{15} = 1$	2.0	220	217 ± 7	9.4(17)	(6.5 ± 0.6)(17)	1.05	6.0	−0.5
NH_2CHO, $v = 0$	2.0	160	157 ± 4	4.0(18)	(3.4 ± 0.2)(18)	1.08	5.7	0.1
$v_{12} = 1$	2.0	160	157 ± 4	4.0(18)	(3.4 ± 0.2)(18)	1.08	5.7	0.1

Table E.4. Same as Table E.2, but for position N1S1.

Molecule	Size ($''$)	$T_{\rm rot,W}$ (K)	$T_{\rm rot,obs}$ (K)	$N_{\rm W}$ ($\rm cm^{-2}$)	$N_{\rm obs}$ ($\rm cm^{-2}$)	$C_{\rm vib}$	Δv ($\rm km\,s^{-1}$)	$v_{\rm off}$ ($\rm km\,s^{-1}$)
CH_3OH, $v = 0$	2.0	173	168 ± 3	2.2(19)	(2.0 ± 0.2)(19)	1.00	4.2	0.0
$v = 1$	2.0	173	168 ± 3	2.2(19)	(2.0 ± 0.2)(19)	1.00	4.2	0.0
$v = 2$	2.0	173	168 ± 3	2.2(19)	(2.0 ± 0.2)(19)	1.00	4.2	0.0
$^{13}CH_3OH$, $v = 0$	2.0	170	169 ± 3	8.0(17)	(8.2 ± 0.5)(17)	1.00	4.2	0.3
C_2H_5OH, $v = 0$	2.0	170	173 ± 2	1.1(18)	(1.15 ± 0.05)(18)	1.46	4.5	0.0
CH_3OCH_3, $v = 0$	2.0	160	154 ± 2	1.0(18)	(1.0 ± 0.1)(18)	1.01	3.5	−0.2
$v_{11} = 1$	2.0	160	154 ± 2	1.0(18)	(1.0 ± 0.1)(18)	1.01	3.5	−0.2
$v_{15} = 1$	2.0	160	154 ± 2	1.0(18)	(1.0 ± 0.1)(18)	1.01	3.5	−0.2
CH_3OCHO, $v = 0$	2.0	200	206 ± 9	1.5(18)	(1.5 ± 0.1)(18)	1.50	4.5	−0.3
$v = 1$	2.0	200	206 ± 9	1.5(18)	(1.5 ± 0.1)(18)	1.50	4.5	−0.3
CH_3CHO, $v = 0$	2.0	150	168 ± 7	2.0(17)	(1.0 ± 0.1)(17)	1.02	4.5	0.0
$v = 1$	2.0	150	168 ± 7	2.0(17)	(1.0 ± 0.1)(17)	1.02	4.5	0.0
$v = 2$	2.0	150	168 ± 7	2.0(17)	(1.0 ± 0.1)(17)	1.02	4.5	0.0
CH_3NCO, $v = 0$	2.0	110	106 ± 7	4.0(16)	(4.0 ± 0.7)(16)	1.00	4.5	0.3
C_2H_5CN, $v = 0$	2.0	170	169 ± 1	1.5(18)	(1.53 ± 0.04)(18)	1.53	5.0	0.7
$v_{12} = 1$	2.0	170	169 ± 1	1.5(18)	(1.53 ± 0.04)(18)	1.53	5.0	0.7
$v_{13} = 2$	2.0	170	169 ± 1	1.5(18)	(1.53 ± 0.04)(18)	1.53	5.0	0.7
$v_{20} = 1$	2.0	170	169 ± 1	1.5(18)	(1.53 ± 0.04)(18)	1.53	5.0	0.7
$v_{21} = 2$	2.0	170	169 ± 1	1.5(18)	(1.53 ± 0.04)(18)	1.53	5.0	0.7
C_2H_3CN, $v = 0$	2.0	175	182 ± 6	5.1(16)	(5.5 ± 3.6)(16)	1.02	4.5	0.5
$v_{11} = 1$	2.0	175	182 ± 6	5.1(16)	(5.5 ± 3.6)(16)	1.02	4.5	0.5
NH_2CHO, $v = 0$	2.0	110	122 ± 3	1.6(18)	(1.2 ± 0.1)(18)	1.04	5.3	0.1
$v_{12} = 1$	2.0	110	122 ± 3	1.6(18)	(1.2 ± 0.1)(18)	1.04	5.3	0.1

Table E.5. Same as Table E.2, but for position N1S2.

Molecule	Size ($''$)	$T_{\rm rot,W}$ (K)	$T_{\rm rot,obs}$ (K)	$N_{\rm W}$ ($\rm cm^{-2}$)	$N_{\rm obs}$ ($\rm cm^{-2}$)	$C_{\rm vib}$	Δv ($\rm km\,s^{-1}$)	$v_{\rm off}$ ($\rm km\,s^{-1}$)
CH_3OH, $v = 0$	2.0	140	140 ± 1	1.5(19)	(1.6 ± 0.1)(19)	1.00	4.0	−0.5
$v = 1$	2.0	140	140 ± 1	1.5(19)	(1.6 ± 0.1)(19)	1.00	4.0	−0.5
$v = 2$	2.0	140	140 ± 1	1.5(19)	(1.6 ± 0.1)(19)	1.00	4.0	−0.5
$^{13}CH_3OH$, $v = 0$	2.0	140	137 ± 3	5.5(17)	(5.5 ± 0.4)(17)	1.00	4.5	0.0
C_2H_5OH, $v = 0$	2.0	130	130 ± 1	5.7(17)	(6.5 ± 0.2)(17)	1.21	4.5	−0.8
CH_3OCH_3, $v = 0$	2.0	130	131 ± 1	9.5(17)	(9.4 ± 0.4)(17)	1.01	4.0	−0.3
$v_{11} = 1$	2.0	130	131 ± 1	9.5(17)	(9.4 ± 0.4)(17)	1.01	4.0	−0.3
CH_3OCHO, $v = 0$	2.0	170	167 ± 5	8.9(17)	(9.4 ± 0.6)(17)	1.27	4.5	−0.8
$v = 1$	2.0	170	167 ± 5	8.9(17)	(9.4 ± 0.6)(17)	1.27	4.5	−0.8
CH_3CHO, $v = 0$	2.0	120	118 ± 4	5.0(16)	(2.5 ± 0.2)(16)	1.00	4.5	−0.4
$v = 1$	2.0	120	118 ± 4	5.0(16)	(2.5 ± 0.2)(16)	1.00	4.5	−0.4
CH_3NCO, $v = 0$	2.0	110	107 ± 12	1.5(16)	(1.4 ± 0.4)(16)	1.00	4.5	0.3
C_2H_5CN, $v = 0$	2.0	140	136 ± 1	5.2(17)	(5.2 ± 0.2)(17)	1.29	5.5	1.0
$v_{13} = 2$	2.0	140	136 ± 1	5.2(17)	(5.2 ± 0.2)(17)	1.29	5.5	1.0
$v_{20} = 1$	2.0	140	136 ± 1	5.2(17)	(5.2 ± 0.2)(17)	1.29	5.5	1.0
$v_{21} = 2$	2.0	140	136 ± 1	5.2(17)	(5.2 ± 0.2)(17)	1.29	5.5	1.0
C_2H_3CN, $v = 0$	2.0	140	129 ± 12	5.0(15)	(4.7 ± 0.9)(15)	1.00	4.0	0.4
NH_2CHO, $v = 0$	2.0	140	147 ± 10	5.3(16)	(4.4 ± 0.9)(16)	1.07	3.5	0.0
$v_{12} = 1$	2.0	140	147 ± 10	5.3(16)	(4.4 ± 0.9)(16)	1.07	3.5	0.0

Table E.6. Same as Table E.2, but for position N1S3.

Molecule	Size ($''$)	$T_{\rm rot,W}$ (K)	$T_{\rm rot,obs}$ (K)	$N_{\rm W}$ ($\rm cm^{-2}$)	$N_{\rm obs}$ ($\rm cm^{-2}$)	$C_{\rm vib}$	Δv ($\rm km\,s^{-1}$)	$v_{\rm off}$ ($\rm km\,s^{-1}$)
CH_3OH, $v = 0$	2.0	120	122 ± 1	1.5(19)	(1.4 ± 0.1)(19)	1.00	4.0	−1.6
$v = 1$	2.0	120	122 ± 1	1.5(19)	(1.4 ± 0.1)(19)	1.00	4.0	−1.6
$v = 2$	2.0	120	122 ± 1	1.5(19)	(1.4 ± 0.1)(19)	1.00	4.0	−1.6
$^{13}CH_3OH$, $v = 0$	2.0	120	121 ± 2	3.0(17)	(3.5 ± 0.2)(17)	1.00	4.5	−1.0
C_2H_5OH, $v = 0$	2.0	115	119 ± 2	2.9(17)	(3.0 ± 0.1)(17)	1.16	5.5	−1.8
CH_3OCH_3, $v = 0$	2.0	110	110 ± 1	5.5(17)	(5.9 ± 0.2)(17)	1.00	3.8	−1.4
$v_{11} = 1$	2.0	110	110 ± 1	5.5(17)	(5.9 ± 0.2)(17)	1.00	3.8	−1.4
CH_3OCHO, $v = 0$	2.0	140	137 ± 2	6.3(17)	(6.5 ± 0.3)(17)	1.14	4.5	−2.0
$v = 1$	2.0	140	137 ± 2	6.3(17)	(6.5 ± 0.3)(17)	1.14	4.5	−2.0
CH_3CHO, $v = 0$	2.0	115	108 ± 5	2.0(16)	(9.3 ± 1.0)(15)	1.00	4.0	−1.7
$v = 1$	2.0	115	108 ± 5	2.0(16)	(9.3 ± 1.0)(15)	1.00	4.0	−1.7
CH_3NCO, $v = 0$	2.0	90	90 ± 8	2.7(15)	(3.1 ± 0.8)(15)	1.00	3.5	0.0
C_2H_5CN, $v = 0$	2.0	115	119 ± 2	1.4(17)	(1.3 ± 0.1)(17)	1.20	5.5	−1.0
$v_{20} = 1$	2.0	115	119 ± 2	1.4(17)	(1.3 ± 0.1)(17)	1.20	5.5	−1.0
C_2H_3CN, $v = 0$	2.0	40	35 ± 2	6.0(14)	(6.1 ± 1.0)(14)	1.00	4.0	0.8
NH_2CHO, $v = 0$	2.0	112	112 ± 16	1.0(15)	(1.0 ± 0.05)(15)	1.03	3.5	−1.0

Table E.7. Same as Table E.2, but for position N1S4.

Molecule	Size ($''$)	$T_{\rm rot,W}$ (K)	$T_{\rm rot,obs}$ (K)	$N_{\rm W}$ ($\rm cm^{-2}$)	$N_{\rm obs}$ ($\rm cm^{-2}$)	$C_{\rm vib}$	Δv ($\rm km\,s^{-1}$)	$v_{\rm off}$ ($\rm km\,s^{-1}$)
CH_3OH, $v = 0$	2.0	100	104 ± 1	6.0(18)	(5.5 ± 0.4)(18)	1.00	4.0	−2.0
$v = 1$	2.0	100	104 ± 1	6.0(18)	(5.5 ± 0.4)(18)	1.00	4.0	−2.0
$v = 2$	2.0	100	104 ± 1	6.0(18)	(5.5 ± 0.4)(18)	1.00	4.0	−2.0
$^{13}CH_3OH$, $v = 0$	2.0	100	102 ± 2	1.2(17)	(1.4 ± 0.1)(17)	1.00	4.2	−1.5
C_2H_5OH, $v = 0$	2.0	100	103 ± 2	2.0(16)	(2.3 ± 0.2)(16)	1.10	4.0	−3.0
CH_3OCH_3, $v = 0$	2.0	100	98 ± 4	1.6(17)	(1.6 ± 0.2)(17)	1.00	3.5	−1.0
CH_3OCHO, $v = 0$	2.0	115	111 ± 2	2.8(17)	(3.0 ± 0.1)(17)	1.07	3.5	−1.8
$v = 1$	2.0	115	111 ± 2	2.8(17)	(3.0 ± 0.1)(17)	1.07	3.5	−1.8
CH_3CHO, $v = 0$	2.0	80	112 ± 56	1.5(15)	(1.51 ± 1.47)(15)	1.00	4.0	−2.5
CH_3NCO, $v = 0$	2.0	89	89 ± 6	≤ 8.0(14)		1.00	4.1	−2.0
C_2H_5CN, $v = 0$	2.0	100	100 ± 5	2.1(16)	(2.2 ± 0.2)(16)	1.11	5.0	−2.0
C_2H_3CN, $v = 0$	2.0	117	117 ± 12	≤ 3.0(14)		1.00	4.1	−2.0
NH_2CHO, $v = 0$	2.0	106	106 ± 17	8.2(14)	(8.2 ± 1.2)(14)	1.02	4.5	−1.5

Table E.8. Same as Table E.2, but for position N1S5.

Molecule	Size ($''$)	$T_{\rm rot,W}$ (K)	$T_{\rm rot,obs}$ (K)	$N_{\rm W}$ ($\rm cm^{-2}$)	$N_{\rm obs}$ ($\rm cm^{-2}$)	$C_{\rm vib}$	Δv ($\rm km\,s^{-1}$)	$v_{\rm off}$ ($\rm km\,s^{-1}$)
CH_3OH, $v = 0$	2.0	110	105 ± 4	4.5(17)	(3.7 ± 0.5)(17)	1.00	4.3	−3.0
$v = 1$	2.0	110	105 ± 4	4.5(17)	(3.7 ± 0.5)(17)	1.00	4.3	−3.0
$^{13}CH_3OH$, $v = 0$	2.0	90	94 ± 8	2.2(16)	(2.7 ± 0.5)(16)	1.00	4.0	−2.5
C_2H_5OH, $v = 0$	2.0	89	89 ± 9	≤ 6.4(15)		1.06	4.1	−2.6
CH_3OCH_3, $v = 0$	2.0	85	84 ± 5	3.0(16)	(2.5 ± 0.3)(16)	1.00	3.5	−2.5
CH_3OCHO, $v = 0$	2.0	100	95 ± 1	1.1(17)	(1.14 ± 0.04)(17)	1.03	3.5	−2.3
$v = 1$	2.0	100	95 ± 1	1.1(17)	(1.14 ± 0.04)(17)	1.03	3.5	−2.3
CH_3CHO, $v = 0$	2.0	86	86 ± 7	≤ 8.0(14)		1.00	3.9	−2.6
CH_3NCO, $v = 0$	2.0	85	85 ± 7	≤ 6.2(14)		1.00	3.9	−2.6
C_2H_5CN, $v = 0$	2.0	98	88 ± 12	2.1(15)	(2.0 ± 0.4)(15)	1.07	4.0	−2.6
C_2H_3CN, $v = 0$	2.0	107	107 ± 12	≤ 3.0(14)		1.00	3.9	−2.6
NH_2CHO, $v = 0$	2.0	102	102 ± 19	5.1(14)	(5.1 ± 0.4)(14)	1.02	4.0	−2.0

Table E.9. Same as Table E.2, but for position N1S6.

Molecule	Size ($''$)	$T_{\rm rot,W}$ (K)	$T_{\rm rot,obs}$ (K)	$N_{\rm W}$ (cm^{-2})	$N_{\rm obs}$ (cm^{-2})	$C_{\rm vib}$	Δv (km s^{-1})	$v_{\rm off}$ (km s^{-1})
CH_3OH, $v = 0$	2.0	100	104 ± 4	2.0(17)	(1.8 ± 0.2)(17)	1.00	3.0	−2.8
$v = 1$	2.0	100	104 ± 4	2.0(17)	(1.8 ± 0.2)(17)	1.00	3.0	−2.8
$^{13}CH_3OH$, $v = 0$	2.0	70	54 ± 6	8.0(15)	(5.8 ± 1.2)(15)	1.00	4.0	−2.5
C_2H_5OH, $v = 0$	2.0	85	85 ± 9	≤ 6.3(15)		1.05	3.9	−2.8
CH_3OCH_3, $v = 0$	2.0	85	86 ± 6	2.5(16)	(2.7 ± 0.4)(16)	1.00	3.5	−2.5
CH_3OCHO, $v = 0$	2.0	100	92 ± 2	9.3(16)	(1.0 ± 0.5)(17)	1.03	3.0	−2.5
$v = 1$	2.0	100	92 ± 2	9.3(16)	(1.0 ± 0.5)(17)	1.03	3.0	−2.5
CH_3CHO, $v = 0$	2.0	83	83 ± 7	≤ 7.0(14)		1.00	3.3	−2.8
CH_3NCO, $v = 0$	2.0	84	84 ± 7	≤ 5.0(14)		1.00	3.3	−2.8
C_2H_5CN, $v = 0$	2.0	90	83 ± 23	8.5(14)	(8.8 ± 3.8)(14)	1.06	3.0	−3.5
C_2H_3CN, $v = 0$	2.0	104	104 ± 13	≤ 2.7(14)		1.00	3.3	−2.8
NH_2CHO, $v = 0$	2.0	100	100 ± 19	≤ 2.5(14)		1.02	3.3	−2.8

Table E.10. Same as Table E.2, but for position N1S7.

Molecule	Size ($''$)	$T_{\rm rot,W}$ (K)	$T_{\rm rot,obs}$ (K)	$N_{\rm W}$ (cm^{-2})	$N_{\rm obs}$ (cm^{-2})	$C_{\rm vib}$	Δv (km s^{-1})	$v_{\rm off}$ (km s^{-1})
CH_3OH, $v = 0$	2.0	100	103 ± 8	8.0(16)	(6.4 ± 1.6)(16)	1.00	2.5	−3.2
$v = 1$	2.0	100	103 ± 8	8.0(16)	(6.4 ± 1.6)(16)	1.00	2.5	−3.2
$^{13}CH_3OH$, $v = 0$	2.0	87	87 ± 5	≤ 2.0(15)		1.00	2.3	−3.1
C_2H_5OH, $v = 0$	2.0	81	81 ± 9	≤ 4.2(15)		1.04	2.3	−3.1
CH_3OCH_3, $v = 0$	2.0	90	90 ± 8	2.3(16)	(2.7 ± 0.5)(16)	1.00	2.3	−2.5
CH_3OCHO, $v = 0$	2.0	100	102 ± 3	7.3(16)	(8.4 ± 0.7)(16)	1.05	2.5	−2.8
$v = 1$	2.0	100	102 ± 3	7.3(16)	(8.4 ± 0.7)(16)	1.05	2.5	−2.8
CH_3CHO, $v = 0$	2.0	79	79 ± 7	≤ 4.5(14)		1.00	2.3	−3.1
CH_3NCO, $v = 0$	2.0	82	82 ± 7	≤ 3.5(14)		1.00	2.3	−3.1
C_2H_5CN, $v = 0$	2.0	60	57 ± 12	2.8(14)	(2.6 ± 0.9)(14)	1.01	2.0	−4.0
C_2H_3CN, $v = 0$	2.0	99	99 ± 13	≤ 2.0(14)		1.00	2.3	−3.1
NH_2CHO, $v = 0$	2.0	98	98 ± 20	≤ 2.0(14)		1.01	2.3	−3.1

Table E.11. Same as Table E.2, but for position N1S8.

Molecule	Size ($''$)	$T_{\rm rot,W}$ (K)	$T_{\rm rot,obs}$ (K)	$N_{\rm W}$ (cm^{-2})	$N_{\rm obs}$ (cm^{-2})	$C_{\rm vib}$	Δv (km s^{-1})	$v_{\rm off}$ (km s^{-1})
CH_3OH, $v = 0$	2.0	81	81 ± 6	8.0(15)	(6.2 ± 1.1)(15)	1.00	2.5	−3.5
$^{13}CH_3OH$, $v = 0$	2.0	80	80 ± 5	≤ 2.0(15)		1.00	2.3	−3.3
C_2H_5OH, $v = 0$	2.0	74	74 ± 9	≤ 4.1(15)		1.03	2.3	−3.3
CH_3OCH_3, $v = 0$	2.0	90	98 ± 21	1.0(16)	(1.1 ± 0.5)(16)	1.00	2.0	−3.5
CH_3OCHO, $v = 0$	2.0	40	36 ± 8	3.0(15)	(2.8 ± 1.1)(15)	1.00	2.5	−3.0
CH_3CHO, $v = 0$	2.0	72	72 ± 7	≤ 3.7(14)		1.00	2.3	−3.3
CH_3NCO, $v = 0$	2.0	79	79 ± 7	≤ 3.3(14)		1.00	2.3	−3.3
C_2H_5CN, $v = 0$	2.0	92	92 ± 12	≤ 2.2(14)		1.08	2.3	−3.3
C_2H_3CN, $v = 0$	2.0	92	92 ± 13	≤ 1.5(14)		1.00	2.3	−3.3
NH_2CHO, $v = 0$	2.0	94	94 ± 20	≤ 2.0(14)		1.01	2.3	−3.3

Table E.12. Same as Table E.2, but for position N1S9.

Molecule	Size ($''$)	$T_{\rm rot,W}$ (K)	$T_{\rm rot,obs}$ (K)	$N_{\rm W}$ (cm^{-2})	$N_{\rm obs}$ (cm^{-2})	$C_{\rm vib}$	Δv (km s^{-1})	$v_{\rm off}$ (km s^{-1})
CH_3OH, $v = 0$	2.0	76	76 ± 6	≤ 3.3(15)		1.00	2.8	−3.5
$^{13}CH_3OH$, $v = 0$	2.0	75	75 ± 5	≤ 1.5(15)		1.00	2.0	−3.5
CH_3OCH_3, $v = 0$	2.0	69	69 ± 6	3.5(15)	(3.6 ± 0.6)(15)	1.00	2.0	−3.5
CH_3OCHO, $v = 0$	2.0	75	75 ± 11	≤ 2.0(15)		1.01	2.0	−3.5
C_2H_5CN, $v = 0$	2.0	88	88 ± 12	≤ 1.6(14)		1.07	2.0	−3.5

Table E.13. Same as Table E.2, but for position N1S10.

Molecule	Size ($''$)	$T_{\rm rot,W}$ (K)	$T_{\rm rot,obs}$ (K)	$N_{\rm W}$ (cm^{-2})	$N_{\rm obs}$ (cm^{-2})	$C_{\rm vib}$	Δv (km s^{-1})	$v_{\rm off}$ (km s^{-1})
CH_3OH, $v = 0$	2.0	71	71 ± 6	≤ 2.5(15)		1.00	2.3	−3.5
$^{13}CH_3OH$, $v = 0$	2.0	70	70 ± 5	≤ 1.5(15)		1.00	2.0	−3.5
CH_3OCH_3, $v = 0$	2.0	65	65 ± 6	≤ 3.0(15)		1.00	2.0	−3.5
CH_3OCHO, $v = 0$	2.0	70	70 ± 11	≤ 1.5(15)		1.01	2.0	−3.5
C_2H_5CN, $v = 0$	2.0	83	83 ± 12	≤ 1.1(14)		1.06	2.0	−3.5

Table E.14. Same as Table E.2, but for position N1W-1.

Molecule	Size ($''$)	$T_{\rm rot,W}$ (K)	$T_{\rm rot,obs}$ (K)	$N_{\rm W}$ (cm^{-2})	$N_{\rm obs}$ (cm^{-2})	$C_{\rm vib}$	Δv (km s^{-1})	$v_{\rm off}$ (km s^{-1})
CH_3OH, $v = 0$	2.0	240	231 ± 6	2.3(19)	(1.9 ± 0.2)(19)	1.00	6.0	3.2
$v = 1$	2.0	240	231 ± 6	2.3(19)	(1.9 ± 0.2)(19)	1.00	6.0	3.2
$v = 2$	2.0	240	231 ± 6	2.3(19)	(1.9 ± 0.2)(19)	1.00	6.0	3.2
$^{13}CH_3OH$, $v = 0$	2.0	270	268 ± 19	9.0(17)	(7.2 ± 1.2)(17)	1.00	6.5	2.2
C_2H_5OH, $v = 0$	2.0	320	319 ± 16	1.4(18)	(1.5 ± 0.1)(18)	3.20	5.0	2.6
CH_3OCH_3, $v = 0$	2.0	315	315 ± 20	≤ 2.7(17)		1.35	5.5	3.5
CH_3OCHO, $v = 0$	2.0	220	250 ± 31	1.3(18)	(1.1 ± 0.3)(18)	1.85	5.0	3.0
$v = 1$	2.0	220	250 ± 31	1.3(18)	(1.1 ± 0.3)(18)	1.85	5.0	3.0
CH_3CHO, $v = 0$	2.0	300	293 ± 16	6.9(17)	(3.1 ± 0.4)(17)	1.15	5.0	2.5
$v = 1$	2.0	300	293 ± 16	6.9(17)	(3.1 ± 0.4)(17)	1.15	5.0	2.5
$v = 2$	2.0	300	293 ± 16	6.9(17)	(3.1 ± 0.4)(17)	1.15	5.0	2.5
CH_3NCO, $v = 0$	2.0	170	141 ± 18	3.0(17)	(1.7 ± 0.5)(17)	1.00	7.4	4.0
C_2H_5CN, $v = 0$	2.0	230	237 ± 5	2.5(18)	(2.1 ± 0.1)(18)	2.30	7.2	2.8
$v_{12} = 1$	2.0	230	237 ± 5	2.5(18)	(2.1 ± 0.1)(18)	2.30	7.2	2.8
$v_{13} = 2$	2.0	230	237 ± 5	2.5(18)	(2.1 ± 0.1)(18)	2.30	7.2	2.8
$v_{20} = 1$	2.0	230	237 ± 5	2.5(18)	(2.1 ± 0.1)(18)	2.30	7.2	2.8
$v_{21} = 2$	2.0	230	237 ± 5	2.5(18)	(2.1 ± 0.1)(18)	2.30	7.2	2.8
C_2H_3CN, $v = 0$	2.0	250	263 ± 6	1.7(18)	(1.8 ± 0.1)(18)	1.11	6.5	3.5
$v_{11} = 1$	2.0	250	263 ± 6	1.7(18)	(1.8 ± 0.1)(18)	1.11	6.5	3.5
$v_{15} = 1$	2.0	250	263 ± 6	1.7(18)	(1.8 ± 0.1)(18)	1.11	6.5	3.5
NH_2CHO, $v = 0$	2.0	180	188 ± 5	2.3(18)	(1.8 ± 0.1)(18)	1.14	5.7	2.3
$v_{12} = 1$	2.0	170	188 ± 5	2.3(18)	(1.8 ± 0.1)(18)	1.14	5.7	2.3

Table E.15. Same as Table E.2, but for position N1W.

Molecule	Size ($''$)	$T_{\rm rot,W}$ (K)	$T_{\rm rot,obs}$ (K)	$N_{\rm W}$ ($\rm cm^{-2}$)	$N_{\rm obs}$ ($\rm cm^{-2}$)	$C_{\rm vib}$	Δv ($\rm km\,s^{-1}$)	$v_{\rm off}$ ($\rm km\,s^{-1}$)
CH_3OH, $v = 0$	2.0	180	183 ± 5	1.5(19)	(1.4 ± 0.2)(19)	1.00	6.0	3.0
$v = 1$	2.0	180	183 ± 5	1.5(19)	(1.4 ± 0.2)(19)	1.00	6.0	3.0
$v = 2$	2.0	180	183 ± 5	1.5(19)	(1.4 ± 0.2)(19)	1.00	6.0	3.0
$^{13}CH_3OH$, $v = 0$	2.0	190	193 ± 7	7.0(17)	(6.8 ± 0.7)(17)	1.00	6.0	2.6
C_2H_5OH, $v = 0$	2.0	230	218 ± 5	6.0(17)	(6.4 ± 0.4)(17)	1.83	5.0	2.6
CH_3OCH_3, $v = 0$	2.0	175	173 ± 8	2.1(17)	(1.8 ± 0.2)(17)	1.03	4.5	3.0
CH_3OCHO, $v = 0$	2.0	180	180 ± 12	9.4(17)	(8.3 ± 1.1)(17)	1.34	5.0	3.5
$v = 1$	2.0	180	180 ± 12	9.4(17)	(8.3 ± 1.1)(17)	1.34	5.0	3.5
CH_3CHO, $v = 0$	2.0	200	197 ± 9	2.0(17)	(1.0 ± 0.1)(17)	1.03	5.0	2.0
$v = 1$	2.0	200	197 ± 9	2.0(17)	(1.0 ± 0.1)(17)	1.03	5.0	2.0
CH_3NCO, $v = 0$	2.0	120	123 ± 18	1.2(17)	(1.1 ± 0.4)(17)	1.00	7.0	3.0
C_2H_5CN, $v = 0$	2.0	200	196 ± 2	1.3(18)	(1.38 ± 0.04)(18)	1.79	7.2	1.7
$v_{12} = 1$	2.0	200	196 ± 2	1.3(18)	(1.38 ± 0.04)(18)	1.79	7.2	1.7
$v_{13} = 2$	2.0	200	196 ± 2	1.3(18)	(1.38 ± 0.04)(18)	1.79	7.2	1.7
$v_{20} = 1$	2.0	200	196 ± 2	1.3(18)	(1.38 ± 0.04)(18)	1.79	7.2	1.7
$v_{21} = 2$	2.0	200	196 ± 2	1.3(18)	(1.38 ± 0.04)(18)	1.79	7.2	1.7
C_2H_3CN, $v = 0$	2.0	170	182 ± 6	9.2(17)	(8.2 ± 1.0)(17)	1.02	6.0	2.0
$v_{11} = 1$	2.0	170	182 ± 6	9.2(17)	(8.2 ± 1.0)(17)	1.02	6.0	2.0
$v_{15} = 1$	2.0	170	182 ± 6	9.2(17)	(8.2 ± 1.0)(17)	1.02	6.0	2.0
NH_2CHO, $v = 0$	2.0	160	165 ± 3	1.4(18)	(1.4 ± 0.1)(18)	1.10	5.7	2.3
$v_{12} = 1$	2.0	160	165 ± 3	1.4(18)	(1.4 ± 0.1)(18)	1.10	5.7	2.3

Table E.16. Same as Table E.2, but for position N1W1.

Molecule	Size ($''$)	$T_{\rm rot,W}$ (K)	$T_{\rm rot,obs}$ (K)	$N_{\rm W}$ ($\rm cm^{-2}$)	$N_{\rm obs}$ ($\rm cm^{-2}$)	$C_{\rm vib}$	Δv ($\rm km\,s^{-1}$)	$v_{\rm off}$ ($\rm km\,s^{-1}$)
CH_3OH, $v = 0$	2.0	155	151 ± 2	1.5(19)	(1.4 ± 0.1)(19)	1.00	5.5	3.0
$v = 1$	2.0	155	151 ± 2	1.5(19)	(1.4 ± 0.1)(19)	1.00	5.5	3.0
$v = 2$	2.0	155	151 ± 2	1.5(19)	(1.4 ± 0.1)(19)	1.00	5.5	3.0
$^{13}CH_3OH$, $v = 0$	2.0	160	155 ± 4	5.5(17)	(5.2 ± 0.4)(17)	1.00	6.0	3.0
C_2H_5OH, $v = 0$	2.0	170	173 ± 4	3.7(17)	(4.2 ± 0.3)(17)	1.46	5.0	3.0
CH_3OCH_3, $v = 0$	2.0	135	130 ± 2	5.0(17)	(5.2 ± 0.3)(17)	1.00	5.0	3.5
$v_{11} = 1$	2.0	135	130 ± 2	5.0(17)	(5.2 ± 0.3)(17)	1.00	5.0	3.5
CH_3OCHO, $v = 0$	2.0	180	166 ± 4	1.1(18)	(1.1 ± 0.1)(18)	1.27	5.0	3.5
$v = 1$	2.0	180	166 ± 4	1.1(18)	(1.1 ± 0.1)(18)	1.27	5.0	3.5
CH_3CHO, $v = 0$	2.0	170	168 ± 9	8.1(16)	(4.0 ± 0.5)(16)	1.02	4.5	2.0
$v = 1$	2.0	170	168 ± 9	8.1(16)	(4.0 ± 0.5)(16)	1.02	4.5	2.0
CH_3NCO, $v = 0$	2.0	100	96 ± 11	5.0(16)	(4.5 ± 1.3)(16)	1.00	6.4	2.5
C_2H_5CN, $v = 0$	2.0	170	168 ± 1	1.3(18)	(1.34 ± 0.04)(18)	1.52	8.0	2.0
$v_{12} = 1$	2.0	170	168 ± 1	1.3(18)	(1.34 ± 0.04)(18)	1.52	8.0	2.0
$v_{13} = 2$	2.0	170	168 ± 1	1.3(18)	(1.34 ± 0.04)(18)	1.52	8.0	2.0
$v_{20} = 1$	2.0	170	168 ± 1	1.3(18)	(1.34 ± 0.04)(18)	1.52	8.0	2.0
$v_{21} = 2$	2.0	170	168 ± 1	1.3(18)	(1.34 ± 0.04)(18)	1.52	8.0	2.0
C_2H_3CN, $v = 0$	2.0	160	168 ± 3	3.5(17)	(3.3 ± 0.2)(17)	1.01	6.5	2.6
$v_{11} = 1$	2.0	160	168 ± 3	3.5(17)	(3.3 ± 0.2)(17)	1.01	6.5	2.6
$v_{15} = 1$	2.0	160	168 ± 3	3.5(17)	(3.3 ± 0.2)(17)	1.01	6.5	2.6
NH_2CHO, $v = 0$	2.0	130	141 ± 3	6.4(17)	(6.4 ± 0.4)(17)	1.06	6.0	2.3
$v_{12} = 1$	2.0	130	141 ± 3	6.4(17)	(6.4 ± 0.4)(17)	1.06	6.0	2.3

Table E.17. Same as Table E.2, but for position N1W2.

Molecule	Size ($''$)	$T_{\rm rot,W}$ (K)	$T_{\rm rot,obs}$ (K)	$N_{\rm W}$ (cm^{-2})	$N_{\rm obs}$ (cm^{-2})	$C_{\rm vib}$	Δv (km s^{-1})	$v_{\rm off}$ (km s^{-1})
CH_3OH, $v = 0$	2.0	135	131 ± 2	1.0(19)	(8.4 ± 0.8)(18)	1.00	5.5	3.0
$v = 1$	2.0	135	131 ± 2	1.0(19)	(8.4 ± 0.8)(18)	1.00	5.5	3.0
$v = 2$	2.0	135	131 ± 2	1.0(19)	(8.4 ± 0.8)(18)	1.00	5.5	3.0
$^{13}CH_3OH$, $v = 0$	2.0	140	135 ± 4	3.3(17)	(3.5 ± 0.3)(17)	1.00	5.0	3.0
C_2H_5OH, $v = 0$	2.0	150	147 ± 3	1.9(17)	(2.2 ± 0.2)(17)	1.30	5.0	3.5
CH_3OCH_3, $v = 0$	2.0	110	109 ± 2	3.2(17)	(3.5 ± 0.2)(17)	1.00	4.0	3.5
$v_{11} = 1$	2.0	110	109 ± 2	3.2(17)	(3.5 ± 0.2)(17)	1.00	4.0	3.5
CH_3OCHO, $v = 0$	2.0	150	144 ± 3	5.9(17)	(6.2 ± 0.3)(17)	1.17	4.0	3.5
$v = 1$	2.0	150	144 ± 3	5.9(17)	(6.2 ± 0.3)(17)	1.17	4.0	3.5
CH_3CHO, $v = 0$	2.0	125	115 ± 4	2.0(16)	(1.0 ± 0.1)(16)	1.00	4.5	2.0
$v = 1$	2.0	125	115 ± 4	2.0(16)	(1.0 ± 0.1)(16)	1.00	4.5	2.0
CH_3NCO, $v = 0$	2.0	90	86 ± 8	1.3(16)	(1.1 ± 0.3)(16)	1.00	6.4	2.5
C_2H_5CN, $v = 0$	2.0	150	151 ± 1	6.3(17)	(6.3 ± 0.2)(17)	1.39	7.3	2.0
$v_{12} = 1$	2.0	150	151 ± 1	6.3(17)	(6.3 ± 0.2)(17)	1.39	7.3	2.0
$v_{13} = 2$	2.0	150	151 ± 1	6.3(17)	(6.3 ± 0.2)(17)	1.39	7.3	2.0
$v_{20} = 1$	2.0	150	151 ± 1	6.3(17)	(6.3 ± 0.2)(17)	1.39	7.3	1.2
$v_{21} = 2$	2.0	150	151 ± 1	6.3(17)	(6.3 ± 0.2)(17)	1.39	7.3	2.0
C_2H_3CN, $v = 0$	2.0	150	153 ± 5	2.5(16)	(2.7 ± 0.2)(16)	1.01	4.5	2.0
$v_{11} = 1$	2.0	150	153 ± 5	2.5(16)	(2.7 ± 0.2)(16)	1.01	4.5	2.0
NH_2CHO, $v = 0$	2.0	130	136 ± 3	3.2(17)	(3.2 ± 0.2)(17)	1.05	5.5	2.0
$v_{12} = 1$	2.0	120	136 ± 3	3.7(17)	(3.2 ± 0.2)(17)	1.05	6.0	2.0

Table E.18. Same as Table E.2, but for position N1W3.

Molecule	Size ($''$)	$T_{\rm rot,W}$ (K)	$T_{\rm rot,obs}$ (K)	$N_{\rm W}$ (cm^{-2})	$N_{\rm obs}$ (cm^{-2})	$C_{\rm vib}$	Δv (km s^{-1})	$v_{\rm off}$ (km s^{-1})
CH_3OH, $v = 0$	2.0	110	107 ± 4	1.5(18)	(1.3 ± 0.1)(18)	1.00	5.0	3.0
$^{13}CH_3OH$, $v = 0$	2.0	120	122 ± 4	1.5(17)	(1.6 ± 0.2)(17)	1.00	5.0	3.0
C_2H_5OH, $v = 0$	2.0	130	133 ± 4	4.9(16)	(5.1 ± 0.5)(16)	1.23	4.5	2.6
CH_3OCH_3, $v = 0$	2.0	90	85 ± 6	4.3(16)	(4.9 ± 0.8)(16)	1.00	3.5	3.0
CH_3OCHO, $v = 0$	2.0	140	135 ± 8	1.3(17)	(1.3 ± 0.2)(17)	1.14	5.0	3.5
$v = 1$	2.0	140	135 ± 8	1.3(17)	(1.3 ± 0.2)(17)	1.14	5.0	3.5
CH_3CHO, $v = 0$	2.0	100	117 ± 28	3.5(15)	(2.6 ± 1.2)(15)	1.00	4.0	2.5
CH_3NCO, $v = 0$	2.0	90	89 ± 21	3.0(15)	(2.8 ± 1.6)(15)	1.00	5.5	2.0
C_2H_5CN, $v = 0$	2.0	130	131 ± 2	1.3(17)	(1.3 ± 0.1)(17)	1.26	7.3	2.0
$v_{20} = 1$	2.0	130	131 ± 2	1.3(17)	(1.3 ± 0.1)(17)	1.26	7.3	2.0
C_2H_3CN, $v = 0$	2.0	130	138 ± 11	3.0(15)	(2.9 ± 0.5)(15)	1.00	5.0	3.9
NH_2CHO, $v = 0$	2.0	125	131 ± 4	5.2(16)	(5.4 ± 0.6)(16)	1.05	5.0	1.5
$v_{12} = 1$	2.0	125	131 ± 4	5.2(16)	(5.4 ± 0.6)(16)	1.05	5.0	1.5

Table E.19. Same as Table E.2, but for position N1W4.

Molecule	Size ($''$)	$T_{\rm rot,W}$ (K)	$T_{\rm rot,obs}$ (K)	$N_{\rm W}$ (cm^{-2})	$N_{\rm obs}$ (cm^{-2})	$C_{\rm vib}$	Δv (km s^{-1})	$v_{\rm off}$ (km s^{-1})
CH_3OH, $v = 0$	2.0	100	90 ± 5	2.5(17)	(1.7 ± 0.3)(17)	1.00	6.0	2.0
$^{13}CH_3OH$, $v = 0$	2.0	100	97 ± 6	4.0(16)	(4.2 ± 0.6)(16)	1.00	4.5	2.6
C_2H_5OH, $v = 0$	2.0	115	115 ± 6	9.2(15)	(8.4 ± 1.3)(15)	1.15	5.5	2.0
CH_3OCH_3, $v = 0$	2.0	77	77 ± 6	≤ 6.5(15)		1.00	4.9	3.4
CH_3OCHO, $v = 0$	2.0	30	23 ± 2	3.0(15)	(3.0 ± 0.7)(15)	1.00	4.0	3.5
CH_3CHO, $v = 0$	2.0	93	93 ± 11	≤ 1.5(15)		1.00	4.9	3.4
CH_3NCO, $v = 0$	2.0	76	76 ± 6	≤ 7.5(14)		1.00	4.9	3.4
C_2H_5CN, $v = 0$	2.0	127	127 ± 7	≤ 8.1(15)		1.24	4.5	2.5
C_2H_3CN, $v = 0$	2.0	128	128 ± 2	≤ 1.0(15)		1.00	4.9	3.4
NH_2CHO, $v = 0$	2.0	123	123 ± 6	≤ 1.3(15)		1.04	5.0	3.0

Table E.20. Same as Table E.2, but for position N1W5.

Molecule	Size ($''$)	$T_{\rm rot,W}$ (K)	$T_{\rm rot,obs}$ (K)	$N_{\rm W}$ ($\rm cm^{-2}$)	$N_{\rm obs}$ ($\rm cm^{-2}$)	$C_{\rm vib}$	Δv ($\rm km\,s^{-1}$)	$v_{\rm off}$ ($\rm km\,s^{-1}$)
CH_3OH, $v = 0$	2.0	94	92 ± 2	1.8(17)	$(1.5 \pm 0.1)(17)$	1.00	5.5	7.0
$^{13}CH_3OH$, $v = 0$	2.0	100	96 ± 18	1.0(16)	$(1.1 \pm 0.4)(16)$	1.00	2.5	7.0
C_2H_5OH, $v = 0$	2.0	105	105 ± 6	$\leq$ 6.1(15)		1.11	3.7	7.4
CH_3OCH_3, $v = 0$	2.0	69	69 ± 6	$\leq$ 5.0(15)		1.00	3.7	7.4
CH_3OCHO, $v = 0$	2.0	50	44 ± 8	5.0(15)	$(5.5 \pm 2.0)(15)$	1.00	2.5	7.0
CH_3CHO, $v = 0$	2.0	84	84 ± 11	$\leq$ 8.0(14)		1.00	3.7	7.4
CH_3NCO, $v = 0$	2.0	72	72 ± 7	$\leq$ 5.5(14)		1.00	3.7	7.4
C_2H_5CN, $v = 0$	2.0	90	94 ± 9	7.6(15)	$(8.2 \pm 1.4)(15)$	1.09	5.5	8.0
C_2H_3CN, $v = 0$	2.0	120	120 ± 2	$\leq$ 1.0(15)		1.00	3.7	7.4
NH_2CHO, $v = 0$	2.0	119	119 ± 6	$\leq$ 8.3(14)		1.03	4.5	7.4

Table E.21. Same as Table E.2, but for position N1W6.

Molecule	Size ($''$)	$T_{\rm rot,W}$ (K)	$T_{\rm rot,obs}$ (K)	$N_{\rm W}$ ($\rm cm^{-2}$)	$N_{\rm obs}$ ($\rm cm^{-2}$)	$C_{\rm vib}$	Δv ($\rm km\,s^{-1}$)	$v_{\rm off}$ ($\rm km\,s^{-1}$)
CH_3OH, $v = 0$	2.0	90	90 ± 3	1.1(18)	$(8.0 \pm 1.1)(17)$	1.00	2.5	7.0
$^{13}CH_3OH$, $v = 0$	2.0	85	81 ± 8	1.3(16)	$(1.5 \pm 0.3)(16)$	1.00	2.9	7.1
C_2H_5OH, $v = 0$	2.0	95	95 ± 6	$\leq$ 4.3(15)		1.08	2.6	7.3
CH_3OCH_3, $v = 0$	2.0	90	89 ± 5	4.5(16)	$(4.1 \pm 0.5)(16)$	1.00	2.0	7.0
CH_3OCHO, $v = 0$	2.0	110	109 ± 4	1.3(17)	$(1.3 \pm 0.1)(17)$	1.06	2.5	7.0
$v = 1$	2.0	110	109 ± 4	1.3(17)	$(1.3 \pm 0.1)(17)$	1.06	2.5	7.0
CH_3CHO, $v = 0$	2.0	75	75 ± 11	$\leq$ 5.0(14)		1.00	2.6	7.3
CH_3NCO, $v = 0$	2.0	68	68 ± 7	$\leq$ 3.5(14)		1.00	2.6	7.3
C_2H_5CN, $v = 0$	2.0	60	68 ± 19	1.3(15)	$(1.5 \pm 0.7)(15)$	1.02	4.3	7.2
C_2H_3CN, $v = 0$	2.0	50	39 ± 4	4.0(14)	$(4.6 \pm 1.0)(14)$	1.00	2.5	8.0
NH_2CHO, $v = 0$	2.0	114	114 ± 7	$\leq$ 2.1(14)		1.03	2.6	7.3

Table E.22. Same as Table E.2, but for position N1W7.

Molecule	Size ($''$)	$T_{\rm rot,W}$ (K)	$T_{\rm rot,obs}$ (K)	$N_{\rm W}$ ($\rm cm^{-2}$)	$N_{\rm obs}$ ($\rm cm^{-2}$)	$C_{\rm vib}$	Δv ($\rm km\,s^{-1}$)	$v_{\rm off}$ ($\rm km\,s^{-1}$)
CH_3OH, $v = 0$	2.0	90	97 ± 8	3.0(17)	$(1.9 \pm 0.6)(17)$	1.00	2.5	7.0
$^{13}CH_3OH$, $v = 0$	2.0	85	81 ± 7	1.1(16)	$(1.2 \pm 0.2)(16)$	1.00	2.9	7.1
C_2H_5OH, $v = 0$	2.0	85	85 ± 6	$\leq$ 3.7(15)		1.05	2.6	7.3
CH_3OCH_3, $v = 0$	2.0	77	76 ± 7	1.5(16)	$(1.4 \pm 0.3)(16)$	1.00	2.0	7.5
CH_3OCHO, $v = 0$	2.0	105	102 ± 2	6.3(16)	$(6.7 \pm 0.4)(16)$	1.05	2.5	7.0
$v = 1$	2.0	105	102 ± 2	6.3(16)	$(6.7 \pm 0.4)(16)$	1.05	2.5	7.0
CH_3CHO, $v = 0$	2.0	66	66 ± 11	$\leq$ 4.0(14)		1.00	2.6	7.3
CH_3NCO, $v = 0$	2.0	64	64 ± 7	$\leq$ 3.5(14)		1.00	2.6	7.3
C_2H_5CN, $v = 0$	2.0	90	111 ± 42	7.0(14)	$(1.0 \pm 0.6)(15)$	1.16	3.0	7.7
C_2H_3CN, $v = 0$	2.0	104	104 ± 3	$\leq$ 5.0(14)		1.00	2.6	7.3
NH_2CHO, $v = 0$	2.0	109	109 ± 7	$\leq$ 1.5(14)		1.02	2.6	7.3

Table E.23. Same as Table E.2, but for position N1W8.

Molecule	Size ($''$)	$T_{\rm rot,W}$ (K)	$T_{\rm rot,obs}$ (K)	$N_{\rm W}$ ($\rm cm^{-2}$)	$N_{\rm obs}$ ($\rm cm^{-2}$)	$C_{\rm vib}$	Δv ($\rm km\,s^{-1}$)	$v_{\rm off}$ ($\rm km\,s^{-1}$)
CH_3OH, $v = 0$	2.0	79	79 ± 8	1.8(16)	(1.4 ± 0.1)(16)	1.00	2.5	7.5
$^{13}CH_3OH$, $v = 0$	2.0	73	73 ± 5	≤ 2.5(15)		1.00	2.5	7.9
C_2H_5OH, $v = 0$	2.0	77	77 ± 6	≤ 3.6(15)		1.03	2.5	7.9
CH_3OCH_3, $v = 0$	2.0	46	46 ± 6	≤ 3.3(15)		1.00	2.5	7.9
CH_3OCHO, $v = 0$	2.0	91	91 ± 8	≤ 2.7(15)		1.03	2.5	7.9
CH_3CHO, $v = 0$	2.7	59	59 ± 11	≤ 4.0(14)		1.00	2.5	7.9
CH_3NCO, $v = 0$	2.0	60	60 ± 7	≤ 3.0(14)		1.00	2.5	7.9
C_2H_5CN, $v = 0$	2.0	98	98 ± 8	2.8(14)	(2.8 ± 0.5)(14)	1.11	3.0	7.0
C_2H_3CN, $v = 0$	2.0	98	98 ± 3	≤ 2.0(14)		1.00	2.5	7.9
NH_2CHO, $v = 0$	2.0	105	105 ± 8	≤ 1.0(14)		1.02	2.5	7.9

Table E.24. Intensity of the continuum corrected for free-free emission and $C^{18}O$ and H_2 column densities for all positions shown in Fig. 3.

Position	$S_{\rm dust}{}^a$ (K)	$\tau_{\rm dust}{}^b$	$N(H_2)_{\rm dust}{}^c$ ($10^{24}\,\rm cm^{-2}$)	$N(C^{18}O)^d$ ($10^{17}\rm cm^{-2}$)	$N(H_2)_{C^{18}O}{}^e$ ($10^{24}\rm cm^{-2}$)	Size^f ($''$)	Δv^g ($\rm km\,s^{-1}$)	$v_{\rm off}{}^h$ ($\rm km\,s^{-1}$)
N1S-1	103.6	0.40(10)	12.8(4)	–	–	–	–	–
N1S	65.9	0.35(9)	11.4(3)	–	–	–	–	–
N1S1	16.0	0.10(2)	3.3(8)	10.8	2.7(5)	2.0	4.5	−0.5
N1S2	6.7	0.05(1)	1.7(4)	4.8	1.2(2)	2.0	4.5	−0.5
N1S3	3.3	0.030(7)	1.0(3)	2.1	0.5(1)	2.0	4.0	−1.8
N1S4	0.9	0.010(4)	0.3(1)	1.0	0.26(5)	2.0	3.5	−3.0
N1S5	0.87	0.010(5)	≤0.3(2)	1.6	0.40(8)	2.0	2.5	−2.6
N1S6	2.7	0.030(8)	≤1.1(3)	1.6	0.40(8)	2.0	2.5	−2.8
N1S7	5.6	0.07(2)	≤2.4(6)	1.6	0.41(8)	2.0	2.5	−3.1
N1S8	–	–	–	1.6	0.39(7)	2.0	2.0	−3.3
N1W-1	27.5	0.29(7)	2.7(7)	≤12.3	≤3.1(6)	2.0	4.5	2.6
N1W	6.6	0.23(6)	1.0(3)	≤9.3	≤2.3(4)	2.0	4.5	2.6
N1W1	3.8	0.18(4)	0.7(2)	8.5	2.1(4)	2.0	4.5	3.0
N1W2	1.0	0.07(2)	0.2(1)	6.3	1.6(3)	2.0	4.5	3.0
N1W3	≤3.3	≤0.02	≤0.8	2.1	0.5(1)	2.0	4.5	3.0
N1W4	≤3.3	≤0.03	≤1.0	0.8	0.20(4)	2.0	4.5	2.0
N1W5	–	–	–	0.3	0.06(1)	2.0	4.0	7.4
N1W6	–	–	–	1.2	0.31(6)	2.0	3.0	7.0
N1W7	–	–	–	3.2	0.8(2)	2.0	2.5	7.3
N1W8	–	–	–	1.5	0.38(7)	2.0	2.0	7.9

Notes. The values in parentheses show the uncertainties in units of the last digit.
[(a)]Measured continuum intensity corrected for free-free emission.[(b)]Opacity of the dust emission assuming $T_{\rm dust} = T_{\rm rot,obs}(C_2H_5OH)$ with $\Delta T_{\rm dust} = 0.2 \times T_{\rm rot,obs}(C_2H_5OH)$.[(c)]$H_2$ column densities derived from dust emission.[(d)]Opacity-corrected $C^{18}O$ column densities taken from the Weeds model at the respective position with $\Delta N(C^{18}O) = 0.15 \times N(C^{18}O)$. [(e)]$H_2$ column densities derived from $C^{18}O$ 1–0 emission.[(f)]Size of the emitting region.[(g)]$FWHM$ of the transitions. [(h)]Offset from the source systemic velocity, which was set to $62\,\rm km\,s^{-1}$.

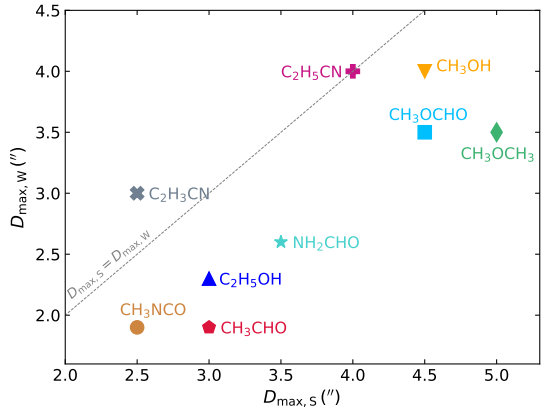

Fig. D.2. Maximum distances to the south $D_{max,S}$ and west $D_{max,W}$ from Sgr B2 (N1) to which a COM is still detected and beyond which only upper limits for column density can be derived. These distances correspond to vertical dashed lines in Fig. 7.

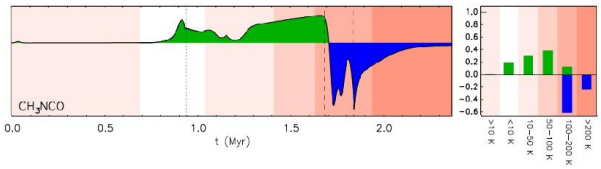

Fig. D.3. Same as in Fig. 13 in Garrod et al. (2022), but for CH_3NCO. It shows the net rate of change in the COM's abundances, summed over all chemical phases, during the cold collapse phase and the subsequent slow warm-up.

Table G.1. Vibrational states of COMs used during the analysis.

COM	vib. states
CH_3OH	$v = 0, v = 1, v = 2$
$^{13}CH_3OH$	$v = 0$
C_2H_5OH	$v = 0$
CH_3OCH_3	$v = 0, v_{11} = 1, v_{15} = 1$
CH_3OCHO	$v = 0, v = 1$
CH_3CHO	$v = 0, v = 1, v = 2$
CH_3NCO	$v = 0$
C_2H_5OH	$v = 0, v_{12} = 1, v_{20} = 1, v_{13} = 2, v_{21} = 2$
C_2H_3CN	$v = 0, v_{11} = 1, v_{15} = 1$
NH_2CHO	$v = 0, v_{12} = 1$

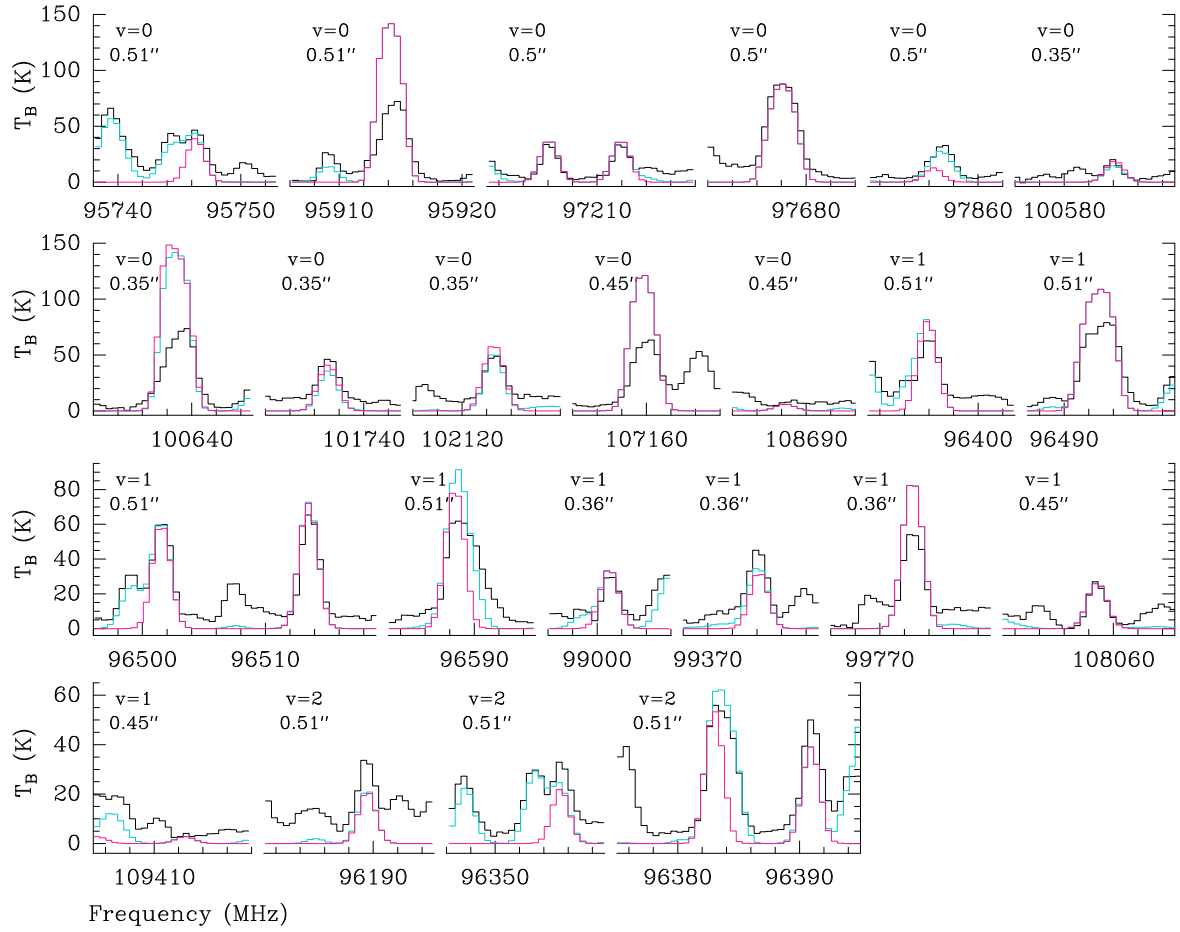

Fig. F.1. Transitions of CH_3OH used to produce the population diagram at position N1S. The observed spectrum is shown in black, the synthetic spectrum of the shown molecule in pink, and the cumulative Weeds model of all COMs, whose spectra have been modelled in this work, in turquoise. The vibrational state and the beam size of the respective spectral window are shown in the upper left corner. The frequency axis shows steps of 2 MHz. Transitions marked with pink stars in Figs. F.2–F.10 are not used for the population diagram.

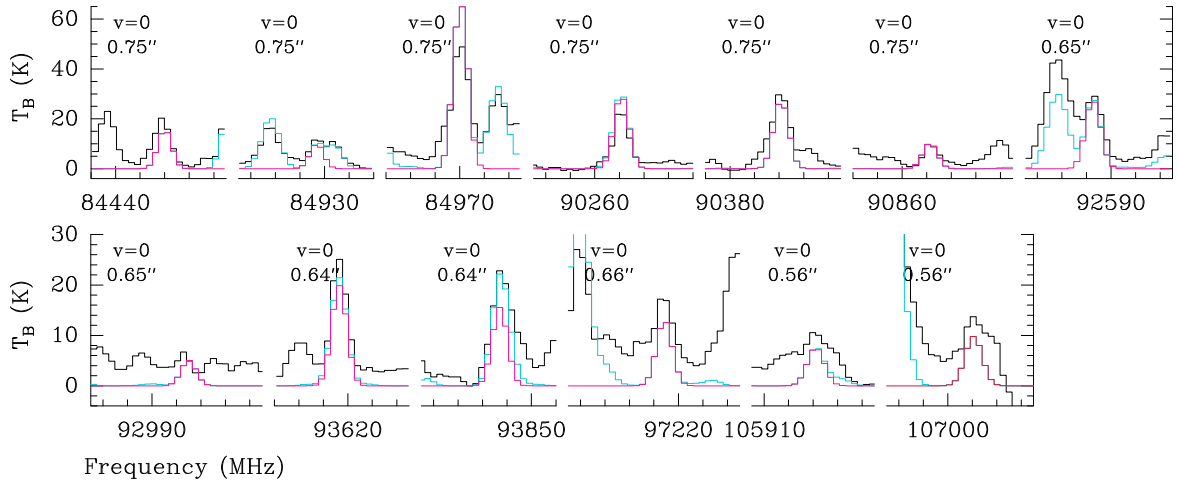

Fig. F.2. Same as Fig. F.1, but for $^{13}CH_3OH$.

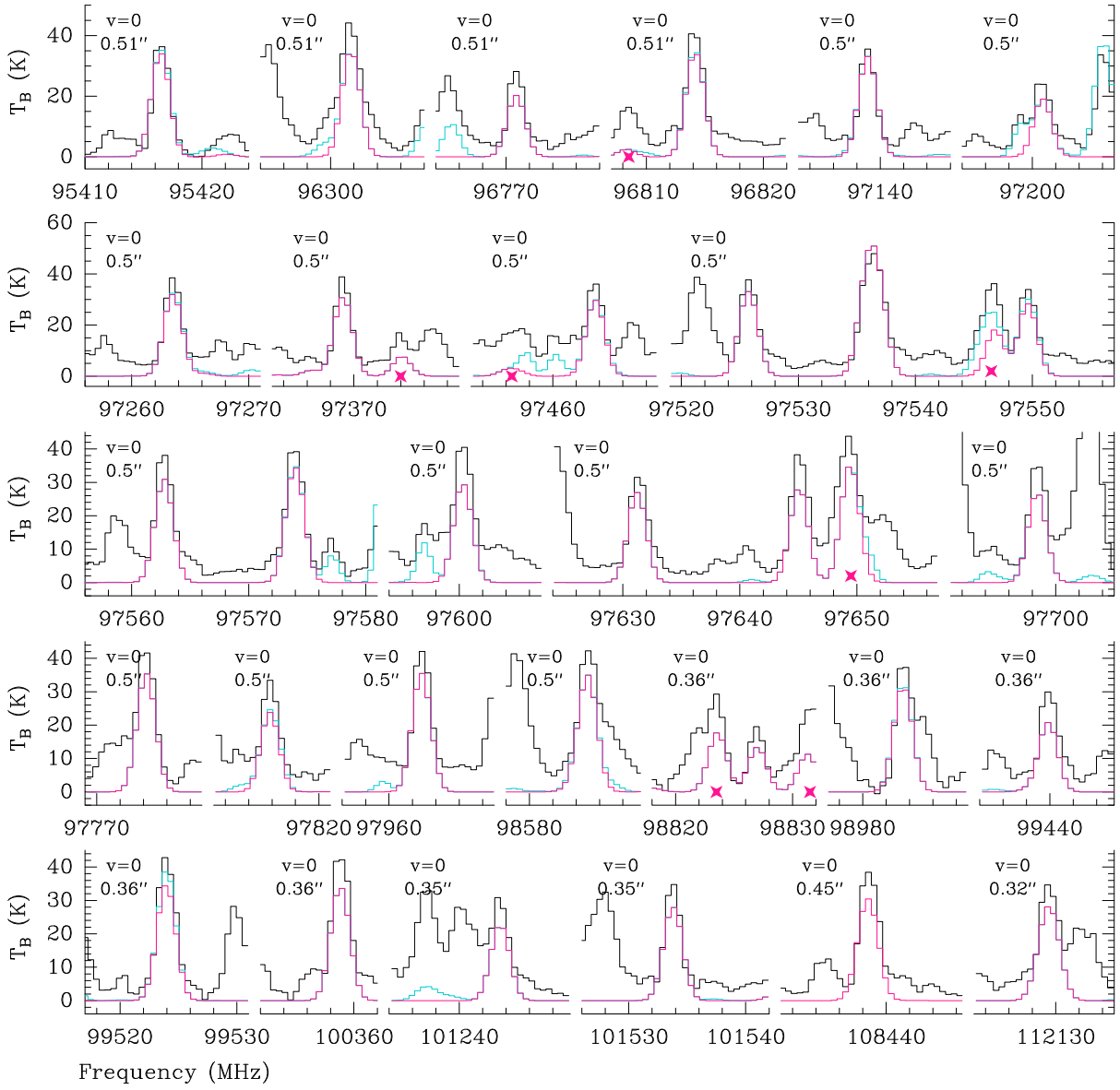

Fig. F.3. Same as Fig. F.1, but for C_2H_5OH.

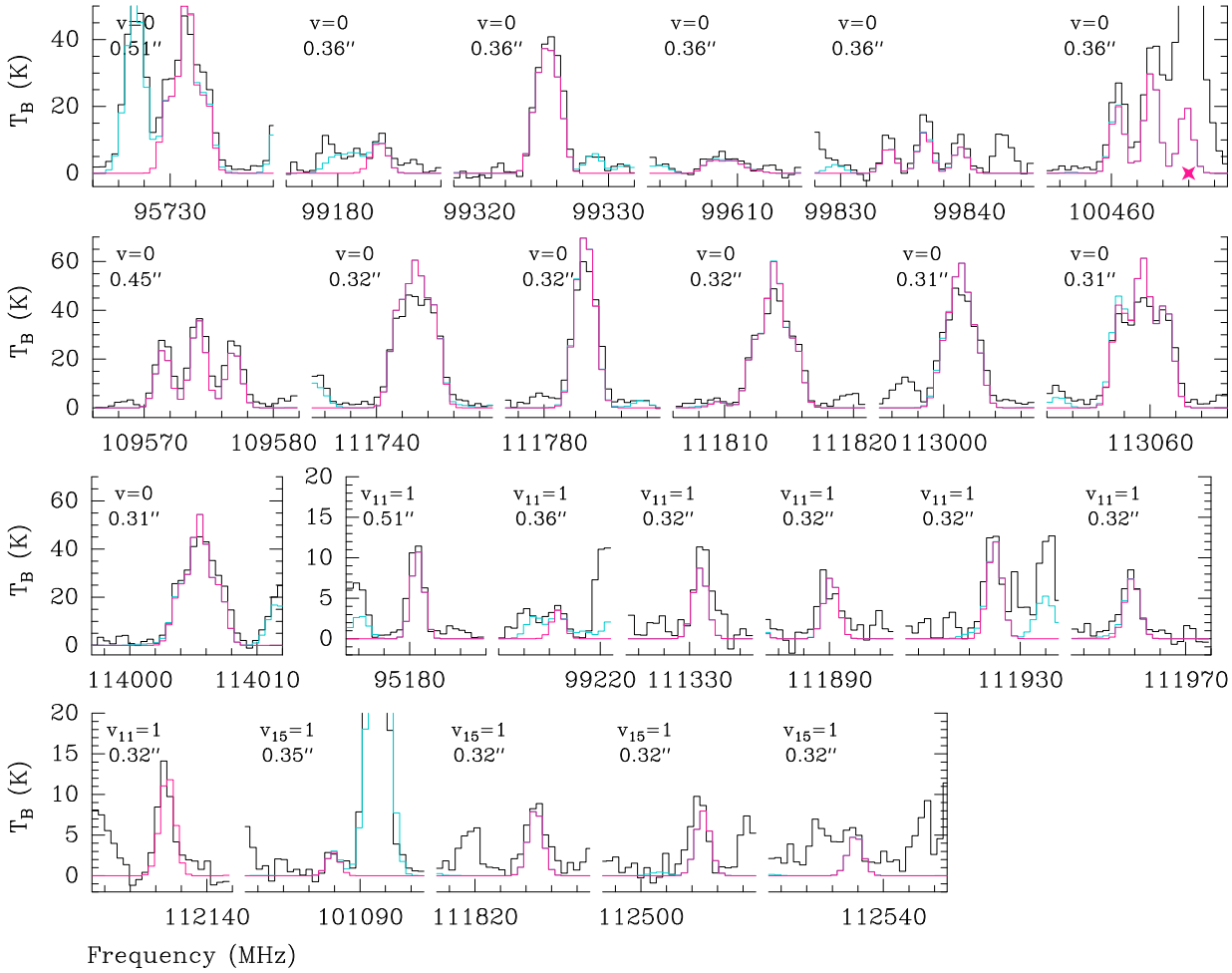

Fig. F.4. Same as Fig. F.1, but for CH_3OCH_3 and at position N1S1.

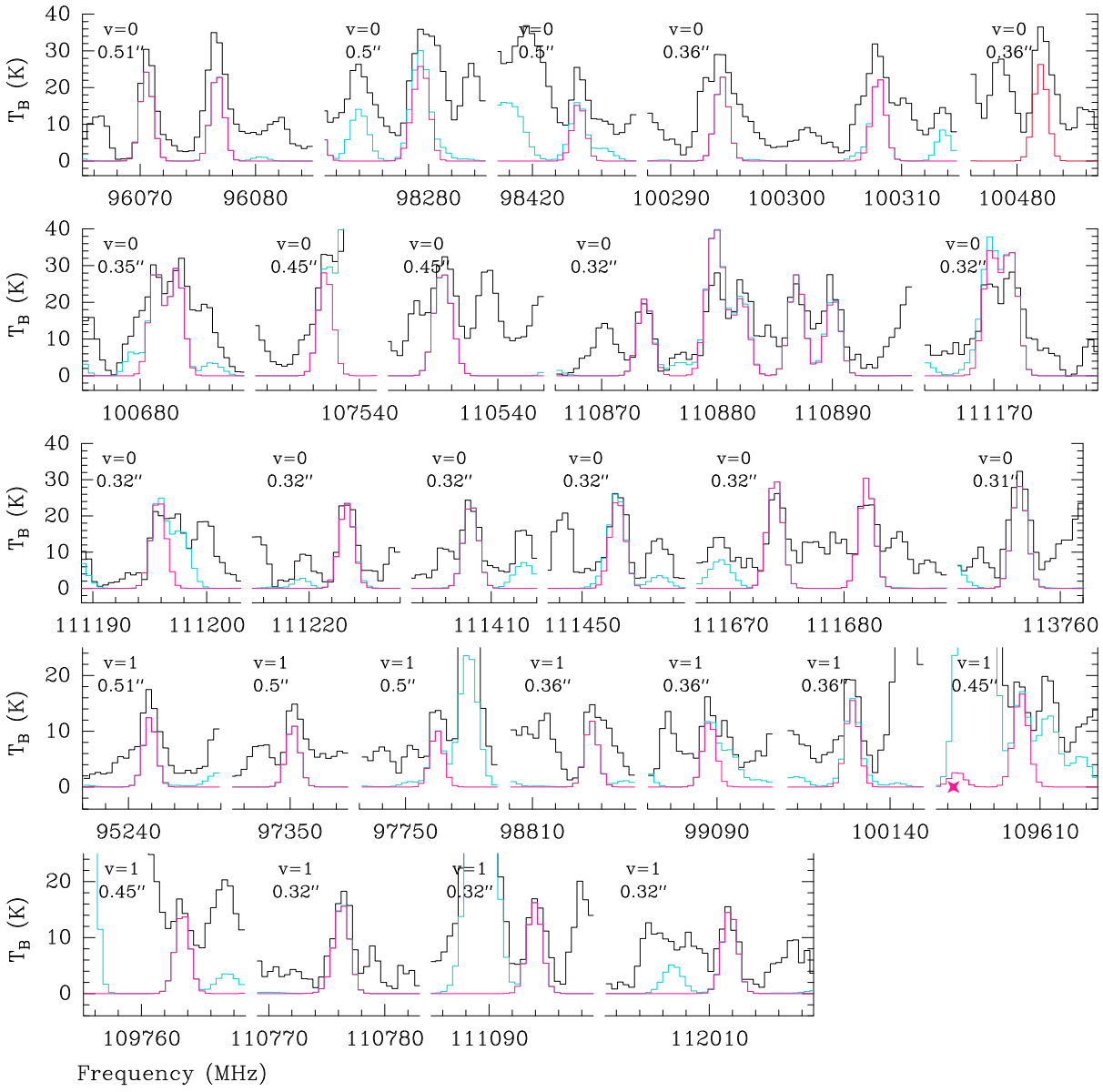

Fig. F.5. Same as Fig. F.1, but for CH_3OCHO.

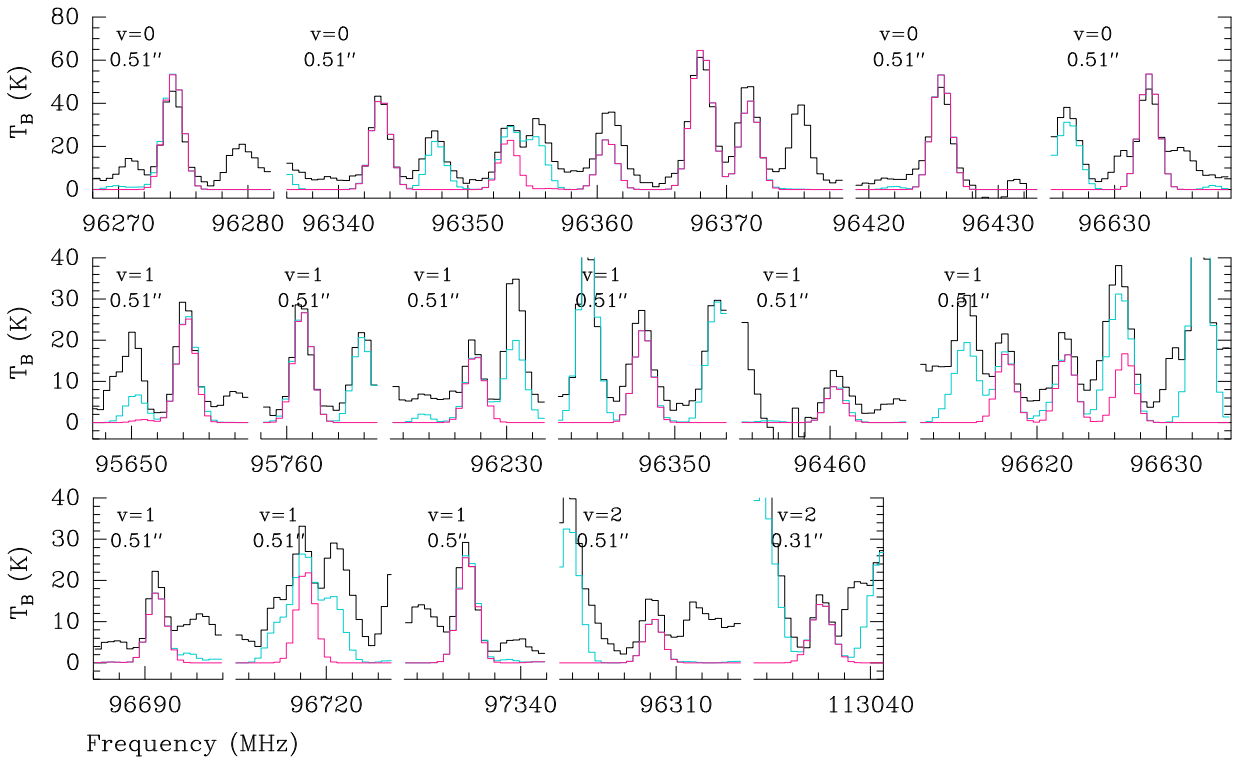

Fig. F.6. Same as Fig. F.1, but for CH_3CHO.

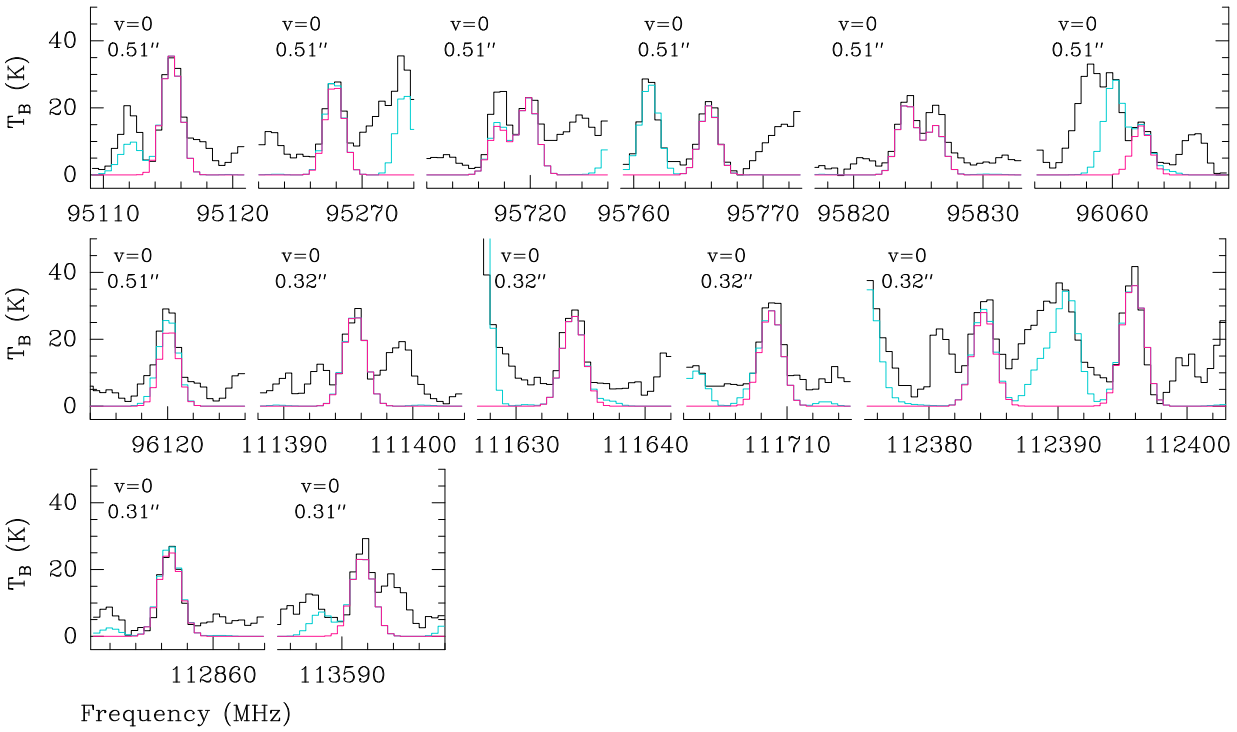

Fig. F.7. Same as Fig. F.1, but for CH_3NCO.

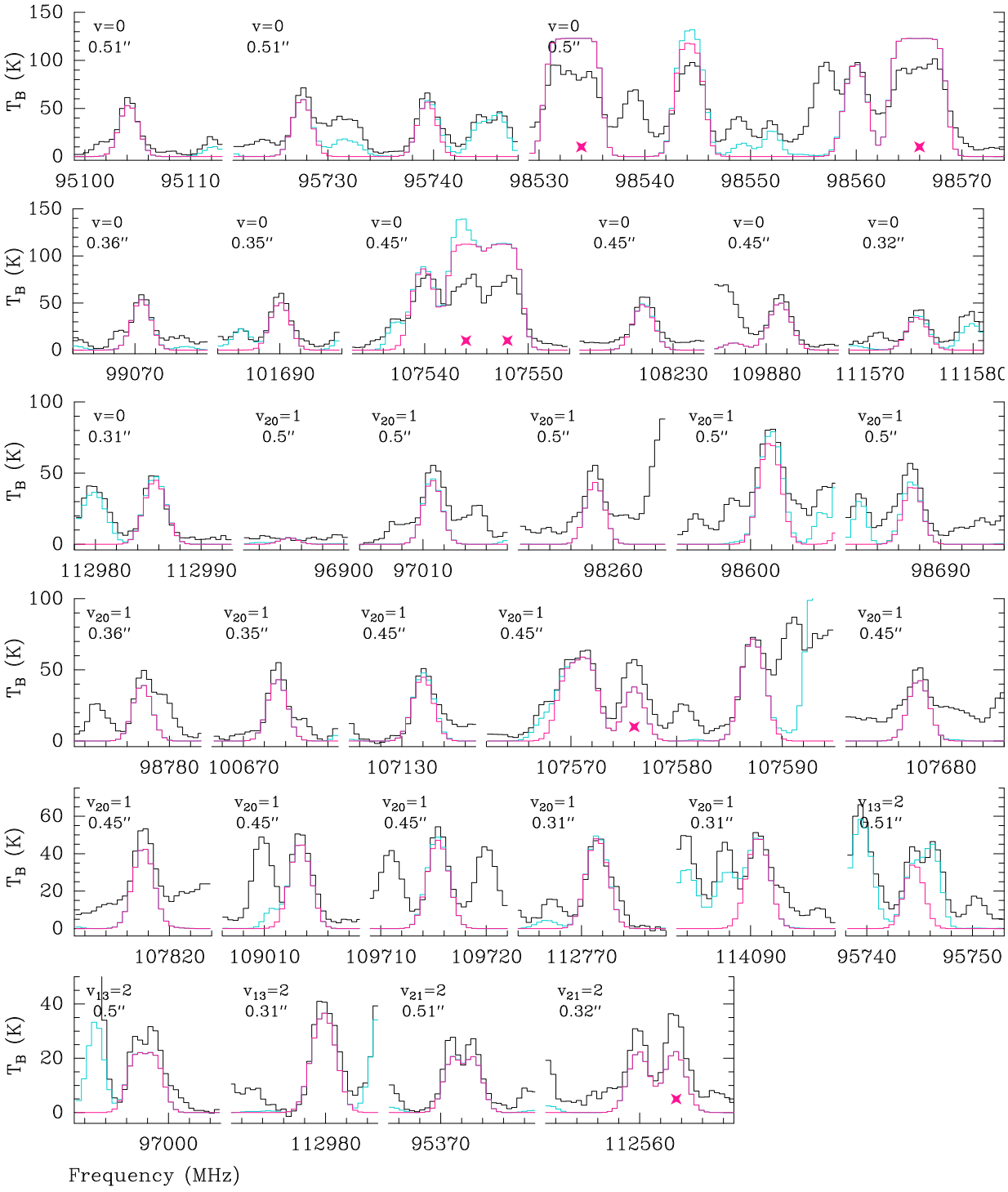

Fig. F.8. Same as Fig. F.1, but for C_2H_5CN.

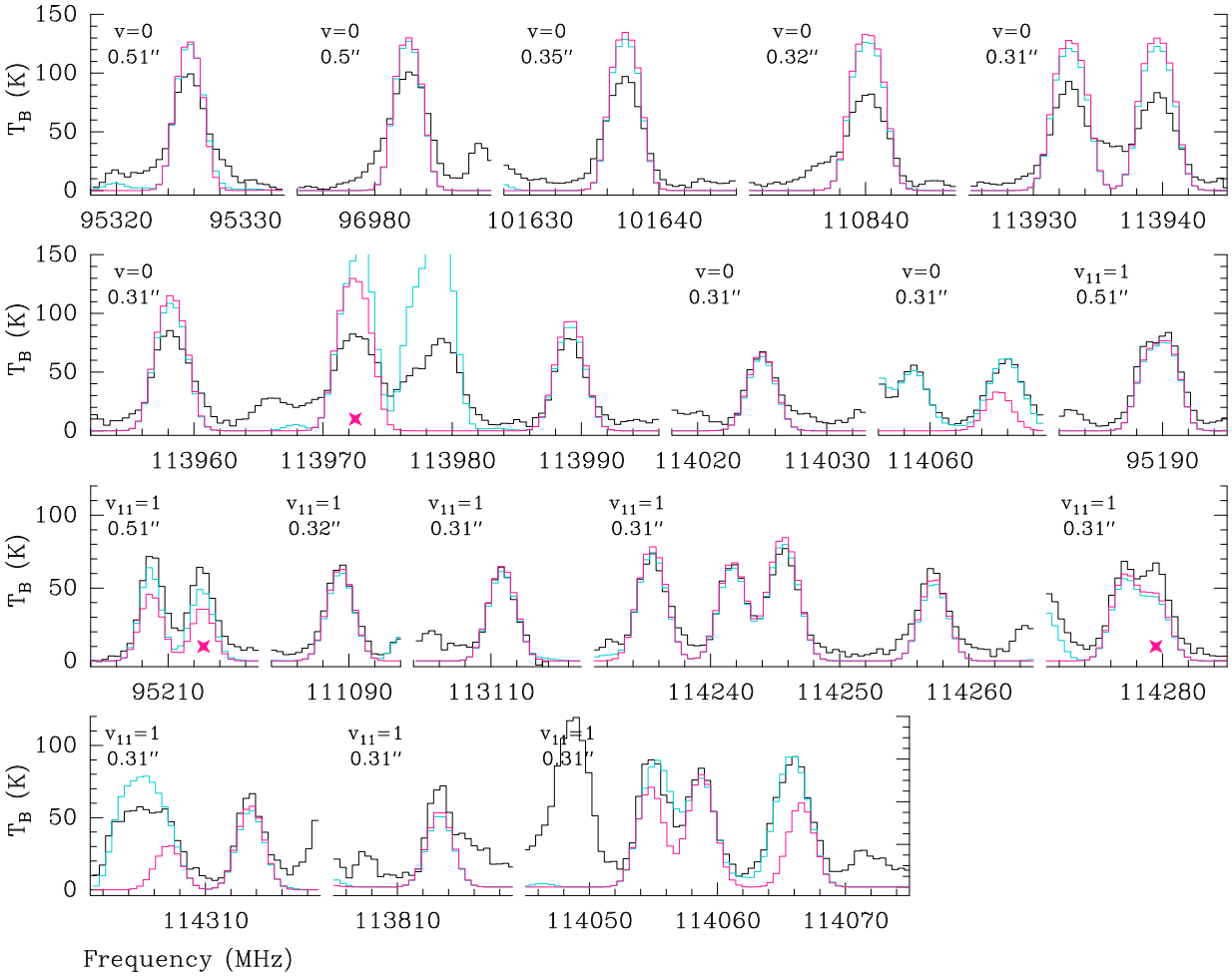

Fig. F.9. Same as Fig. F.1, but for C_2H_3CN.

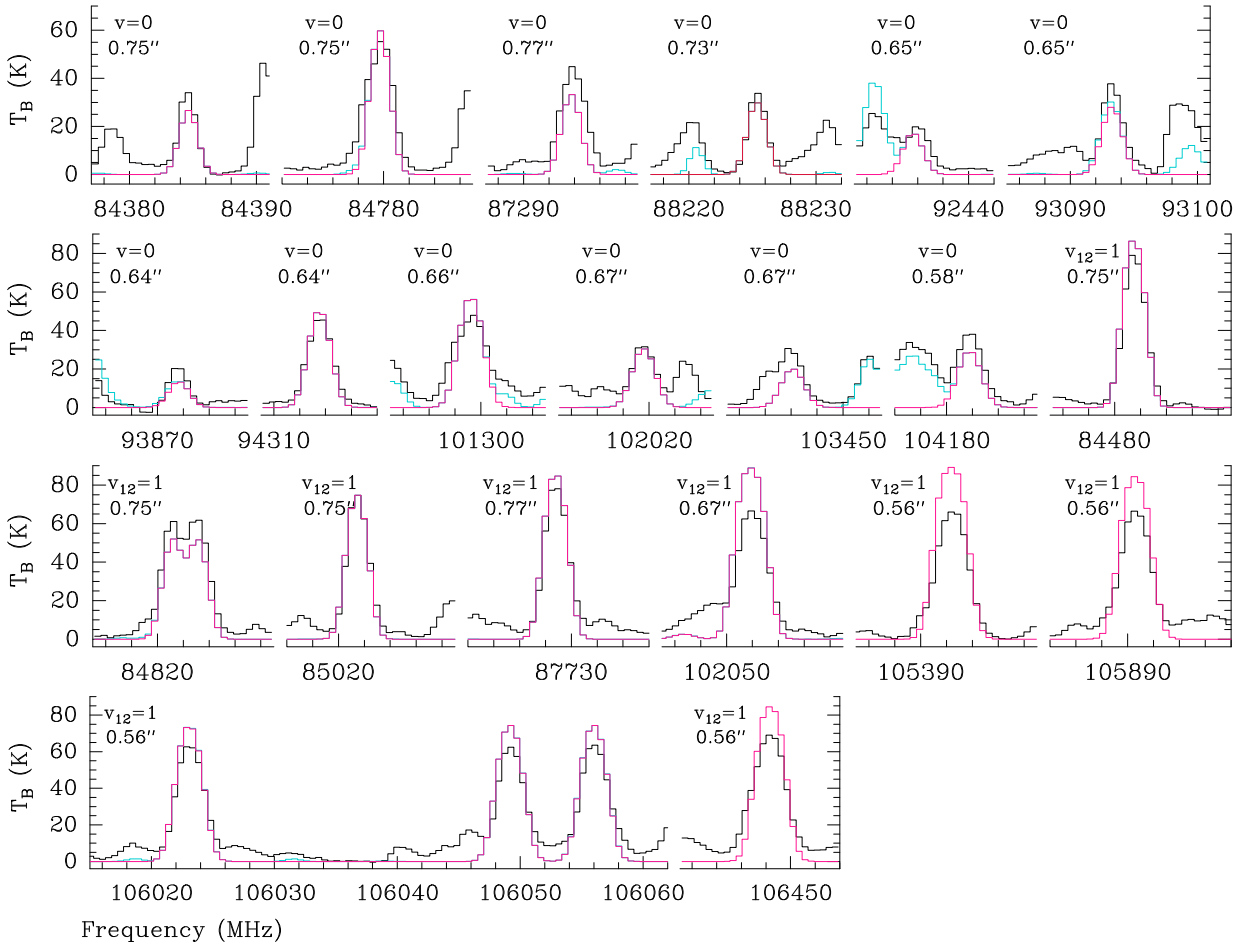

Fig. F.10. Same as Fig. F.1, but for NH_2CHO.

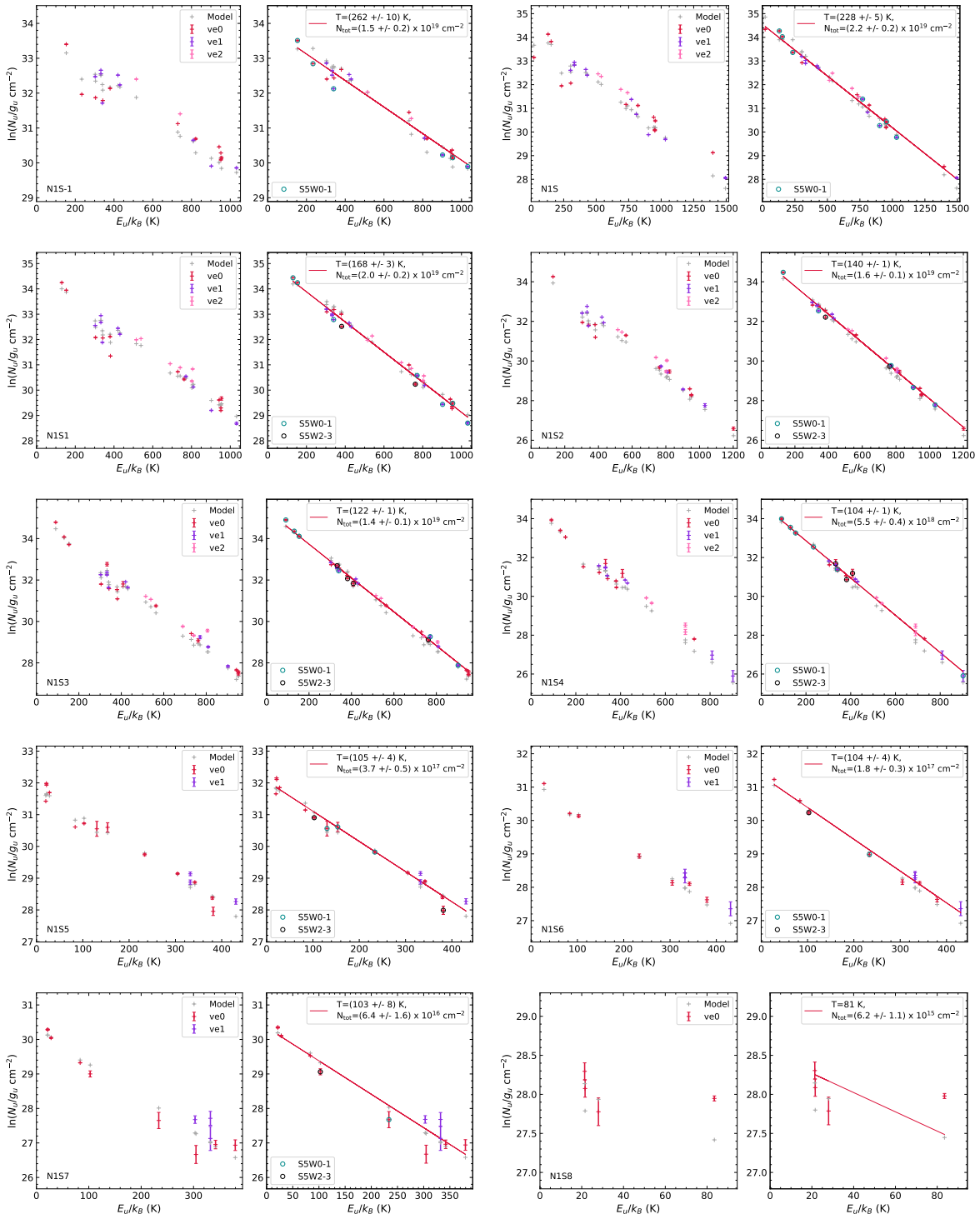

Fig. G.1. Population diagrams of CH_3OH at all positions to the south where the molecule is detected in setups 4–5. Each position takes two plots: the one with the name of the position indicated in the lower left corner and the one to the right. Observed data points are shown in various colours as indicated in the upper right corner of the respective left plot, while synthetic data points are shown in grey. No corrections are applied in the respective left panels, while in the right plots corrections for opacity and contamination by other molecules have been considered for both the observed and synthetic populations. The red line is a linear fit to all observed data points (in linear-logarithmic space). The results of the fits are shown in the respective right panels. Teal and black circles show observed data points from spectral windows 0–1 and 2–3 of observational setup 5, respectively, as indicated in the lower left corner in the right panels.

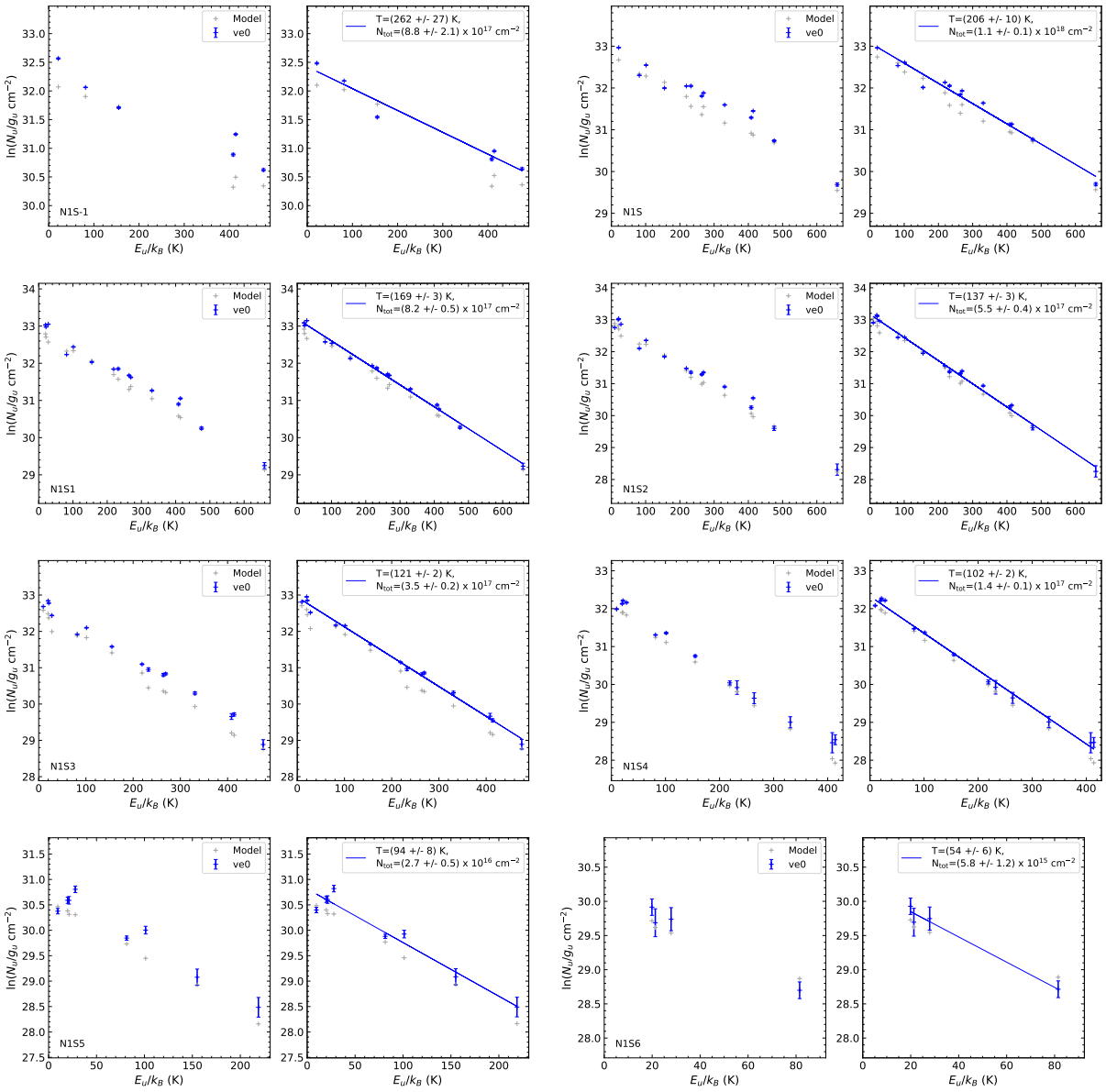

Fig. G.2. Same as Fig. G.1, but for $^{13}CH_3OH$, except that setups 1–3 had to be used due to lack of transitions in setups 4–5. The linear fit to observed data points is shown in blue.

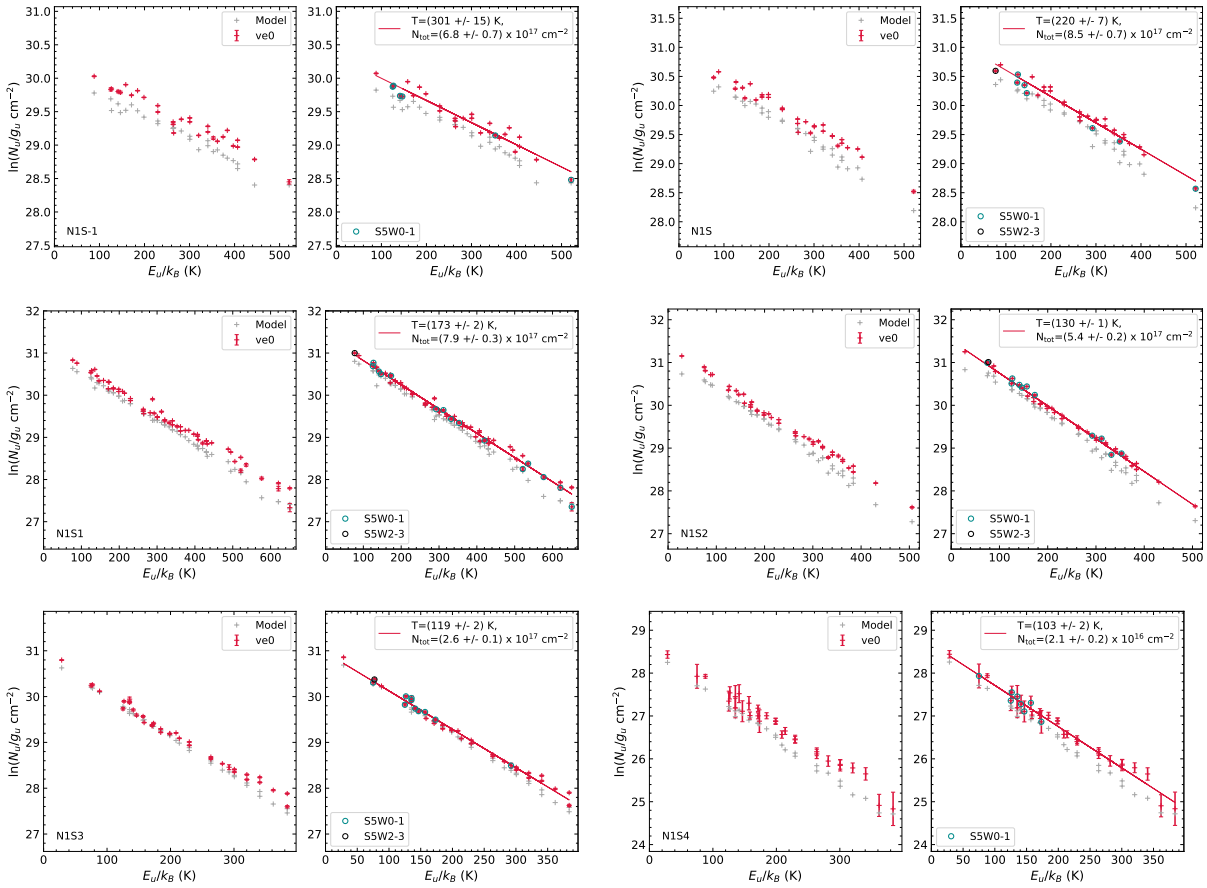

Fig. G.3. Same as Fig. G.1, but for C_2H_5OH.

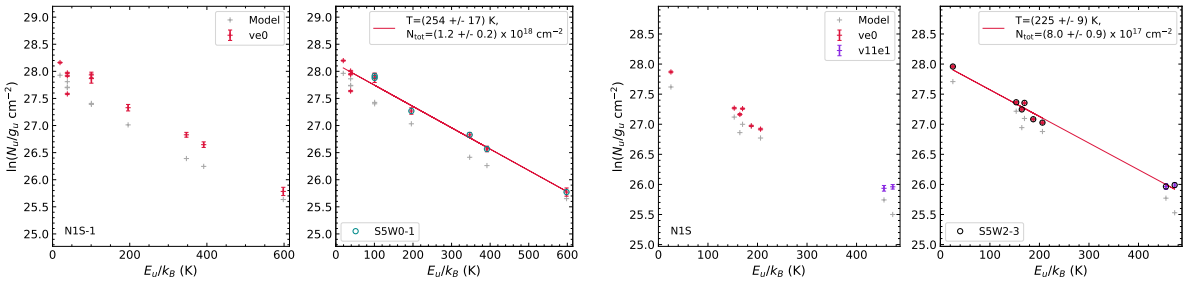

Fig. G.4. Same as Fig. G.1, but for CH_3OCH_3.

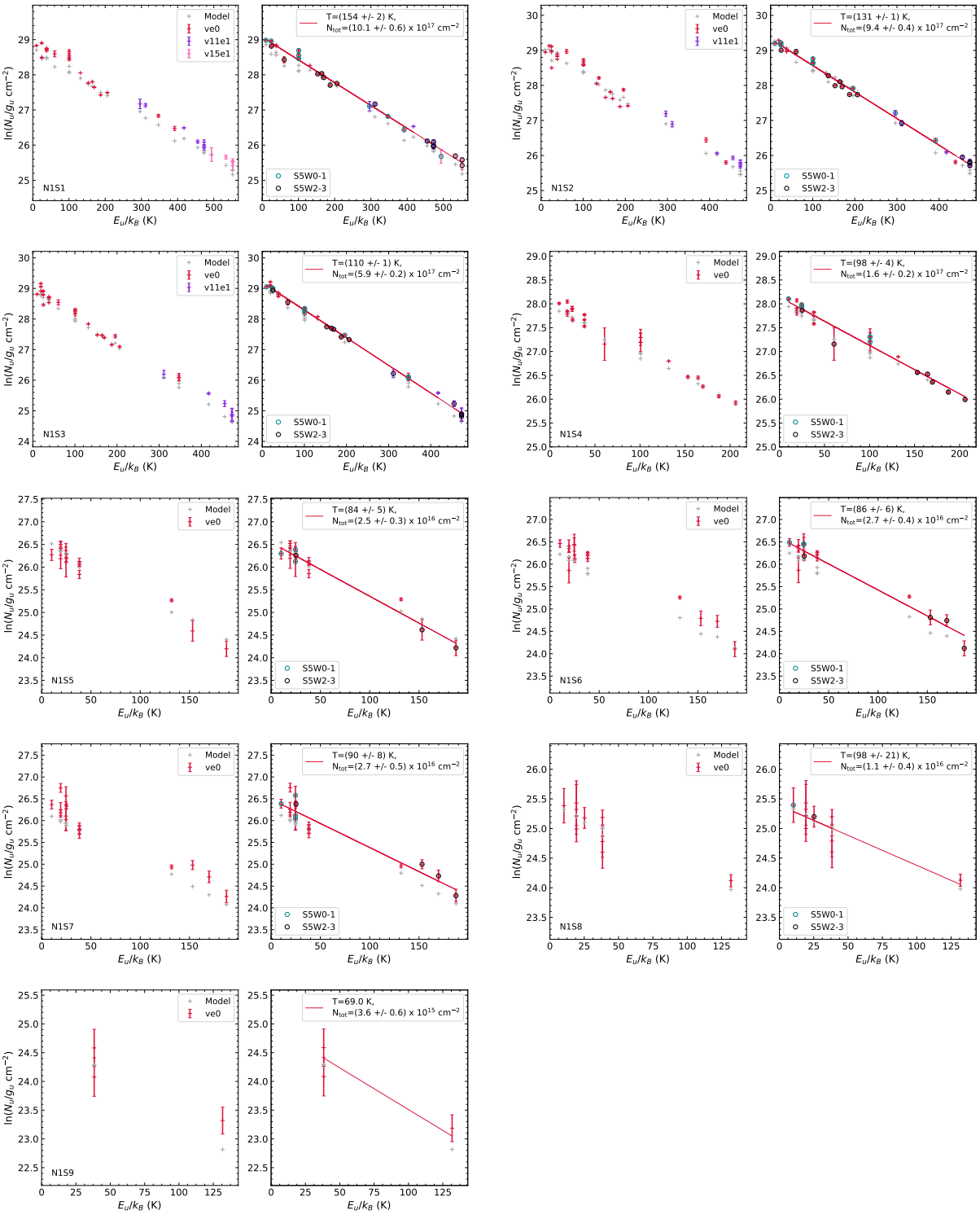

Fig. G.5. Figure G.4 continued.

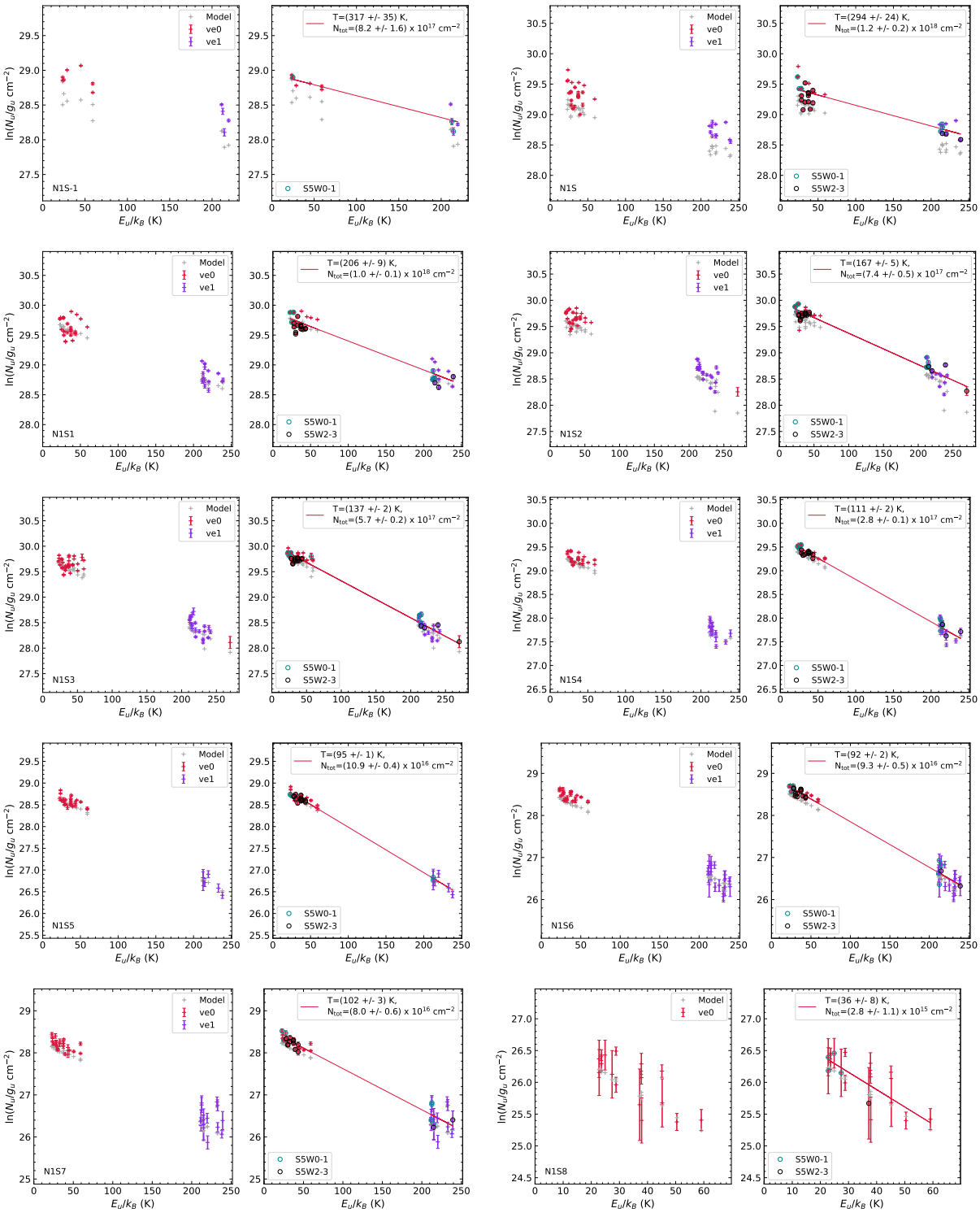

Fig. G.6. Same as Fig. G.1, but for CH_3OCHO.

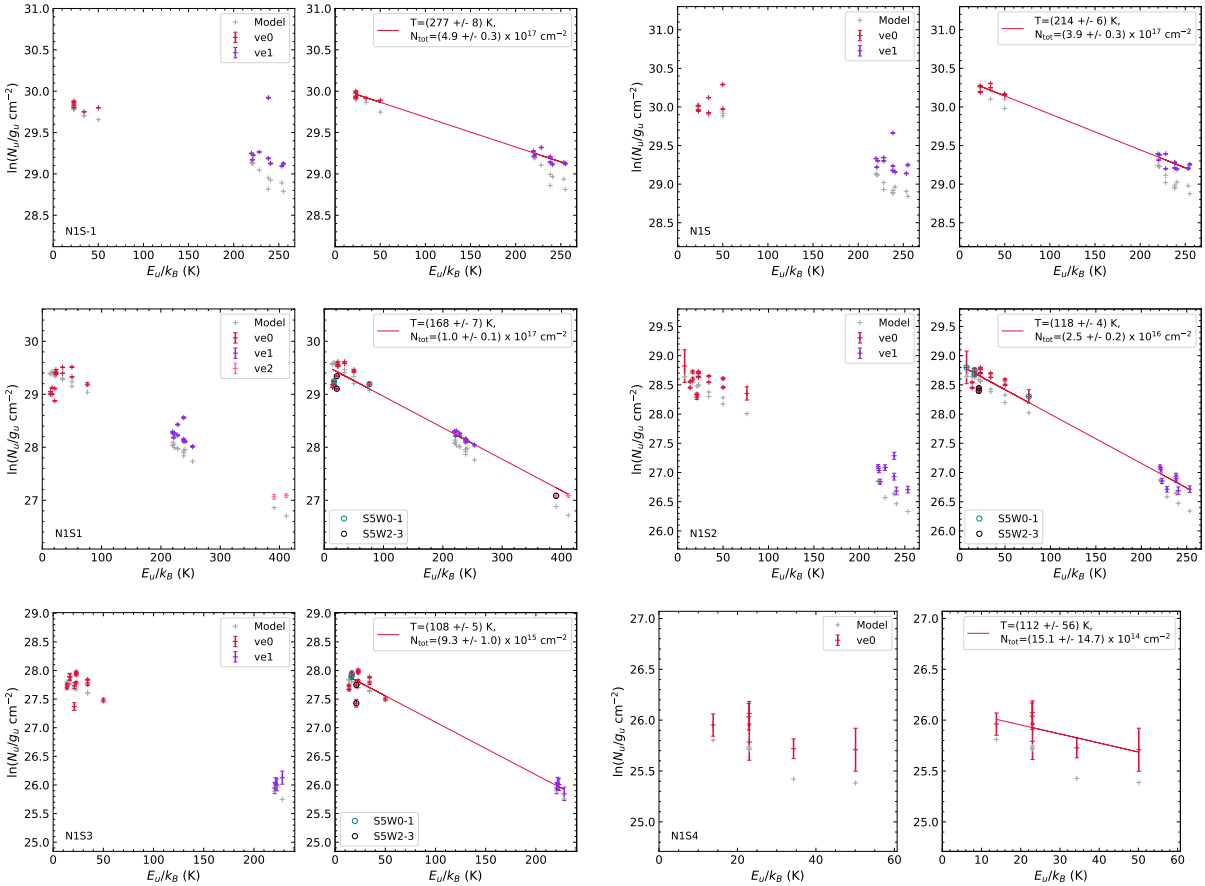

Fig. G.7. Same as Fig. G.1, but for CH_3CHO.

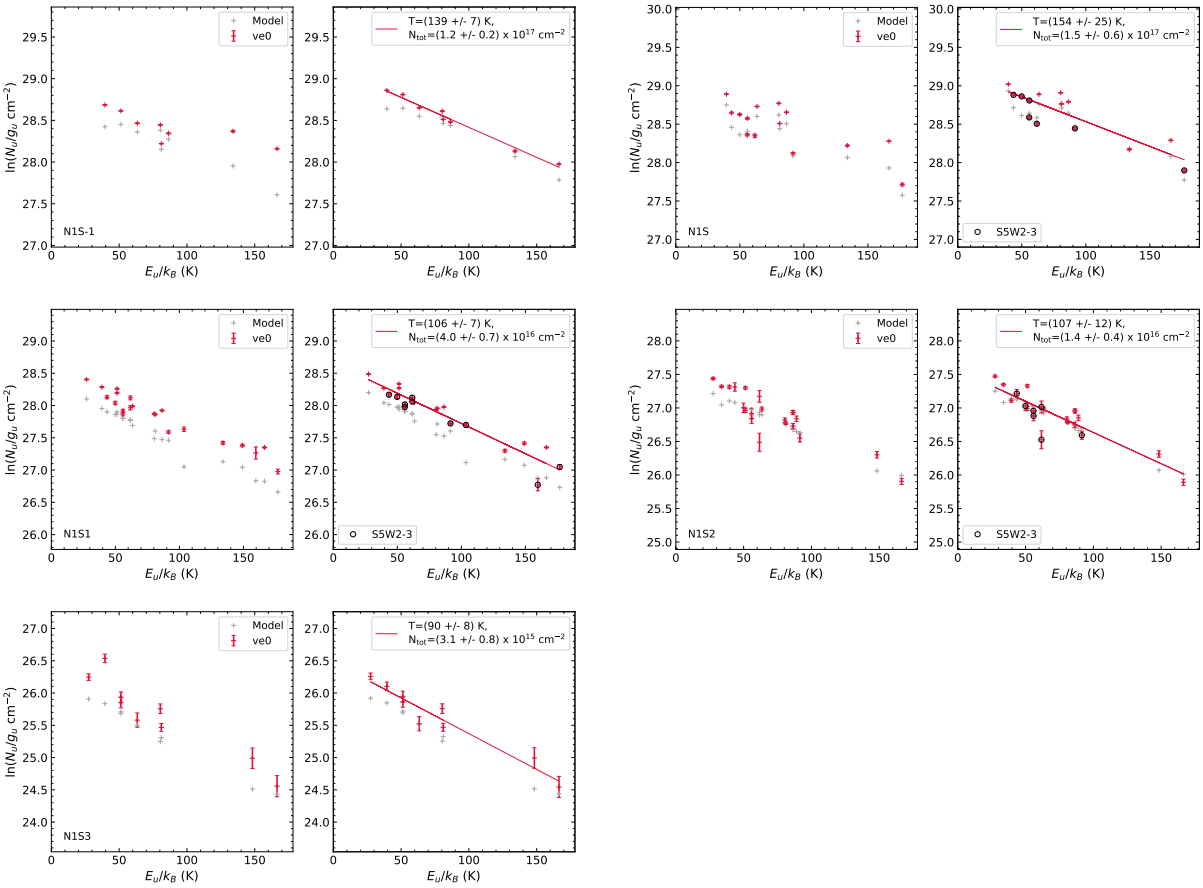

Fig. G.8. Same as Fig. G.1, but for CH_3NCO.

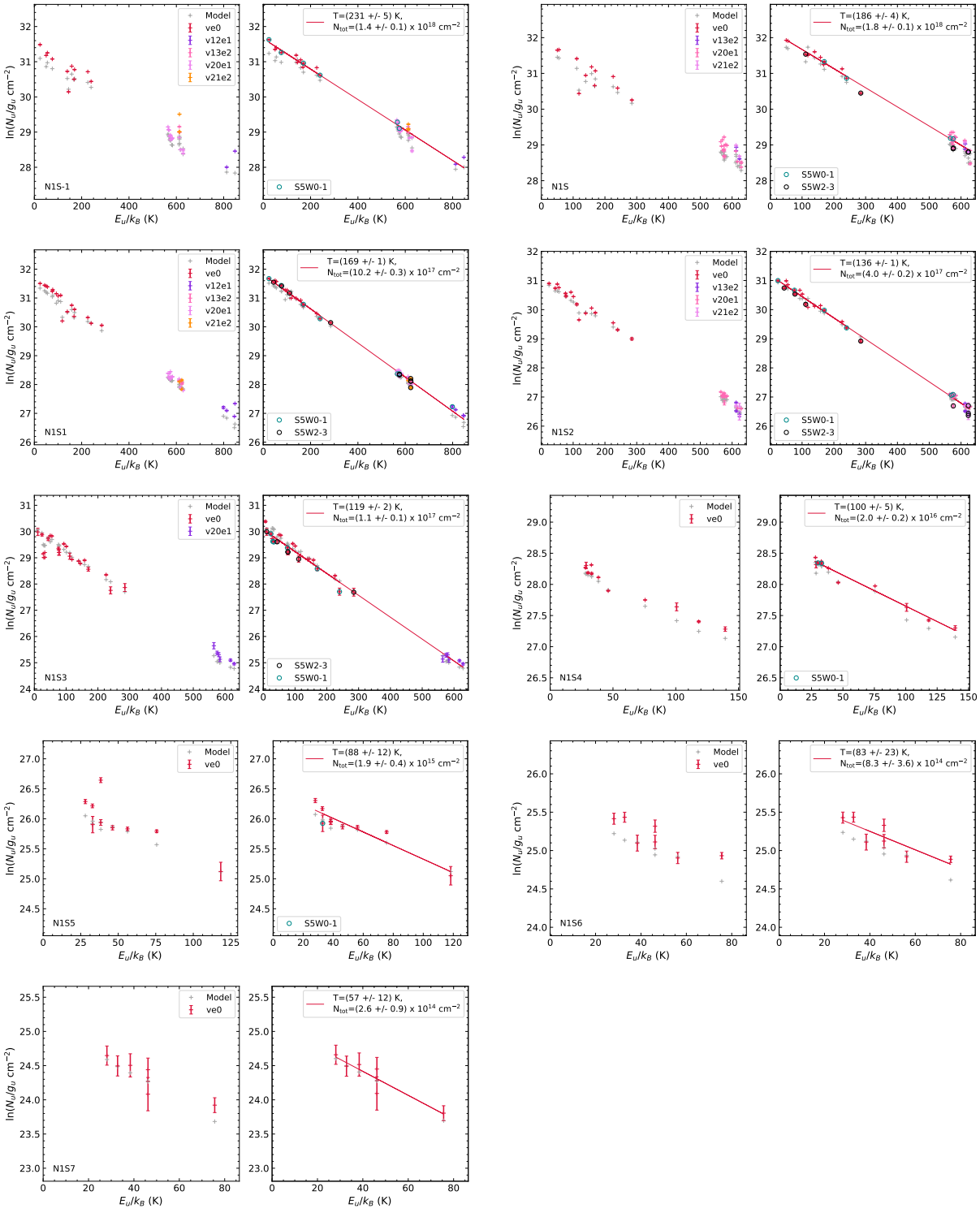

Fig. G.9. Same as Fig. G.1, but for C_2H_5CN.

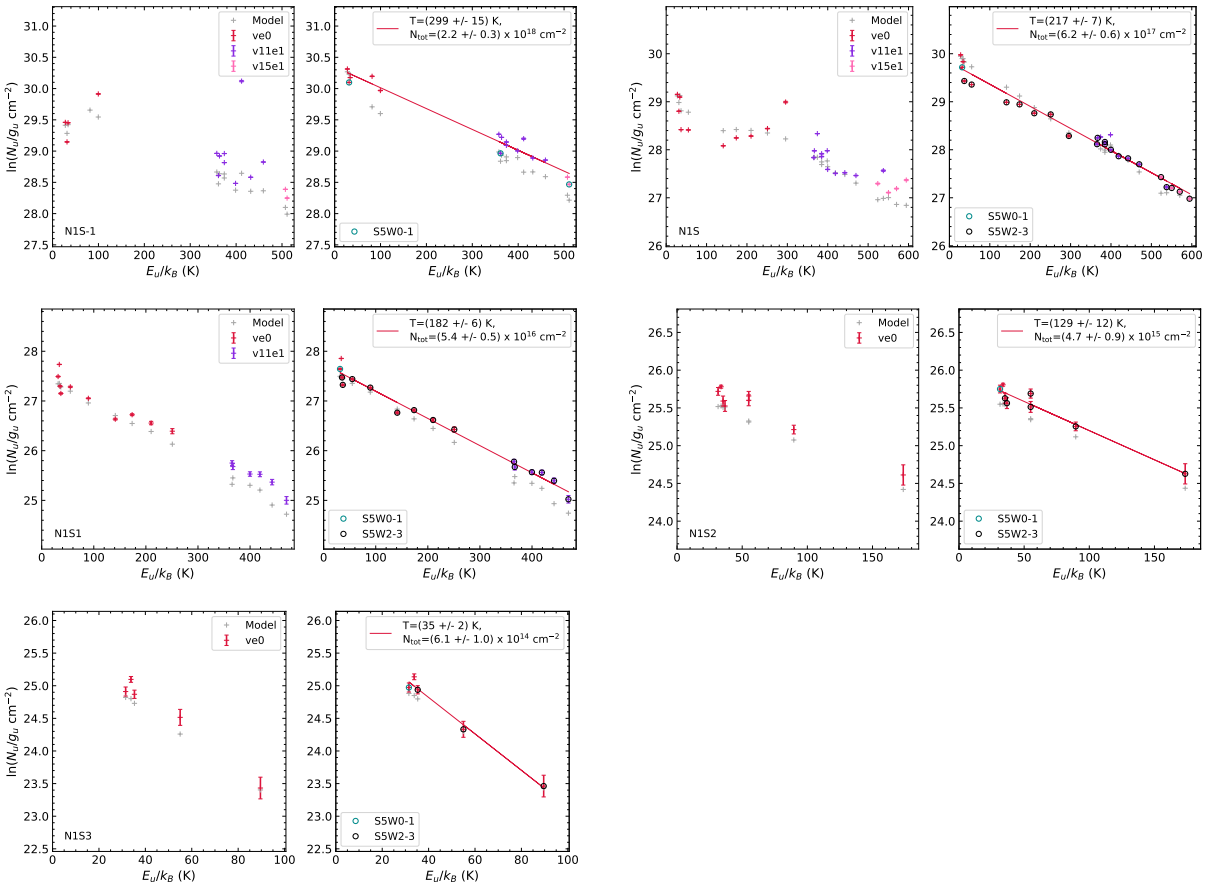

Fig. G.10. Same as Fig. G.1, but for C_2H_3CN.

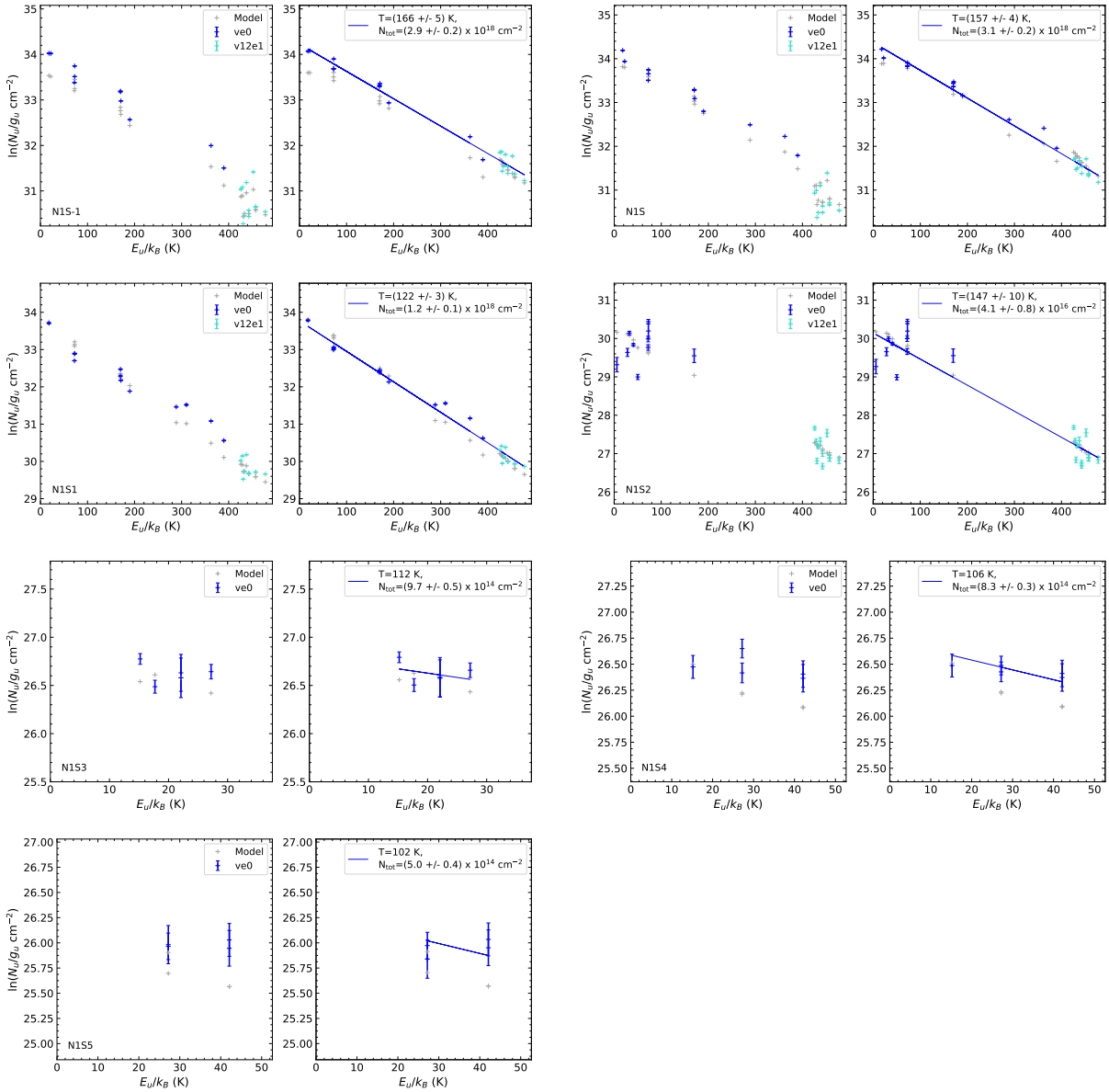

Fig. G.11. Same as Fig. G.1, but for NH_2CHO.

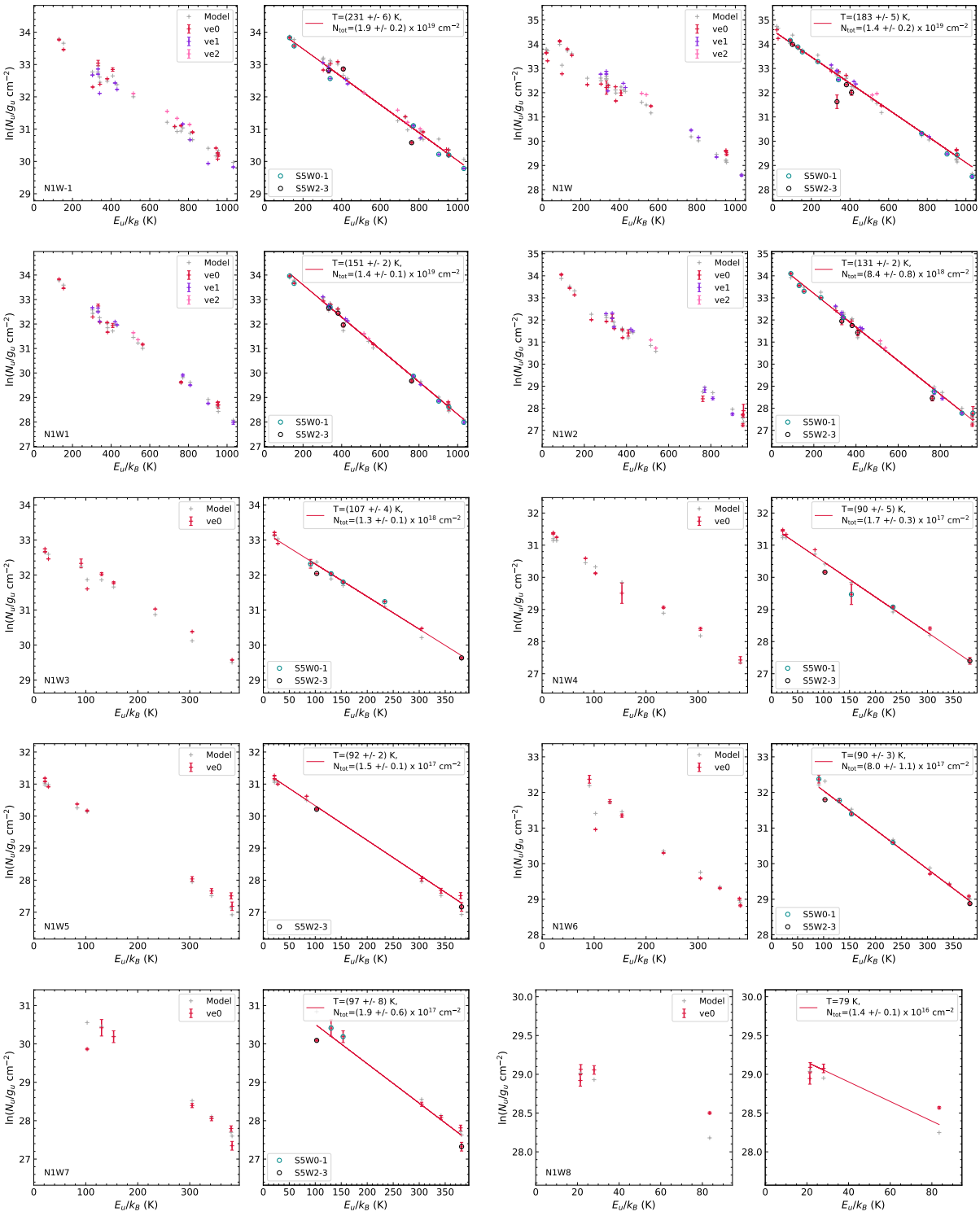

Fig. G.12. Same as Fig. G.1, but for all positions to the west where the molecule is detected.

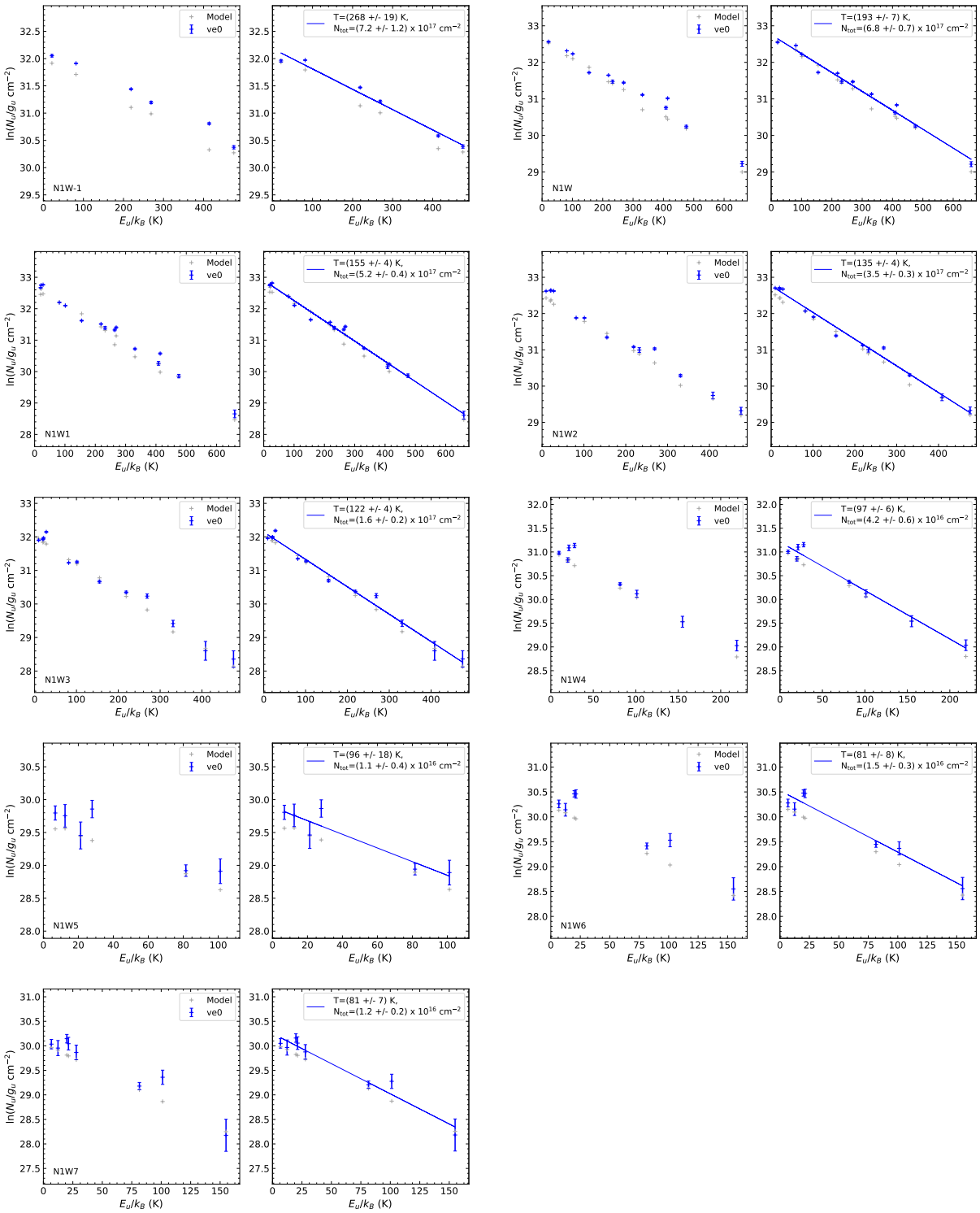

Fig. G.13. Same as Fig. G.1, but for $^{13}CH_3OH$ and for all positions to the west where the molecule is detected, except that setups 1–3 had to be used due to lack of transitions in setups 4–5. The linear fit to observed data points is shown in blue.

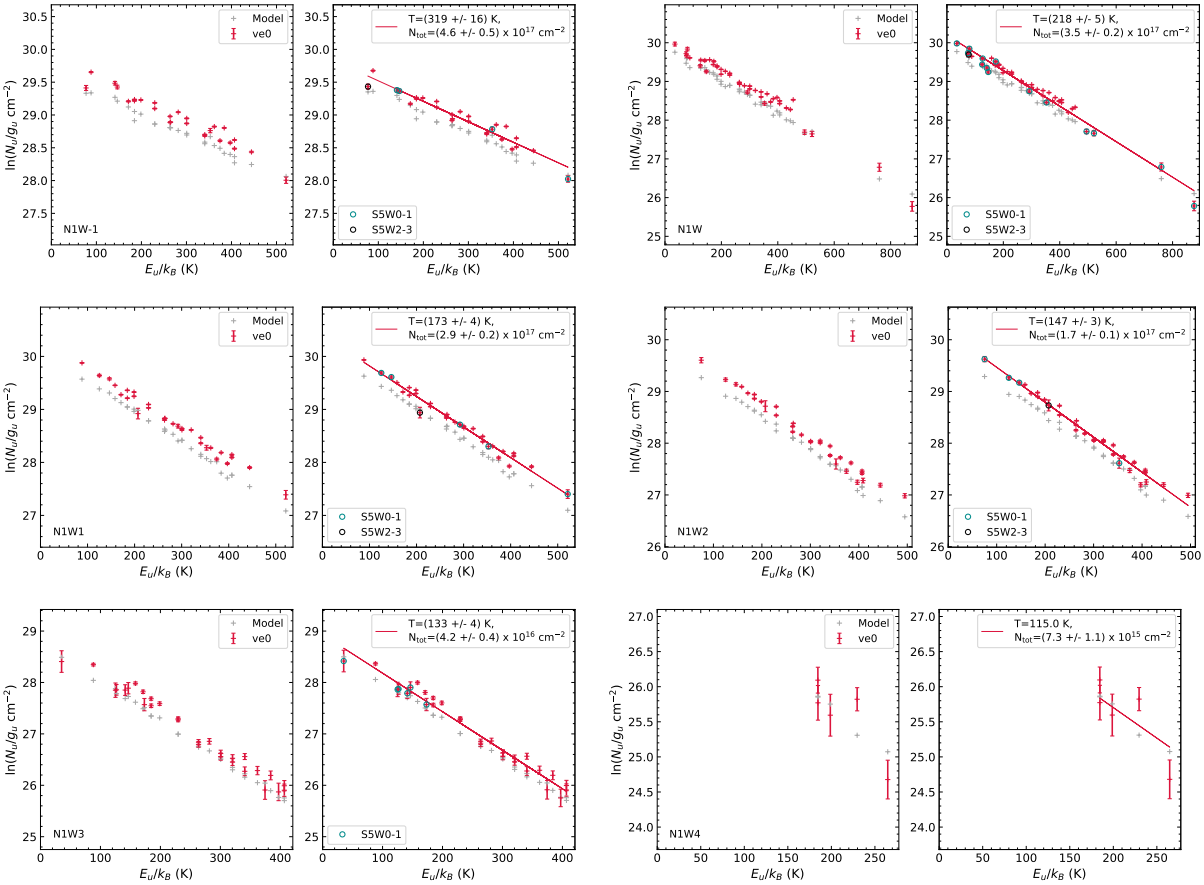

Fig. G.14. Same as Fig. G.1, but for C_2H_5OH and for all positions to the west where the molecule is detected.

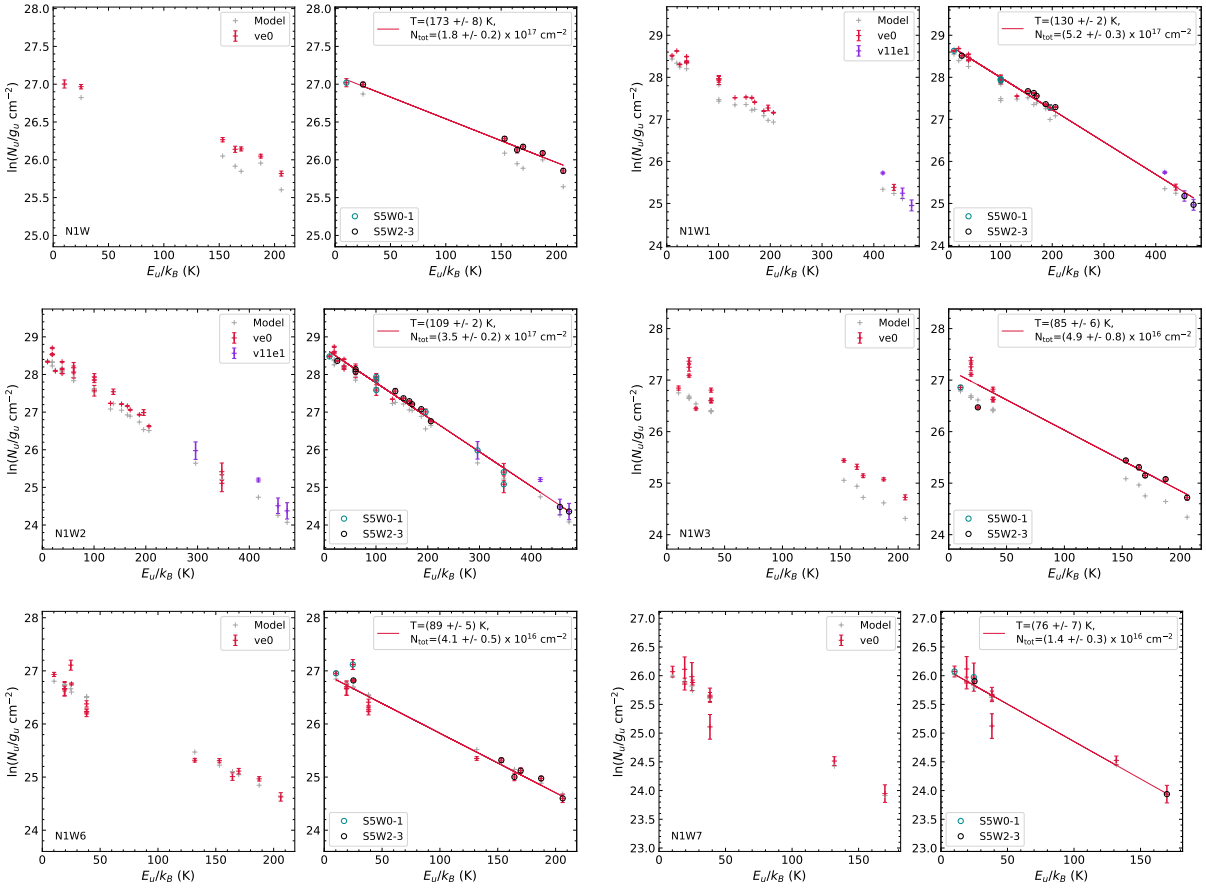

Fig. G.15. Same as Fig. G.1, but for CH_3OCH_3 and for all positions to the west where the molecule is detected.

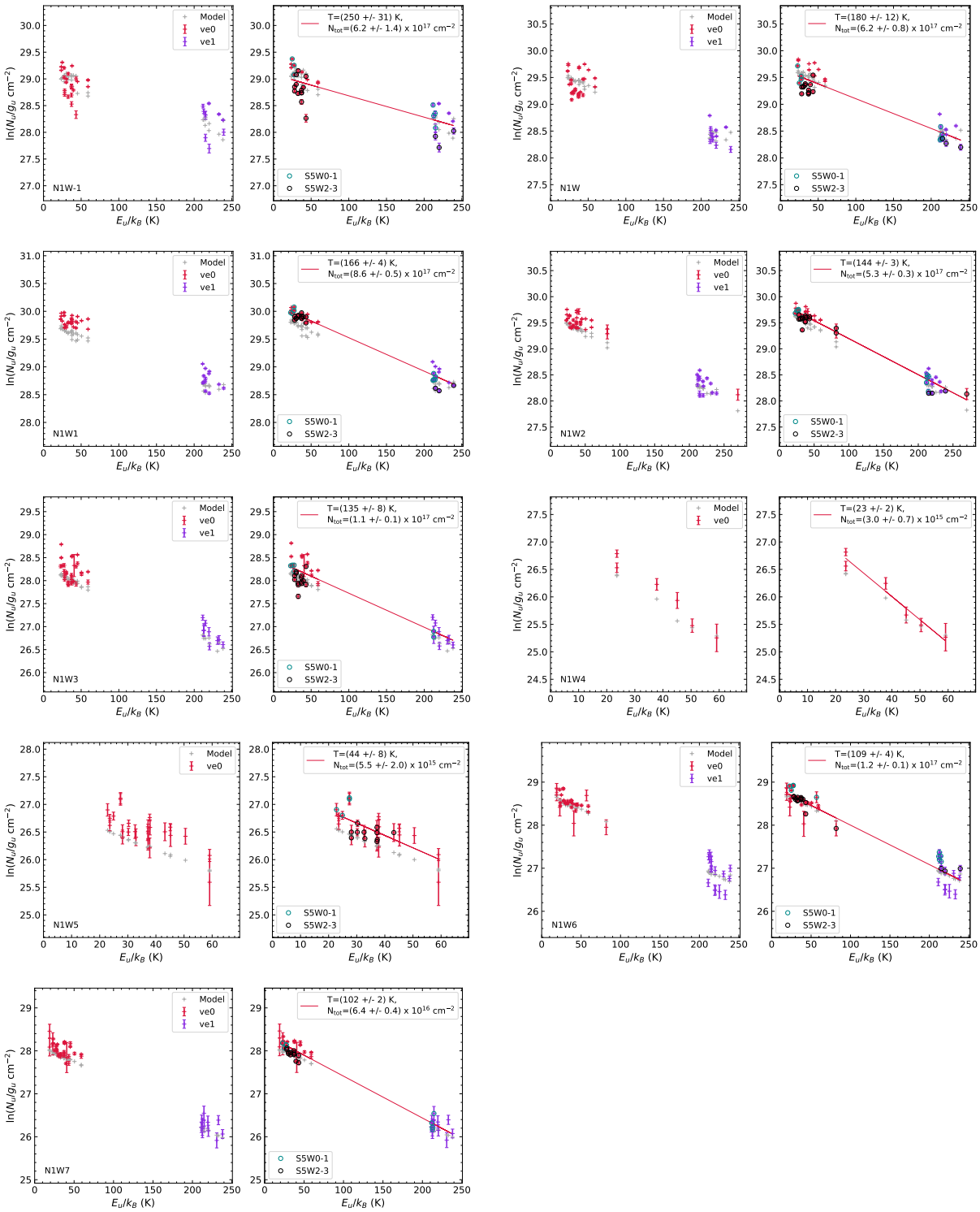

Fig. G.16. Same as Fig. G.1, but for CH_3OCHO and for all positions to the west where the molecule is detected.

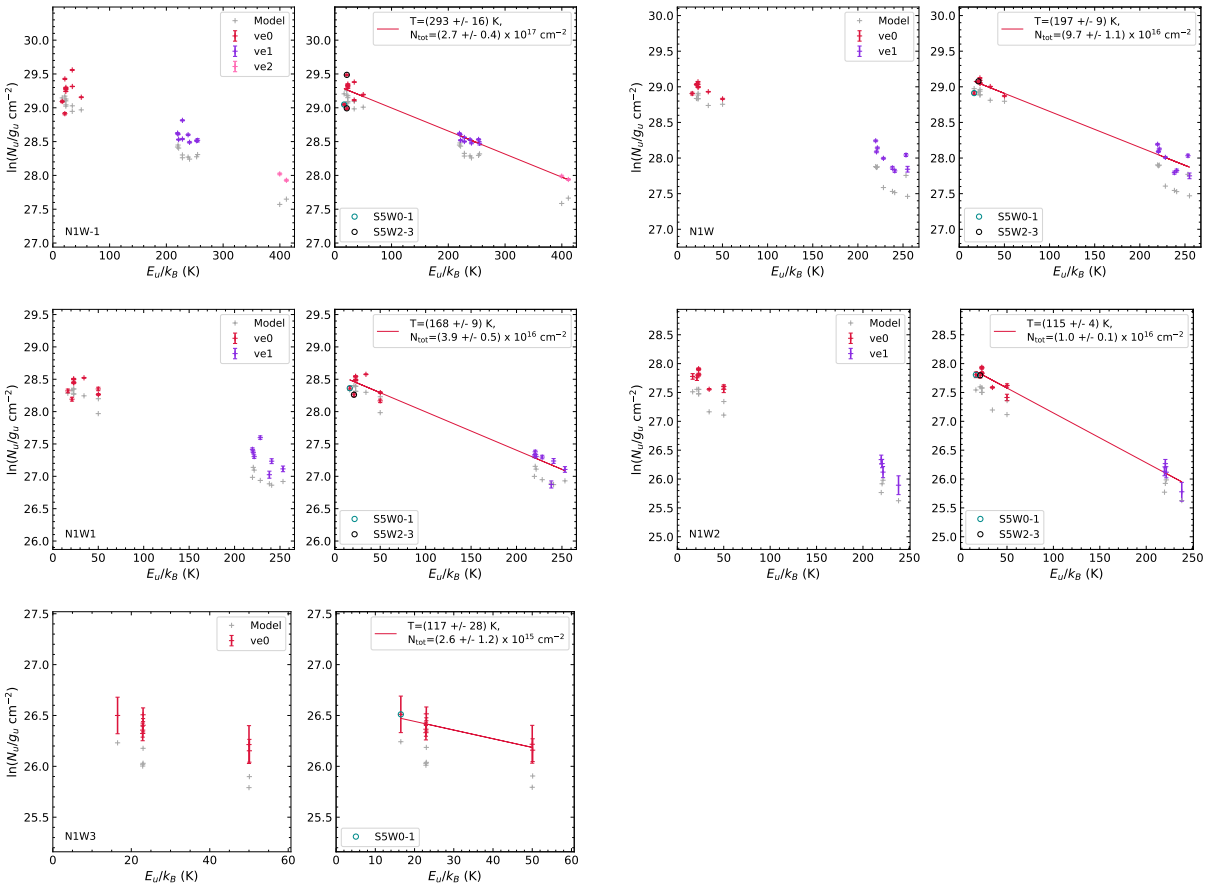

Fig. G.17. Same as Fig. G.1, but for CH_3CHO and for all positions to the west where the molecule is detected.

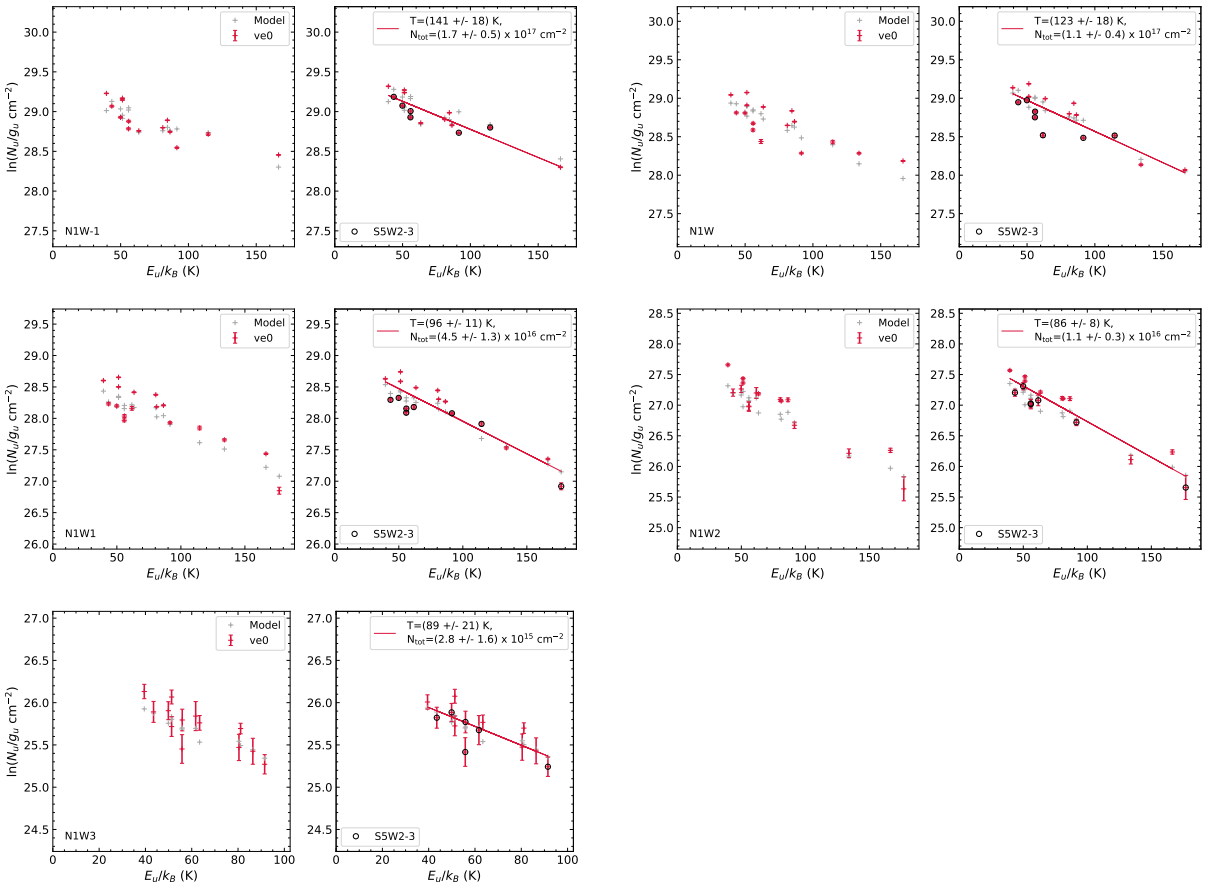

Fig. G.18. Same as Fig. G.1, but for CH_3NCO and for all positions to the west where the molecule is detected.

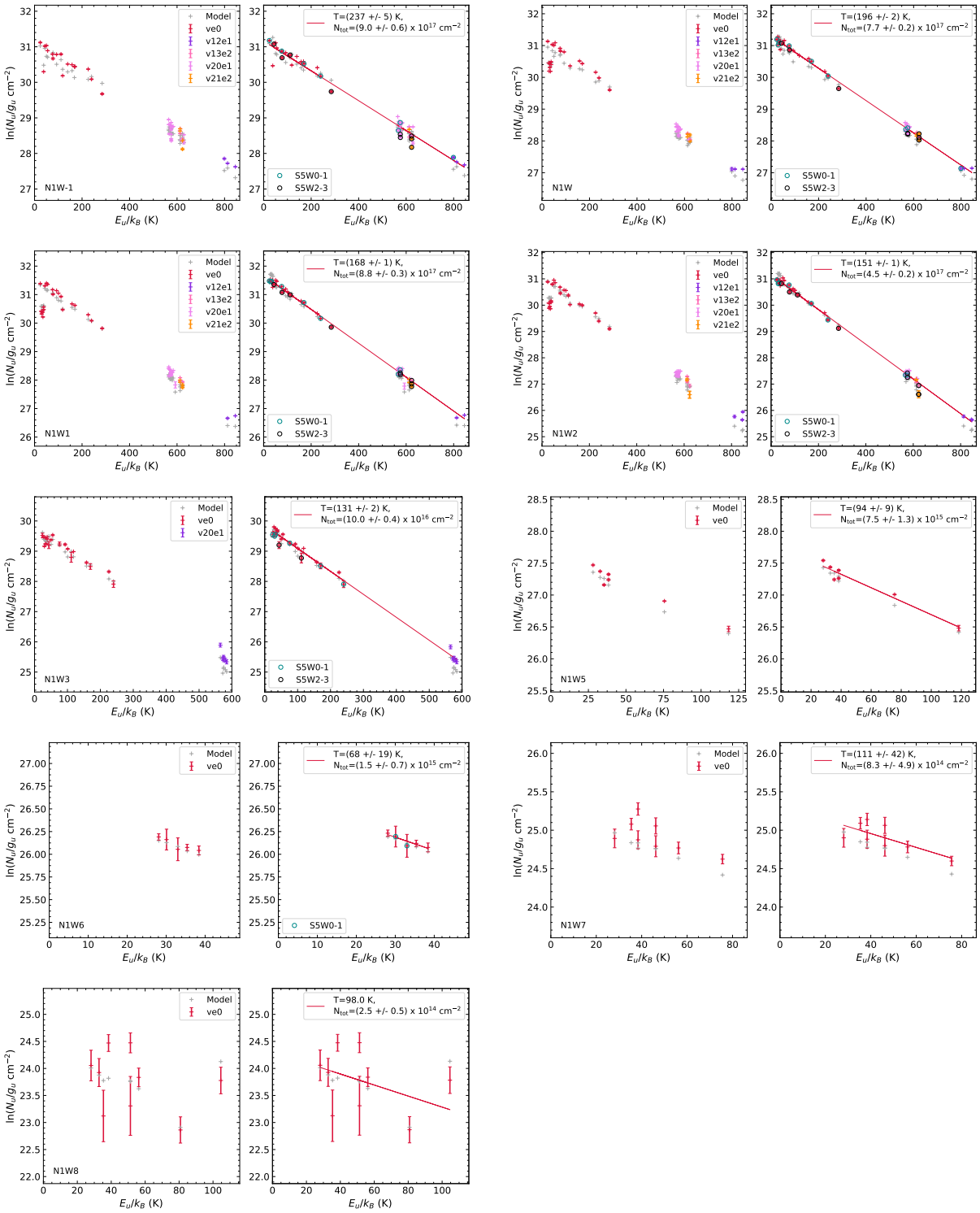

Fig. G.19. Same as Fig. G.1, but for C_2H_5CN and for all positions to the west where the molecule is detected.

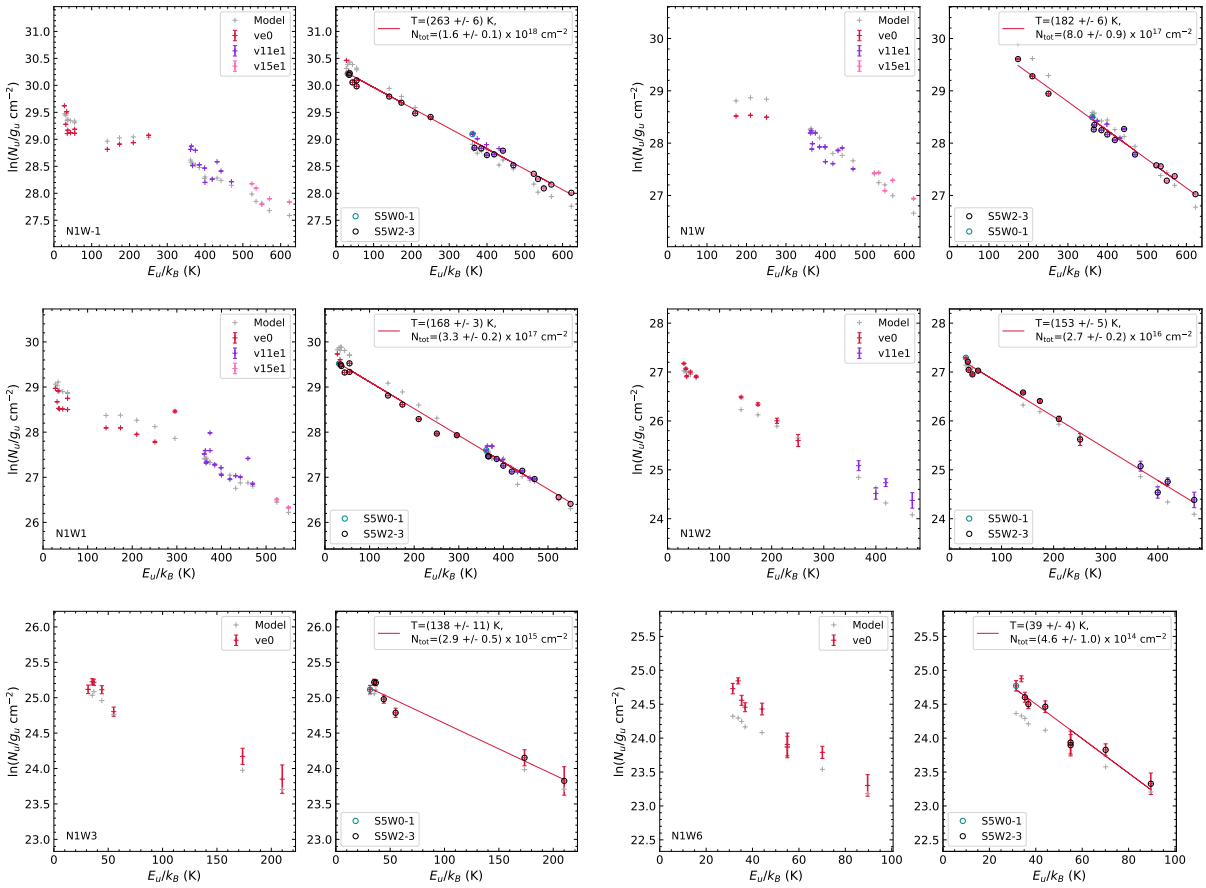

Fig. G.20. Same as Fig. G.1, but for C_2H_3CN and for all positions to the west where the molecule is detected.

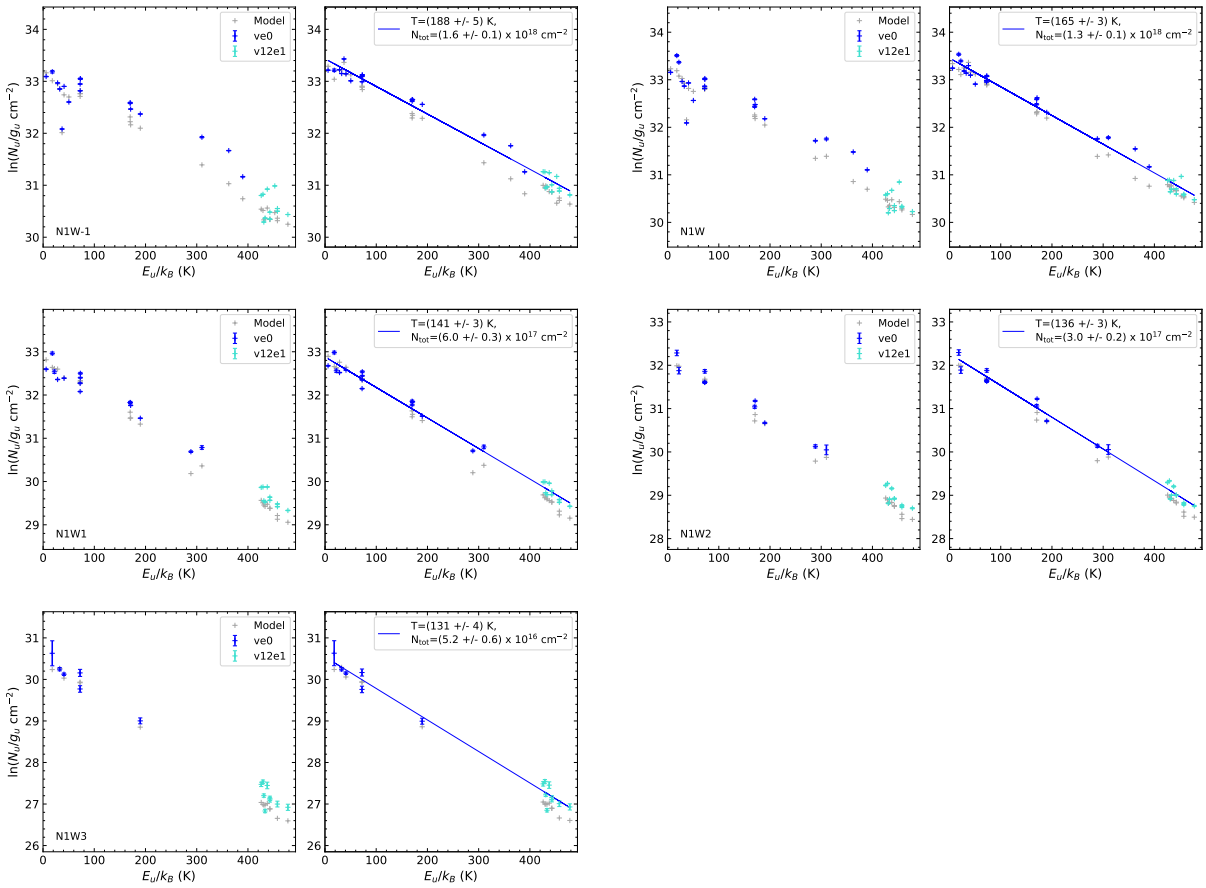

Fig. G.21. Same as Fig. G.1, but for NH_2CHO.

B

Appendix to Chapter 4

B.1 Population diagrams

In Paper I, we derived population diagrams of ten COMs towards multiple positions south- and westwards from the centre of the hot core. In order to compare the results derived here and those for position N1S, we had to derive a few additional population diagrams for HC_3N, HNCO, and CH_3SH towards this position, which were not analysed in Paper I, and show them in Fig. B.1. Population diagrams of various molecules towards N1SE1 are presented in Fig. B.2 and towards N1NW3 in Fig. B.3.

B.2 Additional tables

Tables B.1–B.4 summarise the parameters of the LTE radiative-transfer modelling performed with Weeds and of the population-diagram analysis for each COM and each of the four velocity components, respectively.

B.3 LVINE maps for outflow emission

B.3.1 Integration strategy

Visualising the outflow emission is challenging due to the pervasive line emission close to the hot core's centre that can lead to contamination and the, in some cases, complex line profiles. For each molecule, we made use of two transitions of similar upper-level energies and Einstein A coefficients, because these have similar intensities. The transitions with their properties are listed in Table B.5. By comparing both spectra, we can thus identify emission that comes from other molecules, based on the assumption that such contaminating emission is unlikely to appear at exactly the same velocities in both spectra, as illustrated in Fig. 4.5. We compared the spectra of both transitions over an area of $8'' \times 4''$ around Sgr B2 (N1) by extracting spectra every $0.5''$. Although these transitions were taken from the higher angular-resolution setups 4 and 5, the mean beam sizes can still vary by up to a factor of 1.6 in size or 2.8 in area. Therefore, in the cases where the two selected transitions are covered in two different data cubes, the cube of higher angular resolution was smoothed with a two-dimensional Gaussian kernel to the resolution of the other cube. Overplotting both spectra within

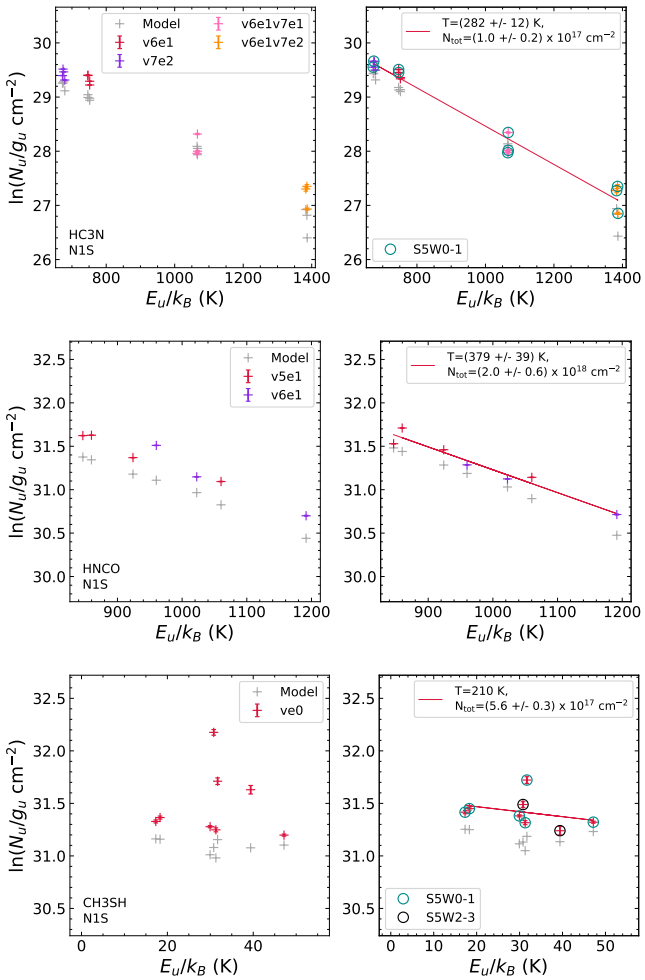

Figure B.1: Population diagrams for HC_3N, HNCO, and CH_3SH at position N1S. Observed data points are shown in various colours as indicated in the top-right corner of the respective left plot, while synthetic data points are shown in grey. No corrections are applied in the respective left panels, while in the right plots corrections for opacity and contamination by other molecules have been considered for both the observed and synthetic populations. The red line is a linear fit to all observed data points (in linear-logarithmic space), where for CH_3SH the temperature was fixed. The results of the fits are shown in the respective right panels. Teal and black circles show observed data points from spectral windows 0–1 and 2–3 of observational setup 5, respectively, as indicated in the bottom-left corner in the right panels.

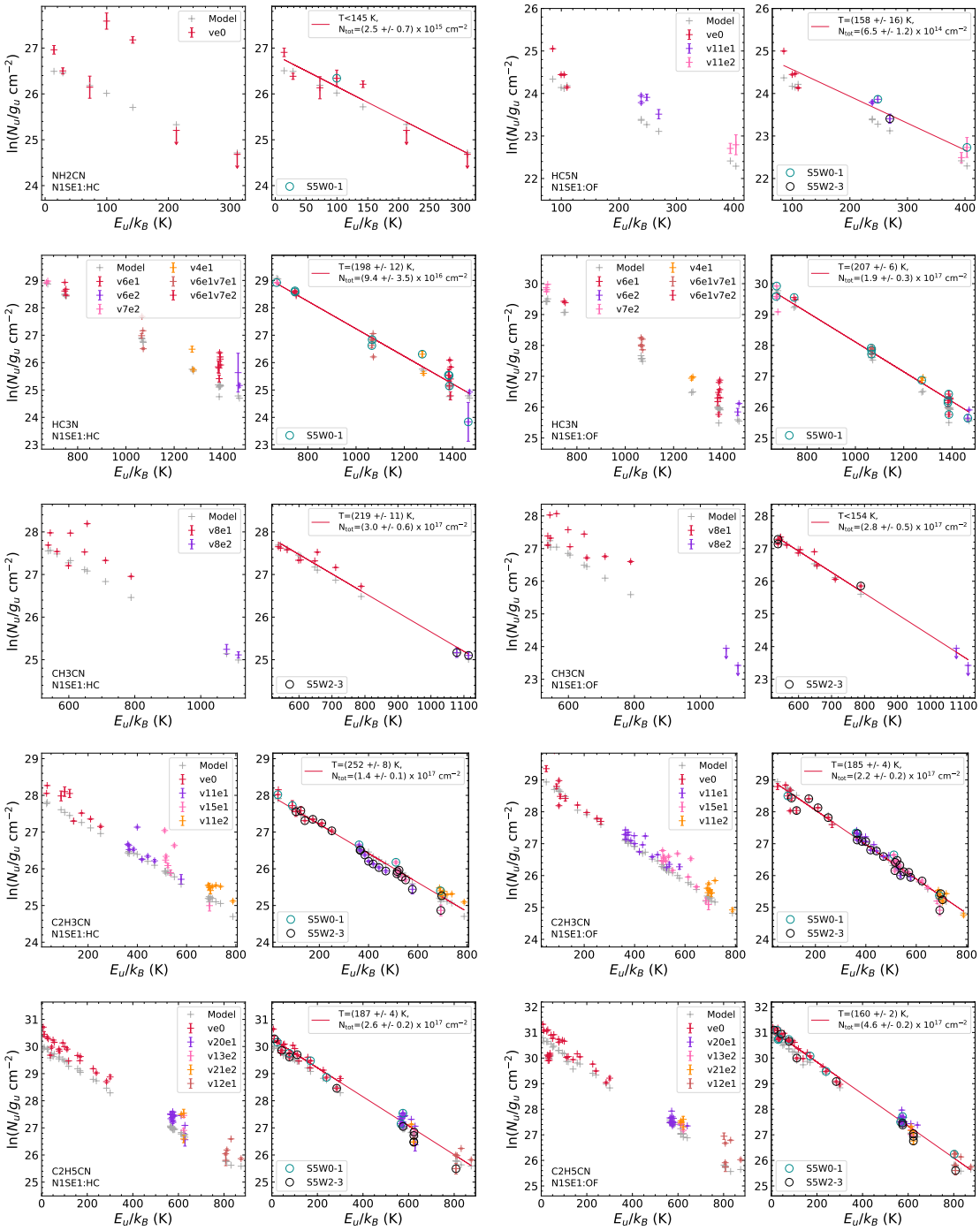

Figure B.2: Same as Fig. B.1, but for multiple molecules at position N1SE1 for the hot-core component (N1SE1:HC) and the outflow component (N1SE1:OF).

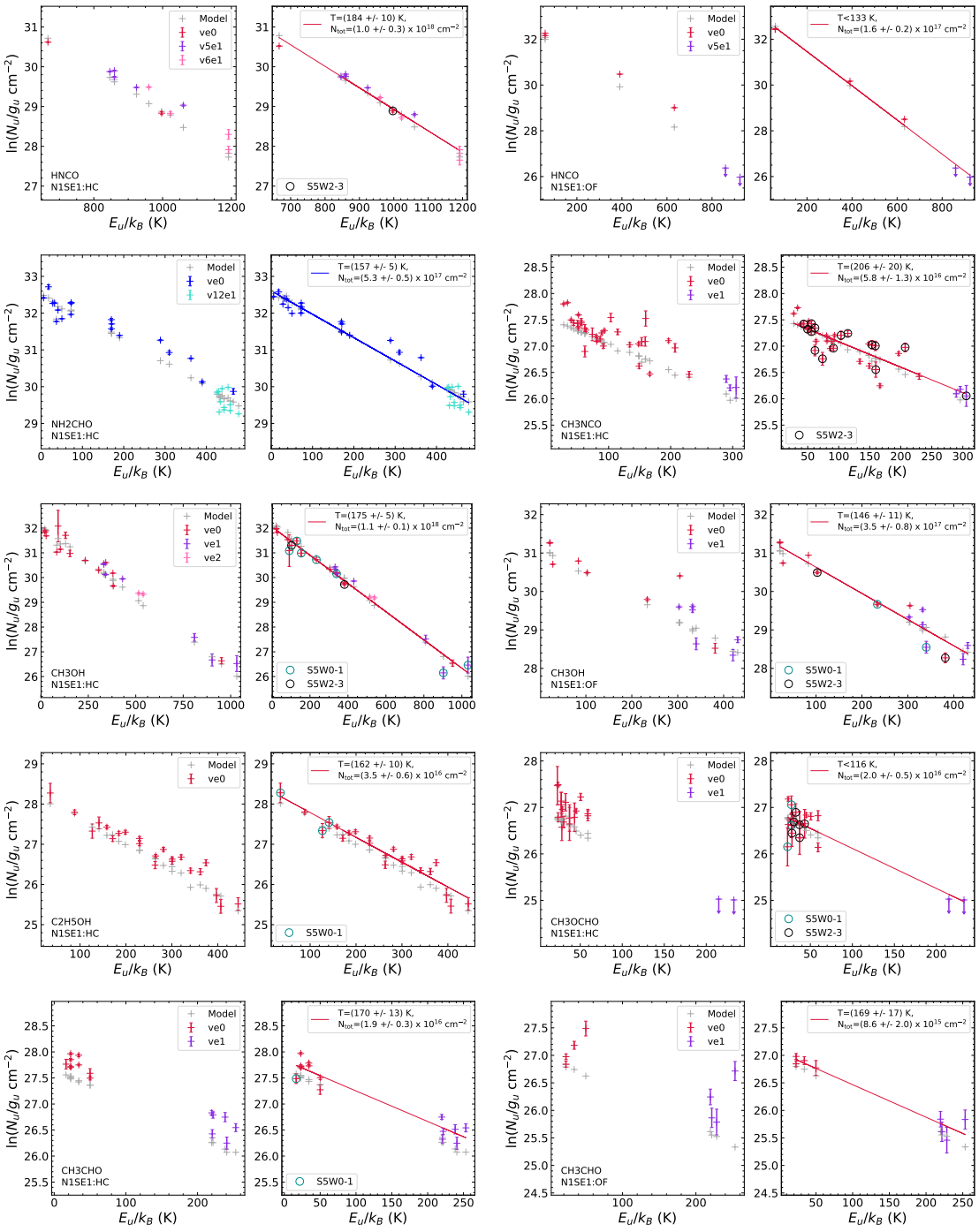

Figure B.2: continued.

Table B.1: Weeds parameters used at N1SE1:HC and results obtained from the population diagrams.

Molecule[a]	Size[b] ($''$)	$T_{\rm rot,W}$[c] (K)	$T_{\rm rot,pd}$[d] (K)	$N_{\rm W}$[e] ($\rm cm^{-2}$)	$C_{\rm vib,W}$[f]	$N_{\rm pd}$[g] ($\rm cm^{-2}$)	$C_{\rm vib,pd}$[h]	Δv[i] ($\rm km\,s^{-1}$)	$v_{\rm off}$[j] ($\rm km\,s^{-1}$)
HC_5N, $v=0$	2.0	180	–	$\leq 3.2(14)$	4.56	–	–	4.6	1.5
HC_3N, $v=0$	2.0	190	198 ± 12	1.9(17)	1.60	$(1.6\pm0.6)(17)$	1.67	5.5	1.0
$v_7=1$	2.0	190	198 ± 12	1.9(17)	1.60	$(1.6\pm0.6)(17)$	1.67	5.5	1.0
$v_7=2$	2.0	190	198 ± 12	1.9(17)	1.60	$(1.6\pm0.6)(17)$	1.67	5.5	1.0
$v_6=1$	2.0	190	198 ± 12	1.9(17)	1.60	$(1.6\pm0.6)(17)$	1.67	5.5	1.0
$v_6=2$	2.0	190	198 ± 12	1.9(17)	1.60	$(1.6\pm0.6)(17)$	1.67	5.5	1.0
$v_4=1$	2.0	190	198 ± 12	1.9(17)	1.60	$(1.6\pm0.6)(17)$	1.67	5.5	1.0
$v_6=1, v_7=1$	2.0	190	198 ± 12	1.9(17)	1.60	$(1.6\pm0.6)(17)$	1.67	6.0	1.2
$v_6=1, v_7=2$	2.0	190	198 ± 12	1.9(17)	1.60	$(1.6\pm0.6)(17)$	1.67	5.5	1.0
CH_3CN, $v=0$	2.0	220	219 ± 11	2.8(17)	1.00	$(3.0\pm0.6)(17)$	1.00	5.5	1.6
$v_8=1$	2.0	220	219 ± 11	2.8(17)	1.00	$(3.0\pm0.6)(17)$	1.00	5.5	1.6
$v_8=2$	2.0	220	219 ± 11	2.8(17)	1.00	$(3.0\pm0.6)(17)$	1.00	5.5	1.6
C_2H_3CN, $v=0$	2.0	250	252 ± 8	1.6(17)	1.09	$(1.5\pm0.1)(17)$	1.09	5.5	1.0
$v_{11}=1$	2.0	250	252 ± 8	1.6(17)	1.09	$(1.5\pm0.1)(17)$	1.09	5.5	1.0
$v_{15}=1$	2.0	250	252 ± 8	1.6(17)	1.09	$(1.5\pm0.1)(17)$	1.09	5.5	1.0
$v_{11}=2$	2.0	250	252 ± 8	1.6(17)	1.09	$(1.5\pm0.1)(17)$	1.09	5.5	1.0
C_2H_5CN, $v=0$	2.0	190	187 ± 4	3.8(17)	1.73	$(4.4\pm0.3)(17)$	1.70	5.0	1.0
$v_{20}=1$	2.0	190	187 ± 4	3.8(17)	1.73	$(4.4\pm0.3)(17)$	1.70	5.0	1.0
$v_{13}=2$	2.0	190	187 ± 4	3.8(17)	1.73	$(4.4\pm0.3)(17)$	1.70	5.0	1.0
$v_{21}=2$	2.0	190	187 ± 4	3.8(17)	1.73	$(4.4\pm0.3)(17)$	1.70	5.0	1.0
$v_{12}=1$	2.0	190	187 ± 4	3.8(17)	1.73	$(4.4\pm0.3)(17)$	1.70	5.0	1.0
NH_2CN, $v=0$	2.0	160	≤ 145	2.6(15)	1.03	$(2.5\pm0.7)(15)$	1.02	4.6	2.2
HNCO, $v=0$	2.0	180	184 ± 10	1.2(18)	1.02	$(1.0\pm0.3)(18)$	1.02	4.5	2.5
$v_5=1$	2.0	180	184 ± 10	1.2(18)	1.02	$(1.0\pm0.3)(18)$	1.02	4.5	2.5
$v_6=1$	2.0	180	184 ± 10	1.2(18)	1.02	$(1.0\pm0.3)(18)$	1.02	4.5	2.5
NH_2CHO, $v=0$	2.0	160	157 ± 5	6.0(17)	1.09	$(5.7\pm0.5)(17)$	1.08	5.5	1.5
$v_{12}=1$	2.0	160	157 ± 5	6.0(17)	1.09	$(5.7\pm0.5)(17)$	1.08	5.5	1.5
CH_3NCO, $v=0$	2.0	200	206 ± 20	5.5(16)	1.00	$(5.8\pm1.3)(16)$	1.00	4.0	2.3
$v=1$	2.0	200	206 ± 20	5.5(16)	1.00	$(5.8\pm1.3)(16)$	1.00	4.0	2.3
CH_3OH, $v=0$	2.0	170	175 ± 5	1.2(18)	1.00	$(1.1\pm0.1)(18)$	1.00	4.5	2.2
$v=1$	2.0	170	175 ± 5	1.2(18)	1.00	$(1.1\pm0.1)(18)$	1.00	4.5	2.2
$v=2$	2.0	170	175 ± 5	1.2(18)	1.00	$(1.1\pm0.1)(18)$	1.00	4.5	2.2
C_2H_5OH, $v=0$	2.0	160	162 ± 10	4.4(16)	1.38	$(4.9\pm0.8)(16)$	1.39	3.7	1.7
CH_3OCH_3, $v=0$	2.0	180	–	$\leq 4.1(16)$	1.03	–	–	4.6	1.5
CH_3OCHO, $v=0$	2.0	115	≤ 116	2.2(16)	1.08	$(2.2\pm0.5)(16)$	1.08	3.0	2.8
CH_3CHO, $v=0$	2.0	170	170 ± 13	3.6(16)	1.08	$(1.9\pm0.3)(16)$	1.02	4.5	1.2
$v=1$	2.0	170	170 ± 13	3.7(16)	1.08	$(1.9\pm0.3)(16)$	1.02	4.5	1.2
CH_3SH, $v=0$	2.0	115	115 ± 41	1.4(16)	1.08	$(1.1\pm0.7)(16)$	1.00	4.4	−0.5
OCS, $v=0$	2.0	215	216 ± 11	3.2(17)	1.07	$(3.1\pm0.4)(17)$	1.07	6.0	1.5
$v_2=1$	2.0	215	216 ± 11	3.2(17)	1.07	$(3.1\pm0.4)(17)$	1.07	6.0	1.5

Notes. [a] COMs and vibrational states used to derive population diagrams. [b] Assumed size of the emitting region. [c] Rotation temperature used for the Weeds model. [d] Rotation temperature derived from the population diagram. [e] Column density used for the Weeds model. [f] Vibrational state correction at temperature $T_{\rm rot,W}$ applied to the column density $N_{\rm W}$ when the partition function does not account for higher-excited vibrational states, where $C_{\rm vib,pd} = C_{\rm vib,pd}(T_{\rm rot,pd})$. [g] Column density derived from the population diagram. [h] Vibrational state correction at temperature $T_{\rm rot,pd}$ applied to N_{pd}, where $C_{\rm vib} = C_{\rm vib}(T_{\rm rot,pd})$. [i] Linewidths ($FWHM$) of the transitions. [j] Offset from the source systemic velocity, which was set to $62\,\rm km\,s^{-1}$.
Values in parentheses show the decimal power, where $x(z) = x\times10^{z}$ or $(x\pm y)(z) = (x\pm y)\times10^{z}$.
Upper limits on $N_{\rm W}$ indicate that a population diagram could not be derived, either because too many transitions are contaminated or the molecule is not detected. Then, the temperature, $FWHM$, and offset velocity values used in Weeds correspond to medians derived from other molecules at this position. Upper limits on $T_{\rm rot,pd}$ indicate when upper limits on integrated intensity for non-detected transitions are used in the population diagrams.

Table B.2: Same as Table B.1, but for position N1SE1:OF.

Molecule	Size ($''$)	$T_{\rm rot,W}$ (K)	$T_{\rm rot,pd}$ (K)	$N_{\rm W}$ ($\rm cm^{-2}$)	$C_{\rm vib,W}$	$N_{\rm pd}$ ($\rm cm^{-2}$)	$C_{\rm vib,pd}$	Δv ($\rm km\,s^{-1}$)	$v_{\rm off}$ ($\rm km\,s^{-1}$)
HC_5N, $v = 0$	2.0	160	158 ± 16	1.8(15)	3.53	(2.2 ± 0.4)(15)	3.44	4.5	−7.3
$v_{11} = 1$	2.0	160	158 ± 16	1.8(15)	3.53	(2.2 ± 0.4)(15)	3.44	4.5	−7.3
$v_{11} = 2$	2.0	160	158 ± 16	1.8(15)	3.53	(2.2 ± 0.4)(15)	3.44	4.5	−7.3
HC_3N, $v = 0$	2.0	200	207 ± 6	3.4(17)	1.69	(3.3 ± 0.5)(17)	1.76	6.5	−7.0
$v_7 = 1$	2.0	200	207 ± 6	3.4(17)	1.69	(3.3 ± 0.5)(17)	1.76	6.5	−7.0
$v_7 = 2$	2.0	200	207 ± 6	3.4(17)	1.69	(3.3 ± 0.5)(17)	1.76	6.5	−7.0
$v_6 = 1$	2.0	200	207 ± 6	3.4(17)	1.69	(3.3 ± 0.5)(17)	1.76	6.5	−7.0
$v_6 = 2$	2.0	200	207 ± 6	3.4(17)	1.69	(3.3 ± 0.5)(17)	1.76	6.5	−7.0
$v_4 = 1$	2.0	200	207 ± 6	3.4(17)	1.69	(3.3 ± 0.5)(17)	1.76	6.5	−7.0
$v_6 = 1, v_7 = 1$	2.0	200	207 ± 6	3.4(17)	1.69	(3.3 ± 0.5)(17)	1.76	6.5	−7.0
$v_6 = 1, v_7 = 2$	2.0	200	207 ± 6	3.4(17)	1.69	(3.3 ± 0.5)(17)	1.76	6.5	−7.0
CH_3CN, $v = 0$	2.0	160	154 ± 0	2.5(17)	1.00	(2.8 ± 0.5)(17)	1.00	6.5	−7.5
$v_8 = 1$	2.0	160	154 ± 0	2.5(17)	1.00	(2.8 ± 0.5)(17)	1.00	6.5	−7.5
$v_8 = 2$	2.0	160	154 ± 0	2.5(17)	1.00	(2.8 ± 0.5)(17)	1.00	6.5	−7.5
C_2H_3CN, $v = 0$	2.0	180	185 ± 4	2.6(17)	1.02	(2.2 ± 0.2)(17)	1.02	5.8	−6.5
$v_{11} = 1$	2.0	180	185 ± 4	2.6(17)	1.02	(2.2 ± 0.2)(17)	1.02	5.8	−6.5
$v_{15} = 1$	2.0	180	185 ± 4	2.6(17)	1.02	(2.2 ± 0.2)(17)	1.02	5.8	−6.5
$v_{11} = 2$	2.0	180	185 ± 4	2.6(17)	1.02	(2.2 ± 0.2)(17)	1.02	5.8	−6.5
C_2H_5CN, $v = 0$	2.0	160	160 ± 2	4.1(17)	1.02	(6.7 ± 0.3)(17)	1.46	6.5	−7.5
$v_{20} = 1$	2.0	160	160 ± 2	4.1(17)	1.02	(6.7 ± 0.3)(17)	1.46	6.5	−7.5
$v_{13} = 2$	2.0	160	160 ± 2	4.1(17)	1.02	(6.7 ± 0.3)(17)	1.46	6.5	−7.5
$v_{21} = 2$	2.0	160	160 ± 2	4.1(17)	1.02	(6.7 ± 0.3)(17)	1.46	6.5	−7.5
$v_{12} = 1$	2.0	160	160 ± 2	4.1(17)	1.02	(6.7 ± 0.3)(17)	1.46	6.5	−7.5
NH_2CN, $v = 0$	2.0	160	–	≤ 4.1(14)	1.03	–	–	6.5	−7.5
HNCO, $v = 0$	2.0	135	≤ 133	1.6(17)	1.00	(1.6 ± 0.2)(17)	1.00	6.5	−7.5
*NH_2CHO, $v = 0$	2.0	160	–	6.5(15)	1.09	–	–	6.0	−6.5
CH_3NCO, $v = 0$	2.0	160	–	≤ 6.0(15)	1.00	–	–	6.5	−7.5
CH_3OH, $v = 0$	2.0	160	146 ± 11	4.0(17)	1.00	(3.5 ± 0.8)(17)	1.00	5.2	−9.8
$v = 1$	2.0	160	146 ± 11	4.0(17)	1.00	(3.5 ± 0.8)(17)	1.00	5.2	−9.8
C_2H_5OH, $v = 0$	2.0	160	–	≤ 1.4(16)	1.38	–	–	6.3	−7.5
CH_3OCH_3, $v = 0$	2.0	160	–	≤ 2.0(16)	1.02	–	–	6.35	−7.5
CH_3OCHO, $v = 0$	2.0	160	–	≤ 1.2(16)	1.24	–	–	6.5	−7.5
CH_3CHO, $v = 0$	2.0	160	169 ± 17	1.5(16)	1.01	(8.7 ± 2.0)(15)	1.02	5.0	−9.3
$v = 1$	2.0	160	169 ± 17	1.5(16)	1.01	(8.7 ± 2.0)(15)	1.02	5.0	−9.3
CH_3SH, $v = 0$	2.0	125	124 ± 25	5.0(16)	1.00	(4.8 ± 1.8)(16)	1.00	6.0	−7.8
OCS, $v = 0$	2.0	170	175 ± 8	3.1(17)	1.03	(3.8 ± 0.5)(17)	1.03	6.5	−7.5
$v_2 = 1$	2.0	170	175 ± 8	3.1(17)	1.03	(3.8 ± 0.5)(17)	1.03	6.5	−7.5

Notes.* The molecule is detected but a population diagram could not be derived due to contamination by the hot-core component.

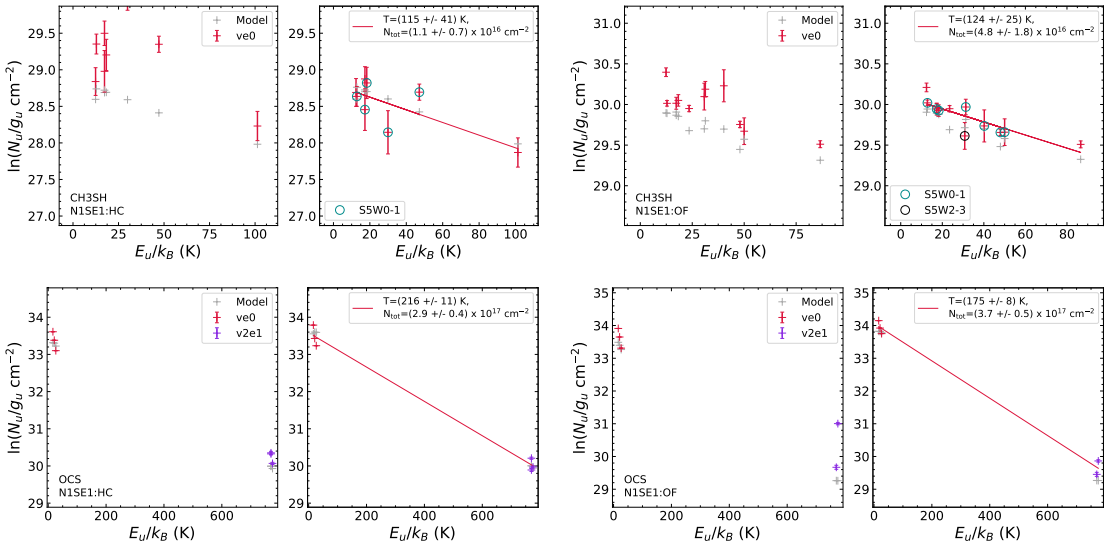

Figure B.2: continued.

Table B.3: Same as Table B.1, but for position N1NW3:HC.

Molecule	Size ($''$)	$T_{\rm rot,W}$ (K)	$T_{\rm rot,pd}$ (K)	$N_{\rm W}$ ($\rm cm^{-2}$)	$C_{\rm vib,W}$	$N_{\rm pd}$ ($\rm cm^{-2}$)	$C_{\rm vib,pd}$	Δv ($\rm km\,s^{-1}$)	$v_{\rm off}$ ($\rm km\,s^{-1}$)
HC_5N, $v=0$	2.0	128	–	$\leq 7.2(13)$	2.39	–	–	4.3	2.5
HC_3N, $v=0$	2.0	140	143 ± 24	6.3(14)	1.26	$(7.5\pm2.5)(14)$	1.27	3.3	2.5
$v_7=1$	2.0	140	143 ± 24	6.3(14)	1.26	$(7.5\pm2.5)(14)$	1.27	3.3	2.5
CH_3CN, $v=0$	2.0	130	126 ± 6	8.0(16)	1.00	$(8.9\pm2.2)(16)$	1.00	4.3	2.5
$v_8=1$	2.0	130	126 ± 6	8.0(16)	1.00	$(8.9\pm2.2)(16)$	1.00	4.3	2.5
C_2H_3CN, $v=0$	2.0	128	–	$\leq 4.0(14)$	1.00	–	–	4.3	2.5
C_2H_5CN, $v=0$	2.0	125	≤ 122	3.1(16)	1.23	$(2.9\pm0.2)(16)$	1.21	5.7	2.4
NH_2CN, $v=0$	2.0	128	–	$\leq 3.5(14)$	1.01	–	–	4.3	2.5
HNCO, $v=0$	2.0	130	120 ± 5	3.5(15)	1.00	$(3.2\pm0.3)(15)$	1.00	5.0	2.8
NH_2CHO, $v=0$	2.0	125	≤ 125	2.7(15)	1.00	$(3.4\pm0.3)(15)$	1.04	4.3	2.7
CH_3NCO, $v=0$	2.0	85	84 ± 7	2.5(15)	1.00	$(2.5\pm0.6)(15)$	1.00	4.0	2.3
CH_3OH, $v=0$	2.0	145	147 ± 5	5.0(18)	1.00	$(4.1\pm0.6)(18)$	1.00	5.7	2.0
$v=1$	2.0	145	147 ± 5	5.0(18)	1.00	$(4.1\pm0.6)(18)$	1.00	5.7	2.0
$v=2$	2.0	145	147 ± 5	5.0(18)	1.00	$(4.1\pm0.6)(18)$	1.00	5.7	2.0
C_2H_5OH, $v=0$	2.0	145	153 ± 6	1.1(17)	1.29	$(1.2\pm0.1)(17)$	1.33	4.0	2.6
CH_3OCH_3, $v=0$	2.0	125	121 ± 4	3.8(17)	1.00	$(3.8\pm0.4)(17)$	1.00	4.2	1.4
$v_{11}=1$	2.0	125	121 ± 4	3.8(17)	1.00	$(3.8\pm0.4)(17)$	1.00	4.2	1.4
CH_3OCHO, $v=0$	2.0	140	150 ± 4	3.5(17)	1.16	$(4.5\pm0.4)(17)$	1.19	4.2	1.4
$v=1$	2.0	140	150 ± 4	3.5(17)	1.16	$(4.5\pm0.4)(17)$	1.19	4.2	1.4
CH_3CHO, $v=0$	2.0	90	79 ± 4	6.0(15)	1.00	$(3.1\pm0.3)(15)$	1.00	4.5	2.8
$v=1$	2.0	90	79 ± 4	6.0(15)	1.00	$(3.1\pm0.3)(15)$	1.00	4.5	2.8
CH_3SH, $v=0$	2.0	128	–	$\leq 7.0(15)$	1.00	–	–	4.3	2.5
OCS, $v=0$	2.0	140	141 ± 5	3.5(17)	1.01	$(3.2\pm0.6)(17)$	1.01	4.5	2.4
$v_2=1$	2.0	140	141 ± 5	3.5(17)	1.01	$(3.2\pm0.6)(17)$	1.01	4.5	2.4

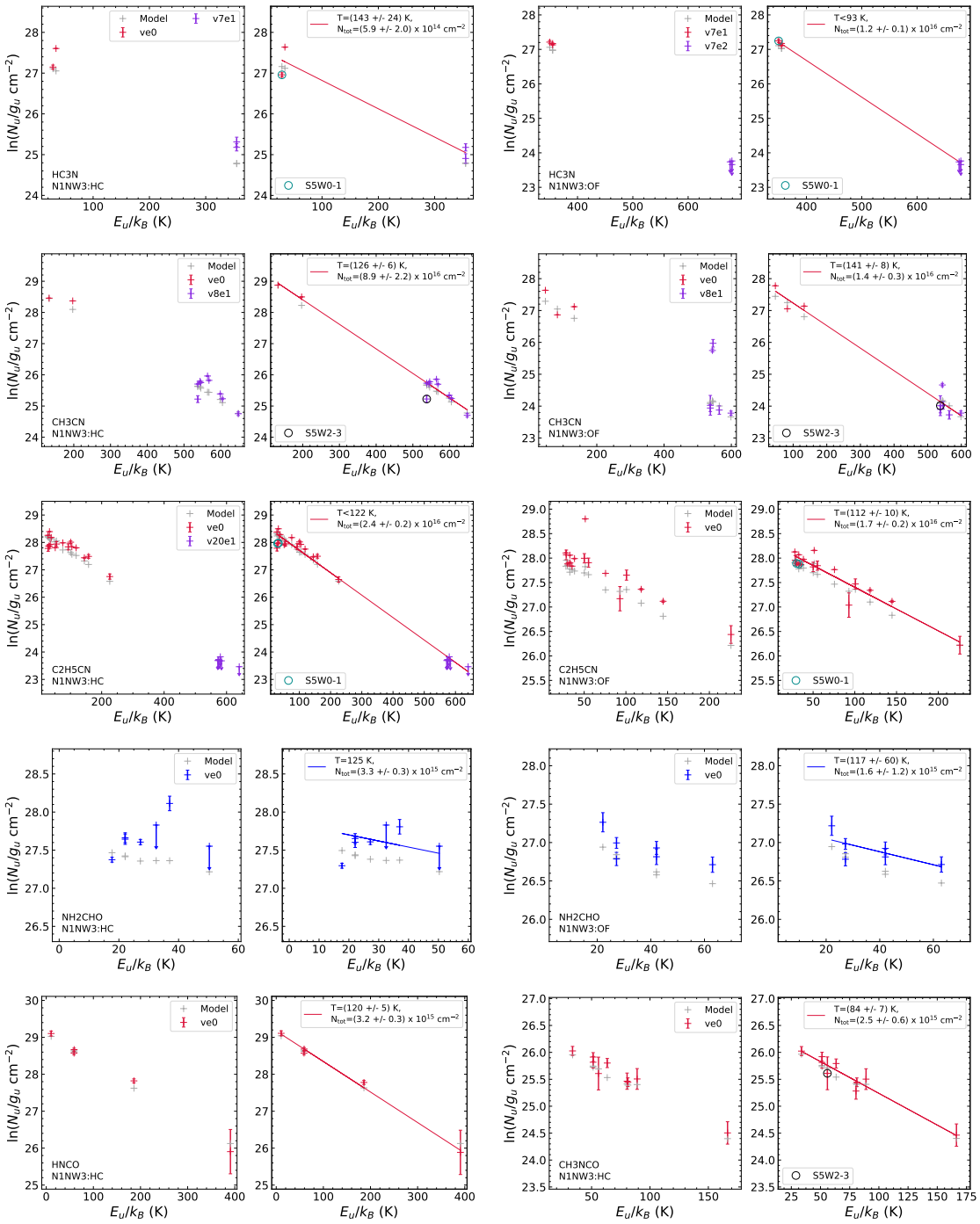

Figure B.3: Same as Fig. B.1, but for multiple molecules at position N1NW3 for the hot-core component (N1NW3:HC) and the outflow component (N1NW3:OF).

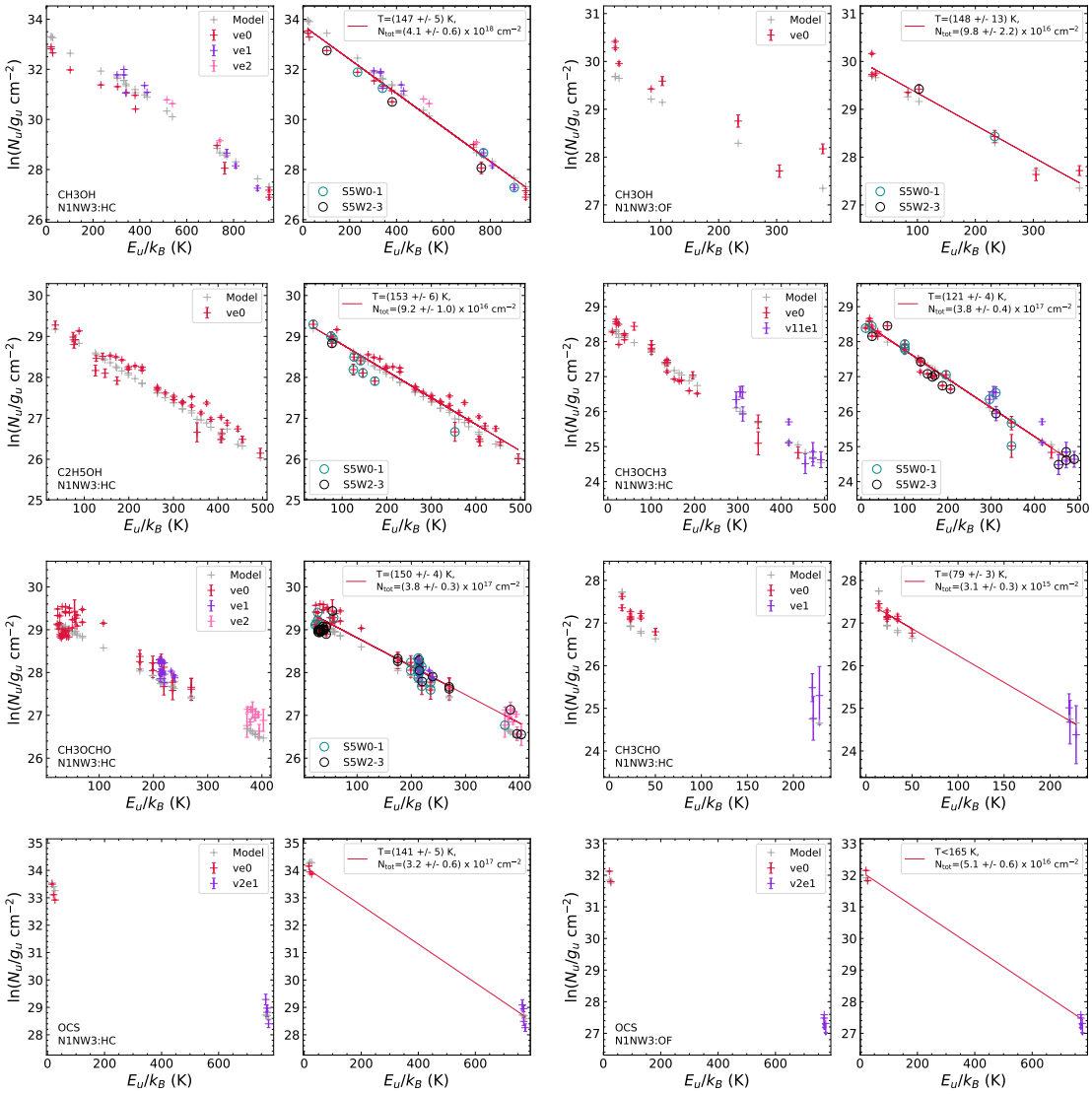

Figure B.3: continued.

Table B.4: Same as Table B.1, but for position N1NW3:OF.

Molecule	Size ($''$)	$T_{\rm rot,W}$ (K)	$T_{\rm rot,pd}$ (K)	$N_{\rm W}$ ($\rm cm^{-2}$)	$C_{\rm vib,W}$	$N_{\rm pd}$ ($\rm cm^{-2}$)	$C_{\rm vib,pd}$	Δv ($\rm km\,s^{-1}$)	$v_{\rm off}$ ($\rm km\,s^{-1}$)
HC_5N, $v = 0$	2.0	129	–	$\leq 9.7(13)$	2.42	–	–	6.0	12.0
HC_3N, $v = 0$	2.0	95	93 ± 0	1.2(16)	1.07	$(1.3 \pm 0.1)(16)$	1.07	6.0	13.0
CH_3CN, $v = 0$	2.0	145	141 ± 8	1.4(16)	1.00	$(1.4 \pm 0.3)(16)$	1.00	6.0	12.0
$v_8 = 1$	2.0	145	141 ± 8	1.4(16)	1.00	$(1.4 \pm 0.3)(16)$	1.00	6.0	12.0
C_2H_3CN, $v = 0$	2.0	129	–	$\leq 1.0(15)$	1.00	–	–	6.0	12.0
C_2H_5CN, $v = 0$	2.0	115	112 ± 10	2.0(16)	1.18	$(2.0 \pm 0.2)(16)$	1.16	8.0	12.0
NH_2CN, $v = 0$	2.0	129	–	$\leq 5.0(14)$	1.01	–	–	6.0	12.0
HNCO, $v = 0$	2.0	129	–	$\leq 1.0(15)$	1.00	–	–	6.0	12.0
NH_2CHO, $v = 0$	2.0	115	117 ± 60	1.5(15)	1.03	$(1.6 \pm 1.2)(15)$	1.03	6.0	11.0
CH_3NCO, $v = 0$	2.0	129	–	$\leq 2.0(15)$	1.00	–	–	6.0	12.0
CH_3OH, $v = 0$	2.0	150	148 ± 13	9.5(16)	1.00	$(1.0 \pm 0.2)(17)$	1.00	5.5	11.5
C_2H_5OH, $v = 0$	2.0	129	–	$\leq 9.7(15)$	1.21	–	–	6.0	12.0
CH_3OCH_3, $v = 0$	2.0	129	–	$\leq 1.0(16)$	1.00	–	–	6.0	12.0
CH_3OCHO, $v = 0$	2.0	129	–	$\leq 1.0(16)$	1.12	–	–	6.0	12.0
CH_3CHO, $v = 0$	2.0	129	–	$\leq 1.5(15)$	1.00	–	–	6.0	12.0
CH_3SH, $v = 0$	2.0	129	–	$\leq 8.5(15)$	1.00	–	–	6.0	12.0
OCS, $v = 0$	2.0	160	≤ 165	5.1(16)	1.02	$(5.2 \pm 0.6)(16)$	1.02	8.0	12.0

Table B.5: Molecular transitions used to derive the LVINE maps shown in Figs. 4.4 and B.4–B.6.

Molecule, vib. state	Transition	ν^a (MHz)	$E_{\rm ul}{}^b$ (K)	$A_{\rm ul}{}^c$ ($10^{-5}\,\rm s^{-1}$)	$g_{\rm ul}{}^d$	$v_r{}^e$ ($\rm km\,s^{-1}$)	$v_b{}^f$ ($\rm km\,s^{-1}$)
HC_3N, $v_7 = 1$	$J = 11 - 10$, $l = 1e$	100322.411 (0.002)	349.7	7.7	23	100	30
	$J = 12 - 11$, $l = 1f$	109598.818 (0.020)	355.0	0.1	25		
HC_5N, $v = 0$	$J = 36 - 35$	95850.335 (0.000)	85.1	9.5	219	90	40
	$J = 42 - 41$	111823.024 (0.000)	115.4	15.1	255		
C_2H_3CN, $v = 0$	$11(1,11) - 10(1,10)$	101637.231 (0.000)	31.5	8.4	69	95	35
	$10(2,8) - 9(2,7)$	95325.476 (0.005)	33.8	6.7	63		
C_2H_5CN, $v = 0$	$11(0,11) - 10(0,10)$	96919.762 (0.050)	28.1	7.5	23	100	30
	$11(2,9) - 10(2,8)$	99681.461 (0.050)	33.0	7.9	23		
HNCO, $v = 0$	$5(1,5) - 4(1,4)$	109495.996 (0.006)	59.0	1.7	11	90	35
	$5(1,4) - 4(1,3)$	110298.089 (0.005)	59.2	1.7	11		
NH_2CHO, $v = 0$	$5(1,5) - 4(1,4)$	102064.267 (0.000)	17.7	7.1	11	85	40
	$5(1,4) - 4(1,3)$	109753.503 (0.000)	18.8	8.8	11		
CH_3OH, $v = 0$	$7(2,5) - 8(1,8)$ A	111289.453 (0.013)	102.7	0.3	60	90	40
	$8(0,8) - 7(1,7)$ A	95169.391 (0.011)	83.5	0.4	68		
CH_3CHO, $v = 0$	$5(2,3) - 4(2,2)$ E	96475.524 (0.003)	23.0	2.5	22	85	45
	$5(1,4) - 4(1,3)$ A	98900.944 (0.003)	16.5	3.1	22		
CH_3SH, $v = 0$	$4(0,4) - 3(0,3)$ $A+$	101139.150 (0.001)	12.1	0.9	9	85	45
	$4(0,4) - 3(0,3)$ E	101284.366 (0.001)	13.6	0.9	9		
	$4(1,3) - 3(1,2)$ E		18.3	0.8	9		
OCS, $v = 0$	$J = 9 - 8$	109463.063 (0.005)	26.3	0.4	19	105	30
	$J = 8 - 7$	97301.208 (0.000)	21.0	0.3	17		
SO_2, $v = 0$	$12(4,8) - 13(3,11)$	107843.470 (0.002)	111.0	0.3	25	105	25
	$7(3,5) - 8(2,6)$	97702.333 (0.002)	47.8	0.2	15		
SO, $v = 0$	$2(3) - 1(2)$	109252.220 (0.100)	21.1	1.1	5	110	15

Notes. $^{(a)}$ Rest frequency with uncertainty in parentheses. $^{(b)}$ Upper-level energy. $^{(c)}$ Einstein A coefficient. $^{(d)}$ Upper-level degeneracy. $^{(e)}$ Outer integration limit for the red-shifted emission. $^{(f)}$ Outer integration limit for the blue-shifted emission.

the same velocity range helped us identifying which part of the blue- and red-shifted emission belongs to the molecule of interest and what is contamination from other species. Based on these spectra, the integration strategy was developed.

The procedure is based on the method of linewidth- and velocity-corrected integrated emission (LVINE) maps, according to which the integration limits in each pixel are adjusted based on variations of peak line velocities and linewidths measured in the spectra of a reference molecule or a set of reference molecules. We used this method in Paper I to determine the integration limits for the hot-core component for each molecule. Therefore, maps of peak velocity, v_t, and linewidth, $FWHM_t$, were derived which are shown in Fig. B.2 in Paper I, using two template transitions. We selected one transition of ethanol at 108.44 GHz with an upper level energy E_u/k of 88 K for positions close to the centre of Sgr B2 (N1) as it remains sufficiently optically thin. At larger distances, that is when the ethanol line is too weak, we used a transition of methanol at 95.91 GHz and an upper level energy of 21 K. Where neither ethanol nor methanol are detected above an intensity threshold of 5σ, where σ was taken from Table 2 in Belloche et al. (2019) for the respective observational setup, we assigned a fixed value of peak velocity and linewidth to that pixel. In this work, the LVINE method was utilised to define the starting points (from the hot-core component) for the integration over the blue- and red-shifted emission. Because ethanol does not show blue- or red-shifted emission and methanol emission remains dominated by the hot-core emission, we took the peak velocities and linewidths from the template maps derived in Paper I. However, during the inspection of the spectra of the two methanol transitions, we noticed that for some pixels at greater distances, we used the fixed values of peak velocity and linewidth although the methanol transition was still detected. This means that the methanol line at these positions was not properly fitted during the derivation of the peak-velocity and linewidth template maps. Therefore, we improved the procedure and used the updated peak-velocity and linewidth maps to produce Figs. 4.4 and B.4–B.6. Since these adjustments are made beyond distances of $3''$ from the hot core's centre, the maps shown in Fig. 4 of Paper I are not severely affected.

The channels where the velocity is $v_t \pm FWHM_t$ were first computed for each pixel. We pushed these limits by two additional channels away from the source velocity to define the inner integration limits of the blue- and red-shifted emission, in order to reduce the contamination from the hot-core component. In that way, however, it is not excluded that we lose some low-velocity outflow emission close to $v_{\rm sys}$. The outer integration limits are set to a fixed value based on the comparison of the spectra of the two transitions for each molecule such that no outflow emission is missed and no contaminating emission, if identified and if possible to avoid, is added to the integration.

For each molecule, the integration strategy uses both selected transitions such that for a given channel the transition with the lowest intensity is used. This is demonstrated with the filled histograms in Fig. 4.5. In that way, we reduce the contribution of contamination by other species. The procedure is slightly more complicated when the intensity of one or both transitions is below 2σ, where σ is the respective noise level in the spectrum, which can be different if the transitions are observed in two observational setups of different sensitivity. In theses cases, we use the spectrum obtained with better sensitivity for integration. The following scheme, which is applied channel-wise, presents the

procedure in detail:

$$
\begin{aligned}
&\text{if } \sigma_1 \leq \sigma_2 \text{ then}\\
&\quad \text{if } T_{2,c} < 2\sigma_2 \text{ then}\\
&\quad\quad \text{if } T_{1,c} < 2\sigma_1 \text{ then}\\
&\quad\quad\quad \text{use } T_{1,c}\\
&\quad\quad \text{else if } 2\sigma_1 \leq T_{1,c} < 2\sigma_2 \text{ then}\\
&\quad\quad\quad \text{use } T_{1,c}\\
&\quad\quad \text{else if } T_{1,c} \geq 2\sigma_2 \text{ then}\\
&\quad\quad\quad \text{use } T_{2,c}\\
&\quad \text{else if } T_{2,c} \geq 2\sigma_2 \text{ then}\\
&\quad\quad \text{if } T_{1,c} \leq T_{2,c} \text{ then}\\
&\quad\quad\quad \text{use } T_{1,c}\\
&\quad\quad \text{if } T_{1,c} > T_{2,c} \text{ then}\\
&\quad\quad\quad \text{use } T_{2,c},
\end{aligned}
$$

where $\sigma_{1,2}$ are the noise levels in spectra 1 and 2 either taken from Table 2 in Belloche et al. (2019) or measured in the smoothed data cubes and c indicates that this runs over each channel within the integration limits. If $\sigma_1 > \sigma_2$, the conditions apply to T_1 and T_2 vice versa. Although the method reduces contamination, it does not avoid everything if in a given channel both spectra contain some contamination.

B.3.2 Details on the outflow morphology

Although the outflow reveals an overall bipolar morphology, there is a lot of additional structure in the form of intensity peaks and more extended features that are described in more detail in the following. Figures B.4–B.6 show again the LVINE maps of the molecules in Fig. 4.4, but the presentation is differently. The right-most panels in Figs. B.4–B.6 are the same as in Fig. 4.4 showing integrated intensities over the full range of blue- and red-shifted velocities as indicated by the dashed coloured lines in Fig. 4.5. This also applies to the left panels (labelled 'all v'), but red- and blue-shifted emissions are shown in separate panels. In addition, we show maps of only the lower- (low-v) and higher-velocity (high-v) emission. The low-velocity maps show emission integrated from the inner integration limits up to half the number of channels used for the full integration interval, while the high-velocity maps include emission from the other half down or up to the outer integration limits Therefore, this division into the low- and high-velocity regimes is again pixel-dependent and each panel in Figs. B.4–B.6 shows maps of integrated intensities over different velocity ranges for each molecule, which has to be kept in mind when comparing the emission morphologies of the molecules in the following. Because the only available transition for SiO at 86.85 GHz severely suffers from absorption, the LVINE method could not be applied, however, we show SiO maps in Fig B.5. For the all-v maps, intensities were integrated as in Fig. 4.2, that is ignoring channels with absorption. The intermediate integration limit was taken from SO. In addition to the LVINE maps, Fig. B.7 shows velocity-channel maps of eight molecules to study changes in the emission morphology within smaller velocity intervals.

Blue-shifted emission

In addition to SO and SiO, extended blue-shifted emission is observed for SO_2, OCS, CH_3SH, HC_3N, HC_5N, C_2H_3CN, and C_2H_5CN, all of which are either N- or S-bearing species, and follows the wider-angle emission of SO and SiO with farthest extension mainly identified in the low-velocity maps. The blue-shifted emission from HNCO and NH_2CHO does spatially extend beyond that of the dense core continuum emission (as indicated with the 3σ contour), however, is more compact (especially NH_2CHO) than for the N- and simple S-bearing species. CH_3OH and CH_3CHO reveal extended blue-shifted emission, however, the morphology seems to rather resemble that of the hot-core emission (cf. Fig. 4 in Paper I). None of the molecules shows the collimated features that we identified in the SO (and SiO) maps in Fig. 4.2 and labelled aB1, aR1, and aR2. There is another nearly bipolar set of blue- and red-shifted collimated features extending from east to west that can be identified in the SO maps in Fig. B.4 (labelled aB2 and aR3). Collimated, blue-shifted emission along aB2 is prominently seen in SiO as well, but its red-shifted emission does not trace aR3. The bipolar structure aB2-aR3 could be another outflow axis, however, we cannot be certain about it as the red-shifted feature aR3 is not clearly observed in Fig. 4.2. Moreover, the blue-shifted emission aB2 runs along the free-free continuum emission of the extended HII region in the northwest (see Fig. 4.2) and may also be associated with it in some way.

Looking into more detail, the peak of SO (and SiO) blue-shifted emission at low velocity (P1) more or less coincides with the peaks of OCS, SO_2, and the N-bearing molecules. Emission from O- and (N+O)-bearing molecules and CH_3SH seems to peak more towards the centre of the hot core. In addition, SO reveals a peak of high-velocity blue-shifted emission (P2), which is almost co-located with a peak in SiO, SO_2 and OCS emission, although the peak of the latter is slightly shifted to the southwest from this SO peak. The N-bearers HC_3N, C_2H_3CN, C_2H_5CN and HNCO also show a peak of high-velocity blue-shifted emission but clearly shifted by $\sim 0.8''$ to the southwest. NH_2CHO emission spatially extends in this direction, CH_3OH as well, but in a different direction than NH_2CHO. For CH_3SH and CH_3CHO there is no clear connection with this peak, which could also be a sensitivity issue. This SO peak does not coincide with a continuum peak, it is rather framed by the continuum (free-free) emission in the north where the HII region seems to meet the emission associated with the hot core. According to Schwörer et al. (2019), there are supposedly also filaments impinging on Sgr B2 (N1) in this region that may be involved in the occurrence of this SO peak in some way (see also Fig. 4.1), when it meets the denser core emission around this position.

There is another peak of high-velocity blue-shifted emission (P3), which is clearly seen in emission of the simple S-bearing molecules, SiO, HC_3N, C_2H_5CN, HNCO, CH_3OH, indicated by one contour for CH_3SH, C_2H_3CN and NH_2CHO, and not seen for HC_5N and CH_3CHO. For HC_5N, this peak may be hidden in the low-v maps due to the smaller overall integration interval. This peak is located at the tip of the high-intensity contours in the low-v panels. All molecules that show this peak also show red-shifted emission above 3σ at this position, except SiO, which may be a consequence of absorption. In addition, there are three water masers associated with this peak, two at blue-shifted and one at red-shifted velocities. On the other hand, there is another peak in blue-shifted emission for many molecules towards the northwest (P4), which also coincides with the location of a cluster of water masers. Generally, the majority of water-maser spots can be associated with blue- or red-shifted emission peaks of the molecules studied here.

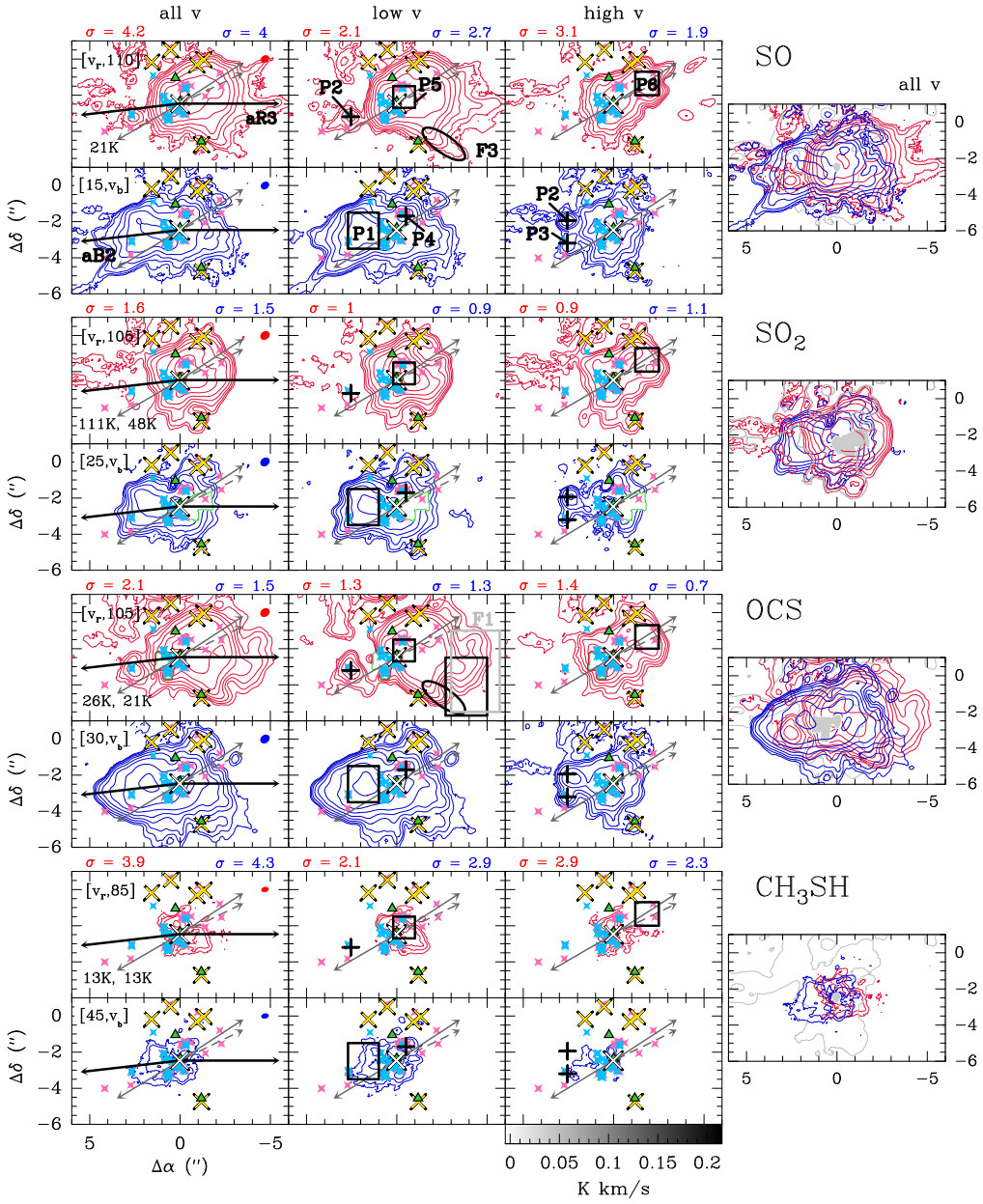

Figure B.4: LVINE maps of blue- and red-shifted emission of S-bearing molecules (blue and red contours, respectively). The left-most panels show maps in which intensities were integrated over the complete velocity interval (all v), where the fixed, pixel-independent outer integration limits (in $\mathrm{km\,s^{-1}}$) are shown in the upper left corner. The maps in the second column (low v) show intensities integrated over half the total velocity interval with velocities closer to v_{sys}, while in the maps in the third column (high v), intensities were integrated over the other half up or down to the outer integration limits. In the right-most panels, the all-v maps of blue- and red-shifted emission are overlaid as in Fig. 4.4. The contour steps start at 5σ and then increase by a factor of 2, where σ is the average noise level measured in an emission-free region in each map and is given at the top of each panel in $\mathrm{K\,km\,s^{-1}}$. The grey contour indicates the 3σ level of the continuum emission at 99 GHz. The closest region around Sgr B2 (N1) is masked out due to high continuum optical depth that depends on frequency and beam size (see Appendix C in Paper I). For OCS and SO_2, the masked region was extended due to contamination by emission from another species that was identified in their spectra. Masks are either shown in white within a green contour or as grey-shaded regions. Grey arrows indicate the directions of the collimated features labelled aB1, aR1, and aR2 in Fig. 4.2. Coloured markers are the same as in Fig. 4.2. Identified intensity peaks P1–P6 and elongated features F1–F3, as well as additional bipolar-like extensions labelled aR3 and aB2 are drawn in black. The upper-level energies of the transitions used to produce the maps are shown in the lower-left corner of the top-left panels, respectively. Other properties of the transitions are summarised in Table B.5. The HPBW is shown in the top-right corner of each each panel in the left-most panels. The position offsets are given with respect to the ReMoCA phase centre.

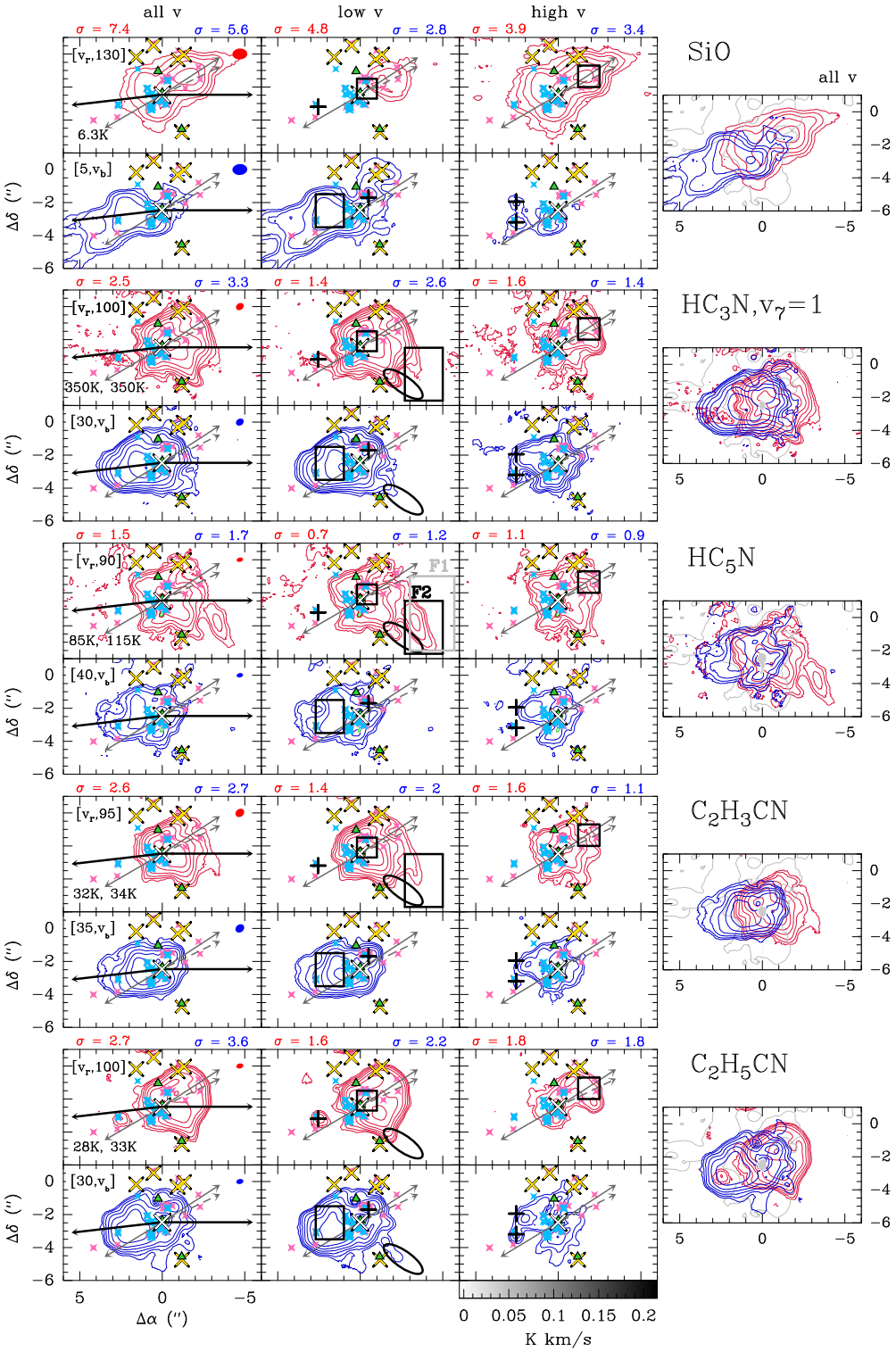

Figure B.5: Same as Fig. B.4, but for N-bearing molecules. The LVINE method could not be used for SiO, because of absorption features. The all-v maps were computed as in Fig 4.2, while the intermediate integration limits that divide the spectrum into the low-v and high-v portions at each pixel was taken from SO.

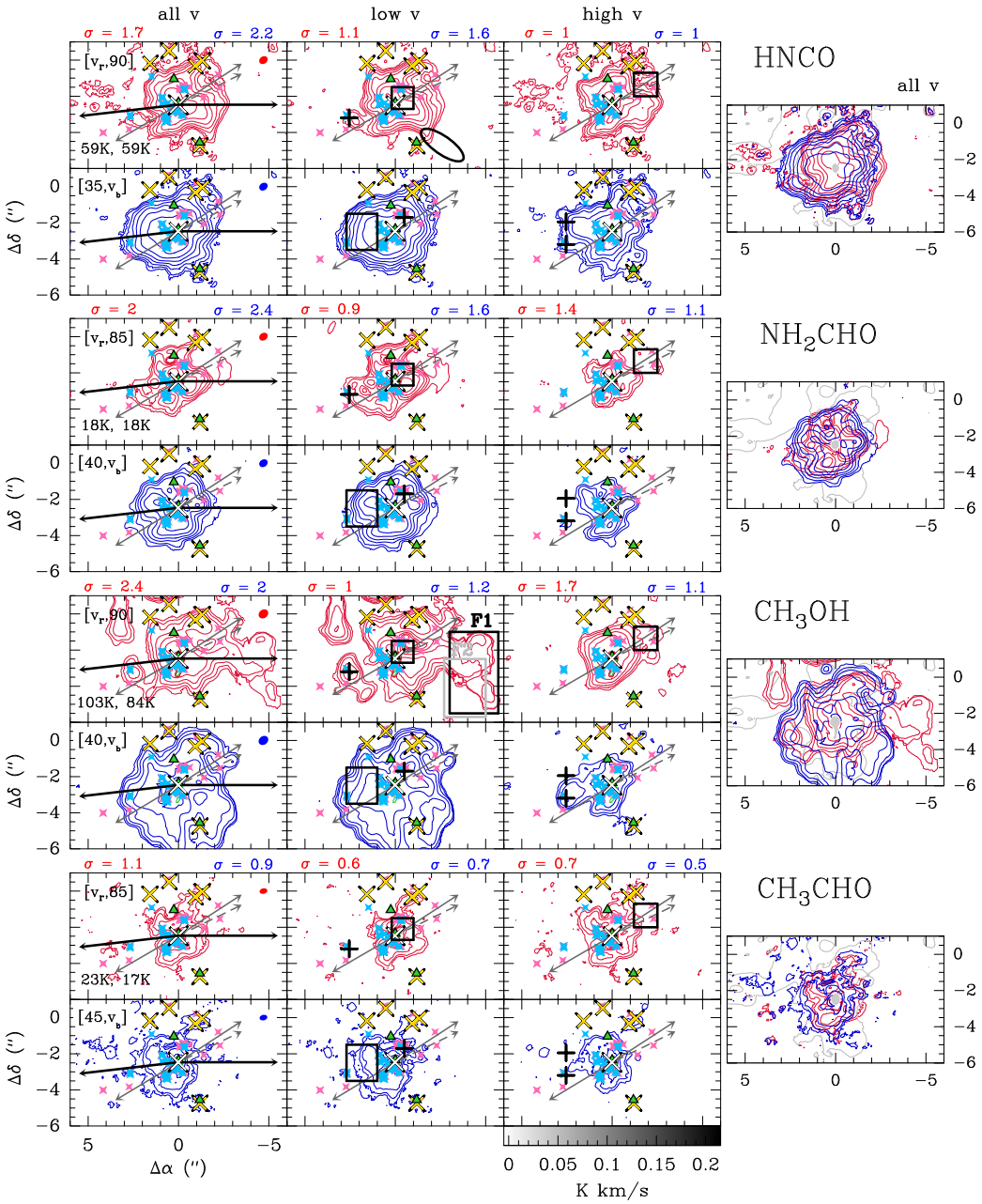

Figure B.6: Same as Fig. B.4, but for (N+O)- and O-bearing molecules.

Red-shifted emission

There are two peaks of SO red-shifted emission: almost right at the centre of the hot core (P5) and at higher velocities at ~2″ to the northwest (P6). The farther, high-velocity peak seems to be embedded in a cavity of continuum emission. The morphologies of SiO, OCS, SO_2, HC_3N, and C_2H_5CN emission closely follow that of SO, except for the collimated features seen in SO further along aR1–aR3. Moreover, the emission of SO_2 and HC_3N peaks more towards the edges of the most intense SO emission at P6, particularly where it seems to be framed by the continuum emission, provided that we are not biased by optical depth. Red-shifted C_2H_3CN emission shows the same trend in the low-v map, but it does not clearly show the high-velocity peak, and HNCO and HC_5N show spatially extended red-shifted emission towards the northwest, but also over the whole hot-core region. Red-shifted emission of CH_3SH, NH_2CHO, and CH_3CHO is only observed towards the more central SO peak. CH_3OH emission shows the extension to the northwest, but also additional structures that we refer to as F1 in Fig. B.6 and that are not seen for other molecules. As mentioned above, there is a prominent peak (P2) coinciding with a peak in high-velocity blue-shifted emission and water masers, that is seen for the majority of molecules, for some more prominently than for others.

Another interesting feature is seen in the red-shifted HC_5N emission that we label F2 in Fig. B.5, which is not observed as prominently in any of the other maps. It is evident in maps of HC_3N ($v_7 = 1$) and C_2H_3CN, however, not with the spatial extent as for HC_5N. It does not coincide with the F1 feature seen in emission of CH_3OH, it is adjacent to it in the south, however. This feature is observed in other transitions of HC_5N, hence, it is not caused by contamination from other molecules in the shown map. We cannot be conclusive on the nature of this feature and why it appears only this prominently in emission of this molecule. There is another feature (F3) that runs almost parallel to F2, which is observed in the maps of SO, OCS, the N-bearing molecules, and HNCO. This feature may be associated with one of the filaments identified by Schwörer et al. (2019, see also Fig. 4.1), but this is not certain.

It is interesting to note that there is a clear lack of emission towards the HII region K3 (green triangle north of the hot-core centre) in the maps of blue-shifted SO, SO_2, OCS, HC_3N, C_2H_3CN, and C_2H_5CN emission. In contrast, for CH_3CHO and NH_2CHO, this lack of emission is rather indicated in the red-shifted emission maps. CH_3OH, HNCO, HC_5N, and CH_3SH do not reveal a clear signature in any map.

B.3.3 Velocity-channel maps

In Fig. B.7 we show velocity-channel maps for a selection of molecules, which includes SiO, SO (109.25 GHz), OCS, CH_3SH, HC_3N, C_2H_5CN, HNCO, and CH_3OH. Each channel map contains integrated intensities over a 10 km s^{-1} velocity interval, where the central velocity is indicated in each map, and the complete velocity range that is shown corresponds to the one used for the LVINE maps. The same integration strategy was applied, where we use two transitions of a molecule to minimise the contamination by other molecules, except for SiO and SO.

We see the same trends as in the integrated intensity maps: strong blue-shifted emission for the simple S-bearing molecules, HC_3N, C_2H_5CN, and HNCO. CH_3SH shows weaker but spatially extended emission. The emission of CH_3OH is spatially extended, but does not follow the morphology of the other molecules. A similar classification of the molecules applies to red-shifted emission extending to the northwestern direction. The most collimated feature in the blue-shifted SiO and SO

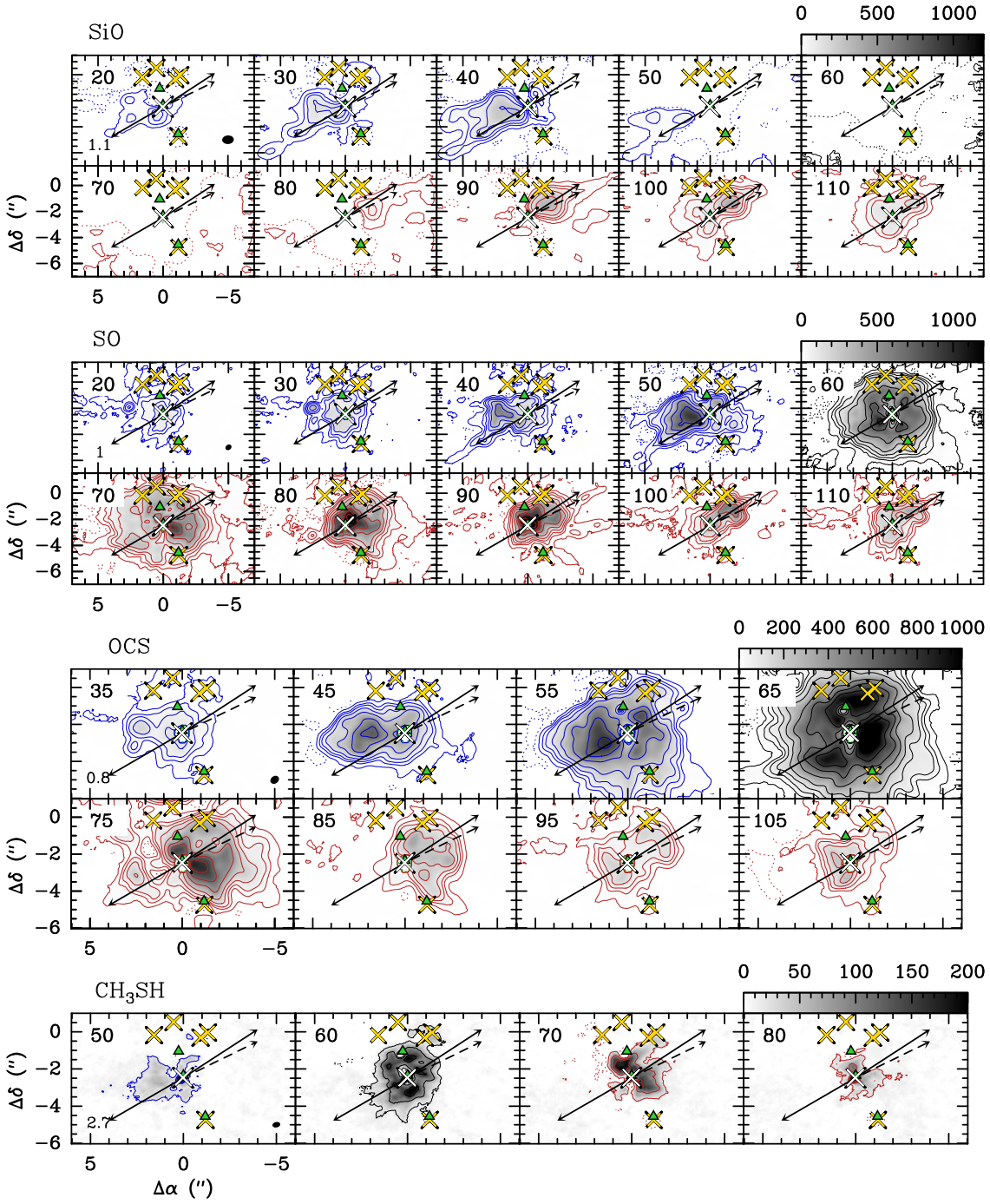

Figure B.7: Velocity-channel maps of various molecules (in grey scale (K km s^{-1}) and contours). The integration strategy is the same as for the maps in Figs. 4.4 and B.4-B.6 (i.e. using two transitions to minimise contamination by other molecules, except for SiO and SO (109.25 GHz)), but in each panel the intensities were integrated over an interval of only 10 km s^{-1}. The respective central velocity in km s^{-1} is shown in the upper left corner. The start and end velocities correspond to the outer integration limits used in Fig. 4.4. For all molecules but SO, the contours are -6σ, 6σ, 30σ, and then increase by a factor of 2, where σ in K km s^{-1} is written in the lower left corner of the lowest-velocity map and was computed using $\sqrt{N} \times rms \times \Delta v$, where N is the number of channels that was integrated over, rms was taken from Table 2 in Belloche et al. (2019), and Δv is the channel separation in km s^{-1}. The SO contours start at 10σ and then increase by factor of 3. Blue contours indicate blue-shifted emission, red contours red-shifted emission, and black contours emission close to the source systemic velocity. Masked regions, arrows, and markers are the same as in Fig. 4.2. The HPBW is shown in the bottom-right corner of the lowest-velocity panel.

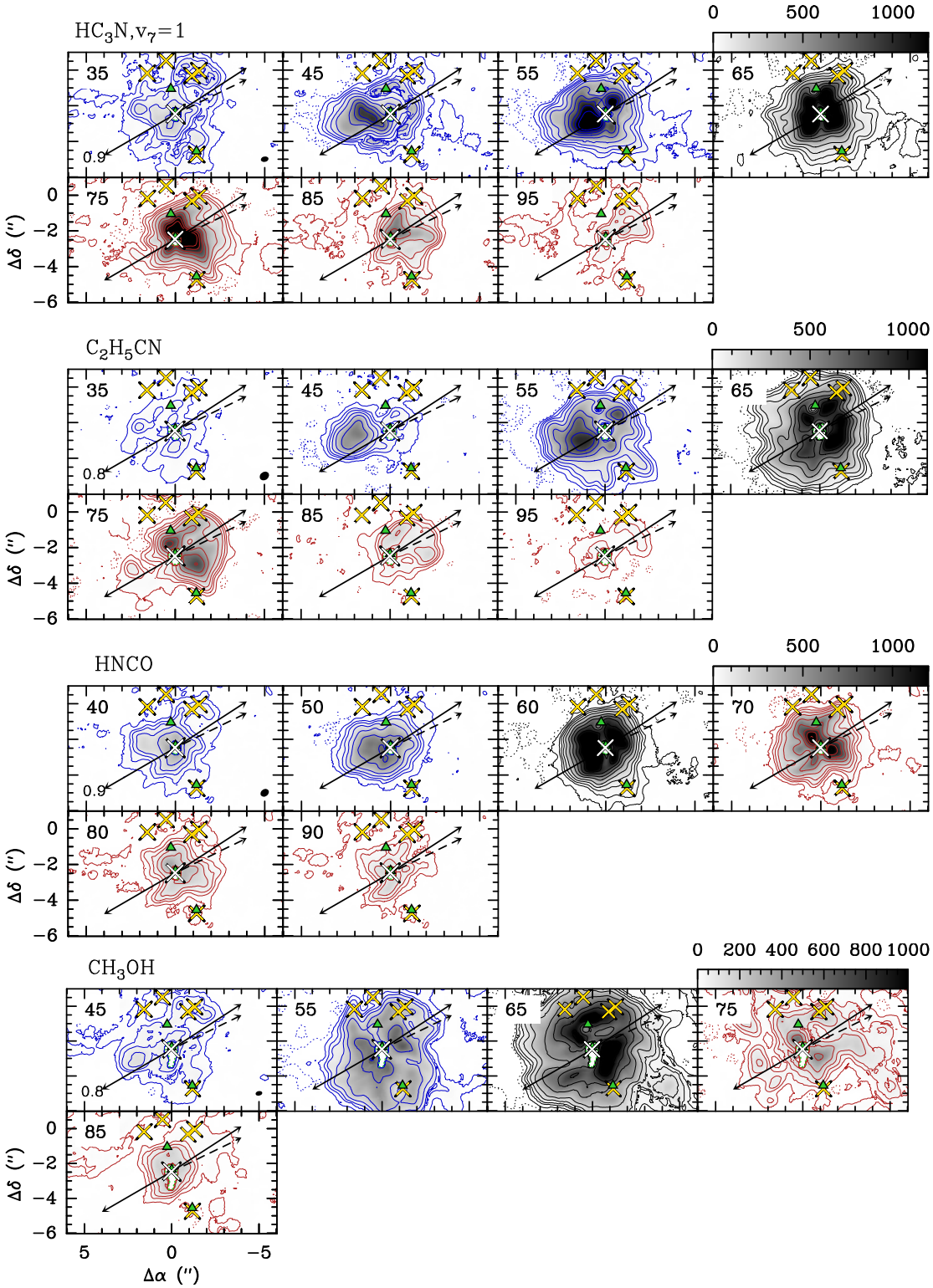

Figure B.7: continued.

emission along arrow aB1 is prominent in the maps at 40–50 km s^{-1}, for SiO even at 20–30 km s^{-1} while the red-shifted feature along aR2 appears at 80–90 km s^{-1}. At higher velocities, the finger-like feature along aR1 can be observed. The collimated features along aR3 and feature F3 become visible at 90 km s^{-1} for SO. For OCS, HC_3N, and C_2H_5CN, feature F3 is observed at 75–85 km s^{-1}.

B.4 Additional figures

Position-velocity diagrams of various COMs and simpler molecules are presented in Fig. B.8. In Figs. B.9–B.11, we show observed and modelled spectra towards positions N1SE1 and N1NW3 of various transitions for those molecules for which abundances were derived in this work. In Fig. B.12 temperatures used in the Weeds models are compared to the values obtained from the population-diagram analysis for both components at N1SE1 and N1NW3, respectively. Column densities of the molecules used in the Weeds models are shown in Fig. B.13 and the comparison of abundances with respect to methanol between Sgr B2 (N1), G0.693, and L1157-B1 in Fig. B.14.

B.5 Molecular abundances in G0.693 and L1157-B1 from the literature

Table B.6: Molecular column densities in G0.693 and L1175–B1 reported by various authors.

	G0.693				L1157–B1	
Molecule	Z18/Z23/RA21	AA15	RT08	RT06	HR* (B1b)	LR**
HC_3N	$7.1 \pm 1.3(14)$	$5.5 \pm 0.3(14)$	–	–	$3.4(13)^{c}$	$4.0(12)^{b}$
HC_5N	$2.6 \pm 0.1(14)$	$3.5 \pm 1.2(13)$	–	–	–	$1.2(12)^{b}$
CH_3CN	$11.5 \pm 0.3(13)$	$28 \pm 3.0(13)$	–	–	$1.0(13)^{d}$	$1.0 \pm 0.5(12)^{e}$
C_2H_3CN	$9.0 \pm 0.1(13)$	$5.1 \pm 1.6(13)$	–	–	–	–
C_2H_5CN	$4.1 \pm 0.4(13)$	$8.1 \pm 1.6(13)$	–	–	–	$< 4.0(12)^{f}$
NH_2CN	$3.1 \pm 0.2(14)$	$1.2 \pm 0.2(14)$	–	–	–	–
HNCO	$3.4 \pm 0.2(15)$	$1.4 \pm 0.1(15)$	–	–	–	$3.3 - 8.4(13)^{b}$
NH_2CHO	$6.3 \pm 1.4(14)/2.5 \pm 0.1(14)$	$5.9 \pm 0.6(13)$	–	–	$8.0(12)^{a}$	$1.7 - 3.6(12)^{b}$
CH_3NCO	$6.6 \pm 0.4(13)$	–	–	–	–	–
CH_3OH	1.6(16)	$1.2 \pm 0.1(17)$	2.1(16)	3.2(16)	$1.3 \pm 0.3(16)^{a}$	$1.0 \pm 0.2(15)^{b}$
C_2H_5OH	2.0(14)	$4.5 \pm 0.9(14)$	–	1.3(15)	–	$4.6 \pm 1.6(13)^{b}$
CH_3OCH_3	$1.1(14)^{\dagger}$	–	–	–	–	$5.0 \pm 1.4(13)^{b}$
CH_3OCHO	–	$\sim 3.5(14)$	1.9(15)	8.3(14)	–	$5.4 \pm 1.4(13)^{b}$
CH_3CHO	–	$2 - 5(14)$	–	1.5(15)	$7.0 \pm 3.0(13)^{a}$	$2.8 \pm 0.8(13)^{b}$
CH_3SH	6.5(14)	–	–	–	–	–
OCS	–	$1.9 \pm 0.1(15)$	–	–	$1.0(15)^{a}$	$4.5 \pm 1.0(13)^{f}$

Notes. Column densities are written as $x(z) = x \times 10^{z}$ cm^{-2} or $(x \pm y)(z) = (x \pm y) \times 10^{z}$ cm^{-2}.
Z18 (N-bearing molecules, Zeng et al. 2018). Z23 (NH_2CHO, Zeng et al. 2023). RA21 (CH_3OH, C_2H_5OH, and CH_3SH, Rodríguez-Almeida et al. 2021). AA15: Armijos-Abendaño et al. (2015). RT06: Requena-Torres et al. (2006). RT08: Requena-Torres et al. (2008). (†) V. Rivilla (private communication).
(∗) High angular resolution; Column densities were obtained from interferometric studies. (∗∗) Low angular resolurion; Column densities were obtained from single-dish observations. $^{(a)}$ SOLIS (Seeds Of Life In Space, Codella et al. 2017, 2020, 2021). $^{(b)}$ ASAI (Astrochemical Survey At IRAM, Mendoza et al. 2014, 2018; Lefloch et al. 2017). $^{(c)}$ Benedettini et al. (2007). $^{(d)}$ Codella et al. (2009). $^{(e)}$ Arce et al. (2008). $^{(f)}$ Sugimura et al. (2011).

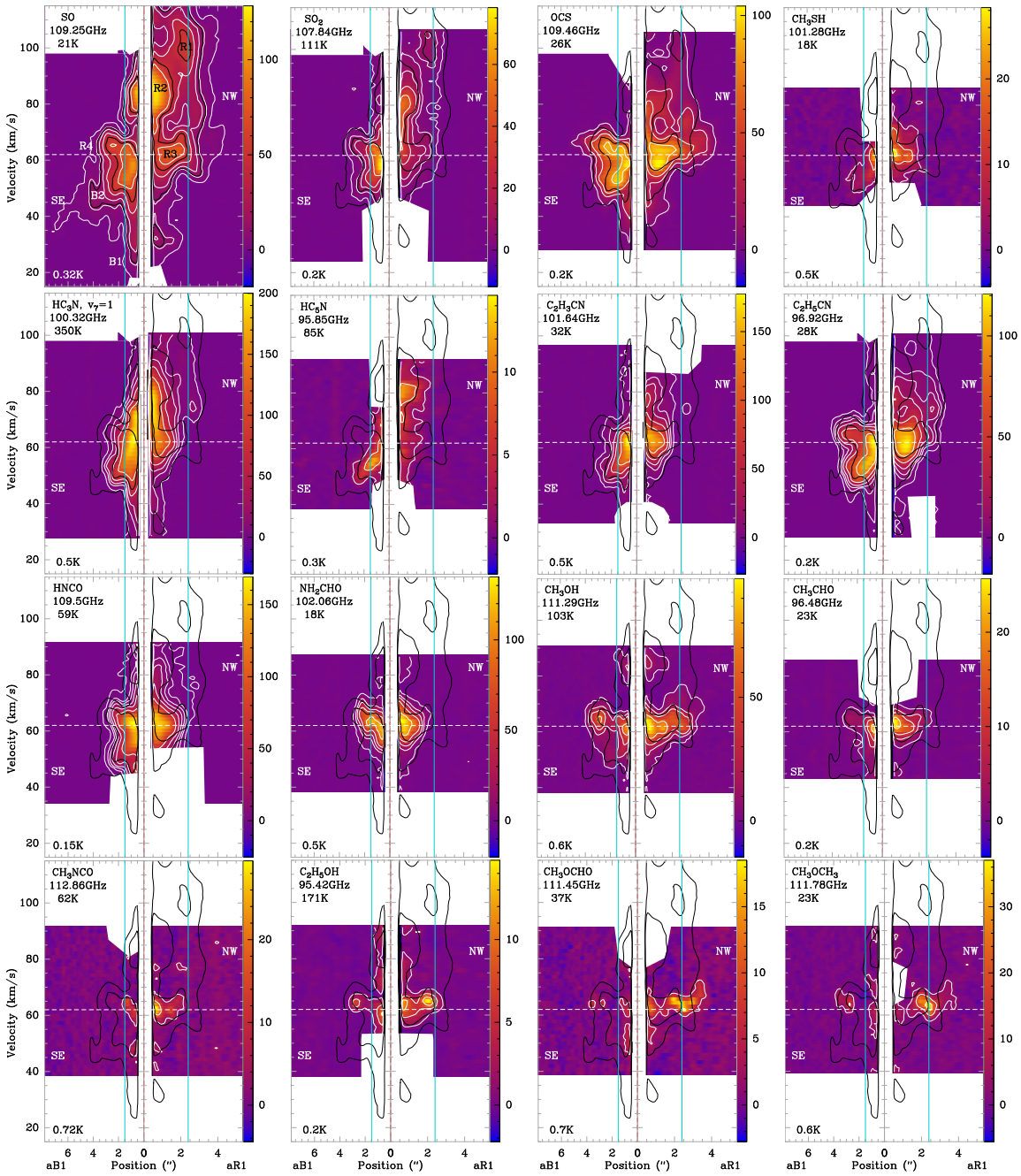

Figure B.8: Position-velocity diagrams along the solid black arrows labelled aB1 and aR1 in Fig. 4.2. Here, the position labelled 0 corresponds to the centre of the hot core. The colour scale and white contours apply to the molecule written in the top-left corner together with the frequency and upper-level energy of the used transition. White contours are at 5σ, 25σ and then increase by a factor 2, where σ was measured in an emission-free region in the respective data cube and is written in the bottom-left corner. Although the region closest to the centre of the hot core and those identified with contaminating emission from other species are masked in white, some weak emission from other molecules may still be included at distances $>1''$ to the SW and NW. Black contours always show SO emission at 30σ and 150σ. The maximum and minimum velocities shown in each map correspond to the outer integration limits used in Figs. B.4–B.6, if existing. The white dashed line marks an average systemic velocity of 62 km s^{-1}. Highlighted features in blue-shifted emission towards the southeast (SE, in the position-position maps) include B1 (elongated along velocity axis), B2 (elongated along both axes). Intensity peaks in red-shifted emission towards the northwest (NW) are labelled R1 and R2, and red-shifted emission close to the systemic velocity are labelled R3 (NW) and R4 (SE). Positions N1SE1 and N1NW3 are indicated with light-blue solid lines.

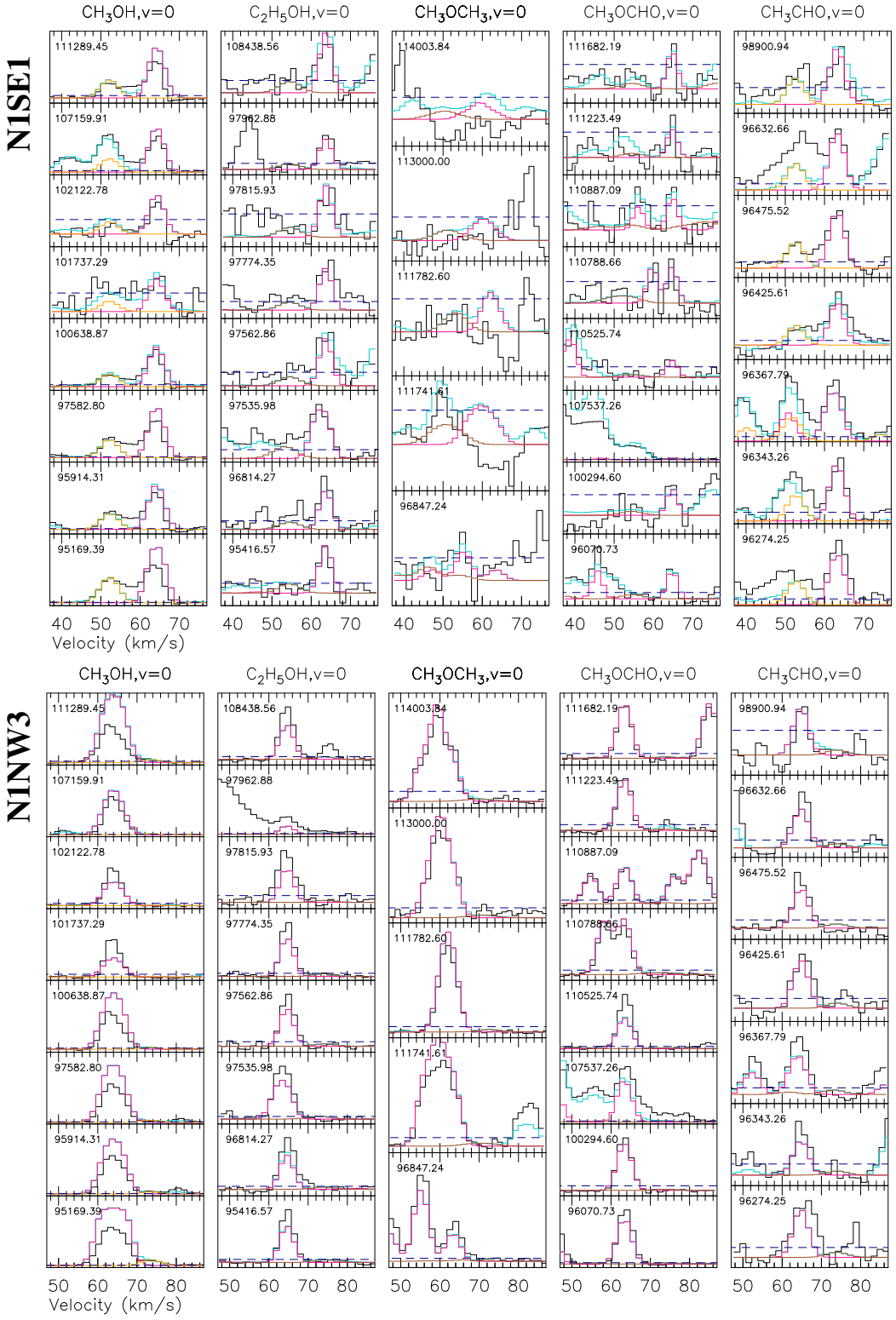

Figure B.9: Observed spectra of O-bearing COMs (black) towards N1SE1 (*top*) and N1NW3 (*bottom*). The modelled spectra of the hot-core component are shown in pink (if detected) or purple (if not), those of the outflow component in orange (if detected) or brown (if not). The complete Weeds model is drawn in turquoise. The dashed line indicates the 3σ threshold for detection, where σ is taken from Table 2 in Belloche et al. (2019). The frequency in GHz at the reference velocity of 62 km s^{-1} is shown in each panel.

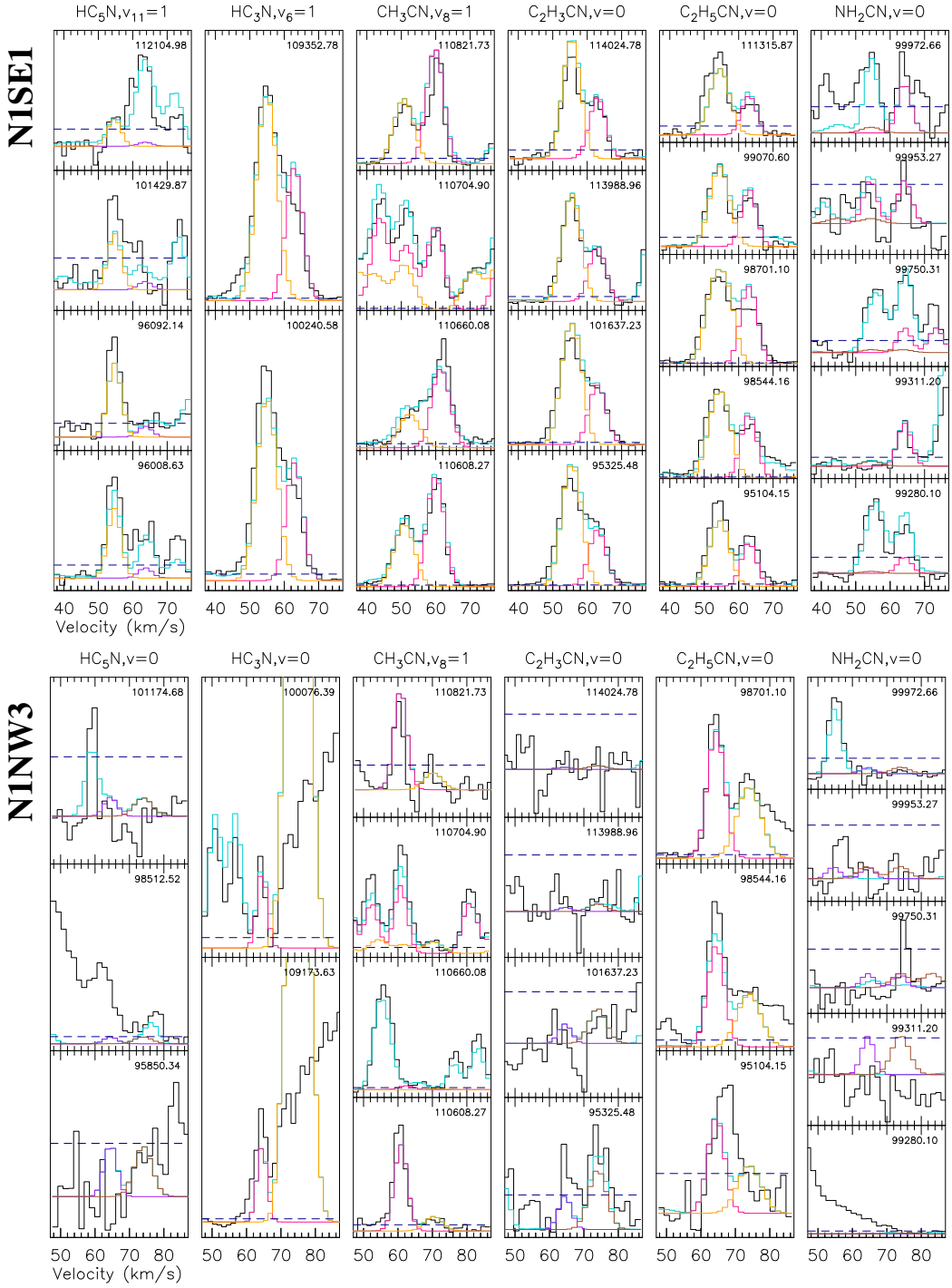

Figure B.10: Same as Fig. B.9, but for N-bearing molecules.

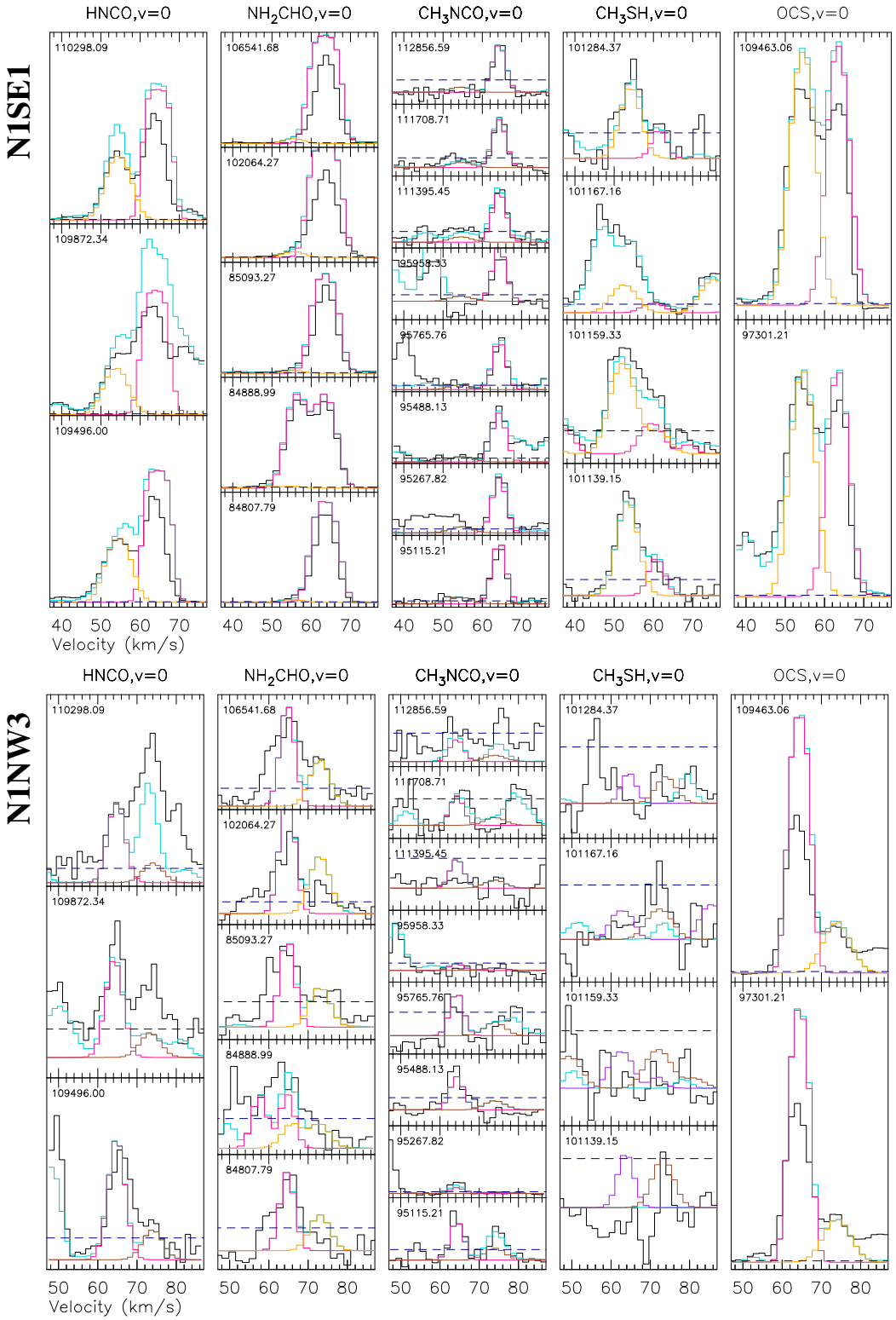

Figure B.11: Same as Fig. B.9, but for (N+O)- and S-bearing molecules.

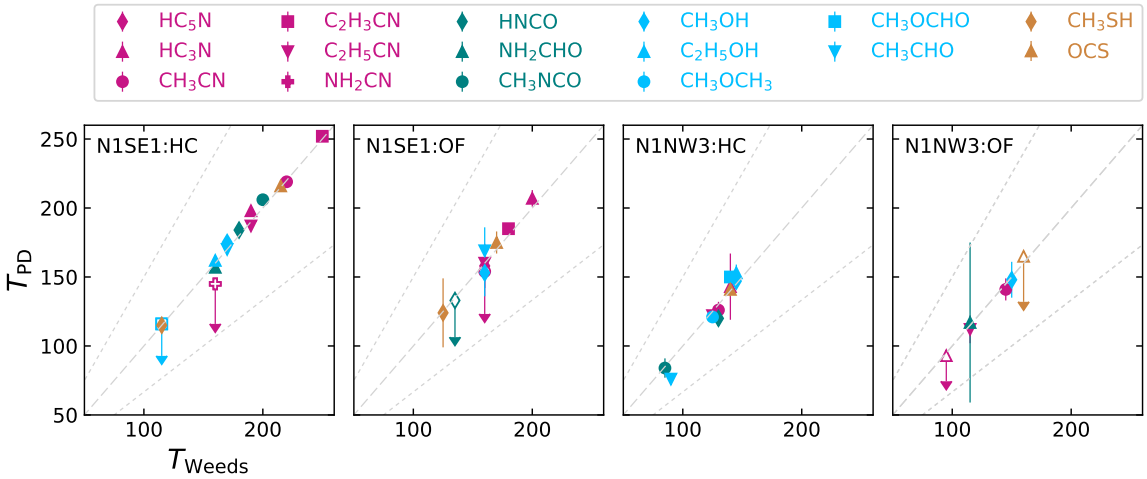

Figure B.12: Comparison of rotational temperatures used for the Weeds models and derived in the population diagrams for the various molecules in the hot-core and outflow components at positions N1SE1 and N1NW3. Pink markers indicate N-bearing species, teal markers (N+O)-bearers, blue O-bearers, and orange S-bearers. Empty markers with arrows indicate upper limits. The grey dashed line shows where temperatures are equal. The two grey dotted lines indicate a factor 1.5 difference from unity.

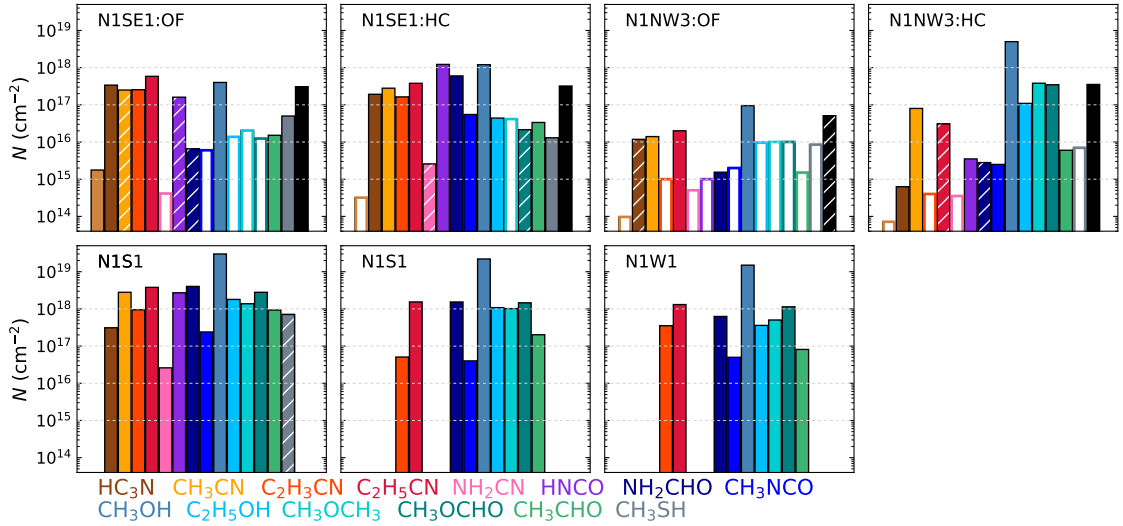

Figure B.13: Column densities of various organic molecules for the outflow (OF) and hot-core (HC) components at positions N1SE1 and N1NW3, as well as at N1S, N1S1, and N1W1. Empty bars indicate upper limits. In all panels hatched bars indicate when the rotational temperature in a population diagram (PD) was fixed (NH_2CN at N1SE1:HC and CH_3SH at N1S), the molecule was detected but a PD could not be derived (NH_2CHO at N1SE1:OF), or only an upper limit for the rotational temperature in the PD was derived.

B.5.1 G0.693

Requena-Torres et al. (2006) performed observations with the IRAM 30 m telescope at an angular resolution of 10–25″ towards multiple clouds located in the Galactic centre region. Their study was focussed on (mainly O-bearing) complex molecules. Amongst these sources, G0.693 was one of the chemically richest, and was observed again in a follow-up study by Requena-Torres et al. (2008) with the Green Bank Telescope (GBT) at lower frequencies, where they confirmed the source as one of the largest repositories of O-bearing organic molecules in the Galactic centre region. Rotational temperatures were derived from rotational diagrams and were found to be < 16 K. Armijos-Abendaño et al. (2015) performed a spectral line survey towards G0.693 at the same position as Requena-Torres et al. (2008) with the Mopra 22 m radio telescope at an angular resolution of 30–40″ covering a variety of simpler and more complex species. Based on a rotational-diagram analysis they derived rotational temperatures of 10–70 K. Zeng et al. (2018) observed the same position with the IRAM 30 m telescope and the GBT at slightly higher angular resolution in order to perform a detailed study on N-bearing molecules. Excitation temperatures and column densities were obtained from an LTE analysis with `madcuba` or from rotational diagrams. The temperatures lie in a range of 10–30 K. The column density of NH_2CHO was recently updated by Zeng et al. (2023) using new observational data obtained with the IRAM 30 m and the Yebes 40 m telescopes. Rodríguez-Almeida et al. (2021) observed the source at the same position with the IRAM 30m and the Yebes 40 m telescopes covering frequencies from 32 to 172 GHz to study mainly S-bearing molecules. Based on modelling with `madcuba` they derived excitation temperatures of ∼15 K. All studies above assume extended emission to derive column densities. The column densities reported for G0.693 by the various studies are summarised in Table B.6.

In Fig. 4.11 we compare abundances with respect to H_2 derived towards G0.693 and at positions in Sgr B2 (N1), including N1S, N1SE1(:OF and HC), and N1NW3:HC. A detailed comparison of the chemical compositions is provided in the following. The key points are summarised in the main text in Sect. 4.4.2. All molecules have higher abundances with respect to H_2 at N1S than in G0.693 by 1–2 orders of magnitude or even more, except for NH_2CN and HC_3N, whose abundances are similar to or higher by a factor of a few than in G0.693, respectively. The picture is not too different for N1SE1:HC. All cyanides and (N+O)-bearing molecules show higher abundances by about two orders of magnitude than in G0.693. Even abundances of HC_3N are enhanced by more than an order of magnitude in N1SE1:HC. The difference in abundance of O-bearing molecules and CH_3SH between N1SE1:HC and G0.693 is sightly smaller than for N1S. The abundance of OCS is higher by more than a factor 10 in N1SE1:HC and the upper limit for HC_5N in N1SE1:HC implies a much lower abundance than in G0.693. In the outflow component at N1SE1, abundances of the cyanides and HC_3N behave similarly as in N1SE1:HC. The abundance of HC_5N is quite similar for G0.693 and N1SE1:OF, while NH_2CN is less abundant by a factor 10 in the latter. Sulphur-bearing molecules are more abundant by about a factor 10 and HNCO is still more abundant by a factor of a few in N1SE1:OF. For the other (N+O)-bearing molecules and most of the O-bearing species, we only derived upper limits, from which we cannot draw conclusions for the comparison to G0.693.

The scatter between the families of molecules is larger in N1NW3:HC. Abundances of CH_3CN and C_2H_5CN are higher by more than two orders of magnitude than in G0.693, while all other N-bearing species are similarly abundant or, more likely, less abundant. All detected O-bearing molecules, except for CH_3CHO, and OCS also have abundances that are higher by two orders of magnitude or more. The abundance of HNCO is similar in both positions, while CH_3NCO and NH_2CHO abundances are

higher by up to a factor 10 in N1NW3:HC.

Molecules that have been observed in G0.693 and that we do not detect in the outflow of Sgr B2 (N1) include, for example, HC_7N (Zeng et al. 2018) and g–C_2H_5SH (Rodríguez-Almeida et al. 2021), with abundances with respect to H_2 of $\sim 1\times10^{-10}$ and $\sim 3\times10^{-10}$, respectively. We derive upper limits on the abundances in N1SE:OF of $\sim 6\times10^{-11}$ and $\sim 3.8\times10^{-9}$, respectively, not including vibrational corrections. In addition, we show a comparison of abundances with respect to methanol in the right column of Fig. B.14. What stands out is, similar to the abundances with respect to H_2, the cyanides are significantly more abundant at N1S and in both components at N1SE1. In Fig. B.14 we also show component N1NW3:OF, however, with mostly upper limits on the abundances in this component, identifying similarities and differences to the chemical content of G0.693 is difficult.

B.5.2 L1157-B1

Abundances that were derived towards L1157-B1 from observations at low angular resolution originate from Arce et al. (2008), Lefloch et al. (2017), Mendoza et al. (2014, 2018), and Sugimura et al. (2011). The first four studies carried out pointed observations towards L1157-B1 with the IRAM 30 m telescope, where the position is not always the same. The observations were performed at 2 and 1.3 mm (Arce et al. 2008) or at 3 mm. Rotational temperatures and column densities were derived based on a rotational-diagram analysis. Values of rotational temperature lie in a range of 10–30 K for O- and (O+N)-bearing species and are higher for N-bearing molecules (50–60 K or higher). Sugimura et al. (2011) performed observations with the NRO 45 m telescope at 3 mm and derived abundances based on the assumption of optically thin emission and a fixed rotational temperature that they took from Arce et al. (2008).

Interferometric observations were performed by Benedettini et al. (2007) and Codella et al. (2009) with the Plateau de Bure Interferometre (PdBI), run by IRAM, and by Codella et al. (2017, 2020, 2021) with the array's successor NOEMA (NOrthern Extended Millimetre Array). The latter studies were carried out as part of the SOLIS (Seeds Of Life In Space) survey (Ceccarelli et al. 2017). All observations yielded an angular resolution of 3–5″ and three of them were done at 3 mm, while for CH_3CN the $8_K - 7_K$ at ~147 GHz was observed (Codella et al. 2009). Rotational temperatures were derived based on a rotational-diagram analysis, which yielded a value of ~10 K for CH_3OH and CH_3CHO (Codella et al. 2020), 73 K for CH_3CN (Codella et al. 2009), and ≥70 K for OCS, which are in agreement with results derived from single-dish observations. Benedettini et al. (2007) and Codella et al. (2017) assumed a value of 80 K and 10 K, respectively, to derive column densities, which they took from previous studies. The column densities derived from single-dish (LR) and interferometric (HR) data are summarised in Table B.6.

From the comparison of abundances with respect to H_2 and methanol in Figs. 4.11 and B.14, respectively, we saw that the gas-phase chemical inventory of L1157-B1 is similar to that in G0.693, the comparison to Sgr B2 (N1) reveals similar differences in abundances with respect to H_2 in Fig. 4.11. Abundances of CH_3CN, C_2H_5CN, and NH_2CHO are higher by two orders of magnitude in N1S, while those of all O-bearing molecules, HNCO, and HC_3N are higher by factors of a few. At N1SE1:HC, abundances of O-bearing molecules are generally more similar to L1157-B1, while CH_3CN, C_2H_5CN, NH_2CHO, and here also HC_3N have higher abundances by a factor 100 or more and HNCO and OCS abundances are higher by a factor 10 or more. The only N-bearing molecule that has a similar or lower abundance than in L1157-B1 is HC_5N. The picture is similar for N1SE1:OF, except that

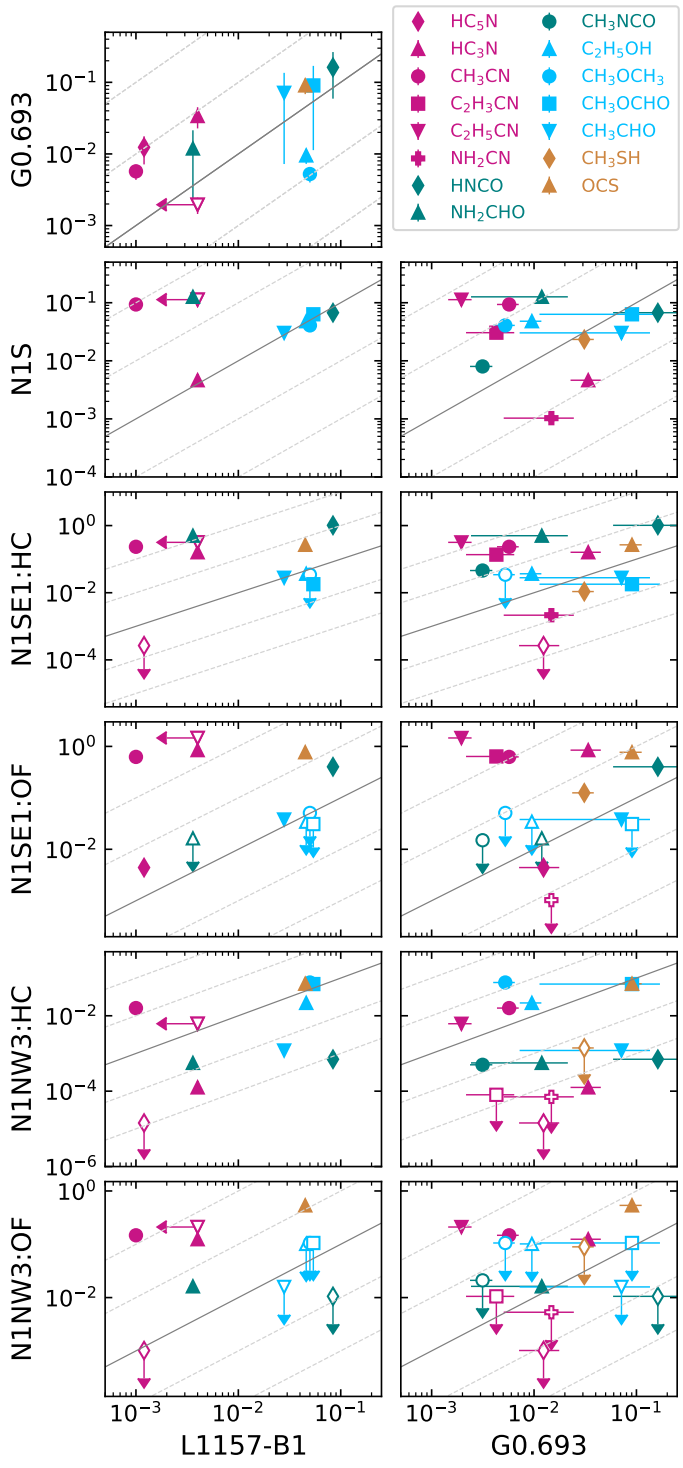

Figure B.14: Same as Fig. 4.11, but for molecular abundances with respect to methanol and additionally showing component N1NW3:OF.

the the (N+O)-bearing species HNCO and NH_2CHO are no longer significantly more abundant than in L1157-B1, and the O-bearing molecules are likely less abundant than in L1157-B1, except for CH_3CHO, which has similar abundances towards both positions. Abundances in N1NW3:HC behave again differently than in other hot-core components in Sgr B2 (N1): all O-bearing molecules, except CH_3CHO, have higher abundances in N1NW3:HC than in L1157-B1 by an order of magnitude or more. These higher abundances are also seen for CH_3CN, C_2H_5CN, and OCS. The abundance for HNCO is lower by factors of a few in N1NW3:HC, while the NH_2CHO abundance is higher by a similar amount. CH_3CHO and HC_3N are similarly abundant in both sources. The overall picture for abundances with respect to CH_3OH shown in Fig. B.14 is again similar to what we see for abundances with respect to H_2.

B.6 Detailed comparison with hot-core models

In Sect. 4.4.3 we introduced the astrochemical models conducted by Garrod et al. (2022, G22 hereafter), which have the goal to predict the chemistry in hot cores. This section provides a detailed comparison between the modelled peak abundances and our observed abundances and a discussion on whether the underlying chemical network of each species used in the models can reproduce the observations or not. In a similar way as in Fig. 13 in Paper I and Fig. 15 in G22, but using abundances with respect to H_2, we compare the modelled peak abundances with the observed ones in Fig. B.15, where we show the results for both components at positions N1SE1, for N1NW3:HC, for N1S and N1S1 (derived in Paper I), and those for G0.693 and L1157-B1 that were discussed in Sect. 4.4.2. The modelled abundances $X_{\rm mod}$ are taken from Table 17 in G22, where we use the values of the slow warm-up (SWU hereafter) in Fig. B.15a, as we found these to best reproduce our observational results in Paper I, and the fast warm-up (FWU hereafter) in Fig. B.15b, as a shorter heating timescale may be closer to what we expect from a shock event. Black crosses indicate molecules for which no value is available. In Fig. B.16 we additionally present the comparison to the model with SWU for abundances with respect to CH_3OH. However, we will focus the following discussion on the abundances with respect to H_2.

B.6.1 N1S and N1S1

Abundances of most molecules at N1S and N1S1 have been derived and compared to the G22 model (assuming SWU) in Paper I. The observed abundance profiles of N- and (N+O)-bearing COMs showed either a plateau or an increasing behaviour at temperatures above 100 K. In particular, the increase of abundances at high temperatures pointed to the COMs' formation partly or solely in the gas phase at these temperatures. The abundance of HC_3N at N1S was derived in this work and is overestimated in the model by factors of a few (FWU) or two orders of magnitude (SWU). A better match with the model may be achieved if HC_3N was more efficiently converted to C_2H_3CN and, eventually, C_2H_5CN on dust grain surfaces. This was suggested as a way to increase the modelled abundances of these cyanides, because they were found to be underestimated by the model in Paper I. Methyl cyanide is predicted to be efficiently produced in the gas phase, mainly from the recombination of CH_3CNH^+ with an electron, where the protonated methyl cyanide is a product of the gas-phase reaction CH_3^+ + HCN. This seems plausible as the CH_3CN abundance, which was previously derived at N1S (Müller et al. 2021), behaves similarly to C_2H_3CN. If we assume a FWU, for which CH_3CN abundances are largely underestimated, the production of the COM has to proceed more efficiently in the model or

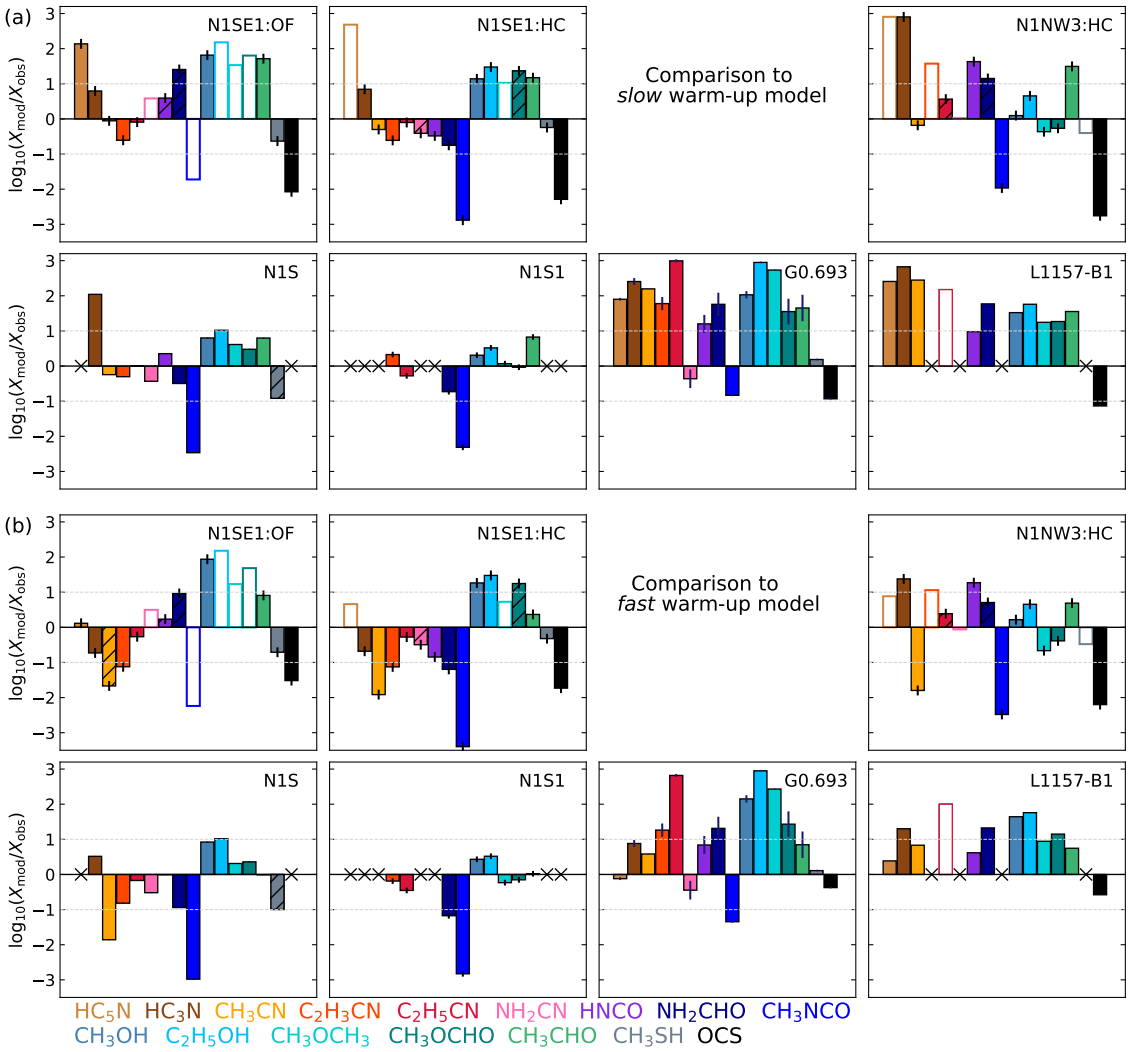

Figure B.15: Comparison between modelled peak abundances with respect to H_2 and the observed abundances towards both components at N1SE1 and N1NW3:HC, N1S, N1S1, G0.693, and L1157-B1. For all observed values, H_2 column densities were derived from $C^{18}O$ emission, except for N1S, for which dust emission was used. The modelled abundances X_{mod} are taken from Table 17 in Garrod et al. (2022), where we use the values of the slow *(a)* and fast *(b)* warm-up models, and multiplied by a factor 2 to roughly convert to abundances with respect to H_2 (from total H). Empty bars indicate lower limits. Hatched bars indicate the same as in Fig. 4.10. Black crosses indicate molecules for which no values are available.

there are additional formation routes (likely in the gas phase) that are currently not considered. The value of NH_2CN column density at N1S was taken from an earlier ReMoCA result for N1S (Kisiel et al. 2022). The molecule is predicted to be solely formed at earliest times during stage 1, that is when the ice mantles start to build. According to G22, a high observed abundance of this molecule suggests that photoprocessing of the ice mantles at these early times could have been significant. This formation at early times would explain the little difference between SWU and FWU.

The peak abundances for most O-bearing COMs were found at positions further away from Sgr B2 (N1) than N1S in Paper I. This can explain why the observed abundances at N1S are lower than the model predictions. In the FWU, there was less time to destroy CH_3OCH_3 and CH_3OCHO, explaining the better agreement with the model. A possible reason for the overproduction of C_2H_5OH was discussed in Paper I. Acetaldehyde is dominantly formed in the gas phase in the models. Therefore, the overproduction at N1S and N1S1 in the SWU models has to have another origin than for the other O-bearing species. Because the abundance is well reproduced for the FWU, maybe the heating timescale is the reason, which was also mentioned in Paper I. The chemical network for CH_3NCO is incomplete, which is likely the main reason for the heavy underestimation of its abundances not only at N1S and N1S1 but all positions shown in Fig. B.15. Formamide forms in both the solid and gas phases in the model, which was also indicated by the observed abundance profiles in Paper I. However, it also gets efficiently destroyed in the gas phase after its thermal desorption, which was not evident in the observed abundance profile. The abundance of HNCO was additionally derived in this work for N1S and seems to agree well with the modelled value. In the model, HNCO is a product of grain-surface chemistry and is efficiently photodissociated in the gas phase after desorption. This destruction pathway for HNCO cannot be inferred from our results, but, for example, it has been used as an explanation for observations towards Sgr B2 (N) (Corby et al. 2015), where HNCO is depleted towards the HII regions.

Methyl mercaptan is purely a product of grain-surface chemistry and is formed mainly via H addition to CS during the collapse as well as the subsequent warm-up phase as can be seen from its panel in Fig. B.17, which assumes a SWU. This kind of figure is an output of the G22 models and such plots were presented for a variety of molecules in Figs. 13–14 in their article. These figures show qualitatively at what times (and temperature regime) of the pre- and protostellar evolution a molecule is dominantly formed (green) or destroyed (blue). The underestimation of CH_3SH abundances in the model may be the consequence of the fact that some input parameters related to sulphur chemistry are still uncertain in chemical models, for example the initial elemental abundance of S (G22) in general or, specifically for CH_3SH, the activation barriers for some of the reactions that eventually lead to the formation of the COM.

B.6.2 N1SE1

A more efficient conversion of HC_3N to C_2H_3CN and C_2H_5CN in the solid phase as proposed in Sect. B.6.1 may help to better match the modelled and observed HC_3N abundances for N1SE1 in the case of the SWU (see Fig. B.15), however, it would lead to a larger discrepancy for the cyanides in this case and does not help at all the results for the FWU. The secure detection of HC_5N at N1SE1:OF may suggest that gas-phase chemistry plays an important role in this component. Not only this molecule but also HC_3N have both efficient formation pathways occurring at around 200 K in the gas phase, where C_2H and HCN react to form HC_3N, which will again react with C_2H to form HC_5N. We show the rate of change of HC_5N abundance in the SWU in Fig. B.17, where it is evident that there are two

periods of efficient gas-phase production: at around 200 K and at $\gtrsim$350 K. At high temperatures during the second period, atomic N is sourced from NH_3 via H abstraction and reacts with hydrocarbons (e.g. C_5H_2), to form HC_5N. Our analysis did not reveal such high temperatures, however, a shock passage in the past could have caused a temporal temperature increase to 400 K or more. In the case of a FWU, there must be additional gas-phase formation routes for CH_3CN, C_2H_3CN, HC_3N, and OCS to better match the observations and the models. A shock may be able to enhance the gas-phase chemistry or trigger additional reactions. This applies to both components at N1SE1.

As already seen for N1S and N1S1, CH_3NCO abundances are heavily underestimated in the model by multiple orders of magnitude, certainly at N1SE1:HC, likely mostly due to an incomplete chemical network. In Paper I we discussed additional formation routes that could potentially increase abundances in the model. Abundances of NH_2CHO are underestimated in the model for N1S, N1S1, and N1SE1:HC, but it is overestimated for the outflow component in both the SWU and FWU. Despite predicted by the G22 models, there was no clear evidence for the destruction of NH_2CHO at high temperatures in Paper I. Therefore we proposed that, for example, the COM's destruction should perhaps be less efficient in the model to better match the observed abundance. Abundances of HNCO behave similarly to those of NH_2CHO at N1SE1, except that the over- or underproduction is not as severe. In the model, NH_2CHO and HNCO are correlated in the sense that they are produced and destroyed at similar periods of time and temperature. A difference is however that HNCO is purely formed on dust grain surfaces. However, it can be a by-product of COM dissociation at high temperatures in the gas phase (Garrod et al. 2008; Tideswell et al. 2010).

The overall larger overestimation of abundances of O-bearing COMs in the model suggests an enhanced destruction of these in N1SE1:HC and even more so in N1SE1:OF in the gas phase after their desorption from the dust grains. Again, this explanation does not apply to CH_3CHO as it is primarily a gas-phase product. Moreover, given that HNCO and NH_2CN are products of grain-surface chemistry and are efficiently destroyed in the gas phase in the model, we would expect them to behave more similarly to the O-bearing COMs. This suggests that either their destruction proceeds less efficiently or they have additional formation routes likely in the gas phase.

As mentioned in Sect. B.6.1, the predictions for CH_3SH may have higher uncertainties due to unknowns in the sulphur chemistry in general and the chemistry of the COM in particular. The underestimation of the OCS abundances by the model is more severe. We show the rate of change for the SWU of the molecule's abundance during the protostellar evolution in Fig. B.17. The molecule is mainly formed towards the end of the collapse phase, where the reaction S + CO produces OCS on the dust grain surfaces. In the current model, the activation barrier for this reaction is set to zero, while this assumption may not actually be correct (Loison et al. 2012). A non-zero activation barrier would however worsen the difference between the model and the observations. There are a few reactions that produce OCS in the gas phase in the model. However, these are currently not able to reproduce the observed abundance.

B.6.3 N1NW3:HC

Molecular abundances behave quite differently in the hot-core component at this position than at N1S or N1SE1. Rotational temperatures at this position are between 80–150 K (see Fig. 4.7), which is when we expect thermal desorption to proceed efficiently (see Paper I). This would explain the better agreement between the model and the observations for the O-bearing molecules in Fig. B.15 and the result for NH_2CN, while gas-phase products such as CH_3CHO, C_2H_3CN, and cyanopolyynes are

overproduced by the model, especially for the SWU. This scenario does not explain the values for CH_3CN, which should behave similarly to, for example, C_2H_3CN, and HNCO, which we would expect to behave similar to the other products of grain-surface chemistry, according to the model.

B.6.4 G0.693 and L1157-B1

Besides a few exceptions, abundances with respect to H_2 are all overproduced by the SWU and FWU models as can be seen in Fig. B.15, which may not be surprising, given that the model is designated to predict the chemistry of hot cores that are known to possess higher abundances of especially COMs than prestellar cores or low-mass protostars. One of the exceptions is NH_2CN, whose abundance is well predicted by the model in G0.693. This suggests that the molecule's formation at early times of stage 1 in the model may indeed be the dominant formation pathway. The other exceptions are OCS and CH_3NCO, for which we know that the chemical network is likely not complete.

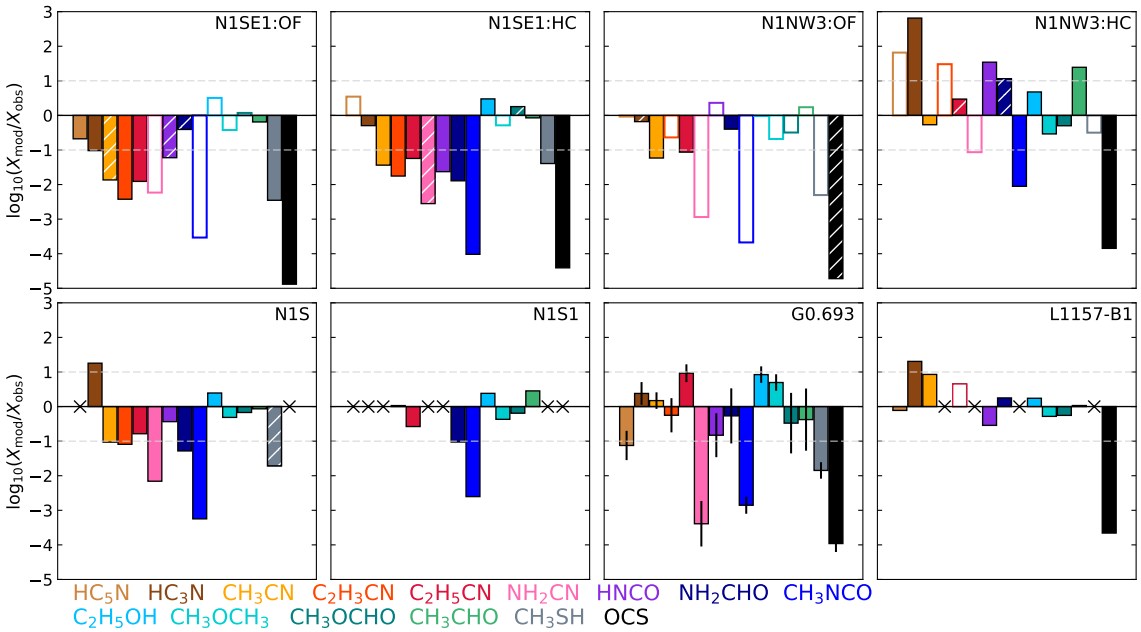

Figure B.16: Comparison between modelled peak abundances with respect to methanol and the observed abundances towards both components at N1SE1 and N1NW3, N1S, N1S1, G0.693, and L1157-B1. The modelled abundances $X_{\rm mod}$ are taken from Table 17 and 18 in Garrod et al. (2022), where we use the values of the slow warm-up model. Empty bars indicate lower limits. Hatched bars indicate the same as in Fig. 4.10. Black crosses indicate molecules for which no values are available.

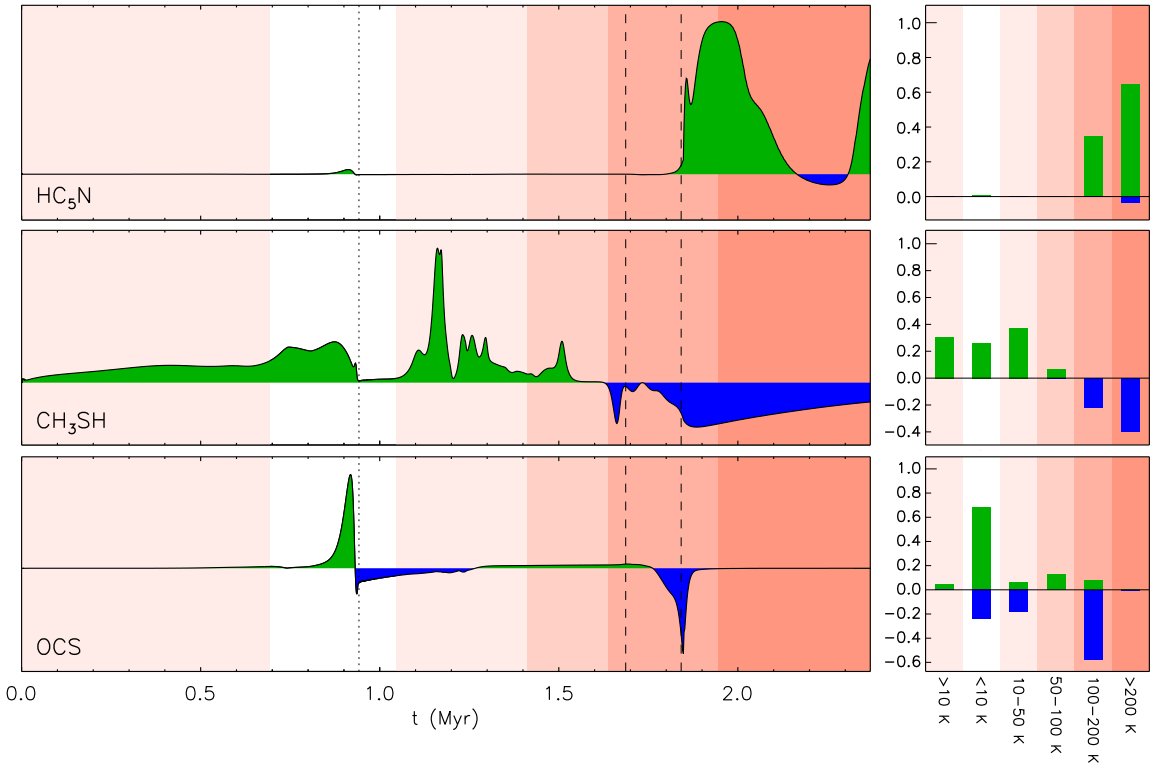

Figure B.17: Same as Fig. 13 in Garrod et al. (2022), but for HC_5N, CH_3SH, and OCS. It shows the net rate of change in the COM's abundances, summed over all chemical phases, during the cold collapse phase and the subsequent slow warm-up. Green represents a net production of the molecule, blue a net destruction. The time axis is divided into several phases marked with different background colours that are associated with the temperature ranges labelled in the right panels. The dotted black line marks the start of the warm-up phase, the two dashed lines indicate the time of thermal desorption of water.

Bibliography

Agúndez, M., Marcelino, N., Tercero, B., et al. 2021, A&A, 649, L4

Allen, V., van der Tak, F. F. S., Sánchez-Monge, Á., Cesaroni, R., & Beltrán, M. T. 2017, A&A, 603, A133

ALMA Partnership, Asayama, S., Biggs, A., et al. 2016, ALMA Cycle 4 Technical Handbook

Altwegg, K., Balsiger, H., Bar-Nun, A., et al. 2016, Science Advances, 2, e1600285

Altwegg, K., Balsiger, H., & Fuselier, S. A. 2019, ARA&A, 57, 113

Andre, P., Ward-Thompson, D., & Barsony, M. 2000, in Protostars and Planets IV, ed. V. Mannings, A. P. Boss, & S. S. Russell, 59

Arce, H. G., Santiago-García, J., Jørgensen, J. K., Tafalla, M., & Bachiller, R. 2008, ApJ, 681, L21

Armijos-Abendaño, J., Martín-Pintado, J., Requena-Torres, M. A., Martín, S., & Rodríguez-Franco, A. 2015, MNRAS, 446, 3842

Bachiller, R. & Pérez Gutiérrez, M. 1997, ApJ, 487, L93

Bacmann, A., Taquet, V., Faure, A., Kahane, C., & Ceccarelli, C. 2012, A&A, 541, L12

Bally, J. 2016, ARA&A, 54, 491

Balucani, N., Ceccarelli, C., & Taquet, V. 2015, MNRAS, 449, L16

Belloche, A., Garrod, R. T., Müller, H. S. P., & Menten, K. M. 2014, Science, 345, 1584

Belloche, A., Garrod, R. T., Müller, H. S. P., et al. 2019, A&A, 628, A10

Belloche, A., Menten, K. M., Comito, C., et al. 2008, A&A, 482, 179

Belloche, A., Meshcheryakov, A. A., Garrod, R. T., et al. 2017, A&A, 601, A49

Belloche, A., Müller, H. S. P., Garrod, R. T., & Menten, K. M. 2016, A&A, 587, A91

Belloche, A., Müller, H. S. P., Menten, K. M., Schilke, P., & Comito, C. 2013, A&A, 559, A47

Beltrán, M. T., Cesaroni, R., Rivilla, V. M., et al. 2018, A&A, 615, A141

Benedettini, M., Viti, S., Codella, C., et al. 2007, MNRAS, 381, 1127

Beuther, H., Churchwell, E. B., McKee, C. F., & Tan, J. C. 2007, in Protostars and Planets V, ed. B. Reipurth, D. Jewitt, & K. Keil, 165

Blake, G. A., Sutton, E. C., Masson, C. R., & Phillips, T. G. 1987, ApJ, 315, 621

Bolatto, A. D., Wolfire, M., & Leroy, A. K. 2013, ARA&A, 51, 207

Bonfand, M., Belloche, A., Garrod, R. T., et al. 2019, A&A, 628, A27

Bonfand, M., Belloche, A., Menten, K. M., Garrod, R. T., & Müller, H. S. P. 2017, A&A, 604, A60

Bonnell, I. A., Bate, M. R., Clarke, C. J., & Pringle, J. E. 2001, MNRAS, 323, 785

Boogert, A. C. A., Gerakines, P. A., & Whittet, D. C. B. 2015, ARA&A, 53, 541

Brunken, N. G. C., Booth, A. S., Leemker, M., et al. 2022, A&A, 659, A29

Burkhardt, A. M., Shingledecker, C. N., Le Gal, R., et al. 2019, ApJ, 881, 32

Busch, L. A., Belloche, A., Garrod, R. T., Müller, H. S. P., & Menten, K. M. 2022, A&A, 665, A96

Calcutt, H., Jørgensen, J. K., Müller, H. S. P., et al. 2018, A&A, 616, A90

Candelaria, T. M., Mills, E. A. C., Meier, D. S., Ott, J., & Butterfield, N. 2023, arXiv e-prints, arXiv:2303.11222

Caselli, P., Hasegawa, T. I., & Herbst, E. 1993, ApJ, 408, 548

Ceccarelli, C., Caselli, P., Fontani, F., et al. 2017, ApJ, 850, 176

Ceccarelli, C., Codella, C., Balucani, N., et al. 2022, arXiv e-prints, arXiv:2206.13270

Choe, J. C. 2023, Physical Chemistry Chemical Physics (Incorporating Faraday Transactions), 25, 16001

Chuang, K. J., Fedoseev, G., Ioppolo, S., van Dishoeck, E. F., & Linnartz, H. 2016, MNRAS, 455, 1702

Chuard, D., Terrier, R., Goldwurm, A., et al. 2018, A&A, 610, A34

Churchwell, E. 2002, ARA&A, 40, 27

Clark, P. C., Glover, S. C. O., Ragan, S. E., Shetty, R., & Klessen, R. S. 2013, ApJ, 768, L34

Codella, C., Benedettini, M., Beltrán, M. T., et al. 2009, A&A, 507, L25

Codella, C., Bianchi, E., Podio, L., et al. 2021, A&A, 654, A52

Codella, C., Ceccarelli, C., Bianchi, E., et al. 2020, A&A, 635, A17

Codella, C., Ceccarelli, C., Caselli, P., et al. 2017, A&A, 605, L3

Collings, M. P., Anderson, M. A., Chen, R., et al. 2004, MNRAS, 354, 1133

Condon, J. J. & Ransom, S. M. 2015, Online lecture slides: Essential Radio Astronomy, https://www.cv.nrao.edu/~sransom/web/Chx1.html

Corby, J. F., Jones, P. A., Cunningham, M. R., et al. 2015, MNRAS, 452, 3969

Crockett, N. R., Bergin, E. A., Neill, J. L., et al. 2015, ApJ, 806, 239

Crockett, N. R., Bergin, E. A., Neill, J. L., et al. 2014, ApJ, 787, 112

Csengeri, T., Belloche, A., Bontemps, S., et al. 2019, A&A, 632, A57

De Pree, C. G., Peters, T., Mac Low, M. M., et al. 2015, ApJ, 815, 123

De Simone, M., Codella, C., Ceccarelli, C., et al. 2020, A&A, 640, A75

Demyk, K., Meny, C., Leroux, H., et al. 2014, PoS, LCDU2013, 044

Draine, B. 2010, Physics of the Interstellar and Intergalactic Medium, Princeton Series in Astrophysics (Princeton University Press)

Draine, B. T. & Li, A. 2007, ApJ, 657, 810

Elitzur, M. 1992, Astronomical Masers, Astrophysics and Space Science Library (Springer Netherlands)

Elitzur, M., Hollenbach, D. J., & McKee, C. F. 1989, ApJ, 346, 983

Elsila, J. E., Glavin, D. P., & Dworkin, J. P. 2009, Meteoritics and Planetary Science, 44, 1323

Endres, C. P., Schlemmer, S., Schilke, P., Stutzki, J., & Müller, H. S. P. 2016, Journal of Molecular Spectroscopy, 327, 95

Erickson, E. F., Knacke, R. F., Tokunaga, A. T., & Haas, M. R. 1981, ApJ, 245, 148

Favre, C., Fedele, D., Semenov, D., et al. 2018, ApJ, 862, L2

Favre, C., Pagani, L., Goldsmith, P. F., et al. 2017, A&A, 604, L2

Fedoseev, G., Chuang, K. J., Ioppolo, S., et al. 2017, ApJ, 842, 52

Fedoseev, G., Cuppen, H. M., Ioppolo, S., Lamberts, T., & Linnartz, H. 2015, MNRAS, 448, 1288

Garcia-Segura, G. & Franco, J. 1996, ApJ, 469, 171

Garrod, R. T. 2013, ApJ, 765, 60

Garrod, R. T., Belloche, A., Müller, H. S. P., & Menten, K. M. 2017, A&A, 601, A48

Garrod, R. T., Jin, M., Matis, K. A., et al. 2022, ApJS, 259, 1

Garrod, R. T., Widicus Weaver, S. L., & Herbst, E. 2008, ApJ, 682, 283

Gaume, R. A., Claussen, M. J., de Pree, C. G., Goss, W. M., & Mehringer, D. M. 1995, ApJ, 449, 663

Geppert, W. D., Hamberg, M., Thomas, R. D., et al. 2006, Faraday Discussions, 133, 177

Gieser, C., Beuther, H., Semenov, D., et al. 2021, A&A, 648, A66

Ginsburg, A., Bally, J., Barnes, A., et al. 2018, ApJ, 853, 171

Goldsmith, P. F. & Langer, W. D. 1999, ApJ, 517, 209

Gómez, L., Rodríguez, L. F., Loinard, L., et al. 2008, ApJ, 685, 333

Gredel, R., Lepp, S., Dalgarno, A., & Herbst, E. 1989, ApJ, 347, 289

Gueth, F. & Guilloteau, S. 1999, A&A, 343, 571

Güsten, R. & Philipp, S. D. 2004, in The Dense Interstellar Medium in Galaxies, ed. S. Pfalzner, C. Kramer, C. Staubmeier, & A. Heithausen, Vol. 91, 253

Hamberg, M., Österdahl, F., Thomas, R. D., et al. 2010, A&A, 514, A83

Hatchfield, H. P., Sormani, M. C., Tress, R. G., et al. 2021, ApJ, 922, 79

Henkel, C., Wilson, T. L., Langer, N., Chin, Y. N., & Mauersberger, R. 1994, Interstellar CNO Isotope

Ratios, ed. T. L. Wilson & K. J. Johnston, Vol. 439, 72–88

Henshaw, J. D., Barnes, A. T., Battersby, C., et al. 2023, in Astronomical Society of the Pacific Conference Series, Vol. 534, Protostars and Planets VII, ed. S. Inutsuka, Y. Aikawa, T. Muto, K. Tomida, & M. Tamura, 83

Herbst, E. & Klemperer, W. 1973, ApJ, 185, 505

Herbst, E. & van Dishoeck, E. F. 2009, ARA&A, 47, 427

Higuchi, A. E., Hasegawa, T., Saigo, K., Sanhueza, P., & Chibueze, J. O. 2015, ApJ, 815, 106

Hirano, N., Liu, S.-Y., Shang, H., et al. 2006, ApJ, 636, L141

Hollenbach, D., Elitzur, M., & McKee, C. F. 2013, ApJ, 773, 70

Hollis, J. M., Lovas, F. J., & Jewell, P. R. 2000, ApJ, 540, L107

Hüttemeister, S., Wilson, T. L., Mauersberger, R., et al. 1995a, A&A, 294, 667

Hüttemeister, S., Wilson, T. L., Mauersberger, R., et al. 1995b, A&A, 294, 667

Indriolo, N., Neufeld, D. A., Gerin, M., et al. 2015, ApJ, 800, 40

Ioppolo, S., Fedoseev, G., Chuang, K. J., et al. 2021, Nature Astronomy, 5, 197

Jacob, A. M., Neufeld, D. A., Schilke, P., et al. 2022, ApJ, 930, 141

Jensen, M. J., Bilodeau, R. C., Safvan, C. P., et al. 2000, ApJ, 543, 764

Jiménez-Serra, I., Martín-Pintado, J., Rivilla, V. M., et al. 2020, Astrobiology, 20, 1048

Jiménez-Serra, I., Rodríguez-Almeida, L. F., Martín-Pintado, J., et al. 2022, A&A, 663, A181

Jiménez-Serra, I., Vasyunin, A. I., Caselli, P., et al. 2016, ApJ, 830, L6

Jin, M. & Garrod, R. T. 2020, ApJS, 249, 26

Jones, P. A., Burton, M. G., Cunningham, M. R., et al. 2012, MNRAS, 419, 2961

Jørgensen, J. K., Belloche, A., & Garrod, R. T. 2020, ARA&A, 58, 727

Jørgensen, J. K., Müller, H. S. P., Calcutt, H., et al. 2018, A&A, 620, A170

Jørgensen, J. K., van der Wiel, M. H. D., Coutens, A., et al. 2016, A&A, 595, A117

Kalenskii, S. V., Slysh, V. I., Goldsmith, P. F., & Johansson, L. E. B. 2004, ApJ, 610, 329

Kauffmann, J., Bertoldi, F., Bourke, T. L., Evans, N. J., I., & Lee, C. W. 2008, A&A, 487, 993

Kenyon, S. J., Calvet, N., & Hartmann, L. 1993, ApJ, 414, 676

Keto, E. 2003, ApJ, 599, 1196

Kisiel, Z., Kolesniková, L., Belloche, A., et al. 2022, A&A, 657, A99

Klein, U. 2006, Lecture notes to Astro841: *Radio astronomy: tools, applications, and impacts* (Argelander Institut für Astronomie, Universität Bonn)

Kruijssen, J. M. D., Dale, J. E., & Longmore, S. N. 2015, MNRAS, 447, 1059

Kwon, W., Looney, L. W., Mundy, L. G., Chiang, H.-F., & Kemball, A. J. 2009, ApJ, 696, 841

Lee, C.-F. 2020, Astronomy and Astrophysics Review, 28, 1

Lefloch, B., Ceccarelli, C., Codella, C., et al. 2017, MNRAS, 469, L73

Lequeux, J., Falgarone, E., & Ryter, C. 2005, The Interstellar Medium, Astronomy and Astrophysics Library (Springer Berlin Heidelberg)

Ligterink, N. F. W. & Minissale, M. 2023, A&A, 676, A80

Lis, D. C., Goldsmith, P. F., Carlstrom, J. E., & Scoville, N. Z. 1993, ApJ, 402, 238

Liu, S.-Y. & Snyder, L. E. 1999, ApJ, 523, 683

Lodders, K. 2003, ApJ, 591, 1220

Loison, J.-C., Halvick, P., Bergeat, A., Hickson, K. M., & Wakelam, V. 2012, MNRAS, 421, 1476

Longmore, S. N., Bally, J., Testi, L., et al. 2013, MNRAS, 429, 987

Loomis, R. A., Cleeves, L. I., Öberg, K. I., et al. 2018, ApJ, 859, 131

Lu, X., Zhang, Q., Kauffmann, J., et al. 2019, ApJ, 872, 171

Mangum, J. G. & Shirley, Y. L. 2015, PASP, 127, 266

Maret, S., Hily-Blant, P., Pety, J., Bardeau, S., & Reynier, E. 2011, A&A, 526, A47

Martín, S., Mangum, J. G., Harada, N., et al. 2021, A&A, 656, A46

Martín, S., Requena-Torres, M. A., Martín-Pintado, J., & Mauersberger, R. 2008, ApJ, 678, 245

Martín-Doménech, R., Muñoz Caro, G. M., Bueno, J., & Goesmann, F. 2014, A&A, 564, A8

Martín-Pintado, J., de Vicente, P., Fuente, A., & Planesas, P. 1997, ApJ, 482, L45

McClure, M. K., Rocha, W. R. M., Pontoppidan, K. M., et al. 2023, Nature Astronomy, 7, 431

McGrath, E. J., Goss, W. M., & De Pree, C. G. 2004, ApJS, 155, 577

McGuire, B. A. 2022, ApJS, 259, 30

McGuire, B. A., Burkhardt, A. M., Kalenskii, S., et al. 2018, Science, 359, 202

McGuire, B. A., Loomis, R. A., Burkhardt, A. M., et al. 2021, Science, 371, 1265

McKee, C. F. & Tan, J. C. 2003, ApJ, 585, 850

Mendoza, E., Lefloch, B., Ceccarelli, C., et al. 2018, MNRAS, 475, 5501

Mendoza, E., Lefloch, B., López-Sepulcre, A., et al. 2014, MNRAS, 445, 151

Mezger, P. G. & Henderson, A. P. 1967, ApJ, 147, 471

Mills, E. A. C., Corby, J., Clements, A. R., et al. 2018, ApJ, 869, 121

Mills, E. A. C. & Morris, M. R. 2013, ApJ, 772, 105

Motte, F., Bontemps, S., & Louvet, F. 2018, ARA&A, 56, 41

Müller, H. S. P., Belloche, A., Lewen, F., et al. 2021, Journal of Molecular Spectroscopy, 378, 111449

Naraoka, H., Takano, Y., Dworkin, J. P., et al. 2023, Science, 379, Issue 9033

Nazari, P., Tabone, B., van't Hoff, M. L. R., Jørgensen, J. K., & van Dishoeck, E. F. 2023, ApJ, 951, L38

Öberg, K. I. & Bergin, E. A. 2021, Physics Reports, 893, 1

Öberg, K. I., Guzmán, V. V., Merchantz, C. J., et al. 2017, ApJ, 839, 43

Oka, T. 2006, Proceedings of the National Academy of Science, 103, 12235

Orozco-Aguilera, M. T., Zapata, L. A., Hirota, T., Qin, S.-L., & Masqué, J. M. 2017, ApJ, 847, 66

Ossenkopf, V. & Henning, T. 1994, A&A, 291, 943

Pagani, L., Bergin, E., Goldsmith, P. F., et al. 2019, A&A, 624, L5

Pagani, L., Favre, C., Goldsmith, P. F., et al. 2017, A&A, 604, A32

Palau, A., Walsh, C., Sánchez-Monge, Á., et al. 2017, MNRAS, 467, 2723

Paulive, A., Shingledecker, C. N., & Herbst, E. 2021, MNRAS, 500, 3414

Pearson, J. C., Müller, H. S. P., Pickett, H. M., Cohen, E. A., & Drouin, B. J. 2010, J. Quant. Spectr. Rad. Transf., 111, 1614

Qin, S. L., Schilke, P., Rolffs, R., et al. 2011, A&A, 530, L9

Reid, M. J., Menten, K. M., Brunthaler, A., et al. 2019, ApJ, 885, 131

Reid, M. J., Menten, K. M., Zheng, X. W., Brunthaler, A., & Xu, Y. 2009, ApJ, 705, 1548

Requena-Torres, M. A., Martín-Pintado, J., Martín, S., & Morris, M. R. 2008, ApJ, 672, 352

Requena-Torres, M. A., Martín-Pintado, J., Rodríguez-Franco, A., et al. 2006, A&A, 455, 971

Riquelme, D., Amo-Baladrón, M. A., Martín-Pintado, J., et al. 2013, A&A, 549, A36

Riquelme, D., Bronfman, L., Mauersberger, R., May, J., & Wilson, T. L. 2010, A&A, 523, A45

Rivilla, V. M., García De La Concepción, J., Jiménez-Serra, I., et al. 2022a, Frontiers in Astronomy and Space Sciences, 9, 829288

Rivilla, V. M., García De La Concepción, J., Jiménez-Serra, I., et al. 2022b, Frontiers in Astronomy and Space Sciences, 9, 829288

Rivilla, V. M., Jiménez-Serra, I., García de la Concepción, J., et al. 2021a, MNRAS, 506, L79

Rivilla, V. M., Jiménez-Serra, I., Martín-Pintado, J., et al. 2021b, Proceedings of the National Academy of Science, 118, e2101314118

Rivilla, V. M., Sanz-Novo, M., Jiménez-Serra, I., et al. 2023, ApJ, 953, L20

Rodríguez-Almeida, L. F., Jiménez-Serra, I., Rivilla, V. M., et al. 2021, ApJ, 912, L11

Rosen, A. L., Offner, S. S. R., Sadavoy, S. I., et al. 2020, Space Science Reviews, 216, 62

Ruaud, M., Loison, J. C., Hickson, K. M., et al. 2015, MNRAS, 447, 4004

Sánchez-Monge, Á., Schilke, P., Schmiedeke, A., et al. 2017, A&A, 604, A6

Sawada, T., Hasegawa, T., Handa, T., & Cohen, R. J. 2004, MNRAS, 349, 1167

Schmiedeke, A., Schilke, P., Möller, T., et al. 2016, A&A, 588, A143

Schnee, S., Enoch, M., Noriega-Crespo, A., et al. 2009, The Astrophysical Journal, 708, 127

Schwörer, A., Sánchez-Monge, Á., Schilke, P., et al. 2019, A&A, 628, A6

Schwörer, A. S. 2020, PhD thesis, University of Cologne, Germany

Shetty, R., Beaumont, C. N., Burton, M. G., Kelly, B. C., & Klessen, R. S. 2012, MNRAS, 425, 720

Shingledecker, C. N., Tennis, J., Le Gal, R., & Herbst, E. 2018, ApJ, 861, 20

Snow, T. P. & McCall, B. J. 2006, ARA&A, 44, 367

Sugimura, M., Yamaguchi, T., Sakai, T., et al. 2011, PASJ, 63, 459

Tan, J. C., Beltrán, M. T., Caselli, P., et al. 2014, in Protostars and Planets VI, ed. H. Beuther, R. S. Klessen, C. P. Dullemond, & T. Henning, 149–172

Tang, Y., Wang, Q. D., & Wilson, G. W. 2021, MNRAS, 505, 2377

Taquet, V., Wirström, E. S., Charnley, S. B., et al. 2017, A&A, 607, A20

Tercero, B., Cernicharo, J., Pardo, J. R., & Goicoechea, J. R. 2010, A&A, 517, A96

Tercero, B., Cuadrado, S., López, A., et al. 2018, A&A, 620, L6

Tideswell, D. M., Fuller, G. A., Millar, T. J., & Markwick, A. J. 2010, A&A, 510, A85

Tielens, A. 2005, The Physics and Chemistry of the Interstellar Medium (Cambridge University Press)

Tychoniec, Ł., van Dishoeck, E. F., van't Hoff, M. L. R., et al. 2021, A&A, 655, A65

van der Marel, N., Booth, A. S., Leemker, M., van Dishoeck, E. F., & Ohashi, S. 2021, A&A, 651, L5

van der Tak, F. F. S. & van Dishoeck, E. F. 2000, A&A, 358, L79

van Dishoeck, E. F. & Blake, G. A. 1998, ARA&A, 36, 317

van 't Hoff, M. L. R., Bergin, E. A., Jørgensen, J. K., & Blake, G. A. 2020, ApJ, 897, L38

Vasyunina, T., Vasyunin, A. I., Herbst, E., et al. 2014, ApJ, 780, 85

Walsh, C., Loomis, R. A., Öberg, K. I., et al. 2016, ApJ, 823, L10

Watanabe, N., Shiraki, T., & Kouchi, A. 2003, ApJ, 588, L121

Wilkins, O. H., Carroll, P. B., & Blake, G. A. 2022, ApJ, 924, 4

Wilson, T., Rohlfs, K., & Huettemeister, S. 2008, Tools of Radio Astronomy, Astronomy and Astrophysics Library (Springer Berlin Heidelberg)

Wilson, T. L., Henkel, C., & Hüttemeister, S. 2006, A&A, 460, 533

Yamamoto, S. 2017, Introduction to Astrochemistry: Chemical Evolution from Interstellar Clouds to Star and Planet Formation, Astronomy and Astrophysics Library (Springer Japan)

Zapata, L. A., Schmid-Burgk, J., & Menten, K. M. 2011, A&A, 529, A24

Zapata, L. A., Schmid-Burgk, J., Rodríguez, L. F., Palau, A., & Loinard, L. 2017, ApJ, 836, 133

Zeng, S., Jiménez-Serra, I., Rivilla, V. M., et al. 2018, MNRAS, 478, 2962

Zeng, S., Jiménez-Serra, I., Rivilla, V. M., et al. 2021, ApJ, 920, L27

Zeng, S., Rivilla, V. M., Jiménez-Serra, I., et al. 2023, MNRAS, 523, 1448

Zeng, S., Zhang, Q., Jiménez-Serra, I., et al. 2020, MNRAS, 497, 4896

Zhang, Y., Tanaka, K. E. I., Tan, J. C., et al. 2022, ApJ, 936, 68

Zucker, C., Speagle, J. S., Schlafly, E. F., et al. 2019, ApJ, 879, 125

List of Figures

List of Tables

Acknowledgements

Many times over the past years when I asked fellow students when astronomy had sparked interest in them, they would tell tell me how they had always been enthusiastic about science since their childhood. This wasn't me. I disliked physics ever since they started teaching us. It wasn't until my astronomy teacher Herr Schüler asked me during class if I had a greater interest in astronomy that the thought of becoming an astrophysicist had settled in my head. In order to pursue this career path, I had to better start liking physics and to improve my knowledge in the subject. On the contrary, a subject that I was always fond of in school was chemistry. Although chemistry has not really played any role during my studies, my passion for it got reignited and I now find myself exploring chemistry in space. Sometimes, I am still surprised by how all this turned out. A big part in all this play the amazing people that I was lucky to meet and work with during my ten years in Bonn and that brought me to this point, where I will soon submit my PhD thesis. Here, I want to give a shout-out to these people. Starting with Herr Schüler, who, by the way, was not only my teacher for astronomy, but also for chemistry. Thank you for knowing before I did!

I would like to thank Prof. Karl Menten for welcoming me so kindly in his group at the MPIfR more than five years ago and for trusting me with a variety of projects during this time. I have frequently been astonished by your widely-varied knowledge in science and life and that you seem to be able to add new insights to whatever discussion. You always have an open ear for problems and doubts but equally also for new scientific ideas. Also, thank you for giving me the opportunity to travel to conferences and to Chile to observe with APEX! These were unforgettable experiences! I would also like to say thank you to Prof. Frank Bigiel, Prof. Jochen Dingfelder, and Prof. Ribana Roscher for agreeing to be part of my thesis evaluation committee.

I am most grateful for my day-to-day advisor Dr. Arnaud Belloche. Thank you for trusting me first with the project on Cha–MMS1 and then with the ReMoCA survey. You taught me basically everything I know, be it the topic or the tools, and you did that with a patience that I can only wish for to have one day. I have always appreciated your way of teaching as there was always enough room for me to explore my own ways of getting a task done. At the same time, your door has been open for one-minute questions or hour-long discussions. I am grateful for any minute that you spent with me on discussing next steps, sharing ideas, improving paper drafts or explaining concepts (anew). Over the past three and a half years, I have grown so fond of the field of astrochemistry, which is certainly also thanks to you and your view on the field. Thank you for being such a great teacher! I would like to complete the ReMoCA four here and express my thanks also to Prof. Rob Garrod and Dr. Holger Müller for sharing their expertise with me and for helping me make sense out of my observations!

I feel extremely grateful to have been able to learn and grow in an environment that was offered by the people in the submm/mm group here at the MPIfR. If need be, they are only a few office doors or en email away. Thank you to all my fellow students (from the group and beyond) that I met along the way and that I could always go to with questions and doubts, but also when I just wanted to chat. In particular, I would like to thank Arshia, Mélisse, Yuxin, and Vivien for the warm welcome when I first

came to your office in 2018. To Arshia, I am so grateful to now call you one of my closest friends! Thank you for always reacting to my 'pspsps', for doing 'think-with-me' sessions, discussing matplotlib colours, for on- and offline tea breaks, going together through the most awkward moments, gossiping, posing in front of telescopes we have never been to together (#coolkids), celebrating astrochemistry, and so much more. Always remember who you are! I would like to highlight a few more names, starting with Dr. Denise Riquelme. Thank you for your constant support and advice even after you have passed on your official duties as my supervisor. Thanks to Dr. Rolf Güsten, for bringing the CMZ paper to the finish line. I am also thankful for Dr. Dirk Muders, for solving all my computer problems, be they serious or silly, always with a smile on your face. I would also like to thank Prof. Dr. Agata Karska for her supportive and encouraging words, her interest in my work and her dedication to promote and support young female researchers in perusing their academic careers. I would like to express my gratitude to all people working in administration: Eva, Boriana (and Fr. Fingas before her), Frau Tran, Frau Mertens, Herr Klug, thank you all for making my live easier! Special thanks to Frau Schneider, you have been the good soul of the institute and made sure everyone's day started with a smile. Thanks to the APEX team in Chile! Observing on site was such an amazing experience that I couldn't even dream of to make when I first thought about becoming an astronomer and one that I will certainly never forget.

A big thank you also to the girls of my dance team. For about eight years, (at least) twice a week, dance practice has added to my good mood on some days and made me forget my problems on others and you guys played a big part in that! Special thanks to Staicy, who went from dance teacher to fellow student to a close friend (and personal driver) over the past decade. Thanks for always supporting me on and off stage! And where Staicy is, her husband Till cannot be far. Thank you for managing to get me through theoretical astrophysics somehow and all your continued help and support along the way! I am beyond grateful for my friends of the first hour in Bonn: Joana, Philipp, Marcel, Henrik, Christian, Mark, Matthias, Gerrit, Julian, (and later your significant others), who have started the adventure of a Bachelor's degree programme in physics with me and are still here, ten years later, to celebrate this next achievement in my life. Thank you for the holiday trips, game and party nights, Trash-TV soirees, and just for making these last ten years an unforgettable adventure! Special thanks to the one household that I was allowed to hold on to during peak Covid–19 times: Joana and Philipp Höllmer, my beloved newly weds! After some initial difficulties, you, Joana, became quickly one of my favourite human beings on this planet. Everything is more fun with you, nights out, nights in, coffee breaks in the institutos, sharing a flat, being your maid of honour, days at the beach with inevitable sunburns, city trips, ER visits, car rides, conferences... . I will miss you infinitely when soon there are almost 9000 km between us. You deserve to achieve everything you reach for. And if you do, call me (I promise, I'll pick up), and if you don't right away and need encouragement, call me too. Thank you, Philipp, for not only tolerating me as Joana's best friend, but for becoming one of my closest friends as well. Thanks to both of you for getting Quante and Noni, what a delight!

Zuletzt möchte ich meiner Mama und meinen Schwestern Mandy und Mona danken. Ihr habt mir beigebracht, schwierigen Lebenslagen stets optimistisch und mit einem Lächeln entgegenzutreten (eine Fähigkeit, die sich im Physikstudium als äußerst hilfreich herausstellte). Schon immer habt mir das Gefühl gegeben, dass ich alles erreichen kann, was ich mir vornehme. Aber ihr seid auch ein Teil davon, der genau das ermöglicht, indem ihr mir bei allen Problemen, vor allem außerhalb des Studiums, mit Rat und Tat zur Seite steht. Und was auch immer das Leben noch für mich bereit hält, ich weiß, dass alles gut wird, weil ihr an meiner Seite seid. Mein Dank gilt auch meiner Oma Ruth und meinem Papa, die leider beide diesen Erfolg in meinem Leben nicht mehr mit mir feiern können, die aber sicherlich auch sehr stolz gewesen wären.